

Torge · Geodesy

Wolfgang Torge

Geodesy

Third completely revised and extended edition



Walter de Gruyter · Berlin · New York 2001

Author

Dr.-Ing. Wolfgang Torge
Institut für Erdmessung
Universität Hannover
Schneiderberg 50
30167 Hannover
Germany

1st edition 1980

2nd edition 1991

This book contains 184 figures.

© Printed on acid-free paper which falls within the guidelines of the ANSI to ensure permanence and durability.

Library of Congress Cataloging-in-Publication Data

Torge, Wolfgang.
[Geodäsie. English]
Geodesy / Wolfgang Torge. – 3rd completely rev. and extended ed.
p. cm.
Includes bibliographical references and index.
ISBN 3-11-017072-8
1. Geodesy. I. Title.
QB281 .T5813 2001
526'.1–dc21

2001028639

Die Deutsche Bibliothek – Cataloging-in-Publication Data

Torge, Wolfgang:
Geodesy / Wolfgang Torge. – 3., completely rev. and extended ed.. –
Berlin ; New York : de Gruyter, 2001
ISBN 3-11-017072-8

© Copyright 2001 by Walter de Gruyter GmbH & Co. KG, 10785 Berlin, Germany

All rights reserved, including those of translation into foreign languages. No part of this book may be reproduced or transmitted in any form or by any means, electronic or mechanical, including photocopy, recording or any information storage and retrieval system, without permission in writing from the publisher.

The use of registered names, trade names, trade marks, etc. in this book, even without a specific statement, does not imply that these names are not protected by the relevant laws and regulations. While the advice and information in this book is believed to be true and accurate at the date of its going to press, neither the author nor the publisher can accept any legal responsibility for any errors or omissions that may be made. The publisher makes no warranty, express or implied, with respect to the material contained herein.

Printed in Germany

Cover design: Rudolf Hübler, Berlin

Printing: Werner Hildebrand, Berlin

Binding: Lüderitz & Bauer-GmbH, Berlin

In memory of

Hans-Georg Wenzel

1945 – 1999

Preface to the Third Edition

The *first edition* of this book was published in 1980 as an English translation of the book "Geodäsie," which was printed in the German language in 1975 within the "Göschen Series" of Walter de Gruyter and Co., Berlin and New York. A thorough revision of the original text was undertaken at that time, but the fundamental structure of the book was retained. The *second edition* (1991) added the remarkable development of space techniques and their effects on positioning and gravity field determination. Though it represented an extension of the first edition, the basic subdivision into six chapters was not altered.

In contrast to the relatively minor changes of the second edition, the *present edition* has been completely revised and significantly extended. This was necessary in order to account for the tremendous changes that geodesy, on the whole, has experienced over the past thirty years, driven by the progress in space techniques and data acquisition and evaluation in general. A particular consequence is that geodesy has transitioned to a three-dimensional concept, based on a global reference system, with far-reaching consequences for geodetic practice. High data rates and improved accuracy require a more rigorous consideration of time as a fourth dimension and has led to a growing contribution to geodynamics research.

The significant extension of the third edition is demonstrated by increases in the number of pages (416 versus 264), the number of figures (184 versus 137), and the number of references. The references increased by about 50 percent to more than 700, half of which are new entries. There are now eight chapters instead of six, and their content more clearly mirrors the fundamental changes of geodesy.

The "*Introduction*" still contains the definition and the over 2000 years history of geodesy. It now also includes the three and four-dimensional geodetic concepts. The survey of geodetic organizations and literature has been updated as well. The new chapter on "*Reference Systems*" comprises the fundamentals of geodetic reference and time systems and their realization and mutual transformation. This information was previously dispersed throughout the book. The third chapter, "*The Gravity Field of the Earth*," is similar to the corresponding chapter in the previous edition, with some additions to the description of the gravity field geometry and the spherical harmonic expansion. The introduction to the geoid is now included here, while the earth tides section has been moved to the last chapter. The next chapter, "*The Geodetic Earth Model*," was extracted from the chapter on geodetic reference systems in the previous edition. A separate treatment appeared necessary, especially due to the

importance of the "Geodetic Reference System 1980" and the "World Geodetic System 1984."

The chapters on measurement and evaluation methods comprise the core of the book and have been completely reorganized and revised. The chapter "*Methods of Measurements*" now starts with a detailed description of atmospheric refraction, which affects all geometric methods of geodesy. The dominating role of satellite geodesy is recognized by treating this subject early. Space for classical methods such as Doppler positioning has been reduced, while the Global Positioning System (GPS) has naturally received increased emphasis (now with 10 pages compared to about 4 in the previous edition). Developing techniques such as satellite-to-satellite tracking and satellite gravity gradiometry have been given separate space. Very Long Baseline Interferometry is now included in the section on geodetic astronomy. Gravimetry was updated with respect to absolute and airborne techniques. Terrestrial geodetic measurements concentrate on combined angle and distance observations over shorter distances and on precise leveling. Discussion of tilt and strain measurements are also found here. The former subdivision of "*Methods of Evaluation*" into astrogeodetic, gravimetric, satellite and combined methods has been replaced by an introductory section on the residual gravity field, two large blocks on positioning and gravity field modeling, and a section on combination solutions. Positioning starts from the three-dimensional model, followed by horizontal positioning and height determination, after proper reductions to the ellipsoid and the geoid, respectively. The effect of topography on gravity field modeling is now discussed in more detail, and a clear distinction is made between global and local modeling, where the astrogeodetic methods have also been included. The combined methods comprise the functional approach by earth models and the statistical approach through least squares collocation.

The seventh and the eighth chapters reflect the effects of the developments in geodesy on national and continental networks and on the geosciences. The chapter on "*Geodetic and Gravimetric Networks*" is now free of computational formulas and concentrates on the design and establishment of networks, with special emphasis on the present transition to three-dimensional networks and absolute gravimetry. The final chapter, "*Structure and Dynamics of the Earth*," has been extracted from the previous edition's chapter on "*Methods of Evaluation, Global Geodesy*." This chapter considers the increasing role which geodesy plays within the geosciences and, consequently, includes an introduction to the geophysical earth model, especially to the upper layers of the earth. Geodetic contributions to geodynamics research are now described more systematically and extensive, ranging from earth rotation over sea level variations, crustal movements, and gravity variations to earth tides.

The text is again illustrated by a large number of figures. Many of the figures depict fundamental geodetic relations, while others show examples of recent instrumentation and geodetic data processing results. The latter case required a thorough revision of the figures and a revision of the associated passages of the text. Among the new examples for geodetic instruments we have geodetic GPS receivers, altimeter satellites, absolute and relative gravimeters, total stations, and digital levels. The results include the International Celestial and Terrestrial Reference Frames, The World Geodetic System 1984 (status 2000), the geopotential model EGM96, the gravimetric geoids for the U.S.A. and for Europe, and the classical and modern networks in those regions, as well as examples of recent geodetic contributions to the investigation of geodynamics.

The primary purpose of the book is to serve as a basic textbook oriented towards students of geodesy, geophysics, surveying engineering, cartography, and geomatics, as well as students of terrestrial and space navigation. The book is also a valuable reference for geoscientists and engineers facing geodetic problems in their professional tasks.

The contents of the book are based in part on lecture courses given at the University of Hannover, Germany and on guest lectures given abroad. The author is indebted to individuals and organizations for providing illustrations; due credit is given in the figure captions. He thanks M.Sc. Kyle Snow, who checked the English text with extreme care, included the formulas and figures, and prepared the manuscript for printing. The majority of the figures have been drawn by cand. geod. Anke Daubner, Dipl.-Ing. Andreas Lindau handled the electronic mailing and text storage, and assisted in the final proof-reading. The staff of the Institut für Erdmessung assisted in manifold ways in the preparation of the manuscript. All this help is gratefully acknowledged. The outstanding cooperation of the publisher, proved over a nearly 30 years association, continued and calls for a cordial thanks to Dr. Manfred Karbe and the staff at Walter de Gruyter.

Hannover, February 2001

Wolfgang Torge

Contents

| | | |
|----------|---|-----------|
| 1 | Introduction | 1 |
| 1.1 | Definition of Geodesy | 1 |
| 1.2 | The Problem of Geodesy | 2 |
| 1.3 | Historical Development of Geodesy | 4 |
| 1.3.1 | The Spherical Earth Model | 4 |
| 1.3.2 | The Ellipsoidal Earth Model | 7 |
| 1.3.3 | The Geoid, Arc Measurements and National Geodetic Surveys | 10 |
| 1.3.4 | Three-dimensional Geodesy | 12 |
| 1.3.5 | Four-dimensional Geodesy | 13 |
| 1.4 | Organization of Geodesy, Literature | 13 |
| 1.4.1 | National Organizations | 13 |
| 1.4.2 | International Collaboration | 14 |
| 1.4.3 | Literature | 15 |
| 2 | Reference Systems | 18 |
| 2.1 | Basic Units and Fundamental Constants | 18 |
| 2.2 | Time Systems | 20 |
| 2.2.1 | Atomic Time, Dynamical Time | 20 |
| 2.2.2 | Sidereal and Universal Time | 21 |
| 2.3 | International Earth Rotation Service | 24 |
| 2.4 | Celestial Reference System | 25 |
| 2.4.1 | Equatorial System of Spherical Astronomy | 26 |
| 2.4.2 | Precession and Nutation | 28 |
| 2.4.3 | International Celestial Reference Frame | 30 |
| 2.5 | Terrestrial Reference System | 31 |
| 2.5.1 | Global Earth-Fixed Geocentric System | 32 |
| 2.5.2 | Polar Motion, Length of Day, Geocenter Variations | 33 |
| 2.5.3 | International Terrestrial Reference Frame | 36 |
| 2.6 | Gravity Field Related Reference Systems | 38 |
| 2.6.1 | Orientation of the Local Vertical | 38 |
| 2.6.2 | Local Astronomic Systems | 39 |

| | | |
|----------|---|-----|
| 3 | The Gravity Field of the Earth | 45 |
| 3.1 | Fundamentals of Gravity Field Theory | 45 |
| 3.1.1 | Gravitation, Gravitational Potential | 45 |
| 3.1.2 | Gravitation of a Spherically Symmetric Earth | 48 |
| 3.1.3 | Properties of the Gravitational Potential | 50 |
| 3.1.4 | Centrifugal Acceleration, Centrifugal Potential | 54 |
| 3.1.5 | Gravity Acceleration, Gravity Potential | 55 |
| 3.2 | Geometry of the Gravity Field | 57 |
| 3.2.1 | Level Surfaces and Plumb Lines | 57 |
| 3.2.2 | Local Gravity Field Representation, Curvatures | 59 |
| 3.2.3 | Natural Coordinates | 64 |
| 3.3 | Spherical Harmonic Expansion of the Gravitational Potential | 66 |
| 3.3.1 | Expansion of the Reciprocal Distance | 67 |
| 3.3.2 | Expansion of the Gravitational Potential | 69 |
| 3.3.3 | Geometrical Interpretation of the Surface Spherical Harmonics | 73 |
| 3.3.4 | Physical Interpretation of the Harmonic Coefficients | 74 |
| 3.4 | The Geoid | 76 |
| 3.4.1 | Definition | 76 |
| 3.4.2 | Mean Sea Level | 78 |
| 3.4.3 | The Geoid as Height Reference Surface | 80 |
| 3.5 | Temporal Gravity Variations | 83 |
| 3.5.1 | Gravitational Constant, Earth Rotation | 83 |
| 3.5.2 | Tidal Acceleration, Tidal Potential | 84 |
| 3.5.3 | Non-Tidal Temporal Variations | 90 |
| 4 | The Geodetic Earth Model | 91 |
| 4.1 | The Rotational Ellipsoid | 91 |
| 4.1.1 | Parameters and Coordinate Systems | 91 |
| 4.1.2 | Curvature | 95 |
| 4.1.3 | Spatial Geodetic Coordinates | 99 |
| 4.2 | The Normal Gravity Field | 102 |
| 4.2.1 | The Level Ellipsoid, Level Spheroids | 103 |
| 4.2.2 | The Normal Gravity Field of the Level Ellipsoid | 104 |
| 4.2.3 | Geometry of the Normal Gravity Field | 111 |
| 4.3 | Geodetic Reference Systems | 114 |
| 5 | Methods of Measurement | 119 |
| 5.1 | Atmospheric Refraction | 119 |

| | | |
|-------|--|-----|
| 5.1.1 | Fundamentals | 120 |
| 5.1.2 | Tropospheric Refraction | 124 |
| 5.1.3 | Ionospheric Refraction | 127 |
| 5.2 | Satellite Observations | 130 |
| 5.2.1 | Undisturbed Satellite Motion | 130 |
| 5.2.2 | Perturbed Satellite Motion | 133 |
| 5.2.3 | Artificial Earth Satellites | 136 |
| 5.2.4 | Direction, Range and Range Rate Measurements: Classical Methods | 139 |
| 5.2.5 | Global Positioning System (GPS) | 142 |
| 5.2.6 | Laser Distance Measurements | 151 |
| 5.2.7 | Satellite Altimetry | 154 |
| 5.2.8 | Satellite-to-Satellite Tracking, Satellite Gravity Gradiometry | 157 |
| 5.3 | Geodetic Astronomy | 159 |
| 5.3.1 | Optical Observation Instruments | 159 |
| 5.3.2 | Astronomic Positioning and Azimuth Determination | 162 |
| 5.3.3 | Reductions | 165 |
| 5.3.4 | Very Long Baseline Interferometry | 167 |
| 5.4 | Gravimetry | 171 |
| 5.4.1 | Absolute Gravity Measurements | 171 |
| 5.4.2 | Relative Gravity Measurements | 178 |
| 5.4.3 | Gravity Reference Systems | 184 |
| 5.4.4 | Gravity Measurements on Moving Platforms | 186 |
| 5.4.5 | Gravity Gradiometry | 191 |
| 5.4.6 | Continuous Gravity Measurements | 193 |
| 5.5 | Terrestrial Geodetic Measurements | 196 |
| 5.5.1 | Horizontal and Vertical Angle Measurements | 196 |
| 5.5.2 | Distance Measurements, Total Stations | 199 |
| 5.5.3 | Leveling | 206 |
| 5.5.4 | Tilt and Strain Measurements | 211 |
| 6 | Methods of Evaluation | 214 |
| 6.1 | Residual Gravity Field | 214 |
| 6.1.1 | Disturbing Potential, Height Anomaly, Geoid Height | 214 |
| 6.1.2 | Gravity Disturbance, Gravity Anomaly, Deflection of the Vertical | 217 |
| 6.1.3 | Statistical Description of the Gravity Field, Interpolation | 220 |
| 6.2 | Three-dimensional Positioning | 226 |
| 6.2.1 | Observation Equations | 226 |
| 6.2.2 | Geodetic Datum | 234 |
| 6.3 | Horizontal Positioning | 239 |
| 6.3.1 | Ellipsoidal Trigonometry | 240 |

| | | |
|----------|--|------------|
| 6.3.2 | Reductions to the Ellipsoid | 243 |
| 6.3.3 | Computations on the Ellipsoid | 245 |
| 6.4 | Height Determination | 249 |
| 6.4.1 | Heights from Geometric Leveling | 249 |
| 6.4.2 | Trigonometrical Heights | 252 |
| 6.4.3 | Heights from GPS | 254 |
| 6.5 | Fundamentals of Gravity Field Modeling | 256 |
| 6.5.1 | The Geodetic Boundary-Value Problem | 256 |
| 6.5.2 | Gravitation of Topography | 260 |
| 6.5.3 | Gravity Reductions to the Geoid | 262 |
| 6.5.4 | Orientation and Scale of Gravity Field Models | 268 |
| 6.6 | Global Gravity Field Modeling | 270 |
| 6.6.1 | Spherical Harmonic Expansions | 271 |
| 6.6.2 | Low-degree Gravity Field Models | 274 |
| 6.6.3 | High-degree Gravity Field Models | 278 |
| 6.7 | Local Gravity Field Modeling | 281 |
| 6.7.1 | Gravimetric Geoid Heights and Deflections of the Vertical | 282 |
| 6.7.2 | Gravimetric Height Anomalies and Surface Deflections of the Vertical | 289 |
| 6.7.3 | The External Gravity Field | 293 |
| 6.7.4 | Astrogeodetic Geoid and Quasigeoid Determination | 294 |
| 6.8 | Combined Methods for Positioning and Gravity Field Determination | 300 |
| 6.8.1 | Earth Models and Optimum Earth Parameters | 301 |
| 6.8.2 | Least Squares Collocation | 303 |
| 7 | Geodetic and Gravimetric Networks | 308 |
| 7.1 | Horizontal Control Networks | 308 |
| 7.1.1 | Design and Observation | 309 |
| 7.1.2 | Computation and Orientation | 311 |
| 7.2 | Vertical Control Networks | 320 |
| 7.3 | Three-dimensional Networks | 323 |
| 7.3.1 | Global and Continental Networks | 323 |
| 7.3.2 | National Networks | 327 |
| 7.4 | Gravity Networks | 330 |
| 8 | Structure and Dynamics of the Earth | 333 |
| 8.1 | The Geophysical Earth Model | 333 |
| 8.2 | The Upper Layers of the Earth | 337 |
| 8.2.1 | Structure of the Earth's Crust and Upper Mantle | 337 |

| | | |
|-------------------|-------------------------------------|-----|
| 8.2.2 | Isostasy | 339 |
| 8.2.3 | Plate Tectonics | 343 |
| 8.2.4 | Interpretation of the Gravity Field | 345 |
| 8.3 | Geodesy and Geodynamics | 350 |
| 8.3.1 | Changes in Earth Rotation | 350 |
| 8.3.2 | Sea Level Variations | 352 |
| 8.3.3 | Recent Crustal Movements | 355 |
| 8.3.4 | Gravity Variations with Time | 359 |
| 8.3.5 | Earth Tides | 362 |
| <i>References</i> | | 369 |
| <i>Index</i> | | 405 |

1 Introduction

1.1 Definition of Geodesy

According to the classical definition of Friedrich Robert Helmert (1880), “*geodesy (γη = earth, διαιω = I divide) is the science of the measurement and mapping of the earth's surface.*” Helmert’s definition is fundamental to geodesy even today. The surface of the earth, to a large extent, is shaped by the earth’s gravity, and most geodetic observations are referenced to the earth’s gravity field. Consequently, the above definition of geodesy includes the determination of the earth’s *external gravity field*. The original focus of geodesy has expanded to include applications in ocean and space exploration. For example, Geodesy, in collaboration with other sciences, now includes the determination of the *ocean floor* and the surfaces and gravity fields of *other celestial bodies*, such as the moon (lunar geodesy) and planets (planetary geodesy). Finally, the classical definition has to be extended to include *temporal variations* of the earth’s surface and its gravity field.

With this extended definition, geodesy is part of the *geosciences and engineering sciences*, including navigation and geomatics (e.g., NATIONAL ACADEMY OF SCIENCES 1978). Geodesy may be divided into the areas of global geodesy, geodetic surveys (national and supranational), and plane surveying. *Global geodesy* includes the determination of the shape and size of the earth, it’s orientation in space, and it’s external gravity field. A *geodetic survey* is for the determination of the earth’s surface and gravity field over a region that typically spans a country or a group of countries. The earth’s curvature and gravity field must be considered in geodetic surveys. In *plane surveying* (topographic surveying, cadastral surveying, engineering surveying), the details of the earth’s surface are determined on a local level, and thus curvature and gravity effects are generally ignored.

There is a close relation between global geodesy, geodetic surveying, and plane surveying. Geodetic surveys are linked to reference frames (networks) established by global geodesy; these surveys adopt the global parameters for the figure of the earth and its gravity field. On the other hand, the results of geodetic surveys may contribute to the work of the global geodesist. Plane surveys, in turn, are generally referenced to control points established by geodetic surveys. Plane surveys are used extensively in the development of national and state map-series, cadastral information systems, and in civil engineering projects. The measurement and data evaluation methods used in national geodetic surveys are often similar to those used in global geodetic work. For instance, space methods (satellite geodesy) have long been a dominant technique in global geodesy and

are now commonly used in regional and local surveys. This requires a more detailed knowledge of the gravity field at the regional and local scales.

With the corresponding classification in the English and French languages, the concept of "*geodesy*" (la géodésie, "höhere Geodäsie" after Helmert) in this text refers only to global geodesy and geodetic surveying. The concept of "*surveying*" (la topométrie, Vermessungskunde or "niedere Geodäsie" after Helmert) shall encompass plane surveying.

In this volume, geodesy is treated only in the more restrictive sense as explained above (excluding plane surveying), and limited to the planet earth. Among the numerous textbooks on surveying we mention KAHMEN and FAIG (1988), KAHMEN (1997), ANDERSON and MIKHAIL (1998), BANNISTER et al. (1998). For lunar and planetary geodesy see BILLS and SYNNOTT (1987), KAULA (1993), and NEREM (1995a); numerical values of astrometric and geodetic parameters are given by Yoder (1995).

1.2 The Problem of Geodesy

Based on the concept of geodesy defined in [1.1], the problem of geodesy may be described as follows:

"The problem of geodesy is to determine the figure and external gravity field of the earth and of other celestial bodies as a function of time, from observations on and exterior to the surfaces of these bodies."

This *geodetic boundary-value problem* incorporates a geometric (figure of the earth) and a physical (gravity field) formulation; both are closely related.

By the *figure of the earth* we mean the physical and the mathematical surface of the earth as well as a geodetic reference earth, e.g., MORITZ (1990).

The *physical surface* of the earth is the border between the solid or fluid masses and the atmosphere. The *ocean floor* is included in this formulation, being the bounding surface between the solid terrestrial body and the oceanic water masses. The irregular surface of the solid earth (continental and ocean floor topography) cannot be represented by a simple mathematical (analytical) function. It is therefore described point wise by the *coordinates of control points*. Given an adequately dense control network, the detailed structure of this surface can be determined by interpolation of data from terrestrial topographic and hydrographic surveying (KRAUS 1992/97, KRAUS and SCHNEIDER 1988/90, HAKE and GRÜNREICH 1994, KAHMEN 1997). On the other hand, the *ocean surfaces* (70% of the earth's surface) are easier to represent. If we neglect the effects of ocean

currents and other "disturbances", the ocean surfaces form a part of a level or equipotential surface of the earth's gravity field (surface of constant gravity potential). We may think of this surface as being extended under the continents and identify it as the *mathematical figure of the earth*, which can be described by a condition of equilibrium (HELMERT 1880/1884). J.B. LISTING (1873) designated this level surface as *geoid*.

The great mathematician and geodesist *Carl Friedrich Gauss* (1777 – 1855) had already referred to this surface: "What we call surface of the earth in the geometrical sense is nothing more than that surface which intersects everywhere the direction of gravity at right angles, and part of which coincides with the surface of the oceans" (C.F. Gauss: "Bestimmung des Breitenunterschiedes zwischen den Sternwarten von Göttingen und Altona," Göttingen 1828), see also MORITZ (1977).

The description of the geoid's properties is the physical aspect of the problem of geodesy. In solving this problem, the earth's surface and the geoid are considered as bounding surfaces in the earth's gravity field, the field to which geodetic observations are referenced. Based on the law of gravitation and the centrifugal force (due to the earth's rotation), the *external gravity field* of the earth, or any other celestial body, can be modeled analytically and described by a large number of model parameters. A geometric description is given by the infinite number of *level surfaces* extending completely or partially (as the geoid) exterior to the earth's surface.

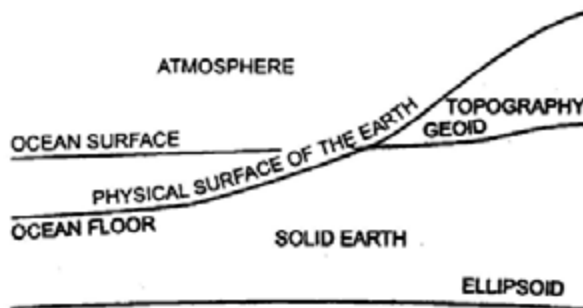


Fig. 1.1. Physical surface of the earth, geoid, and ellipsoid

Reference systems are introduced in order to describe the orientation of the earth and other bodies in space (celestial reference system) as well as their surface geometry and gravity fields (terrestrial reference system). The definition and realization of these systems has become a major part of global geodesy; the use of three-dimensional Cartesian coordinates in Euclidean space is adequate in this context. However, due to the demands of practitioners, *reference surfaces* are introduced to distinguish between curvilinear surface coordinates for horizontal positioning and heights above some zero-height surface for vertical positioning.

Because of its simple equation, an *ellipsoid* of rotation, flattened at the poles, is well suited for describing horizontal positions, and consequently is used as a reference surface in geodetic surveying. In plane surveying, the *horizontal plane* is generally a sufficient reference surface. Because of its physical meaning, the geoid (or any other reference defined in the earth's gravity field) is well suited as a reference surface for heights. For many applications, a *geodetic reference earth* (earth model, normal earth) is needed. It is realized through a *mean-earth ellipsoid* that optimally approximates the geometry (geoid) and the gravity field of the earth. Fig. 1.1 shows the mutual location of the surfaces to be determined in geodesy.

The body of the earth and its gravity field are subject to *temporal variations* of secular, periodic, and abrupt nature, which can occur globally, regionally, and locally. These variations also influence the orientation of the earth. Modern geodetic measurement and evaluation techniques are used to detect these variations to a high level of accuracy. If time-independent results are required, geodetic observations must be corrected for temporal variations. By determining temporal variations, the science of geodesy contributes to the investigation of the kinematic and dynamic properties of the terrestrial body. Accordingly, the figure of the earth and the external gravity field must be considered as time dependent quantities: "Four-dimensional geodesy" (MATHER 1973).

1.3 Historical Development of Geodesy

The formulation of the problem of geodesy as described in [1.2] did not fully mature until the nineteenth century. However, the question of the figure of the earth was contemplated in antiquity. In fact, geodesy together with astronomy and geography are among the oldest sciences dealing with the planet earth. Superseding the use of the *sphere* as a model for the earth [1.3.1], the oblate *rotational ellipsoid* became widely accepted as the model of choice in the first half of the eighteenth century [1.3.2]. The significance of the *gravity field* was also recognized in the nineteenth century, leading to the introduction of the geoid [1.3.3]. In the second half of the twentieth century, satellite techniques permitted the realization of the *three-dimensional* concept of geodesy [1.3.4]. A drastic increase in the accuracy of geodetic observations required that time variations be taken into account. This led to the concept of *four-dimensional* geodesy [1.3.5]. Extensive material on geodetic history is found in TODHUNTER (1873), FISCHER (1975), BIALAS (1982), SMITH (1986) and LEVALLOIS (1988).

1.3.1 The Spherical Earth Model

Various opinions on the figure of the earth prevailed in the past, e.g., the notion of an *earth disk* encircled by oceans (*Homer's Iliad* ~ 800 B.C., *Thales of Milet* ~

600 B.C.). Considering the sphere aesthetically appealing, *Pythagoras* (~ 580 – 500 B.C.) and his school proposed a spherical shaped earth. By the time of *Aristotle* (384 – 322 B.C.), the spherical concept was generally accepted and even substantiated by observations. For example, observers noted the round shadow of the earth in lunar eclipses and the apparent rising of an approaching ship on the horizon. In China the spherical shape of the earth was recognized in the first century A.D.

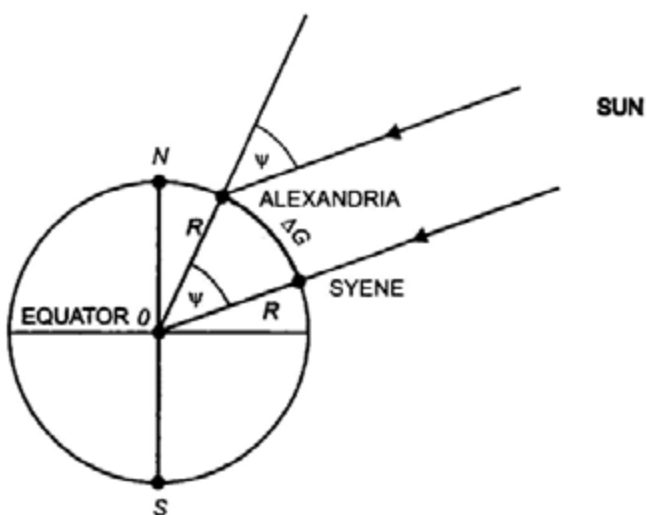


Fig. 1.2. Arc measurement of Eratosthenes

The founder of geodesy is *Eratosthenes* of Alexandria (276 – 195 B.C.), who, based on the assumption of a spherical earth, deduced the earth radius from measurements (SCHWARZ 1975). The principle of the *arc-measurement* method developed by Eratosthenes was still applied in modern time: from geodetic measurements, the length ΔG of a meridian arc is determined; astronomical observations furnish the associated central angle ψ (Fig. 1.2). The radius of the earth is then given by

$$R = \frac{\Delta G}{\psi}. \quad (1.1)$$

Eratosthenes found that at the time of the summer solstice the rays of the sun descended vertically into a well in Syene (modern day Assuan). Whereas in Alexandria (approximately on the same meridian as Syene), the sun's rays formed an angle with the direction of the plumb line. From the length of the shadow of a vertical staff ("gnomon") produced in a hemispherical shell ("skaphe"), Eratosthenes determined this angle as 1/50 of a complete circle, i.e., $\psi = 7^\circ 12'$.

From Egyptian cadastre maps, which were based on the information of "bematists" (step counters), Eratosthenes estimated the distance from Syene to Alexandria to be 5000 stadia. With the length of an Egyptian stadium assumed as 148.5 m, the earth radius is computed to be 5909 km from Eratosthenes estimations. This value departs from the radius of a mean spherical earth (6371 km) by only -7%. Another ancient determination of the earth's radius is attributed to *Posidonius* (135 – 51 B.C.). Using the meridian arc from Alexandria to Rhodes, he observed the star Canopus to be on the horizon at Rhodes, while at a culmination height of $7^{\circ}30'$ at Alexandria, which again equals the central angle between the cities.

During the middle ages in Europe, the question of the figure of the earth was not pursued further. Documentation from China shows that an astronomic-geodetic survey between 17° and 40° latitude was carried out by the astronomers *Nankung Yueh* and *I-Hsing* around 725 A.D. in order to determine the length of a meridian. A 1° arc length was measured directly with ropes by the Arabs (~ 827 A.D.) northwest of Bagdad by the caliphate of *Al-Mámún*. At the beginning of the modern age, the French physician *Fernel* (1525) observed the geographical latitudes of Paris and Amiens using a quadrant. He computed the corresponding surface distance from the number of rotations of a wagon wheel.

Later arc measurements based on the spherical earth model benefited from fundamental advances in instrumentation technology (1611, *Kepler* telescope) and methodology. After the initial application of *triangulation* by *Gemma Frisius* (1508 – 1555) in the Netherlands, and by *Tycho Brahe* (1546 – 1601) in Denmark, the Dutchman *Willebrord Snellius* (1580 – 1626) conducted the first triangulation to determine the figure of the earth, HAASBROECK (1968). Snellius used triangulation to measure the arc between Bergen op Zoom and Alkmaar (Holland). The hitherto inaccurate arc length estimate by direct measurement was replaced by an indirect procedure. The angles of a triangulation network were observed with high precision instruments, and the scale was accurately determined by precise measurement of short baselines. With proper reduction of the observations to the meridian, the length of arc could be accurately calculated. A direct length measurement using a chain was employed by *Norwood* when determining the meridian arc between London and York (1633 – 1635).

The method of *reciprocal zenith angles* is yet another technique that has been used to determine the central angle between points on a meridian arc. The Italian fathers *Grimaldi* and *Riccioli* used this method in 1645 between Bologna and Modena (Fig. 1.3). The central angle may be computed from the zenith angles z_1 and z_2 observed at locations P_1 and P_2 according to

$$\psi = z_1 + z_2 - \pi . \quad (1.2)$$

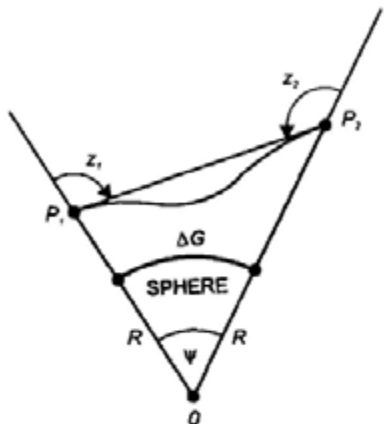


Fig 1.3. Central angle and reciprocal zenith angles

This procedure does not yield satisfactory results due to the inaccurate determination of the curvature of light rays (refraction anomalies).

Through the initiative of the Academy of Sciences (founded in Paris, 1666), France assumed the leading role in geodesy in the seventeenth and eighteenth centuries. In 1669 – 1670 the French abbey *J. Picard* measured the meridian arc through Paris between Malvoisine and Amiens with the aid of a triangulation network; he was the first to use a telescope with cross hairs. The value Picard obtained for the radius of the earth (deviation of +0.01%) aided *Newton* in the verification of the law of gravitation, which he had formulated in 1665 – 1666.

1.3.2 The Ellipsoidal Earth Model

In the sixteenth and seventeenth centuries, new observations and ideas from astronomy and physics decisively influenced the perception of the figure of the earth and its position in space. N. *Copernicus* (1473 – 1543) achieved the transition from the *geocentric* universe of *Ptolemy* to a *heliocentric* system (1543: "De revolutionibus orbium coelestium"), which *Aristarchus of Samos* (~ 310 – 250 B.C.) had already postulated. J. *Kepler* (1571 – 1630) discovered the laws of planetary motion (1609: "Astronomia nova...", 1619: "Harmonices mundi"), and G. *Galilei* (1564 – 1642) established the fundamentals for mechanical dynamics (law of falling bodies and law of pendulum motion).

In 1666, the astronomer *J. D. Cassini* observed the flattening of the poles of Jupiter. On an expedition to Cayenne to determine martian parallaxes (1672 – 1673), the astronomer *J. Richer* discovered that a one-second pendulum regulated in Paris needed to be shortened in order to regain oscillations of one second. From this observation, and on the basis of the law of pendulum motion, one can infer an increase in gravity from the equator to the poles. This effect was

confirmed by *E. Halley* when comparing pendulum measurements in St. Helena to those taken in London (1677 – 1678).

Building on these observations and on his theoretical work on gravitation and hydrostatics, *Isaac Newton* (1643 – 1727) developed an earth model based on physical principles: "Philosophiae Naturalis Principia Mathematica" (1687). Based on the law of gravitation, Newton proposed a rotational ellipsoid as an equilibrium figure for a homogeneous, fluid, rotating earth. The flattening

$$f = \frac{a - b}{a} \quad (1.3)$$

(a = semimajor axis, b = semiminor axis of the ellipsoid) of Newton's ellipsoid was 1/230. He also postulated an increase in gravity acceleration from the equator to the poles proportional to $\sin^2 \varphi$ (φ = geographical latitude). At the same time, the Dutch physicist *Christian Huygens* (1629 – 1695), after having developed the principle of pendulum clocks and the law of central motion, calculated an earth model flattened at the poles ("Discours de la Cause de la Pesanteur," 1690). Shifting the source of the earth's attractive forces to the center of the earth, he obtained a rotationally-symmetric equilibrium-surface with a meridian curve of fourth order and flattening of 1/576.

Arc measurements at various latitudes were required to verify the proposed ellipsoidal earth-models. Theoretically, the length of a one-degree arc (meridian arc for a difference of 1° in latitude), in the case of flattened poles, should increase pole-ward from the equator. The ellipsoidal parameters a, b or a, f can be computed from two arc measurements.

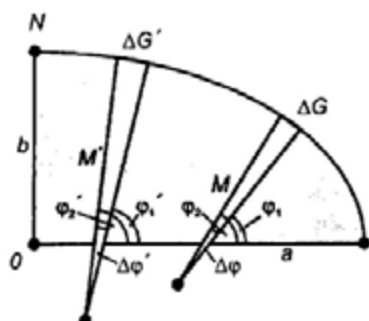


Fig. 1.4. Latitude arc measurement

We distinguish between arc measurements along an ellipsoidal meridian (latitude arc measurement), along a parallel (longitude arc measurement), and arc measurements oblique to the meridian.

For the computations in a *latitude arc-measurement* (Fig. 1.4), the angles $\Delta\varphi = \varphi_2 - \varphi_1$ and $\Delta\varphi' = \varphi'_2 - \varphi'_1$ are formed from the observed geographic latitudes $\varphi_1, \varphi_2, \varphi'_1$, and φ'_2 . The corresponding meridian arcs ΔG and $\Delta G'$ are obtained from triangulation networks. For short arcs, one can replace the meridian ellipse by the osculating circle having the meridian radius of curvature $M = M(\varphi)$ evaluated at the mean latitude $\varphi = (1/2)(\varphi_1 + \varphi_2)$, where M is also a function of the ellipsoidal parameters a, f . From $\Delta G = M \Delta\varphi$ and $\Delta G' = M' \Delta\varphi'$, a and f may be determined. The larger the latitude interval $\varphi' - \varphi$, the more accurate the computed flattening; whereas, the accuracy of the semi-major axis length a depends in particular on the lengths of the meridian arcs.

For *longitude arc measurements*, corresponding relations are used between the arc lengths measured along the parallels and the difference of the geographical longitudes observed at the end points of the arcs. Arc measurements *oblique to the meridian* require a proper azimuth determination for reduction to the meridian.

Initial evaluations of the older arc measurements (*Snellius, Picard*, among others) led to an earth model elongated at the poles. The same result was obtained by *La Hire, J. D.* and *J. Cassini*. They extended the arc of Picard north to Dunkirk and south to Collioure (1683 – 1718), with a latitude difference of $8^{\circ}20'$. The computations from two arc segments yielded a "negative" flattening of $-1/95$, which can be attributed primarily to measurement errors in the astronomic latitudes. The intense dispute between the supporters of Newton and those of the Cassinis over the figure of the earth was resolved by two further arc measurement campaigns sponsored by the French Academy of Sciences.

Maupertuis and *Clairaut*, among others, participated in the expedition to Lapland (1736 – 1737). The results of the Lapland arc measurement (average latitude $66^{\circ}20'$ and latitude interval $57'.5$) confirmed the polar flattening. Using the arc measurement of the meridian through Paris (revised by *Cassini de Thury* and *La Caille*, 1739 – 1740) the flattening was computed as $1/304$. On a second expedition (1735 – 1744) to Peru (modern day Ecuador), an arc at an average latitude $1^{\circ}31' S$ and with $3^{\circ}7'$ amplitude was determined by *Bouguer, La Condamine* and *Godin*. Combining this information with the Lapland arc led to a flattening of $1/210$. The flattening of the earth at the poles was thereby demonstrated by *geodetic* measurements.

A *synthesis* between the physical and the geodetic evidence of the ellipsoidal shape of the earth was finally achieved by *A. C. Clairaut* (1713 – 1765). The theorem (1743), which bears his name, permits the computation of the flattening

from two gravity measurements at different latitudes, cf. [4.2.2]. A first application of Clairaut's theorem is due to *P. S. Laplace* (1799), who from only 15 gravity values derived a flattening of $1/330$. The wider application of this "gravimetric method" suffered from the lack of accurate and well distributed gravity measurements and from the difficulty of reducing the data to the earth ellipsoid. Such problems were not overcome until the twentieth century.

With the rotational ellipsoid commonly accepted as a model for the earth, numerous *arc measurements* were conducted up to the twentieth century. These measurements generally served as a basis for geodetic surveys, see [1.3.3]. The meridian arc through Paris was extended by *Cassini de Thury* and was included in the first triangulation of France (1733 – 1750). A geodetic connection between the astronomical observatories in Paris and Greenwich (1784 – 1787) was the beginning of the national survey of Great Britain, with the final extension of the Paris meridian arc to the Shetland islands. Particular significance was attained by a measurement on the meridian through Paris, between Barcelona and Dunkirk (1792 – 1798), commissioned by the French National Assembly and carried out by *Delambre* und *Méchain*. The results served for the definition of the meter as a natural unit of length (1799). These observations, combined with the Peruvian arc measurement, yielded an ellipsoidal flattening of $1/334$.

1.3.3 The Geoid, Arc Measurements and National Geodetic Surveys

As recognized by *P. S. Laplace* (1802), *C. F. Gauss* (1828), *F. W. Bessel* (1837), and others, the assumption of an ellipsoidal-earth model is no longer tenable at a high level of accuracy. The deviation of the physical plumb line, to which the measurements refer, from the ellipsoidal normal then can no longer be ignored. This deviation is known as the *deflection of the vertical*. While adjusting several arc measurements for determination of the ellipsoidal parameters, contradictions were found which greatly exceeded the observational accuracy. An initial adjustment of arc measurements was carried out in 1806 by *A. M. Legendre* in his treatise "Sur la méthode des moindres carrées". *C. F. Gauss* was the first to adjust a triangulation network (in and around Brunswick, 1803 – 1807) by the method of least squares (GERARDY 1977).

This led to the improved definition of the "figure of the earth" by *Gauss* and *Bessel*, who clearly distinguished between the physical surface of the earth, the geoid as the mathematical surface, and the ellipsoid as a reference surface approximating it, cf. [1.2]. With the definition of geodesy [1.1], *F. R. Helmert* made the transition to the actual concept of the figure of the earth (MORITZ 1990).

Friedrich Robert Helmert (1843 – 1917), one of the most distinguished geodesists of modern times, was professor of geodesy at the technical university at Aachen and later director of the Prussian Geodetic Institute in Potsdam and of the Central Bureau of the "Internationale Erdmessung". Through his work, geodesy has experienced decisive impulses, the effects of which are still felt

today. In his fundamental monograph (1880/1884), *Heimert* established geodesy as a proper science (WOLF 1993, HARNISCH and HARNISCH 1993).

Despite the discrepancies found from the adjustments, arc measurements continued to be used to determine the dimensions of the earth ellipsoid. However, the deflections of the vertical, being a physically phenomena and hence having systematic characteristics, were treated as random observational errors. As a consequence, this method provided parameters for *best-fitting* ellipsoids, approximating the geoid in the area of the triangulation chains. Many of these ellipsoids have been introduced as "*conventional*" ellipsoids for calculating the national geodetic surveys, and thus arc measurements increasingly became part of the geodetic surveys. Established by triangulation, these national surveys provided control points for mapping, which remain the basis for many national geodetic reference systems today (TORGE 1997). Gravity observations were carried out at most arc measurements and at dedicated campaigns, especially after the foundation of the "Mitteleuropäische Gradmessung", cf. [1.4.2].

We mention the historically important arc of *Gauss* (arc measurement between Göttingen and Altona 1821 – 1824, invention of the Heliotrope, adjustment according to the method of least squares) and its extension to the triangulation of the kingdom of Hannover (until 1844). Initiated by the Danish astronomer *H. Chr. Schumacher*, this arc should become part of a central European meridian arc, running from Denmark to Bavaria (triangulation by *J. G. Soldner*, 1808 – 1828) and further south. *Bessel* and *Baeyer* carried out an arc measurement oblique to the meridian in East Prussia (1831 – 1838), which connected the Russian triangulations (*W. Struve, C. Tenner*) with the Prussian and Danish networks and finally with the French-British arc along the meridian of Paris. Some *long arcs* linking national triangulation-chains were built up over a 100 year period. Some of these were not completed until 1950's, while others were never finished, owing to the replacement of classical geodetic observation techniques by satellite surveying methods. These long arcs include the American meridian arc (Alaska – Tierra del Fuego), the North American longitude arc along the 39° parallel between the Atlantic and the Pacific Oceans, the West European-African arc along the meridian of Paris (Shetlands – Algeria), the Arctic Ocean to Mediterranean Sea meridian arc (Hammerfest – Crete) and the African 30° east meridian arc tied to it (Cairo – Cape Town), the European-Asiatic longitude arc measurements at 48° (Brest – Astrachan) and at 52° latitude (Ireland – Ural Mountains), as well as the latitude and longitude arc measurements in India (*G. Everest, W. Lambdon*).

Since the 1880's, *vertical control networks* were established by geometric leveling within the frame of the national geodetic surveys but *independently* from the horizontal control systems. Heights were referred to a level surface close to the geoid and defined by the mean sea level as observed at a tide gauge. The

geoid was not needed in this separate treatment of horizontal position and height, but it played a major role as a geometric representation of the earth's gravity field.

An inevitable presupposition for the evaluation of large-scale arc measurements, triangulations, and leveling was the regulation of the *measuring units*. It was nearly one century after the introduction of the *meter* in France that a large number of countries agreed upon a definition for the meter at the International Meter Convention in Paris in 1875. Following a recommendation of the "Europäische Gradmessung" in 1883, the International Meridian Conference (Washington, D. C., 1884) adopted the Greenwich meridian as the initial meridian for longitude and the universal day (mean solar day) as the *time unit* referenced to the meridian.

1.3.4 Three-dimensional Geodesy

The three-dimensional concept of geodesy consists of the common treatment of horizontal and vertical positioning within the same mathematical model. This was suggested already by BRUNS (1878), who proposed to determine the surface of the earth pointwise using a spatial polyhedron together with all exterior level surfaces. However, three-dimensional computations were not carried out in practice due to the uncertainty of trigonometric derived height differences over large distances and due to the absence of geoid heights above the ellipsoid, which were required for the proper treatment of geometric leveling.

The concept of three-dimensional geodesy was revived by MARUSSI (1949) and HOTINE (1969), while in 1945 Molodenski demonstrated that the physical surface of the earth and its external gravity field can be determined from surface measurements only, without needing the geoid, MOLODENSKI (1958).

VÄISÄLÄ (1946) introduced *Stellar triangulation* from high altitude balloons as a first step to realize the three-dimensional concept. This technique was followed by *electromagnetic distance measurements* in the 1950's and 1960's, using both terrestrial and airborne methods. Satellite geodesy provided a technological breakthrough after the launch of the Russian satellite Sputnik I in 1957. Observations to orbiting satellites were used to establish control points in a three-dimensional system, and provided valuable gravity field information. Beginning in the 1980's, the NAVSTAR *Global Positioning System (GPS)* now dominates geodetic measuring techniques. The practical problems of geodesy today include the connection of classical horizontal and vertical control networks to the global reference system established by space methods. A particular problem is the determination of the geoid with respect to a global reference ellipsoid.

Recently, *kinematic methods* have gained great importance, especially with the use of GPS. The measuring systems, or their components, are carried on moving

platforms (e.g., satellite, airplane, ship, car) and, by continuous positioning (navigation), provide data referring to the geodetic reference system.

1.3.5 Four-Dimensional Geodesy

The beginning of four-dimensional geodesy may be reckoned from the detection of *polar motion* by *F. Küstner* (1884 – 1885) and first observations of the *earth tides* by *E.v. Rebeur-Paschwitz* (1889 – 1893). Monitoring of *crustal deformations* related to seismic activities began in Japan and the U.S.A. about 100 years ago. Interest in this phenomena was motivated by powerful seismic events, such as the San Francisco earthquake of 1906. In Fennoscandia, precise leveling and tide gauge registrations began in the 1880's and were used to determine the region's large-scale *vertical uplift* caused by postglacial rebound.

Today, the variations of the *earth's rotation* and the movements of the *tectonic plates* are regularly observed through global networks, and a number of regional control networks have been set up, especially at tectonic plate boundaries. *Gravity variations* with time are derived from the analysis of satellite orbits (large-scale) and terrestrial networks (small-scale). The *earth tides* have also been modeled successfully using terrestrial and satellite methods.

Large efforts continue worldwide to measure and analyze all types of geodynamic phenomena by geodetic methods, for instance that described in the NASA (1983) Geodynamics Program, see also MUELLER and ZERBINI (1989).

In the future, geodetic observations will experience a further increase of accuracy and an increase in resolution in space and time. Longer observation series will permit the detection of long-term changes of the earth and its gravity field. Global geodesy and geodetic surveys must take these temporal changes into account. With improved modeling, the four-dimensional aspect of geodesy will increasingly be employed in the evaluation and presentation of geodetic products (LAMBECK 1988, BRUNNER and RIZOS 1990).

1.4 Organization of Geodesy, Literature

1.4.1 National Organizations

The problems of *global geodesy* may be solved only with the international cooperation of institutions involved in nation-wide geodetic work, together with international geodetic services, cf. [1.4.2]. *University* institutes and departments (e.g., geodesy, geophysics, astronomy, and space sciences) pursue fundamental research. In some countries, *academy* or *governmental* institutes are also engaged in geodetic research (China: Institute of Geodesy and Geophysics, Wuhan;

Finland: Finnish Geodetic Institute; Germany: Deutsches Geodätisches Forschungsinstitut, München, Geoforschungszentrum Potsdam; Russia: Institute of Physics of the Earth, Moscow). The *geodetic surveys* are carried out according to the guidelines of the official survey system, either by central agencies or by decentralized institutions (Australia: Australian Surveying and Land Information Group; Canada: Geodetic Survey Division, National Resources Canada, China: National Bureau of Surveying and Mapping; France: Institut Géographique National; Germany: State geodetic surveys in cooperation with the federal Bundesamt für Kartographie und Geodäsie BKG; Great Britain: Ordnance Survey; India: Survey of India; Japan: Geographical Survey Institute; Russia: Federal Service of Geodesy and Cartography; South Africa: Surveys and Land Information; U.S.A.: National Geodetic Survey, National Oceanic and Atmospheric Administration NOAA, (formerly U.S. Coast and Geodetic Survey)).

In addition to these, a number of non-geodetic institutions, in the course of their special tasks and projects, are also concerned with geodetic problems. These groups develop theory, measuring systems and methods, and in particular are involved with the collection and evaluation of geodetic data. We mention *space agencies* (e.g., Goddard Space Flight Center of NASA, Greenbelt, Md.; Centre National d'Etudes Spatiales, Toulouse), *geologic and hydrographic services* (China: State Seismological Bureau; France: Bureau des Recherches Géographiques et Minières; Germany: Bundesanstalt für Geowissenschaften und Rohstoffe, Bundesamt für Seeschiffahrt und Hydrographie; Great Britain: Institute of Geological Sciences, Institute of Oceanographic Sciences; U.S.A.: U.S. Geological Survey, U.S. Naval Observatory), *University departments* (e.g., Jet Propulsion Laboratory, California Institute of Technology, Pasadena, Cal.; Lamont Doherty Earth Observatory, Columbia Univ., Palisades, N.Y.) and *military agencies* (e.g., U.S.A.: National Imagery and Mapping Agency NIMA, formerly Defense Mapping Agency). More details may be found in Journal of Geodesy 74 (2000): 142 – 154.

1.4.2 International Collaboration

At the beginning of the arc measurements in the kingdom of Hanover (1821), C. F. Gauss had already expressed his desire for international collaboration. According to Gauss, this geodetic network would be connected to neighboring triangulation networks, aiming toward an eventual merger of the European observatories. Organized international collaboration originated with the memorandum by the Prussian general J. J. Baeyer (1794 – 1885): "Über die Größe und Figur der Erde, eine Denkschrift zur Begründung einer Mitteleuropäischen Gradmessung" (1861). In 1862, the "Mitteleuropäische Gradmessung" was founded in Berlin as the first international scientific association of significance; Baeyer became its first president. After expanding to the "Europäische Gradmessung" (1867) and to the "Internationale Erdmessung" ("Association Géodésique Internationale," 1886), the association engaged in fruitful activity,

which was especially inspired by the works of *Helmert* as director of the Central Bureau (LEVALLOIS 1980, TORGE 1996).

After the dissolution of the "Internationale Erdmessung" during the first World War, the "*International Union of Geodesy and Geophysics*" (IUGG) was founded in 1919. Today this organization has a membership of 75 countries. It consists of one geodetic and six geophysical associations. The "*International Association of Geodesy*" (IAG) is directed by a President who is elected every four years, and who is assisted by a Vice President and a General Secretary. The IUGG and IAG meet at General Assemblies at four-year intervals. In addition, numerous symposia and scientific conferences are organized to treat special themes; among these are the IAG Scientific Assemblies, which are held between the General Assemblies.

The IAG consists of five sections: Positioning, Advanced Space Technology, Determination of the Gravity Field, General Theory and Methodology, Geodynamics. *Commissions* are established for continuing problems, whereas transient problems are treated by *special study groups*. In addition, the IAG, in collaboration with other scientific organizations, maintains the following permanent services: International GPS Service (IGS) with the Central Bureau at the Jet Propulsion Laboratory, Pasadena, California; Bureau Gravimetrique International (BGI), Toulouse; International Geoid Service (IGeS), Milano; International Center for Earth Tides (ICET), Brussels; International Earth Rotation Service (IERS) with the Central Bureau at the Bundesamt für Kartographie und Geodäsie (BKG), Frankfurt, a.M. (and until December 31, 2000: Observatoire de Paris); Permanent Service for Mean Sea Level, Bidston Observatory, Merseyside, U.K.; Bureau International des Poids et Mesures-Time Section, Sèvres; International Laser Ranging Service (ILRS) and International VLBI Service for Geodesy and Astrometry (IVS), since 1999. The IAG also maintains an information and a bibliographic service and organizes summer schools in many parts of the world (IAG 1997). A restructuring of IAG is under discussion and may lead to major changes (SCHWARZ 2000a).

1.4.3 Literature

References to textbooks for geodesy and related fields (mathematics, physics, astronomy, geophysics, surveying engineering and mapping) will be found in the running text. A list of geodetic and geodetically relevant publication series is given in *Journal of Geodesy* 74 (2000): 155 – 162.

We mention in particular the *Journal of Geodesy* (formerly *Bulletin Géodésique* and *Manuscripta Geodaetica*, Springer: Berlin-Heidelberg-New York), which is the official journal of the IAG. The results of each General Assembly of the IAG are compiled in the *Travaux (Proceedings)*. National reports are collected and

stored at the Central Bureau of the IAG. The proceedings of IAG symposia are published in a separate series (Springer).

Among the recent *scientific-technical journals* in the field of geodesy, geophysics, navigation, and surveying we mention in particular: Acta Geodaetica, Geophysica et Montanistica Hungarica (Hungary), Acta Geodaetica et Cartographica Sinica (China), Annali di Geofisica (Italy), Artificial Satellites (Poland), Australian Journal of Geodesy, Photogrammetry and Surveying, The Australian Surveyor, Bollettino de Geodesia e Scienze Affini (Italy), Allgemeine Vermessungsnachrichten (Germany), Bollettino die Geofisica Teorica ed Applicata (Italy), EOS Transactions (American Geophysical Union), Geodesia (The Netherlands), Geomatica (Canada), Geodeziya i Aeroseymka, Geodeziya i Kartografiya (Russia), Geophysical Journal International (U.K.), Geophysical Research Letters (U.S.A.), Geophysics (U.S.A.), GPS-World (U.S.A.), GPS Solutions (U.S.A.), Journal of Earthquake Prediction Research (China/Russia), Journal of Geodynamics (The Netherlands), Journal of the Geodetic Society of Japan, Journal of Geophysical Research (U.S.A.), Journal of Surveying Engineering (U.S.A.), Marine Geodesy (U.S.A.), The Journal of Navigation (U.S.A.), Österreichische Zeitschrift für Vermessungswesen und Geoinformation (Austria), Physics and Chemistry of the Earth A: Solid Earth and Geodesy (The Netherlands), Reviews of Geophysics and Space Physics (U.S.A.), Revista Cartografica (Mexico), Surveying and Land Information Systems (U.S.A.), Studia Geophysica et Geodaetica (Czech Republic), Survey Review (U.K.), Surveys in Geophysics (The Netherlands), Tectonophysics (The Netherlands), Vermessung, Photogrammetrie und Kulturtechnik (Switzerland), Zeitschrift für Vermessungswesen (Germany).

Technical Reports are issued by university and research institutes, as well as by some governmental agencies. We mention here: Bull. d'Inf. Bureau Gravimetrique International, Toulouse; Bull. d'Inf. Marées Terrestres, Brussels; Bull. Earthquake Research Inst., Univ. of Tokyo; Bull. Geograph. Survey Inst., Tokyo; Geod. Geophys. Arb. in der Schweiz, Schweiz. Geod. Komm., Zürich; Geowiss. Mittl. Studieng. Verm.wesen, TU Wien; IERS Techn. Notes, Paris; IGS Techn. Reports JPL, Pasadena, U.S.A.; Journal of Wuhan Technical University of Surveying and Mapping; Mitt. Bundesamt Kart. u. Geod., Frankfurt a.M.; Mitt. Geod. Inst. Univ. Bonn; Mitt. Geod. Inst. TU Graz; Mitt. Inst. Geod. Photogr. ETH Zürich; NASA Goddard Space Flight Center Rep., Greenbelt, Md.; Nat. Survey and Cadastre, Geod. Div. Techn. Rep., Copenhagen; Nederlandse Comm. voor Geodesie Publ.; NIMA Techn. Rep., Washington D.C.; NOAA-NOS-National Geod. Survey Techn. Rep., Rockville, Md.; Publ./Rep. Finnish Geod. Inst. Helsinki; Publ. Division of Geomatics, Univ. of Calgary; Rep. Dep. of Geodetic Science and Surveying, The Ohio State Univ., Columbus, Ohio; Rep. on Geodesy, Inst. of Geodesy and Geod. Astronomy, Warsaw Univ. of Technology; Math. and Phys. Geodesy, TH Delft; Schriftenreihe d. Institute d. Fachber. Vermessungswesen, Univ. Stuttgart;

Schriftenr. Univ. Studiengang Vermessungswesen, Univ. der Bundeswehr, München; Univ. Rep. School of Geomatic Engineering, Univ. of New South Wales, Sydney; Veröff. Bayer. Komm. für die Internationale Erdmessung, München; Veröff. Deutsche Geod. Komm., München; Wiss. Arb. Fachr. Vermessungswesen, Univ. Hannover.

2 Reference Systems

Reference systems are introduced in order to model geodetic observations as a function of unknown parameters of interest. The coordinate systems are defined in terms of orientation, metrics, and curvature; they are three-dimensional in principle (HEITZ 1988). A fourth dimension, time, enters through the mutual motion of the earth and other celestial bodies and through the earth's deformations. As with the earth, reference systems can be defined for the moon and the planets in the solar system.

Basic units and fundamental constants are foundational to the geodetic measurement and modeling process [2.1]. Time systems are based either on processes of quantum physics or on the daily rotation of the earth [2.2]. Global reference systems are realized through reference frames, e.g., the ITRF, which is established and maintained by the International Earth Rotation Service [2.3]. We distinguish between the space-fixed celestial reference system [2.4] and the earth-fixed terrestrial reference system [2.5] (KOVALEVSKY et al. 1989). In addition, gravity related reference systems have to be introduced, as most geodetic observations refer to the earth's gravity field [2.6].

2.1 Basic Units and Fundamental Constants

Length, mass, and time are basic quantities used in geodesy. The units for these quantities are the meter (m), the kilogram (kg), and the second (s) respectively. They are defined through the International System of Units (Système International d'Unités SI), established in 1960 by the 11th General Conference of Weights and Measures (CGPM) in Paris (MARKOWITZ 1973, BIPM 1991). The definitions are as follows:

- The *meter* is the length of the path traveled by light in vacuum during a time interval of $1/299\,792\,458$ of a second (CGPM 1983).
- The *kilogram* is the unit of mass; it is equal to the mass of the international prototype of the kilogram (CGPM 1901).
- The *second* is the duration of $919\,263\,1770$ periods of the radiation corresponding to the transition between the two hyperfine levels of the ground state of the cesium-133 atom (CGPM 1967).

The establishment and maintenance of the reference standards for these units is the task of the *Bureau International des Poids et Mesures* (BIPM), located in Sèvres, France. BIPM cooperates with the national laboratories of standards under the guidelines of the International Meter Convention (1875). These national laboratories include the National Institute of Standards and

Technology, Gaithersburg, Md., U.S.A.; the National Physical Laboratory, Teddington, U.K.; and the Physikalisch-Technische Bundesanstalt, Braunschweig, Germany.

The *realization* of the *meter* is based on interferometric measurements (relative uncertainty 10^{-12}) using light with highly stable frequencies (stabilized lasers). The international *kilogram* prototype has been kept in BIPM since 1889; national prototypes are related to it with an uncertainty of 10^{-9} . The BIPM Time Section (until 1987: Bureau International de l'Heure BIH, Paris) defines the *second* (relative uncertainty 10^{-14}) and the atomic time scale, cf. [2.2.1].

Previous definitions of the meter and the second were based on natural measures. The *meter* was intended to be one ten-millionth part of the meridian quadrant passing through Paris. Its length was derived from an arc measurement, cf. [1.3.2], and realized in 1799 by a prototype meter bar called "mètre des archives" (legal meter). Following the International Meter Convention, a more stable version (platinum-iridium bar) was manufactured (international meter). It has been preserved since 1889 at the BIPM. This definition (uncertainty 10^{-7}) was valid until 1960 when, for the first time, the wavelength of a certain spectral line of light became the defining quantity.

Since ancient times, the natural measure for *time* has been the daily rotation of the earth about its axis. The mean solar day, cf. [2.2.2], was determined by astronomic observations, and the second was defined as $1/86400$ part of that day. From the 1930's on, it became obvious that this definition was uncertain by about 10^{-7} due to the irregularities of the earth's rotation, cf. [2.5.2].

As a supplementary SI unit, the *radian* (rad) is used for *plane angles*:

- The radian is the plane angle between two radii of a circle subtended by an arc on the circumference having a length equal to the radius.

Geodesy, astronomy, and geography also use the *sexagesimal graduation* with 1 full circle = 360° (degrees), $1^\circ = 60'$ (minutes), and $1' = 60''$ (seconds, also arcsec). With 2π rad corresponding to 360° , an angle α is transformed from radian to degree by

$$\alpha(^{\circ}) = \rho(^{\circ})\alpha \text{ rad}, \rho^{\circ} = 180^{\circ}/\pi. \quad (2.1)$$

Among the *fundamental constants* used in geodetic models is the *velocity of light* in a vacuum, which is by definition (1983)

$$c = 299\,792\,458 \text{ ms}^{-1}, \quad (2.2)$$

and the *gravitational constant* (CODATA system of physical constants 1986), which is defined as

$$G = (6.672\ 59 \pm 0.000\ 85) \times 10^{-11} \text{ m}^3 \text{ kg}^{-1} \text{ s}^{-2}. \quad (2.3)$$

Cavendish carried out the first experimental determination of G in 1798 with a torsion balance. Current work concentrates on increasing the relative accuracy of G to better than 10^{-4} . This includes investigations into dependence of G on material, external influences, distance and direction, as well as non-inverse-square properties of gravitation (GILLIES 1987, FISCHBACH and TALMADGE 1999).

Other units and constants used in geodesy, astronomy, and geophysics will be introduced in the corresponding chapters, see also AHRENS (1995), BURŠA (1995), GROTEK (2000).

2.2 Time Systems

Time plays a fundamental role in geodesy. This is due to the fact that most measurement methods use the signal travel-time of electromagnetic waves for positioning, and that a uniform time scale is also needed in order to model the motion of artificial satellites. On the other hand, a time system is required for describing the relative motion of the earth in the solar system with respect to inertial space and for describing earth deformations due to internal and external forces.

Time systems are defined by the unit for a time interval and by a time epoch. They are based either on the definition of the SI second [2.2.1] or on the diurnal rotation of the earth about its axis [2.2.2]. Fundamental descriptions of time systems are found in MUELLER (1969), MORITZ and MUELLER (1987), SEIDELMANN (1992).

2.2.1 Atomic Time, Dynamical Time

A uniform time-scale of high accuracy is provided by the *International Atomic Time* (Temps Atomique International: TAI). It corresponds to the definition of the SI second, cf. [2.1], which has been made approximately equal to the second of the formerly used ephemeris-time. The latter was defined by the motion of the earth about the sun and determined through long-term astronomic observations. The origin of TAI was chosen so that its epoch (January 1, 1958, 0 h) coincided with the corresponding epoch of Universal Time UT1, cf. [2.2.2]. The TAI day comprises 86400 s, and the Julian Century has 36525 TAI days.

TAI is *realized* by a large set (more than 200) of atomic clocks (mostly cesium beam frequency standards providing long-term stability and a few hydrogen

masers) maintained at about 60 laboratories around the world. Clock comparisons are performed at a number of timing centers, employing GPS observations for time links, cf. [5.2.5]. From these local determinations, a weighted mean is calculated at the BIPM Time Section. The relative frequency-stability of TAI is between a few 10^{-15} (over minutes to days) and 10^{-11} (over years). Due to relativistic effects, the readings of the atomic clocks are reduced to a common height reference (SI second "on the geoid").

The motions of celestial bodies and artificial satellites have to be described by a strictly uniform time scale (inertial time). This is provided by a *dynamical time*, which is based on motions of bodies in the solar system. Dynamical time scales refer either to the barycenter of the solar system (Barycentric Dynamic Time TDB) or to the geocenter (Terrestrial Time TT). The TT unit is practically equivalent to TAI, with a constant difference resulting from the epoch definition of TAI:

$$TT = TAI + 32.184 \text{ s.} \quad (2.4)$$

Dynamical time is used in celestial mechanics with Newton's equations of motion, e.g., as an argument for the astronomical ephemeris of the moon and the sun.

2.2.2 Sidereal and Universal Time

The diurnal rotation of the earth provides a natural measure for time. Corresponding time systems are introduced in order to relate earth-based observations to a space-fixed system: Sidereal and Universal (solar) Time. Hereby, two periodic motions of the earth play a role (Fig. 2.1):

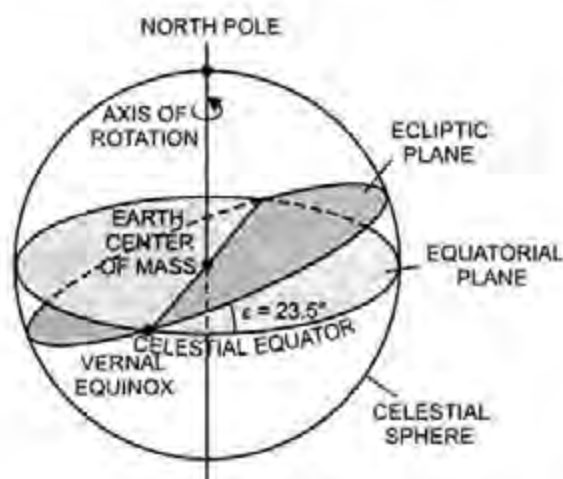


Fig. 2.1 Earth rotation, equatorial plane, and ecliptic plane

- the *diurnal rotation* (spin) of the earth about its polar axis. This rotational axis approximately coincides with the axis of maximum moment of inertia, and it passes through the earth's center of mass, cf. [2.5.2]. The *equatorial plane* is perpendicular to the axis of rotation,
- the *annual revolution* of the earth around the sun. Following Kepler's laws, the earth describes an ellipse with the sun at one of its focal points. Minor perturbations arise due to the gravitation of the moon and other planets. The plane of the earth's orbit is called the *ecliptic plane*; it has an obliquity of about 23.5° with respect to the equatorial plane.

By circumscribing the unit sphere around the center of the earth, simple geometric relations are obtained. The *celestial equator* and the *ecliptic* are defined by the intersections of the sphere with the corresponding planes. The *vernal equinox* (also first point of Aries) is the intersection of the ecliptic and the equator where the sun passes from the southern to the northern hemisphere.

Sidereal time is directly related to the rotation of the earth. *Local Apparent (or true) Sidereal Time* (LAST) refers to the observer's (local) meridian; it is equal to the hour angle of the (true) vernal equinox (Fig. 2.2), cf. [2.4.1]. The vernal equinox is affected by precession and nutation and experiences long and short-periodic variations, cf. [2.4.2]. If nutation is taken into account, we obtain *Local Mean Sidereal Time* (LMST), referring to the mean vernal equinox. For the Greenwich meridian the corresponding hour angles are called *Greenwich Apparent Sidereal Time* (GAST) and *Greenwich Mean Sidereal Time* (GMST). The astronomic longitude Λ is the angle between the meridian planes of the observer and Greenwich. It is given by, cf. [2.6.2]

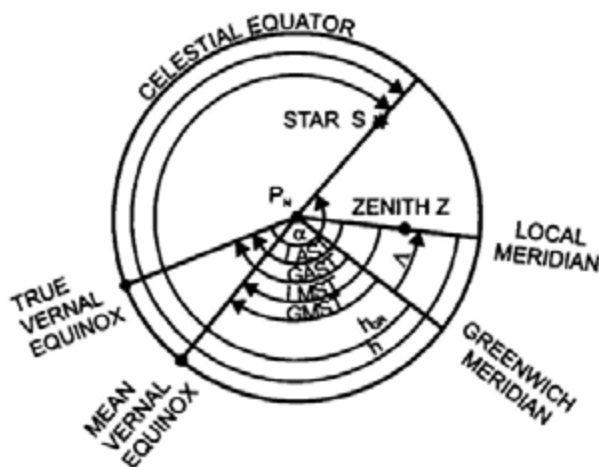


Fig. 2.2. Rectascension, sidereal time, hour angle, and longitude

$$\Delta = \text{LAST} - \text{GAST} = \text{LMST} - \text{GMST}. \quad (2.5)$$

LAST is determined from astronomical observations to fixed stars and extragalactic radio sources. The mean sidereal time scale is still affected by precession (long-periodic). The *mean sidereal day* is the fundamental unit; it corresponds to the time interval of two consecutive transits of the mean vernal equinox through the meridian.

For practical reasons, *solar time* is used in everyday life. It is related to the apparent diurnal motion of the sun about the earth. Since this revolution is not uniform, a "mean" sun is introduced which moves with constant velocity along the equator and coincides with the true sun at the vernal equinox. *Mean solar time* is equal to the hour angle of the mean sun plus 12 hours. If referred to the Greenwich mean astronomical meridian, cf. [2.5.1], it is termed *Universal Time* (UT). Its fundamental unit is the *mean solar day*, being the interval between two transits of the fictitious sun through the meridian.

The conversion of Universal Time to Greenwich Mean Sidereal Time is rigorously possible and is given by a series development with time defined by the International Astronomical Union (MORITZ and MUELLER 1987). Since the orbital motion of the earth is about 1° per day ($360^\circ/365\text{d}$), the year has one day more in sidereal days than in solar days. We have the following approximation:

$$1 \text{ mean sidereal day} = 1 \text{ mean solar day} - 3\text{m}55.90\text{s} = 86164.10\text{s}. \quad (2.6)$$

The earth's rotation rate is $15.041\,07''/1\text{s}$, and its angular velocity is

$$\omega = 2\pi/86\,164.10\text{s} = 7.292\,115 \times 10^{-5} \text{ rad s}^{-1}. \quad (2.7)$$

Universal time is obtained from a network of stations operating within the frame of the International Earth Rotation Service, cf. [2.3]. The observed local time UT0 refers to the instantaneous rotation axis, which is affected by polar motion, cf. [2.5.2]. In order to compare the results of different stations, reductions to a *Conventional Terrestrial Pole* are applied. The reduction in astronomic longitude $\Delta\Lambda_p$ corresponds to a change in time, cf. [5.3.3]. It transforms UT0 to UT1, which refers to the conventional terrestrial system, cf. [2.5.3]:

$$\text{UT1} = \text{UT0} + \Delta\Lambda_p. \quad (2.8)$$

The precision of UT1 is about 0.01 to 0.02 ms at a 1d resolution.

UT1, as well as Greenwich Mean Sidereal Time, still contains the variations of the earth's rotation with time, which are of secular, periodic, and irregular character, cf. [2.5.2]. An approximation to a uniform time scale can be achieved by modeling the seasonal variations of annual and semiannual type. With the corresponding reduction $\Delta\Lambda_s$, we obtain

$$\text{UT2} = \text{UT0} + \Delta\Lambda_p + \Delta\Lambda_s . \quad (2.9)$$

A practical time scale, as needed in navigation for instance, has to provide a uniform unit of time and maintain a close relationship with UT1. This led to the introduction of the *Coordinated Universal Time* (UTC). Its time interval corresponds to atomic time TAI, cf. [2.2.1], and its epoch differs by not more than 0.9s from UT1. In order to keep the difference

$$|\text{DUT1}| = |\text{UT1} - \text{UTC}| < 0.9 \text{ s} , \quad (2.10)$$

"leap seconds" are introduced to UTC when necessary. UTC is provided by the BIPM Time Section and broadcasted by time signal stations, while DUT1 is calculated by the IERS, cf. [2.3].

Among the continuously broadcasting time stations are DCF77/Mainflingen (77.5 kHz), HBG/Prangins (75 kHz); MSF/Rugby (60 kHz) in Europe; WWV resp. WWVB/Ft. Collins, Colorado (2500 to 20000 kHz resp. 60 kHz); and WWVH/Kauai, Hawaii (2500 to 15000 kHz).

2.3 International Earth Rotation Service

The International Earth Rotation Service (IERS) is in charge of providing and maintaining conventional celestial and terrestrial reference frames. These frames are a realization of the reference systems recommended by the International Astronomical Union (IAU) and the International Union of Geodesy and Geophysics (IUGG). IERS is also responsible for the determination of the orientation parameters of the earth as functions of time, which relate the two frames to each other (SEIDELMANN 1992, REIGBER and FEISSEL 1997).

Established by the IAU and IUGG, the IERS has operated since January 1, 1988. It collects, analyzes, and models observations of a global network of astronomic and geodetic stations (about 300 sites in 1996), operating either permanently or for a certain time span. Observation techniques include Very Long Baseline Interferometry (VLBI), Lunar Laser Ranging (LLR), Global Positioning System (GPS), Satellite Laser Ranging (SLR), and DORIS (Doppler Orbit determination and Radio positioning Integrated on Satellite), cf. [5.2] to [5.3].

The different types of observations are evaluated at the respective IERS coordinating centers and then combined by an adjustment at the IERS Central Bureau. The results include the positions (coordinates) of both the extragalactic radio sources and the terrestrial stations, the earth orientation parameters (EOP), and other information. With respect to the EOP, VLBI provides information about precession, nutation, polar motion, and UT1, cf. [2.4.2], [2.2.2]. Satellite techniques contribute to the daily interpolation of UT and to the determination of polar motion, cf. [2.5.2]. The results are disseminated through bulletins, annual reports, and technical notes. The combined solutions have an accuracy of $\pm 0.0003''$ for EOP and ± 0.01 m for the positions of the terrestrial stations, cf. [2.4], [2.5]. The evaluation of the observations is based on the IERS Conventions, which are consistent with the IAU and IUGG/IAU recommendations for reference systems (McCARTHY 1996), cf. [2.4.2], [4.3].

Among the early international agreements on positioning and time were the introduction of the Greenwich zero meridian and Universal Time (1884). The first fundamental catalogue of selected stars was published in the 1880's, which started a series of star catalogues providing the positions of fixed stars.

International activities of monitoring the earth's rotation date back to 1899, when the *International Latitude Service* (ILS) started to determine polar motion through latitude observations at five observatories located around the globe on the $39^{\circ}08'$ northern parallel. After extension to the *International Polar Motion Service* (IPMS), and in cooperation with the *Bureau International de l'Heure* (BIH) established in 1912, about 50 astronomical observatories contributed to the determination of polar motion and time. An accuracy of $\pm 0.02''$ resp. ± 1 ms was reached for mean values over 5 days. IPMS and the earth rotation section of BIH have been replaced by IERS, while the BIH activities on time are continued at the BIPM, cf. [2.2.1].

2.4 Celestial Reference System

An inertial system is needed in order to describe the motions of the earth and other celestial bodies in space, including those of artificial satellites. Such a system is characterized by Newton's laws of motion; it is either at rest or in the state of a uniform rectilinear motion without rotation. A space-fixed system (celestial reference system) represents an approximation to an inertial system and can be defined by appropriate conventions: Conventional Inertial System (CIS). The coordinate frame for such a system is provided by spherical astronomy [2.4.1]. The spatial orientation of this frame varies with time, and therefore, modeling of the variations is required [2.4.2]. The International Celestial Reference Frame represents the realization of the celestial reference system [2.4.3], KOVALEVSKY et al. (1989), SEIDELMANN (1992).

2.4.1 Equatorial System of Spherical Astronomy

The coordinates of the celestial reference-system are defined by the *equatorial system* of spherical astronomy (MUELLER 1969, EICHHORN 1974). We introduce a three-dimensional Cartesian coordinate system with the origin at the center of mass of the earth (geocenter). The Z-axis coincides with the rotational axis of the earth. The X and Y-axes span the equatorial plane, with the X-axis pointing to the vernal equinox and the Y-axis forming a right-handed system (Fig. 2.3), cf. [2.2.2].

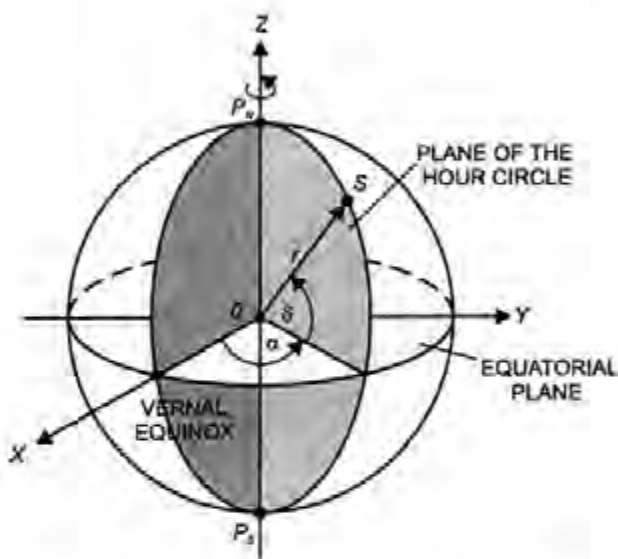


Fig. 2.3. Astronomic equatorial system

In the sequel, we shall also shift the origin of this system to the position of an observer on the earth (topocenter) or to the barycenter of the solar system. The directions to celestial bodies then vary with different definitions of the origin (parallaxes), cf. [5.3.3]. Since the earth's radius is negligibly small compared to the distances to stars and extragalactic radio sources, no distinction is necessary between a topocentric and a geocentric system.

We circumscribe the unit sphere (celestial sphere) about the earth. The rotational axis meets the sphere at the celestial north and south poles P_N and P_S . The great circles perpendicular to the celestial equator, which contain the celestial poles, are called *hour circles*, and the small circles parallel to the equator are termed *celestial parallels*.

The *right ascension* α is the angle measured in the plane of the equator between the planes of the hour circles passing through the vernal equinox and the celestial body S ; it is reckoned from the vernal equinox anticlockwise. The

declination δ is the angle measured in the plane of the hour circle between the equatorial plane and the line OS (positive from the equator to P_N and negative to P_S).

The position of a *celestial body* S can be described either by the Cartesian coordinates X,Y,Z , or by the spherical coordinates α,δ,r (r = distance from the origin O). We have the transformation

$$\mathbf{r} = \begin{pmatrix} X \\ Y \\ Z \end{pmatrix} = r \begin{pmatrix} \cos\alpha \cos\delta \\ \sin\alpha \cos\delta \\ \sin\delta \end{pmatrix}. \quad (2.11)$$

In geodesy, only directions are important for stars and extragalactic sources. With $r = 1$, α and δ describe the position of S on the unit sphere. They can also be expressed by the lengths of the corresponding arcs on the equator and the hour circle.

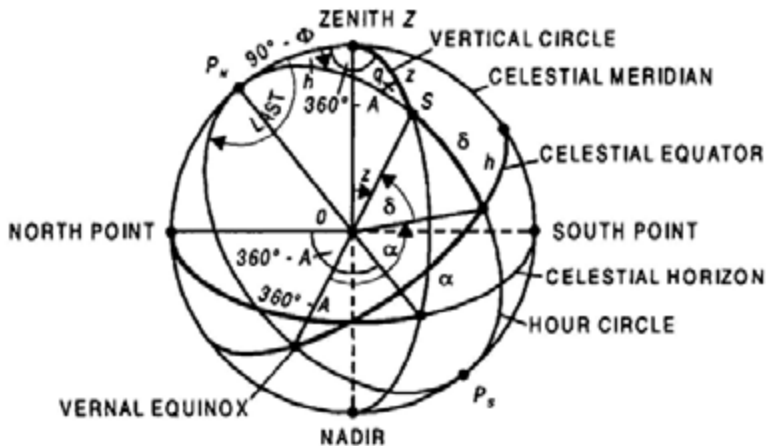


Fig. 2.4. Astronomic equatorial and horizon system

We introduce the local *meridian plane* of the observer, spanned by the local vertical (direction of the plumb line) and the rotational axis, after a parallel shift from the geocenter to the topocenter. The *zenithal point* Z is the intersection of the vertical with the unit sphere, and the *celestial meridian* is the great circle through Z and the poles (Fig. 2.4). The *hour angle* h is measured in the equatorial plane between the celestial meridian through Z and the hour circle of S , reckoned from the upper meridian toward west. Because of the earth's rotation, the hour angle system (h,δ) depends on time. The h,δ -system is rotated, with respect to the α,δ -system, about the polar axis by the angle of sidereal time LAST, cf. [2.2.2]. We have the relation (Fig. 2.2)

$$\text{LAST} = h + \alpha, \quad (2.12)$$

which is used with time determination, cf. [5.3.2].

2.4.2 Precession and Nutation

The earth's axis of rotation, which has been introduced as the Z-axis, changes its spatial orientation with time. As a consequence, the position (α, δ) of a celestial body varies, with a superposition of long and short-periodic effects (MORITZ and MUELLER 1987, SEIDELMANN 1992, DICKEY 1995).

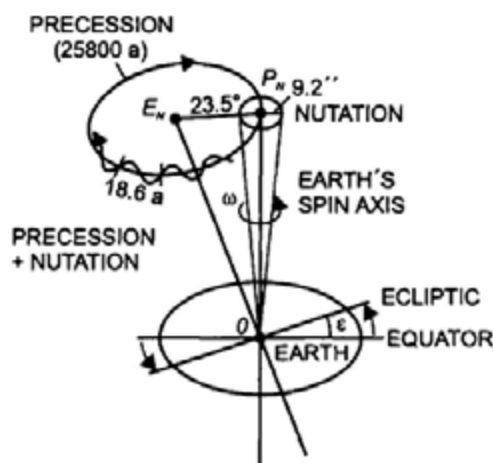


Fig. 2.5. Precession and nutation

The *lunisolar precession* is a long-periodic effect caused by the gravitation of the moon and the sun on the equatorial bulge of the earth. This creates a force couple (torque) which tends to turn the equatorial plane into the plane of the ecliptic (Fig. 2.5). In combination with the moment of the earth's rotation, the earth's axis describes a gyration of a cone with a generating angle of 23.5° (corresponding to the obliquity of the ecliptic ε), about the northern pole of the ecliptic E_N . The vernal equinox moves clockwise along the ecliptic at a rate of $50.3''/\text{year}$, making a complete revolution in about 25800 years. The gravitation of the planets causes a slow dislocation of the earth's orbit and thereby an additional migration of the vernal equinox along the equator and a change in ε : *planetary precession*. The sum of the lunisolar and the planetary precession is termed *general precession*.

The precession is superimposed by short-periodic effects known as *nutation*, which has periods between 5 days and 18.6 years. These periods are mainly due

to the time variations of the inclination of the moon's orbit with respect to the ecliptic (appr. 5°). Other components have semiannual and semimonthly periods and stem from the oscillations of the sun and moon between the earth's northern and southern hemisphere.

Precession and nutation can be modeled as a function of time using the ephemerides of the moon, the sun, and the planets. The IAU (1976) theory of *precession* provides three time-dependent Eulerian rotation angles for reducing the positions of celestial bodies to a common reference. For the reference epoch J 2000.0 (Julian epoch January 1, 2000, 12^h TDB, cf. [2.2.1]), we have the fundamental constants "general precession in longitude at the ecliptic" ($5029.0965''/\text{century}$) and "obliquity of the ecliptic" ($23^\circ 26' 21.412''$).

The IAU (1980) theory of *nutation* describes this effect by a rotation about the cone of precession. The deviation of the true pole from the mean pole is modeled by two time-dependent parameters. Hereby, the earth is regarded as an elliptical, rotating, elastic, and ocean-free body with solid inner and liquid outer cores (WAHR 1981, SEIDELMANN 1992). For the epoch J 2000.0 the constant of nutation is $9.2025''$.

The IAU models for precession and nutation define the reference pole for the international celestial reference frame (Celestial Ephemeris Pole CEP). CEP is free of diurnal or quasidiurnal nutation terms (amplitudes $< 0.001''$) with respect to the space- or earth-fixed coordinate systems. It is also referred to as the pole of the instantaneous equatorial system, cf. [2.4.3].

The IAU models for precession and nutation provide a precision of $\pm 0.001''$ at 5 to 7 days resolution. An improved theory has been developed at the IERS based on recent VLBI and LLR data. Larger offsets ($< 0.02''$) of the celestial pole from CEP have been found; these are published regularly by IERS (McCARTHY 1996). GPS also contributes to the determination of the short-periodic nutation terms (ROTHACHER et al. 1999).

According to an IAU recommendation, the IAU (1976/1980) models for precession and nutation shall be replaced by January 1, 2003. The new model is the IAU 2000A (precision $\pm 0.0002''$), as published in the IERS conventions 2000. CEP will then be substituted by the Celestial Intermediate Pole (CIP), as defined by the model for periods greater than two days together with additional time-dependent corrections provided by IERS.

The instantaneous position of a celestial body, cf. [2.4.1], is called *true position* at the epoch t . By accounting for nutation, we obtain the *mean position* at epoch t , which refers to the mean celestial equator and the mean vernal equinox, cf. [2.2.2]. If precession is also taken into account, we get the mean position at the reference epoch J 2000.0.

2.4.3 International Celestial Reference Frame

The International Celestial Reference System (ICRS), as recommended by IAU, is based on the general theory of relativity, with the time coordinate defined by the international atomic time (ARIAS et al. 1995, MA and FEISSEL 1997). ICRS approximates a space-fixed conventional inertial-system (CIS) with the origin at the barycenter of the solar system. It is assumed that no global rotation of the system exists. This implies that the defining sources are either free from proper motion (component of spatial motion tangent to the celestial sphere) or that this motion can be modeled. The coordinate axes are defined by the celestial reference pole and the vernal equinox as provided by the IAU models for precession and nutation. They are realized through mean directions to extraterrestrial fiducial objects: stellar or radio source CIS (MUELLER 1988), cf. [2.4.2].

The *stellar system* is based on the stars of the Fundamental Catalogue FK5 (FRICKE et al. 1988). It provides the mean positions (α, δ) and the proper motions (generally $< 1''/\text{year}$) of 1535 fundamental stars for the epoch J 2000.0, with precisions of $\pm 0.01\ldots 0.03''$ and $\pm 0.05''/\text{century}$ respectively. A supplement to FK5 contains additional stars up to an apparent magnitude of 9.5. The mean equator and the mean vernal equinox for J 2000.0 are realized by the FK5 catalogue, with an accuracy of $\pm 0.05''$. Due to refraction uncertainties, earth-based astrometry can hardly improve this accuracy.

Astromonic space missions have significantly improved the realization of a stellar CIS. The HIPPARCOS astrometry satellite (ESA, 1989 – 1993) was used to construct a network by measuring large angles between about 100000 stars (up to an apparent magnitude of 9) covering the entire sky. The reference frame thus established provides an accuracy of $\pm 0.001''$ and $\pm 0.0005''/\text{year}$ for proper motion (HIPPARCOS 1995, KOVALEVSKY et al. 1997). From improved FK5 data and HIPPARCOS results, an FK6 catalogue has been developed for a small number of stars (340 “astrometrically excellent”), resulting in an improvement of proper motion as compared to the HIPPARCOS catalogue (WIELEN et al. 1999). Future astrometric space missions will employ optical interferometry and thus increase the positional accuracy to $\pm 0.00001''$ (BROSCH and DICK 1996).

The *radio source system* is based on extragalactic radio sources (quasars and other compact sources). It was adopted as ICRS by the IAU in 1997 and has superseded the previous stellar system (FK5) since 1998. Due to the large distances (> 1.5 billion light years), these sources do not show a measurable proper motion. The system is realized through the International Celestial Reference Frame (ICRF), established and maintained by IERS (McCARTHY 1996, MA et al. 1998). ICRF contains the coordinates (equatorial system, epoch J 2000.0) of more than 600 objects. About 200 of them are well observed

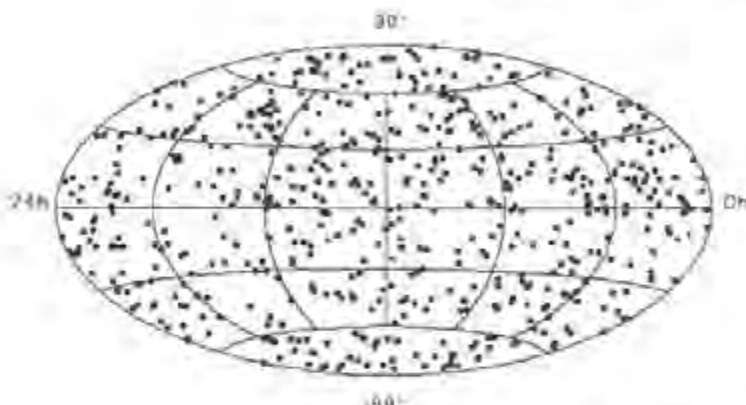


Fig. 2.6. International Celestial Reference Frame (ICRF), from IERS (1995): Missions and goals for 2000

"defining sources," and 100 more are used for densification and connection to the stellar-fixed reference system (Fig. 2.6). The southern sky is not as well covered, as the telescopes are concentrated in the northern hemisphere. The coordinates of the radio sources are determined by radio astronomy, with a precision of better than $\pm 0.001''$ on the average and $\pm 0.0003''$ for the most precisely observed objects (MA and FEISSEL 1997, BROSCHE und SCHUH 1999).

The link between the stellar and the radio source CIS is given with an accuracy of $\pm 0.05\ldots 0.1''$, which corresponds to the uncertainty of FK5. This connection will be improved by the results of the astrometric space missions (optical signals from a limited number of radio sources) to $\pm 0.001''$ or better for the epoch of observation.

2.5 Terrestrial Reference System

An *earth-fixed* reference system is introduced for positioning and navigation on and close to the earth's surface and for describing the earth's gravity field as well as other physical parameters. It is defined by a three-dimensional geocentric coordinate system [2.5.1]. The orientation of this system changes with time and with respect to the solid earth's body as well as to the celestial reference system [2.5.2]. The system is realized by the IERS International Terrestrial Reference Frame, which includes its relation to the International Celestial Reference Frame [2.5.3].

2.5.1 Global Earth-Fixed Geocentric System

An earth-fixed (i.e., rotating with the earth) system of spatial Cartesian-coordinates X, Y, Z is used as the fundamental terrestrial coordinate system (Fig. 2.7). Its origin is at the earth's center of mass (geocenter), being defined for the whole earth including hydrosphere and atmosphere. The Z -axis is directed towards a conventional "mean" terrestrial (north) pole. The "mean" equatorial plane is perpendicular to it and contains the X and Y -axes. A "mean" rotational axis and equatorial plane has to be introduced because the rotation of the earth changes with respect to the earth's body over time, cf. [2.5.3]. The XZ -plane is generated by the conventional "mean" meridian plane of Greenwich, which is spanned by the mean axis of rotation and the Greenwich zero meridian, to which Universal Time refers, cf. [2.2.2]. The Z and X -axes are realized indirectly through the coordinates of terrestrial "fiducial" stations, cf. [2.5.3]. The Y -axis is directed so as to obtain a right-handed system.

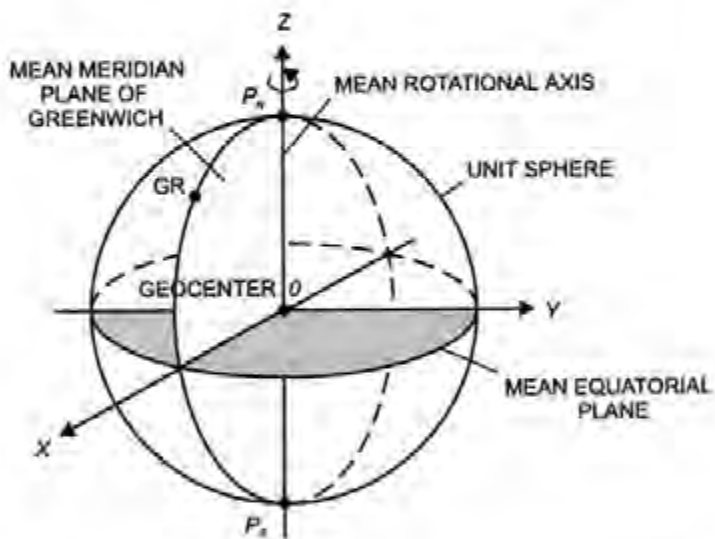


Fig. 2.7. Earth-fixed geocentric Cartesian system

The instantaneous axis of rotation is the common starting point for defining the Z -axes of the space-fixed and the earth-fixed reference systems. By referring to a reference epoch, the dependence on time is modeled, cf. [2.4.2], [2.5.2]. The directions of the X -axes of both systems differ by the angle of Greenwich mean sidereal time GMST, cf. [2.2.2].

In order to describe analytically certain physical properties of the earth (gravity field, magnetic field, topography, etc.), *spherical coordinates* r, ϑ, λ are employed. Here r = radial distance from the geocenter, ϑ = polar distance (colatitude), and λ = geocentric longitude. Instead of ϑ , the geocentric latitude

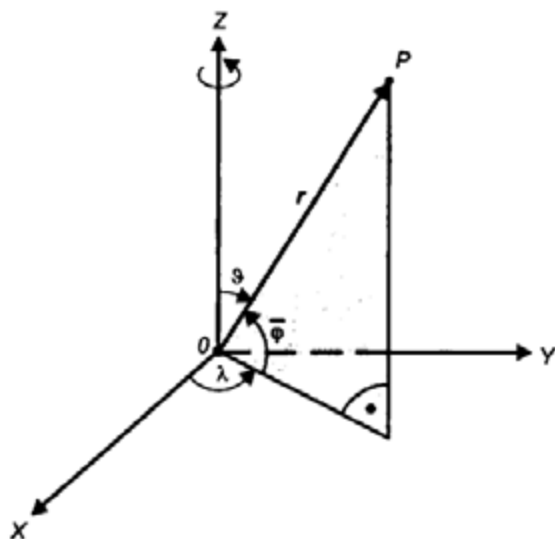


Fig. 2.8. Cartesian and spherical coordinates

$$\bar{\varphi} = 90^\circ - \vartheta \quad (2.13)$$

can be used (Fig. 2.8). The position of the point P is then given by the positional vector

$$\mathbf{r} = \begin{pmatrix} X \\ Y \\ Z \end{pmatrix} = r \begin{pmatrix} \sin \vartheta \cos \lambda \\ \sin \vartheta \sin \lambda \\ \cos \vartheta \end{pmatrix}. \quad (2.14)$$

2.5.2 Polar Motion, Length of Day, Geocenter Variations

The rotation of the earth can be described by a vector directed to the north pole of the instantaneous axis of rotation and by the angular velocity ω , see (2.7).

Direction and magnitude of the rotational vector *change with time* due to astronomical and geophysical processes. These processes include variations of the lunar and solar gravitation and mass redistributions in the atmosphere, the hydrosphere, the solid earth, and the liquid core. The changes are secular, periodic or quasiperiodic, and irregular in nature (LAMBECK 1980, MORITZ and MUELLER 1987, DICKEY 1995), cf. [8.3.1].

Polar motion (or wobble) is the motion of the rotation axis relative to the earth's crust as viewed from the earth-fixed reference system. It directly affects

the coordinates of stations on the earth's surface and the gravity vector. Polar motion consists of several components:

- A free oscillation with a period of about 435 days (*Chandler period*), with an amplitude of 0.1" to 0.2", in a counterclockwise sense as viewed from the north pole. The Chandler wobble is due to the fact that the spin axis of the earth does not coincide exactly with a principal axis of inertia.

For a rigid earth, this would lead to a gyration of the rotational axis about the principal axis of inertia with a period of $A/(C-A) = 305$ days (Euler period). Here C is the earth's polar moment of inertia, and $A = B$ is the mean equatorial moment (rotational symmetry assumed). The difference between the Chandler and the Euler period results from the non-rigidity of the earth. This consideration neglects the fact that there is a small deviation between the axis of rotation and the axis of angular momentum, which is invariable in space. However, the deviation is less than 0.001" with periods < 1 d.

- The Chandler wobble is superposed by an *annual oscillation* forced by seasonal displacements of air and water masses. It proceeds in the same direction as the Chandler wobble with amplitudes of 0.05" to 0.1".
- A *secular motion* of the pole has been observed for more than 100 years. The motion consists of an irregular drift of about 0.003"/year in the direction of the 80° W meridian. Secular motion is mainly due to the melting of the polar ice and to large-scale tectonic movements; it attains large amounts over geological epochs: *polar wander*.
- More *irregular variations* occur at time scales from a few days to years with amplitudes up to 0.02". They originate primarily from mass redistributions within the atmosphere, but variations due to ocean volume changes, ground water variations, and earthquakes also occur.

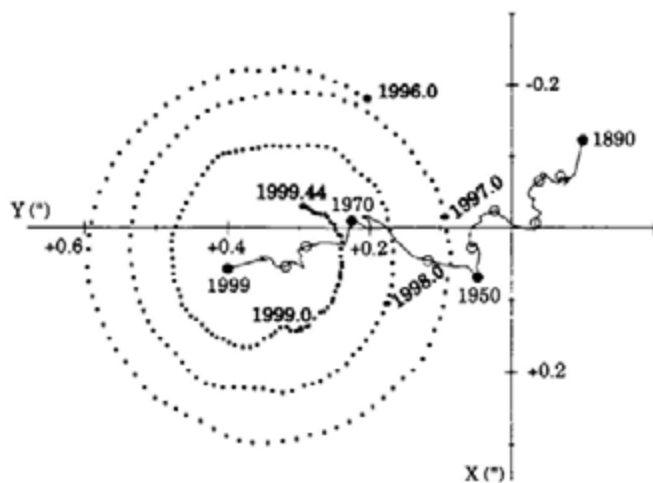


Fig. 2.9. Polar motion 1996 – 1999, and mean pole displacement 1890 – 1999, from IERS Annual Report 1998

The superposition of these components results in a slightly perturbed spiral like curve of the instantaneous pole with a slowly advancing mean position (Fig. 2.9). Over one year, the deviations from the mean position remain $< 0.3''$, corresponding to 9 m on the earth's surface.

The reference for describing the actual position of the pole with respect to the solid earth is provided by the *IERS reference pole*. It agrees within $\pm 0.03''$ with the *Conventional International Origin* (CIO), which was defined by the mean position of the north pole as determined between 1900.0 and 1906.0. The position of the instantaneous pole (Celestial Ephemeris Pole, cf. [2.4.2]) with respect to the reference pole is given by the rectangular coordinates x_p , y_p , which are defined in the plane tangential to the pole. The x_p -axis is in the direction of the Greenwich mean meridian (consistent with the previous BIH zero meridian), and the y_p -axis is directed along the 90°W meridian. These plane coordinates are usually expressed as spherical distances (in units of arcsec) on the unit sphere.

The *angular velocity* ω of the earth's rotation, as monitored from the earth, changes with time. Relative changes may reach several 10^{-8} , which corresponds to several ms for one day. The variations are generally described by the excess revolution time with respect to 86 400 s and then called *Length Of Day* (LOD). They are derived by comparing astronomical time determinations, which deliver Universal Time UT1, with the uniform time scales TAI or UTC, cf. [2.2.2].

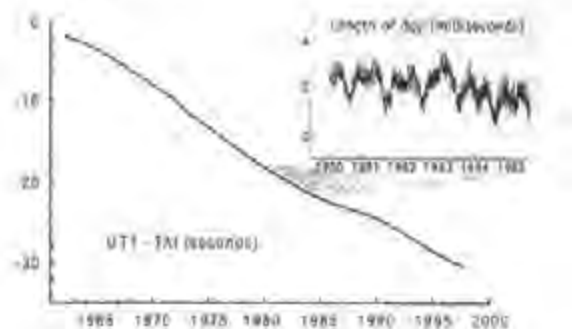


Fig. 2.10. Difference between atomic time scale TAI and Universal time UT1 (1962-1998) and length of day (LOD 1979-1987), from IERS Inform. 1998

The following components of LOD variations have been observed (Fig. 2.10):

- A *secular decrease* in the angular velocity of the earth's rotation is caused mainly by tidal friction. It lengthens the day by about 2 ms/century (STEPHENSON and MORRISON 1994).

- Fluctuations over *decades* are due to motions in the earth's liquid core and to slow climatic variations.
- The *tides* of the solid earth and the oceans produce variations of about 1 ms with long (annually) and short (monthly and less) periodic parts.
- *Seasonal* effects are explained by atmospheric excitation, with contributions from water and ice budget variations.
- More *irregular* oscillations stem from different sources, such as terrestrial mass displacements (earthquakes), solar activity, and atmospheric events, e.g., El Niño.

While the effect of polar motion on observations is dependent on location, LOD changes act uniformly on all points. The pole coordinates and LOD, as well as ω , are provided as *Earth Orientation Parameters* (EOP) by the IERS with daily resolution and accuracy of $\pm 0.0003''$ resp. ± 0.02 ms or better (REIGBER and FEISSEL 1997).

The position of the *geocenter* (origin of the terrestrial reference system) changes slightly in time with respect to the monitoring observatories. Annual and semiannual variations have been found, with amplitudes of several mm/year, from the analysis of satellite orbits. The variations are caused primarily by mass redistributions in the atmosphere and the oceans and by continental water variations. Through the coordinates of the ITRF stations, cf. [2.5.3], the geocenter is given with an accuracy of a few mm (DONG et al. 1997, RAY 1999).

2.5.3 International Terrestrial Reference Frame

The International Terrestrial Reference System is realized by the IERS through a global set of space geodetic observing sites. The geocentric Cartesian coordinates and velocities of the observing sites comprise the International Terrestrial Reference Frame (ITRF). The stations participating in the ITRF carry out observations either continuously or at certain time intervals (Fig. 2.11). Observations are made on twelve of the larger tectonic plates, which permits the derivation of station velocities related to plate tectonics, cf. [8.2.3].

Annual realizations of the ITRF are published by the IERS. The ITRF97 is comprised of the geocentric positions (X, Y, Z) for more than 550 stations at about 320 sites and corresponding site velocities (BOUCHER et al. 1999). The accuracy of the results depends on the observation techniques and is maximum for VLBI, SLR, and GPS observations ($\pm 0.5 \dots 2$ cm and $\pm 1 \dots 3$ mm/year resp.). Several time variable effects are taken into account, including displacements due to the solid earth tides, ocean and atmospheric loading effects, and postglacial rebound, cf. [8.2.2]. The ITRF solutions satisfy the condition of no residual net-rotation relative to the plate tectonics model NNR-NUVEL1A; vertical movements are not allowed at all, cf. [8.2.3]. The orientation of the

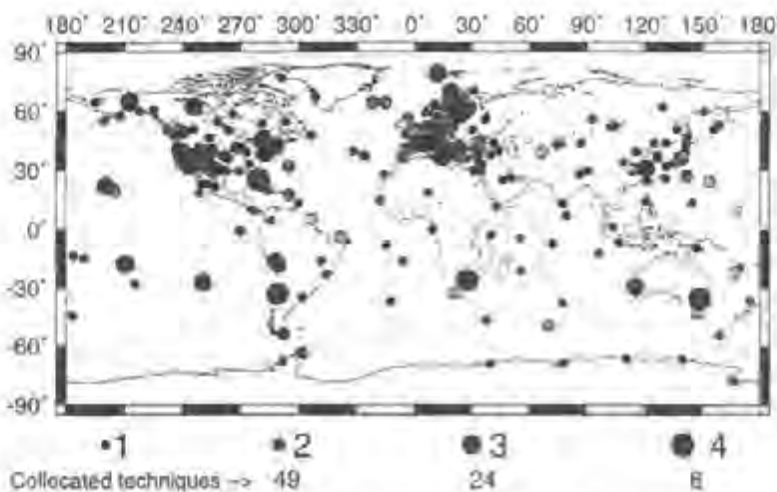


Fig. 2.11. International Terrestrial Reference Frame (ITRF) sites 1997, from BOUCHER et al. (1999)

ITRF is given with respect to the IERS reference pole and reference meridian, cf. [2.5.2]. The actual (time t) position vector \mathbf{r} of a point on the earth's surface is derived from its position at the reference epoch (t_0) by

$$\mathbf{r}(t) = \mathbf{r}_0 + \dot{\mathbf{r}}_0(t - t_0), \quad (2.15)$$

where \mathbf{r}_0 and $\dot{\mathbf{r}}_0$ are the position and velocity respectively at t_0 .

The relation between the celestial (ICRS) and the terrestrial (ITRS) reference systems is given by spatial rotations, which depend on the earth rotation parameters introduced in [2.2.2], [2.4.2], [2.5.2], SEEBER (1993), McCARTHY (1996), RICHTER, BU. (1995). The complete transformation from the celestial to the terrestrial system reads as

$$\mathbf{r}(\text{ITRS}) = \mathbf{R}_z(-x_p) \mathbf{R}_y(-y_p) \mathbf{R}_x(\text{GAST}) \mathbf{N}(t) \mathbf{P}(t) \mathbf{r}(\text{ICRS}). \quad (2.16)$$

The position vector as given in the ICRS is first transformed by the precession matrix $\mathbf{P}(t)$ from the reference epoch t_0 (J 2000.0) to the observation epoch t . The nutation matrix $\mathbf{N}(t)$ then transforms from the mean to the instantaneous true equator and vernal equinox. The Eulerian angles in these two rotation matrices are given in the models for precession and nutation, cf. [2.4.2]. The apparent Greenwich sidereal time GAST, cf. [2.2.2], is used to rotate the system about the Z-axis:

$$\mathbf{R}_3(\text{GAST}) = \begin{pmatrix} \cos(\text{GAST}) & \sin(\text{GAST}) & 0 \\ -\sin(\text{GAST}) & \cos(\text{GAST}) & 0 \\ 0 & 0 & 1 \end{pmatrix}, \quad (2.17)$$

with GAST calculated from UT1. Finally, counterclockwise rotations about the X and Y -axes are computed as functions of the pole coordinates x_p and y_p (small angles), cf. [2.5.2].

$$\mathbf{R}_1(-y_p) = \begin{pmatrix} 1 & 0 & 0 \\ 0 & 1 & -y_p \\ 0 & y_p & 1 \end{pmatrix}, \quad \mathbf{R}_2(-x_p) = \begin{pmatrix} 1 & 0 & x_p \\ 0 & 1 & 0 \\ -x_p & 0 & 1 \end{pmatrix}. \quad (2.18)$$

Equations (2.17) and (2.18) provide the transformation from the instantaneous space-fixed system to the conventional terrestrial system.

2.6 Gravity Field Related Reference Systems

Most geodetic and astronomic observations on or close to the earth's surface refer to the earth's gravity field by orientation along the local vertical. Consequently, local gravity-field-related reference systems are introduced for the modeling of these observations. The orientation of the local systems with respect to the global reference system is given by astronomic latitude and longitude [2.6.1]. These orientation parameters are used for transformation from the local systems into the global system and back [2.6.2].

2.6.1 Orientation of the Local Vertical

The direction of the plumb line (local vertical) with respect to the global geocentric system is given by two angles (Fig. 2.12). The *astronomic (geographic) latitude* Φ is the angle measured in the plane of the meridian between the equatorial plane and the local vertical through the point P . It is reckoned positive from the equator northward and negative to the south. The angle measured in the equatorial plane between the Greenwich meridian plane and the plane of the meridian passing through P is the *astronomic (geographic) longitude* Λ ; it is reckoned positive toward the east. The *gravity potential* W locates P in the system of level surfaces $W = \text{const.}$, cf. [3.2.1]. The *local astronomic meridian plane* is spanned by the local vertical at P and a line parallel to the rotational axis, cf. [2.4.1].

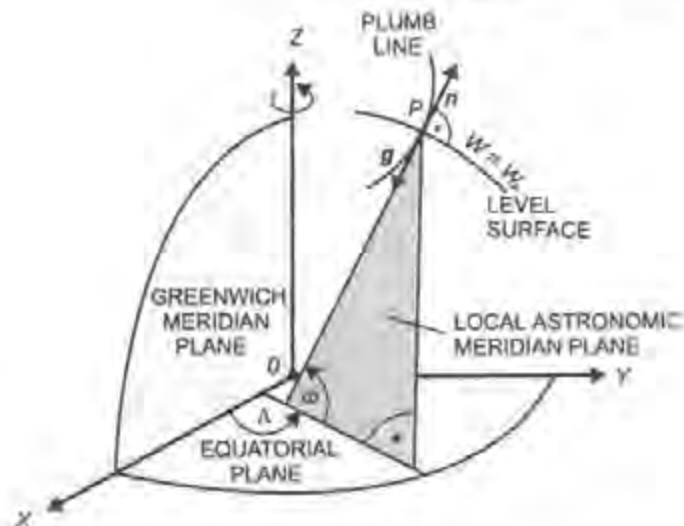


Fig. 2.12. Astronomic latitude and longitude

We introduce the outer surface normal \mathbf{n} (unit vector), which is normal to the level surface $W = W_p$ and passes through P . It is directed to the zenith, which is opposite of the direction of the gravity vector \mathbf{g} . From Fig. 2.12, we see that

$$\mathbf{n} = -\frac{\mathbf{g}}{g} = \begin{pmatrix} \cos \Phi \cos \Lambda \\ \cos \Phi \sin \Lambda \\ \sin \Phi \end{pmatrix}, \quad (2.19)$$

Latitude Φ and longitude Λ can be determined by the methods of geodetic astronomy, cf. [5.3]. Together with the potential W , they form a triple of three-dimensional coordinates defined in the gravity field, cf. [3.2.3].

2.6.2 Local Astronomic Systems

Geodetic and astronomic observations are tied to the direction of the plumb line at the point of observation and thereby to the earth's gravity field. An exception is distance measurements, which are independent of the reference system. Thus, these observations establish local gravity-field related systems; *Local astronomic systems* (Fig. 2.13). Their origin is at the point of observation P . The z -axis coincides with the local vertical and points toward the zenith. The x -axis (north) and the y -axis (east) span the horizontal plane, which is tangent to the level surface $W = W_p$. This x,y,z -system is left-handed.

Observable geometric quantities include astronomic azimuths, horizontal directions and angles, zenith angles, spatial distances, and leveled height differences.

The *astronomic azimuth* A is the angle measured in the horizontal plane between the astronomic meridian of P and the vertical plane spanned by the vertical through P and the target point P_t . It is positive as measured from the x -axis in a clockwise direction. *Horizontal directions and angles* may be regarded as azimuths lacking orientation, or as azimuth differences. The *zenith angle* (zenith distance) z is the angle measured in the vertical plane between the local vertical and the line joining P and P_t . It is positive as measured from the outer surface normal. The *spatial distance* s is the length of the straight line joining P and P_t . *Geometric leveling* also refers to the local vertical, providing a height difference with respect to $W = W_P$ over a very short distance. It may be regarded as the boundary case for trigonometric heighting, with a zenith angle of 90° . *Gravity measurements* and measurements of *gravity gradients* also refer to the local astronomic system.

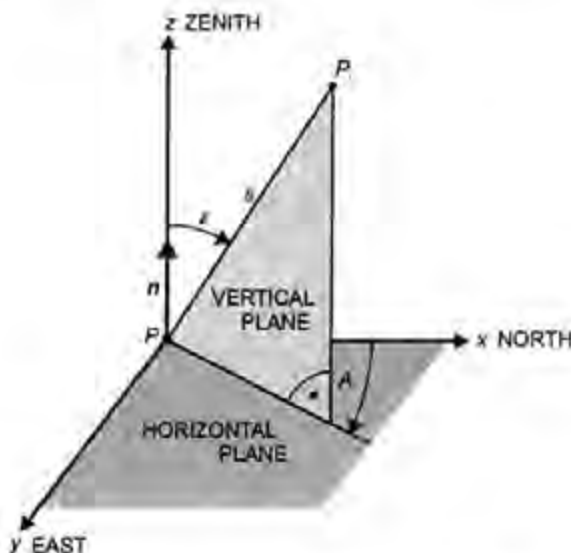


Fig. 2.13. Local astronomic system

According to Fig. 2.13, the position vector between P and P_t is given by

$$\mathbf{x} = \begin{pmatrix} x \\ y \\ z \end{pmatrix} = s \begin{pmatrix} \cos A \sin z \\ \sin A \sin z \\ \cos z \end{pmatrix}. \quad (2.20)$$

The local astronomic system is used for astronomic and geodetic applications.

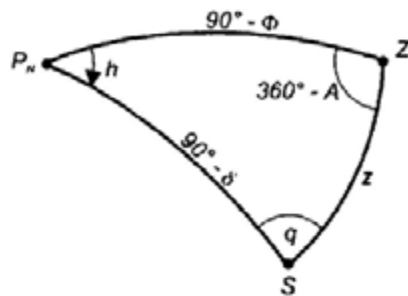


Fig. 2.14. Astronomic triangle

In *geodetic astronomy*, only direction measurements (zenith angles and azimuths) to celestial bodies are performed. The local system is called the *horizon system*, and the origin is named topocenter. The points of intersection of the plumb-line direction with the celestial sphere are known as the zenithal point Z and the nadir point Z' . The intersection of the horizontal plane with the celestial sphere is the celestial horizon. The azimuth in astronomy is usually reckoned from the south point and is considered positive westward to the north. The relation between the horizon system and the equatorial hour angle system, cf. [2.4.1], is given by the astronomic triangle (Fig. 2.14), see also Fig. 2.4. It is formed on the celestial sphere by the vertices P_N (north pole), Z (zenithal point), and S (celestial body). The triangle contains the compliments to declination ($90^\circ - \delta$) and astronomic latitude ($90^\circ - \Phi$), the hour angle h , the zenith angle z , the explement of the azimuth ($360^\circ - A$), and the parallactic angle q . From spherical astronomy we obtain the transformations

$$\left. \begin{aligned} \cos A \sin z &= \sin \delta \cos \Phi - \cos \delta \cos h \sin \Phi \\ \sin A \sin z &= -\cos \delta \sin h \\ \cos z &= \sin \delta \sin \Phi + \cos \delta \cos h \cos \Phi \end{aligned} \right\}. \quad (2.21)$$

Here the azimuth A is reckoned in the geodetic sense, i.e., positive from the north.

The transition to the α, δ -system (α = right ascension) is given by the local apparent sidereal time LAST, see (2.12):

$$\alpha = \text{LAST} - h. \quad (2.22)$$

Astronomic longitude Λ is obtained by comparing LAST with the Greenwich sidereal time (2.5):

$$\Lambda = \text{LAST} - \text{GAST}. \quad (2.23)$$

Equations (2.21) to (2.23) are the fundamental equations for determining Φ , Λ and A from measurements of z and GAST at given α , δ , cf. [5.3.2]. Equation (2.21) also follows from (2.20) if we take (2.11) and (2.29) into account.

For geodetic applications, the observations carried out in the local astronomic systems have to be transformed into the global geocentric system for further use in establishing geodetic control networks.

Due to the non-parallelism of the plumb lines, the orientation of the local systems depends on position and thus changes rapidly from place to place. Computations in one individual system are therefore admissible only in very limited areas when applying formulas of plane geometry.

The plumb line direction can be referred to the global geocentric-system by means of the "orientation" parameters astronomic latitude Φ and longitude Λ (Fig. 2.15). After a parallel shift of the global system into the local one (Fig. 2.16), we transform the latter one to a right-handed system by applying the reflection matrix

$$\mathbf{S}_2 = \begin{pmatrix} 1 & 0 & 0 \\ 0 & -1 & 0 \\ 0 & 0 & 1 \end{pmatrix}. \quad (2.24)$$

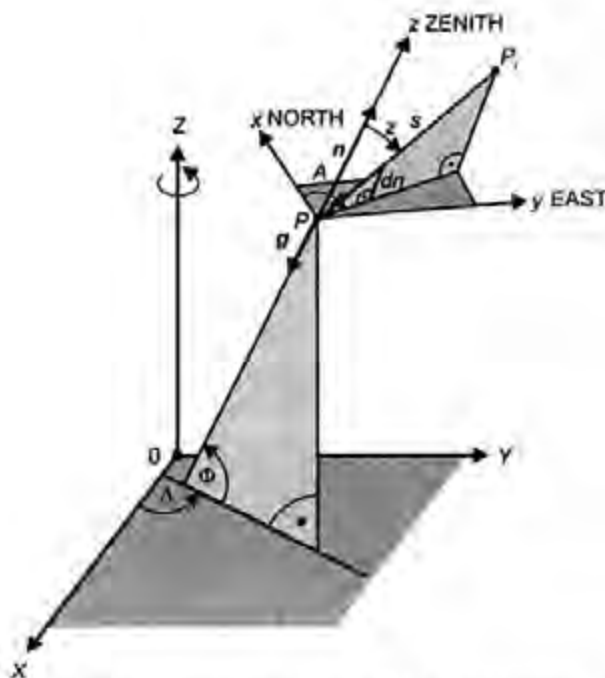


Fig. 2.15. Local astronomic and global geocentric system

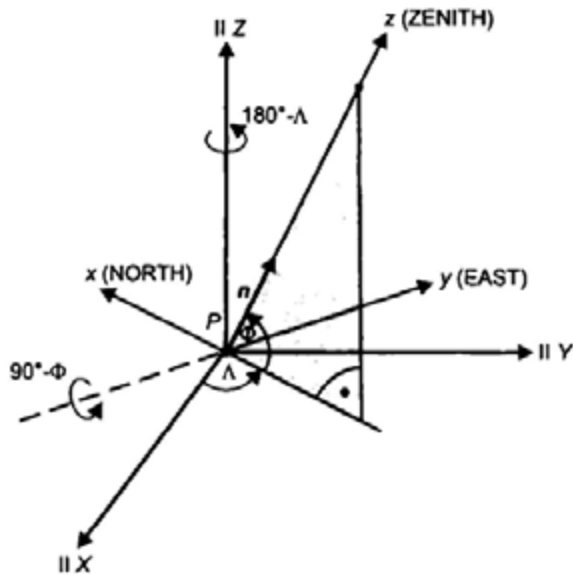


Fig. 2.16 Transformation between the local astronomic and the geocentric system

We then rotate the local system by $90^\circ - \Phi$ around the (new) y -axis and by $180^\circ - \Lambda$ around the z -axis with the rotation matrices

$$\mathbf{R}_2(90^\circ - \Phi) = \begin{pmatrix} \sin \Phi & 0 & -\cos \Phi \\ 0 & 1 & 0 \\ \cos \Phi & 0 & \sin \Phi \end{pmatrix} \quad \text{and}$$

$$\mathbf{R}_3(180^\circ - \Lambda) = \begin{pmatrix} -\cos \Lambda & \sin \Lambda & 0 \\ -\sin \Lambda & -\cos \Lambda & 0 \\ 0 & 0 & 1 \end{pmatrix}. \quad (2.25)$$

Coordinates differences between P_i and P in the geocentric system are thus obtained by

$$\Delta \mathbf{X} = \mathbf{A} \mathbf{x}, \quad (2.26)$$

with \mathbf{x} given by (2.20) and

$$\Delta \mathbf{X} = \begin{pmatrix} \Delta X \\ \Delta Y \\ \Delta Z \end{pmatrix}. \quad (2.27)$$

The transformation matrix reads as

$$\mathbf{A} = \mathbf{R}_3(180^\circ - \Lambda) \mathbf{R}_2(90^\circ - \Phi) \mathbf{S}_2 =$$

$$\begin{pmatrix} -\sin \Phi \cos \Lambda & -\sin \Lambda & \cos \Phi \cos \Lambda \\ -\sin \Phi \sin \Lambda & \cos \Lambda & \cos \Phi \sin \Lambda \\ \cos \Phi & 0 & \sin \Phi \end{pmatrix}. \quad (2.28)$$

The inversion of (2.26) is performed easily considering that \mathbf{A} is orthonormal:

$$\mathbf{A}^{-1} = \mathbf{A}^T.$$

We obtain

$$\mathbf{x} = \mathbf{A}^{-1} \Delta \mathbf{X}, \quad (2.29)$$

with

$$\mathbf{A}^{-1} = \begin{pmatrix} -\sin \Phi \cos \Lambda & -\sin \Phi \sin \Lambda & \cos \Phi \\ -\sin \Lambda & \cos \Lambda & 0 \\ \cos \Phi \cos \Lambda & \cos \Phi \sin \Lambda & \sin \Phi \end{pmatrix}. \quad (2.30)$$

Equations (2.27) to (2.30) are the basic equations for the evaluation of local geodetic measurements within the three-dimensional reference frame, cf. [6.2.1].

3 The Gravity Field of the Earth

The external gravity field plays a fundamental role in geodesy. This is because the figure of the earth has evolved under the influence of gravity, and most geodetic observations refer to gravity. Modeling of the observations thus requires knowledge of the gravity field. In addition, the analysis of the gravity field yields information on the structure of the earth's interior; in this way geodesy contributes to geophysics, cf.[8.2.4].

The fundamental quantities gravitation and gravity, together with their corresponding potentials, are introduced in [3.1], where the main properties of the gravity field are also described. The geometry of the gravity field is especially important for local applications [3.2], while the spherical harmonic expansion provides a powerful tool for a global gravity-field representation [3.3]. The geoid, as a physically defined reference surface for heights, is of basic interest in geosciences and engineering [3.4]. Gravity variations with time can be modeled in part (tidal effects), but to a large degree this work is still in the research stage [3.5].

The theory of the gravity field is extensively treated in geodetic and geophysical literature (e.g., HEISKANEN and VENING-MEINESZ 1958, HEISKANEN and MORITZ 1967, JEFFREYS 1970, PICK et al. 1973, GROTEK 1979).

3.1 Fundamentals of Gravity Field Theory

A body rotating with the earth experiences the gravitational force of the masses of the earth [3.1.1] to [3.1.3], and other celestial bodies as well as the centrifugal force due to the earth's rotation [3.1.4]. The resultant is the force of gravity [3.1.5]. In the case of artificial satellites, it is noted that a satellite does not rotate with the earth; hence, only gravitation acts on the satellite.

3.1.1 Gravitation, Gravitational Potential

According to Newton's law of gravitation (1687), two point masses m_1 and m_2 attract each other with the gravitational force (attractive force)

$$\mathbf{K} = -G \frac{m_1 m_2}{l^2} \frac{\mathbf{l}}{l}, \quad (3.1)$$

where G is the gravitational constant, cf. [2.1],

$$G = 6.673 \times 10^{-11} \text{ m}^3 \text{ kg}^{-1} \text{ s}^{-2}, \quad (3.2)$$

and l is the distance between the masses. The vectors \mathbf{K} and \mathbf{l} point in opposing directions. The SI-unit of K is m kg s^{-2} .

By setting the mass at the attracted point P to unity, (3.1) transforms into the gravitational acceleration (henceforth also termed gravitation):

$$\mathbf{b} = -G \frac{m \mathbf{l}}{l^2}. \quad (3.3)$$

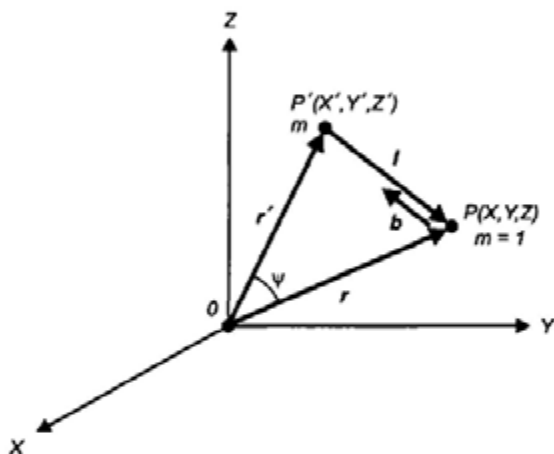


Fig. 3.1. Gravitation

\mathbf{b} originates at P and is directed towards the source point P' . The vector \mathbf{l} may be expressed by the position vectors \mathbf{r} and \mathbf{r}' (Fig. 3.1), e.g., in the global Cartesian X,Y,Z -system:

$$\mathbf{l} = \mathbf{r} - \mathbf{r}', \quad \mathbf{r}^T = (X, Y, Z), \quad \text{and} \quad \mathbf{r}'^T = (X', Y', Z'), \quad (3.4)$$

with

$$l = \|\mathbf{l}\| = \sqrt{(X - X')^2 + (Y - Y')^2 + (Z - Z')^2}.$$

The unit of the acceleration b is ms^{-2} .

As gravitation depends only on the distance between the attracting mass and the attracted point, it does not depend on the choice of the coordinate system. While global applications require a

geocentric coordinate system, local coordinate systems are useful for problems of limited spatial extent.

The *earth* is composed of an infinite number of differential mass elements dm . The gravitation on the unit mass at P results from the integral over the individual contributions. Equation (3.3) correspondingly transforms to

$$\mathbf{b} = \mathbf{b}(\mathbf{r}) = -G \iiint_{\text{earth}} \frac{\mathbf{r} - \mathbf{r}'}{|\mathbf{r} - \mathbf{r}'|^3} dm. \quad (3.5)$$

The mass element dm can be expressed by the volume density $\rho = \rho(\mathbf{r}')$ and the volume element dV :

$$dm = \rho dV, \quad (3.6)$$

where ρ is expressed in kg m^{-3} .

The representation of gravitational acceleration, the gravity field, and related computations are simplified if the scalar quantity "potential" is used instead of the vector quantity "acceleration." Because the gravitational field is invariant to rotations:

$$\operatorname{curl} \mathbf{b} = \mathbf{0}, \quad (3.7)$$

the vector \mathbf{b} may be represented as the gradient of a potential V (e.g., KELLOGG 1929, SIGL 1985):

$$\mathbf{b} = \operatorname{grad} V. \quad (3.8)$$

For a *point mass* m , see (3.3), we have

$$V = \frac{GM}{l}, \text{ with } \lim_{r \rightarrow \infty} V = 0. \quad (3.9)$$

For the *earth*, see (3.5) and (3.6), we obtain

$$V = V(\mathbf{r}) = G \iiint_{\text{earth}} \frac{dm}{l} = G \iiint_{\text{earth}} \frac{\rho}{l} dV, \quad \lim_{r \rightarrow \infty} V = 0. \quad (3.10)$$

The potential at P indicates the work that must be done by gravitation in order to move the unit mass from infinity ($V = 0$) to P . The unit of potential is $\text{m}^2 \text{s}^{-2}$.

If the density function $\rho = \rho(\mathbf{r})$ was known for the earth, (3.5) resp. (3.10) would permit calculation of the gravitation as a function of position. In reality, more detailed density information is available for the upper layers of the earth only, while global models merely consider radial density changes, cf. [3.1.2], [8.1]. Consequently, gravity-field *observations* have to be used in order to model the exterior gravity field.

3.1.2 Gravitation of a Spherically Symmetric Earth

To a first approximation, the earth can be viewed as a sphere with a centrally symmetric density structure, i.e. composed of spherical shells with constant density, cf. [8.1]. We calculate the gravitation in the interior and exterior of this model using the system of spherical coordinates r, ϑ, λ introduced in (2.14). For this purpose, the orientation of the system is changed such that the ϑ -axis coincides with the line joining the coordinate origin O and the calculation point P (Fig. 3.2).

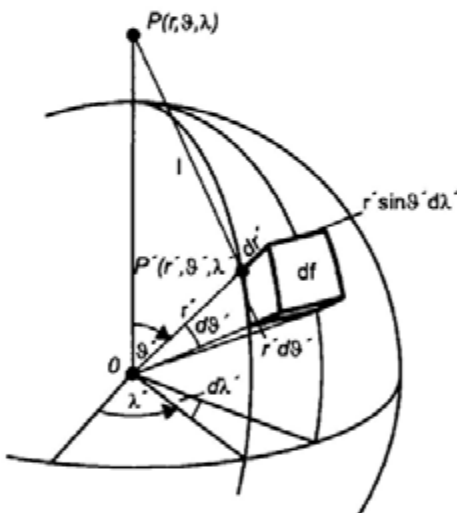


Fig. 3.2. Surface element of a spherical shell

The potential of a homogeneous *spherical shell* of radius r' with infinitesimal thickness dr' and density ρ is given in analogy to (3.10) by

$$V' = G\rho dr' \iint_f \frac{df}{l}. \quad (3.11)$$

Here, integration is over the surface of the shell f and

$$df = r'^2 \sin \vartheta' d\vartheta' d\lambda' \quad (3.12)$$

is the surface element. Inserting (3.12) into (3.11) gives

$$V' = G\rho r'^2 dr' \int_{\lambda'=0}^{2\pi} \int_{\vartheta'=0}^{\pi} \frac{\sin \vartheta'}{l} d\vartheta' d\lambda'. \quad (3.13)$$

A distinction is now made in the integration as to whether the attracted point P is exterior or interior to the spherical shell.

For an attracted point lying in the *exterior* ($r > r'$), the potential is given by integration of (3.13):

$$V'_e = 4\pi G\rho \frac{r'^2}{r} dr' = G \frac{dm'}{r}. \quad (3.14)$$

Here,

$$dm' = 4\pi\rho r'^2 dr' \quad (3.15)$$

represents the mass of the spherical shell. The potential of the *spherical earth* composed of concentric homogeneous shells is

$$V_e = G \iiint_{\text{earth}} \frac{dm'}{r} = \frac{GM}{r}. \quad (3.16)$$

Hence, it is equal to the potential of the entire mass M of the earth concentrated at the center of mass. The gravitation follows from

$$b_e = -\frac{\partial V_e}{\partial r} = \frac{GM}{r^2}. \quad (3.17)$$

With $GM = 398.6 \times 10^{12} \text{ m}^3 \text{s}^{-2}$ and the radius of the earth $R = 6371 \text{ km}$, the value of the potential at the surface of the earth ($r = R$) amounts to $V = 6.26 \times 10^7 \text{ m}^2 \text{s}^{-2}$, and the gravitation is $b = 9.82 \text{ ms}^{-2}$.

For a point in the *interior* ($r < r'$), we obtain from (3.13) for the potential of the spherical shell:

$$V'_i = 4\pi G\rho r' dr' = \frac{G dm'}{r'}. \quad (3.18)$$

Here, V' is constant; therefore, the gravitation is zero:

$$b'_i = -\frac{\partial V'_i}{\partial r} = 0. \quad (3.19)$$

The potential inside an *earth* constructed of *shells* includes the contribution of V'_i (3.14) due to the masses interior to the sphere $r = \text{const}$. It is also comprised of V'_i (3.18), which is due to the spherical shell having thickness $R - r$:

$$V'_i = \frac{4\pi G}{r} \int_0^r \rho r'^2 dr' + 4\pi G \int_r^R \rho r' dr'. \quad (3.20)$$

For a *homogeneous* earth ($\rho = \text{const.}$) we have

$$V'_i = \frac{4}{3}\pi G \rho r^2 + 2\pi G \rho (R^2 - r^2) = 2\pi G \rho \left(R^2 - \frac{r^2}{3} \right). \quad (3.21)$$

The gravitation of the earth composed of *shells* is

$$b_i = -\frac{\partial V'_i}{\partial r} = G \frac{m'}{r^2} \quad (3.22)$$

with

$$m' = 4\pi \int_0^r \rho r'^2 dr' \quad (3.23)$$

according to (3.15), which represents the mass inside the sphere $r = \text{const}$. The masses outside this sphere have no effect on the gravitation. For a *homogeneous* sphere, (3.22) and (3.23) transform to

$$b_i = \frac{4}{3}\pi G \rho r. \quad (3.24)$$

3.1.3 Properties of the Gravitational Potential

We now investigate the fundamental properties of the gravitational potential and its first and second derivatives.

Starting from the potential (3.10)

$$V = G \iiint_{\text{earth}} \frac{dm}{l}, \quad (3.25)$$

gravitation is given by the gradient (3.8) through the components, see (3.5),

$$\frac{\partial V}{\partial X} = V_x = -G \iiint_{\text{earth}} \frac{X - X'}{l^3} dm, \text{ etc.} \quad (3.26)$$

The second derivatives read as

$$\frac{\partial^2 V}{\partial X^2} = V_{xx} = -G \iiint_{\text{earth}} \frac{dm}{l^3} + 3G \iiint_{\text{earth}} \frac{(X - X')^2}{l^5} dm, \text{ etc.} \quad (3.27)$$

We now have to distinguish between the cases where the attracted point P lies exterior or interior to the earth's masses, cf. [3.1.2]. Here, we neglect the mass of the atmosphere (about 10^{-6} of the total mass) and the variations of gravitation with time (maximum relative effect about 10^{-7}). The earth's surface S then constitutes a boundary surface between the mass-free exterior space and the earth's interior.

If P lies exterior to the surface S , then $l > 0$ always. Then according to (3.25) - (3.27), the potential and its first and second derivatives are single-valued, finite and continuous functions, vanishing at infinity.

We now apply the Laplacian differential operator $\Delta = \operatorname{div} \operatorname{grad}$ to V . In the X, Y, Z -system, this reads as

$$\Delta V = V_{xx} + V_{yy} + V_{zz}. \quad (3.28)$$

When introducing (3.27) into (3.28), the first and second terms cancel each other. This leads to *Laplace's differential equation* of second order, which governs the exterior gravitational field:

$$\Delta V = 0. \quad (3.29)$$

Continuous functions having continuous first and second order derivatives and fulfilling (3.29) are called *harmonic functions*.

If the attracted body lies *inside* the body of the earth, then the case $l = 0$ is possible. This requires special attention because of the discontinuity of $1/l$.

To this end, we consider P enclosed by a sphere K (center at P_0 , radius p),

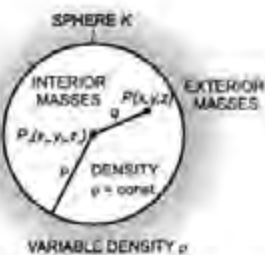


Fig. 3.3. Gravitational potential inside the earth

where p is chosen sufficiently small so that the density $\rho = \text{const.}$ inside K (Fig. 3.3). The potential at P is composed of the contributions from masses lying interior and exterior to K . From (3.10) and (3.21) and using

$$R = p, \quad r = q = \sqrt{(X - X_0)^2 + (Y - Y_0)^2 + (Z - Z_0)^2},$$

we find

$$V = G \iiint_{\text{earth}-K} \frac{dm}{l} + 2\pi G\rho \left(p^2 - \frac{q^2}{3} \right).$$

In the limits $p \rightarrow 0$ and $q \rightarrow 0$, agreement is obtained with the expression for the exterior potential (3.10). Differentiation yields

$$V_x = -G \iiint_{\text{earth}-K} \frac{X - X'}{l^3} dm - \frac{4}{3}\pi G\rho(X - X_0), \text{ etc.}$$

As $q \rightarrow 0$, we also have $X - X_0 = Y - Y_0 = Z - Z_0 \rightarrow 0$, so that once again we obtain agreement with the exterior case (3.26). The second derivatives are given by

$$V_{xx} = -G \iiint_{\text{earth}-K} \frac{1}{l^3} dm + 3G \iiint_{\text{earth}-K} \frac{(X - X')^2}{l^5} dm - \frac{4}{3}\pi G\rho, \text{ etc.}$$

For $q \rightarrow 0$, the last term does not vanish:

$$V_{xx} = -\frac{4}{3}\pi G\rho, \text{ etc.} \quad (3.30)$$

The gravitational potential and its first derivatives are thus single-valued, finite, and continuous in the interior as well. According to (3.30), the second derivatives exhibit discontinuities at abrupt changes in density. Inserting (3.30) into (3.28), we get *Poisson's differential equation*:

$$\Delta V = -4\pi G \rho . \quad (3.31)$$

Hence, V is not a harmonic function in the interior of the earth.

Finally, we mention *Gauss' integral formula*, which connects the normal derivatives $\partial V / \partial n_s$ on any boundary surface S (which in general is not an equipotential surface) and the second derivatives contained in the Laplace operator (3.28):

$$\iint_S \frac{\partial V}{\partial n_s} dS = \iiint_V \Delta V dv . \quad (3.32)$$

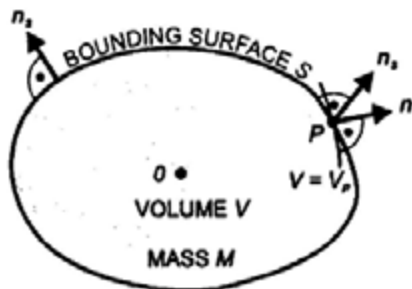


Fig. 3.4. Outer surface normal on the bounding surface and on the equipotential surface

Here, v is the volume of the body of surface S (Fig. 3.4). The left-side term may be interpreted as "gravitational flux" through S . As shown in potential theory, it is proportional to the total mass

$$M = \iiint_v dm = \iiint_v \rho(\mathbf{r}') dv \quad (3.33)$$

according to

$$\iint_S \frac{\partial V}{\partial n_s} dS = -4\pi GM . \quad (3.34)$$

Taking the limit at the source point P' in (3.34), equation (3.32) reduces to Poisson's differential equation (3.31) and to Laplace's differential equation for the exterior space ($\rho = 0$). Based on Gauss' formula, basic relationships can be established between observations in the gravity field and parameters describing the surface S , cf. [6.5.1].

3.1.4 Centrifugal Acceleration, Centrifugal Potential

The centrifugal force acts on an object of mass on the earth's surface. It arises as a result of the rotation of the earth about its axis. We assume here a rotation of constant angular velocity ω about the rotational axis, with the axis assumed fixed with the earth. The small effects of time variations of the rotational vector can be taken into account by reductions, cf. [2.5.2]. The centrifugal acceleration

$$\mathbf{z} = (\boldsymbol{\omega} \times \mathbf{r}) \times \boldsymbol{\omega} = \omega^2 \mathbf{p} \quad (3.35a)$$

acting on a unit mass is directed outward and is perpendicular to the spin axis (Fig. 3.5). With the geocentric latitude $\bar{\varphi}$, we have

$$p = r \cos \bar{\varphi}$$

and the magnitude

$$z = |\mathbf{z}| = \omega^2 r \cos \bar{\varphi}. \quad (3.35b)$$

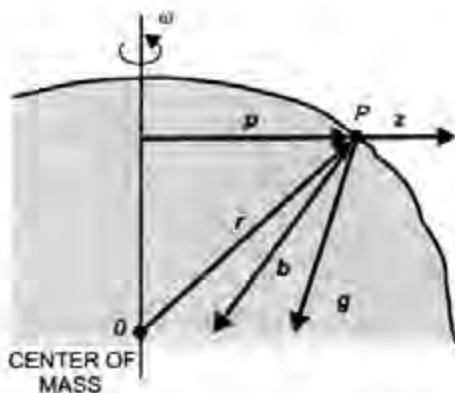


Fig. 3.5. Gravitation, centrifugal acceleration, and gravity

The angular velocity

$$\omega = 7.292\,115 \times 10^{-5} \text{ rad s}^{-1} \quad (3.36)$$

is known with high accuracy from astronomy, cf. [2.2.2]. Consequently, $z = |\mathbf{z}|$ can be calculated if the position of P is known.

As the Z -axis of the earth-fixed X, Y, Z -system coincides with the axis of rotation, cf. [2.5.1], we have

$$\mathbf{p} = \begin{pmatrix} X \\ Y \\ 0 \end{pmatrix}, \quad p = |\mathbf{p}| = \sqrt{X^2 + Y^2}.$$

With

$$\mathbf{z} = \text{grad } Z, \quad (3.37)$$

we introduce the *centrifugal potential*

$$Z = Z(p) = \frac{\omega^2}{2} p^2, \quad \lim_{p \rightarrow 0} Z = 0. \quad (3.38)$$

Remark: Here, the symbols z and Z are used for the centrifugal acceleration and potential respectively. They were introduced earlier for local and global coordinates and will be employed again as such in later sections.

Differentiating twice and applying the Laplacian operator yields

$$\Delta Z = 2\omega^2. \quad (3.39)$$

Therefore, the analytic function Z , as opposed to V (3.29), is not harmonic.

For points on the equator of the earth, the centrifugal potential has a value of $1.1 \times 10^5 \text{ m}^2 \text{s}^{-2}$, and the centrifugal acceleration is 0.03 ms^{-2} ($\approx 0.3\%$ of gravitation). At the poles, we have $Z = 0$ and $z = 0$.

3.1.5 Gravity Acceleration, Gravity Potential

The gravity acceleration, or *gravity* \mathbf{g} (Latin: *gravitas*), is the resultant of gravitation \mathbf{b} and centrifugal acceleration \mathbf{z} (Fig. 3.5):

$$\mathbf{g} = \mathbf{b} + \mathbf{z}. \quad (3.40)$$

By multiplying with the mass m of the attracted point, we obtain the force of gravity

$$\mathbf{F} = m\mathbf{g}. \quad (3.41)$$

The direction of \mathbf{g} is referred to as the direction of the *plumb line* (vertical); the magnitude g is called gravity intensity (often just gravity). With (3.10) and (3.38), the *gravity potential* of the earth becomes

$$W = W(\mathbf{r}) = V + Z = G \iiint_{\text{earth}} \frac{\rho}{l} dv + \frac{\omega^2}{2} p^2. \quad (3.42)$$

It is related to the *gravity acceleration* by

$$\mathbf{g} = \text{grad } W. \quad (3.43)$$

In the X, Y, Z -system, we have

$$\mathbf{g}^T = (\text{grad } W)^T = (W_x, W_y, W_z). \quad (3.44)$$

Taking (2.19) into account, we obtain the components of gravity expressed by the plumb line parameters Φ, Λ :

$$\mathbf{g} = -g\mathbf{n} = -g \begin{pmatrix} \cos \Phi \cos \Lambda \\ \cos \Phi \sin \Lambda \\ \sin \Phi \end{pmatrix}. \quad (3.45)$$

The property

$$\text{curl } \mathbf{g} = \text{curl grad } W = 0 \quad (3.46)$$

follows from the corresponding properties of gravitation and centrifugal acceleration and can also be expressed by the conditions

$$W_{xx} = W_{yy}, \quad W_{xz} = W_{zx}, \quad W_{yz} = W_{zy}. \quad (3.47)$$

W and its first derivatives are single-valued, finite, and continuous in the whole space as a consequence of the characteristics of V and Z . Exceptions are the uninteresting cases $r \rightarrow \infty$ (then also $Z \rightarrow \infty$) and $g = 0$ (direction of the plumb line is not unique). Due to the behavior of V , the second derivatives of W are discontinuous inside the earth at abrupt density changes. For geodesy, the most

important surface of discontinuity is the physical surface of the earth, with a density jump from 1.3 kg m^{-3} (density of air) to 2700 kg m^{-3} (mean density of the upper crust).

From (3.31) and (3.39), we obtain the generalized Poisson differential equation

$$\Delta W = -4\pi G\rho + 2\omega^2. \quad (3.48)$$

In outer space ($\rho = 0$), it becomes the generalized Laplace differential equation

$$\Delta W = 2\omega^2. \quad (3.49)$$

With the conditions (3.47) and (3.48) resp. (3.49), the gravity potential W possesses only five (out of nine) mutually independent second derivatives. They are closely related to the curvature of the level surfaces and the plumb lines, cf. [3.2.2].

Because of the flattening at the earth's poles and the centrifugal acceleration, g depends on the latitude. The value of gravitation for a spherical model, 9.82 ms^{-2} , cf. [3.1.2], decreases at the equator and increases at the poles of an ellipsoidal model. The centrifugal acceleration further diminishes the equatorial value, while gravitation at the poles is not influenced by centrifugal acceleration, cf. [3.1.4]. As a result, gravity varies between 9.78 ms^{-2} (equator) and 9.83 ms^{-2} (poles), see also [4.3].

3.2 Geometry of the Gravity Field

A geometrical representation of the gravity field is given by the level surfaces and the plumb lines [3.2.1]. Local field properties are described by the curvatures of level surfaces and plumb lines [3.2.2], and a system of "natural" coordinates can be based on these properties [3.2.3].

3.2.1 Level Surfaces and Plumb Lines

The surfaces of constant gravity potential

$$W = W(\mathbf{r}) = \text{const.} \quad (3.50)$$

are designated as *equipotential* or *level surfaces* (also geopotential surfaces) of gravity. As a result of an infinitesimal displacement $d\mathbf{s}$, and in view of (3.43), the potential difference of differentially separated level surfaces (Fig. 3.6) is given by

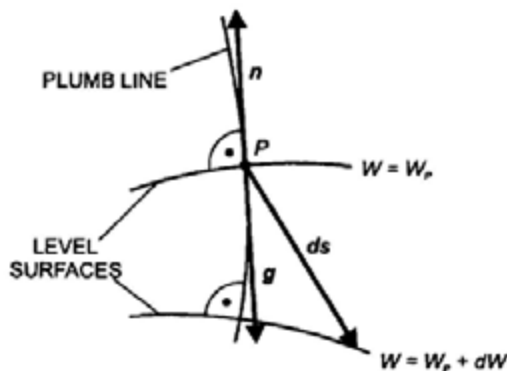


Fig. 3.6. Neighboring level surfaces

$$dW = \mathbf{g} \cdot d\mathbf{s} = g d\mathbf{s} \cos(\mathbf{g}, d\mathbf{s}). \quad (3.51)$$

This means that the derivative of the gravity potential in a certain direction is equal to the component of the gravity along this direction. Since only the projection of $d\mathbf{s}$ along the plumb line enters into (3.51), dW is independent of the path. Hence, no work is necessary for a displacement along a level surface $W = \text{const.}$; the level surfaces are *equilibrium* surfaces.

If $d\mathbf{s}$ is taken along the level surface $W = W_p$, then it follows from $dW = 0$ that $\cos(\mathbf{g}, d\mathbf{s}) = \cos 90^\circ = 0$: gravity is normal to $W = W_p$. The level surfaces are intersected at right angles by the *plumb lines*. The tangent to the plumb line is called the *direction* of the plumb line and has been defined already in [3.1.5]. If $d\mathbf{s}$ is directed along the outer surface normal \mathbf{n} , then, because $\cos(\mathbf{g}, \mathbf{n}) = \cos 180^\circ = -1$, the following important relationship exists:

$$dW = -g d\mathbf{n}. \quad (3.52)$$

It provides the link between the potential difference (a physical quantity) and the difference in height (a geometric quantity) of neighboring level surfaces. According to this relation, a combination of gravity measurements and (quasi) differential height determinations, as provided by geometric leveling, delivers gravity potential differences, cf. [5.5.3].

If g varies on a level surface, then, according to (3.52), the distance $d\mathbf{n}$ to a neighboring level surface also changes. Therefore, the level surfaces are not parallel, and the plumb lines are space curves. As a consequence of the gravity increase of 0.05 ms^{-2} from the equator to the poles, the level surfaces of the earth converge toward the poles by $0.05 \text{ ms}^{-2} / 9.8 \text{ ms}^{-2}$, or 5×10^{-3} , in a relative sense. Consequently, two level surfaces that are 100.0 m apart at the equator are separated by only 99.5 m at the poles (Fig. 3.7).

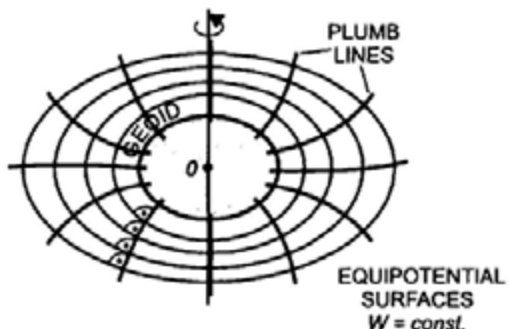


Fig. 3.7. Equipotential surfaces and plumb lines close to the earth

The level surfaces inside the earth and in the exterior space are closed spheroidal surfaces. The geoid is the level surface that approximates mean sea level. Because of its importance as a reference surface for heights, it will be treated separately in [3.4]. As an outer limit in the realm of the definition of gravity, one may consider the level surface for which the gravitation and centrifugal acceleration in the equatorial plane cancel each other. The equatorial radius of this surface would be 42 200 km.

The concept of the level surface was introduced by *MacLaurin* (1742), whereas *Clairaut* (1743) thoroughly discussed level surfaces and plumb lines as a whole. *BRUNS* (1878) included the determination of the exterior level surfaces in their entirety in the fundamental problem of geodesy.

3.2.2 Local Gravity Field Representation, Curvatures

From the properties of the potential function $W = W(\mathbf{r})$, it follows that the level surfaces which lie entirely in the exterior space are analytical surfaces; that is, they have no salient or singular points, cf. [3.1.5], and can be expanded in Taylor series. Level surfaces extending partially or completely inside the earth exhibit discontinuities in the second derivatives where density jumps occur. These surfaces can thus be constructed from pieces of different analytical surfaces only.

Using the local astronomic x,y,z -system introduced in [2.6.2], we develop the potential W in the vicinity of the origin P into a series. This local representation reads as

$$\begin{aligned} W = & W_p + W_x + W_y + W_z + \frac{1}{2} (W_{xx}x^2 + W_{yy}y^2 + W_{zz}z^2) \\ & + W_{xy}xy + W_{xz}xz + W_{yz}yz + \dots \end{aligned} \quad (3.53)$$

Here, $W_x = \partial W / \partial x$, $W_{xx} = \partial^2 W / \partial x^2$, $W_{yy} = \partial^2 W / \partial y^2$, etc. represent the first and second order partial derivatives at P in the local system. If the calculation point is located on the level surface through P , we have

$$W = W_P, \quad W_x = W_y = 0, \quad W_z = -g.$$

By solving for z , we get the equation of the *level surface* in the neighborhood of P :

$$z = \frac{1}{2g} (W_{xx}x^2 + 2W_{xy}xy + W_{yy}y^2). \quad (3.54)$$

Here, we have neglected terms of third and higher order, taking into account that z is of second order compared to x and y , due to the small curvature of the level surfaces.

The *curvature* of the *level surface* at P along an azimuth A is described by the curvature of the normal section (intersection of the vertical plane with the surface), which is called *normal curvature*. The well-known formula for the depression of a sphere (local approximation to the level surface) with respect to the horizontal x,y -plane gives

$$z = -\frac{s^2}{2R_A}, \quad (3.55)$$

with s = distance from P and R_A = radius of curvature in the azimuth A (Fig. 3.8). We substitute x,y with the local polar coordinates s,A

$$x = s \cos A, \quad y = s \sin A$$

and introduce (3.55) into (3.54). The *normal curvature* then reads as

$$k = \frac{1}{R_A} = -\frac{1}{g} (W_{xx} \cos^2 A + 2W_{xy} \sin A \cos A + W_{yy} \sin^2 A). \quad (3.56)$$

For the x and y -directions ($A = 0^\circ$ and $A = 180^\circ$), we obtain the curvatures

$$k_x = \frac{1}{R_x} = -\frac{W_{xx}}{g}, \quad k_y = \frac{1}{R_y} = -\frac{W_{yy}}{g}, \quad (3.57)$$

where R_x and R_y are the corresponding curvature radii. Analogously, the geodetic torsion in the direction of the meridian (expressing the change of

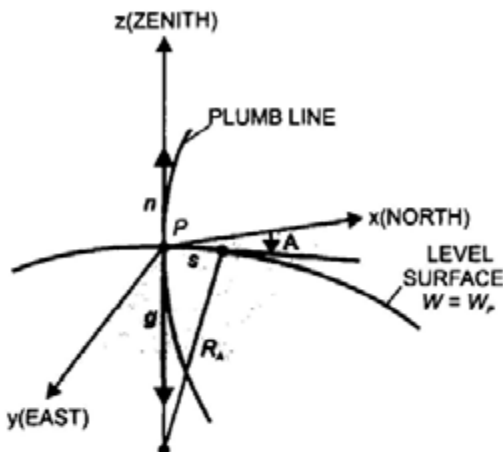


Fig. 3.8. Curvature of level surfaces and plumb lines

direction normal to the meridian) is given by

$$t_x = -\frac{W_{yy}}{g}. \quad (3.58)$$

The normal curvature assumes its extreme values in the mutually perpendicular directions of *principal curvature* A_1 and $A_2 = A_1 \pm 90^\circ$. By considering the extrema, we find

$$\tan 2A_{1,2} = 2 \frac{W_{yy}}{W_{xx} - W_{yy}}. \quad (3.59)$$

Introducing (3.59) into (3.56) yields the corresponding principal curvatures

$$\frac{1}{R_{A(1,2)}} = -\frac{1}{g} (W_{xx} + W_{yy} \tan A_{1,2}). \quad (3.60)$$

The *mean curvature* of the level surface is given by

$$J = \frac{1}{2} (k_x + k_y) = -\frac{1}{2g} (W_{xx} + W_{yy}). \quad (3.61)$$

Outside the masses of the earth, the *plumb lines* can also be described analytically. In the local astronomic system, the equation of the plumb line is given by

$$x = x(s), \quad y = y(s), \quad z = z(s), \quad (3.62)$$

where s is the arc length reckoned in the direction of gravity (Fig. 3.8). The line element along s thus differs from gravity only by the "scale factor" g :

$$g \begin{pmatrix} x' \\ y' \\ z' \end{pmatrix} = \begin{pmatrix} W_x \\ W_y \\ W_z \end{pmatrix}, \quad (3.63)$$

with $x' = ds/dx$, etc. The curvature vector of the plumb line lies in the principal normal through P and thus in the horizontal plane. It reads as

$$\begin{pmatrix} x'' \\ y'' \\ z'' \end{pmatrix} = \kappa \begin{pmatrix} \cos A \\ \sin A \\ 0 \end{pmatrix}, \quad (3.64)$$

where κ is the total curvature, and A is the azimuth of the principal normal. Differentiating (3.63) with respect to s , and considering that at P : $x' = y' = 0, z' = -1$, a substitution into (3.64) yields

$$\kappa = -\frac{W_x}{g \cos A} = -\frac{W_{yz}}{g \sin A} \quad (3.65)$$

and

$$A = \arctan \frac{W_y}{W_x}. \quad (3.66)$$

The *curvatures* of the projections of the plumb line on the x,z -plane ($A = 0^\circ$) and y,z -plane ($A = 90^\circ$) follow from (3.65):

$$\kappa_x = -\frac{W_x}{g}, \quad \kappa_y = -\frac{W_{yz}}{g}, \quad (3.67)$$

where

$$\kappa = \sqrt{\kappa_x^2 + \kappa_y^2}.$$

From (3.56) to (3.67), we recognize that the curvatures of the level surfaces and the plumb lines depend on the second derivatives of the gravity potential. Consequently, they experience discontinuities at abrupt density changes, as discussed for the potential function, cf. [3.1.5].

The *gravity gradient tensor* (*Eötvös tensor*) is comprised of the second derivatives of W as follows:

$$[W_{ij}] = \text{grad } \mathbf{g} = \text{grad}(\text{grad } W) = \begin{pmatrix} W_{xx} & W_{xy} & W_{xz} \\ W_{yx} & W_{yy} & W_{yz} \\ W_{zx} & W_{zy} & W_{zz} \end{pmatrix}. \quad (3.68)$$

With (3.57), (3.58), (3.67), and $W_z = -g$, it can be transformed into the *Marussi tensor*

$$[w_{ij}] = -\frac{[W_{ij}]}{g} = \begin{pmatrix} k_x & t_x & K_x \\ t_x & k_y & K_y \\ K_x & K_y & \frac{1}{g} \frac{\partial g}{\partial z} \end{pmatrix}, \quad (3.69)$$

which completely describes the geometry of the gravity field (GRAFAREN 1986, MORITZ and HOFMANN-WELLENHOF 1993). As already stated in [3.1.5], (3.68) resp. (3.69) only contain five independent elements.

The Eötvös tensor (3.68) includes the *gravity gradient*

$$\text{grad } \mathbf{g} = -\begin{pmatrix} W_{xy} \\ W_{yz} \\ W_{zx} \end{pmatrix} = \begin{pmatrix} \partial g / \partial x \\ \partial g / \partial y \\ \partial g / \partial z \end{pmatrix}, \quad (3.70)$$

which describes the variation of gravity in the horizontal plane and in the vertical direction. The horizontal gradient is formed by the components $\partial g / \partial x$ and $\partial g / \partial y$, and points in the direction of maximum gravity increase in the horizontal plane. The vertical component (often called vertical gradient) $\partial g / \partial z$ describes the gravity change with height. If we combine the generalized Poisson equation (3.48) with the mean curvature (3.61), we get

$$\Delta W = W_{xx} + W_{yy} + W_{zz} = -2gJ - \frac{\partial g}{\partial z} = -4\pi G\rho + 2\omega^2$$

or

$$\frac{\partial g}{\partial z} = -2gJ + 4\pi G\rho - 2\omega^2. \quad (3.71)$$

This relation was found by BRUNS (1878). It connects the vertical gradient with the mean curvature of the level surface and offers a possibility to determine this curvature from gravity measurements, cf. [5.4.5].

3.2.3 Natural Coordinates

We introduce a system of non-linear "natural" coordinates Φ, Λ, W defined in the gravity field. Astronomical latitude Φ and astronomical longitude Λ describe the direction of the plumb line at the point P . They have been introduced already in [2.6.1] as orientation parameters of the local gravity field system with respect to the global geocentric system. The gravity potential W locates P in the system of level surfaces $W = \text{const.}$ (Fig. 2.12). Hence, P is determined by the non-orthogonal intersection of the coordinate surfaces $\Phi = \text{const.}$, $\Lambda = \text{const.}$, and the surface $W = \text{const.}$ The coordinate lines (spatial curves) are called astronomic meridian curve ($\Lambda, W = \text{const.}$), astronomic parallel curve ($\Phi, W = \text{const.}$), and isozenithal line ($\Phi, \Lambda = \text{const.}$).

The natural coordinates can be determined by measurements. Astronomic positioning provides latitude and longitude, cf. [5.3.2]. Although W cannot be measured directly, potential differences can be derived from leveling and gravity measurements and then referred to a selected level surface, e.g., the geoid, cf. [5.5.3].

The relationship between the global X, Y, Z -system and the Φ, Λ, W -system is obtained from (3.45):

$$\mathbf{g} = \text{grad } W = -g \begin{pmatrix} \cos \Phi \cos \Lambda \\ \cos \Phi \sin \Lambda \\ \sin \Phi \end{pmatrix}. \quad (3.72)$$

Solving for the natural coordinates yields the highly non-linear relations:

$$\left. \begin{aligned} \Phi &= \arctan \frac{-W_z}{\sqrt{W_x^2 + W_y^2}} \\ \Lambda &= \arctan \frac{W_y}{W_x} \\ W &= W(X, Y, Z) \end{aligned} \right\}. \quad (3.73)$$

Differential relations between the *local* Cartesian coordinates x, y, z (local astronomic system) and the *global* Φ, Λ, W -system are given by

$$d\Phi = \frac{\partial \Phi}{\partial x} dx + \frac{\partial \Phi}{\partial y} dy + \frac{\partial \Phi}{\partial z} dz, \text{ etc.,}$$

where dx, dy , and dz can be derived from local measurements, cf. [2.6.2].

The partial derivatives of Φ and Λ describe the change of the plumb line direction when moving in the gravity field. This corresponds to the curvature of the level surface (when moving in the horizontal plane) and of the plumb line (when moving vertically). We have the following relations:

$$\left. \begin{aligned} \frac{\partial \Phi}{\partial x} &= k_x, \quad \frac{\partial \Phi}{\partial y} = \frac{\cos \Phi \partial \Lambda}{\partial x} = t_x, \quad \frac{\partial \Phi}{\partial z} = \kappa_x \\ \frac{\cos \Phi \partial \Lambda}{\partial y} &= k_y, \quad \frac{\cos \Phi \partial \Lambda}{\partial z} = \kappa_y \\ \frac{\partial W}{\partial x} &= 0, \quad \frac{\partial W}{\partial y} = 0, \quad \frac{\partial W}{\partial z} = -g \end{aligned} \right\}, \quad (3.74)$$

where the curvature and torsion parameters are given by (3.57), (3.58), and (3.67). Introducing (3.74) into the differential relations leads to the transformation

$$\begin{pmatrix} d\Phi \\ \cos \Phi d\Lambda \\ dW \end{pmatrix} = \begin{pmatrix} k_x & t_x & \kappa_x \\ t_x & k_y & \kappa_y \\ 0 & 0 & -g \end{pmatrix} \begin{pmatrix} dx \\ dy \\ dz \end{pmatrix}, \quad (3.75)$$

which again contains the elements of the Marussi tensor (3.69), see GRAFARENDE (1972), MORITZ and HOFMANN-WELLENHOF (1993).

As the orientation of the local systems changes from point to point, the differentials dx , dy , dz are imperfect ones, with loop closures differing from zero:

$$\oint dx \neq 0, \oint dy \neq 0, \oint dz \neq 0. \quad (3.76)$$

Φ, Λ, W , on the other hand, possess perfect differentials with

$$\oint d\Phi = 0, \oint d\Lambda = 0, \oint dW = 0. \quad (3.77)$$

Equation (3.75) offers the possibility to transform local observable-quantities (azimuths, horizontal directions and angles, zenith angles, distances, potential differences from leveling and gravity) to the global gravity field system, where the astronomic latitude and longitude coordinates are also observable.

A theory of "intrinsic geodesy" based on the differential geometry of the gravity field has been developed by MARUSSI (1949, 1985), see also HOTINE (1969). Using only observable quantities, reductions to conventional reference systems are completely avoided. On the other hand, in order to practically evaluate (3.75), a detailed knowledge of the curvature of the gravity field would be necessary. This would require a dense survey of the second derivatives of the gravity potential, as the curvature close to the earth's surface is rather irregular. Present gravity models do not sufficiently provide this information, and gravity gradiometer techniques are either time consuming or not yet operational, cf. [5.4.5]. But even with a better knowledge of the curvature of the gravity field, the transfer of coordinates would hardly be made in the system of natural coordinates, due to the complex structure of the gravity field.

3.3 Spherical Harmonic Expansion of the Gravitational Potential

Because the density function $\rho = \rho(\mathbf{r})$ of the earth is not well known, the gravitational potential $V = V(\mathbf{r})$ cannot be computed by Newton's law of gravitation using (3.10). However, a convergent series expansion of V is possible in the exterior space as a special solution of Laplace's differential equation (3.29). It can be easily derived from an expansion of the reciprocal distance appearing in Newton's law [3.3.1], [3.3.2], see KELLOGG (1929), SIGL (1985), BLAKELEY (1996). This solution corresponds to a spectral decomposition of the gravitational field [3.3.3]. The coefficients of the series expansion provide the amplitudes of the respective spectral parts [3.3.4]. Any observable functional of V can be evaluated for the determination of these coefficients, thus allowing a global analytical representation of the gravitational field, cf. [6.6.1].

3.3.1 Expansion of the Reciprocal Distance

Applying the law of cosines to the triangle $OP'P$ (Fig. 3.1), we obtain

$$\frac{1}{l} = \left(r^2 + r'^2 - 2rr' \cos\psi \right)^{-\frac{1}{2}} = \frac{1}{r} \left(1 + \left(\frac{r'}{r} \right)^2 - 2 \frac{r'}{r} \cos\psi \right)^{-\frac{1}{2}} \quad (3.78)$$

for the reciprocal distance $1/l$ appearing in (3.10), between the attracted point P and the attracting point P' . Here, ψ is the central angle between the directions from O to P and O to P' respectively. If $1/l$ is expanded in a series converging for $r' < r$, and if the terms are arranged according to increasing powers of r'/r , then it follows that

$$\frac{1}{l} = \frac{1}{r} \sum_{l=0}^{\infty} \left(\frac{r'}{r} \right)^l P_l(\cos\psi). \quad (3.79)$$

The $P_l(\cos\psi)$ terms represent polynomials of l^{th} degree in $\cos\psi$. They are known as *Legendre polynomials* (zonal harmonics), and they are computed for the argument $t = \cos\psi$ by means of

$$P_l(t) = \frac{1}{2^l \times l!} \times \frac{d^l}{dt^l} (t^2 - 1)^l. \quad (3.80a)$$

A rapid calculation is possible with the recurrence formula (WENZEL 1985)

$$P_l(t) = \frac{2l-1}{l} t P_{l-1}(t) - \frac{l-1}{l} P_{l-2}(t), \quad l \geq 2, \quad (3.80b)$$

with $P_0 = 1$, $P_1 = t$.

We now introduce the unit sphere σ around the origin of the coordinates O (Fig. 3.9). The projections of OP and OP' on σ , together with the north pole projection N , form a spherical triangle. It contains the spherical coordinates ϑ, λ and ϑ', λ' , and the central angle ψ appears as a spherical distance on σ , see also [2.5.1]. Spherical trigonometry provides the following relationship

$$\cos\psi = \cos\vartheta \cos\vartheta' + \sin\vartheta \sin\vartheta' \cos(\lambda' - \lambda).$$

The corresponding decomposition of $P_l(\cos\psi)$ leads to

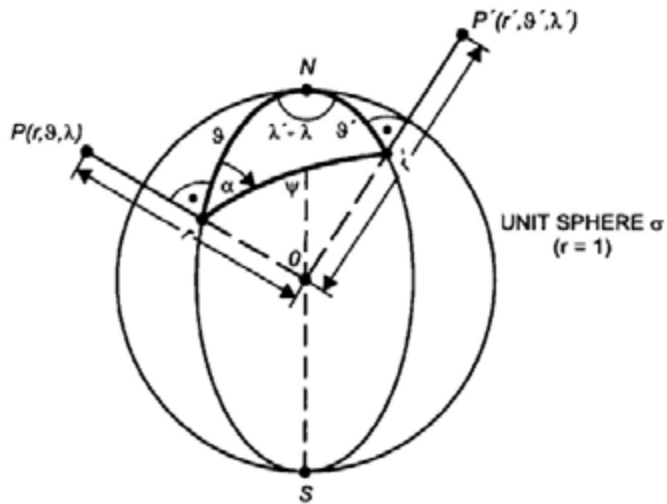


Fig. 3.9. Spherical polar triangle on the unit sphere, spherical coordinates

$$\begin{aligned}
 P_l(\cos \psi) &= P_l(\cos \vartheta) P_l(\cos \vartheta') \\
 &+ 2 \sum_{m=1}^l \frac{(l-m)!}{(l+m)!} (P_{lm}(\cos \vartheta) \cos m\lambda P_{lm}(\cos \vartheta') \cos m\lambda' \\
 &+ P_{lm}(\cos \vartheta) \sin m\lambda P_{lm}(\cos \vartheta') \sin m\lambda'). \tag{3.81}
 \end{aligned}$$

Again, the $P_l(t)$ are the Legendre polynomials with the argument $t = \cos \vartheta$ or $t = \cos \vartheta'$. The *associated* Legendre functions of the first kind, $P_{lm}(t)$ (l = degree, m = order), are obtained by differentiating $P_l(t)$ m times with respect to t :

$$P_{lm}(t) = (1-t^2)^{\frac{m}{2}} \frac{d^m}{dt^m} P_l(t). \tag{3.82}$$

Up to degree 3, the Legendre polynomials and the associated Legendre functions are given as follows:

$$P_0 = 1, P_1 = \cos \vartheta, P_2 = \frac{3}{2} \cos^2 \vartheta - \frac{1}{2}, P_3 = \frac{5}{2} \cos^3 \vartheta - \frac{3}{2} \cos \vartheta \tag{3.83a}$$

and

$$\left. \begin{aligned} P_{1,1} &= \sin \vartheta, \quad P_{2,1} = 3 \sin \vartheta \cos \vartheta, \quad P_{2,2} = 3 \sin^2 \vartheta \\ P_{3,1} &= \sin \vartheta \left(\frac{15}{2} \cos^2 \vartheta - \frac{3}{2} \right), \quad P_{3,2} = 15 \sin^2 \vartheta \cos \vartheta, \quad P_{3,3} = 15 \sin^3 \vartheta \end{aligned} \right\}. \quad (3.83b)$$

A series development for the calculation of $P_{lm}(t)$ is given in HEISKANEN and MORITZ (1967, p.24). By substituting (3.81) into (3.79), the expansion of $1/l$ into spherical harmonics is completed.

The functions

$$\left. \begin{aligned} Y_{lm}^c(\vartheta, \lambda) &= P_{lm}(\cos \vartheta) \cos m\lambda \\ Y_{lm}^s(\vartheta, \lambda) &= P_{lm}(\cos \vartheta) \sin m\lambda \end{aligned} \right\}, \quad (3.84)$$

which appear in (3.81), are called *Laplace's surface spherical harmonics*. They characterize the behavior of the developed function (here $1/l$) on the unit sphere, cf. [3.3.3]. The *orthogonality* relations are valid for these functions, i.e., the integral over the unit sphere of the product of any two different functions is zero:

$$\iint_{\sigma} Y_{lm}^i Y_{nq}^k d\sigma = 0 \quad (3.85a)$$

for $n \neq l$, $q \neq m$, or $k \neq i$. For the product of two equal functions Y_{lm}^c or Y_{lm}^s , we have

$$\iint_{\sigma} Y_{lm}^2 d\sigma = \begin{cases} \frac{4\pi}{2l+1} & \text{for } m=0 \\ \frac{2\pi}{2l+1} \frac{(l+m)!}{(l-m)!} & \text{for } m \neq 0 \end{cases}, \quad (3.85b)$$

see HEISKANEN and MORITZ (1967, p.29).

3.3.2 Expansion of the Gravitational Potential

We substitute the spherical harmonic expansion of $1/l$, (3.79) and (3.81), into the volume integral (3.10):

$$\begin{aligned}
 V = & \frac{G}{r} \sum_{l=0}^{\infty} \sum_{m=0}^l k \frac{(l-m)!}{(l+m)!} \times \\
 & \left. \frac{1}{r^l} \left(\begin{array}{l} P_{lm}(\cos \vartheta) \cos m\lambda \iiint_{\text{earth}} r'' P_{lm}(\cos \vartheta') \cos m\lambda' dm \\ + P_{lm}(\cos \vartheta) \sin m\lambda \iiint_{\text{earth}} r'' P_{lm}(\cos \vartheta') \sin m\lambda' dm \end{array} \right) \right). \quad (3.87) \\
 k = & \begin{cases} 1 & \text{for } m=0 \\ 2 & \text{for } m \neq 0 \end{cases}
 \end{aligned}$$

In abbreviated form this development can be expressed as

$$V = \sum_{l=0}^{\infty} V_l = \sum_{l=0}^{\infty} \frac{Y_l(\vartheta, \lambda)}{r^{l+1}}, \quad (3.88)$$

where the V_l are called *solid spherical harmonics*, and the $Y_l(\vartheta, \lambda)$ are linear combinations of the surface spherical harmonics (3.84).

For $l = 0$, the integration yields the potential of the earth's mass M concentrated at the center of mass (3.16). We extract this term, introduce the semimajor axis a of the earth ellipsoid as a constant, and denote the mass integrals by C_{lm} , S_{lm} (spherical harmonic coefficients). The gravitational potential expanded in spherical harmonics is then written as

$$V = \frac{GM}{r} \left(1 + \sum_{l=1}^{\infty} \sum_{m=0}^l \left(\frac{a}{r} \right)^l (C_{lm} \cos m\lambda + S_{lm} \sin m\lambda) P_{lm}(\cos \vartheta) \right). \quad (3.89)$$

The *harmonic coefficients* (also Stokes' constants) are given by

$$\begin{aligned}
 C_{l0} = C_l &= \frac{1}{M} \iiint_{\text{earth}} \left(\frac{r'}{a} \right)^l P_l(\cos \vartheta') dm \quad \text{and} \\
 \left. \begin{cases} C_{lm} \\ S_{lm} \end{cases} \right\} &= \frac{2}{M} \times \frac{(l-m)!}{(l+m)!} \iiint_{\text{earth}} \left(\frac{r'}{a} \right)^l P_{lm}(\cos \vartheta') \begin{cases} \cos m\lambda' \\ \sin m\lambda' \end{cases} dm \quad \text{for } m \neq 0
 \end{aligned} \quad (3.90)$$

The following coefficients are sometimes used, particularly in satellite geodesy:

$$J_l = -C_l, \quad J_{lm} = -C_{lm}, \quad K_{lm} = -S_{lm}. \quad (3.91)$$

Calculations in the gravitational field become more convenient with the (fully) *normalized* spherical harmonic functions $\bar{P}_{lm}(\cos\vartheta)$. They are computed from the conventional harmonics, (3.80) and (3.82), according to

$$\bar{P}_{lm}(t) = \sqrt{k(2l+1)\frac{(l-m)!}{(l+m)!}} P_{lm}(t), \quad k = \begin{cases} 1 & \text{for } m=0 \\ 2 & \text{for } m \neq 0 \end{cases}, \quad (3.92)$$

with $t = \cos\vartheta$, etc. Recursive formulas are also available for the calculation of the normalized harmonics and its derivatives (PAUL 1978, TSCHERNING et al. 1983, WENZEL 1985):

$$\begin{aligned} \bar{P}_{lm}(t) = & \left[\frac{(2l+1)(2l-1)}{(l+m)(l-m)} \right]^{1/2} t \bar{P}_{l-1,m}(t) - \\ & \left[\frac{(2l+1)(l+m-1)(l-m-1)}{(2l-3)(l+m)(l-m)} \right]^{1/2} \bar{P}_{l-2,m}(t) \end{aligned} \quad (3.93a)$$

for $l > m+1$

with

$$\begin{aligned} \bar{P}_0 &= 1, \quad \bar{P}_1 = \sqrt{3} \cos\vartheta, \quad \bar{P}_2 = \frac{1}{2} \sqrt{5} (3 \cos^2\vartheta - 1), \\ \bar{P}_{1,1} &= \sqrt{3} \sin\vartheta, \quad \bar{P}_{2,1} = \sqrt{15} \sin\vartheta \cos\vartheta, \quad \bar{P}_{2,2} = \frac{1}{2} \sqrt{15} \sin^2\vartheta \end{aligned} \quad (3.93b)$$

and the control

$$\sum_{m=0}^l \bar{P}_{lm}(t)^2 = 2l+1. \quad (3.93c)$$

In addition to the orthogonality relation (3.85) for the surface harmonics, we now also have

$$\frac{1}{4\pi} \iint_{\sigma} \left(\bar{P}_{lm} \begin{Bmatrix} \cos m\lambda \\ \sin m\lambda \end{Bmatrix} \right)^2 d\sigma = 1 \quad (3.94)$$

over the unit sphere σ . According to (3.92), for an expansion of the gravitational potential analogous to (3.89), the harmonic coefficients are now given by

$$\begin{Bmatrix} \bar{C}_{lm} \\ \bar{S}_{lm} \end{Bmatrix} = \sqrt{\frac{(l+m)!}{k(2l+1)(l-m)!}} \begin{Bmatrix} C_{lm} \\ S_{lm} \end{Bmatrix}, \quad k = \begin{cases} 1 & \text{for } m=0 \\ 2 & \text{for } m \neq 0 \end{cases}. \quad (3.95)$$

Equation (3.89), or the corresponding equations employing fully normalized harmonics ((3.92) and (3.95)), represent a spherical solution of Laplace's differential equation (3.29). It can also be derived straightforwardly by the method of variable separation, after substituting the Cartesian coordinates with spherical coordinates (HEISKANEN and MORITZ 1967, pp.18 ff.).

The expansion converges outside a sphere of radius $r = a$, which just encloses the earth (Brillouin sphere). After the theorem of Runge-Krarup, an expansion of V into converging spherical harmonics can also be used in the interior of the earth, down to a sphere completely inside the earth and close to its surface (Bjerhammar sphere), KRARUP (1969), MORITZ (1980, p.69). Such an expansion represents an arbitrarily good approximation of the outer gravitational field. Naturally, this analytical extension does not satisfy the Poisson equation (3.31) of the actual gravitational field in the earth's interior.

With present accuracies of the determination of the earth's gravity field, the gravitation of the *atmosphere* cannot be neglected. As the density of the atmosphere primarily depends on height, corresponding models can be used to calculate the potential and the gravitation of the atmosphere as a function of height. These calculations are based on the relations derived for the potential inside an earth constructed of homogeneous spherical shells, cf. [3.1.2]. With an atmospheric mass of 5.32×10^{18} kg, we get a potential value of $55.6 \text{ m}^2 \text{s}^{-2}$ for $h = 0$, and $54.8 \text{ m}^2 \text{s}^{-2}$ for $h = 100 \text{ km}$. This effect is taken into account by corresponding reductions, cf. [4.3].

The extension of the spherical harmonic expansion for V to the *gravity potential* W is performed easily by adding the centrifugal potential Z (3.38). If we express the distance p to the rotational axis by spherical coordinates (2.14), the centrifugal potential reads as

$$Z = \frac{\omega^2}{2} r^2 \sin^2 \vartheta \quad (3.96a)$$

or, after introducing the Legendre polynomial P_2 according to (3.83a), as

$$Z = \frac{\omega^2}{3} r^2 (1 - P_2(\cos \vartheta)). \quad (3.96b)$$

By adding (3.96) to (3.89) we get the expansion for the gravity potential.

3.3.3 Geometrical Interpretation of the Surface Spherical Harmonics

We now discuss the properties of the surface spherical harmonics (3.84), which describe the behavior of the gravitational potential on the unit sphere. The zero points of these functions divide the surface into regions with alternating signs, bounded by meridians and parallels.

For the order $m = 0$, we obtain the Legendre polynomials $P_l(\cos \vartheta)$. Because of their independence of the geographical longitude λ , they divide the surface into zones of positive and negative signs: *zonal harmonics*. These harmonics possess l real zeros in the interval $0 \leq \vartheta \leq \pi$. For even l , the sphere is divided symmetrically with respect to the equator $\vartheta = 90^\circ$, and the case for odd l results in an asymmetric division. The $P_{lm}(\cos \vartheta)$ for $m \neq 0$ have $(l-m)$ zeros in the interval $0 < \vartheta < \pi$. Because of the multiplication by $\cos m\lambda$ or $\sin m\lambda$, the surface harmonics are longitude dependent, furnishing $2m$ zeros in the interval $0 \leq \lambda \leq \pi$: *tesseral harmonics*. Finally, for $m=l$, the dependence on ϑ disappears, and the sphere is divided into sectors of alternating signs: *sectorial harmonics* (Fig. 3.10).

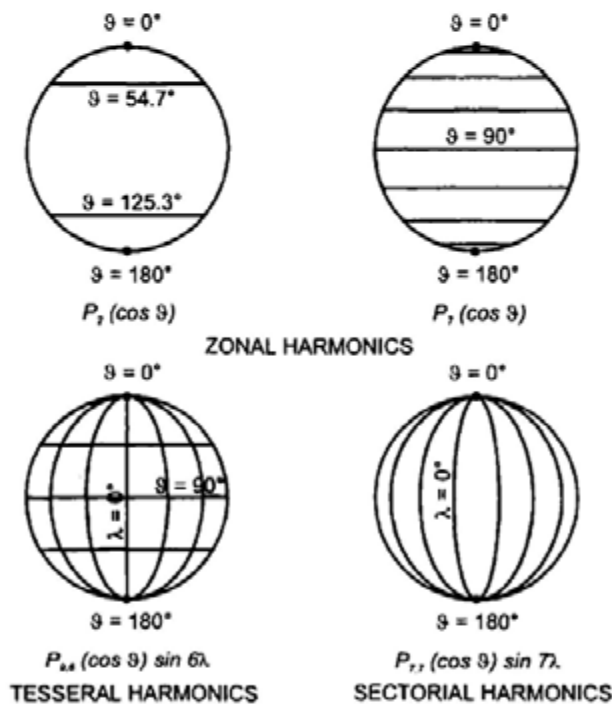


Fig. 3.10. Spherical harmonics on the unit sphere, with alternating positive (grey) and negative (white) sign

The amplitudes of the individual terms given by the surface harmonics are determined by the harmonic coefficients. For example, the series has only zonal harmonics for an earth rotationally symmetric with respect to the Z-axis; the coefficients with $m \neq 0$ must all vanish. For a mass distribution symmetric with respect to the equator, the zonal harmonic coefficients with odd l must be absent.

Summarizing, we state that the spherical harmonic expansion of the gravitational potential represents a *spectral decomposition* of the gravitational field. The field is separated into structures of wave-length $360^\circ/l$, corresponding to a spatial resolution of $180^\circ/l$. With increasing height, the field is smoothed by the factor $(a/r)^l$.

3.3.4 Physical Interpretation of the Harmonic Coefficients

The spherical harmonic expansion has transformed the single volume integral over the earth's masses (3.10) into an infinite series. The harmonic coefficients now carry mass integrals for the individual contribution of the corresponding wave-length to the total potential. The lower degree harmonics have a simple physical interpretation.

As already stated above, the zero degree term ($l=0$) represents the potential of a homogeneous or radially layered spherical earth, see (3.16):

$$V_0 = \frac{GM}{r}. \quad (3.97)$$

The terms of degree one and two ($l=1,2$) can be calculated from (3.90) by introducing the harmonic functions P_m (3.83) and subsequently transforming the spherical coordinates to Cartesian coordinates using (2.14). For $l=1$, this yields

$$C_1 = \frac{1}{aM} \iiint_{\text{earth}} Z' dm, \quad C_{1,1} = \frac{1}{aM} \iiint_{\text{earth}} X' dm, \quad \text{and} \quad S_{1,1} = \frac{1}{aM} \iiint_{\text{earth}} Y' dm. \quad (3.98)$$

As known from mechanics, the integrals divided by the mass M are the coordinates of the center of mass of the earth. Since we have placed the origin of the coordinate system at the center of mass, we have

$$C_1 = C_{1,1} = S_{1,1} = 0. \quad (3.99)$$

For $l=2$, we obtain

$$\begin{aligned}
 C_2 &= \frac{1}{a^2 M} \iiint_{\text{earth}} \left(Z'^2 - \frac{X'^2 + Y'^2}{2} \right) dm, \quad C_{2,1} = \frac{1}{a^2 M} \iiint_{\text{earth}} X' Z' dm, \\
 S_{2,1} &= \frac{1}{a^2 M} \iiint_{\text{earth}} Y' Z' dm, \quad C_{2,2} = \frac{1}{4a^2 M} \iiint_{\text{earth}} (X'^2 - Y'^2) dm, \\
 S_{2,2} &= \frac{1}{2a^2 M} \iiint_{\text{earth}} X' Y' dm.
 \end{aligned} \tag{3.100}$$

These expressions are functions of the moments of inertia

$$\begin{aligned}
 A &= \iiint (Y'^2 + Z'^2) dm, \quad B = \iiint (X'^2 + Z'^2) dm, \\
 C &= \iiint (X'^2 + Y'^2) dm
 \end{aligned} \tag{3.101}$$

and of the products of inertia

$$D = \iiint Y' Z' dm, \quad E = \iiint X' Z' dm, \quad F = \iiint X' Y' dm \tag{3.102}$$

with respect to the axes of the global X, Y, Z -system. If we neglect polar motion, the Z -axis coincides with one principal axis of inertia (maximum moment of inertia). Consequently, we have

$$D = E = 0.$$

F , on the other hand, would only become zero if the X -axis coincided with one of the equatorial principal-axes of inertia. Due to the conventional definition of the X -axis (Greenwich meridian), F does not vanish.

Using the above expressions for A , B , C , and F , the harmonic coefficients of second degree may also be formulated as follows:

$$\begin{aligned}
 C_2 &= \frac{1}{a^2 M} \left(\frac{A+B}{2} - C \right), \quad C_{2,1} = S_{2,1} = 0, \\
 C_{2,2} &= \frac{B-A}{4a^2 M}, \quad S_{2,2} = \frac{F}{2a^2 M}
 \end{aligned} \tag{3.102}$$

$J_2 = -C_2$ is also known as *dynamical form factor*. It characterizes the polar flattening of the earth's body by the difference between the mean equatorial moment of inertia (with $A \approx B$) and the polar moment of inertia. As this is the largest deviation from a spherical earth model, the numerical value for C_2 is

three orders of magnitude larger than the values of the successive coefficients. Slight contributions to the ellipsoidal form of the earth also come from the even zonal harmonics of higher degree, mainly $l = 4$ and $l = 6$. The coefficients $C_{2,2}$ and $S_{2,2}$ describe the asymmetry of the equatorial mass distribution in relation to the rotational axis (ellipticity of the equator) and the torsion of the corresponding principal axes of inertia with respect to the conventional X and Y -directions, cf. also [4.2.1]. If the odd zonal harmonic-coefficients differ from zero, the corresponding terms in the expansion of V represent an asymmetric mass distribution with respect to the equatorial plane, cf. [3.3.3]. The main contribution comes from C_3 , and may be geometrically interpreted as a difference in the flattening for the northern and the southern hemisphere. Numerical values for the coefficients are given in [6.6.2].

3.4 The Geoid

The geoid is of fundamental importance for geodesy, oceanography, and physics of the solid earth. Due to the demands for, and achievable accuracy of, a modern geoid, the classical definition of the geoid must be reconsidered today [3.4.1]. In geodesy and oceanography, the geoid serves as a height reference surface for describing continental and sea surface topography [3.4.2], [3.4.3]. Geophysics exploits the geoid as a gravity field representation revealing the distribution of deeper located masses, cf. [8.2.4].

3.4.1 Definition

The geoid has been introduced by C. F. Gauss as a refined model of the figure of the earth, cf. [1.2]. It was defined by Gauss as the equipotential surface of the earth's gravity field coinciding with the mean sea level of the oceans.

This physical *definition* considers the waters of the oceans as freely-moving homogeneous matter, subject only to the force of gravity and free from variations with time. Upon attaining a state of equilibrium, the surface of such idealized oceans would assume a level surface of the gravity field. The ocean surface may be regarded as being extended under the continents, e.g., by a system of conducting tubes.

With the gravity potential value W_0 , the *equation* of the geoid reads as

$$W = W(\mathbf{r}) = W_0. \quad (3.103)$$

It follows from the properties of the gravity potential W , that the geoid is a closed and continuous surface, cf. [3.1.3]. As it extends partially inside the solid

earth (under the continents), its curvature will display discontinuities at abrupt density changes. Thus, although not being an analytical surface in a global sense, it may be sufficiently well approximated by a spherical harmonic development, cf. [3.3.2].

The problem of downward continuation of the gravity field into the earth's masses presupposes knowledge about the density distribution of the atmospheric and topographic masses. Geoid calculations consequently depend on the corresponding assumptions (STRYKOWSKI 1998), cf. [6.5.3].

As well known from oceanography, mean sea level is not an equilibrium surface in the earth's gravity field, due to ocean currents and other quasi-stationary effects. In addition, sea surface variations with time can only be partially reduced by averaging over time or modeling. Hence, mean sea level still varies over longer time spans, cf. [3.4.2].

Consequently, a *refined geoid definition* is needed at the "cm" accuracy level (RIZOS 1982, RAPP 1983a). By applying a minimum condition on the deviations between mean sea level and the geoid, the geoid could be defined as the equipotential surface which best fits mean sea level at a certain epoch (MATHER 1978, RAPP 1995a).

Another choice would be to define the geoid as the level surface which optimally fits mean sea level at a selected set of tide gauges used for defining the vertical datum of national or continental height systems, cf. [3.4.3]. Such a definition would lead to only small corrections for the existing height systems but not result in a best fit over the oceans.

The geoid definition also has to include the treatment of the *permanent tidal effects*, cf. [3.5.2]. There are three different definitions possible. The *mean geoid* includes the direct effect of attraction and the indirect effect of deformation. It would coincide with an "undisturbed" sea level; hence it is of interest for oceanography. For the *non-tidal geoid*, the total tidal-effect would be eliminated. This would agree with the theoretical demand of geodesy to have no masses outside the boundary surface "geoid", cf. [6.5.3]. As the response of the earth to the permanent tidal part is not known, the *zero-geoid* is preferred in geodesy. Here, the attraction part is eliminated but the permanent deformation retained. This definition takes into account the fact that positioning also refers to a deformed earth (IAG resolution, Gen. Ass. Hamburg 1983, EKMAN 1989). With respect to a best-fitting reference ellipsoid, cf. [4.3], the geoid deviates by ± 30 m; maximum deviations reach about ± 100 m, cf. [6.6.3].

Finally, a refined geoid definition should also consider *variations with time*, which result from the displacements of terrestrial masses, cf. [3.5.3]. Such a definition then would refer to a certain epoch.

3.4.2 Mean Sea Level

The ocean surface does not coincide with a level surface (e.g. the geoid) of the earth's gravity field; the deviations are called *sea surface topography* (SST, also dynamic ocean topography). *Instantaneous* SST is affected by temporal variations of long-term, annual, seasonal, and short-term character, occurring at different scales. Averaging the ocean surface over time (at least over one year) or modeling ocean tides provides *mean sea level* (MSL) for the corresponding time interval. Even after reducing all time-dependent parts, a quasi-stationary SST would remain. It is caused by nearly constant oceanographic and meteorological effects, which generate ocean currents and ocean surface slopes. The r.m.s. variation is ± 0.6 to ± 0.7 m, and the maximum deviation from the geoid is about ± 1 m or more (LISITZIN 1974).

Short term variations of the sea surface (waves) are averaged out in the mean value over time (e.g., at tide gauge observations over one hour) or by the smoothing effect of the "footprints" in satellite altimetry, cf. [5.2.7]. *Tidal effects* can deviate considerably between the open ocean and shelf areas, adjacent seas, and coastal zones. This is due to unequal water depths and to the fact that the continents impede the movement of water. On the open sea, the tidal amplitude is less than one meter (r.m.s. variation ± 0.3 m), while it can amount to several meters in coastal areas (Bay of Fundy, Nova Scotia: more than 15 m).

Oceanic tidal models are based on Laplace's tidal equations. These models take bathymetry, tide gauge data, and in more recent solutions, satellite altimetry and satellite orbit analyses into account. The models solve for about 10 to 12 partial tides (annual, semiannual, monthly, fortnightly, daily, and half-daily). They are provided either in grid form ($1^\circ \times 1^\circ$, $0.5^\circ \times 0.5^\circ$) or as a spherical harmonic expansion (SCHWIDERSKI 1980, 1983, ANDERSEN et al. 1995). Ocean tide models have also been derived by global gravity modeling (SCHWINTZER et al. 1997, LEMOINE et al. 1998). The accuracy of the oceanic tidal models amounts to a few cm on the open oceans but is less at shelf areas and close to the coast.

Fluctuations of annual, semiannual, and seasonal character are of *meteorological* origin (atmospheric pressure, winds), of *oceanographic* nature (ocean currents, differences in water density as a function of temperature, salinity and pressure), and are also due to a variable *water budget* (changing water influx as a result of meltwater, monsoon rains, etc.). The amplitude of these variations is on the order of 0.1 to 1 m, and scales of a few 100 km are found, e.g., at meandering ocean streams and eddies (NEREM 1995b). In addition, a *secular rise* of about 1 to 2 mm/a has been observed over the last 100 years. This trend is expected to increase, reaching 0.5 to 1 m over the next century, due to climate changes producing a thermal expansion of the water masses, a melting of the polar ice caps and the glaciers, and isostatic movements (LAMBECK 1988, HANNAH 1989).

Mean sea level can be derived from tide gauge records, satellite altimetry, and oceanographic methods.

Tide gauges (mareographs) continuously record the height of the water level with respect to a height reference surface close to the geoid, cf. [3.4.3]. Averaging the results over long time intervals (month, year) eliminates most variations with time. In order to fully remove the tidal period of a complete lunar cycle (nutation), the record should extend over 18.6 years, cf. [2.4.2]. The precision of the mean monthly and annual values is better than ± 1 cm. These results may be systematically disturbed if the tide gauge location is not directly linked to the open ocean and data is thereby affected by local sea level anomalies (swell in shallow waters, estuary effects at river mouths). In addition, local or regional vertical crustal movements (sedimentary subsidence, postglacial uplift, etc.) may act at the tide gauge location and systematically influence (bias) the sea level registration. These movements may reach a few mm/a (EKMAN 1993, MITCHUM 1994).

Tide gauge data are available for over 1750 stations worldwide, but only a few stations cover a time span of a few centuries (at Amsterdam registrations go back to 1700), WOODWORTH (1997). In the open oceans, pressure tide gauges contribute in monitoring sea surface variability but lack connection to continental height systems (TOLKATCHEV 1996). Tide gauges along the continental coasts generally have been connected to the geodetic height control system, thus permitting the derivation of MSL from the geoid or a zero height reference close to it. Sea level slopes up to several 0.1 m/1000 km and more have been detected by this method, cf. [3.4.3].

Satellite altimetry directly provides sea surface topography with respect to an ellipsoidal reference surface, cf. [5.2.7]. With the exception of the polar regions, satellite altimeters cover the oceans with repeated tracks (e.g., with a 10 days repetition rate at TOPEX/POSEIDON) and permit derivation of mean sea surface heights to an accuracy of a few cm. The solutions are derived over a certain time period (e.g., one year) and are provided in grids of a few minutes of arc (ANZENHOFER et al. 1996, RAPP and YI 1997). Sea surface topography is obtained by referring these results to a geoid model. If the altimetric solutions for different epochs are compared, sea surface variations with time can be determined, MINSTER et al. 1995, cf. [8.3.2].

Oceanographic methods derive sea surface topography from measurements at sea (LAMBECK 1988, RUMMEL and ILK 1995). *Steric leveling* assumes that equipotential and isobaric surfaces coincide at a certain depth (e.g., 2000 m): level of no motion. Using water density values derived from salinity, temperature, and pressure data, the equation of hydrostatic equilibrium yields the gravity potential difference (or the dynamic height) between the ocean surface and the reference level of no motion. This method is applicable in the deep oceans (STURGES 1974). *Geostrophic leveling* (dynamic leveling) is based on the hydrodynamic equations and uses observed ocean current velocities. It can also be applied in shelf areas.

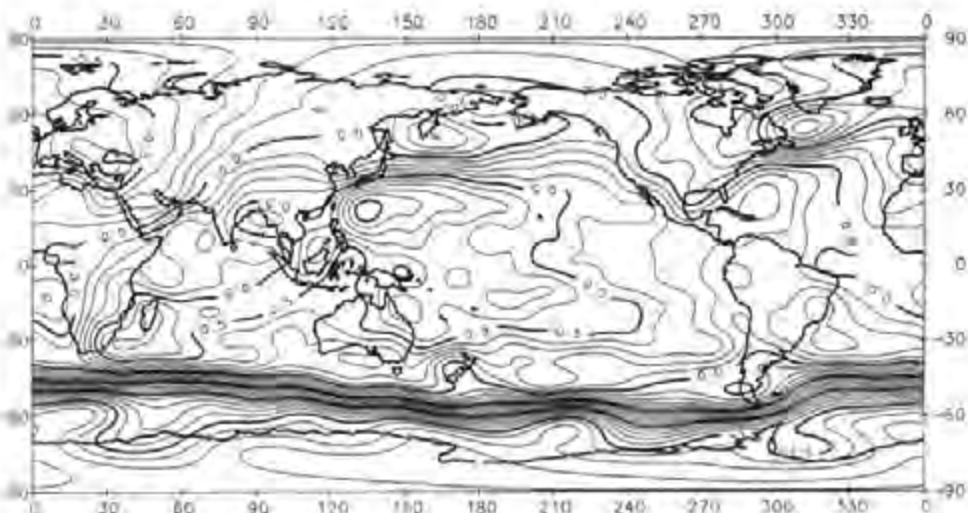


Fig. 3.11. Sea surface topography, spherical harmonic expansion up to degree 20, contour line interval 0.1 m, after LEMOINE et al. (1998)

Oceanic sea surface topography models have been developed that correspond to a spherical harmonic expansion up to degree 36 (or a minimum wave-length of 10°) with an accuracy of a few cm to 0.1 m (LEVITUS 1982). Satellite altimetry solutions, partly in combination with gravity field modeling, are available up to degree 20, for time spans over 5 to 10 years, and with an accuracy of better than 0.1 m (SCHWINTZER et al. 1997, LEMOINE et al. 1998), Fig. 3.11. Quasi-stationary sea surface topography is characterized by an increase from the polar regions toward the equator and by strong inclinations along the main ocean currents.

3.4.3 The Geoid as Height Reference Surface

The geoid is used in geodesy, cartography, and oceanography as a reference surface for heights and depths (continental and ocean bottom topography, as well as sea surface topography). A point P can be attributed to a specified level surface by its gravity potential W (Fig. 3.12). With respect to the geoid potential W_0 , the "height" of P is given by the negative potential difference to the geoid, which is called the *geopotential number* C . We get from (3.52)

$$C = W_0 - W_P = - \int_{P_0}^P dW = \int g \, dn. \quad (3.104)$$

The integral is independent of the path; hence, P_0 is an arbitrary point on the geoid. C can be determined from geometric leveling and gravity measurements along any path between P_0 and P .

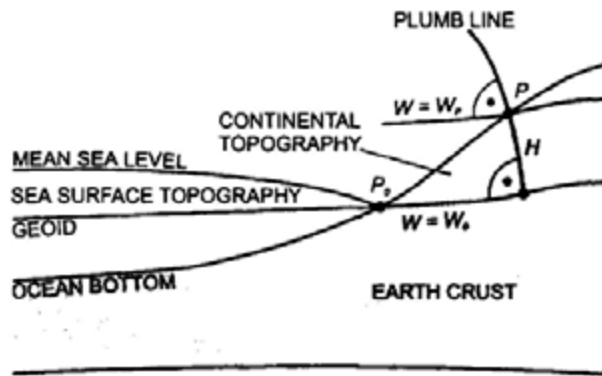


Fig. 3.12. Geoid, mean sea level, continental and sea surface topography

The geopotential number is an ideal measure for describing the behavior of masses (e.g., water masses) in the gravity field. It could be used as a "height" in several applications, as in hydraulic engineering and oceanography. A more general use is limited by the potential unit $\text{m}^2 \text{s}^{-2}$, which is in contradiction to the obvious demand for a metric height system that employs the "meter" unit.

In order to achieve a certain agreement with the numerical value of the height in meters, the geopotential unit (gpu) $10 \text{ m}^2 \text{s}^{-2}$, or kgalm, is also used for the geopotential number. With $g \approx 9.8 \text{ ms}^{-2}$, the values of C are about 2% smaller than the corresponding height values.

The *dynamic height* H^{dyn} is obtained by dividing the geopotential number through a constant gravity value. Usually the normal gravity γ_0^{45} calculated for the surface of the level ellipsoid at 45° latitude is used, cf. [4.2.2]:

$$H^{\text{dyn}} = \frac{C}{\gamma_0^{45}} . \quad (3.105)$$

The surfaces $H^{\text{dyn}} = \text{const.}$ remain equilibrium surfaces. Hence, points located on the same level surface have the same dynamic height. Unfortunately, a geometric interpretation of the dynamic heights is not possible, and larger corrections are necessary in order to convert leveling results into dynamic height differences, cf. [6.4.1]. Because of this, dynamic heights have not been widely used in geodesy but are used in oceanography, cf. [3.4.2].

National or continental height systems, and terrain-data based on them (topographic maps, digital terrain models), use either orthometric or normal heights.

The *orthometric height* H is defined as the linear distance between the surface point and the geoid, reckoned along the curved plumb line (Fig. 3.12). This definition corresponds to the common understanding of "heights above sea level". Expanding the right-hand side of (3.104) in H and integrating along the plumb line from P_0 ($H = 0$) to P (H) we obtain

$$H = \frac{C}{\bar{g}}, \quad \bar{g} = \frac{1}{H} \int_0^H g \, dH. \quad (3.106)$$

\bar{g} is the mean gravity along the plumb line; gravity values inside the earth are required for its calculation. This is performed by introducing a model of the density distribution of the topographic masses. As this distribution is known only imperfectly, the accuracy of computed orthometric heights depends on the accuracy of the density model. In addition, points of equal orthometric height deviate slightly from a level surface, which is due to the non-parallelism of the level surfaces, cf. [3.2.1]. These drawbacks are compensated by the fact that orthometric heights represent the geometry of the topographic masses. Geometric leveling only needs small corrections for the transformation into orthometric height differences, cf. [6.4.1].

In order to avoid any hypothesis on the distribution of the topographic masses, *normal heights* H^N have been introduced and are used in a number of countries. The mean gravity \bar{g} in (3.106) is replaced by the mean normal gravity $\bar{\gamma}$ along the normal plumb line, which is only slightly curved:

$$H^N = \frac{C}{\bar{\gamma}}, \quad \bar{\gamma} = \frac{1}{H^N} \int_0^{H^N} \gamma \, dH^N. \quad (3.107)$$

$\bar{\gamma}$ can be calculated in the normal gravity field of an ellipsoidal earth model. The reference surface for the normal heights is the quasi-geoid, which is close to the geoid but not a level surface. It deviates from the geoid on the mm to cm-order at low elevations and may reach one-meter deviation in the high mountains. On the oceans, geoid and quasigeoid practically coincide, cf. [6.1.1].

The *zero height surface* (vertical datum) of national height systems generally is defined by the mean sea level derived from tide gauge records over a certain time interval. These reference surfaces only approximate the geoid, due to the sea surface topography and local anomalies, with deviations up to one meter, cf. [3.4.2].

The adjustment of continental-wide leveling networks provides heights that refer to one common level surface. By comparing with the mean sea level obtained at tide gauges, sea level slopes that partially agree with oceanic leveling results have been found, cf. [3.4.2]. MSL at the Pacific coast of the U.S.A. is about 1 m higher than at the Atlantic coast (ZILKOSKI et al. 1995), and the mean Baltic Sea level is estimated to be about 0.5 m above MSL of the Mediterranean Sea (GRONWALD 1963). On the other hand, there are also larger discrepancies of a few 0.1 m between the results of geometric and oceanic leveling. These can be traced back to differently defined reference surfaces, to the particular behavior of MSL along the coastlines, and to systematic errors in geometric leveling over long distances (FISCHER 1977). It should be mentioned that older leveling networks have often been adjusted without any gravity reduction, or by substituting actual gravity with normal gravity. A unification of the different vertical datum systems to a world-wide standard thus would require vertical shifts to a common reference (global geoid definition) and a uniform treatment of the height measurements (RUMMEL and TEUNISSEN 1988, RAPP 1995b), cf. [7.2].

3.5 Temporal Gravity Variations

Gravity changes with time may be divided into effects due to a time dependent gravitational constant and variations of the earth's rotation [3.5.1], tidal accelerations [3.5.2], and variations caused by terrestrial mass displacements [3.5.3]. These changes are of global, regional, or local character and occur either at well-known frequencies (tides) or at time scales ranging from secular to abrupt (LAMBECK 1988, MUELLER and ZERBINI 1989).

3.5.1 Gravitational Constant, Earth Rotation

Based on cosmological considerations, DIRAC (1938) postulated a secular decrease of the *gravitational constant G*, with relative changes of $\dot{G}/G = -10^{-10}$ to $-10^{-11}/a$ ($\dot{G} = dG/dt$). Even to this day, laboratory experiments and the analysis of long-term observations to artificial satellites and the moon have not supported the assumption $\dot{G} \neq 0$ (GILLIES 1987, BURŠA 1995).

The *earth's rotational vector ω* is subject to secular, periodic, and irregular variations, leading to changes of the centrifugal acceleration \mathbf{z} , cf. [2.5.2]. In a spherical approximation, the radial component of \mathbf{z} enters into gravity, cf. [3.1.4]. By multiplying (3.35b) with $\cos\bar{\varphi}$ ($\bar{\varphi}$ = geocentric latitude), we obtain

$$z_r = -\omega^2 r \cos^2 \bar{\varphi}. \quad (3.108)$$

Differentiation yields the effect of changes in latitude (polar motion) and angular velocity (length of day) on gravity:

$$\delta z_r = \omega^2 r \sin 2\bar{\varphi} d\bar{\varphi} - 2\omega r \cos^2 \bar{\varphi} d\omega. \quad (3.109)$$

Polar motion does not exceed a few $0.1''/\text{a}$, and rotation changes are at the order of a few ms. Hence, corresponding gravity variations on the earth's surface ($r = 6371 \text{ km}$) remain less than $0.1 \mu\text{ms}^{-2}$ and $0.01 \mu\text{ms}^{-2}$ respectively.

3.5.2 Tidal Acceleration, Tidal Potential

Tidal acceleration is caused by the superposition of lunisolar gravitation (and to a far lesser extent planetary gravitation) and orbital accelerations due to the motion of the earth around the barycenter of the respective two-body system (earth-moon, earth-sun etc.). The periods of these orbital motions are about 28 days for the moon and 365 days for the sun, and the gravimetric tidal effect is on the order of 10^{-7} g (MELCHIOR 1983, ZUERN and WILHELM 1984, WENZEL 1997a).

For a *rigid earth*, the tidal acceleration at a given point can be determined from Newton's law of gravitation and the ephemerides (coordinates) of the celestial bodies (moon, sun, planets). The computations are carried out separately for the individual two-body systems (earth-moon, earth-sun etc.), and the results are subsequently added, with the celestial bodies regarded as point masses.

We consider the geocentric coordinate system to be moving in space with the earth but not rotating with it (revolution without rotation). All points on the earth experience the same orbital acceleration in the geocentric coordinate system (see Fig. 3.13 for the earth-moon system). In order to obtain equilibrium, orbital acceleration and gravitation of the celestial bodies have to cancel in the earth's center of gravity. Tidal acceleration occurs at all other points of the earth. The acceleration is defined as the difference between the gravitation \mathbf{b} , which depends on the position of the point, and the constant part \mathbf{b}_0 , referring to the earth's center:

$$\mathbf{b}_r = \mathbf{b} - \mathbf{b}_0. \quad (3.110)$$

The tidal acceleration deforms the earth's gravity field symmetrically with respect to three orthogonal axes with origin at the earth's center. This tidal acceleration field experiences diurnal and semidiurnal variations, which are due to the rotation of the earth about its axis.

If we apply the law of gravitation to (3.110), we obtain for the moon (m)

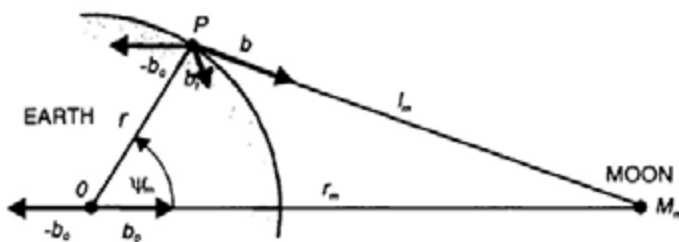


Fig. 3.13. Lunar gravitation, orbital acceleration, and tidal acceleration

$$\mathbf{b}_t = \frac{GM_m}{l_m^2} \frac{\mathbf{l}_m}{l_m} - \frac{GM_m}{r_m^2} \frac{\mathbf{r}_m}{r_m}. \quad (3.111)$$

Here, M_m = mass of the moon, and l_m and r_m = distance to the moon as reckoned from the calculation point P and the earth's center of gravity O respectively. We have $\mathbf{b}_t = \mathbf{0}$ for $l_m = r_m$. Corresponding relations hold for the earth-sun and earth-planet systems.

We now make the transition from the tidal acceleration to the *tidal potential*:

$$\mathbf{b}_t = \text{grad } V_t = \text{grad}(V - V_0). \quad (3.112)$$

In the geocentric system, using spherical coordinates r_m, ψ_m , the law of gravitation yields the potential of a point mass according to (3.9):

$$V = \frac{GM_m}{l_m} \quad (3.113a)$$

with

$$l_m = \left(r^2 + r_m^2 - 2rr_m \cos \psi_m \right)^{\frac{1}{2}}. \quad (3.113b)$$

The potential of the homogeneous \mathbf{b}_0 -field is given by multiplying b_0 with $r \cos \psi_m$:

$$V_0 = \frac{GM_m}{r_m^2} r \cos \psi_m. \quad (3.114)$$

Inserting (3.113) and (3.114) into (3.112), and adding an integration constant so that $V_t = 0$ for $r = 0$ and $l_m = r_m$, we get for the tidal potential

$$V_t = GM_m \left(\frac{1}{l_m} - \frac{1}{r_m} - \frac{r \cos \psi_m}{r_m^2} \right). \quad (3.115)$$

The tidal potential, and functionals thereof, can be calculated either from the ephemerides of the celestial bodies or from a spherical harmonic expansion. Tidal potential catalogues are based primarily on the latter method, as the series expansions converge rapidly close to the earth's surface ($r = R$), with $r/r_m = 1/60$ for the moon and a corresponding relation of $1/23600$ for the sun. The results from calculations employing the ephemerides serve as a control for the tidal potential catalogues.

We develop (3.113b) into a series according to (3.79). When inserting into (3.115), the terms of degree zero and one cancel and we obtain

$$V_t = \frac{GM_m}{r_m} \sum_{l=2}^{\infty} \left(\frac{r}{r_m} \right)^l P_l(\cos \psi_m), \quad (3.116)$$

where $P_l(\cos \psi_m)$ are the Legendre polynomials. The largest contribution ($\approx 98\%$) stems from degree two. Restricting ourselves now to the degree $l = 2$, and inserting P_2 (3.83) in the form

$$\cos^2 \psi_m = \frac{1}{2} (\cos 2\psi_m + 1),$$

we get the *main term* of the tidal potential series

$$V_t = \frac{3}{4} GM_m \frac{r^2}{r_m^3} \left(\cos 2\psi_m + \frac{1}{3} \right). \quad (3.117)$$

For $r = R$, and neglecting the slight variation of r_m , the expression before the parentheses is called *Doodson's tidal constant*. It is $2.628 \text{ m}^2 \text{ s}^{-2}$ for the moon and $1.208 \text{ m}^2 \text{ s}^{-2}$ for the sun. Hence, the solar tides amount to 46% of the lunar tides.

Differentiating (3.117) generates the *tidal acceleration*. The *radial component* (positive outward) is found to be

$$b_r = \frac{\partial V_t}{\partial r} = \frac{3}{2} GM_m \frac{r}{r_m^3} \left(\cos 2\psi_m + \frac{1}{3} \right). \quad (3.118)$$

The *tangential* component (positive in the direction toward the moon) is

$$b_\psi = -\frac{\partial V_t}{r \partial \psi} = \frac{3}{2} GM_m \frac{r}{r_m^3} \sin 2\psi_m. \quad (3.119)$$

Equations (3.117) to (3.119) permit calculation of the tidal effects on the level surfaces, on gravity, and on the plumb line direction for a rigid earth.

Taking the relation (3.52) between a potential change and the vertical shift of a level surface into account, we obtain a tidal-induced increase of the level surface. This amounts to 0.36m for the moon and 0.16m for the sun at $\psi = 0^\circ$ and 180° respectively. At $\psi = 90^\circ$ and 270° , we have a decrease of 0.18m and 0.08m respectively. For stationary systems, the level surfaces would experience a corresponding deformation, and freely moving masses of water would assume the form of one of these surfaces (equilibrium tide), Fig. 3.14.

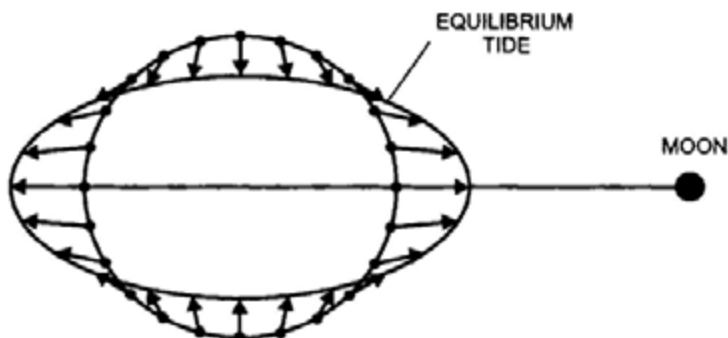


Fig. 3.14. Tidal acceleration and equilibrium tide

According to (3.118), gravity changes (opposite sign) would vary between $-1.1 \mu\text{ms}^{-2}$ (moon) and $-0.5 \mu\text{ms}^{-2}$ (sun) for $\psi = 0^\circ$ (zenithal position); and $+0.5 \mu\text{ms}^{-2}$ (moon) and $+0.3 \mu\text{ms}^{-2}$ (sun) for $\psi = 90^\circ$ and 135° . Changes in the direction of the *plumb line* are given by b_ψ/g . There is no tidal effect at $\psi = 0^\circ$ and 90° . Maximum values occur at $\psi = 45^\circ$ and 135° , with fluctuations of $\pm 0.017''$ (moon) and $\pm 0.008''$ (sun).

Equation (3.117) provides the dependence of the tidal potential on the zenith angle (and the distance) to the celestial body. The variation of the tidal potential and acceleration is more easily recognized if we change to the earth-fixed coordinate system $(\bar{\varphi}, \lambda)$ for the point of calculation and to the equatorial system of astronomy (δ, h) for the celestial body, cf. [2.4.1]. Following (2.21), we have (for the moon) the relation

$$\cos \psi_m = \sin \bar{\varphi} \sin \delta_m + \cos \bar{\varphi} \cos \delta_m \cos h_m \quad (3.120)$$

with the hour angle given by (2.22) and (2.23):

$$h_m = \text{LAST} - \alpha_m = \lambda + \text{GAST} - \alpha_m. \quad (3.121)$$

Substituting into (3.117) yields *Laplace's tidal equation* (for the moon):

$$V_i = \frac{3}{4} GM_m \frac{r^2}{r_m^3} \left\{ \left(\frac{1}{3} - \sin^2 \bar{\varphi} \right) \left(1 - 3 \sin^2 \delta_m \right) + \right. \\ \left. \sin 2\bar{\varphi} \sin 2\delta_m \cos h_m + \cos^2 \bar{\varphi} \cos^2 \delta_m \cos 2h_m \right\}. \quad (3.122)$$

The quantities r_m , δ_m , and h_m vary with time, having different periods. The first term, which is independent of the earth's rotation, exhibits long-periodic variations (14 days for the moon, 1/2 year for the sun). It also contains a non-periodic part, which only depends on latitude, causing a permanent deformation of the level surfaces including the geoid, cf. [3.4.1]. Using (3.52), and taking the inclination of the ecliptic into account, the geoid is thus lowered by 0.19 m at the poles and raised by 0.10 m at the equator (EKMAN 1989).

The second term oscillates with diurnal periods because of the daily rotation of the earth as expressed by the hour angle h , and the third term introduces semidiurnal periods. Long-periodic terms enter through the declination δ and the right ascension α . As seen from (3.122), long-periodic and semidiurnal tides are symmetric about the equator, while the diurnal tides are antisymmetric. The diurnal tide has its maximum at $\varphi = \pm 45^\circ$ and vanishes at the equator and the poles, while the semidiurnal tide reaches its maximum at the equator and is zero at the poles. The long-periodic tides have a maximum at the poles.

Each of the three tidal constituents in (3.122) varies in a complicated way, since they contain products of different time varying functions. However, the ephemerides of the moon and the sun can be expressed as harmonic functions of five fundamental astronomic quantities, considering that these quantities essentially change uniformly with time (MELCHIOR 1983). Introducing these harmonic series into (3.122) yields a spectral analysis of the tidal potential, and with (3.118) and (3.119) we get a spectral analysis of the tidal acceleration. Thus, potential and acceleration are represented by the sum of time-dependent cosine functions having constant periods and amplitudes and phases that depend on latitude and height (partial tides). Tab. 3.1 gives the periods and amplitudes of the main gravimetric partial tides for $\varphi = 45^\circ$.

A first expansion for the moon and the sun was carried out by DOODSON (1921). The development by CARTWRIGHT and TAYLER (1971) and CARTWRIGHT and EDDEN (1973) contains 505 partial tides (uncertainty less than 1nms^{-2}) and was recommended by IAG for the computation of the tides of the rigid earth (RAPP 1983b). A recent tidal catalogue by HARTMANN and WENZEL (1995)

is based on a spherical harmonic development to degree 6 (moon) and degree 3 (sun) and includes the effects of Venus, Mars, and Jupiter (4 orders of magnitude smaller than the tidal effects of moon and sun). It also takes the flattening of the earth into account. This catalogue provides 12 935 partial tides with an accuracy of $\pm 0.001 \text{ nm s}^{-2}$, WENZEL (1996).

As the earth is not a rigid body, it reacts in a different way to the tidal force. The solid earth behaves mainly as an elastic body: *earth's body tides*. In the oceans, tidal oscillations depend on the ocean-bottom topography, with large differences occurring at the coastlines and at the shelf areas: *ocean tides*, ZAHEL (1997). While the measurement of tidal effects will be discussed in [5.4.6] and [5.5.4], the theory of earth tides and results of earth-tide observations are given in [8.3.5].

Tab. 3.1. Principal Gravimetric Partial Tides for $\bar{\varphi} = 45^\circ$, $h = 0$

| symbol | name | period (solar hours) | amplitude (nm s^{-2}) |
|----------------------------|--------------------------------------|----------------------------|-------------------------------------|
| long-periodic waves | | | |
| M0 | const. <i>l</i> tide | ∞ | 102.9 |
| S0 | const. <i>s</i> tide | ∞ | 47.7 |
| Ssa | declin. tide to S0 | 182.62 d | 14.8 |
| Mm | ellipt. tide to M0 | 27.55 d | 16.8 |
| Mf | declin. tide to M0 | 13.66 d | 31.9 |
| diurnal waves | | | |
| O1 | main diurnal <i>l</i> tide | 25.82 h | 310.6 |
| P1 | main diurnal <i>s</i> tide | 24.07 h | 144.6 |
| Q1 | ellipt. tide to O1 | 26.87 h | 59.5 |
| K1 | main diurnal <i>ls</i> decl. tide | 23.93 h | 436.9 |
| semi-diurnal waves | | | |
| M2 | main <i>l</i> tide | 12.42 h | 375.6 |
| S2 | main <i>s</i> tide | 12.00 h | 174.8 |
| N2 | ellipt. tide to M2 | 12.66 h | 71.9 |
| K2 | declin. tide to M2, S2 | 11.97 h | 47.5 |
| ter-diurnal waves | | | |
| M3 | terdiurn. <i>l</i> tide | 8.28 h | 5.2 |

3.5.3 Non-tidal Temporal Variations

The terrestrial gravity field is affected by a number of variations with time due to mass redistributions in the atmosphere, the hydrosphere, and the solid earth. These processes take place at different time scales and are of global, regional, and local character (WAGNER and MCADOO 1986, MUELLER and ZERBINI 1989, TORGE 1993).

Long-term global effects include postglacial rebound, melting of the ice caps and glaciers, as well as sea level changes induced by atmospheric warming; slow motions of the earth's core and mantle convection also contribute. Subsidence in sedimentary basins and tectonic uplift are examples of regional effects. Groundwater variations are primarily of seasonal character, while volcanic and earthquake activities are short-term processes of more local extent.

The magnitude of the resulting gravity variations depends on the amount of mass shifts and is related to them by the law of gravitation. As seen from (3.5), a shift of the observer also affects gravitation, especially where height changes play a dominant role. Research and modeling of these variations is still in the beginning stages. Large-scale variations have been found from satellite-derived gravity field models, but small-scale effects can be detected only by terrestrial gravity measurements. Simple models have been developed for the relation between atmospheric and hydrological mass shifts and gravity changes, cf. [5.4.1]. Generally, gravity changes produced by mass redistributions do not exceed the order of 10^{-9} to 10^{-8} g, while geoid changes remain less than 1 mm/a, cf. [8.3.4].

4 The Geodetic Earth Model

A geodetic earth model is used as a reference for the actual surface and external gravity field of the earth. It should provide a good fit to the geoid and to the gravity field, and thus allow the linearization of non-linear geodetic problems. On the other hand, the mathematical formation of the model should be simple and possibly permit calculations by closed formulas. The model should serve as a standard for applications not only in geodesy and cartography but also in astronomy and geophysics; it should satisfy the demands and needs of these disciplines too.

Based on these considerations, the level ellipsoid has been introduced. It possesses a simple geometry, and coordinate systems that refer to it approximate the "natural" coordinate system sufficiently well [4.1]. The ellipsoid's mass and rotation provide a "normal" gravity field, which can be calculated if the ellipsoid surface is defined to be in equilibrium [4.2]. State of the art earth models are recommended from time to time as a standard and are given the name Geodetic Reference System [4.1.3].

4.1 The Rotational Ellipsoid

The rotational ellipsoid was introduced as a geometrical figure of the earth in the 18th century, cf. [1.3.2]. By fitting its dimension and orientation to the geoid, it approximates this level surface within about 100 m. The geometry of the ellipsoid can be described in a simple manner, together with ellipsoidal surface coordinates and curvature [4.1.1], [4.1.2]. The use of global and local three-dimensional ellipsoidal systems provides an approximation to the corresponding systems of the actual earth and permits the separation between horizontal position and height [4.1.3].

Geometry and coordinate systems of the ellipsoid are well documented in geodetic literature, e.g., GROSSMANN (1976), BOMFORD (1980), HECK (1995), HEITZ (1988).

4.1.1 Parameters and Coordinate Systems

The rotational ellipsoid is generated by rotating the meridian ellipse about its minor axis. The shape of the ellipsoid is described by two geometric parameters, the *semimajor axis* a and the *semiminor axis* b (Fig. 4.1). Generally, b is replaced by a smaller quantity, describing the (small) polar flattening of the

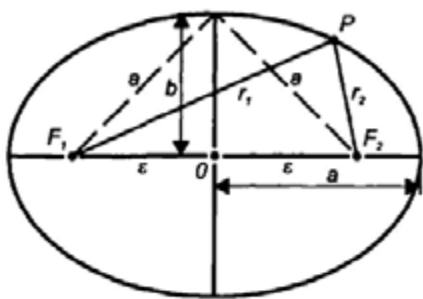


Fig. 4.1. Meridian Ellipse

ellipsoid, which is more suitable for series expansions. We have the (geometrical) *flattening*

$$f = \frac{a - b}{a}, \quad (4.1a)$$

the *first eccentricity*

$$e = \frac{\sqrt{a^2 - b^2}}{a}, \quad (4.1b)$$

and the *second eccentricity*

$$e' = \frac{\sqrt{a^2 - b^2}}{b}. \quad (4.1c)$$

The following relations hold among those quantities:

$$\frac{b}{a} = 1 - f = \sqrt{1 - e^2} = \frac{1}{\sqrt{1 + e'^2}} = \frac{e}{e'}. \quad (4.2)$$

From the geometric definition of the ellipse as the curve having a constant value for the sum of the distances r_1 and r_2 to the focal points F :

$$r_1 + r_2 = 2a,$$

we derive the *linear eccentricity*

$$e = \sqrt{a^2 - b^2}. \quad (4.3)$$

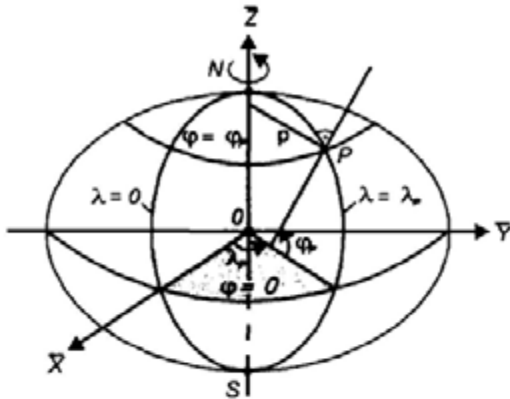


Fig. 4.2. Geodetic coordinates latitude and longitude

We now introduce a spatial $\bar{X}, \bar{Y}, \bar{Z}$ -Cartesian coordinate system (Fig. 4.2). The origin of the system is situated at the center of the ellipsoid O . The \bar{Z} -axis coincides with the minor axis of the ellipsoid. The equation of the surface of the ellipsoid is then given by

$$\frac{\bar{X}^2 + \bar{Y}^2}{a^2} + \frac{\bar{Z}^2}{b^2} - 1 = 0. \quad (4.4)$$

The system of *geodetic surface coordinates* is defined by the ellipsoidal *latitude* φ and *longitude* λ (also geodetic latitude and longitude). φ is the angle measured in the meridian plane between the equatorial plane (\bar{X}, \bar{Y} -plane) of the ellipsoid and the surface normal at P . Longitude λ is the angle measured in the equatorial plane between the zero meridian (\bar{X} -axis) and the meridian plane of P . Here, φ is positive northward and negative southward, and λ is positive as reckoned toward the east. The ellipsoidal *meridian plane* is formed by the surface normal and the \bar{Z} -axis. φ and λ are defined to have angular values, but they may also be considered as curvilinear surface coordinates. The *coordinate lines* of this orthogonal system are the meridians ($\lambda = \text{const.}$) and the parallels, or circles of latitude, ($\varphi = \text{const.}$). With

$$\bar{X} = p \cos \lambda, \quad \bar{Y} = p \sin \lambda, \quad (4.5)$$

we introduce the radius of the circle of latitude

$$p = \sqrt{\bar{X}^2 + \bar{Y}^2} \quad (4.6)$$

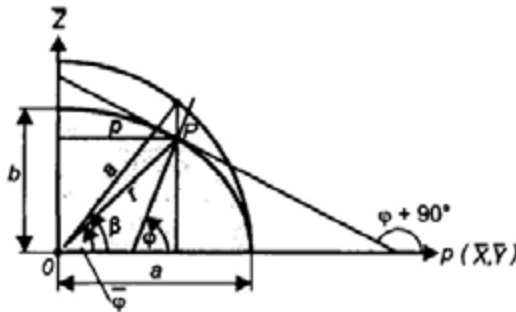


Fig. 4.3. Geodetic, reduced, and geocentric latitude

as a new variable (Fig. 4.2). Substituting p into (4.4) and differentiating yields the slope of the ellipsoidal tangent at P (Fig. 4.3):

$$\frac{d\bar{Z}}{dp} = -\left(\frac{b}{a}\right)^2 \frac{p}{\bar{Z}} = -\cot \varphi. \quad (4.7)$$

By combining (4.4) and (4.7), and substituting p with (4.5), the parametric representation of the *meridian ellipse* follows:

$$\begin{aligned} \bar{X} &= \frac{a^2 \cos \varphi \cos \lambda}{(a^2 \cos^2 \varphi + b^2 \sin^2 \varphi)^{1/2}}, \quad \bar{Y} = \frac{a^2 \cos \varphi \sin \lambda}{(a^2 \cos^2 \varphi + b^2 \sin^2 \varphi)^{1/2}}, \\ \bar{Z} &= \frac{b^2 \sin \varphi}{(a^2 \cos^2 \varphi + b^2 \sin^2 \varphi)^{1/2}}. \end{aligned} \quad (4.8)$$

Instead of φ , other latitude parameters are used for special applications. The *geocentric latitude* $\bar{\varphi}$ has already been introduced together with the longitude λ and the geocentric distance r as spherical coordinate, cf. [2.5.1]. From Fig. 4.3, the corresponding equation of the *ellipse* is given by

$$p = r \cos \bar{\varphi}, \quad \bar{Z} = r \sin \bar{\varphi}, \quad (4.9)$$

where p follows from (4.5).

The *reduced latitude* β is obtained by projecting (parallel to the \bar{Z} -axis) from the ellipse to the concentric circle of radius a (Fig. 4.3). Since the ratio of the elliptical to the circular ordinates is b/a (ellipse as the affine image of the circle), we have

$$p = a \cos \beta, \quad \bar{Z} = \frac{b}{a} a \sin \beta = b \sin \beta. \quad (4.10)$$

Using β instead of φ formally transforms ellipsoidal formulas into spherical formulas.

Comparing (4.9) and (4.10) with (4.7) provides the transformation between φ , $\bar{\varphi}$, and β :

$$\begin{aligned} \tan \bar{\varphi} &= \left(\frac{b}{a} \right)^2 \tan \varphi = (1 - e^2) \tan \varphi \\ \tan \beta &= \frac{b}{a} \tan \varphi = \sqrt{1 - e^2} \tan \varphi \end{aligned} . \quad (4.11a)$$

A series expansion yields the differences in the angles:

$$\varphi - \bar{\varphi} = \frac{e^2}{2} \sin 2\varphi + \dots = 2(\varphi - \beta). \quad (4.11b)$$

The maximum difference occurs at $\varphi = 45^\circ$, with $(\varphi - \bar{\varphi}) = 690''$.

4.1.2 Curvature

The meridians and parallels are the *lines of curvature* of the rotational ellipsoid. The principal *radii of curvature* are therefore in the plane of the meridian and in the plane of the prime vertical perpendicular to the meridian plane (Fig. 4.4).

The curvature of the *meridian* (M = curvature radius) as a plane curve $\bar{Z} = \bar{Z}(p)$ in the \bar{Z}, p -plane is given by

$$\frac{1}{M} = - \frac{d^2 \bar{Z}/dp^2}{\left(1 + (d\bar{Z}/dp)^2\right)^{3/2}}. \quad (4.12)$$

With (4.7) and its derivative, and taking (4.2) into account, we obtain the meridian radius of curvature

$$M = \frac{a(1 - e^2)}{(1 - e^2 \sin^2 \varphi)^{3/2}}. \quad (4.13)$$

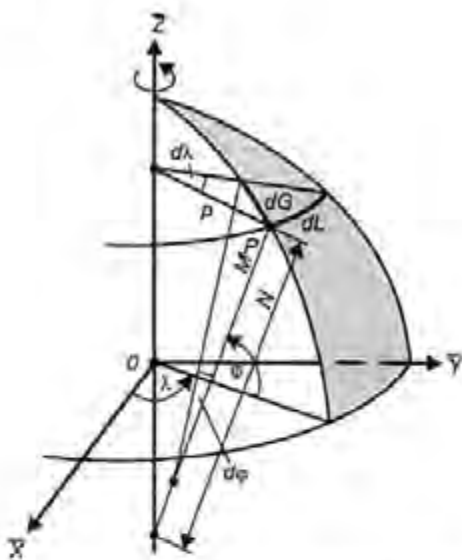


Fig. 4.4. Curvature of the rotational ellipsoid

The plane of a parallel circle (oblique section of the rotational ellipsoid) and the vertical plane in the same tangential direction intersect at point P with the angle φ . The theorem of Meusnier (regarding surface curvatures, see, e.g., STOKER 1969) provides the radius of curvature in the *prime vertical*:

$$N = \frac{P}{\cos \varphi}. \quad (4.14)$$

Because of rotational symmetry, the origin of N is on the spin axis. Inserting (4.6) and (4.8) into (4.14), one obtains

$$N = \frac{a}{(1 - e^2 \sin^2 \varphi)^{\frac{3}{2}}}. \quad (4.15)$$

A comparison of (4.13) and (4.15) shows that $N \geq M$. At the poles ($\varphi = \pm 90^\circ$), the polar radius of curvature becomes

$$c = M_{90} = N_{90} = \frac{a^2}{b}. \quad (4.16)$$

At the equator ($\varphi = 0^\circ$) the values are

$$M_0 = \frac{b^2}{a}, \quad N_0 = a. \quad (4.17)$$

The curvature of the *normal section* of an ellipsoidal, or geodetic, azimuth α is computed according to *Euler's formula* by

$$\frac{1}{R_\alpha} = \frac{\cos^2 \alpha}{M} + \frac{\sin^2 \alpha}{N}. \quad (4.18)$$

Here, R_α is the radius of curvature. The *geodetic azimuth* α is defined as the angle measured in the horizontal plane between the ellipsoidal meridian plane of P and the vertical plane containing the normal to P and the target point; α is reckoned from north in the clockwise direction. The *mean curvature* \bar{J} is given by

$$\bar{J} = \frac{1}{2} \left(\frac{1}{M} + \frac{1}{N} \right). \quad (4.19)$$

The *arc lengths* of the *coordinate lines* of the φ, λ -system are computed using M and N . For the arc elements of the meridian and the parallel respectively, we obtain (Fig. 4.4)

$$dG = M d\varphi, \quad dL = N \cos \varphi d\lambda. \quad (4.20)$$

With (4.13), the length of the *meridian arc* (starting at the equator) becomes

$$G = \int_0^\varphi M d\varphi = a(1 - e^2) \int_0^\varphi \frac{d\varphi}{(1 - e^2 \sin^2 \varphi)^{3/2}}. \quad (4.21a)$$

Equation (4.21a) can be reduced to an elliptic integral of the second kind, which cannot be evaluated in a closed form (KUTTERER 1998). Practical computations may be based on numerical integration (e.g., by Simpson's rule) or on a binomial expansion of the denominator. Subsequent term-by-term integration yields

$$G = a(1 - e^2) \left(\left(1 + \frac{3}{4} e^2 + \dots \right) \varphi - \left(\frac{3}{8} e^2 + \dots \right) \sin 2\varphi + \dots \right). \quad (4.21b)$$

Short arcs ($\Delta\varphi = \varphi_2 - \varphi_1 < 1^\circ$) can be calculated by a rapidly converging Taylor expansion. Expanding about the middle latitude $\varphi_M = (\varphi_1 + \varphi_2)/2$ yields

$$\Delta G_{1,2} = G_2 - G_1 = \left(\frac{dG}{d\varphi} \right)_{\varphi_M} \Delta\varphi + \dots \quad (4.21c)$$

According to (4.20), the arc length of a *circle of latitude* between the geodetic longitudes λ_1 and λ_2 is given by

$$\Delta L = \int_{\lambda_1}^{\lambda_2} N \cos \varphi d\lambda = N \cos \varphi (\lambda_2 - \lambda_1). \quad (4.22)$$

With $a = 6\ 378\ 137$ m, $b = 6\ 356\ 752$ m, and $e^2 = 0.006\ 694\ 380$ (for numerical values see [4.3]), we get for the radii of curvature at the poles and at the equator

$$c = 6\ 399\ 594 \text{ m}, \quad M_0 = 6\ 335\ 439 \text{ m}, \quad N_0 = a.$$

The arc lengths along the meridian and the parallel for $\varphi = 50^\circ$ are

$$\begin{aligned} \Delta G(\Delta\varphi = 1^\circ) &= 111\ 229 \text{ m}, & \Delta L(\Delta\lambda = 1^\circ) &= 71\ 696 \text{ m}, \\ \Delta G(\Delta\varphi = 1') &= 1853.8 \text{ m}, & \Delta L(\Delta\lambda = 1') &= 1194.9 \text{ m}, \\ \Delta G(\Delta\varphi = 1'') &= 30.90 \text{ m}, & \Delta L(\Delta\lambda = 1'') &= 19.92 \text{ m}. \end{aligned}$$

Local approximations to the ellipsoid use the *Gaussian osculating sphere* of radius

$$R_G = \sqrt{M(\varphi_0)N(\varphi_0)}. \quad (4.23)$$

At the latitude φ_0 it has the same Gaussian curvature as the ellipsoid.

Global approximations can be based on a sphere with the *mean radius*

$$R_m = \frac{1}{3}(2a + b), \quad (4.24a)$$

the radius derived from equality of *volumes* (i.e., volume of sphere = volume of ellipsoid)

$$R_v = \sqrt[3]{a^2 b}, \quad (4.24b)$$

or the radius for a sphere having a surface area equal to that of the ellipsoid. The latter one results from an integration over the ellipsoidal surface elements dG and dL (4.20), which after a series expansion yields

$$R_s = b \left(1 + \frac{2}{3} e^2 + \frac{3}{5} e^4 + \dots \right)^{1/2}. \quad (4.24c)$$

The numerical values for these three approaches agree within a few meters, which leads to a global value of $R = 6371$ km.

4.1.3 Spatial Geodetic Coordinates

The ellipsoidal surface coordinate system (φ, λ) can be extended to a spatial system by introducing the height h of the point P above the ellipsoid measured along the surface normal (Fig. 4.5). The point Q on the ellipsoid thus is obtained by projecting the point P along the ellipsoidal normal (Helmert projection). The spatial coordinates φ, λ, h are designated as geodetic coordinates.

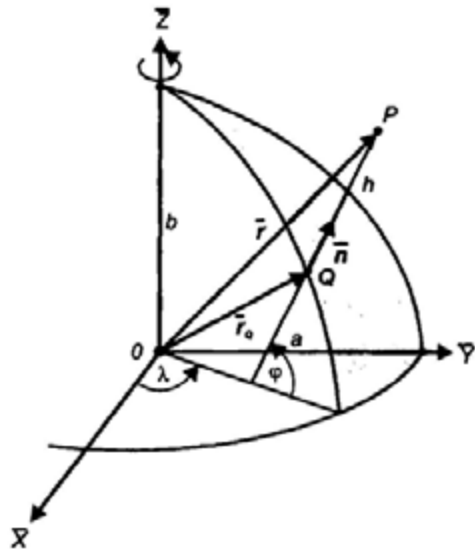


Fig. 4.5. Spatial geodetic coordinates

The *coordinate surfaces* ($\varphi = \text{const.}$, $\lambda = \text{const.}$, $h = \text{const.}$) of this system are orthogonal. The *coordinate lines* (φ -line = geodetic meridian, λ -line = geodetic parallel, h -line = ellipsoidal normal) represent planar curves.

In (4.8) we substitute the first eccentricity e^2 for the semiminor axis b , taking (4.15) into account; the coordinate vector for the point Q on the ellipsoid (4.8) then transforms into

$$\bar{\mathbf{r}}_Q = \begin{pmatrix} \bar{X}_Q \\ \bar{Y}_Q \\ \bar{Z}_Q \end{pmatrix} = N \begin{pmatrix} \cos\varphi \cos\lambda \\ \cos\varphi \sin\lambda \\ (1-e^2)\sin\varphi \end{pmatrix}. \quad (4.25)$$

For the point P , we get according to Fig. 4.5

$$\bar{\mathbf{r}} = \bar{\mathbf{r}}_Q + h\bar{\mathbf{n}}, \quad (4.26a)$$

with the surface normal

$$\bar{\mathbf{n}} = \begin{pmatrix} \cos\varphi \cos\lambda \\ \cos\varphi \sin\lambda \\ \sin\varphi \end{pmatrix}, \quad (4.26b)$$

or

$$\bar{\mathbf{r}} = \begin{pmatrix} \bar{X} \\ \bar{Y} \\ \bar{Z} \end{pmatrix} = \begin{pmatrix} (N+h)\cos\varphi \cos\lambda \\ (N+h)\cos\varphi \sin\lambda \\ ((1-e^2)N+h)\sin\varphi \end{pmatrix}. \quad (4.27)$$

The *inverse problem* can be solved for φ and h only by iterative methods. From (4.27) we get (HEISKANEN and MORITZ 1967, p.183)

$$h = \frac{\sqrt{\bar{X}^2 + \bar{Y}^2}}{\cos\varphi} - N, \quad \varphi = \arctan \frac{\bar{Z}}{\sqrt{\bar{X}^2 + \bar{Y}^2}} \left(1 - e^2 \frac{N}{N+h} \right)^{-1}. \quad (4.28)$$

$$\lambda = \arctan \frac{\bar{Y}}{\bar{X}}$$

The iteration process may start with $h = 0$, which results in a first approximation for φ , and so on. Close to the earth's surface ($h \ll N$) the process converges quickly. Efficient methods have also been developed for large heights (BORKOWSKI 1989, SJÖBERG 1999). Closed formulas with negligible residual

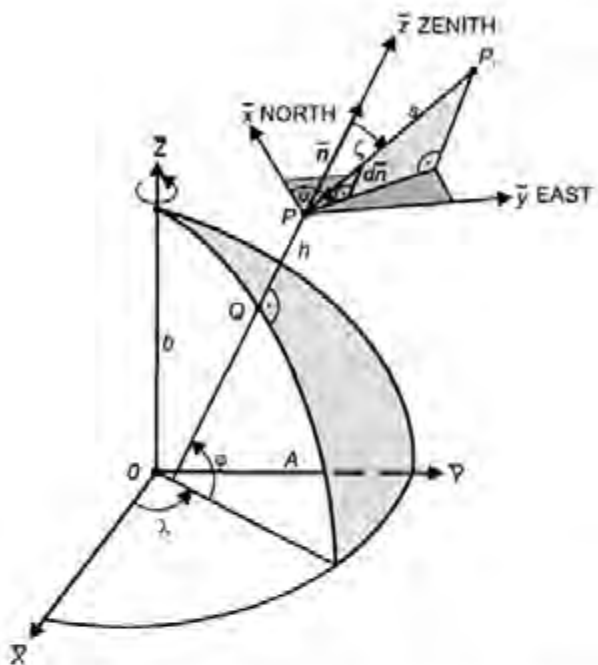


Fig. 4.6. Global and local ellipsoidal system

errors are given by BOWRING (1985). The transformation (4.28) is a standard problem in satellite geodesy, cf. [6.2.1].

Local ellipsoidal (geodetic) systems are introduced in analogy to the local astronomic systems, cf. [2.6.2], and represent an approximation to them (Fig. 4.6). With the origin at the point P , the local system is connected to the ellipsoidal vertical (outer surface normal \bar{n} to the ellipsoid) through the geodetic latitude and longitude (4.26). The \bar{z} -axis is directed towards the ellipsoidal zenith, with the \bar{x}, \bar{y} -plane being perpendicular to it. The \bar{x} -axis points to the ellipsoidal north (direction of the meridian), and the \bar{y} -axis points towards east (left-handed system).

A target point P_r is described with respect to P by the geodetic (ellipsoidal) azimuth α , introduced already in [4.1.2], the ellipsoidal zenith angle ζ_r , and the straight distance s between P and P_r . The zenith angle is measured in the vertical plane between the ellipsoidal vertical and the connecting line and reckoned positively from the zenith. These polar coordinates can be transformed into the local $\bar{x}, \bar{y}, \bar{z}$ -system by a relation corresponding to (2.20):

$$\begin{pmatrix} \bar{x} \\ \bar{y} \\ \bar{z} \end{pmatrix} = s \begin{pmatrix} \cos \alpha \sin \zeta_r \\ \sin \alpha \sin \zeta_r \\ \cos \zeta_r \end{pmatrix}. \quad (4.29)$$

After applying the reflection matrix S_2 (2.24), the local system is transformed to the global $\bar{X}, \bar{Y}, \bar{Z}$ -system by the rotation matrices $R_2(90^\circ - \varphi)$ and $R_3(180^\circ - \lambda)$, which correspond to (2.25) and (2.26):

$$\Delta\bar{\mathbf{X}} = \bar{\mathbf{A}}\bar{\mathbf{x}}, \quad (4.30)$$

with

$$\Delta\bar{\mathbf{X}} = (\Delta\bar{X}, \Delta\bar{Y}, \Delta\bar{Z})^T \quad (4.31)$$

and

$$\begin{aligned} \bar{\mathbf{A}} &= R_3(180^\circ - \lambda)R_2(90^\circ - \varphi)S_2 \\ &= \begin{pmatrix} -\sin\varphi\cos\lambda & -\sin\lambda & \cos\varphi\cos\lambda \\ -\sin\varphi\sin\lambda & \cos\lambda & \cos\varphi\sin\lambda \\ \cos\varphi & 0 & \sin\varphi \end{pmatrix}. \end{aligned} \quad (4.32)$$

The inversion of (4.32) gives

$$\bar{\mathbf{x}} = \bar{\mathbf{A}}^{-1}\Delta\bar{\mathbf{X}}, \quad (4.33)$$

with

$$\bar{\mathbf{A}}^{-1} = \bar{\mathbf{A}}^T = \begin{pmatrix} -\sin\varphi\cos\lambda & -\sin\varphi\sin\lambda & \cos\varphi \\ -\sin\lambda & \cos\lambda & 0 \\ \cos\varphi\cos\lambda & \cos\varphi\sin\lambda & \sin\varphi \end{pmatrix}, \quad (4.34)$$

which corresponds to (2.29) and (2.30).

4.2 The Normal Gravity Field

A "normal" gravity field may be referenced to the rotational ellipsoid by considering the latter to be a "level" ellipsoid. This earth model is now generally accepted as a geodetic reference system; higher order models do not offer any advantage [4.2.1]. The external gravity field of the level ellipsoid can be determined unambiguously from the parameters defining it [4.2.2]. The geometry of the normal gravity field is of special interest for geodetic applications [4.2.3].

4.2.1 The Level Ellipsoid, Level Spheroids

By adding the total mass M and the rotational angular velocity ω to the geometric parameters a and f of the rotational ellipsoid, we introduce an ellipsoidal gravity field composed of gravitation and centrifugal acceleration: *normal gravity field*. In addition, we require the surface of this ellipsoid to be a level surface of its own gravity field. According to the theorem of *Stokes-Poincaré*, the gravity field then is uniquely defined in the space exterior to the ellipsoid.

Theorem of *Stokes-Poincaré*: if a body of total mass M rotates with constant angular velocity ω about a fixed axis, and if S is a level surface of its gravity field enclosing the entire mass, then the gravity potential in the exterior space of S is uniquely determined by M , ω , and the parameters defining S .

The earth model thus defined is called a *level* (or *equipotential*) *ellipsoid*. Instead of a , f , M and ω , other sets of four independent parameters may be used for its definition. If the parameters are given values which correspond to the real earth, then an optimum approximation to the geometry of the geoid and to the external gravity field is achieved: *mean earth ellipsoid*, cf. [6.8.1]. The theory of the level ellipsoid has been developed by *P. Pizetti* (1894), *C. Somigliana* (1929), and others (HEISKANEN and MORITZ 1967, p.64).

From the physical point of view, an earth model is required which is in *hydrostatic equilibrium*. All its level surfaces then coincide with the surfaces of equal density and equal pressure. Deviations from this model would indicate stress in the earth's body, cf. [8.1]. The theory of equilibrium figures has been discussed since the days of *Newton* and *Clairaut*, cf. [1.3.2], see LEDERSTEGER (1956/1969), MORITZ (1990).

In the above definition of the level ellipsoid, nothing has been stated regarding the interior mass distribution. But from the theory of equilibrium figures, it follows that only the homogeneous ellipsoids of *MacLaurin* exist in equilibrium. On the other hand, the surface of an equilibrium figure constructed of shells of equal density, and thus corresponding more to the real structure of the earth, is not an ellipsoid. Nevertheless, a layered structure of the interior mass of the level ellipsoid that approximates the actual situation, and sufficiently well reproduces the gravity field of the level ellipsoid, can be found (MORITZ 1968a). The maximum deviation between the level surfaces and the surfaces of equal density are on the order of f^2 only, and the differences in stress at the model remain considerably smaller than in the real earth. The level surface thus can also serve as a bounding surface for a *geophysical earth model* (MARUSSI et al. 1974).

There have been several attempts to construct earth models with a better fit to the geoid and the external gravity field than that provided by the level ellipsoid. A physical approximation consists of reference figures derived from truncated spherical harmonic expansions of the gravity potential of the earth: *level spheroids*. By assuming symmetry about the equator and truncating at the degree $l = 2$ (*Brun's spheroid*) and $l = 4$ (*Helmer's spheroid*), we obtain surfaces of the fourteenth and twenty-second order respectively. The deviations from the rotational ellipsoid having the same axes are on the $O(f^2)$ for $l = 2$ and $O(f^3)$ for $l = 4$. From the harmonic coefficients $C_{2,2}$ and $S_{2,2}$ (3.102), a *triaxial ellipsoid* can also be calculated as a geometrical approximation to the geoid. This results in a difference of 70 m between the radii of the equatorial principal axes of inertia (corresponding to an equatorial flattening of 1/90 000), where the larger radius is directed to 345° longitude (BURŠA 1995).

These higher order earth models do not significantly reduce the deviations between the geoid and the level ellipsoid. On the other hand, computations related to these surfaces and their gravity fields become more complicated. Finally, they are not suitable as physical normal figures. Although, for instance, triaxial rotational ellipsoids exist as equilibrium figures (homogeneous ellipsoids of *Jacobi*), such an ellipsoid would yield a completely unnatural form when using the actual values for the angular velocity and mass of the earth.

4.2.2 The Normal Gravity Field of the Level Ellipsoid

The external gravity field of the level ellipsoid (normal gravity field) can be modeled by *closed formulas* in the system of *ellipsoidal coordinates* β, λ, u . The reduced latitude β and the geodetic longitude λ have been introduced in [4.1.1]. The third coordinate u is the semiminor axis of the ellipsoid with constant linear eccentricity ε , see (4.3), which passes through the point P (Fig. 4.7). From (4.20), and putting $\sqrt{u^2 + \varepsilon^2}$ for the semimajor axis, the transformation from the ellipsoidal coordinates to the Cartesian ones is given by

$$\begin{pmatrix} \bar{X} \\ \bar{Y} \\ \bar{Z} \end{pmatrix} = u \begin{pmatrix} \sqrt{1 + (\varepsilon/u)^2} \cos \beta \cos \lambda \\ \sqrt{1 + (\varepsilon/u)^2} \cos \beta \sin \lambda \\ \sin \beta \end{pmatrix}. \quad (4.35)$$

For $\varepsilon = 0$, the β, λ, u -system with $\beta = 90^\circ - \vartheta$ and $u = r$ degenerates into the system of spherical coordinates (2.14).

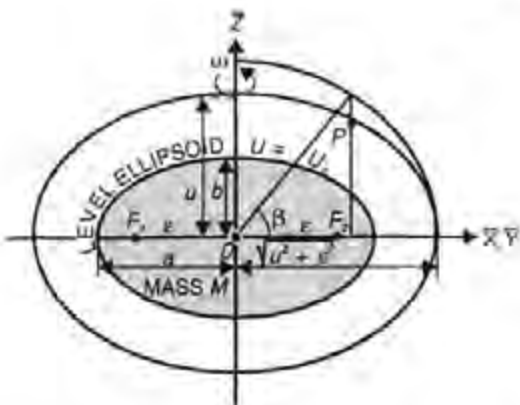


Fig. 4.7. Level ellipsoid and ellipsoidal coordinates

We denote the vector of *normal gravity* by γ and the normal gravity *potential* by U . In analogy to (3.43), we have

$$\gamma = \text{grad } U . \quad (4.36a)$$

With respect to the global $\bar{X}, \bar{Y}, \bar{Z}$ -system, γ is given in analogy to (3.72) by

$$\gamma = -\gamma \begin{pmatrix} \cos \varphi \cos \lambda \\ \cos \varphi \sin \lambda \\ \sin \varphi \end{pmatrix} . \quad (4.36b)$$

Corresponding to (3.42), U is composed of the gravitational potential V_E and the potential of the centrifugal acceleration Z_E :

$$U = V_E + Z_E . \quad (4.37)$$

The gravitational potential satisfies Laplace's differential equation (3.29) in the space exterior to the ellipsoid that contains the total mass.

By expressing Laplace's equation in ellipsoidal coordinates, we get a solution based on ellipsoidal harmonics. Adding the centrifugal potential (3.38), and taking both rotational symmetry and the condition of the ellipsoid surface as a level surface into account, we obtain a closed expression for the normal gravity potential (HEISKANEN and MORITZ 1967, p.64):

$$U = \frac{GM}{\varepsilon} \arctan \frac{\varepsilon}{u} + \frac{\omega^2}{2} a^2 \frac{q}{q_0} \left(\sin^2 \beta - \frac{1}{3} \right) + \frac{\omega^2}{2} (u^2 + \varepsilon^2) \cos^2 \beta . \quad (4.38)$$

Here, q is an auxiliary quantity depending only on the geometric parameters ε and u . On the ellipsoid surface ($u = b$), it is denoted q_0 :

$$q = \frac{1}{2} \left(\left(1 + 3 \frac{u^2}{\varepsilon^2} \right) \arctan \frac{\varepsilon}{u} - 3 \frac{u}{\varepsilon} \right), \quad q_0 = q_{u=b}. \quad (4.39)$$

Hence, in agreement with Stokes' theorem, cf. [4.2.1], the normal gravity potential is determined by four parameters (a, b, M, ω). It does not depend on the geodetic longitude. If one puts $u = b$ and $q = q_0$ in (4.38), then the potential of the *level ellipsoid* reads

$$U_0 = \frac{GM}{\varepsilon} \arctan \frac{\varepsilon}{b} + \frac{\omega^2}{3} a^2. \quad (4.40)$$

The normal gravity γ is perpendicular to the level ellipsoid, so that in accordance with (4.36), only the orthogonal component appears in the derivative of U (4.38). If the geodetic latitude φ is used instead of the reduced latitude β , then for the *normal gravity* on the *ellipsoid* we obtain the formula of *Somigliana* (1929):

$$\gamma_0 = \frac{a\gamma_a \cos^2 \varphi + b\gamma_b \sin^2 \varphi}{\sqrt{a^2 \cos^2 \varphi + b^2 \sin^2 \varphi}}. \quad (4.41a)$$

For numerical computations, the form

$$\gamma_0 = \gamma_a \frac{1 + k \sin^2 \varphi}{\left(1 - e^2 \sin^2 \varphi\right)^{1/2}} \text{ with } k = \frac{b\gamma_b}{a\gamma_a} - 1 \quad (4.41b)$$

is more convenient (MORITZ 2000).

Here, the normal gravity, which depends on latitude only, is represented by the four parameters a, b, γ_a (normal gravity at the equator), and γ_b (normal gravity at the pole). The ellipsoidal parameters $a, b, M, \omega, \gamma_a, \gamma_b$ appearing in (4.38) and (4.41) are interrelated according to the theorem of *Pizetti*

$$2 \frac{\gamma_a}{a} + \frac{\gamma_b}{b} = \frac{3GM}{a^2 b} - 2\omega^2 \quad (4.42)$$

and the theorem of *Clairaut*

$$f + \beta = \frac{\omega^2 a}{\gamma_a} (1 + e'^2)^{-1/2} \left(1 + e' \frac{3 \left(1 + \frac{1}{e'^2} \right) \left(1 - \frac{1}{e'} \arctan e' \right) - 1}{\left(1 + \frac{3}{e'^2} \right) \arctan e' - \frac{3}{e'}} \right). \quad (4.43)$$

Thus, only four independent parameters are remaining. In (4.43), besides the second eccentricity e' and the geometric flattening f , there is also the *gravity flattening*

$$\beta = \frac{\gamma_b - \gamma_a}{\gamma_a}. \quad (4.44)$$

The abbreviation β is used for both the reduced latitude and the gravity flattening; confusion is not to be anticipated.

The normal gravity in the *exterior space* is obtained by partial differentiation of (4.38). Near the ellipsoid, a Taylor series expansion with respect to the ellipsoidal height is sufficient, see below.

Application of normal gravity field formulas, (4.38) to (4.43), is often facilitated by *series expansions* with respect to f , or some other quantity that describes the polar flattening.

We start with the spherical harmonic expansion of the gravitational potential. Due to the symmetry with respect to the rotational axis (tesseral terms = 0) and the equatorial plane (odd zonal terms = 0), we obtain, upon adding the centrifugal potential (3.96a) expressed in spherical coordinates, the *potential of normal gravity* in terms of Legendre polynomials, cf. [3.3.1],

$$U = \frac{GM}{r} \left(1 - \sum_{n=1}^{\infty} \left(\frac{a}{r} \right)^{2n} J_{2n} P_{2n}(\cos \vartheta) \right) + \frac{\omega^2}{2} r^2 \sin^2 \vartheta. \quad (4.45)$$

If P_2 is substituted from (3.83a), the expansion up to $n = 1$ (corresponding to $l = 2$) yields

$$U = \frac{GM}{r} \left(1 - \left(\frac{a}{r} \right)^2 J_2 \left(\frac{3}{2} \cos^2 \vartheta - \frac{1}{2} \right) + \frac{\omega^2}{2GM} r^3 \sin^2 \vartheta \right). \quad (4.46)$$

Solving for r and setting $U = U_0$ gives the *radius vector* to the level ellipsoid, where we have put $r = a$ on the right side:

$$r = \frac{GM}{U_0} \left(1 - J_2 \left(\frac{3}{2} \cos^2 \vartheta - \frac{1}{2} \right) + \frac{\omega^2 a^3}{2GM} \sin^2 \vartheta \right). \quad (4.47)$$

The *normal gravity* γ follows from the derivative of (4.46) with respect to r :

$$\gamma = \frac{GM}{r^2} \left(1 - 3 \left(\frac{a}{r} \right)^2 J_2 \left(\frac{3}{2} \cos^2 \vartheta - \frac{1}{2} \right) - \frac{\omega^2}{GM} r^3 \sin^2 \vartheta \right). \quad (4.48)$$

If we substitute either $\vartheta = 90^\circ$ (equator) or 0° (pole) in (4.47) and (4.48), then we obtain either the semimajor axis a and the equatorial gravity or the semiminor axis b and the polar gravity of the ellipsoid. Using these values, the *geometric flattening* f (4.1a) and the gravity flattening β (4.44) may be computed according to

$$f = \frac{3}{2} J_2 + \frac{m}{2}, \quad \beta = -\frac{3}{2} J_2 + 2m. \quad (4.49)$$

Here,

$$m = \frac{\omega^2 a^2 b}{GM} \approx \frac{\omega^2 a}{\gamma_a} \quad (4.50)$$

is the ratio of the centrifugal acceleration to the normal gravity at the equator.

From (4.48) and (4.49), we arrive at an approximation to the theorem of *Pizetti* (4.42)

$$GM = a^2 \gamma_a \left(1 - f + \frac{3}{2} m \right) \quad (4.51)$$

and an approximation to *Clairaut's theorem* (4.43)

$$f + \beta = \frac{5}{2} m. \quad (4.52)$$

Substituting (4.49) and (4.50) into (4.48), we obtain *Newton's gravity formula*, cf. [1.3.2] :

$$\gamma_0 = \gamma_a (1 + \beta \sin^2 \varphi). \quad (4.53)$$

If two γ_0 gravity values are known on the ellipsoid (gravity reduction problem) at different geographic latitudes φ , then γ_a and β may be computed from (4.53). With known values for the semimajor axis a and the angular velocity ω , (4.50) supplies the quantity m . Finally, Clairaut's theorem (4.52) yields the geometric flattening f , which thus can be determined from gravity values. Application of this principle to the real earth - that is, deriving geometric form parameters from physical quantities - leads to the gravimetric method of physical geodesy, cf. [6.5.1].

The relations above (linear in f , β , and m) may also be derived by series expansions of the closed formulas. They had already been found by *Clairaut* ("Theorie de la Figure de la Terre" 1743). The expansion up to terms of the order f^2 yields (IAG 1971)

$$f = \frac{3}{2}J_2 + \frac{m}{2} + \frac{9}{8}J_2^2 + \frac{15}{28}J_2m + \frac{3}{56}m^2, \quad (4.54)$$

$$\beta = -f + \frac{5}{2}m - \frac{17}{14}fm + \frac{15}{4}m^2, \quad (4.55)$$

$$m = \frac{\omega^2 a^2 b}{GM}, \quad (4.56)$$

$$\gamma_0 = \gamma_a (1 + \beta \sin^2 \varphi + \beta_1 \sin^2 2\varphi), \quad \beta_1 = \frac{1}{8}f^2 - \frac{5}{8}fm. \quad (4.57)$$

One of the first applications of Clairaut's theorem was made by *Helmert* (1901). An adjustment to the gravity formula (4.57) of about 1400 free-air reduced gravity values yielded the parameters $\gamma_a = 9.7803 \text{ ms}^{-2}$ and $\beta = 0.005302$, with a flattening of $f = 1/298.3$.

The harmonic coefficients of second and fourth degree may be computed from f and m as follows:

$$J_2 = \frac{2}{3}f - \frac{m}{3} - \frac{1}{3}f^2 + \frac{2}{21}fm, \quad J_4 = -\frac{4}{5}f^2 + \frac{4}{7}fm. \quad (4.58)$$

For today's accuracy requirements, an expansion up to $n = 3$ (corresponding to $l = 6$) is generally adequate. That is, the expansion has to include the terms of the order f^3 (COOK 1959). Developments up to the order f^5 have been given by CHEN (1982).

Near the earth's surface, a Taylor series expansion with respect to the ellipsoidal height h is sufficient for the derivation of the normal gravity in the *exterior space*:

$$\gamma = \gamma_0 + \left(\frac{\partial \gamma}{\partial h} \right)_0 h + \frac{1}{2} \left(\frac{\partial^2 \gamma}{\partial h^2} \right)_0 h^2 + \dots \quad (4.59)$$

The partial derivative $\partial \gamma / \partial h$ is obtained by applying Bruns' equation (3.71) to the exterior space:

$$\frac{\partial \gamma}{\partial h} = -2\gamma \bar{J} - 2\omega^2, \quad (4.60)$$

where \bar{J} is the mean curvature of the ellipsoid (4.19). A series expansion up to the order of f leads to the vertical component of the normal gravity gradient

$$\frac{\partial \gamma}{\partial h} = -2 \frac{\gamma}{a} (1 + f + m - 2f \sin^2 \varphi). \quad (4.61)$$

The second derivative can be derived from a spherical approximation of γ , see (3.17). With

$$\gamma = \frac{GM}{r^2}, \quad \frac{\partial \gamma}{\partial r} = -2 \frac{GM}{r^3} = -2 \frac{\gamma}{r}$$

we obtain

$$\frac{\partial^2 \gamma}{\partial r^2} = \frac{6GM}{r^4} = 6 \frac{\gamma}{r^2}. \quad (4.62)$$

Inserting the above into (4.59), with $r = a$ and $\gamma = \gamma_0$, leads to the normal gravity as a function of φ and h :

$$\gamma = \gamma_0 \left(1 - \frac{2}{a} (1 + f + m - 2f \sin^2 \varphi) h + \frac{3}{a^2} h^2 \right). \quad (4.63)$$

For higher altitudes, γ has to be derived by differentiating the normal gravity potential (4.38) either in the β, λ, u -system or, after corresponding transformation, in the φ, λ, h or the ϑ, λ, r -system, cf. HEISKANEN and MORITZ 1967, p.228.

With $\gamma = 9.81 \text{ ms}^{-2}$ and $a = 6378 \text{ km}$, we get $\partial\gamma/\partial h = -3.08 \mu\text{ms}^{-2}/\text{m}$ and $\partial^2\gamma/\partial h^2 = 1.5 \times 10^{-6} \mu\text{ms}^{-2}/\text{m}^2$. More detailed numerical values are given in [4.3]. In gravity reductions the value $-3.086 \mu\text{ms}^{-2}/\text{m}$ is used conventionally.

4.2.3 Geometry of the Normal Gravity Field

The geometry of the normal gravity field is represented by the spheropotential surfaces and the normal plumb lines.

The *spheropotential surfaces* are surfaces of constant normal gravity potential

$$U = U(\mathbf{r}) = \text{const.} \quad (4.64)$$

With the exception of the surface of the level ellipsoid ($U = U_0$), spheropotential surfaces deviate from ellipsoids and are not parallel to each other. The *normal plumb lines* intersect the spheropotential surfaces orthogonally. Due to the non-parallelism of the level surfaces, they are slightly curved in the plane of the meridian (Fig. 4.8).

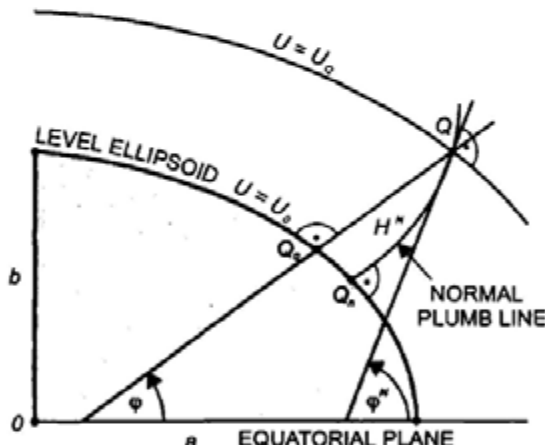


Fig. 4.8. Spheropotential surfaces, normal plumb line, normal height

In order to describe the geometry of the normal gravity field, "normal" geodetic coordinates φ^N, λ^N, U are introduced. They are defined in analogy to the "natural" coordinates Φ, Λ, W of the actual gravity field, cf. [3.2.3]. They refer to the point Q , which is related to the surface point $P(\Phi, \Lambda, W)$ by the conditions:

$$\varphi_Q^N = \Phi_P, \quad \lambda_Q^N = \Lambda_P, \quad U_Q = W_P. \quad (4.65)$$

The surface thus defined in a point-wise manner approximates the physical surface of the earth, with deviations less than 100 m and less than one arcmin respectively. This surface is called the *telluroid* (HIRVONEN 1960). It is not a level surface of the normal gravity field, but it resembles the earth's surface.

The *normal geodetic latitude* φ^N is the angle measured in the meridian plane between the equatorial plane of the ellipsoid and the direction of the normal plumb line. It differs from the geodetic latitude φ , introduced in [4.1.1], by the small angle $\delta\varphi^N$. This difference is a result of the plumb line curvature (Fig. 4.8), see below. The *normal geodetic longitude* λ^N is equal to the geodetic longitude λ . The *normal gravity potential* U relates the point Q to the level surface $U = U_Q$.

Instead of U , the potential difference $U_0 - U_Q$ to the level ellipsoid may be used. With the geopotential number $C = W_0 - W_p$ (3.104), and the condition $U_Q = W_p$, we also have $U_0 = W_0$. From this, we may derive the *normal height* H^N , already introduced in [3.4.3], by

$$H^N = \frac{U_0 - U_Q}{\bar{\gamma}} = \frac{W_0 - W_p}{\bar{\gamma}}. \quad (4.66)$$

Hence, H^N is defined as the distance between Q and the level ellipsoid measured along the normal plumb line. To a good approximation, H^N may be measured along the ellipsoidal normal passing through the surface point. According to (3.107), $\bar{\gamma}$ is the mean normal gravity between the ellipsoid and Q . Substituting γ from (4.63) into (3.107) and integrating yields

$$\bar{\gamma} = \gamma_0 \left(1 - \frac{1}{a} (1 + f + m - 2f \sin^2 \varphi) H^N \right). \quad (4.67)$$

Hence, $\bar{\gamma}$ may be computed rigorously in an iterative manner. Since C can be derived from measurements, the normal height can be determined without any hypothesis. Extending the normal heights downward from the earth's surface yields the *quasigeoid*, which is used as a reference surface for heights, cf. [3.4.3].

The normal geodetic coordinates $\varphi^N, \lambda^N, H^N$ have gained special importance for the direct determination of the physical surface of the earth according to the theory of Molodenski, cf. [6.5.1]. Normal heights have been introduced for a number of national height systems, cf. [3.4.3], [7.2].

The *curvature* of the *spheropotential surfaces* is described by the second derivatives of U , in analogy to the actual gravity field, see (3.57), (3.58). In the

local ellipsoidal system, the curvatures in the direction of the meridian and the parallel are given by

$$k_{\bar{x}}^N = -\frac{U_{\bar{x}}}{\gamma}, \quad k_{\bar{y}}^N = -\frac{U_{\bar{y}}}{\gamma}. \quad (4.68)$$

The geodesic *torsion* is zero due to the rotational symmetry of the level ellipsoid:

$$t_{\bar{x}}^N = -\frac{U_{\bar{y}}}{\gamma} = 0. \quad (4.69)$$

On the ellipsoid, the curvature is given by the principal radii of curvature M and N , see (4.13), (4.14):

$$k_{\bar{x}(0)}^N = \frac{1}{M}, \quad k_{\bar{y}(0)}^N = \frac{1}{N}. \quad (4.70)$$

Taking the rotational symmetry into account, and following (3.67), we get for the curvature of the projections of the *normal plumb line* onto the \bar{x}, \bar{z} and the \bar{y}, \bar{z} -plane respectively:

$$\kappa_{\bar{x}}^N = -\frac{U_{\bar{x}}}{g}, \quad \kappa_{\bar{y}}^N = -\frac{U_{\bar{y}}}{g} = 0. \quad (4.71)$$

On the level ellipsoid, we have with (4.20)

$$U_{\bar{x}(0)} = -\left(\frac{\partial \gamma}{\partial \bar{x}}\right)_0 = -\left(\frac{\partial \gamma}{M \partial \varphi}\right)_0. \quad (4.72)$$

Introducing the derivative $\partial \gamma / \partial \varphi$ from (4.53) and inserting into (4.71) yields with sufficient approximation

$$\kappa_{\bar{x}}^N = \frac{\beta}{M} \sin 2\varphi \quad (4.72a)$$

with $\beta =$ gravity flattening (4.44). For the change of the normal gravity along the meridian, we thus get

$$\left(\frac{\partial \gamma}{\partial \bar{x}} \right)_0 = \gamma_0 \frac{\beta}{M} \sin 2\varphi = 8.2 \sin 2\varphi \text{ n s}^{-2}, \quad (4.72b)$$

which corresponds to $8.2 \text{ nms}^{-2}/\text{m}$ at $\varphi = 45^\circ$. Together with the relation $U_{\bar{z}} = -\partial \gamma / \partial \bar{z}$, (4.68) to (4.72) completely define the Marussi tensor (3.69) for the normal gravity field. According to (3.75), the differential transformation from the local to the global geodetic system is also provided by the curvature parameters.

Finally, we derive the differences between the geodetic coordinates φ, λ and the normal geodetic coordinates φ^N, λ^N :

$$\varphi = \varphi^N + \delta\varphi^N, \quad \lambda = \lambda^N. \quad (4.73)$$

From (4.71) and (4.72) we obtain

$$d\varphi^N = - \int_0^{H^N} \kappa_{\bar{x}}^N dH^N = -\frac{\beta}{M} \sin 2\varphi H^N.$$

And with $\beta = 0.0053$ and $M \approx a = 6371 \text{ km}$ we get

$$\delta\varphi^N = -0.00017'' \sin 2\varphi H^N, \quad (4.74)$$

where H^N is in meters.

4.3 Geodetic Reference Systems

Geodetic reference systems provide numerical values for the parameters of a geodetic earth model. The systems are recommended by the International Union of Geodesy and Geophysics (IUGG) and represent the best parameter values for a designated epoch. The systems generally serve as a standard over a long time span for geodesy and related disciplines such as astronomy, cartography, geophysics, engineering, and navigation. Actual best values are determined at shorter time intervals and published by the International Association of Geodesy, cf. [6.8.1].

In the 19th and early 20th century, the geometric parameters of reference ellipsoids were derived from various terrestrial data sets and then introduced as a reference for national geodetic surveys, cf. [1.3.3], [7.1.2]. Normal gravity formulae referred to these ellipsoids have been derived since about 1900 and used for national gravimetric surveys. These regional or local reference systems

may be regarded as precursors of the present global systems, based on the theory of the level ellipsoid.

All reference systems are supposed to be geocentric, with the Z-axes coinciding with the earth's axis of rotation and the direction of the X-axis pointing to the Greenwich meridian. While the earlier reference systems may have large deviations from the geocentric system, recent reference systems agree at the "cm"-order. The orientation of geodetic systems with respect to the earth is described by the "Geodetic Datum", cf. [6.2.2].

Geodetic reference systems based on the theory of the level ellipsoid were first introduced in 1924/1930. At the IUGG General Assembly in Madrid 1924, Hayford's ellipsoid was introduced as the *International Ellipsoid*, with the parameters

$$a = 6378388 \text{ m}, f = 1/297.0. \quad (4.75a)$$

The General Assembly in Stockholm (1930) adopted the gravity formula established by G. Cassini for Hayford's ellipsoid:

$$\gamma_0 = 9.780\,49 \left(1 + 0.005\,2884 \sin^2 \varphi - 0.000\,0059 \sin^2 2\varphi \right) \text{ ms}^{-2}. \quad (4.75b)$$

This corresponds to the normal gravity formula (4.57), assuming a level ellipsoid.

The geometric parameters a and f were calculated by J. F. Hayford (1909) from astrogeodetic observations in the U.S.A. W. A. Heiskanen (1928) determined the equatorial gravity from an adjustment of isostatically reduced gravity values. The international reference system of 1924/1930 is thus defined by the four parameters a, f, γ_0, ω . The corresponding ellipsoid has been applied in numerous geodetic surveys; also, the normal gravity formula has found broad acceptance.

At the General Assembly of the IUGG in Luzern (1967), the 1924/1930 reference system was replaced by the *Geodetic Reference System 1967* (GRS67), see IAG (1971). It was defined by the following parameters:

$$a = 6\,378\,160 \text{ m}, GM = 398\,603 \times 10^9 \text{ m}^3 \text{ s}^{-2}, J_2 = 1082.7 \times 10^{-6}. \quad (4.76a)$$

The angular velocity of the earth's rotation

$$\omega = 7.292\,115\,146\,7 \times 10^{-5} \text{ rad s}^{-1}, \quad (4.76b)$$

not mentioned in the IUGG resolution, was adopted as the fourth parameter. The reference ellipsoid corresponding to this definition was declared a level ellipsoid.

The calculation of the semimajor axis was based on astrogeodetic observations collected over the entire earth, which were transformed into a uniform system by the inclusion of gravimetric data. Observations of space probes yielded the geocentric gravitational constant, which includes the mass of the atmosphere. The dynamic form factor was derived from the orbit perturbations of artificial satellites, and the angular velocity was adopted from astronomy. The GRS67 has been used especially for scientific problems and for a number of recently established geodetic networks.

At the IUGG General Assembly in Canberra (1979), the *Geodetic Reference System 1980* (GRS80) was introduced. It is also based on the theory of the geocentric equipotential ellipsoid, with the defining constants (MORITZ 2000):

$$\left. \begin{array}{ll} a = 6378137 \text{ m} & \text{equatorial radius of the earth} \\ GM = 398\,600.5 \times 10^9 \text{ m}^3 \text{ s}^{-2} & \text{geocentric gravitational constant of the earth} \\ & \quad (\text{including the atmosphere}) \\ J_2 = 1\,082.63 \times 10^{-6} & \text{dynamical form factor of the earth,} \\ & \quad (\text{excluding the permanent tidal deformation}) \\ \omega = 7.292\,115 \times 10^{-5} \text{ rad s}^{-1} & \text{angular velocity of the earth.} \end{array} \right\} \quad (4.77a)$$

With $M_{\text{atm}} = 0.88 \times 10^{-6} M_{\oplus}$, we have $GM_{\text{atm}} = 0.35 \times 10^9 \text{ m}^2 \text{ s}^{-2}$.

The system is consistent with the 1976 IAU system of astronomical constants, cf. [2.4.2].

With respect to the orientation, it is stated that the minor axis of the reference ellipsoid be parallel to the direction defined by the Conventional International Origin and that the primary meridian be parallel to the zero meridian of the BIH adopted longitudes, cf. [2.5.2].

The equatorial radius has been derived from laser distance measurements to satellites, satellite altimetry, and Doppler positioning, with an uncertainty of $\pm 0.5 \text{ m}$. The calculation of the geocentric gravitational constant was based on space probes and lunar and satellite laser data ($\pm 0.1 \times 10^{-9}$), while the value for the dynamic form factor was taken from global gravity models ($\pm 5 \times 10^{-9}$).

Numerical values for derived parameters include (MORITZ 2000):

geometric constants, cf. [4.1.1], [4.1.2]:

| | | |
|--|-------------------------------------|---------|
| $b = 6\ 356\ 752.3141\text{ m}$ | semiminor axis | (4.77b) |
| $\varepsilon = 521\ 854.0097\text{ m}$ | linear eccentricity (4.3) | |
| $c = 6\ 399\ 593.6259\text{ m}$ | polar radius of curvature (4.16) | |
| $e^2 = 0.006\ 694\ 380\ 022\ 90$ | first eccentricity (e) (4.1b) | |
| $e'^2 = 0.006\ 739\ 496\ 775\ 48$ | second eccentricity (e') (4.1c) | |
| $f = 0.003\ 352\ 810\ 681\ 18$ | flattening (4.1a) | |
| $1/f = 298.257\ 222\ 101$ | reciprocal flattening | |
| $G = 10\ 001\ 965.7293\text{ m}$ | meridian quadrant (4.21a) | |

physical constants, cf. [4.2.2]:

| | | |
|---|---------------------------------------|---------|
| $U_0 = 62\ 636\ 860.850\text{ m}^2\text{ s}^{-2}$ | normal potential at ellipsoid (4.40) | (4.77c) |
| $J_4 = -0.000\ 002\ 370\ 912\ 22$ | spherical harmonic coefficient (4.45) | |
| $J_6 = 0.000\ 000\ 006\ 083\ 47$ | spherical harmonic coefficient (4.45) | |
| $J_8 = -0.000\ 000\ 000\ 014\ 27$ | spherical harmonic coefficient (4.45) | |
| $m = 0.003\ 449\ 786\ 003\ 08$ | (4.50) | |
| $\gamma_a = 9.780\ 326\ 7715\text{ m s}^{-2}$ | normal gravity at equator (4.41) | |
| $\gamma_b = 9.832\ 186\ 3685\text{ m s}^{-2}$ | normal gravity at pole (4.41) | |
| $\beta = 0.005\ 302\ 440\ 112$ | (4.44) | |
| $k = 0.001\ 931\ 851\ 353$ | (4.41b) | |

Normal gravity can be computed by the closed formula (4.41) or the series expansion

$$\gamma_0 = \gamma_a \left(1 + 0.005\ 279\ 0414 \sin^2 \varphi + 0.000\ 023\ 2718 \sin^4 \varphi + 0.000\ 000\ 1262 \sin^6 \varphi + 0.000\ 000\ 0007 \sin^8 \varphi \right), \quad (4.78a)$$

which is accurate to $10^{-3}\text{ }\mu\text{m s}^{-2}$. The conventional series (4.57) has an accuracy of only $1\mu\text{m}^{-2}$:

$$\gamma_0 = 9.780\ 327 \left(1 + 0.005\ 3024 \sin^2 \varphi - 0.000\ 0058 \sin^2 2\varphi \right) \text{ m s}^{-2}. \quad (4.78b)$$

Inserting the values for the GRS80 into (4.63) yields the change of normal gravity with height:

$$\gamma = \gamma_0 - \left(3.0877 \times 10^{-3} - 4.3 \times 10^{-6} \sin^2 \varphi \right) h + 0.72 \times 10^{-6} h^2 \text{ ms}^{-2} \quad (4.79)$$

with h in km. A development accurate to 10 nm s^{-2} for heights up to 10 km is given by WENZEL (1989).

According to the definition of GM, γ_0 refers to the total mass of the earth including the atmosphere. If normal gravity values are required on the ellipsoid, or within the range of the atmosphere, the effect of the air masses above the calculation point must be subtracted from γ_0 . The corresponding reduction

amounts to $-8.7 \mu\text{ms}^{-2}$ ($h = 0$), $-4.7 \mu\text{ms}^{-2}$ ($h = 5 \text{ km}$), and $-0.1 \mu\text{ms}^{-2}$ ($h = 30 \text{ km}$), ECKER and MITTERMAYER (1969).

5 Methods of Measurement

Modeling of geodetic parameters is based on observations taken on the earth's surface and in its exterior space. Different measurement methods are available, delivering geometric or physical quantities. Geometric methods rely primarily on electromagnetic waves and thus are influenced by atmospheric refraction [5.1]. The measurement methods may be divided into

- observations employing artificial satellites as targets (including the moon) or sensors: satellite observations [5.2],
- observations to fixed stars and extragalactic radio sources: geodetic astronomy [5.3],
- terrestrial gravity and gravity gradient measurements: gravimetry [5.4],
- determination of coordinate differences between points on the surface of the earth: terrestrial geodetic measurements [5.5].

The measurement methods depend on available technology, where electronics governs data collection and online data-processing (KAHMEN 1978, SCHLEMMER 1996). Satellite techniques now dominate global and regional surveys, while terrestrial methods are used for interpolation in space and time. Accuracy limits are governed by calibration errors and elimination or reduction of disturbing influences such as temperature, atmospheric pressure, magnetic field variations, microseismicity, atmospheric refraction, and local instabilities. Thus the inherent precision of the respective technique may deteriorate by a factor of two to three, or more.

5.1 Atmospheric Refraction

In practically all geodetic measurements, electromagnetic waves serve as signal carriers; this includes the methods of satellite and terrestrial geodesy as well as geodetic astronomy. From the broad spectrum of electromagnetic waves, the visible light (380 to 780 nm, corresponding to 7.9 to $3.8 \cdot 10^{14}$ Hz), the near infrared (up to 1 μm), and the microwave parts (1 mm to 1 m, corresponding to 300 GHz to 300 MHz) are used. When traveling through the atmosphere, the waves experience changes in velocity and curvature of the path, depending on the physical state of the atmosphere [5.1.1]. Signal propagation is different in the troposphere and the ionosphere and has to be treated separately [5.1.2], [5.1.3].

Different methods have been developed in order to eliminate or reduce the effects of atmospheric refraction on geodetic measurements. These include

instrument design, observation methodology, and the use of atmospheric models based on data collected on the earth's surface and in space. The individual strategies will be discussed in the chapters that pertain to measurement methods, see also BRUNNER (1984a), DE MUNCK and SPOELSTRA (1992).

Acoustic waves are employed for positioning on, and mapping of, the ocean floor and the bottom of rivers and lakes. The propagation of these waves through water differs from their behavior in vacuum and depends on water properties, cf. [5.5.2].

5.1.1 Fundamentals

According to *Fermat's principle*, the path s of an electromagnetic wave is determined by the condition of a minimum travel time Δt of the wave (MORITZ and HOFMANN-WELLENHOF 1993, p.158):

$$\Delta t = \int_{\text{path}} dt = \int_{\text{path}} \frac{ds}{v} = \min . \quad (5.1)$$

The velocity v differs from the velocity in vacuum c (2.2) by the *index of refraction* n (also called refractive index):

$$n = \frac{c}{v} . \quad (5.2)$$

For a gaseous medium, $n > 1$ is proportional to the density of the gas. If the medium is dispersive for a certain spectral domain, n also depends on the wavelength: *dispersion*. An average value for n near the earth's surface is 1.0003. Instead of n , the *refractivity*

$$N = (n - 1) \cdot 10^6 \quad (5.3)$$

is frequently used.

Inserting (5.2) into (5.1) yields

$$\Delta t = \frac{1}{c} \int_{\text{path}} n ds = \min . \quad (5.4)$$

By setting

$$n ds = d\bar{s} ,$$

(5.4) can also be expressed as a minimum condition for the “electromagnetic” path length (Fig. 5.1):

$$\bar{s} = \int_{\text{path}} d\bar{s} = \int_{\text{path}} n ds = \min . \quad (5.5)$$

Solving the variational problem (5.5) yields the path \bar{s} , but requires the knowledge of n along the path.

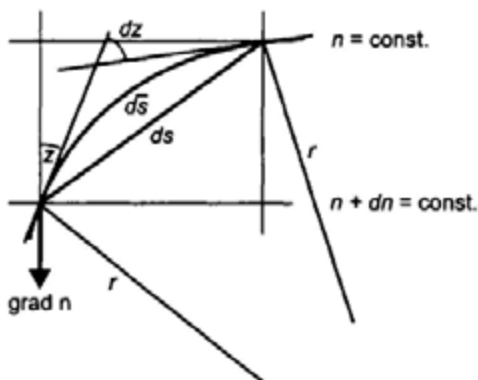


Fig. 5.1. Ray bending in the atmosphere

The effect of refraction on *distance* is given by the difference between the actual path length \bar{s} and the straight-line s (chord):

$$\bar{s} - s = \int_{\text{path}} n ds - \int_0^s ds = \int_0^s (n - 1) ds + \left(\int_{\text{path}} n ds - \int_0^s n ds \right). \quad (5.6)$$

The first term on the right side accounts for the difference in length due to the longer travel time in the atmosphere, while the second term represents the effect of the bending of the ray (JANES et al. 1991).

The refraction effect on *curvature* can be estimated by assuming that the air density is stratified horizontally (Fig. 5.1). Snell's law describes the bending of the ray as it passes through layers of varying refractive index, which corresponds to Fermat's principle:

$$n \sin z = \text{const.} \quad (5.7a)$$

Or for two points P_1 and P_2 :

$$n_1 \sin z_1 = n_2 \sin z_2 . \quad (5.7b)$$

Under the above assumption, the angle between the normal to the surface $n = \text{const.}$ and the tangent to the ray with curvature $1/r$ is the zenith angle z . Differentiation of (5.7) yields

$$\sin z \, dn + n \cos z \, dz = 0 .$$

With

$$dn = (\text{grad } n) \cdot d\mathbf{s} = |\text{grad } n| \cos z \, ds ,$$

we obtain the curvature

$$\frac{1}{r} = \frac{dz}{ds} = - \frac{|\text{grad } n|}{n} \sin z . \quad (5.8)$$

By separating the horizontal and the vertical component of $\text{grad } n$, we get the curvatures of the ray projected into the horizontal and the vertical planes. The corresponding effects on horizontal and vertical angles are called *horizontal* (lateral) and *vertical* refraction, respectively.

Horizontal refraction is about one to two orders of magnitude less than vertical refraction. Neglecting it yields a simplified formula for the curvature of *vertical refraction*:

$$\frac{1}{r} = - \frac{1}{n} \frac{dn}{dh} \sin z , \quad (5.9a)$$

where h is the height, cf. [4.1.3].

In *terrestrial* geodetic measurements, we have $n \approx 1$ and $z \approx 90^\circ$, which leads to

$$\frac{1}{r} = - \frac{dn}{dh} . \quad (5.9b)$$

Instead of $1/r$, the *coefficient of refraction* k is often used. It is defined as the ratio between the radius of the earth R and the curvature radius r :

$$k = \frac{R}{r} = - R \frac{dn}{dh} . \quad (5.10)$$

The vertical *refraction angle* δ is the effect of refraction on observed zenith angles (Fig. 5.2). It results from integrating $1/r$ resp. dn/dh along the path:

$$\delta = \frac{1}{s} \int_0^s (s - s_i) \frac{dn}{dh} ds . \quad (5.11a)$$

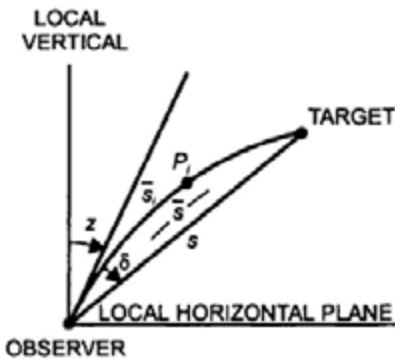


Fig 5.2. Vertical refraction

Here the local vertical gradient of n is weighted according to the distance from the observer; values from closer distances receive a greater weight. For a spherical arc ($r = \text{const.}$), and taking (5.10) into account, (5.11a) reduces to

$$\delta = \frac{k}{2R} s . \quad (5.11b)$$

In most geodetic applications, the signal is transferred by a modulation of the carrier wave. This can be regarded as a superposition of a group of waves with different frequencies. While *phase velocity* v_{ph} , introduced in (5.2), refers to the monochromatic carrier wave, the center of a short wave group (signal energy) travels with the *group velocity*

$$v_{gr} = v_{ph} - \lambda \frac{dv_{ph}}{d\lambda} . \quad (5.12)$$

In a dispersive medium, we have $n = n(\lambda)$ and $dv_{ph}/d\lambda \neq 0$ (LEICK 1995). Taking (5.2) into account delivers the corresponding *group refractive index*

$$n_{gr} = n_{ph} - \lambda \frac{dn_{ph}}{d\lambda} = n_{ph} + f \frac{dn_{ph}}{df} , \quad (5.13)$$

with f = frequency, cf. [5.1.2], [5.1.3].

For *standard air* (temperature 273.15 K, air pressure 1013.25 hPa, humidity 0.0 hPa, CO₂ content 0.0375 %), the *phase refractivity* may be calculated as follows (IAG resolution, Gen. Ass. Birmingham 1999):

$$N_{ph} = (n_{ph} - 1)10^6 = 287.6155 + \frac{1.62887}{\lambda^2} + \frac{0.01360}{\lambda^4}, \quad (5.14)$$

where λ is the carrier wave length in μm , and n_{ph} is the corresponding phase refractive index. The *group refractivity* is given by

$$N_{gr} = (n_{gr} - 1)10^6 = 287.6155 + \frac{4.88660}{\lambda^2} + \frac{0.06800}{\lambda^4}, \quad (5.15)$$

with n_{gr} = group refractive index.

According to (5.6) and (5.11), the refraction effect on distances and angles depends on the index of refraction and its gradient along the path of the ray, which behave differently in the troposphere than in the ionosphere.

5.1.2 Tropospheric Refraction

The *troposphere* is the lower layer of the atmosphere. It extends to a height of about 9 km at the poles and 16 km at the equator. Weather processes take place in tropospheric region, where nearly 90% of the atmospheric masses are concentrated. The *tropopause* as a boundary layer separates the troposphere from the *stratosphere*, which extends to about 50 km. The troposphere, tropopause, and stratosphere are electronically neutral. The index of refraction n depends on temperature T , pressure p and humidity e . For visible light, the troposphere behaves as a dispersive medium, cf. [5.1.1]. The refractive index decreases with height and becomes nearly 1 at about 40 km. Tropospheric refraction is the combined effect from the ground to this "effective" height. Above 50 km the atmosphere is ionized, cf. [5.1.3].

The *meteorological parameters* T , p , e not only depend strongly on height but also on latitude, land/ocean distribution, topography, vegetation, and local conditions. These variables produce large to small-scale anomalies of n . Variations with time are of long-term, seasonal, daily, and turbulent character. Rapid fluctuations are especially pronounced close to the earth's surface, up to 10 to 30 m above the ground.

Temperature T decreases in the troposphere almost linearly with height h according to

$$dT/dh \approx -0.0065^\circ\text{C}/\text{m}, \quad (5.16a)$$

followed by a slight increase in the stratosphere. Horizontal temperature gradients may reach a few $^\circ\text{C}/100 \text{ km}$. Close to the ground, temperature variations are pronounced, including temperature inversion during night time and convection at noon.

Air pressure p decreases exponentially with height. Assuming hydrostatic equilibrium, the vertical pressure gradient depends on density ρ and gravity g . Near the surface of the earth, this leads to

$$dp/dh = -\rho g = -0.034 \frac{P}{T} = -0.12 \text{ hPa/m} \quad (5.16b)$$

at standard conditions ($T = 288 \text{ K}$, $p = 1013 \text{ hPa}$).

Humidity is rather irregularly distributed and concentrated in a layer of a few km above ground, where strong variations also occur with time. Humidity is measured by the water vapour pressure e , which is about 10 to 20 hPa at mid-latitudes close to the surface. It tends to decrease with height, with a mean value of

$$de/dh = -0.0035 \text{ hPa/m} \quad (5.16c)$$

near the ground.

Empirical relations have been derived between the index of refraction and the meteorological parameters for both light and microwaves (BOMFORD 1980, p.42, LANGLEY 1998).

With atmospheric conditions different from the standard air, cf. [5.1.1], the group refractivity of visible *light* and near *infrared* waves in ambient moist air is (IAG resolution, Gen. Ass.Birmingham 1999):

$$N_i = (n_i - 1)10^6 = \frac{273.15}{1013.25} \frac{p}{T} N_g - 11.27 \frac{e}{T}, \quad (5.17)$$

with T in Kelvin, p and e in hPa. Equation (5.17) is also valid for unmodulated light with the corresponding phase refractivity (5.14).

The refractivity of *microwaves* (independent of the wavelength) is given by the formula of Thayer (1974)

$$N_m = (n_m - 1)10^6 = 77.60 \frac{p}{T} - 13 \frac{e}{T} + 3.78 \cdot 10^5 \frac{e}{T^2}, \quad (5.18)$$

which is practically identical with the formula of Essen and Froome (IAG resolution, Gen. Ass. Berkeley 1963).

The first term on the right side of (5.18) represents a "dry" component of the refractivity. It contributes about 90% to the total tropospheric refraction in the lower 15 km and can be modeled from surface pressure, assuming hydrostatic equilibrium. The "wet" component, as expressed by the terms depending on e (especially the last one), is extremely difficult to model but approaches zero at around a height of 10 km.

In order to keep the error in the index of refraction less than 10^{-6} , the meteorological parameters in (5.17) and (5.18) have to be determined to about $\pm 1^\circ\text{C}$ for temperature, $\pm 3.5 \text{ hPa}$ for pressure, and $\pm 25 \text{ hPa}$ (light) resp. $\pm 0.2 \text{ hPa}$ (microwaves) for humidity.

Differentiating (5.17) and (5.18) with respect to the height h yields the dependence of the *curvature* on the meteorological parameters. Neglecting minor terms and taking (5.16b) into account, we obtain for the surface near layers

$$\frac{dN_l}{dh} = -78 \frac{P}{T^2} \left(0.034 + \frac{dT}{dh} \right) - \frac{11}{T} \frac{de}{dh} \quad (5.19a)$$

for *light*. For *microwaves*, the last term on the right side (wet component) changes to

$$+ \frac{3.7 \cdot 10^5}{T^2} \frac{de}{dh}. \quad (5.19b)$$

Thus according to (5.10), the *coefficient of refraction* k has to be determined for light with an accuracy of $\pm 2^\circ\text{C}$ in temperature, $\pm 6 \text{ hPa}$ in air pressure, and $\pm 0.0002^\circ\text{C}/\text{m}$ in the temperature gradient in order to achieve a relative accuracy of 1%. For microwaves, the admissible errors may be two times larger. The gradient of the water vapor pressure should be determined with $\pm 0.005 \text{ hPa/m}$ for light and $\pm 0.0001 \text{ hPa/m}$ for microwaves. Hence, the most critical parameters are the vertical gradients of temperature and, especially for microwaves, of the water vapor pressure. According to (5.11b), an error of 1% in k would produce an error in the refraction angle of $\pm 0.2''$ over a distance of 10 km and $\pm 0.4''$ over 25 km.

In the layers close to the ground, the strong variations of the meteorological parameters in space and time lead to corresponding changes in the *coefficient of refraction*, with pronounced seasonal and day/night variations (HOEPCKE 1966). Under average daytime conditions with a clear sky, and for heights between 40 m and 100 m above the ground, we have for *light*

$$k_l = 0.13 \text{ or } r_l = 8R, \quad (5.20a)$$

and for *microwaves*

$$k_m = 0.25 \text{ or } r_m = 4R. \quad (5.20b)$$

Tropospheric models generally assume concentric spherical layers and azimuthal symmetry and neglect variations with time. Global models are provided by standard atmospheres in the form of vertical profiles for temperature, pressure, and density. The U.S. standard atmosphere (1976) approximates mean mid-latitude conditions for dry air. Latitudinal and seasonal departures are given by supplements, NOAA (1966, 1976).

More refined refraction models have been developed for the reduction of geodetic measurements; these models employ observed surface data as input (HOPFIELD 1969, SAASTAMOINEN 1972/1973, NEILL 1996). A "mapping function" takes into account the increase in refraction with larger zenith angles z . A simple approximation is given by $1/\cos z$ for elevation angles that are not too small.

The path delays that GPS (Global Positioning System) *signals* experience when passing through the atmosphere, cf. [5.2.5], can be exploited for tropospheric and ionospheric monitoring (DAVIS et al. 1996). By separating the "dry" component from the *tropospheric* signal delay, the integrated perceptible *water vapor* can be estimated from the "wet" component (Bevis et al. 1992). Permanent GPS networks, cf. [7.3.1], supply this information on global and regional scales, with high temporal resolution.

Atmospheric sounding by *radio occultation* is possible with spaceborne GPS receivers installed on Low Earth Orbiters (LEO's), YUNK and MELBOURNE (1996). Here, the GPS signal is tracked after rising or before setting of the GPS satellite. The observed Doppler shift induced by atmospheric bending is used for constructing profiles of atmospheric density, pressure, temperature, and water vapor content, and evaluated for developing tropospheric models.

5.1.3 Ionospheric Refraction

As part of the higher atmosphere, the ionosphere is characterized by the presence of free, negatively-charged electrons and positive ions. Ionization is caused primarily by the impact of solar ultraviolet radiation and consequently depends on the density of the atmospheric gas and the intensity of the radiation. The ionosphere covers the region between 50 km and 1500 km above the earth, with a maximum electron density at a height of 200 to 300 km.

The ionosphere acts like a mirror at frequencies below 30 MHz. Radio waves of higher frequencies pass through the ionosphere but experience frequency-dependent effects (dispersive medium). Measurements to targets above the ionosphere are also affected by the electron concentration in the plasmasphere,

which extends up to a height of several earth radii above the equator and does not exist at the poles (KLOBUCHAR 1991, WANNINGER 1995).

The *index of refraction* depends primarily on the number N_e of electrons per m^3 : *electron density*. As a first order approximation, the *phase* refractive index is given by

$$n_{\text{ph}} = 1 - K \frac{N_e}{f^2}, \quad (5.21)$$

with the constant $K = 40.28 \text{ m}^3 \text{s}^{-2}$ and f = frequency. Higher terms of the order $1/f^3$ and $1/f^4$ also depend on the intensity of the earth's magnetic field and the direction of the signal propagation. In daytime, N_e (el/m^3) varies between about $10^8 \dots 10^{10}$ (60 to 90 km) over 10^{11} (105 to 160 km) to $10^{11} \dots 10^{12}$ (160 to 180 km) and 10^{12} (300 to 400 km).

As seen from (5.2) and (5.21), the phase velocity is larger than the velocity of light in vacuum, which corresponds to a larger wavelength of the signal compared to vacuum. Since signal propagation follows the group velocity, we insert (5.21) into (5.13) and obtain the group refractive index

$$n_{\text{gr}} = 1 + K \frac{N_e}{f^2}. \quad (5.22)$$

Inserting (5.21) resp. (5.22) into (5.6) delivers the difference between the electromagnetic path length \bar{s} and the straight-line connection s . This yields for carrier phase (n_{ph}) and for range (n_{gr}) observations respectively:

$$(\bar{s} - s)_{\text{ph}} = -(\bar{s} - s)_{\text{gr}} = -\frac{K}{f^2} \int_0^s N_e ds, \quad (5.23)$$

where the small effect of the path's bending has been neglected.

The integral of the electron density along the path is called *total electron content* (TEC):

$$\text{TEC} = \int_0^s N_e(s) ds. \quad (5.24)$$

It gives the number of electrons along the signal path in a cylindrical column with a cross section of 1 m^2 . Its unit is $1 \text{ TECU} = 10^{16} \text{ electrons/m}^2$. For a spherically-layered ionosphere, we may introduce the electron content along a

vertical column of height h and relate it to the TEC along the path by an oblique factor F ("mapping function"):

$$\text{TEC} = F \int_0^h N_e(h) dh. \quad (5.25)$$

For $z < 70^\circ$, we have $F \approx 1/\cos z_i$, with z_i = zenith angle at the subionospheric point P_i (Fig. 5.3). P_i is located at the "mean height" h_i of the ionosphere (single-layer model), with, e.g., $h_i = 350$ km. z_i can be calculated from h_i and the zenith angle z measured from the ground:

$$\sin z_i = \frac{R}{R + h_i} \sin z, \quad (5.26)$$

R = radius of the earth.

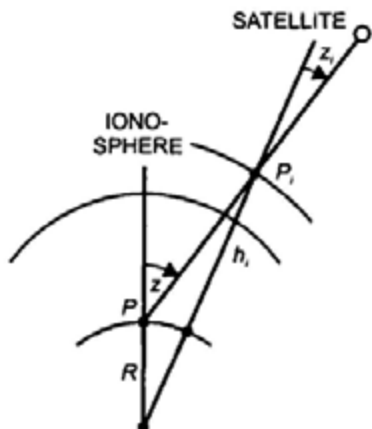


Fig. 5.3. Ionospheric refraction

The electron content in the ionosphere varies strongly with time. There are pronounced variations of daily, seasonal, and about an 11-year (solar activity cycle) period. Superimposed on to these more regular variations are irregular disturbances. Short-term scintillations occur primarily in the equatorial zones but also in the polar and auroral regions (magnetic storms). Traveling ionospheric disturbances of wavelike structure proceed with horizontal speeds between 100 and 1000 m/s at scales of some 10 to 1000 km and at periods from several minutes to a few hours.

Ionospheric models describe the distribution of N_e in space and time; they are based on the dependency of the ionospheric state on the position of the sun. Assuming a spherical shell distribution, they provide a smoothly varying TEC along vertical profiles and a mapping function for inclined signal propagation.

Among these models are the International Reference Ionosphere (IRI) 1995 and the GPS-broadcast model (KLOBUCHAR 1991). These models may deviate from reality by some 10%, due to the ionospheric disturbances. Refined models include observed ionospheric parameters and sunspot numbers (BROWN et al. 1991, KLEUSBERG 1998). The dispersion effect, on the other hand, allows us to eliminate most of the ionospheric refraction effects by employing two frequencies for signal propagation, cf. [5.2.4], [5.2.5], [5.2.7].

The ionospheric delay of GPS signals provides information on the structure and temporal behavior of the ionosphere. By analyzing the two carrier waves used to eliminate ionospheric refraction, cf. [5.5.2], the total electron content (TEC) along the line of sight from the receiver to the GPS satellite can be measured. The results of global GPS ground networks are used to generate global maps of TEC. Space-based GPS data, cf. [5.1.2], will significantly improve this ionospheric imaging, especially the vertical resolution (YUNK and MELBOURNE 1996).

5.2 Satellite Observations

Satellite geodesy utilizes artificial satellites and the moon as extraterrestrial targets or sensors. For a point mass earth model, the orbital motion of a satellite is described by Kepler's laws [5.2.1]. The actual gravitational field and non-gravitational forces create orbital "perturbations" [5.2.2]. Satellites used for geodetic applications differ in design, equipment, and orbit according to the respective observation technique and the mission purpose [5.2.3]. Classical measurement methods, introduced and employed from the 1960's to the 1980's, demonstrated the efficiency of satellite observations for establishing large-region geodetic control networks and gravitational field determination [5.2.4]. Today, the Global Positioning System (GPS) governs three-dimensional positioning at all scales [5.2.5], while laser distance-measurements primarily contribute to global reference networks [5.2.6]. By monitoring the ocean surface, satellite altimetry contributes to gravity field modeling [5.2.7], and high-resolution global gravity field recovery is expected from future satellite-to-satellite tracking and gravity gradiometry missions [5.2.8].

The theory of satellite orbits and satellite measurement methods are treated in textbooks and monographs on satellite geodesy, e.g., KAULA (1966), SCHNEIDER (1988), SEEBER (1993).

5.2.1 Undisturbed Satellite Motion

After the satellite has separated from the carrier, it begins its unrestrained revolution about the earth. We assume the gravitational point mass model, cf. [3.1.2], and neglect the mass of the satellite with respect to the earth's mass. If we also neglect perturbations of non-gravitational type and the effect of other

celestial bodies (two-body problem), Newton's second law of motion provides the *equation of motion* in the gravitational field:

$$\ddot{\mathbf{r}} = \text{grad } V = -\frac{GM}{r^2} \frac{\mathbf{r}}{r}. \quad (5.27)$$

\mathbf{r} is the geocentric position vector of the satellite and $\ddot{\mathbf{r}} = d^2\mathbf{r}/dt^2$ its acceleration, M and V are the mass and the gravitational potential of the earth respectively, cf. (3.16). The integration of the vectorial second-order differential equation (5.27) introduces six integration constants, e.g., position and velocity at a given epoch.

The fundamental theory on the two-body problem is given by celestial mechanics (BROUWER and CLEMENCE 1961, KOVALEVSKY 1989, SCHNEIDER 1992/1993). Such works also address the fundamentals of orbit perturbations, orbit computation, and the treatment of three and multi-body problems.

Johannes Kepler (1571-1630) derived three laws of planetary motion from the astronomic observations collected by *Tycho de Brahe* (1546-1601). *Keplerian motion* provides a geometric description of the equation of motion for an undisturbed central motion.

According to Kepler's laws, the satellite moves in an elliptical orbit. One focal point of the ellipse, with semimajor axis a and first eccentricity e (not to be confused with the corresponding parameters of the earth ellipsoid), coincides with the center of mass of the earth. In the orbital system (Fig. 5.4), the position of the satellite is described by the distance r from the center of mass and the true anomaly v . The true anomaly is the geocentric angle between the directions to the satellite and perigee. Instead of v , the eccentric anomaly E can be used, with the relations

$$r = a(1 - e \cos E), \tan v = \frac{\sqrt{1 - e^2} \sin E}{\cos E - e}. \quad (5.28)$$

With Kepler's third law, the mean (angular) velocity

$$\bar{n} = \sqrt{\frac{GM}{a^3}} \quad (5.29)$$

is introduced, describing a mean orbital motion. The mean anomaly

$$\bar{M} = \bar{n}(t - T) \quad (5.30)$$

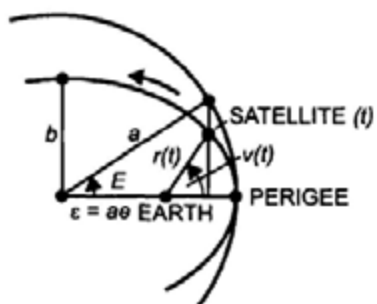


Fig. 5.4. Satellite orbital system

represents yet another parameter for describing the satellite's position in the orbit. It is generally preferred because it increases *linearly* with time. T is the epoch of the passage through the perigee, the closest approach to the earth. From \bar{M} , E can be computed iteratively using Kepler's equation:

$$\bar{M} = E - e \sin E . \quad (5.31)$$

The orbital system is transformed into the space-fixed equatorial system, cf. [2.4.1], by three rotations (Fig. 5.5). The right ascension of the ascending node Ω and the inclination i provide the orientation of the orbital plane in space. The argument of perigee ω orients the ellipse in the orbital plane. From the result of this transformation, we obtain the geocentric position vector (2.11) as a function

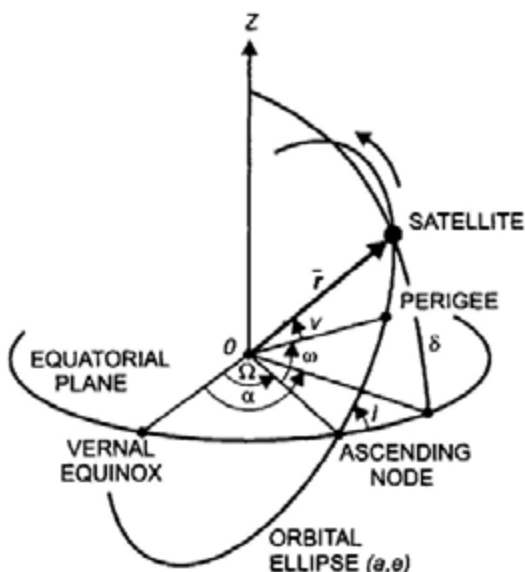


Fig. 5.5. Orbital and equatorial system

of the six Keplerian elements a , e , Ω , i , ω , and v (or equivalently E , \bar{M} , or T):

$$\mathbf{r} = r \begin{pmatrix} \cos \delta \cos \alpha \\ \cos \delta \sin \alpha \\ \sin \delta \end{pmatrix} = r \begin{pmatrix} \cos(\omega + v) \cos \Omega - \sin(\omega + v) \sin \Omega \cos i \\ \cos(\omega + v) \sin \Omega - \sin(\omega + v) \cos \Omega \cos i \\ \sin(\omega + v) \sin i \end{pmatrix}, \quad (5.32a)$$

with

$$r = \frac{a(1-e^2)}{1+e \cos v}. \quad (5.32b)$$

The six Keplerian parameters completely describe the orbital motion of the undisturbed satellite. They correspond to the integration constants of the equation of motion (5.27) and are used for the approximation of satellite orbits.

5.2.2 Perturbed Satellite Motion

The actual orbit of a satellite departs from the Keplerian orbit due to the effects of various "disturbing" forces. This includes the non-spherical parts of the earth's gravitation, the gravitational effects of moon and sun, atmospheric air drag, and solar radiation pressure, among others. These disturbing forces cause variations in time in the orbital elements (orbital perturbations) of secular, long, and short-periodic nature. The actual orbit can be viewed as the envelope of Keplerian ellipses, which are given at each instant by the actual orbital elements (osculating ellipses).

In order to account for the complete *gravitation* of the earth, the gravitational potential of a spherically symmetric earth must be amended by the *perturbing potential* R (not to be confused with the *disturbing* potential [6.1.1]):

$$V = \frac{GM}{r} + R. \quad (5.33)$$

According to equations (3.89) to (3.91), R can be expressed by a spherical harmonic expansion of the gravitational potential V through the harmonic coefficients J_{lm} , K_{lm} ($l \geq 2$). By substituting (5.33) into (5.27), the *equation of motion* now reads

$$\ddot{\mathbf{r}} = -\frac{GM}{r^2} \frac{\mathbf{r}}{r} + \text{grad } R. \quad (5.34a)$$

The spherical coordinates r, ϑ, λ (2.14) used in the expansion of V can be replaced by the orbital elements according to (5.28) and (5.32), see also Fig. 5.4. R then is described by the time-variable Keplerian orbital parameters and the harmonic coefficients:

$$R = R(a, e, \Omega, i, \omega, \bar{M}, J_{lm}, K_{lm}). \quad (5.34b)$$

The second-order differential equation (5.34) can be transformed into a system of first-order differential equations. They represent the time rates of the orbital parameters as a function of partial derivatives of the perturbing potential (i.e., of the harmonic coefficients) with respect to them. These first-order differential equations are known as Lagrange's perturbation equations (KAULA 1966, p.29, SEEBER 1993, p.75):

$$\left. \begin{aligned} \frac{da}{dt} &= \frac{2}{na} \frac{\partial R}{\partial \bar{M}} \\ \frac{de}{dt} &= \frac{1-e^2}{na^2 e} \frac{\partial R}{\partial \bar{M}} - \frac{\sqrt{1-e^2}}{na^2 e} \frac{\partial R}{\partial \omega} \\ \frac{d\omega}{dt} &= -\frac{\cos i}{na^2 \sqrt{1-e^2} \sin i} \frac{\partial R}{\partial i} + \frac{\sqrt{1-e^2}}{na^2 e} \frac{\partial R}{\partial e} \\ \frac{di}{dt} &= \frac{\cos i}{na^2 \sqrt{1-e^2} \sin i} \frac{\partial R}{\partial \omega} - \frac{1}{na^2 \sqrt{1-e^2} \sin i} \frac{\partial R}{\partial \Omega} \\ \frac{d\Omega}{dt} &= \frac{1}{na^2 e \sqrt{1-e^2} \sin i} \frac{\partial R}{\partial i} \\ \frac{d\bar{M}}{dt} &= n - \frac{1-e^2}{na^2 e} \frac{\partial R}{\partial e} - \frac{2}{na} \frac{\partial R}{\partial a} \end{aligned} \right\}. \quad (5.35)$$

The influence of the *gravitation of moon and sun* on a satellite can be calculated by corresponding extension of (5.27), which leads to the equation of motion for a four-body problem. As a result, a satellite orbit experiences secular and long-periodic perturbations, which may reach 100 m and more. In addition, *solid earth* and *ocean tides*, cf. [8.3.5], especially affect low-flying satellites. Corresponding corrections are based on the ephemeris of the moon and sun and on earth and ocean tide models.

Air drag is caused by friction of the satellite with atmospheric particles. It is proportional to the velocity of the satellite and depends on atmospheric density and the effective cross-sectional area to mass ratio. With increasing altitude, the air drag decreases rapidly and approaches zero at about 1000 km. Air drag

effects are corrected using high-altitude atmospheric models such as CIRA72 (Cospar International Reference Atmosphere 1972), cf. [5.1.2].

High-altitude satellites are especially affected by *solar radiation pressure* due to incident photons. The resulting perturbations depend on the attitude of the satellite with respect to the sun, the area to mass ratio, the reflectivity, and the solar flux. The earth-reflected solar radiation pressure (albedo) remains significantly smaller than the direct effect. Modeling of the radiation pressure effects is difficult, especially for satellites of complex structure. *Electromagnetic interactions* with the magnetic field of the earth occur in the ionosphere; however, they are small and can be considered by corrections. At the present level of accuracy, relativistic effects also have to be taken into account.

Orbit determinations are based on analytical or numerical methods (BOCCALETI and PUCACCO 1996/1999). For *analytical solutions*, all acting forces are expressed by rigorous relations and integrated in closed form. A first order approximation is already provided by the solution of (5.35). The position vector at any epoch t is given by the orbital elements at an initial epoch t_0 , the parameters of the gravitational field, and other models of disturbing forces:

$$\mathbf{r} = \mathbf{r}(a_0, e_0, \Omega_0, i_0, \omega_0, \bar{M}_0; GM, J_{lm}, K_{lm}; \dots; t). \quad (5.36)$$

For *numerical methods*, all forces are calculated for a particular position of the satellite and used as a starting condition for a step-wise integration. Classical astronomic methods for orbit determination are used, as developed by *Cowell* (integration of the total force) or *Encke* (integration of the difference to an osculating Kepler ellipse). Conventional integration methods based on a polynomial fit to consecutive points (e.g., the *Runge-Kutta* method) provide a rigorous solution.

The analytical method is rather laborious, and difficulties arise at applying it to non-gravitational forces. It is well suited for estimating the effects of perturbing forces on the satellite's orbit and for the planning of satellite missions and projects. Numerical methods are simple and generally applicable. They are used nearly exclusively today.

With precise models for the perturbing forces, orbit predictions can be extended to several revolutions of the satellite. Predicted orbits for individual satellites are published by the responsible agencies, while navigation satellites transmit their own orbital data, cf. [5.2.4], [5.2.5]. Precise orbit determinations are necessary for positioning and satellite altimetry. On the other hand, an orbit analysis can be used for deriving or improving the harmonic coefficients of the gravitational field, cf. [6.6.2].

Under good satellite tracking, and with precise models of both the gravitational field and the non-gravitational forces available, the ephemeris of laser and altimeter satellites can be determined with an accuracy of a few cm for short arcs (fractions of a day) and with dm-accuracy for long arcs (few days). The orbital data of high-altitude navigation satellites are predicted with an accuracy of a few m, and orbital post-processing using tracking data of dedicated networks reaches sub-dm accuracy, cf. [5.2.5].

5.2.3 Artificial Earth Satellites

Since the launch of Sputnik I (1957), artificial earth satellites have been used for geodetic purposes such as positioning and the determination of the earth's gravity field and rotation parameters. Only a few satellite missions have been designed exclusively for geodetic applications. However, a large number of satellites developed for navigation, remote sensing, and geophysics were and are used extensively in geodesy.

A satellite can be regarded as a moving *target* at high altitude and then used mainly for positioning. Because the satellite's orbit is affected by the gravitational field of the earth, the satellite may also serve as a *sensor* for gravitation. Satellites may reflect incident light only (passive satellites), or they may carry on board subsystems such as transmitters/receivers, different type sensors, clocks, and computers (active satellites). In the latter case, an energy supply is required, and lifetime is rather limited.

The mean *orbital velocity* of a satellite moving in an approximately circular orbit ($r = a$) is given from (5.29) by

$$\bar{v} = a\bar{n} = (GM/r)^{1/2}. \quad (5.37)$$

For a satellite close to the earth ($h = 1000$ km), we obtain, with $r = R + h = 7370$ km, a velocity of 7.4 km/s. Kepler's third law yields the period of revolution $U = 2\pi r/\bar{v} = 104$ min.

The intersection of the orbital plane with a non-rotating earth represents a great circle on the earth's surface: *subsatellite track*. The rotation of the earth causes a western displacement of subsequent satellite orbits (Fig. 5.6), with a shift on the equator given by

$$\Delta\lambda = 360^\circ \frac{U}{\text{sidereal day}} = 15^\circ \cdot U[\text{h}] = 0.25^\circ \cdot U[\text{min}]. \quad (5.38)$$

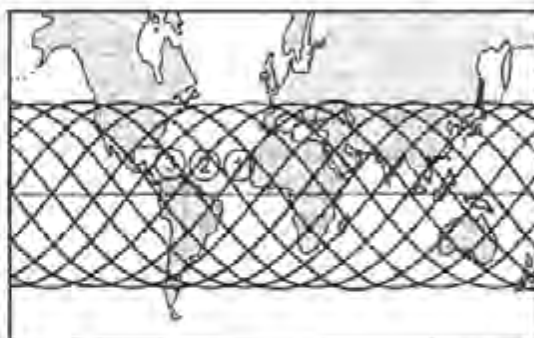


Fig. 5.6. Subsatellite tracks

The latitude range of the subsatellite tracks is determined by the inclination of the satellite.

The following aspects have to be considered during the *design* (choice of orbital parameters) of *satellite missions* for geodetic applications:

For *positioning*, the network geometry of the ground stations and the satellites plays a primary role. Simultaneous direction measurements from two ground stations to a satellite form a plane, and the intersection of planes provides positions. Range measurements utilize the intersection of spheres, whereas range differences, derived from Doppler-frequency shifts, use the intersection of hyperboloids. Satellites at high altitudes are less influenced by gravitational and air drag perturbations and therefore preferred.

Low altitude satellites are required for the determination of the *gravitational field*. This is mainly due to the attenuation factor $(a_e/r)^l$ in the spherical harmonic expansion of the gravitational potential (a_e = semimajor axis of the earth ellipsoid), cf. [3.3.2]. Consequently, the relative errors of the harmonic coefficients increase rapidly at higher degrees l . For $l = 20$, the amplitude of the corresponding structure of wavelength 2000 km is only 5% at a satellite altitude of 1000 km, as compared to the earth's surface. This attenuation is increased by the fact that the harmonic coefficients become smaller with increasing degree and order, cf. [6.6.2]. In order to resolve the gravitational field with a certain degree l at the equator, it follows from (5.38) that the satellite has to perform $2l$ revolutions/day, or a longer observation time is required. As seen from (5.35), the recovery of the harmonic coefficients strongly depends on the satellite's inclination. Corresponding satellite coverage is needed in order to avoid ill conditioning; too small inclinations and eccentricities must be avoided.

Gravitational field determination can be based on range and range-rate measurements between satellites and ground stations, as well as between satellites. A high field resolution is achieved by gravity gradiometers carried on

board low-flying satellites. Satellite altimetry provides the distance to sea level and thus a high-resolution approximation to the geoid, cf. [3.4.2]. Both an orientation into the vertical and a high orbital accuracy is required in that case.

Non-gravitational perturbing effects can be reduced by a small cross-sectional surface and large mass; a spherical shape offers special advantages. Atmospheric drag and solar radiation pressure may also be compensated by a drag-free system. In such a system, a proof mass is shielded by a shell attached to the satellite. The mass is affected only by gravitation, while surface forces act in addition on the shell. By continuously measuring the position changes between proof mass and shell, a feedback system keeps the satellite centered on the proof mass.

In order to detect *variations with time*, in position (point velocities), and in the gravitational field, long-term observations have to be carried out, preferably by the same satellite system.

Satellites used in geodesy may be equipped with the following techniques, of which combinations are used in many missions:

- *Direction* measurements have been made available by a sun-light reflecting skin (early balloon satellites), by flashing light devices, and by mirror arrays, cf. [5.2.4],
- transmitters/receivers serve for the continuous emission/reception of modulated radio waves used for *distance* and *Doppler* measurements, cf. [5.2.4], [5.2.5],
- retroreflector arrays of fused silica corner cubes reflect laser light pulses and are employed for *laser distance* measurements, cf. [5.2.6],
- vertical distance measurements to the ocean surface are performed by *radar altimeters*, cf. [5.2.7],
- gravitational *gradiometers* measure the gravitational gradient within the body of the satellite, cf. [5.2.8].

Dedicated systems have been developed specifically for precise *orbit determination*. They consist of space, ground, and control segments. The French DORIS (Doppler Orbitography and Radio positioning Integrated by Satellite) system is based on a worldwide network of beacons emitting radio signals (2 GHz) that are received and processed as Doppler frequency shifts on board the satellite. The German PRARE (Precision Range and range Rate Experiment) is a space borne, two-way, dual-frequency microwave system (2.2 and 8.5 GHz), where the double signal travel time is calculated in the space segment. These systems have operated on different satellites since the 1990's, cf. [5.2.7], and are also exploited for positioning of the ground stations. The radial-orbit accuracy achieved a few cm to 1 dm, and velocities are derived to within ± 0.1 to 0.3 mm/s.

GPS receivers are increasingly installed on satellites for precise orbit determination; they deliver similar accuracies to those discussed above (YUNCK and MELBOURNE 1996).

High demands are placed on the determination of *time*. At orbital velocities of several km/s, the time epoch has to be determined to $\pm 1 \mu\text{s}$ in order to keep orbital errors less than 1 cm. Distance measurements to satellites require time interval measurements to $\pm 0.1 \text{ ns}$ in order to obtain cm-accuracy. Rubidium or cesium frequency standards, which are tied to UTC by time signals, are capable of this level of accuracy. Quartz oscillators can be used in satellite receivers if an external control is provided, e.g., through the satellite system, cf. [5.2.5].

More details on satellites employed in geodesy are given in the following chapters.

5.2.4 Direction, Range and Range Rate Measurements: Classical Methods

Satellite observations began in 1957. They were based partly on methods developed for the observation of the moon and of balloons. While some of the classical techniques applied up to the 1980's are no longer of importance, other such methods have been developed further and are still used extensively today. Some results of the early satellite missions are still of relevance for the strengthening and orientation of geodetic networks and for the calculation of earth models, cf. [6.8.1].

Direction measurements to satellites prevailed until about 1970 and led for the first time to global and regional three-dimensional networks. They also provided the low-degree harmonic coefficients of the gravitational potential.

For optical direction measurements, an illuminated satellite is photographed on film or glass plates together with the fixed stars.

Balloon satellites reflecting both sunlight (e.g., Pageos, 1966-1972, diameter of 30 m, $i = 87^\circ$, $h = 2800$ to 5600 km) and light flashes from active satellites were used. Ballistic cameras (e.g., Wild BC4) mounted azimuthally were easy to operate and had a large field of view. Equatorially-mounted astronomic cameras could follow the motion of the stars. Using a large focal length, even faint stars could be detected and observed with high precision. Orbital cameras were designed so that they could also follow the motion of a satellite.

Upon developing the photographs and identifying the stars, the satellite and star image points were measured on a precision comparator ($\pm 1 \mu\text{m}$). The plate coordinates of the satellite were then transformed to the spatial directions right ascension and declination, whereby the transformation parameters were derived from the known directions to the stars, cf. [2.4.1]. Since the satellite travels in the atmosphere, astronomic refraction reduction as applied to the stars, cf. [5.3.3], had to be reduced by the satellite refraction (Fig. 5.28), with

$$\Delta z_{\text{sat}} = 0.48'' \frac{\tan z}{h[1000 \text{ km}]} . \quad (5.39)$$

The accuracy of the direction measurements was $\pm 0.2''$ to $2''$. An increase in accuracy was not possible mainly due to scintillation effects and comparator measuring errors.

The Japanese satellite EGS (also Ajisai, $h = 1500$ km) is a recent example of direction measurements. The satellite is equipped with both mirror and laser reflectors. By rotation of the satellite about its axis, incident sunlight is reflected periodically with two flashes per second.

Microwave distance-measurements were employed in the 1960's and still play a fundamental role today.

The Secor (Sequential Collation of Range) system used modulated microwaves (two frequencies) emitted from ground stations and re-transmitted from transponders on board the satellites. Distances were derived from signal's travel time, using the phase comparison method, cf. [5.5.2]. Using this method and employing spatial trilateration, isolated geodetic networks were connected to a global reference system. The precision obtained was a few m, although systematic errors up to several 10 m also occurred.

From the 1970's to the 1980's, *Doppler positioning* became an operational tool for establishing or improving geodetic networks. By orbital analysis, it also delivered improved geopotential models and earth rotation parameters.

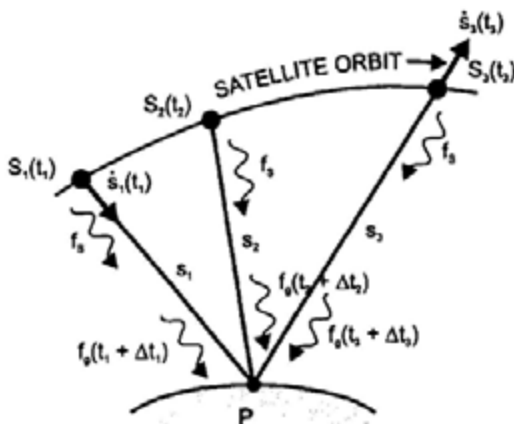


Fig. 5.7. Satellite Doppler positioning

With Doppler measurements, a transmitter aboard a satellite S continuously emits a stable frequency f_s (Fig. 5.7). A signal is received at the ground station with the frequency f_g and a time shift Δt with respect to the transmission time t . f_g is shifted against f_s due to the relative velocity $\dot{s} = ds/dt$ between the satellite and the observer (Doppler effect):

$$f_g - f_s = -\frac{f_s}{c} \dot{s}. \quad (5.40)$$

The Doppler frequency shift is proportional to \dot{s} ; a reversal in sign occurs at the time of the closest approach of the satellite to the observer ($\dot{s} = 0$). In principle, a range difference (range rate) can be determined from (5.40) by integration over time. In practice, f_g is compared with a constant reference frequency f_0 generated within the Doppler receiver, with $f_0 \approx f_s$. Integration over a time interval yields the Doppler count

$$N_y = \int_{t_i + \Delta t_i}^{t_j + \Delta t_j} (f_0 - f_g) dt. \quad (5.41)$$

With (5.40), we obtain the observation equation

$$N_y = (f_0 - f_s)(t_j - t_i) + \frac{f_0}{c}(s_j - s_i), \quad (5.42)$$

which provides the range rate $s_j - s_i$ from the Doppler counts.

As with any microwave technique, Doppler measurements do not depend on weather conditions, and they allow large amounts of data to be accumulated within short time intervals. Today, Doppler measurements are used with several satellite missions and with the DORIS positioning system, cf. [5.2.3].

The *Navy Navigation Satellite System* (NNSS) or *Transit System* was an important application of Doppler measurements (KOUBA 1983, ANDERLE 1986). Developed as a navigation system for the U.S. Navy, it was opened to civil use early on and operated successfully between 1964 and 1996. Positioning was based on 4 to 7 Transit satellites in orbit ($h = 1100$ km, $i = 90^\circ$), which continuously transmitted frequencies of 150 and 400 MHz. With the orbital planes of the satellites evenly distributed in longitude, and due to earth rotation, a satellite became visible at least every two hours along the equator. The satellite orbits were determined by Doppler measurements from four tracking stations located in the U.S.A. Initially they referred to the World Geodetic System 1972 (WGS72) and later to WGS84, cf. [5.2.5]. The satellites transmitted their "broadcast ephemeris" at two-minute intervals, together with UTC time signals, with an accuracy of ± 10 to 20 m. "Precise ephemeris" (± 1 to 2 m) were later made available to authorized users. A number of Doppler receivers were built as portable units for geodetic purposes. These contained a reference oscillator, a microprocessor, a data-recording unit, the antenna, and an energy supply.

The influence of ionospheric refraction was practically eliminated by the use of two frequencies, cf. [5.1.3], and tropospheric refraction was computed using atmospheric models and observed meteorological data, cf. [5.1.2]. The positional error of ± 10 to 30 m, obtained at the observation of a single satellite pass, could be reduced to ± 2 to 5 m (broadcast ephemeris) with 30 to 50

passes and to ± 0.5 to 1 m using precise ephemeris. Relative positioning employed simultaneous observations on two or more stations, which strongly reduced orbital and refraction errors and led to baseline accuracies of ± 0.2 to 0.5 m (SEEBER et al. 1982).

With the GPS-system becoming operational, the NNSS system was no longer maintained.

5.2.5 Global Positioning System (GPS)

The NAVSTAR/GPS (Navigation System with Time and Range/ Global Positioning System) is a radio navigation system based on satellites. It is operated by the U.S. Department of Defense (DOD), which started development of the system in 1973. The first GPS satellites were launched in 1978, and the system became fully operational in 1993. GPS provides real time navigation and positioning by one-way microwave distance measurements between the satellites and the GPS receivers. Early on, the use of GPS for geodetic applications was investigated (BOSSLER et al. 1980), and GPS positioning is now extensively employed in geodesy at all scales, including the determination of variations with time. Several textbooks on GPS are available, e.g., WELLS (1986), LEICK (1995), HOFMANN-WELLENHOF et al. (1997), see also SEEBER (1993), and for the actual state, TEUNISSEN and KLEUSBERG (1998a), MCDONALD (1999).

The *basic idea* of GPS is to have at least four satellites above the horizon available 24 hours everywhere on the earth. In principle, the three-dimensional coordinates of the receiver's antenna can be derived from three observed distances. The computation is based on the known ephemeris of the satellites and the intersection of spherical shells. As the clocks of the satellite and the receiver are not synchronized, a fourth distance measurement is necessary in order to determine the clock synchronization error. Therefore, the original distances derived from the travel time of a signal are called *pseudoranges* (Fig. 5.8).

We distinguish between the space, the control, and the user segment of GPS.

The *space segment* consists of 21 *satellites* (plus 3 additional spares) arranged in six nearly circular orbits ($i = 55^\circ$, 12 h period of revolution) at an altitude of about 20 200 km (Fig. 5.9, Fig. 5.10). Due to the limited lifetime of a satellite (10 years on the average), a regular replacement is scheduled in blocks, which are intended to correspond to improvements in satellite technology (block II/IIA consisted of 28 satellites launched between 1989 and 1998).

Atomic clocks (2 rubidium and 2 cesium clocks per satellite) provide a high-precision frequency standard, with 10^{-12} to 10^{-13} relative long-term stability, cf. [2.2.1]. They produce the fundamental frequency of 10.23 MHz. By

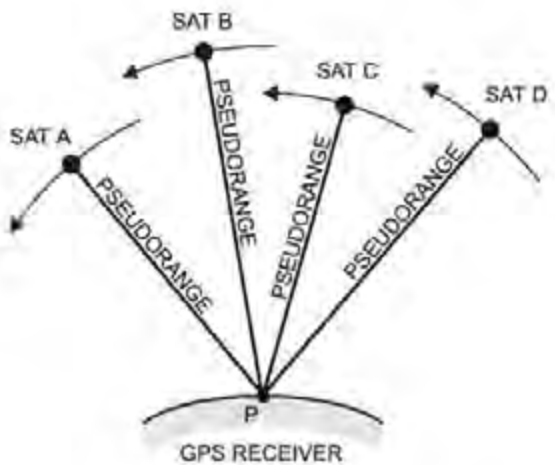


Fig. 5.8. GPS positioning

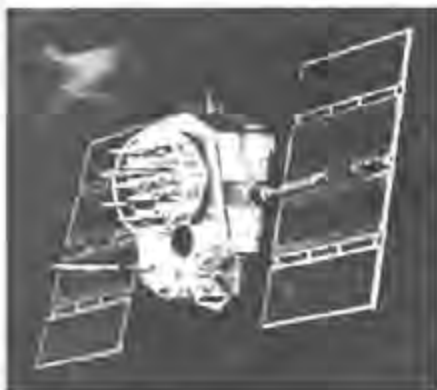


Fig. 5.9. GPS (Global Positioning System) satellite, courtesy The Aerospace Corporation, El Segundo, CA, U.S.A.



Fig. 5.10. GPS orbit constellation

multiplication, the L1 (1575.42 MHz $\hat{=}$ 19.05 cm wavelength) and the L2 (1227.60 MHz $\hat{=}$ 24.45 cm) *carrier waves* are derived and continuously emitted. L1 and L2 serve as carriers for two code modulations and for a data signal (navigation message). The codes are given as binary signals (+1 and -1 sequence) in a pseudo-random noise (PRN) form (Fig. 5.11). The *C/A-code* (coarse/acquisition code) is modulated on L1 only, with a frequency of 1.023 MHz ($\hat{=}$ 293 m wavelength) and a repetition rate of 1 ms. The *P-code* (precise code) is modulated on L1 and L2 and has a frequency of 10.23 MHz ($\hat{=}$ 29.3 m wavelength) and a repetition sequence of 266 days. It primarily serves for

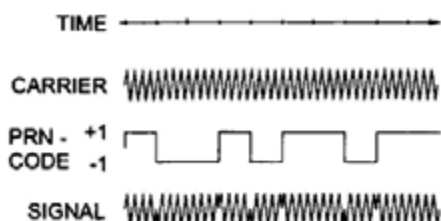


Fig. 5.11. GPS signals

precise navigation and is reserved to authorized users. The *navigation message* is transmitted on L1 and L2. It contains the satellite's ephemeris (Keplerian elements and certain time derivatives and orbital correction terms), a clock correction with respect to GPS-time, the coefficients of a ionospheric refraction model, and information on the status of the GPS system. The broadcast ephemeris are accurate to a few m and approach sub-meter accuracy.

With GPS being fully operational, an *accuracy deterioration* for civil users has been introduced by DOD. The *Precise Positioning Service* (PPS) provides all GPS signals, and thus the full accuracy of the system (± 10 to 20 m or better) to authorized users (mainly U.S. military). The *Standard Positioning Service* (SPS) only delivers the C/A-code, while the P-code is encrypted by Anti-Spoofing (AS), which results in the non-accessible Y-code.

Between 1990 and 2000, the fundamental frequency of the satellite clocks was destabilized, and the ephemeris data were manipulated by *Selective Availability* (SA). This introduced errors in the pseudoranges, which degraded the absolute accuracy to about 100 m in horizontal position and 150 m in height. For geodetic purposes, these effects were largely eliminated by differential techniques. The suspension of SA led to an accuracy improvement in positioning and time transfer, reaching the accuracy available for authorized users.

The GPS *control segment* is responsible for maintaining the operation of the GPS satellites. It consists of the master control station (Colorado Springs, CO, U.S.A.) and five globally distributed monitoring stations. The stations are equipped with cesium standards and GPS receivers. They continuously measure pseudoranges to all satellites and transfer the results to the master station. After computation of the satellite orbits and the clock correction, the (extrapolated) broadcast ephemeris and GPS time are transmitted to the satellites for storage and retransmission by three ground antennas collocated with monitoring stations. This operational control system is supplemented by a number of additional monitoring stations (in 1999: 7 stations) operated by the U.S. National Imagery and Mapping Agency (NIMA).

The GPS ephemerides refer to an earth-fixed system, as defined by the coordinates of the monitoring stations: *World Geodetic System* (WGS).

WGS has been developed by DOD since the end of the 1950's (realizations WGS 60, WGS 72, and WGS 84). The system is intended to serve for mapping, charting, positioning and navigation, following international standards for geodetic reference systems. The defining parameters of the latest version of WGS 84 are as follows (SLATER and MALYS 1998, NIMA 2000):

- semimajor axis $a = 6378137 \text{ m}$,
- reciprocal flattening $1/f = 298.257\,223\,563$,
- geocentric gravitational constant $GM = 398\,600.4418 \times 10^9 \text{ m}^3\text{s}^{-2}$, which includes the atmospheric part $GM_{\text{atm}} = 0.35 \times 10^9 \text{ m}^3\text{s}^{-2}$,
- angular velocity of the earth's rotation $\omega = 7.292115 \times 10^{-5} \text{ rad s}^{-1}$.

WGS 84 thus practically coincides with the Geodetic Reference System 1980, cf. [4.3]. The associated gravity field is given by the global geopotential model EGM 96, complete to degree and order 360, cf. [6.6.3].

The coordinates of the monitoring stations are given for the epoch 1997.0, taking earth tides (tide-free system), cf. [3.4.1], and plate tectonic motions into account. The accuracy of the WGS 84 coordinates is $\pm 0.05 \text{ m}$, which is also the level of agreement between WGS 84 and the International Terrestrial Reference Frame (ITRF), cf. [2.5.3].

GPS-time (unit SI second) is defined by the cesium clocks of the control segment stations. It agreed with UTC on January 5, 1980 and differs from it by a nearly integer number of seconds. This difference is increasing because no "leap seconds" are introduced to the GPS time scale, cf. [2.2.2]. The actual difference between GPS-time and UTC is part of the GPS navigation message ($\pm 0.1 \mu\text{s}$). GPS is a very efficient system of *time dissemination*. A clock comparison is possible with an accuracy of $\pm 100 \text{ ns}$ and $\pm 10 \text{ ns}$ and better with differential techniques. Special GPS-time receivers are available as C/A one-channel instruments and operate in an automatic mode (LARSON and LEVINE 1999).

A similar satellite navigation system has been developed in the former Soviet Union since the 1970's. GLONASS (Global Navigation Satellite System) also operates as a one-way ranging system. It has been operational since 1996 (ANGLEY 1997a, ZARRAO et al. 1998). Its space segment comprises 24 (including 3 spares) satellites, arranged at a regular spacing of 45° in three nearly circular orbits ($i = 64.8^\circ$, $h = 19\,100 \text{ km}$, revolution time about 11.2 h). The orbits are spaced 120° apart from each other, with five satellites always being visible. The satellites transmit on two frequency bands (1602-1615 MHz, 1246-1256 MHz) with *different* frequencies for each satellite (contrary to GPS). On the other hand, the C/A- and P-code modulations are the same for all satellites. There is no degradation of the GLONASS signals. The satellites are equipped with laser retroreflectors for laser tracking. The control segment consists of a master control station near Moscow and secondary stations distributed over the territory of the former Soviet Union.

The GLONASS results refer to the reference system PZ90, which is based on the Soviet geodetic reference system SGS85. Transformation parameters to WGS84 are known with an accuracy of a few m (MISRA and ABBOT 1994). GLONASS uses its own time system (UTC + 3 hours) which is synchronized to UTC within 1 μ s by the use of leap-seconds.

A European navigation satellite system called GALILEO has been discussed since 1999. It may employ four carrier frequencies, and the intended on-line positional accuracy is 10 m (95%), once every second (DIVIS 1999).

The *user segment* is composed of the many *GPS receivers* operating in navigation, geodesy, and surveying. The main components of a receiver include the antenna, the receiver electronics, the microprocessor, the oscillator, the memory, the user interface, and a power supply. An additional telemetry unit can be used for data transfer between different receivers (differential mode).

The signals transmitted from the satellites are received and amplified by the antenna. After identification, the signals are processed to pseudoranges in the channels of the receiver electronics. One channel is generally responsible for the tracking of one satellite. Hence, a minimum of four channels is necessary to determine position and time. Modern receivers contain 12 or more channels for each frequency (multi-channel technique). The microprocessor controls the operation of the receiver and calculates the three-dimensional position of the antenna in WGS84 and the velocity and azimuth of moving objects. A quartz oscillator is used for generating the reference frequency, which is approximately synchronized with GPS-time. All data (pseudoranges, phases, time, navigation message) are stored in receiver memory for post-processing, which is typical for multi-station observation sessions employed in geodesy, cf. [6.2.1]. The user interface includes a keyboard and a display, which provides a communication link between the user and receiver. Power is provided by internal, rechargeable nickel-cadmium batteries.

Geodetic GPS receivers deliver high accuracies in the static and kinematic mode (BOUCHER 1987, LANGLEY 1997b). This is achieved by dual-frequency (L1 and L2) multi-channel instruments with the P-code and the full carrier wave available on L1 and L2. Other characteristics include low receiver-noise in code and carrier phase, a high data rate (> 1 Hz), and a large memory capacity. The antenna phase center should be stable and protected against multipath effects.

The Macrometer (1982) was the first GPS receiver for geodetic applications (code-free, single frequency, 6 parallel channels). The Texas Instruments TI4100 (1984) provided all geodetically relevant observables (P and C/A-code pseudoranges, carrier phases on L1 and L2) in a multiplex channel technique (SEEBER et al. 1985). The efficiency of geodetic receivers is discussed in the literature (e.g., COORS et al. 1998). Fig. 5.12 to 5.14 show some examples. Combined GPS/GLONASS receivers are also available (Fig. 5.15). They are able to track any combination of GPS and GLONASS satellites (12 to 21 will be visible with fully deployed systems). This will



Fig. 5.12. GPS continuously operating reference station (CORS) with receiver (GPS total station 4700) and choke ring antenna, courtesy Trimble Navigation Ltd., Sunnyvale, CA, U.S.A.



Fig. 5.13. Geodetic GPS dual-frequency receiver (GPS total station SR530), with terminal TR500 and telemetry antenna, courtesy Leica Geosystems AG, Heerbrugg, Switzerland



Fig. 5.14. Geodetic GPS dual-frequency receiver (GePoS Experience) with antenna, courtesy Zeiss/Spectra Precision AB, Danderyd, Sweden



Fig. 5.15. GPS/GLONASS receiver with antenna, courtesy JAVAD Positioning Systems/TOPCON, Paramus, NJ, U.S.A.

improve the satellites-receiver geometry and the availability of satellites, as well as the integrity of the solution, and lead to a higher accuracy for absolute positioning with broadcast ephemeris.

A distinction is made between code and carrier phase measurements for GPS-positioning.

Code measurements employ the travel time Δt of a signal between the satellite and the antenna of the receiver. The time difference is determined by cross-correlating an arriving code sequence with a code copy generated in the receiver. Multiplication of Δt with the velocity of light c gives the distance between the satellite and the antenna, cf. [5.1.1]. Considering the clock synchronization error δt , the *observation equation* for the *pseudoranges* R reads as

$$R = c \Delta t = s + c \delta t . \quad (5.43a)$$

The distance is given by

$$s = \left((X_s - X_p)^2 + (Y_s - Y_p)^2 + (Z_s - Z_p)^2 \right)^{1/2} , \quad (5.43b)$$

where X_s, Y_s, Z_s and X_p, Y_p, Z_p are the geocentric coordinates of the satellite and the ground stations respectively. Using the transmitted broadcast ephemeris, the receiver clock correction and the coordinates of the ground station can be derived by simultaneous measurements to four satellites. Equation (5.43) presupposes that atmospheric refraction effects are taken into account by proper reductions (see below).

The measurement noise governs the accuracy limit for this method. Accuracy depends on the wavelength and is at the m-level for C/A-code and at the dm-level for P-code. If used as a standard method in navigation, a positional accuracy of about 10 m is achieved.

Pseudorange differences can be derived from integrated *Doppler frequency shifts* (Doppler counts) of the carrier frequency according to (5.41) and (5.42). The differences are used for the determination of velocity in navigation. Doppler solutions also play a role in the removal of ambiguities, which occur with carrier phase measurements. The method is not suitable for real-time positioning due to the long observation time required.

Relative (differential) GPS methods determine differences of coordinates between two or more stations. This is accomplished either by simultaneous observations on the stations, including at least one with known coordinates, or by using correction data provided by permanently operating reference stations. Corresponding DGPS-Services for navigation deliver range corrections derived from the differences between observed and calculated pseudoranges at reference stations. Accuracies of a half to a few m are achieved over distances between about 50 and several 100 km.

Geodesy and surveying require accuracies of at least two orders of magnitude better than that required for navigation. This is achieved by *carrier phase*

measurements. Due to the shorter wavelength of carrier phases, the measurement noise is only in the mm to sub-mm-range (BEUTLER et al. 1987).

The carrier phase is detected by comparing the received carrier signal with the reference frequency generated in the receiver after subtraction of the code. In order to reconstruct L2 under AS conditions (P-code encryption), different techniques have been developed, such as squaring of L2 (eliminates the code signal) and cross-correlation of L1 and L2. The measured phase difference

$$\Delta\varphi = \varphi_c - \varphi_0 \quad (5.44)$$

(φ_c, φ_0 = phase of the carrier and reference waves respectively) is related to the distance s by

$$\Delta\varphi = \frac{2\pi}{\lambda} (s - N\lambda + c\delta t), \quad (5.45)$$

which is well known from terrestrial distance measurements, cf. [5.5.2]. N is an integer number of complete carrier cycles within the range s , and δt is the receiver clock synchronization error. The *ambiguity* introduced by N poses a primary problem for the evaluation of (5.45). Among the algorithms available for ambiguity determination, we have the inclusion of ambiguity-free Doppler solutions, the combination of code and carrier phases, and statistical search methods applied to combinations of L1 and L2. Difficulties arise when the phase lock is lost due to signal obstruction. Such sudden jumps of the carrier phase by an integer number of cycles are called *cycle slips*. They are either removed during preprocessing or taken into account by introducing an additional ambiguity for the affected pseudorange.

The GPS signals experience path delays while traveling through the atmosphere. *Ionospheric refraction*, cf. [5.1.3], causes range errors at the m to 100 m order of magnitude (KLOBUCHAR 1991). Using the satellite message, a reduction can be applied to the travel time when only a single-frequency receiver is available. Two-frequency receivers allow application of (5.23) to the frequencies f_1 and f_2 , which leads to the distance (code measurement)

$$s = \frac{s_1 f_1^2 - s_2 f_2^2}{f_1^2 - f_2^2}. \quad (5.46)$$

In (5.46) the ionospheric refraction is eliminated, and s_1 and s_2 are the observed distances on L1 and L2 respectively. A corresponding equation can be derived for carrier phase observations. *Tropospheric refraction* may cause delays on the order of one m (zenith direction) to 10 m (close to the horizon).

Refraction is accounted for by tropospheric models and observed surface weather data, cf. [5.1.2]. The "wet" component remains a critical part of these reductions; an improved determination is possible by water vapor radiometers, which measure the water vapor content along the path.

Multipath effects result from signal reflection near the antenna. They affect code and carrier measurements and may produce errors on the order of cm to dm. A reduction of these effects is possible by a proper design of the antenna and by careful site selection. The antenna's phase center (close to the geometric center) varies in dependence on the satellite's elevation and azimuth; this must be taken into account by calibration (MENGE et al. 1998).

The *error budget* of GPS is composed of orbital and satellite clock errors, residual refraction effects, and receiver errors. Orbital errors are at the order of a few m (Standard Positioning Service).

High-quality GPS data and orbits are available for post-processing through the International GPS Service (IGS), which operates under the auspices of IAG, cf. [7.3.1]. IGS provides, among other things, a precise and a "rapid" GPS ephemeris. The precise ephemeris is available after 7 days and has a precision of about $\pm 3\ldots 5$ cm. The "rapid" ephemeris is available after 24 hours and is only slightly less precise. Satellite clock parameters are given with a precision of ± 1 ns. The accuracy of these products should be close to the precision.

Clock errors are about 1 m. The residual errors of ionospheric refraction reach only a few cm with two-frequency receivers, while tropospheric model errors may attain one dm. The receiver noise is roughly about 0.1% of the signal's wavelength, which corresponds to a dm-order of magnitude with the C/A- code and 1 to 2 mm with the P-code (LANGLEY 1997b). Phase center variations of the antenna may reach a few cm.

The *accuracy* of GPS positioning also depends on the geometric constellation of the satellites with respect to the receivers and on the duration of the observation time. A longer observation time increases the accuracy, especially for long baselines and for the height component. The accuracy of the kinematic mode (moving GPS receiver) is lower than that of the static mode.

The accuracy of an observed pseudorange can be expressed by its standard deviation (also user equivalent range error). The strength of the satellite geometry is characterized by a quantity called "Positional Dilution of Precision" (PDOP). It is defined as the ratio between the standard deviation of a position derived from a certain satellite constellation and the standard deviation of an observed pseudorange (LANGLEY 1999). The numerator of this quotient follows from the trace of the coordinates covariance matrix, which depends on the design of the network, e.g., SEEBER (1993, p.292). PDOP values can be calculated in advance and serve for the planning of observations and for rapid information on expected positioning quality. For instance, a PDOP value of 3 means that the accuracy of positioning is three times worse than the accuracy of the

pseudorange observation. If separated into the horizontal and the vertical components, it turns out that the determination of heights is less accurate than horizontal positioning by a factor of about two. This results from the fact that all observed satellites are above the receiver but distributed over the total horizon.

Relative positioning (differential GPS) significantly reduces the errors that occur in absolute positioning, especially orbital and refraction errors. This is especially valid for shorter baselines, due to the correlation of these errors at the two ground stations. For orbital errors, a (pessimistic) rule of thumb allows an estimate of the error to be expected in a baseline (length b) from the orbital error dr :

$$\frac{db}{b} = \frac{dr}{s}, \quad (5.47)$$

where s is the distance between the satellite and the receiver (maximum 25 000 km). Hence, if an accuracy of 1 cm is required for the baseline, the orbital error should not exceed 2.5 m at $b = 100$ km and 0.25 m at $b = 1000$ km. When the precise ephemerides from the IGS are used, orbital errors no longer play a large role. The obtainable accuracy of relative positioning with good PDOP conditions and in the static mode is about

$$\pm(3\dots5 \text{ mm} + 0.5\dots1 \times 10^{-6} \text{ s})$$

for the horizontal coordinates. In the kinematic mode, this reduces to

$$\pm(10\dots20 \text{ mm} + 1\dots2 \times 10^{-6} \text{ s}).$$

Height determination is less accurate by about a factor of two.

The Global Positioning System has drastically changed surveying methods in geodesy, navigation, and other applications. This is mainly due to the high accuracy achieved with static and kinematic positioning, real-time evaluation, and operational flexibility. Direct visibility between the ground stations is not necessary; only visibility to the satellites is required. The system is weather independent and usable day and night. The use of GPS is still increasing and is strongly supported by global and regional GPS services, cf. [7.3.1], [7.3.2].

5.2.6 Laser Distance Measurements

Laser distance measurements may be made to satellites equipped with corner cube reflectors: *Satellite Laser Ranging* (SLR). This method offers high accuracy due to the favorable propagation of laser light in the atmosphere. It

also offers a low-cost, long-lifetime space segment. On the other hand, SLR depends on weather conditions and requires a considerable operational effort at the ground segment.

At the ground station, laser pulses are emitted at epoch t , reflected at the satellite, and received again at epoch $t + \Delta t$. If refraction effects are taken into account by corresponding reductions, the distance is obtained by

$$s = \frac{c}{2} \Delta t . \quad (5.48)$$

Nowadays, travel time of the photons can be measured with an accuracy of ± 10 to 100 ps, which corresponds to a ranging accuracy of ± 1.5 to 15 mm (BENDER 1992).

Many *satellites* (about 30 in 1999) are equipped with laser reflector arrays for precise orbit determination, e.g., satellites carrying radar altimeters for ocean height determination, cf. [5.2.7]. Dedicated SLR missions for positioning and geodynamic research include the satellites Starlette (France, 1975, $h = 800$ to 1100 km, $i = 50^\circ$), Lageos 1 and 2 (U.S.A., 1976/1992, $h \approx 5900$ km, $i = 110^\circ/52^\circ$, COHEN et al. 1985), Ajisai (Japan, 1986, $h = 1500$ km, $i = 50^\circ$), and Etalon 1 and 2 (USSR, 1989, $h \approx 19\,000$ km, $i = 65^\circ$). These satellites are spherical in shape (diameter 0.2 to 2 m) and possess a favorable surface-to-mass ratio (Fig. 5.16). The GLONASS satellites and a few GPS satellites also carry laser retroreflectors on board.

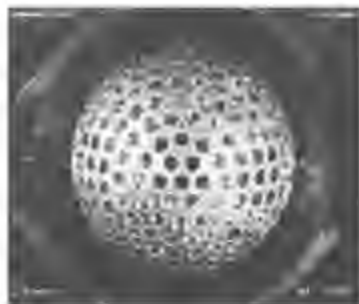


Fig. 5.16. Laser satellite LAGEOS, courtesy National Aeronautics and Space Administration (NASA)

Laser distance *measuring systems* have developed rapidly since the 1960's. They consist of the laser unit (Nd:Yag-laser = Yttrium-aluminum garnet crystal doped with neodymium ions), the transmitting and receiving optics (telescopes), and the receiver electronics (secondary-electron photomultiplier). The mechanical mounting provides an automatic tracking of the satellite's pre-

calculated orbit. Due to atmospheric disturbances and reflection, only a few laser pulses (photons) return. The travel time is measured by a time-interval counter and an atomic clock, regularly compared with UTC. A process computer controls the complete measurement and registration.

About 50 *laser-satellite-systems* are operating worldwide (as of 1999), either in the stationary or mobile mode. The Wettzell laser ranging system employs a Nd:Yag laser (532 nm) and a 75 cm telescope. It operates with high-energy short pulses (pulse length 180 ps, pulse energy 100 mJ) at a pulse repetition rate of 1 to 10 Hz in the single-shot mode. Visible and /or infrared light is used, allowing a day-and-night operation to satellites at altitudes between 800 and 40 000 km and to the earth's moon (DASSING et al. 1992), Fig. 5.17. Further developments are directed to reduce the pulse length to some 10 ps and to reduce the pulse energy. The emission of short-pulse trains increases the probability of single photon detection.



Fig. 5.17. 75 cm telescope, Wettzell Laser Ranging System (WLRS), Fundamentalstation Wettzell, Germany, courtesy Bundesamt für Kartographie und Geodäsie (BKG), Frankfurt a.M., Germany

Mobile systems have been developed in the U.S.A. (NASA) and in Germany/Netherlands, among others (SILVERBERG 1978). Operating with low energy and single-photon detection, these systems are employed mainly for the investigation of recent crustal movements, cf. (8.3.3). A transportable, integrated geodetic-observatory has been developed by BKG (Bundesamt für Kartographie und Geodäsie, Germany). In addition to the laser unit, it includes a VLBI module and GPS unit. It is employed for strengthening fundamental reference networks, especially in the southern hemisphere.

The *accuracy* of laser distance measurements depends on the pulse length, the stability of the photomultiplier, and the time resolution. Atmospheric refraction effects may reach 2 m at the zenith and 10 m at an elevation of 10°; they are corrected with standard atmospheric models. Depending on the satellite's altitude, some 100 to 1000 distances are measured during one passage, with a

single shot precision of ± 5 to 10 mm. By compressing the data to "normal points" (average over 30 s to 120 s at Lageos), sub-cm precision is achieved.

Laser reflectors have been placed on the moon by the Apollo 11 (1969), 14, and 15 missions and by Luna 21/ Lunokhod 2. These reflectors provide targets for *lunar laser ranging* (BENDER et al. 1973). Pulsed lasers with a tightly bundled beam and a powerful telescope are necessary in order to recapture the weak returning signal (single photon technique). The tracking system must provide a 2 arcsec pointing accuracy.

Observations to the moon have been carried out regularly since 1969 by the McDonald Observatory, University of Texas, and by systems operating in Hawaii and Grasse/France. Results have also been provided by laser stations in Australia and Germany (Weizell). The accuracy of these measurements is about 1 cm. They especially contribute to investigations of the dynamics of the earth-moon system and on terrestrial geodynamic processes (SMITH et al. 2000).

5.2.7 Satellite Altimetry

Satellite altimetry is based on a satellite-borne *radar altimeter* that transmits pulses in the vertical direction to the earth's surface. The ocean surface reflects the pulses perpendicularly, and the measurement of the travel time Δt furnishes the height of the satellite above the instantaneous sea surface (Fig. 5.18):

$$a = \frac{c}{2} \Delta t . \quad (5.49a)$$

(The denotation a should not be confused with the abbreviation for the semimajor axes of the satellite's orbit and the earth ellipsoid). A proper reduction of atmospheric refraction effects is presupposed in (5.49).

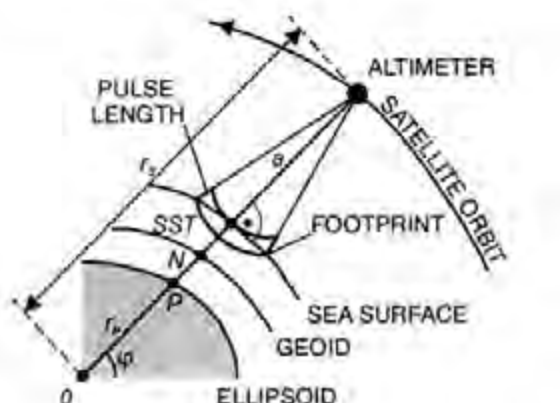


Fig. 5.18. Satellite altimetry

In spherical approximation, this observation can be expressed as

$$a = r_s - r_p - (N + \text{SST}), \quad (5.49b)$$

where r_s and r_p are the geocentric distances to the satellite and to the subsatellite point P on the ellipsoid; N is the geoid height and SST the height of the surface topography. Satellite tracking provides r_s and positioning gives r_p . Altimetry thus delivers information on the geoid and on sea surface topography. Ellipsoidal formulas are given by GOPALAPILLAI (1974).

Radar altimeters operate in the 14 GHz frequency range with short (a few ns) pulses and a high-pulse frequency (e.g., 100 pulses/s). The effects of beam divergence and finite pulse length result in measurements that refer to a "mean" sea surface within a circular "footprint" (few km diameter); short-wavelength features of the ocean (waves) are thereby smoothed out. For example, by averaging the measurements over 1 s, the along-track resolution is about 7 km. Satellite altimetry missions are designed to provide either an exact repetition of ground tracks (days to weeks) or a dense pattern of profiles. The different modes are achieved by orbital maneuvers (KNUDSEN 1993). The latter is for determination of the altimetric geoid and the former for investigation of ocean variability (Fig. 5.19).

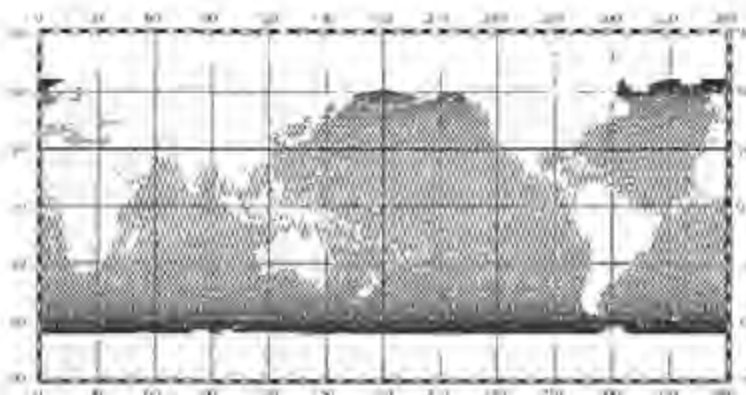


Fig. 5.19. TOPEX/Poseidon subsatellite tracks covered within the 9.9 days repeat cycle, from BOSCH (2001)

The first global survey with a radar altimeter was accomplished by the Geos-3 satellite (U.S.A., 1975-1978). The oceanographic satellites SEASAT (1978) and GEOSAT (U.S.Navy, 1985-1989) carried improved altimeter systems and operated in heights close to 800 km with 108° inclination and repetition rates of 3 and 17 days (TAPLEY et al. 1982, MCADOO and SANDWELL 1988). The European Remote Sensing Satellites ERS-1 (1991) and ERS-2 (1995) operate at similar heights

with 98° inclination (Fig. 5.20). Repetition rates are 35 and 168 days respectively, and ground track distances at the equator are 80 km and 8 km respectively for geodetic missions (KOCH 1989, JGR 1998). The NASA/CNES (French space agency) TOPEX/Poseidon satellite (1992, 5.3 and 13.6 GHz) is placed in a circular orbit at an altitude of 1340 km and an inclination of 63°. Repetition time is 10 days, and the equatorial ground track interval 316 km (FU et al. 1994, CHENEY et al. 1995), see Fig. 5.21.



Fig. 5.20. European Remote Sensing (altimeter) Satellite ERS, courtesy European Space Agency (ESA)



Fig. 5.21. TOPEX/Poseidon (altimeter) satellite, courtesy JPL/NASA, Pasadena, CA, U.S.A.

High radial-orbit accuracy is required for satellite altimetry. Consequently, the satellites are equipped with laser reflectors, with some having active systems such as Doppler transmitters, C-band radar transponders, and GPS. The space-borne orbit determination systems DORIS and PRARE have been installed on the TOPEX/Poseidon and ERS-2 respectively (TAPLEY et al. 1995, ANDERSEN et al. 1998), cf. [5.2.3]. Further orbital improvements have been achieved by "tailored" gravitational field models developed for a dedicated altimeter mission (TAPLEY et al. 1996). The orbital error thus has been reduced to about ± 0.5 m for the GEOS-3 mission, to ± 3 cm for TOPEX/Poseidon, and to a range of ± 5 to 10 cm for ERS-1. For the evaluation of a region sampled multiple times with high spatial-resolution altimeter profiles, the track crossover discrepancies are adjusted by minimum conditions with time-dependent, low-order polynomial models (e.g., shift and inclination) applied on the individual tracks (van GYSEN and COLEMAN 1997). Residual orbit and other long-term errors are further reduced in this way, cf. [6.6.3].

The altimeter instrumental noise is now less than 2 to 3 cm (TOPEX/Poseidon, ERS). Corrections have to be applied for systematic instrumental (bias and drift) and sea-state effects as well as for tropospheric and ionospheric path delay (modeling, use of two frequencies for TOPEX/Poseidon), cf. [5.1.3]. After reduction of the ocean tides and large-scale air pressure effects, the altimetric

results refer to the quasi-stationary sea surface and yield its height with an accuracy of ± 5 to 10 cm.

5.2.8 Satellite-to-Satellite Tracking, Satellite Gravity Gradiometry

High-resolution gravity-field determination from space requires low-orbiting satellites and highly sensitive sensors, cf. [5.2.3]. This is achieved by satellite-to-satellite tracking and satellite gravity gradiometry (COLOMBO 1989, SNEEUW and ILK 1997, ILK 2000).

Satellite-to-satellite tracking (SST) employs microwave systems for measuring range rates between two satellites. High-low (one high and one low-flying satellite) and low-low (two low-flying satellites at the same altitude) configurations have been designed (RUMMEL et al. 1978), Fig. 5.22. The basic observables are the range rates (radial velocities) and changes of the range rates, which are due to gravitational and non-gravitational "disturbing" forces, cf. [5.2.2]. The gravitational field parameters (harmonic coefficients) can be derived after proper compensation of the surface forces. In order to achieve a gravity field resolution of 100 km, the orbital altitude of the lower satellite must not exceed a few 100 km. The relative velocity between the satellites has to be determined with an accuracy of ± 1 to 10 $\mu\text{m/s}$, and precise tracking should be guaranteed by high-altitude satellite systems (GPS) and ground stations.

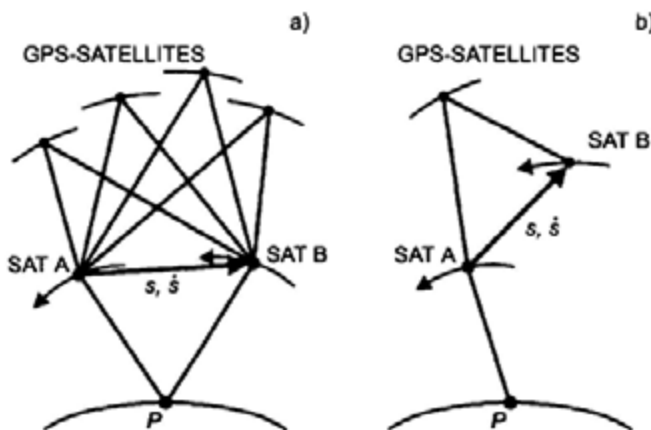


Fig. 5.22. Satellite-to-satellite tracking: a) low-low mode, b) high-low mode

SST experiments started in the 1970's, for example, between GEOS-3 and the geostationary satellite ATS-6 (nearly circular equatorial orbit, $h = 36\,000$ km). The CHAMP (Challenging Mini-Satellite Payload for Geophysical Research and Application) satellite (Germany, launch in 2000) began at an altitude of 450 km, which will be reduced to 300 km within the mission time of 5 years. It moves in a nearly circular polar-orbit ($i=83^\circ$). The satellite (dimensions 4 m x 1 m x

1.6 m) carries a GPS receiver (high-low mode tracking), laser reflectors, a three-axes accelerometer ($\pm 10^{-4} \text{ ms}^2$, for measuring and later compensation of the surface forces), and magnetometer systems (Fig. 5.23). A gravity field recovery up to degree and order 50 is expected (REIGBER et al. 2000).



Fig. 5.23. Champ satellite, courtesy Geoforschungszentrum (GFZ) Potsdam, Germany

The GRACE (Gravity Recovery and Climate Experiment) mission (U.S.A./Germany, launch scheduled for 2001, mission duration 5 years) will employ two satellites of the CHAMP type in the low-low mode about 200 to 300 km apart at an initial orbit altitude of 450 km ($i = 89.5^\circ$). The relative range measurements between the satellites will be integrated by GPS tracking. A gravity field resolution up to degree and order 150 to 180 will be achieved, with accuracies of ± 10 to $30 \mu\text{ms}^2$ for the gravity anomalies and ± 0.1 m for the geoid.

An essential mission goal is the detection and monitoring of large-scale gravity field variations with time, cf. [8.3.4].

Satellite gravity gradiometry determines the components of the gravitational gradient tensor (second derivatives of the gravitational potential). On the earth's surface, gravity gradiometry has been employed since about 1900 with sensor pairs (accelerometers) sensitive to local changes of the gravity field in a certain direction. By different orientation of the sensors, different components of the gravity gradient can be determined, cf. [5.4.5]. For space-borne applications, the attenuation of the gravity field with height (at a few 100 km height, the off-diagonal elements of the gradient tensor are a few 10^{-9} s^2 only) requires a high accuracy for the second derivatives (at the order of 10^{-11} to 10^{-13} s^2), which can be achieved with conventional or superconducting electronics (WELLS 1984, PAIK et al. 1988). High demands are posed on the attitude control of the sensor pairs and on the drift of the accelerometers. Surface forces cancel when the output of an accelerometer pair is differenced (MORITZ 1968c).

ESA is planning a dedicated gradiometry mission GOCE (launch 2004?), with a drag-free satellite ($h = 270$ km, $i = 97^\circ$) in a sun-synchronous near circular orbit. Tracking will be performed by GPS, and earth-pointing orientation is provided by star trackers. Accelerometer pairs ($\pm 10^{-12} \text{ s}^2$) will be arranged over three mutually orthogonal directions, with baselines of 70 cm. A mission duration of 12 months should provide a gravity field resolution up to degree and order 300, with accuracies of about $\pm 10 \mu\text{ms}^{-2}$ (gravity anomalies) and $\pm 1 \text{ cm}$ (geoid). The low-degree potential terms will be determined primarily through GPS tracking, while the higher degrees will result from gradiometry (RUMMEL 1986, RUMMEL et al. 2000b).

5.3 Geodetic Astronomy

Classical geodetic astronomy is concerned with the determination of astronomic latitude, longitude, and azimuth from ground-based optical direction measurements to fixed stars, which also requires time determination (MUELLER 1969, SCHÖDLBAUER 2000). Several types of observational instruments are available for this purpose [5.3.1], and different methods of observation have been developed [5.3.2]. A number of reductions are necessary in order to refer the observations to the celestial reference frame [5.3.3].

Geodetic astronomy is based on spherical astronomy (EICHHORN 1974, KOVALEVSKY 1995). Its importance has decreased since the development of efficient satellite positioning and gravimetric methods and is now restricted to more local applications of gravity field (plumb line direction) and azimuth determinations. On the other hand, radio waves emitted from extragalactic sources are used extensively in order to derive base-line vectors between fundamental terrestrial stations and to determine earth-rotation parameters: Very Long Base Line Interferometry [5.3.4].

5.3.1 Optical Observation Instruments

Optical observations to fixed stars are carried out in the local astronomic (horizon) system. The direction to a star is determined by the astronomic azimuth A and the zenith angle z (sometimes the altitude or elevation angle $90^\circ - z$ is used), cf. [2.6.2]. Due to the movement of the observer with respect to the stars, simultaneous time measurements are required.

Astronomic instruments are either permanently installed in observatories or constructed as transportable devices for field operation.

Observations of highest precision with *stationary* instruments have been utilized by the former International Time Service and International Polar Motion Service. Among other instruments, the photographic zenith tube has been employed. In this case, stars near the zenith are photographed symmetrically with respect to the meridian. The zenith angles and the hour angles can be

determined from the tracks of the stars. The direction of the vertical is established by a mercury pool. Comparable precision ($\pm 0.05''$) was achieved by the Danjon prism astrolabe. Thereby, the time is determined when a star crosses the horizontal circle of a given zenith angle. These astronomic observatory measurements are no longer of significance for geodesy, as celestial and terrestrial reference-frames are now established by other space techniques, cf. [2.3].

The *universal instrument* was employed for field measurements of first-order precision ($\pm 0.1''$ to $0.3''$). It consists of a high-precision theodolite, cf. [5.5.1], of very stable design with a few attachments for astronomic observations.

An angled telescope with a horizontal eyepiece permits observations near the zenith. To eliminate personal errors, the movable thread of the registering micrometer is driven to follow the star so that impulses are generated and recorded at uniform intervals. The suspension level serves to measure the tilt of the horizontal axis. The Horrebow level, mounted at right angles to the horizontal axis, registers any changes in the tilt of the telescope. The Kern DKM3-A and the Wild T4 universal theodolites were used widely (Fig. 5.24).



Fig. 5.24. Universal instrument
Kern DKM3-A, courtesy Kern/Leica
Geosystems AG, Heerbrugg,
Switzerland



Fig. 5.25. ZEISS Ni2 level with prism
astrolab, courtesy Carl Zeiss,
Oberkochen, Germany

The *prism astrolab* is used for the simultaneous observation of astronomic latitude and longitude. With this device, one measures the transit times of those stars that cross the same small-circle parallel to the horizon (almucantar). The constant zenith distance (usually $\approx 30^\circ$) is realized by a prism placed in front of the telescope, and the direction of the vertical is defined by the surface of a pool of mercury or by a compensator pendulum. Astrolabe attachments are

particularly common. These are mounted either on a theodolite (e.g., the Wild T3 astrolabe with a mercury pool) or on an automatic level (Zeiss Ni2 astrolabe), DEICHL (1975), Fig. 5.25.

Transportable zenith cameras are also used for rapid determination of latitude and longitude. Such an instrument consists of a camera oriented in the direction of the plumb line (focal length 300 to 1000 mm, relative aperture $\approx 1:5$), which can be rotated around the plumb-line axis in any azimuth. In addition to a timing device, the instrument is also furnished with two levels that are arranged at right angles to each other (Fig. 5.26).



Fig. 5.26. Transportable zenith camera, Institut für Erdmessung, Universität Hannover

The field of stars near the zenith is photographed for two positions of the camera differing by 180° in azimuth. After the photographic plates are developed (exposure time 1 s), the star tracks and the intersection of the lines connecting the fiducial marks are measured on a comparator. The transformation of the plate coordinates into the α, δ -system provides the rectascension and the declination of the zenith point, after averages are taken and corrections are made for the reading of the levels. The observations (several plates) require one half to one hour, including instrumental setup and disassembly. The attainable accuracy is $\pm 0.5''$ or better (BIRARDI 1976, SEEBER and TORGE 1985).

Recent developments in the CCD (charge-coupled device) technique allow creation of an electronic image of the stars. The principle of a CCD is based on the photoelectric effect produced on a semiconductor plate. The number of collected photoelectrons is proportional to the light received. A CCD matrix is composed of a number of linear arrays. CCD's with 2000×2000

pixels and more are available with pixel dimensions of $10 \mu\text{m}$ and less and a resolution of 0.1 pixels. Using an image processing unit and a PC, an automatic evaluation of star observations is achieved, reaching similar accuracies as with photographic methods (KOVALEVSKY 1995, GERSTBACH 1996).

For *time determination*, an accuracy of $\pm 1 \text{ ms}$ is needed in optical geodetic astronomy. This is provided by quartz clocks, which are based on quartz crystal oscillators (frequency stability $10^{-8} \dots 10^{-9}$ over a few hours) and are synchronized by time signals, cf. [2.2.2]. A simple time measurement is possible with a GPS receiver, cf. [5.2.5]. In order to record the time of a star transit through the horizontal or vertical thread of a telescope, or the time of taking a star image, a registration device (chronograph) has to be implemented in the observation system.

5.3.2 Astronomic Positioning and Azimuth Determination

The determination of astronomic latitude, longitude and azimuth is based on the relations given in [2.6.2], where the star positions (α, δ) are given by star catalogues, cf. [2.4.3]. We mention here only a few of the many methods developed in geodetic astronomy.

In determining the *astronomic latitude* Φ , it is required, according to (2.21), to ascertain the zenith angle z and the hour angle h . The latter quantity has to be derived from the rectascension α and the measured time, see (2.22). By differentiating (2.21) with respect to the observed quantities, we obtain differential formulas for estimating the effect of observational errors on the results and for finding optimum configurations for the observations. For the latitude we obtain

$$d\Phi = -\frac{1}{\cos A} dz - \cos \Phi \tan A dh . \quad (5.50)$$

An error in z has a minimum effect for meridian transits of the star, and an error in h has no effect on Φ in that case.

For an upper culmination (the smaller zenith angle) of a northern star ($A = 0^\circ$) or a southern star ($A = 180^\circ$), the latitude is given by (see also Fig. 2.4)

$$\Phi = \delta_N - z_N \text{ and } \Phi = \delta_S + z_S \quad (5.51)$$

respectively. Measuring the meridian zenith angle (e.g., to Polaris) is therefore most suitable for the determination of the latitude.

If one observes a pair of stars consisting of both a northern and a southern star having approximately the same zenith angle, averaging (5.51) significantly reduces the uncertainties in z due to refraction (*Sterneck* method):

$$\Phi = \frac{1}{2}(\delta_N + \delta_S) + \frac{1}{2}(z_S - z_N). \quad (5.52)$$

In the *Horrebow-Talcott* method, the small difference between the meridian zenith angle of the northern and southern stars in a star pair is measured by a registering micrometer. The optical axis in each case is adjusted to the same zenith angle using the Horrebow level that is mounted on the horizontal axis. Since accurate circle and time readings are not required, this method provides very precise results ($\pm 0.1''$ when about 20 star pairs are observed).

The *astronomic longitude* Λ is given by the difference between the local sidereal time LAST and the Greenwich sidereal time GAST (2.23):

$$\Lambda = \text{LAST} - \text{GAST}, \quad (5.53)$$

where 1 s corresponds to $15''$. According to (2.22), LAST is related to the hour angle h :

$$\text{LAST} = h + \alpha. \quad (5.54)$$

h can be computed from the zenith angle according to (2.21). If the latitude is known, we have:

$$\cos h = \frac{\cos z - \sin \Phi \sin \delta}{\cos \Phi \cos \delta}. \quad (5.55)$$

Converting measured universal time UT to GAST allows the determination of Λ .

By differentiating (2.21), we get

$$dh = -\frac{dz}{\sin A \cos \Phi} - \frac{\cot A}{\cos \Phi} d\Phi. \quad (5.56)$$

The effect due to errors in z is minimum when observations are made on the prime vertical ($A = 90^\circ$), while the effect here is zero for errors in Φ . The influence of refraction is largely eliminated when observing east and west stars of the same altitude that are symmetric with respect to the meridian. On the other hand, by observing the time of transit across the meridian ($h = 0$) we get

$\text{LAST} = \alpha$. An accuracy of ± 0.01 to 0.02 s is obtained from approximately 30 transits.

The accuracy of the determination of longitude depends primarily on the systematic errors of the observer, the instrument, and the time comparison. If the determinations are made by the same observer, using the same instrument and the same time signal transmitting station, as well as the same stars, then longitude differences are essentially free from these errors. Longitude determinations of high accuracy have thus been carried out as measurements of differences with respect to a reference station.

An economical method to determine the latitude and longitude simultaneously is known as the method of *position lines*.

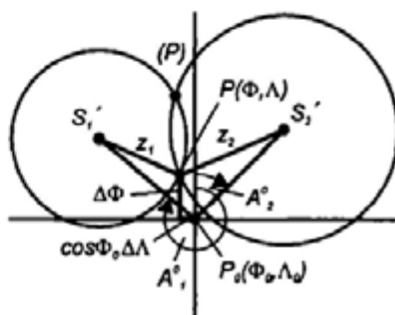


Fig. 5.27. Method of position lines

The zenith angles z_1, z_2 of two stars $S_1(\alpha_1, \delta_1), S_2(\alpha_2, \delta_2)$ are observed at sidereal times $\text{LAST}_1, \text{LAST}_2$ and at azimuths A_1, A_2 . If S_1, S_2 are projected on the earth's surface, then the intersections of the circles centered at the projections S'_1, S'_2 having radii z_1, z_2 represent two geometric positions P and (P) for the point of observation (Fig. 5.27). Near P , the circles can be replaced by their tangent lines (position lines). The intersection of these lines yields an approximation to P . Computationally, one obtains the corrections $\Delta\Phi = \Phi - \Phi_0$ and $\Delta\Lambda = \Lambda - \Lambda_0$ upon introducing an approximate position $P_0(\Phi_0, \Lambda_0)$. When observations are made with the prism astrolabe, cf. [5.3.1], the zenith angle predetermined by the prism is treated as an additional unknown. One obtains accuracies of a few $0.1''$ from about 20 stars evenly distributed above the horizon.

A *zenith camera* also permits the simultaneous determination of latitude and longitude. From the coordinates α_z, δ_z of the zenith, derived from the observations, we obtain

$$\Phi = \delta_z, \quad \Lambda = \alpha_z - \text{GAST}, \quad (5.57)$$

cf. [5.3.1], see also Figs. 2.2, 2.4.

If the latitude is known, then the azimuth A can be obtained, according to (2.21), from the hour angle h derived from the sidereal time and the rectascension (5.54):

$$\tan A = \frac{\sin h}{\sin \Phi \cos h - \cos \Phi \tan \delta}. \quad (5.58)$$

Differentiation of (2.21) yields

$$dA = \frac{\cos q \cos \delta}{\sin z} dh + \cot z \sin A d\Phi, \quad (5.59)$$

where q is the parallactic angle, cf. [2.6.2]. An error in h has a minimum effect for $\delta \approx 90^\circ$ (stars near the pole). For some 10 observations, we get an accuracy of $\pm 0.3''$ to $0.5''$. The azimuth of a terrestrial target is obtained by additionally measuring the angle between the directions to the star and the target.

5.3.3 Reductions

In order to refer the "observed" positions (epoch t) of fixed stars to the system of the star catalogue (mean positions at the reference epoch t_0), several reductions have to be applied.

- *Astromic refraction* causes an apparent increase in the star's altitude (Fig. 5.28). The true zenith angle z is obtained from the observed quantity z' by adding the astromic refraction angle Δz_{**} :

$$z = z' + \Delta z_{**}. \quad (5.60)$$

According to (5.10) and (5.11), the refraction angle depends on the vertical gradient of the refractive index along the path. For a standard atmosphere (temperature 288.15 K, atmospheric pressure 1013.25 hPa), we obtain for $z' < 70^\circ$:

$$\Delta z_0 = 57.08'' \tan z' - 0.067'' \tan^3 z'. \quad (5.61)$$

For actual conditions (temperature T , pressure p), we have the transformation

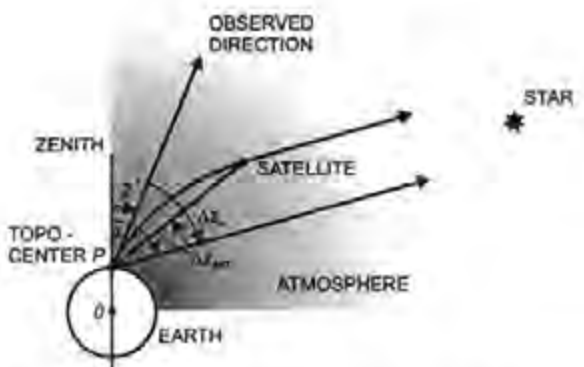


Fig. 5.28. Astronomic and satellite refraction

$$\Delta z_{\text{atm}} = \Delta z_0 \frac{p}{1013} \frac{288}{T}, \quad (5.62)$$

(SAASTOMAINEN 1972/1973, KOVALEVSKY 1995). The accuracy of Δz_{atm} varies between a few $0.01''$ and a few $0.1''$ and depends strongly on systematic deviations from the atmospheric model (turbulences, slope of the atmospheric layers).

- The *diurnal aberration* is an apparent displacement in direction resulting from the finite velocity of light and the relative velocity of the observer with respect to the stars, due to the earth's rotation. The corresponding reduction reaches a maximum of $0.3''$ at the equator.
- The *geocentric* (or diurnal) *parallax* represents the difference between the topocentric and the geocentric direction; it can be neglected for star observations, cf. [2.4.1].

Through these reductions, the "observed" position is transformed to the "apparent" position (apparent place) at epoch t . The reduction from the "mean" position (epoch t_0) to the apparent position (epoch t) involves the following steps:

- Applying *precession* and *proper motion* for the time interval $t - t_0$ transforms the mean position (t_0) to the mean position at epoch t , cf. [2.4.2], [2.4.3].
- Accounting for *nutation* transforms the mean position (t) to the true position (t). The origin of the system is still at the barycenter of the solar system.
- The transition to the (geocentric) apparent position (t) is performed by accounting for the apparent directional changes arising from the orbital motion of the earth around the sun (*annual aberration*, up to $20''$) and the

difference between the heliocentric and the geocentric directions (*annual parallax*, less than $1''$).

Instead of reducing from the mean position (t_0) to the apparent position (t), astronomic almanacs that contain the apparent places of fundamental stars for a particular year (Apparent Places of Fundamental Stars, Astronomisches Recheninstitut Heidelberg) can be used.

Finally, we must consider that the results (astronomic positions and azimuths) refer to the instantaneous spin-axis of the earth. The results must be transformed into the IERS reference pole (ICRF) by applying reductions for polar motion, cf. [2.5.2]. Multiplying the polar motion rotation matrix (2.18) with the unit vector of the local vertical (2.19) gives the reductions for latitude, longitude, and azimuth (MUELLER 1969, p.86):

$$\begin{aligned}\Delta\Phi_p &= \Phi_{\text{ICRF}} - \Phi = -(x_p \cos \Lambda - y_p \sin \Lambda) \\ \Delta\Lambda_p &= \Lambda_{\text{ICRF}} - \Lambda = -(x_p \sin \Lambda + y_p \cos \Lambda) \tan \Phi, \\ \Delta A_p &= A_{\text{ICRF}} - A = -(x_p \sin \Lambda + y_p \cos \Lambda) \sec \Phi\end{aligned}\quad (5.63)$$

where x_p, y_p are the pole coordinates with respect to ICRF.

5.3.4 Very Long Baseline Interferometry

Extragalactic radio sources (quasars = quasi-stellar radio sources, radio galaxies) emit waves in the cm to dm range, which can be detected by large antennas (radio telescopes) used in radio astronomy. The approximate angular resolution of such a telescope is given by the wavelength/diameter ratio, and thus it is limited to a few arcmin for telescope diameters less than 100 m. By employing a receiving system of two widely (a few 1000 to 10 000 km) separated radio telescopes (baseline), the resolution can be increased to $\pm 0.001''$ and better: *Very Long Baseline Interferometry* (VLBI), MORITZ and MUELLER (1987, p.381).

The wave train from an extragalactic radio source arrives at the telescope P_2 with a phase difference Φ with respect to the telescope P_1 . Φ is related to the time delay τ , the time the wave requires to travel the path difference $c\tau$ (c = velocity of light in vacuum), Fig. 5.29. Due to the earth's rotation, Φ and τ depend on time t . The following relations are valid:

$$\Phi(t) = 2\pi \frac{c}{\lambda} \tau(t) = 2\pi v \tau(t), \quad (5.64)$$

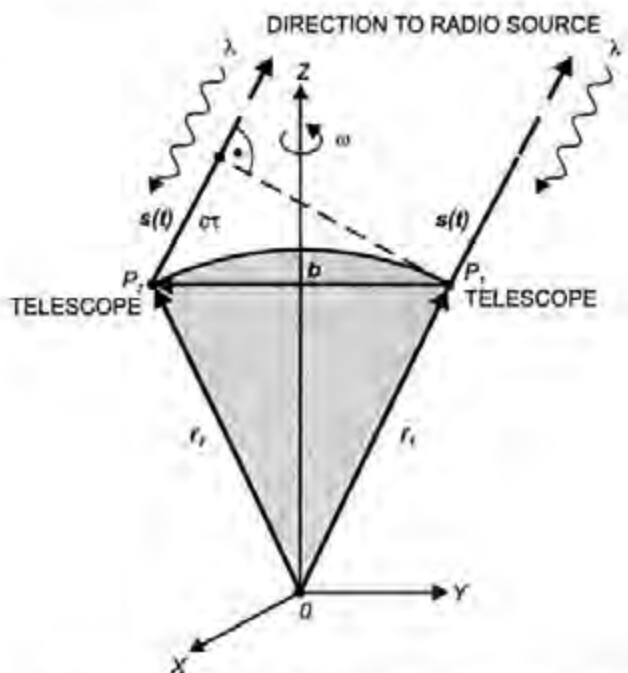


Fig. 5.29. Very Long Baseline Interferometry

where λ and v are the respective wavelength and the frequency of the received radio wave. We introduce the baseline vector

$$\mathbf{b}_{\text{IRS}} = \mathbf{r}_2 - \mathbf{r}_1 = \begin{bmatrix} X_2 - X_1 \\ Y_2 - Y_1 \\ Z_2 - Z_1 \end{bmatrix}, \quad (5.65)$$

described in the terrestrial geocentric system (2.14) and the unit vector to the quasar:

$$\mathbf{s}_{\text{ICRS}} = \begin{bmatrix} \cos \alpha \cos \delta \\ \sin \alpha \cos \delta \\ \sin \delta \end{bmatrix}, \quad (5.66)$$

given in the celestial reference system (2.11). After transformation of \mathbf{s} to the terrestrial system according to (2.16), we obtain, see Fig. 5.29,

$$\tau(t) = -\frac{1}{c} \mathbf{b} \cdot \mathbf{s}(t). \quad (5.67)$$

The negative sign takes the direction of \mathbf{s} into account, which is opposite to the direction of wave propagation. By comparing the two wave trains received at P_1 and P_2 , interferences are obtained. The *frequency* of the interference *fringes* (maxima and minima) changes due to the earth's rotation:

$$f(t) = \frac{1}{2\pi} \frac{d\Phi(t)}{dt}. \quad (5.68)$$

With (5.64) and (5.67), the fringe frequency can be expressed as

$$f(t) = v \frac{d\tau(t)}{dt} = -\frac{v}{c} \mathbf{b} \cdot \dot{\mathbf{s}}(t), \quad (5.69)$$

$\dot{\mathbf{s}} = d\mathbf{s}/dt$. Equations (5.67) and (5.69) represent the VLBI *observation equations* (CAMPBELL and WITTE 1978, CARTER et al. 1985).

The VLBI observables are the time delay τ (or the phase delay, respectively) and the delay rate $d\tau/dt$. They are derived by a comparison of the signals, which are recorded on magnetic tape, along with the precise time provided by hydrogen maser frequency standards. Typically, 10 to 20 sources are tracked over periods of 3 to 6 minutes several times over a 24-hour observation session. The data tapes are sent to a correlator center where they are replayed and the signals processed (MARK III and recently MARK IV correlator, CLARK et al. 1987). The correlation function furnishes the delay and the delay rate between the two stations. The observable τ represents a group delay, while Φ is a phase delay, cf. [5.1.1], which involves the problem of ambiguity resolution, cf. [5.2.5]. The fringe frequency (delay rate) observation is free of this problem but of less importance due to its lower accuracy as compared to the delay observation and since it allows only the determination of a reduced set of parameters (SEEBER 1993, p.430).

Reductions are applied for the daily aberration, cf. [5.3.3], for systematic clock differences (clock synchronization), for the effects of the tropospheric refraction, cf. [5.1.2], and for relativistic effects. The effect of the ionosphere is compensated for by observing in two frequency-bands, namely 2.2 and 8.4 GHz, cf. [5.1.3]. Main *error* sources result from timing (± 1 ps) and frequency instabilities ($\pm 10^{-15}$ over a few days) as well as from tropospheric models. The determination of the "wet" component plays a major part in this aspect, cf. [5.1.2]. Attempts have been made to measure the water vapor content along the signal path by water vapor radiometers in order to estimate the wet component with cm-accuracy. The vertical baseline component is mainly affected by the uncertainty of the wet component.

Among the *parameters* to be estimated from (5.67) and (5.69) are the components of the baseline vector in the terrestrial reference system (cm accuracy). Global solutions for a given epoch deliver a precision of a few mm for the coordinates and annual station velocities accurate to a mm/a. They also yield earth rotation parameters, cf. [2.5.3]. These parameters enter into the models through the transformation between the terrestrial and the celestial system. They can be determined with an accuracy better than 0.001" (pole coordinates) and 0.1 ms (UT1), with a one-day resolution, cf. [2.5.2]. In addition, corrections to the precession and nutation models can be derived from VLBI (ROBERTSON et al. 1985, CAMPBELL et al. 1992).



Fig. 5.30. 20m-radio telescope, Fundamentalstation Wettzell, courtesy Bundesamt für Kartographie und Geodäsie (BKG), Frankfurt a.M., Germany

Today, around 20 stationary radio telescopes participate in international programs in order to establish the reference frames, to determine the earth rotation parameters, and to derive station velocities, especially within the International Earth Rotation Service. The stations are mainly located in North America, Europe, and Japan, Fig. 5.30. Mobile radio telescopes have been developed for rapid surveying of regions with recent crustal movements, such as California or the Eastern Mediterranean, and to fill gaps of the terrestrial reference system in the southern hemisphere.

5.4 Gravimetry

Gravimetry deals with the measurement of the gravity intensity (gravity) and the gravity gradient by terrestrial methods on or close to the earth's surface (MARSON and FALLER 1986, TORGE 1989). "Absolute" gravity measurements refer directly to the standards of length and time [5.4.1], while "relative" measurements use a counterforce for the determination of gravity differences [5.4.2]. A global gravity reference system is needed in order to refer local and regional gravity networks to a common standard [5.4.3]. Gravity measurements on moving platforms are valuable for areas difficult to access [5.4.4]. Local gravity-field information can be obtained by the measurement of the gravity gradient [5.4.5]. The continuous record of gravity provides gravity variations with time, especially the gravimetric earth tides [5.4.6].

The *unit* of gravity in the SI-system is ms^{-2} . The units $\text{mGal} = 10^{-5} \text{ ms}^{-2}$ and $\mu\text{Gal} = 10^{-8} \text{ ms}^{-2} = 10 \text{ nms}^{-2}$ are still in widespread use in geodesy and geophysics and derived from the unit Gal (after Galileo) of the former cgs-system.

5.4.1 Absolute Gravity Measurements

An "absolute" gravity measurement determines the gravity g from the fundamental acceleration quantities length and time. We distinguish between the pendulum and the free-fall method, both introduced by Galileo Galilei (1564 – 1642), FALLER and MARSON (1988), TORGE (1991).

The pendulum method is no longer applied today but governed gravimetry for about 300 years. Because of its fundamental importance, and because recent results are still part of some gravity networks, a short introduction is given here.

The *pendulum method* is based on the measurement of the period and the length of a freely swinging pendulum. For a *mathematical* pendulum (point mass m suspended on a weightless wire of length l) we have the equation of oscillation

$$ml\ddot{\varphi} + mg \sin \varphi = 0, \quad (5.70)$$

with the phase angle $\varphi = \varphi(t)$, and the angular acceleration $\ddot{\varphi} = d^2\varphi/dt^2$ (Fig. 5.31). Integration over a full period leads to an elliptical integral. After expansion into a series, we obtain the period T of oscillation

$$T = 2\pi \sqrt{\frac{l}{g}} \left(1 + \frac{\varphi_0^2}{16} + \dots \right), \quad (5.71)$$

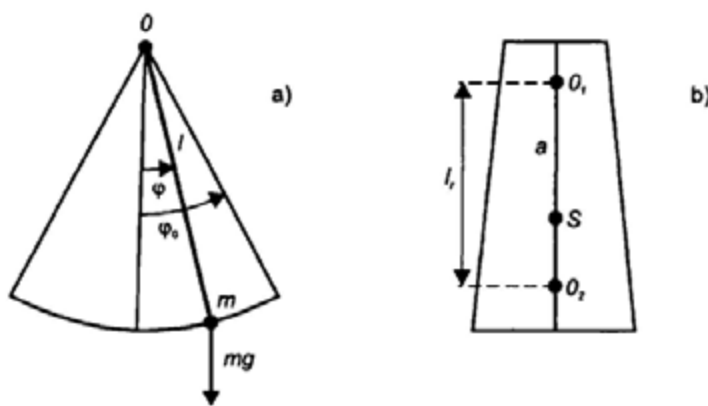


Fig. 5.31. Absolute pendulum method: a) mathematical pendulum, b) reversible pendulum

where the amplitude φ_0 is kept small. Thus, gravity is derived from the measurement of T and l .

A mathematical pendulum is difficult to realize. Equations (5.70) and (5.71) also hold for a *physical* pendulum if l is replaced by the reduced pendulum length

$$l_r = \frac{J}{ma}. \quad (5.72)$$

Here, J is the moment of inertia with respect to the axis of rotation O , m the total mass, and a the distance between O and the center of mass. The *reversible pendulum* is characterized by two axes of rotation, for which, after a corresponding adjustment, the same oscillation time is achieved. The distance between the two axes is equal to the reduced pendulum length, thus avoiding the direct determination of J , m , and a (Fig. 5.31).

The reversible pendulum was introduced by *Kater* (1818), and a limited number of observations were carried out, primarily after the 1860's (transportable devices by *Repsold* and others). After the fundamental gravity determination in Potsdam, cf. [5.4.3], only a few more experiments were performed. Due to errors in determining the length of the swinging pendulum, the accuracy achieved remained at a few μms^2 (*SCHÜLER* et al. 1971).

The *free-fall method* is based on the equation of motion

$$m\ddot{z} = mg(z) \quad (5.73)$$

of a freely falling body. Here m is mass; z is along the local vertical axis, and $\ddot{z} = d^2z/dt^2$ (Fig. 5.32). Assuming a homogeneous gravity field along the falling distance, double integration of (5.73) yields the free-fall equation

$$z = z_0 + \dot{z}_0 t + \frac{g}{2} t^2. \quad (5.74)$$

Equation (5.74) relates the position z of the falling body at the time t to gravity. The integration constants z_0 and \dot{z}_0 represent z and $\dot{z} = dz/dt$ at the starting time of the experiment ($t = 0$).

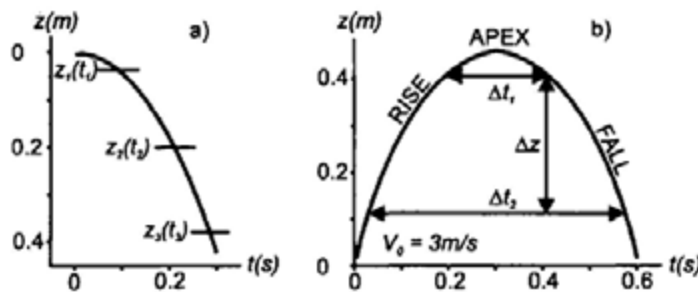


Fig. 5.32. Distance-time diagram: a) free-fall method, b) symmetrical rise and fall

z_0 and \dot{z}_0 slightly deviate from zero due to problems in accurately defining the starting position and small microseismic accelerations. The gravity change along the falling distance (non-homogeneous gravity field) is taken into account by introducing the vertical gradient $\partial g/\partial z$ into (5.74) and by referring the final gravity value to a fixed reference height, e.g. 1 m (NIEBAUER 1989).

If at least three position/time pairs are measured, z_0 and \dot{z}_0 can be eliminated in (5.74), and gravity is given by

$$g = 2 \frac{(z_3 - z_1)(t_2 - t_1) - (z_2 - z_1)(t_3 - t_1)}{(t_3 - t_1)(t_2 - t_1)(t_3 - t_2)}. \quad (5.75)$$

For the *symmetrical rise and fall*, the test mass is thrown vertically upward and falls back after having reached the apex (Fig. 5.32). It is sufficient to measure time at the same two positions during rise and fall. Evaluation of (5.74) yields

$$g = \frac{8\Delta z}{\Delta t_2^2 - \Delta t_1^2}, \quad (5.76)$$

with $\Delta z = z_2 - z_1$, $\Delta t_1 = t_3 - t_2$, $\Delta t_2 = t_4 - t_1$.

Generally, more than the necessary number of position/time pairs is measured. Equation (5.74) then serves as observation equation for a least squares adjustment of g , z_0 , and \dot{z}_0 .

Accuracy demands for absolute gravimetry are at the order of 10^{-9} g or 10^{-8} ms $^{-2}$. Hence, for a falling distance of 0.2 m (falling time 0.2 s), accuracies of ± 0.2 nm and ± 0.1 ns are required for position and time respectively. This is achieved by interferometric distance measurements and simultaneous electronic timing.

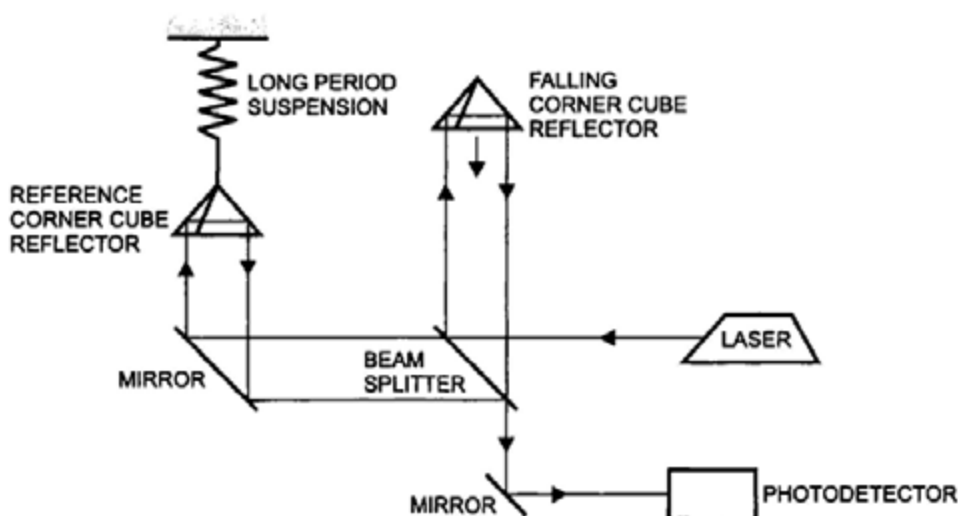


Fig. 5.33. Michelson interferometer principle

For recent free-fall gravimeters, a polarization or iodine stabilized He-Ne gas laser ($\lambda = 633$ nm) serves as the length standard and an atomic (rubidium) frequency normal as the time standard. A Michelson interferometer is used for the distance measurement, with two corner cube reflectors as the main components (Fig. 5.33). One of the reflectors is fixed and serves as a reference; the other one represents the falling body. By splitting the laser light into a measurement and a reference beam, and superimposing them again after parallel reflection, light interferences occur. The zero crossings of this fringe signal have a distance of $\lambda/2$, and the fringe frequency increases with time due to the velocity increase according to $\dot{z}(t) = gt$ (Fig. 5.34). The zero crossings are

sensed by a photodiode, converted to an electronic signal, amplified, triggered, and counted. A time measurement (atomic clock and time interval counter) is carried out after a preset number n of zero crossings, which corresponds to a falling distance of

$$\Delta z = n \frac{\lambda}{2}. \quad (5.77)$$

The experiments are performed in vacuum (10^{-4} Pa) in order to eliminate air resistance. Microseismicity is to a large part absorbed by long-period ($T > 10$ s) compensation devices. A further reduction is achieved by randomization, performing a large number (several 100 to a few 1000) of drops per station. For the rise and fall method, systematic errors that are proportional to the falling body's velocity (residual air drag, timing errors) cancel.

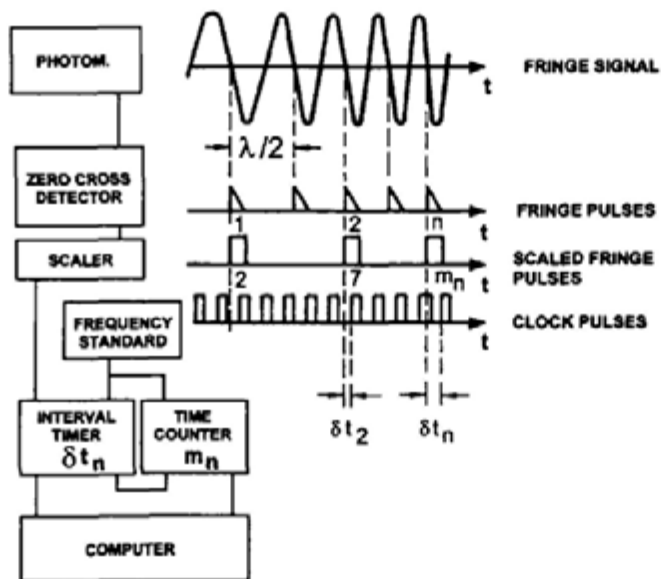


Fig. 5.34. Timing of scaled fringe pulses, after ZUMBERGE (1981)

Several *reductions* have to be applied to the observed gravity values. The gravimetric earth tides can be reduced with an accuracy of a few $0.01 \mu\text{ms}^{-2}$ in most parts of the world, cf. [8.3.5]. The *polar motion* reduction, according to (3.109) and (5.63), is given by

$$\delta g_{\text{pole}} = -\delta_{\text{pole}} \omega^2 R \sin 2\varphi (x_p \cos \lambda - y_p \sin \lambda), \quad (5.78a)$$

with ω = rotational velocity of the earth, R = earth radius, and x_p and y_p = coordinates of the instantaneous pole with respect to the IERS reference pole.

The geodetic coordinates φ, λ sufficiently approximate astronomic latitude and longitude. The factor $\delta_{\text{pole}} = 1.2$ accounts for the earth's elasticity, cf. [5.4.6]. The direct (gravitation) and indirect (deformation) effect of *air pressure* variations is taken into account by a reduction

$$\delta g_p = 3(p - p_n) \text{nms}^{-2}, \quad (5.78b)$$

with p = actual air pressure, and p_n = normal air pressure as given by a standard atmosphere, both in hPa (NIEBAUER 1988). The reduction of the adjusted gravity value from the reference height to ground is performed by relative gravity measurements, with an accuracy of ± 0.01 to $0.02 \mu\text{ms}^{-2}$, cf. [5.4.5].

The long-term *stability* of the length and time standards is controlled by calibration of the laser (10^{-9} to 10^{-10} frequency stability) and the atomic clock (10^{-10}). The *repeatability* of the gravimeter system can be checked by regular measurements at a reference station (Fig. 5.35), while the *accuracy* should be estimated by comparisons with other instruments, cf. [5.4.3].

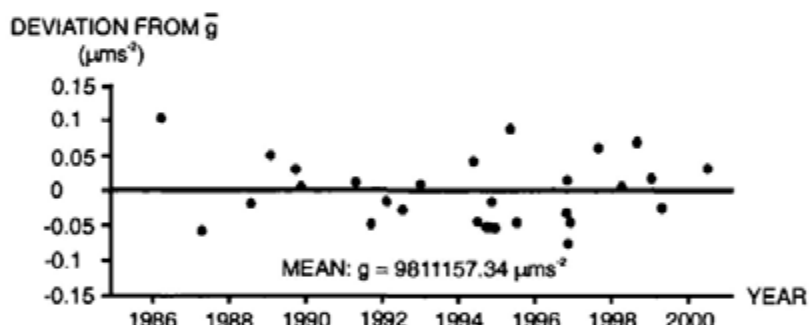
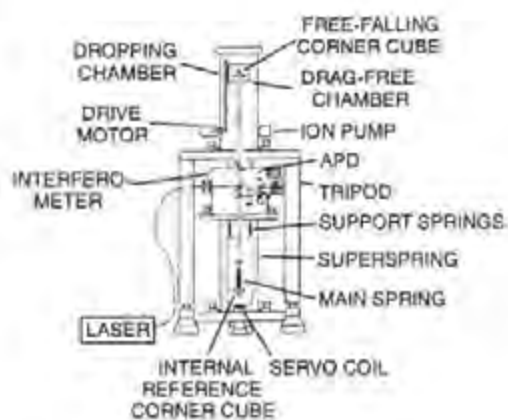


Fig. 5.35. Long-term stability control of JILAG-3 absolute gravimeter at the reference station Clausthal, Germany

The *accuracy* of absolute gravity measurements depends strongly on site conditions. Stable sites (hard bedrock, low man-made noise) provide better results than locations in sediments, close to the coast, or in urban environment. The drop-to-drop scatter (± 0.05 to \pm a few μms^{-2}) is reduced by a large number of measurements. The adjusted station gravity-value is generally derived with a standard deviation of ± 0.01 to $0.03 \mu\text{ms}^{-2}$. The accuracy is at the order of a few $0.01 \mu\text{ms}^{-2}$, due to unmodeled systematic effects of the instrument (e.g., floor recoil) or the environment (atmospheric loading, ground water variations). Systematic discrepancies between different instruments may reach $0.05 \mu\text{ms}^{-2}$ and more, cf. [5.4.3].

The free-fall method was developed in the 1950's (*Violet and Sakuma* at the BIPM Sèvres, *Cook* at the National Physical Laboratory, Teddington). A transportable instrument was designed and employed by *Faller* in 1968. Among the presently operating transportable gravimeters are the JILA (Joint Institute for Laboratory Astrophysics, Boulder, CO, U.S.A.) and the FG5 (Micro-g Solutions Inc., U.S.A.) free-fall instruments (*FALLER* et al. 1983, *NIEBAUER* et al. 1995). Around 200 position/time data pairs are collected over one drop, evenly distributed in distance over the drop length of 20 cm, and adjusted on-line to a fitting parabola. The falling object moves in a co-accelerated 'drag-free' chamber. The chamber eliminates residual air drag and serves, by adequate acceleration, for dropping and catching the corner cube as well as for transporting it back to the initial position. The reference corner cube is isolated from ground motions by a "super-spring", which by a feed-back system electronically generates effective free-oscillation periods between 30 and 60 s. While the JILA gravimeters have a horizontal interferometer basis, the FG5 instruments employ a vertical basis (Figs. 5.36, 5.37). The vertical basis eliminates the influence of floor vibration and tilt on the optical path length. The instruments are disassembled for transportation (FG5: 240 kg in 8 containers). Setting up at a station requires about two hours, and observations are generally carried out over one to two days, depending on local noise (*TORGE* et al. 1987, *KLOPPING* et al. 1997). A portable modification of the FG5 gravimeter can be used in outdoor environment on quiet sites, providing a precision of $\pm 0.1 \mu\text{ms}^{-2}$ in 10 minutes.



5.36. Free-fall gravimeter FG5 principle, courtesy Micro-g Solutions, Inc., Arvada, CO, U.S.A.



5.37. Free-fall gravimeter FG5 view, courtesy Micro-g Solutions, Inc., Arvada, CO, U.S.A.

Transportable *rise-and-fall* instruments have been developed by the Istituto di Metrologia "G. Colonnelli", Torino, Italy (*ALASIA* et al. 1982) and by Jaeger S.A., France (*SAKUMA* 1983). An option for the rise-and-fall mode is also available for the FG5 gravimeter.

An *ocean-bottom* absolute gravimeter has been constructed primarily for monitoring long-term gravity variations in geodynamically active zones (*ZUMBERGE* and *CANUTESON* 1995).

5.4.2 Relative Gravity Measurements

A “relative” gravity measurement yields the gravity difference between two stations or variations of gravity with time, cf. [5.4.6]. Either time or length is measured, keeping the other quantity fixed. As a consequence, relative measurements can be performed more easily than absolute ones.

For the *pendulum method*, the oscillation periods T_1 and T_2 of the same pendulum are measured at two stations P_1 and P_2 . From (5.71) we obtain

$$\frac{g_2}{g_1} = \frac{T_1^2}{T_2^2} \quad (5.79)$$

or, after simple transformation, the gravity difference

$$\Delta g_{1,2} = g_2 - g_1 = -2g_1 \frac{T_2 - T_1}{T_2} + g_1 \frac{(T_2 - T_1)^2}{T_2^2}. \quad (5.80)$$

The relative pendulum method has been employed extensively since v. Sternbeck (1887) developed a transportable device (pendulum length 25 cm, two pendulums swinging on the same support in opposite phase in order to eliminate floor recoil effects). Although the systematic effects that are independent of time and position cancel with this differential method, the accuracy could not be increased over a few μms^{-2} due to problems in keeping the pendulum length constant during a field survey. The method was superseded in the 1930's by elastic spring gravimeters. The pendulum method was used until the 1960's for establishing gravimeter calibration lines, exploiting the fact that pendulum results are given in the unit of acceleration and do not need to be calibrated.

Relative *gravity meters* use a counterforce in order to keep a test mass in equilibrium with gravity. Gravity changes in space or time are monitored by corresponding changes of the counterforce, which are transformed to the gravity unit by a calibration function. An elastic counterforce is used nearly exclusively, but magnetic counterforces are also employed in instruments operating on moving platforms and in the stationary mode, cf. [5.4.4], [5.4.6].

The elastic spring *gravimeter* is based on the principle of a spring balance. If gravity changes, the spring length will also change in order to maintain static equilibrium between gravity and the elastic force. According to *Hooke's law*, the strain is proportional to the stress for small elongations. We distinguish between translational systems (seldom used) and rotational systems.

In a *translational system* (vertical spring balance), the condition of equilibrium is given by (Fig. 5.38a)

$$mg - k(l - l_0) = 0, \quad (5.81)$$

where k is the spring constant and l (resp. l_0) is the length of the spring with (resp. without) a load. Applying (5.81) on a gravity difference Δg furnishes a linear relationship between Δg and the observed difference in length Δl :

$$\Delta g = \frac{k}{m} \Delta l = \frac{g}{l - l_0} \Delta l. \quad (5.82)$$

An undamped spring generates a harmonic oscillation with the proper frequency

$$\omega_0 = \sqrt{k/m} \quad (5.83)$$

and the oscillation time

$$T_0 = 2\pi \sqrt{\frac{m}{k}} = 2\pi \sqrt{\frac{l - l_0}{g}}. \quad (5.84)$$

By differentiation, we obtain the mechanical *sensitivity*

$$\frac{dl}{dg} = \frac{m}{k} = \frac{T_0^2}{4\pi^2}. \quad (5.85)$$

In order to assess gravity changes with a relative accuracy of 10^{-3} , length changes of a 0.1 m long spring would have to be determined to ± 1 nm.

Rotational systems (lever spring balance) consist of a lever that supports a mass m and rotates about an axis O . Equilibrium can be produced through a horizontal torsion spring or through a vertically or obliquely acting helical spring. The equilibrium of the torques for the *lever torsion spring balance* (Fig. 5.38b) yields

$$mg \cos \alpha - \tau(\alpha_0 + \alpha) = 0, \quad (5.86)$$

where a = length of the lever, α = angle between the horizontal and the lever, τ = torsion constant, and α_0 = pretension angle of the spring. This non-linear system becomes a linear one for $\alpha = 0$, with

$$\Delta g = \frac{\tau}{ma} \Delta \alpha. \quad (5.87)$$

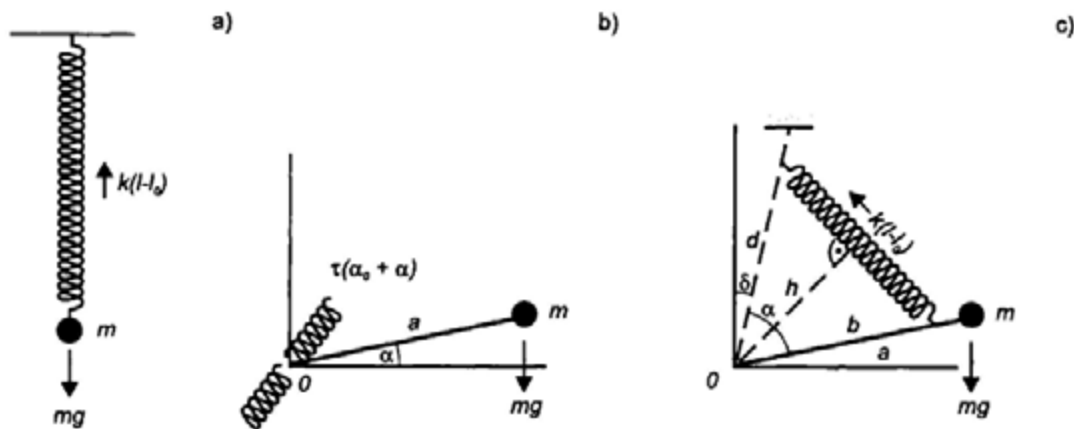


Fig. 5.38. Elastic spring gravimeter principle: a) vertical spring balance, b) lever torsion spring balance, c) general lever spring balance

For the *general lever spring balance*, the spring counterforce acts under an arbitrary angle on the lever carrying the mass. The line connecting the rotation axis O with the point where the spring is mounted deviates by an angle δ from the vertical (Fig. 5.38c). With the distance

$$h = (bd/l)\sin \alpha \quad (5.88a),$$

the equilibrium condition for the torques reads

$$mg a \sin(\alpha + \delta) - kbd \frac{l - l_0}{l} \sin \alpha = 0. \quad (5.88b)$$

The sensitivity of this non-linear system can be significantly increased by approximating the torques of gravity and of the elastic spring (astatization). With a zero-length spring ($l_0 = 0$), we have the sensitivity

$$\frac{d\alpha}{dg} = \frac{\sin(\alpha + \delta)\sin \alpha}{g \sin \delta}. \quad (5.89)$$

High sensitivity is achieved at a small angle δ and $\alpha \approx 90^\circ$. For $a = 0.1$ m, $\alpha + \delta = 90^\circ$, and $\delta = 100''$, displacements have to be measured with $\pm 2 \mu\text{m}$ in order to obtain a relative accuracy of 10^{-8} . Compared to the linear system, the sensitivity is thus increased by a factor of 2000.

The required accuracies of $0.1 \mu\text{ms}^{-2}$, or better, place high demands on the reading systems as well as on the stability of the counterforce with time.

Optical and/or electrical reading systems are used to observe the position of the test mass. A capacitive position-indicator is usually employed and is connected to a digital readout unit. The *zero-method* is preferred for the measurement of the displacement, with a compensation device for restoring the zero position. Mechanical compensation is performed by a measurement screw, while electronic feedback systems are not affected by screw errors (RÖDER et al. 1988).

The *elasticity* of the spring should exhibit a time stability of 10^{-8} over several hours, which is the time interval required for transporting the gravimeter between the stations of a large-scale network, cf. [7.4]. Spring materials include NiFe alloys (small thermoelastic coefficient) and fused quartz (large but linear thermoelastic coefficient, small coefficient of thermal expansion). In addition, the measurement system has to be protected against changes in temperature (thermostat), air pressure (air-tight sealing), and magnetic field (shielding of metal alloy springs). The effects of mechanical shocks and vibrations can be reduced by a damping device, in addition to air-damping.

Spring gravimeters have been developed since the 1930's for use in geophysical exploration. From the 1950's, instruments were available which could be used for establishing large-scale gravity networks. Most of these early gravimeters had a limited measuring range (e.g. 2000 μms^{-2}) and required a reset screw for changing to another gravity range (Askania gravimeter: torsion spring balance, metal alloy; Worden gravimeter: fused quartz system with horizontal beam and vertical counter spring). The LaCoste and Romberg astatized gravimeters employ a metal zero-length spring, acting at 45° inclination on the horizontal beam (model G: 70 000 μms^{-2} range, measuring screw with 10 μms^{-2} per one rotation), KRIEG (1981), KANNIGESER (1983), Fig. 5.39. Recently developed instruments are microprocessor-controlled and are highly automated. They employ capacitive transducers and electronic feedback systems with worldwide

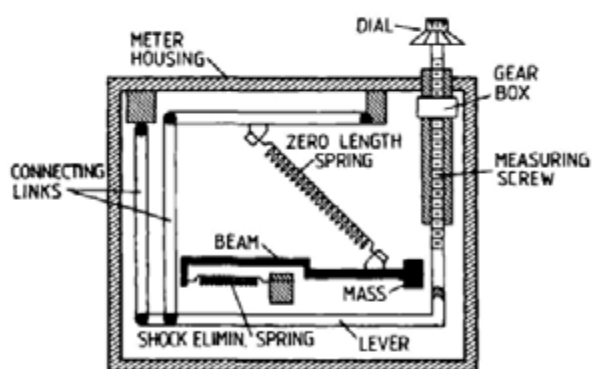


Fig. 5.39. LaCoste and Romberg gravimeter principle, courtesy LaCoste and Romberg, Inc., Austin, Texas, U.S.A.



Fig. 5.40. LaCoste and Romberg gravimeter (Graviton-EG), courtesy LaCoste and Romberg, Inc., Austin, TX, U.S.A



Fig. 5.41. Scintrex Autograph CG-3M gravimeter, courtesy Scintrex, Concord, Ontario, Canada

range. Self-leveling, a high data acquisition rate, and on-line evaluation (data compression and analysis, earth tides reduction, drift control) are further characteristics (Scintrex CG-3 Autograph: Worden type quartz system; LaCoste and Romberg model E-meter), FALK (1995), BONVALOT et al. (1998), Figs. 5.40, 5.41.

Options of conventional land gravimeters include underwater and bore-hole instruments. After sealing in a pressure and water protected diving bell, an *underwater gravimeter* is lowered to the sea bottom and remotely operated from on board a survey vessel. The underwater gravimeters are used mainly in the shelf areas, BEYER et al. (1966). Bore-hole gravimeters are characterized by small dimensions and remote-controlled operation at high temperatures.

Air/sea gravimeters will be described in [5.4.4] and recording (earth tides) gravimeters in [5.4.6].

Despite all measures to protect the gravimeter's measuring system against environmental disturbances, the zero reading changes with time: drift and tares. The *drift* is caused by aging of the spring material (approximating zero after some years) and short-term changes which occur during a field survey. This "transportation" drift results from reactions of the spring to vibrations and small shocks, uncompensated temperature fluctuations, and elastic aftereffects after unclamping the lever. It depends on the spring material and on measurement conditions and can reach a few $\mu\text{ms}^{-2}/\text{day}$. Larger mechanical shocks may produce sudden *tares* of the same order of magnitude or more. The drift is determined by repeated station occupations during one day and subsequent modeling. Different methods have been developed depending on the instrumental behavior and the network structure; among them are the profile, the star, and the step method (Fig. 5.42).

After reducing the gravimeter reading for the earth tides, cf. [8.3.5], the drift function can be modeled by a low-order polynomial with time (Fig. 5.43):

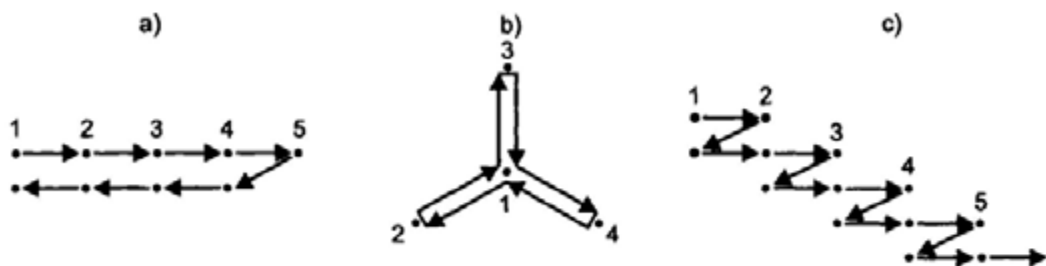


Fig. 5.42. Drift determination methods: a) profile method, b) star method, c) step method

$$D(t) = d_1(t - t_0) + d_2(t - t_0)^2 + \dots, \quad (5.90)$$

with t_0 = starting time (e.g., beginning of the survey) and d_1, d_2 = drift parameters. The network adjustment delivers the drift parameters, based on repeated observations, cf. [7.4].

The gravimeter reading z (in counter units) is converted to the gravity unit by means of the *calibration* function:

$$g = F(z). \quad (5.91)$$

$F(z)$ depends on the physical and geometrical parameters of the measuring system, see (5.82), (5.87), (5.89), which cannot be determined with the desired

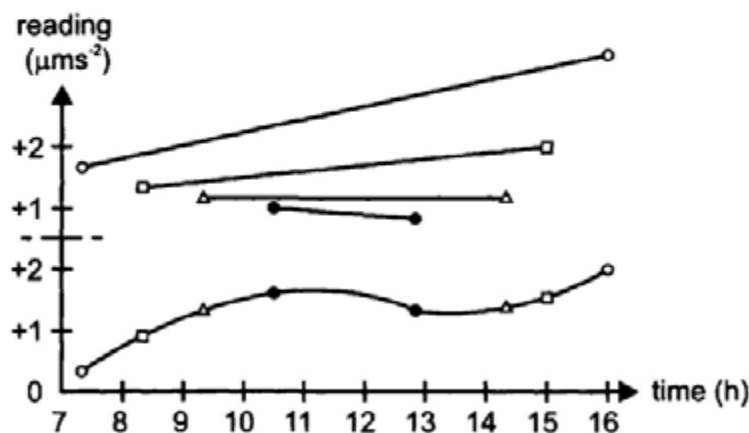


Fig. 5.43. Drift determination (profile method)

accuracy. Therefore, the calibration function is derived by comparing reading differences with known differences of gravity. A low degree polynomial (linear "scale factor" and eventually small non-linearities due to the properties of the feed-back system) provides the transformation from the readings (stations i, j) to the gravity difference:

$$\Delta g_{ij} = g_j - g_i = Y_1(z_j - z_i) + Y_2(z_j^2 - z_i^2) + \dots, \quad (5.92)$$

with Y_1, Y_2 = calibration coefficients. Periodic calibration terms may be added for taking cyclic errors of a measuring screw into account.

Laboratory and field methods are available for determining the coefficients of the calibration function. In the *laboratory*, gravity changes can be simulated and compared with the corresponding gravimeter readings. The tilt-table method uses the inclination by a known angle for producing an apparent gravity variation, and the mass method uses the defined change of the gravimeter mass. Special methods have been developed for recording gravimeters, cf. [5.4.6]. *Calibration lines* provide gravity differences, determined by absolute gravimeters, and may be densified by relative gravimetry. The calibration-line surveys exploit the fact that gravity varies with latitude and height (KANNGIESER et al. 1983). The limited gravity range of these lines only allows determination of an approximate value for the linear calibration factor; an improved estimate must be based on a global gravity-reference-system, cf. [5.4.3]

The *accuracy* of gravity differences ($\Delta g < 1000$ to $2000 \mu\text{ms}^{-2}$) observed with well calibrated and drift-controlled instruments is ± 0.1 to $0.2 \mu\text{ms}^{-2}$. Repeated measurements and the use of several instruments increase the accuracy to ± 0.05 to $0.1 \mu\text{ms}^{-2}$ and $\pm 0.02 \mu\text{ms}^{-2}$ for local ties (TORGE 1984, BECKER et al. 2000).

5.4.3 Gravity Reference Systems

Gravity reference systems provide homogeneity of gravimetric surveys by realizing a gravity standard through the gravity values of a selected number of stations.

The need to establish a global reference system arose at the end of the 19th century when larger sets of absolute and relative pendulum measurements had to be combined. The *Potsdam Gravity System* was introduced in 1909 by IAG. It was based on reversible pendulum measurements carried out in the Geodetic Institute Potsdam by Kühnen and Furtwängler (1898 – 1904). Relative pendulum ties to national base stations transferred the absolute value to other parts of the world. Since the 1930's, new absolute and relative gravity measurements revealed that the Potsdam gravity value was $140 \mu\text{ms}^{-2}$ too high and that transfer errors of several $10 \mu\text{ms}^{-2}$ had occurred.

The Potsdam Gravity System was superseded by the *International Gravity Standardization Net 1971* (IGSN71), recommended by the I.U.G.G. (MORELLI et al. 1974). This network contains 1854 gravity stations (among them about

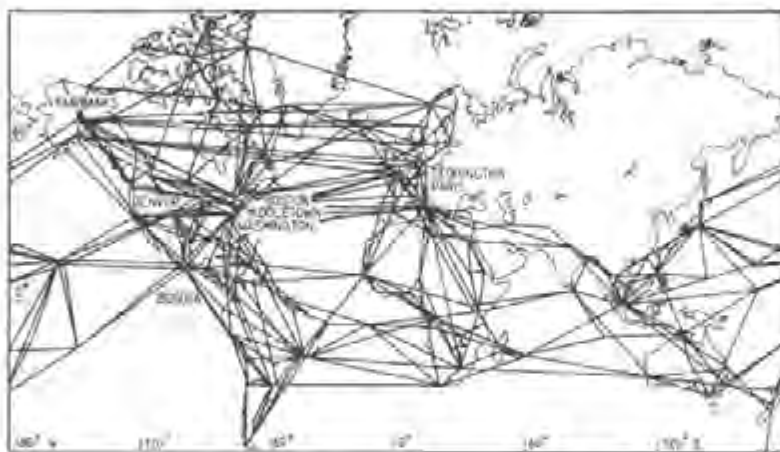


Fig. 5.44. International Gravity Standardization Net 1971 (IGSN71): absolute gravity stations and selected network ties, after MORELLI et al. (1974)

500 primary stations) determined by 10 absolute and about 25 000 relative measurements, including 1200 relative pendulum ties (Fig. 5.44). The mean uncertainty of the adjusted gravity values is less than $\pm 1 \mu\text{ms}^{-2}$. High relative-accuracy is provided at gravimeter calibration lines, which extend in the north-south direction in America, Europe and Africa, and in the western Pacific. Meanwhile the IGSN71 has been extended to previously uncovered parts of the world. Regional networks have been connected to IGSN71, or transformed (shift and scale factor) to it, with the help of identical stations. The IGSN71 gravity values can be used to derive the linear calibration factor of relative gravimeters with a relative accuracy of some 10^{-5} .

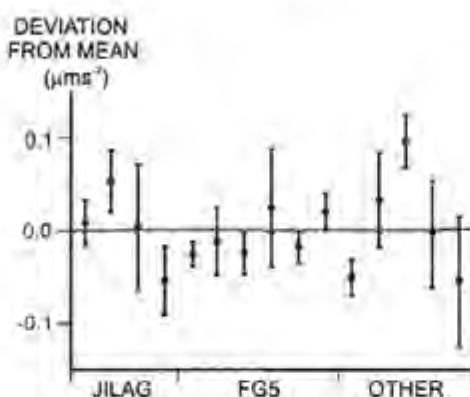


Fig. 5.45. Absolute gravimeter comparison, BIPM Sevres 1997: Deviations from mean value and standard deviations for JILAG-, FG5- and other gravimeters, after ROBERTSSON et al. (2001).

With the increasing availability of transportable *absolute gravimeters* of accuracy of $0.05 \mu\text{ms}^{-2}$ and better, the gravity reference can be established independently from a global system with any gravity survey (TORGE 1998). The linear calibration factors of relative gravimeters then are derived from the absolute values available in the survey area. The IGSN71 consequently does not need a readjustment but rather is improved continuously by networks based on absolute gravimetry. This strategy requires a regular quality control of the absolute gravimeter systems, cf. [5.4.1]. International comparisons have been carried out since the 1980's at the BIPM, Sèvres (Fig. 5.45). For advanced absolute gravimeters, both the r.m.s. scatter around the BIPM mean value and the long-term stability is a few $0.01 \mu\text{ms}^{-2}$, which characterizes the present state of the realization of the gravity standard (ROBERTSSON et al. 2001).

5.4.4 Gravity Measurements on Moving Platforms

Kinematic methods have been developed for rapid and high-resolution gravimetric surveys in areas of having challenging environmental conditions, such as oceans, the polar regions, high mountains, and tropical forests. Ships and airplanes are predominantly used as platforms, but helicopters and land vehicles also have been employed for local surveys. Compared to stationary gravimetry, additional difficulties arise in kinematic gravimetry, including problems with orientation of the gravity sensor and with separating gravity from non-gravitational accelerations (DEHLINGER 1978, BROZENA and PETERS 1995, CANNON and LACHAPELLE 1997).

The principle of kinematic gravimetry is based on Newton's *equation of motion*. In the local astronomic system (also called local level system), cf. [2.6.2], the gravity vector is expressed by:

$$\mathbf{g}' = \ddot{\mathbf{r}}' - \mathbf{R}_b' \mathbf{f}^b + (\mathbf{2}\omega_{ie}' + \omega_{ei}') \times \dot{\mathbf{r}}', \quad (5.93)$$

where $\ddot{\mathbf{r}} = d^2\mathbf{r}/dt^2$ is the platform acceleration, $\dot{\mathbf{r}}$ the platform velocity (\mathbf{r} = position vector), and \mathbf{f} is the vector of measured acceleration (also called specific force). It is assumed that the accelerometers are fixed to the vehicle, which requires a transformation from the vehicle's body frame b to the local level system i . The corresponding rotation matrix \mathbf{R} contains the orientation angles between the two frames. As the platform moves with $\dot{\mathbf{r}}$ with respect to the earth, inertial accelerations arise. These accelerations are taken into account by the last term in (5.93). ω_{ie}' and ω_{ei}' are vectors of angular velocities of the earth's rotation with respect to the inertial frame i and of the platform's rotation with respect to the earth-fixed frame e , respectively.

Operational sea and airborne gravimetry employs modified land gravimeters mounted on a damped two-axes stabilized platform. Stabilization occurs in the

local-level frame by two gyroscope/accelerometer pairs operating in a feed-back mode. For this “scalar” gravimetry, only the *magnitude* of gravity is determined, and (5.93) reduces to

$$g = f_z - \ddot{z} + 2\omega \cos \varphi \sin \alpha v + \frac{v^2}{r}. \quad (5.94)$$

Here, f_z and \ddot{z} are the vertical components of the specific force and the platform acceleration, ω = angular velocity of the earth rotation, φ = geodetic latitude, α = geodetic azimuth, v = platform velocity with respect to the earth, and r = distance to the earth's center. For the static case, (5.94) transforms into the equilibrium conditions of relative gravimetry, cf. [5.4.2].

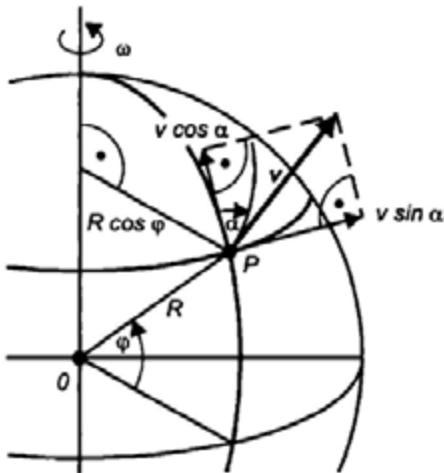


Fig. 5.46. Eötvös effect

The velocity dependent terms on the right side of (5.94) represent the *Eötvös reduction*. From Fig. 5.46, it can be identified as the Coriolis acceleration, which increases (for a west-east directed course) the angular velocity of the earth rotation, and the centrifugal acceleration arising from the platform's angular velocity v/r around the center of the earth. Close to the earth ($r = R = 6371$ km) the Eötvös reduction amounts to

$$\delta g_{\text{Eö}} = 40v \cos \varphi \sin \alpha + 0.012v^2 \mu \text{ms}^{-2}, \quad (5.95)$$

with v in km/h. The second term is small for sea gravimetry but attains large values with airborne applications. As velocities can be determined by GPS navigation with an accuracy of 0.05 m/s, the uncertainty of the Eötvös reduction is now less than $10 \mu \text{ms}^{-2}$.

Instead of using a stabilized platform, the gravity sensor can be rigidly connected to a vehicle. GPS supported inertial navigation systems (INS) are employed with this *strapdown inertial gravimetry*, characterized by a high digital data rate. In the scalar mode, only one approximately-vertical accelerometer is used, while in the vector mode three orthogonally mounted accelerometers determine the specific force vector. According to (5.93), the orientation between the body and the local level frame is needed continuously and is calculated from the output of the INS gyros. Due to the high demands on attitude control, vector gravimetry is still in the experimental stage. Demands are less stringent for scalar gravimetry, especially if the output of the accelerometer triad is used for the determination of the magnitude of gravity (rotation invariant scalar gravimetry), JEKELI (1995), TIMMEN et al. (1998), WEI and SCHWARZ (1998).

The methods for separating *gravity* from *non-gravitational* accelerations depend on the frequency of the accelerations and differ for sea and airborne gravimetry.

High-frequency vibrations can be strongly reduced by the damping of the measuring system. For *sea gravimetry* (stabilized platform), "disturbing" accelerations occur with periods between 2 and 20 s, and they may reach amplitudes of 0.1 g. Due to low ship velocity (10 to 20 km/h) and the nearly constant reference surface (sea level), low-pass filtering sufficiently suppresses the *vertical* accelerations. By averaging the recorded data over time intervals of 1 to 5 minutes, mean gravity values over some 0.1 to 2 km are thus obtained. The effect of *horizontal* accelerations remains small because of the stabilization. Off-leveling effects generally can be neglected (attitude accuracy about 10"). More critical are cross-coupling effects, which occur with horizontal lever spring gravimeters between the horizontal and the vertical component of the disturbing acceleration. They may reach $50 \mu\text{ms}^{-2}$ or more and must be corrected using the horizontal acceleration records. Vertical line gravimeters are free from these errors.

For *airborne gravimetry*, accelerations vary with periods from 1 to 300 s (long-periodic eigenmotion of the airplane) and with amplitudes up to 0.01 g and more. Large airplane velocities (250 to 450 km/h) prevent an effective filtering, and thus with a long filter-length (several minutes) only mean gravity values over some 10 km are obtained. Consequently, accelerations have to be determined independently by differential GPS (carrier phase measurements) through the second time derivative of position or the first time derivative of velocity. Over water and ice areas, radar and laser altimetry can also be employed for height determination. Heights are needed in order to reduce the gravity data to a common reference level, by the free air reduction, cf. [6.5.3].

In 1923, F.A. Vening-Meinesz constructed a three-pendulum instrument for gravity measurements in a submerged submarine; world-wide cruises followed until the 1960's. Since that time, *sea gravimeters* (e.g., Askania, LaCoste and Romberg) mounted on gyro-stabilized platforms have operated on board surface vessels, helicopters (1980's), and airplanes (1990's). Since the 1990's,



Fig. 5.47. Gravity sensor Gss30 and gyrostabilized platform KT 30, courtesy Bodenseewerk Geosystem, Überlingen, Germany

these campaigns have also been supported by GPS. A vertical spring is employed in the Bodenseewerk straight-line gravimeter (Fig. 5.47).

Force-balanced *accelerometers*, as developed for inertial navigation, are small and robust with respect to strong dynamics but have less resolution and larger drift rates than conventional land gravimeters. For a linear system, the proof mass is constrained to move in only one direction and maintained at the zero position by an electromagnetic field. The electrical current needed to maintain zero is proportional to the acceleration. Depending on the direction of the sensitive axis, dedicated components of the specific force are measured (BELL and WATTS 1986, NEUMAYER and HEHL 1995), Fig. 5.48. Force-balanced accelerometers are especially suited for use under rough conditions on sea and in air; they have also been employed on board deep sea vessels (COCHRAN et al. 1999). Similar properties are found with *vibrating string* gravimeters. Here, gravity measurements are based on the fact that the vibrational frequency of a string under tension is proportional to the square root of g (BOWIN et al. 1972).

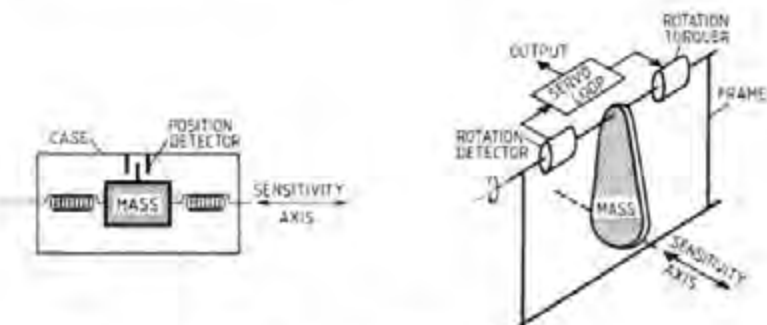


Fig. 5.48. Force-balanced accelerometer principle: translational (suspended mass) system (left) and rotational (pendulum) system (right)

Sea and airborne gravimetric surveys generally are carried out along parallel tracks. Orthogonal tracks serve for control and accuracy improvement by adjustment of the cross-over discrepancies. Sea gravimetry has been concentrated in regions of geological interest and in shelf areas, while recent airborne surveys have covered areas lacking in gravity field information (Greenland, arctic ocean, Antarctica, Switzerland), FORSBERG and BROZENA (1993), KLINGELÉ et al. (1997), Fig. 5.49.



Fig. 5.49. Sea gravimetry profiles (1965-1972). Western Mediterranean Sea, Osservatorio Geofisico Sperimentale, Trieste, after FINETTI and MORELLI (1973)

The accuracy of sea and airborne gravity measurements (data recording generally with 1 s average) depends on the survey conditions (sea state, air turbulence, ship and aircraft properties, flight altitude and velocity), on attitude errors, and, for airborne gravimetry, on the separation between gravity and disturbing accelerations. Accuracies of ± 5 to $20 \mu\text{ms}^{-2}$ are achieved with sea gravimetry with a resolution of about 1 km along track (track distances 5 to 10 km). Airborne gravimetry generally is carried out at flight heights of a few km, but low speed and elevation (several 100 m) surveys are also performed, especially with helicopters (HAMMER 1983). A resolution of 5 to 10 km is routinely obtained now (helicopter 1 km), with accuracies of ± 20 to $50 \mu\text{ms}^{-2}$ (helicopter $5 \mu\text{ms}^{-2}$). An increase in resolution and accuracy by a factor of two is expected (GUMERT 1995). It must be remembered that the attenuation of the gravity field with height, cf. [3.3.3], prevents a high frequency resolution at high flight altitudes.

5.4.5 Gravity Gradiometry

The *gravity gradient tensor* (3.68) contains local gravity field information, and thus is of interest for high-resolution gravity field determination. It is generally expressed in the local astronomic (local level) system, cf. [3.2.2]. The unit of the components of $\text{grad } g$ is s^{-2} . In view of the magnitude of the components and the measuring accuracy, they are generally expressed in $10^{-9} s^{-2} = \text{ns}^{-2}$, traditionally called *Eötvös unit* (E).

A *gravity gradiometer* determines the components of $\text{grad } g$, either all or several or linear combinations of them, by exploiting the different reaction of neighboring proof masses to the gravity field. A gradiometer unit consequently consists of two gravity sensors (mostly accelerometers) rigidly connected and generally orientated in the local level system. Taylor expansions of gravity in the two sensors 1 and 2, with respect to the center of mass C of the system, and differences in the output of the sensors (specific force f) yields in the stationary mode

$$\mathbf{f}_2 - \mathbf{f}_1 = (\text{grad } \mathbf{g})_C (\mathbf{r}_2 - \mathbf{r}_1)', \quad (5.96)$$

with $\mathbf{r}_1, \mathbf{r}_2$ = position vectors of the sensors in the local level system. A gradiometer system is composed of several gradiometer units orientated in different directions in order to derive the corresponding components (Fig. 5.50). Rotation of the gradiometer units in the gravity field provides another means for the determination of different components.

On the earth's surface, *gravimeters* can be used to approximate the components of $\text{grad } g$ by measuring gravity differences between adjacent stations. The horizontal gradient (W_x, W_y) can be derived with a precision of $\pm 10 \text{ ns}^{-2}$ from gravity profiles or area surveys, with station distances of 10 to 100 m (HAMMER

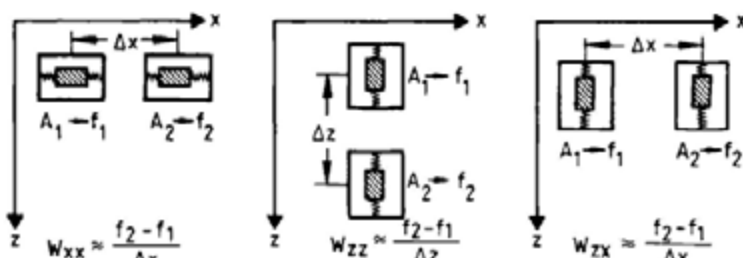


Fig. 5.50. Gravity gradiometer translational system principle with longitudinal (left and center) and transverse (right) constellation

1979). The *vertical* component W_z can be determined with the same precision by repeated relative gravity measurements on tripods, with heights up to 3 m (RÖDER et al. 1985).

The *torsion balance*, developed by R.v.Eötvös around 1900, was the first dedicated gravity gradiometer. It consists of two equal masses situated at different heights and rigidly connected by a beam system. At the center of mass the system is suspended by a torsional thread. Equilibrium of the torques acting on the masses is achieved by horizontal rotation, which depends on the components $W_{yy} - W_{xx}$, W_{yy} , W_{zz} , W_{yz} . These quantities and the zero position of the beam are determined by observing the beam direction at five different azimuths. A precision of ± 1 to 3 ns^{-2} was obtained (MUELLER et al. 1963). The torsion balance was widely employed in applied geophysics between 1920 and 1940.

Terrestrial gravity-gradiometry in the stationary mode is time consuming and strongly affected by small local mass anomalies. Topographic reductions have to be taken into account even in the immediate surrounding (within 100 m), which limits the application to flat or moderate hilly areas.

Measurements on *moving platforms* allow rapid data collection (e.g., in a 1 s rate or more). With airborne and satellite applications, cf. [5.2.7], topographic effects are significantly reduced. In the kinematic mode, the gradiometer system is mounted on a gyro-stabilized platform. The effects of the platform's rotation about the earth have to be taken into account, cf. [5.4.4]. Due to differencing, non-gravitational forces of linear type cancel with this method.

A gravity gradiometer survey system for automobile and airplane applications has been developed at Bell Aerospace, with a precision of 10 ns^{-2} and a resolution of a few km (JEKELI 1988a, VASCO and TAYLOR 1991). It consists of three gradiometer units, each equipped with two accelerometer pairs, mounted orthogonally on a slowly rotating disk (Fig. 5.51). The gradiometer units are combined under different orientation on a gyro-stabilized platform. Superconducting technology may greatly reduce vibrational and long-term effects and provide a precision of 1 ns^{-2} . Airborne or shipborne surveys could then resolve the gravity field down to 1 km or less and by integration give an accuracy of $1 \mu\text{ms}^{-2}$ for gravity (PAIK et al. 1997).

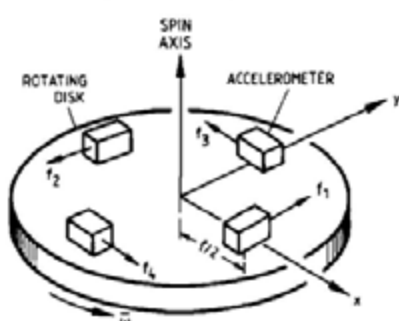


Fig. 5.51. Rotating gravity gradiometer principle, after JEKELI (1988a)

5.4.6 Continuous Gravity Measurements

Continuous gravity records contain information on earth tides and ocean tidal loading, free oscillations and the nearly diurnal free wobble of the earth, inner core translation, polar motion, and volcanic and earthquake activity (ZÜRN et al. 1997, CROSSLEY et al. 1999), cf. [8.3.5]. These effects occur at time scales between seconds and several years and have amplitudes of about 1 to 1000 (tides) nms^{-2} . Hence, a *recording gravimeter* should provide a resolution of 0.01 to 1 nms^{-2} and a high stability with time (low drift rates). It should be time-controlled within ± 10 ms. In order to reduce environmental effects (temperature changes, microseismicity, local inclinations), recording gravimeters generally are installed at underground sites (basement, tunnel).

Recording gravimeters operate in an electronic feedback mode, cf. [5.4.2], over a limited measuring range, e.g., $10 \mu\text{ms}^{-2}$. The voltage output is proportional to gravity and first undergoes an analogue filtering in order to reduce the high-frequency noise. It is then digitized by an A/D converter. Digital filtering delivers a data set (1 to 10 s samples), which is stored on a PC. Further numerical filtering and data reduction may be appropriate as well as the reduction of spikes due to earthquakes and the interpolation of data gaps (WENZEL 1996). An analogue output offers a convenient on-line control of the data acquisition.

Spring-type and superconducting gravimeters are used for gravity recording (MELCHIOR 1983).

Elastic spring gravimeters can be employed if supplemented with a low-pass filter, a recording unit, and a quartz clock. Special earth tide gravimeters have also been developed and are characterized by long-term stability (e.g., by a double thermostat). Recent land gravimeters offer the option of an earth tides mode through increased sensitivity, large memory, and computer-controlled remote operation. The long-term drift of these instruments has to be removed by filtering. Consequently, only short-period effects (e.g., diurnal and higher-frequency tides) can be determined, at a noise level of a few 0.1 to 1nms^{-2} .

For the *superconducting* gravimeter, the gravity acting on the proof mass (Nb sphere) is compensated by a magnetic counterforce (Fig. 5.52). The magnetic field is generated by superconducting coils and thus is extremely stable with time. The position of the mass is monitored by a capacitive detector and held fixed by a feedback coil. Liquid helium provides the superconducting state at a temperature of 4.2 K. The measuring system is kept in an insulating Dewar vessel (Fig. 5.53). For long-term remote operation, a reduced size option is available with no need for liquid helium refilling (GOODKIND 1991, RICHTER

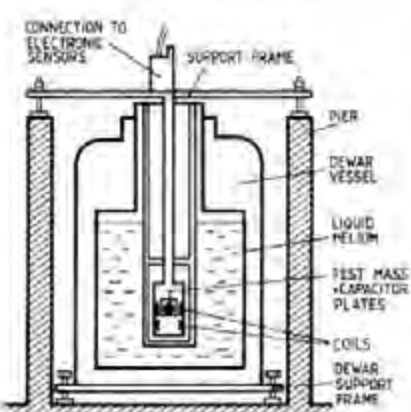


Fig. 5.52. Superconducting gravimeter principle, after GWR-Instruments information and RICHTER (1987)



Fig. 5.53. RSG remote controlled tidal superconducting gravimeter view, courtesy of GWR-Instruments Inc., San Diego, CA, U.S.A.

1995, WARBURTON and BRINTON 1995). The instrumental drift of a superconducting gravimeter is very small (on the order of $10 \text{ nms}^{-2}/\text{a}$), and may be modeled by an exponential function. Absolute gravity measurements can be used to control the drift at longer time intervals. From tidal analysis, a noise level between 0.01 to 0.1 nms^{-2} (short periods) and 1 to 10 nms^{-2} (very long time intervals) has been found (HINDERER et al. 1994, NEUMEYER and DITTFELD 1997).

Calibration of a recording gravimeter is performed by relative and absolute methods. A *relative* calibration is realized by parallel registration with a "calibrated" gravimeter or by recording on a station with well-known tidal parameters. *Absolute* calibration is generally performed on a vertical-gravimeter calibration line. Laboratory calibration procedures include the artificial periodic acceleration on a vertically-oscillating platform, the controlled vertical displacement of large external masses, and the parallel registration with an absolute gravimeter. Accuracies of a few 0.1 % are achieved (RICHTER et al. 1995, FRANCIS 1997). The instrumental phase shift is determined by recording the gravimeter's response to a defined impulse.

The gravity signal is strongly correlated with *atmospheric pressure*. A linear regression with local air pressure (between -2.5 and $-3.5 \text{ nms}^{-2}/\text{hPa}$) reduces the main part of this effect. More refined models are available which also take the air pressure around the station and the elastic response of the earth's crust into account (MERRIAM 1992). Variations of *groundwater* level and *precipitation* also affect the gravity record (order of some 10 nms^{-2}) but are difficult to model (VIRTANEN 2000).

Longer (several months and more) gravity records can be subjected to a *tidal analysis*. It is based on the spectral decomposition of the observed signal into a number of partial tides. By comparing the observations (hourly samples, atmospheric pressure effects reduced) with the gravimetric tides for a rigid earth, cf. [3.5.2], deviations in amplitude and phase are found, which depend on the earth's elastic response to the tidal forces. For the partial tide i , this is expressed by the *amplitude factor*

$$\delta_i = A_i(\text{obs}) : A_i(\text{theor}), \quad (5.97)$$

with A_i = observed resp. calculated (solid earth) amplitude, and the *phase shift*

$$\Delta\Phi_i = \Phi_i(\text{obs}) - \Phi_i(\text{theor}), \quad (5.98)$$

with Φ_i = observed resp. calculated phase. The observation equation for a least squares *spectral analysis* then reads

$$l(t) = \sum_{i=1}^n \delta_i A_i(\text{theor}) \cos(\omega_i t + \Phi_i(\text{theor}) + \Delta\Phi_i), \quad (5.99)$$

with $l(t)$ = recorded gravity value at time t , and ω_i = circular frequency for the partial tide i (WENZEL 1976, 1997).

Elastic spring gravimeters allow the determination of 10 to 20 partial tides (mainly diurnal, semidiurnal, terdiurnal), with an observation time of 4 to 6 months. Superconducting gravimeters can resolve up to 40 tides (including semiannual and annual) by registration over several years. The gravimetric factor for polar motion has also been derived from long-term series. As an example, a 158 days registration with a LaCoste and Romberg feedback gravimeter at Hannover ($\varphi = 52.387^\circ\text{N}$, $\lambda = 9.713^\circ\text{E}$, $H = 50$ m) yielded for the lunar diurnal tide O1

$$\delta(\text{O1}) = 1.151 \pm 0.001, \Delta\Phi(\text{O1}) = 0.16^\circ \pm 0.08^\circ$$

and for the semidiurnal tide M2

$$\delta(\text{M2}) = 1.188 \pm 0.0005, \Delta\Phi(\text{M2}) = 1.70^\circ \pm 0.03^\circ$$

(TIMMEN and WENZEL 1994a). The factor for O1 is close to the observed global value 1.155, while the M2 result differs due to ocean load and attraction, cf. [8.3.5].

A global data bank for tidal gravity measurements (more than 300 stations) is maintained at the International Center for Earth Tides in Brussels (MELCHIOR 1994).

5.5 Terrestrial Geodetic Measurements

Terrestrial geodetic measurements are carried out by directly observing geometric quantities between points on the earth's surface. The majority of the observations refer to the gravity field of the earth through orientation in the local astronomic systems. The measurement of horizontal and zenith angles [5.5.1] and distances [5.5.2] allows relative positioning, where combined instruments (total stations) are generally used. Very precise height differences are provided by leveling [5.5.3]. Strain and tilt measurements serve for detecting local changes of distances and inclination with time [5.5.4].

Due to the high accuracy and economy of satellite-based measurement techniques, terrestrial geodetic measurements are used primarily for interpolating satellite-derived results or in areas where satellite methods fail or need terrestrial support (underground and underwater positioning, forests, urban areas, engineering surveys, local geodynamics).

Inertial surveying provides kinematic three-dimensional positioning by evaluating accelerometer measurements on a moving gyro-stabilized platform. The influence of the gravity field has to be taken into account by reductions. The method is mainly used for station densification in control networks, especially for mapping purposes. The accuracy achieved depends on distance and is about $\pm (0.1 \text{ m} + 10 \times 10^{-6} \text{ s})$. SCHWARZ (1986), JEKELI (2001).

Terrestrial methods are treated in textbooks on surveying, e.g., KAHMEN and FAIG (1988), BANNISTER et al. (1998). Classical surveying instruments are described by DEUMLICH (1988), while the actual state is dealt with in JOECKEL und STOBER (1999), and DEUMLICH and STAIGER (1999). KAHMEN (1978) and SCHLEMMER (1996) concentrate on the fundamentals of electronics employed in geodetic instruments, while Brunner (1984b) deals with the effects of atmospheric refraction.

5.5.1 Horizontal and Vertical Angle Measurements

The *horizontal angle* is defined as the angle measured in the horizontal plane of the local astronomic system between two vertical planes. It is formed by the difference in horizontal *directions* to the target points which define the vertical planes. The *vertical angle* is the angle measured in the vertical plane between the horizontal plane and the direction to the target point. Generally the *zenith angle*, the complement to 90° , is introduced instead of the vertical angle, cf. [2.6.2].

A *theodolite* is used for measuring horizontal and vertical angles. The principal components of this instrument are a horizontal and a vertical circle with graduation, a telescope capable of being rotated about the vertical and the horizontal axes, and a mechanism for reading the circles. In order to orientate

the theodolite with respect to the plumb line direction, it is equipped with spirit or electronic levels.

Regarding the reading of the circle graduation, we distinguish between optical and electronic or digital theodolites.

Optical theodolites of highest precision were developed since the second half of the 18th century and were then used until the 1960's for first order triangulation (with the Kern DKM3 and the Wild T3 theodolites being the latest developments) at station distances of 30 to 60 km. They were characterized by very stable construction and circle diameters of 100 to 250 mm. Circle graduation errors were less than 0.5", and reading accuracy reached 0.1" by using a coincidence microscope with micrometer screw. The lens aperture of the telescope was 60 to 70 mm and the magnification 30 to 40 or more. Standard deviations of $\pm 0.2''$ to $0.4''$ have been achieved for an adjusted horizontal direction, cf. [7.1.1].

Today, horizontal angles are measured only over maximum distances of a few km for densification surveys or dedicated local networks. *Electronic theodolites* (lens aperture 40 to 45 mm, magnification of 30 or more) are available for this purpose and have superseded the optical analogue instruments (Fig. 5.54). Generally, the electronic theodolite is combined with a distance meter to produce a total station, cf. [5.5.2].

The horizontal and vertical circles of an electronic theodolite are either coded or carry an incremental graduation. Reading is microprocessor-controlled and performed by optical-electronic scanning and subsequent interpolation (electronic micrometer). Electronic levels and a dual-axes compensator serve for leveling the instrument; a residual tilt correction may also be applied automatically. Collimation and horizontal axis errors are either eliminated by measurement at both positions of the telescope or corrected internally. An accuracy of $\pm 0.5''$ to 1" is obtained for a direction observed in two positions.

Gyrotheodolites have been developed for the determination of astronomic azimuths by combining a theodolite with a gyroscope. The principle of the gyroscope is based on the fact that a rapidly rotating gyro with horizontal spin axis swings into the north direction due to the mutual effects of the gyro's spin, the earth's gravity, and the earth's rotation. An accuracy of $\pm 3''$ can be obtained from 20 individual measurements. Gyrotheodolites are employed primarily for mining and tunnel surveys, Fig. 5.55.

For the measurement of *zenith angles*, the theodolite is equipped with a reading index for the vertical circle. By leveling the index either manually (spirit level) or automatically, the local vertical is realized with an accuracy of a few 0.1". With electronic theodolites (circle diameter about 70 mm, electronic levels with 2"/2 mm) an accuracy of $\pm 0.5''$ to 2" is obtained for an observed zenith angle.



Fig. 5.54. Electronic theodolite (Leica T 1800), courtesy Leica Geosystems AG, Heerbrugg, Switzerland



Fig. 5.55. Gyrotheodolite (Gyromat 2000), courtesy Deutsche Montan Technologie (DMT), Essen, Germany

Further processing of zenith angles, cf. [6.4.2], requires the consideration of errors due to vertical refraction.

The *refraction angle* depends on the coefficient of refraction (5.11) and thereby on the meteorological conditions along the path of light, particularly the vertical gradient of temperature, see (5.19). Generally, the refraction angle is derived from meteorological data taken at the endpoints of the observation line. This easily leads to errors of a few arcsec and more for distances larger than a few km. According to (5.11b), the effect of this error on the height difference increases with the square of the distance and reaches the order of a few decimeters over a few km. The error of the observed zenith angle, on the other hand, only propagates with distance and thus remains at the order of a few cm.

An approximately symmetric behavior of refraction is to be expected for *simultaneous* observations at the endpoints, especially with cloudy weather and prior to the isothermal conditions of the evening and if the ray of light is more than 15 to 20 m above the ground. The uncertainty of the refraction angle remains less than 1" for distances below 10 to 25 km. This has led to the method of observing reciprocal simultaneous zenith-angles.

For the direct determination of the refraction angle, the *dispersion* of the light may be utilized, cf. [5.1.1]. As the light path at shorter wavelengths has a greater curvature than at longer ones, the use of two different wavelengths causes a difference between the two angles of refraction at the target point. This dispersion angle depends on the effective coefficients of refraction along the light path. Neglecting the small influence of water vapor pressure, it is proportional to the refraction angle but about two orders of magnitude smaller. The main error source of the measurement of the dispersion angle is atmospheric turbulence. Experiments at distances less than 20 km gave uncertainties of ± 1 to $2"$ for the refraction angle. An eventual application of

dispersometers probably will be restricted to distances of a few km (WILLIAMS and KAHMEN 1984).

5.5.2 Distance Measurements, Total Stations

Terrestrial distances represent important geometric quantities for positioning. They provide geometric relations between points and establish the scale of classical geodetic networks.

Until about 1960, the scale of triangulation networks, constructed from angle measurements, was derived from *base lines* having lengths of 5 to 10 km. Measuring rods and, since 1900, wires or tapes served to measure the base line length. With the Jäderin (1880) method, freely hanging invar (NiFe alloy) wires 24 m in length were used, characterized by a small coefficient of thermal expansion. The relative accuracy of the more recent base lines amounts to 10^{-6} , which corresponds to 1 mm/ 1 km.

For field calibrations of wires and tapes, several international *calibration lines* were established by interferometric methods. Starting from the length of a standard meter, the *Väisälä* light interference comparator provided an optical multiplication up to base line lengths of 864 m (relative accuracy $\pm 10^{-7}$).

Electromagnetic distance measurements started at the end of the 1940's. They either use light waves ($\lambda = 0.4$ to $0.8 \mu\text{m}$) and the near infrared (up to $\lambda = 1 \mu\text{m}$) or microwaves ($\lambda = 1$ to 10 cm) as carriers of the measuring signal (RUEGER 1997, JOECKEL und STOBER 1999). The travel time of the signal serves as a measure for the distance.

Microwaves are hardly absorbed by the atmosphere and allow the measurement of large distances (50 km and more) even under unfavorable weather conditions. The effect of humidity on refraction, on the other hand, is great and may significantly deteriorate the results. Distances measured by *light waves* are about one order of magnitude more accurate, but their use may be limited by visibility disturbances (haze, fog), cf. [5.1.2].

Time measurement is performed by the pulse or the phase comparison method.

For the *pulse method*, the transmitter emits a pulse which is reflected at the target and observed at the receiver. An electronic timer measures the time Δt that the signal requires to travel forth and back along the distance s . We have

$$s = \frac{c}{2} \Delta t , \quad (5.100)$$

where we assume that refraction effects have been taken into account by corresponding corrections, cf. [5.1.1]. If the uncertainty in distance is to remain less than 5 mm, the time of propagation must be obtained to an accuracy of ± 0.03 ns. This high accuracy demand can be fulfilled by short (a few ns) laser pulses, electronic counting with a high frequency oscillator, and averaging the results of a large amount (e.g., 1000) of individual measurements, cf. also [5.2.6].

For the *phase comparison method*, a high-frequency carrier wave is sent out by the transmitter and modulated continuously (amplitude or frequency modulation), with modulation frequencies between about 10 and 100 MHz. The corresponding half wavelength (because of the double distance traveled by the signal) serves as a "yard stick" (about 1 to 10 m) in surveying the distance (Fig. 5.56). The phase shift found between the transmitted and the received signal represents the residual part of the distance above an integral number of complete wavelengths.

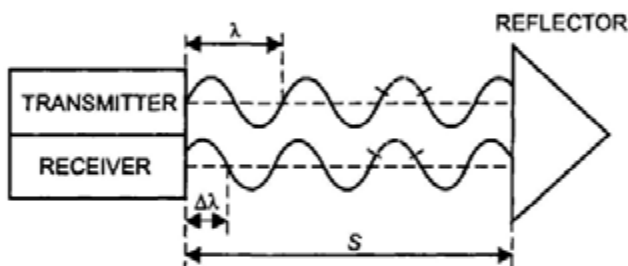


Fig. 5.56. Phase comparison method principle

Travel time Δt and phase shift $\Delta\Phi$ are related through

$$\Delta t = \frac{N + \Delta\varphi/2\pi}{f}, \quad (5.101)$$

with N = number of complete periods, and the modulation frequency

$$f = \frac{v}{\lambda} = \frac{c}{n\lambda}, \quad (5.102)$$

n = refractive index, cf. [5.1.1]. Substituting (5.101) and (5.102) into (5.100), and assuming that refraction is corrected separately, delivers the distance

$$s = \frac{\lambda}{2} \left(N + \frac{\Delta\varphi}{2\pi} \right). \quad (5.103)$$

With the residual part of a wavelength

$$\Delta\lambda = \frac{\Delta\varphi}{2\pi} \lambda, \quad (5.104)$$

the distance can also be expressed by

$$s = N \frac{\lambda}{2} + \frac{\Delta\lambda}{2}. \quad (5.105)$$

Hence, a distance measuring unit consists of an oscillator and transmitter, a receiver, a phase meter, and a microprocessor. With a digital phase detector, the measuring process can be fully automatized; the resolution achievable is 10^{-3} to 10^{-4} , which corresponds to a mm-precision. The number N is determined automatically by applying several slightly different modulation frequencies generated by frequency division.

Terrestrial *microwave* distance measurements started with the development of the tellurometer by *T. L. Wadley* (1956). Here, the master station emitted a modulated (modulation frequencies between 7.5 and 150 MHz) carrier wave ($\lambda = 8$ mm to 10 cm), which was retransmitted from the active transponder (receiver and transmitter). Measurement of ranges up to 70 km and more were obtained. The accuracy strongly depended on refraction uncertainties and could reach

$$\pm(10 \dots 15 \text{ mm} + 3 \times 10^{-6} \text{ s}).$$

Electro-optical distance measurements trace back to the first geodimeter developed by *E. Bergstrand* (1948). Long-range distance meters used laser light (He-Ne gas laser) with modulation frequencies between 15 and 50 MHz and were able to measure distances up to 60 km on clear days, with an accuracy of

$$\pm(1 \dots 5 \text{ mm} + 1 \dots 2 \times 10^{-6} \text{ s}).$$

Microwave and long-range electro-optical distance measurements have been carried out extensively from the 1950's to the 1970's. The measurements were primarily for establishing first order control networks and for strengthening existing horizontal control, cf. [7.1.1]. Long-range distance meters have become obsolete, as large-scale positioning is carried out nowadays almost exclusively by satellite methods.

Today, terrestrial distance measurements are restricted to ranges of a few km and about 10 km maximum. Visible light and (mostly) near infrared are used, either in the pulse or (mainly) in the phase comparison method. Pure distance

meters are available for special applications (partly suitable to be mounted on a theodolite), Fig. 5.57, but generally electronic *total stations* are employed, measuring distances, horizontal directions and zenith angles simultaneously.



Fig. 5.57. Pulsed infrared laser distance meter (Leica Di 3000S), courtesy Leica Geosystems AG, Heerbrugg, Switzerland

The measuring range of a distance measuring unit depends on the number of prisms posted on the target station. With pulsed infrared laser light (gallium arsenide diode), distances up to 5 km (1 prism) or 10 to 20 km (multiple prisms) can be observed with an accuracy of

$$\pm(3\dots5\text{ mm} + 1 \times 10^{-6}\text{ s})$$

and within a measuring time of a few seconds.

With the phase comparison method, using modulated infrared light, distances up to 2 to 3 km can be measured with one prism with an accuracy of

$$\pm(1\dots2\text{ mm} + 1\dots2 \times 10^{-6}\text{ s}).$$

When integrated into a total station, the microprocessor-controlled operation also includes the (partly) automatic searching and pointing of the target, leveling by a two-axes compensator (range 5', precision $\pm 0.3''$), measurement of horizontal direction and zenith angle, data storage in the internal memory, refraction corrections with standard or actual meteorological data, transformation from polar to local Cartesian coordinates, and a graphic display (FEIST et al. 1998), Figs. 5.58, 5.59.

The *calibration* of electronic distance meters includes the control of the modulation frequency by a frequency meter and the determination of the instrumental constants (zero point correction and possible cyclic errors) on a comparator or on a short (about 1 km) calibration line. Calibration lines are usually partitioned into several sections and determined by laser interferometry



Fig. 5.58. Total station (Trimble TTS 500), courtesy Trimble Navigation Ltd., Sunnyvale, CA, U.S.A.



Fig. 5.59. Total station (Geodimeter System 600), courtesy Spectra Precision AB, Danderyd, Sweden

or with a short-range distance meter of high precision.

The error budget of distance measurements contains a constant part that depends on uncertainties in timing or phase measurement and on the zero point stability. The distance dependent part is determined by errors of the modulation frequency and by refraction effects.

The *meteorological parameters* generally are measured only at the instrument and at the target point, and the arithmetic mean is introduced with the refraction reduction. This value may not be representative for the entire distance, and thus a limiting factor for precise distance measurements is set (ILIFFE and DODSON 1987). Measurements conducted under the same atmospheric conditions may be highly correlated, but this correlation can be significantly reduced if observations are carried out under different conditions (HÖPCKE 1965).

Special distance meters have been developed in order to measure shorter base lines with very *high precision* (calibration lines, local geodynamic control). These developments are based either on instrumental refinements and better determination of the refraction effects or on the use of two or three different wavelengths.

The Mekometer ME 5000 uses a He-Ne laser as a light source, with a polarization modulated wavelength of 0.6 m (FROOME 1971, MEIER and LOSER 1986), Fig. 5.60. The modulation frequency is automatically adjusted such that the distance becomes an integer number of wavelengths and is measured with a frequency meter. The Geomensor (COM-RAD, England) uses a Xenon flash tube as light source (SCIERER 1985). Meteorological data are provided by a special sensor unit. Distances of 5 km can be measured with one prism, and a precision of

$$\pm(0.1 \dots 0.2 \text{ mm} + 0.2 \times 10^{-6} \text{ s})$$

may be obtained. However, refraction effects may increase the distance-dependent contribution to $0.5 \times 10^{-6} \text{ s}$ (DODSON and FLEMING 1988).



Fig. 5.60. Distance meter Mekometer ME 5000, courtesy Leica Geosystems AG, Heerbrugg, Switzerland

If the distance is measured with different wavelengths, the effect of *dispersion* can be exploited, cf. [5.1.1]. For light waves, the difference in the distances obtained with "blue" and "red" light particularly depends on the influence of temperature and atmospheric pressure on the index of refraction. If an additional microwave measurement is performed, the effect of humidity is then reflected mainly in the deviation of the microwave results from the light results. From (5.14), (5.15), (5.17), and (5.18), a relation between the geometric length of the path and the differences between the distances obtained with different light waves and a microwave can be established. A resolution of a few 0.01 mm is required at these small differences in order to obtain mm-accuracy for the distance. The terrameter has been developed as a two-wave instrument (He-Cd laser 441.6 nm, He-Ne laser 632.8 nm) to measure distances with a precision of ± 0.1 mm (LANGBEIN et al. 1987). By adding a microwave ($\lambda = 3$ cm) and employing a light modulation frequency of 3 GHz, the relative accuracy of this method could be increased to 10^{-7} and better (HUGGETT and SLATER 1975).

The *refraction corrections* which have to be applied to the observed distances before further processing can be split up into three parts (HÖPCKE 1966). The distance \bar{s}_0 read on the instrument is based on a standard value n_0 for the refractive index calculated from standard temperature and air pressure (5.17). If a more realistic value \bar{n} is available from local meteorological measurements, the relation

$$\bar{s} \bar{n} = \bar{s}_0 n_0 \quad (5.106)$$

provides a first *velocity correction*

$$k_s = \bar{s} (n_0 - \bar{n}). \quad (5.107)$$

As seen from (5.20a), the radius of the light curve differs from the earth's radius ($r \approx 8 R$). Hence, the light passes through atmospheric layers with a greater density and refractive index than estimated by the mean value \bar{n} , calculated from the endpoint data. With (5.10) and the coefficient of refraction $k = 0.13$, we obtain

$$\frac{dn}{dh} = -\frac{k}{R} = -20 \times 10^{-6} / \text{km}, \quad (5.108a)$$

which can be used to derive a second velocity correction

$$k_{\Delta n} = -(k - k^2) \frac{\bar{s}^3}{12R^2}. \quad (5.108b)$$

This correction is less than 1 mm over a distance of 15 km and can be neglected generally.

For three-dimensional computations, the *chord distance* s is required. By assuming a spherical arc with radius r we have

$$s = 2r \sin \frac{\bar{s}}{2r},$$

or after a series expansion

$$s = 2r \left(\frac{\bar{s}}{2r} - \frac{1}{6} \left(\frac{\bar{s}}{2r} \right)^3 + \dots \right).$$

Introducing (5.10) yields the curvature reduction

$$k_r = -k^2 \frac{\bar{s}^3}{24R^2}, \quad (5.109)$$

which is part of the reduction formula (5.6). This reduction is less than 0.1 mm for a distance of 15 km and can be neglected. By adding (5.107) to (5.109), we obtain the total reduction from the observed distance to the chord:

$$s - \bar{s}_0 = \bar{s} (\eta_0 - \bar{\eta}) - \frac{2k - k^2}{24R^2} \bar{s}^3. \quad (5.110)$$

The reduction from the chord distance to the length of the normal section and the geodesics on the ellipsoid will be given in [6.3.2].

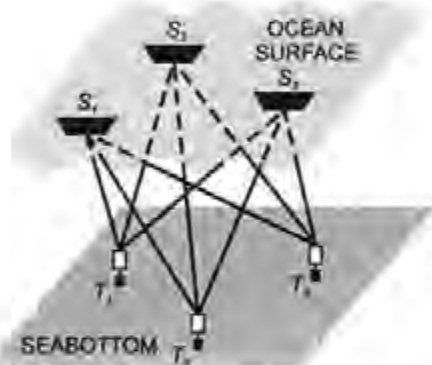


Fig. 5.61. Acoustic positioning on the sea bottom (T = transponder, S = transmitter)

Control points have been established locally on the *ocean floor* mainly for geodynamic investigations (e.g., sea floor spreading at active ridge zones). Control points are usually arranged in arrays of 3 to 4 stations, with station separation of 5 to 10 km. *Acoustic waves* (velocity about 1500 m/s in water) are used exclusively for relative positioning, with acoustic transponders powered by batteries or sources of nuclear energy. Acoustic signals (5 to 20 kHz) are emitted from a ship-borne transducer and sent back by the transponders. The slant range is calculated from the propagation time of the signal traveling forth and back. Spatial trilateration then provides the relative positions (RINNER 1977), Fig. 5.61. With microsecond timing, the accuracy of the acoustic wave method is determined by the sound velocity, which depends on temperature, salinity, and water pressure. cm-accuracy can be achieved over a few km (CHADWELL et al. 1998). The relation to the global reference system is established by GPS-positioning on board of the surface vessel.

5.5.3 Leveling

In *geometric leveling*, differences in height are determined using horizontal lines of sight between points in close proximity to each other. Leveling is conducted with a *leveling instrument* (level) and two vertically posted leveling rods (Fig. 5.62). The leveled height difference Δh between the rods is given by the difference between the backsight (b) and the foresight (f) reading:

$$\delta n = b - f . \quad (5.111)$$

The *leveling instrument* consists primarily of a measuring telescope capable of rotation about the vertical axis. The line of sight is brought into the horizontal either by a coincidence bubble in conjunction with a tilting screw or, for most modern instruments, automatically by a compensator that is comprised mainly of a gravity pendulum (first introduced with the ZEISS Ni2 in 1950). A setting accuracy of $\pm 0.1''$ to $0.4''$ is achieved by both methods. The use of a compensator increases the speed of leveling, but spirit levels offer advantages if high-frequency oscillations (traffic, wind) occur, due to better damping.

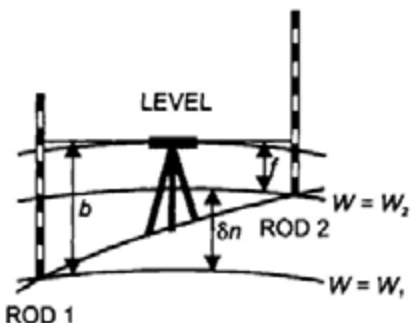


Fig. 5.62. Geometric leveling principle

High-precision levels employ telescopes with an aperture of 40 to 50 mm and a magnification of 30 to 40. Distances between the level and the rods are kept within 30 to 40 m. Setting-up the instrument in the middle of two subsequent rod positions is typical, as it eliminates errors due to non-parallelism of the collimation and the bubble axes as well as symmetric refraction effects. In the *analogue* mode, the leveling rods carry two graduation lines on invar tape, displaced against each other and numbered differently in order to detect reading errors. The line of sight is adjusted to the closest graduation mark by means of a parallel plate mounted in front of the objective's lens. The amount of the displacement is measured by a micrometer (Fig. 5.63).

Digital levels were introduced with the Wild NA 2000 (INGENSAND 1990). They are used in connection with invar staffs that carry a binary code (Fig. 5.64). A code section around the horizontal sight is projected on a CCD sensor in the image plane of the telescope. A subsequent processing of the image by a microprocessor includes electronic scanning (A/D conversion) and correlation with a digital reference signal, whereby the automatically measured distance has to be taken into account (MEIER-HIRMER 1997, RUEGER and BRUNNER 2000).



Fig. 5.63. Bubble level (Wild/ Leica N3), courtesy Leica Geosystems AG, Heerbrugg, Switzerland



Fig. 5.64. Digital level (Zeiss DiNi 12), courtesy Zeiss/Spectra Precision AB, Danderyd, Sweden

In order to transfer heights over larger distances, the individual leveled differences are summed. For one set-up, the non-parallelism of the level surfaces may be neglected (quasi-differential method). The observed difference δn then corresponds to the height difference of the level surfaces passing through the rod sites. Summing the individual differences between two bench marks P_1 and P_2 yields the "raw" leveled height difference

$$\Delta n_{1,2} = \sum_1^2 \delta n . \quad (5.112)$$

At longer distances, the effect of the non-parallelism may reach the cm-order of magnitude and more, cf. [3.2.1]. Hence Δn depends on the path taken and does not provide a unique height in any height system. A unique height determination can be achieved only by considering gravity g , that is by referring to potential differences ΔW . According to (3.52) we have

$$\Delta W_{1,2} = W_2 - W_1 = - \int_1^2 g dn \approx - \sum_1^2 g \delta n . \quad (5.113)$$

Thus potential differences can be determined without any hypothesis from leveling and surface gravity. In order to obtain height differences in any specific height system from the raw leveling results, gravity reductions have to be applied, cf. [6.4.1].

The accuracy of precise leveling depends on many influences. Some of the leveling errors behave in a random manner and propagate with the square root of the number of individual set-ups. Other errors are of systematic type and may propagate with distance in a less favorable way. Hence particular attention must

be afforded to reduce them, by instrumental measures and modeling or by employing dedicated measurement methods.

Important *error sources* include (KUKKAMÄKI 1980):

- Misleveling of the instrument. This random type error is of the order of a few 0.1" and results in an error of a few 0.01 mm for an individual height difference. Systematic effects arise from a residual adjustment error of the bubble or an imperfect operation of the compensator and cause an "obliquity of the horizon". These effects cancel when measuring in two opposite positions of the compensator.
- Magnetic effects on the compensator. These are kept small generally, but a regular control is advisable.
- Rod graduation errors. This includes a "mean" scale error, errors of the individual graduation marks, and effects of thermal expansion. Routine calibrations deliver the corresponding corrections, with a remaining random part less than 5 to 10 μm (SCHLEMMER 1984).
- Rod inclination errors. These errors can be kept sufficiently small by properly adjusting the rod bubble and carefully holding the rod in the vertical position.
- Vertical refraction. This depends mainly on the vertical temperature gradient, cf. [5.1.2]. The irregular part (shimmer) acts as a random error (± 0.01 mm under cloudy skies). Systematic influences occur particularly with measurements made in terrain with steep slopes or those made close to the ground. The effects may reach 0.01 to 0.1 mm per 1 m height difference. They can be modeled in part by a refraction correction, with the vertical temperature gradient as a function of height (KUKKAMÄKI 1938). More refined models are available, which include other meteorological and hydrological data, terrain slope, and orientation with respect to the sun (ANGUS-LEPPAN 1984).
- Vertical movements of the instrument and the rods. These errors depend on the stability of the ground and on the manner in which the instrument is set up; movements of 0.01 to 0.1 mm per station are possible. Movements proportional to time are cancelled by an observation succession b_1, f_1, f_{II}, b_{II} (I, II = scales of the rod). In addition, from the mean of forward and backward leveling runs, those rod movements are eliminated which are proportional to time and which occur while the instrument is brought to the next station.
- Earth tides effects. The tidal effect on the plumb line causes periodic inclinations of the line of sight. The inclinations can be modeled by the horizontal tidal component acting in the azimuth of the leveling line. Starting from (3.119) and taking the elasticity of the earth into account, the tidal reduction for the moon reads

$$\delta_{t(m)} = 0.06 \sin 2\psi_m \cos(\alpha_m - \alpha) s \text{ mm/km} . \quad (5.114)$$

Here, α_m and α are the azimuths of the moon and of the leveling line, and ψ_m the geocentric central angle between the directions to the moon and the computation point. s is the length of the leveling line in km. The same equation is valid for the sun, with an effect of 46% of that for the moon (KUKKAMAKI 1949).

In order to eliminate or reduce systematic errors, precise leveling is always carried out with equal back and foresights ("leveling from the middle") at less

than 50 m distance. Observations should be performed during cloudy weather, preferably in the morning and in the evening hours. Line of sights very close to the ground (0.5 m or less) should be avoided. Leveling is always conducted twice, in opposing directions and possibly under different meteorological conditions. For a 1 km double-run leveling, one can attain a standard deviation of 0.2 to 1.0 mm. Residual systematic effects (especially those due to local vertical movements and refraction) may cause small correlations between the height differences obtained from the forward and backward runs and affect the results of large network adjustments (LUCHT 1972).

The time needed for precise leveling can be significantly reduced by employing a *motorized* procedure, whereby the instrument and the rods are carried in and operated from an automobile. This mode also reduces time dependent errors and partially eliminates asymmetric refraction effects, as the line of sight is more remote from the ground (PESCHEL 1974, BECKER 1987).

For leveling across broad *waterways* and inlets of the *sea*, several methods have been developed:

- In *reciprocal leveling*, approximately horizontal sights to specially designed targets are taken simultaneously with a precise level from both sides of the waterway. For longer series of observations including a change of the instruments, height differences over 1 to 2 km can be determined with a precision of ± 1 to 2 mm (JELSTRUP 1955, KAKKURI 1966).
- *Hydrostatic leveling* is based on the principle of communicating tubes. A hose filled with water (free of air bubbles, uniform temperature) is laid between the shores of the watercourse to be bridged. The water level observed at the vertical ends of the hose belong to the same level surface (GRABOWSKI 1987). The method may be applied for ranges up to 20 km (Fehmarn-Belt/Baltic Sea) and delivers mm-precision (ANDERSEN 1992). In the Netherlands, it is used in an operational mode (WAALEWIJN 1964).
- In *hydrodynamic leveling* (geostrophic leveling), the height is transferred over the waterway utilizing water level records, which have to be reduced for the effects of sea surface topography, cf. [3.4.2]. This implies the development of a hydrodynamic model, which takes water velocity, wind drag, water depth and bottom friction, atmospheric pressure, water density, and gravity and Coriolis force into account. The method has been applied, for instance, for a height transfer over the British channel (70 km) and over the Fehmarn-Belt (CARTWRIGHT and CREASE 1963, WÜBBELMANN 1992) with a precision of about 1 cm.

5.5.4 Tilt and Strain Measurements

Tilt and strain observed on the surface of the earth indicate the response of the earth's crust to external and internal forces such as earth tides, tectonic processes, and seismic and volcanic activities. Tilt and strain are dimensionless quantities and are given in radian or arcsec and extension (positive sign) or compression per distance, respectively.

Over time intervals of years to decades, long-term tilt and strain can be determined from repeated observations of geodetic control networks using satellite and terrestrial techniques, cf. [8.3.3]. Tiltmeters and strainmeters (also called extensometers), on the other hand, have been developed in order to monitor continuously local deformations (MELCHIOR 1983, AGNEW 1986, ZÜRN 1997a).

Short-term (up to one day) tilt and strain is dominated by tidal deformations and is at the order of 10^{-8} to 10^{-7} , which correspond to inclinations of 0.002" to 0.02" and lengths changes of 0.01 to 0.1 $\mu\text{m}/\text{m}$. *Long-term* effects of tectonic origin generally are only at the order of a few $10^{-7}/\text{year}$. Episodic effects related to seismic or volcanic events may reach the same order of magnitude and more over a few hours to a few weeks and months. Consequently, the instrumental sensitivity of tilt and strainmeters should be at least about 10^{-9} to 10^{-10} , and the stability with time should be better than $10^{-7}/\text{year}$.

Tiltmeters measure the inclination of the earth's surface with respect to the local vertical. Two mutually perpendicular sensors are needed in order to completely determine the tilt, which are usually orientated in the NS and EW-directions. Tiltmeters have been designed as horizontal and vertical pendulums, bubble levels, and long water tubes (ZÜRN et al. 1986).

Horizontal pendulums consist of two nearly vertical threads that support an approximately horizontal beam with an attached mass (Zöllner suspension), Fig. 5.65. Because of the small inclination of the rotational axis with respect to the vertical, a tilt of the support (basis about 30 cm) or a plumb line variation cause a strongly amplified angular deflection (astatization), which may be further enlarged optically. Fused quartz (*Verbaandert-Melchior* pendulum) or metallic alloys are used as pendulum material in order to keep thermal effects small. Calibration is performed by controlled tilting of the instrument (VAN RUYMBEKE 1976). Among the *vertical pendulums* is the Askania borehole instrument, which may operate in depths of 20 to 60 m. The pendulum's (length 60 cm) suspension allows it to swing freely, and the deflections are sensed by two three-plate capacitive transducers installed at right angles to each other. The pendulum is calibrated by displacing a small mass over a known distance (FLACH 1976). Short-base *bubble levels* with electric sensors and *water-tube tiltmeters* with lengths of several 100 m have also been used. For the water-tube tiltmeters, water level variations at the endpoints of the tube are measured by capacitive or interferometric methods (KÄÄRIÄINEN 1979, SLATER 1983).

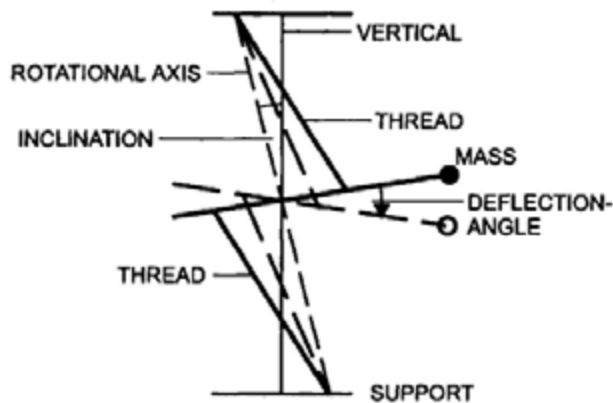


Fig. 5.65. Zöllner horizontal pendulum principle

Strainmeters measure relative displacements of the earth's crust (KING and BILHAM 1973). For a complete determination of the strain tensor, which contains six independent components, a strain meter array should be arranged with orientation in different spatial directions, although in most cases only horizontal strainmeters have been installed.

Short-baseline strainmeters (baseline length 10 to 30 m and more) are represented by *invar wires* and fused *quartz tube* rods. One end is fixed to a rock, and the crustal displacement is measured at the other end by inductive or capacitive transducers (KING and BILHAM 1976). *Laser strainmeters* apply the Michelson interferometer principle. Operated in an evacuated tube, they can measure distances up to 1 km with nm resolution (BERGER and LEVINE 1974, WYATT et al. 1990).

Among the *instrumental errors* of tiltmeters and strainmeters are the uncertainties of the calibration (about 0.1 to 1 %) and the direct effects of temperature and air pressure variations, which are kept small by the selection of the material and appropriate shielding. Long-term drift effects are at the order of 10^{-6} to 10^{-7} /year and to a large part are due to problems inherent with the sensor-rock coupling. Effects induced by *meteorological* and *hydrological* variations (air temperature, air pressure, solar radiation, rainfall, groundwater) pose severe problems in interpreting the results, especially for tiltmeters. These disturbances have pronounced daily and seasonal periods but also happen at other time scales. Modeling of these effects is still in its infancy, but their influence can be reduced by installing the instruments below the earth's surface, in tunnels, mines, natural caves, and boreholes.

Geologic, topographic, and cavity effects may cause large local distortions of the tiltmeter and strainmeter data. This is due to variable rock properties including local fractures, irregular topography, and different cavity reactions to deformation. Local distortion may reach 10 to 15% and more, leading to non-

representative results (HARRISON 1976). Attempts to model these effects have been only partly successful (SATO and HARRISON 1990, WYATT et al. 1990, KOHL and LEVINE 1995). Consequently, in addition to carefully selecting the observation site, preference now is given either to short-base tiltmeters and strainmeters operating in deep boreholes or to long-baseline instruments. In the latter case, local effects are reduced by integrating over a large distance of some 10 to some 100 m.

Tiltmeter and strainmeter results primarily contribute to earth tide research in the short-periodic part and to the detection of anomalous tilt and strain related to coseismic and volcanic activity, cf. [8.3.3].

6 Methods of Evaluation

Geodetic evaluation methods may be separated into positioning and gravity field determination. This separation is possible because positioning only requires an approximate knowledge of the gravity field, and gravity field modeling needs only approximate positions. The linearization of the gravity field is essential in both cases, and it permits a statistical description [6.1]. Nowadays, positioning is based on three-dimensional models [6.2], while classical strategies distinguished between horizontal positioning [6.3] and height determination [6.4]. Gravity field modeling utilizes some basic observables and can be formulated as a boundary-value problem of potential theory [6.5]. Global models are derived mainly from the results of space geodesy [6.6], whereas local gravity field estimation is primarily based on terrestrial data [6.7]. Special methods have been developed for combining positioning and gravity field determination [6.8].

Geodetic evaluation methods are described in textbooks on geodesy, e.g., LEDERSTEGER (1956/1969), HEISKANEN and MORITZ (1967), GROTH (1979), MORITZ (1980), VANÍČEK and KRAKIWSKY (1986), HECK (1995).

6.1 Residual Gravity Field

The actual gravity field can be sufficiently well approximated by the normal gravity field of the level ellipsoid, cf. [4.2.2], which results in linear relations between the observations and the unknown parameters. The fundamental quantity of the residual gravity field is the disturbing potential. It is closely related to the height anomaly and the geoid height [6.1.1]. The residual gravity vector generally is expressed by the gravity anomaly and the deflection of the vertical [6.1.2]. The residual gravity field may be treated by statistical methods, which is of interest in gravity field interpolation and modeling [6.1.3].

6.1.1 Disturbing Potential, Height Anomaly, Geoid Height

Approximation of the actual gravity potential W (3.42) by the normal gravity potential U (4.37) leads to the *disturbing potential* (also anomalous potential) T defined at the point P :

$$T_P = W_P - U_P. \quad (6.1)$$

W and U contain a gravitational and a centrifugal part. As the centrifugal acceleration of the earth is known with high accuracy, cf. [3.1.4], we may

assume that the centrifugal parts of W and U are identical. The disturbing potential then is formed by the difference of the gravitation of the earth and of the level ellipsoid, and thus is a harmonic function outside the earth's masses. Hence, it obeys Laplace's differential equation (3.29)

$$\Delta T = 0, \quad (6.2)$$

where Δ = Laplace operator. T can be expanded into spherical harmonics, in analogy to the corresponding developments for the gravitational potentials (3.89) and (4.45). Expressed in spherical coordinates r, ϑ, λ , the disturbing potential as a spatial function reads, in abbreviated form, see (3.88):

$$T = T(r, \vartheta, \lambda) = \sum_{l=2}^{\infty} \left(\frac{a}{r} \right)^{l+1} T_l(\vartheta, \lambda). \quad (6.3)$$

In its full form the disturbing potential is given by

$$T = \frac{GM}{r} \sum_{l=2}^{\infty} \left(\frac{a}{r} \right)^l \sum_{m=0}^l (\Delta C_{lm} \cos m\lambda + \Delta S_{lm} \sin m\lambda) P_{lm}(\cos \vartheta). \quad (6.4)$$

Comparing (6.3) and (6.4) yields the surface spherical harmonics

$$T_l = \frac{GM}{a} \sum_{m=0}^l (\Delta C_{lm} \cos m\lambda + \Delta S_{lm} \sin m\lambda) P_{lm}(\cos \vartheta). \quad (6.5)$$

Due to the properties of U , only the even zonal harmonic coefficients ΔC_l differ from C_l , while all the other coefficients are identical with the coefficients of the actual gravity field, cf. [4.2.2]. The development of (6.3) and (6.4) starts at $l = 2$ since equality of the masses of the earth and the ellipsoid is assumed, as is coincidence of the center of the earth's masses with the center of the ellipsoid, cf. [3.3.4].

The disturbing potential is closely related to the vertical distance between P and the point Q located on the spheroidal surface $U = U_Q$, cf. [6.5.1]. Q is associated with P by the condition

$$U_Q = W_p, \quad (6.6)$$

cf. [4.2.3], Fig. 6.1. This distance is called *height anomaly* ζ . Geometrically, it is the difference between the ellipsoidal height h and the normal height H^N (3.107), (4.66):

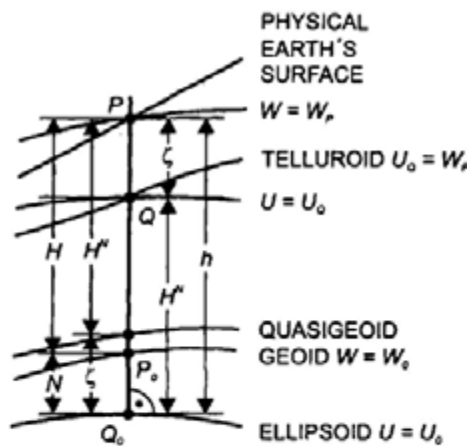


Fig. 6.1. Ellipsoidal, normal and orthometric height

$$\zeta = h - H^N, \quad (6.7)$$

where we have neglected the slight curvature of the normal plumb line. The surface for which (6.6) holds at every point is called the *telluroid* (HIRVONEN 1960). A corresponding relation holds at any point in the exterior space.

The telluroid represents an approximation to the physical surface of the earth. By extending H^N downward from P we obtain the *quasigeoid*, and ζ becomes the distance between the level ellipsoid $U = U_g$ and the quasigeoid, which is often used as a zero height surface, cf. [3.4.3]. ζ is also called quasigeoid height.

If P is located on the geoid, we obtain the *geoid height* N (also called geoid undulation) as the vertical distance between the ellipsoid and the geoid. A geometric definition follows by differencing the ellipsoidal height h and the orthometric height H (3.106):

$$N = h - H, \quad (6.8)$$

where the effect of the plumb line curvature has been neglected.

The difference between the geoid height and the height anomaly is equal to the difference between the normal height and the orthometric height and follows from (3.106) and (3.107):

$$N - \zeta = H^N - H = \frac{\bar{g} - \bar{y}}{\bar{y}} H = \frac{\Delta g_s}{\bar{y}} H. \quad (6.9)$$

The difference depends on the height and thus is zero on the oceans. It also depends on the “mean” gravity anomaly $\bar{g} - \bar{\gamma}$, which corresponds to the Bouger anomaly Δg_B , cf. [6.5.3].

6.1.2 Gravity Disturbance, Gravity Anomaly, Deflection of the Vertical

The gravity vector \mathbf{g} at P can be approximated by the vector of normal gravity $\boldsymbol{\gamma}$, which leads to the *gravity disturbance*

$$\delta \mathbf{g}_P = \mathbf{g}_P - \boldsymbol{\gamma}_P, \quad (6.10)$$

Fig. 6.2. Neglecting the small angle between the directions of \mathbf{g} and $\boldsymbol{\gamma}$ (deflection of the vertical), we obtain the magnitude

$$\delta g_P = g_P - \gamma_P. \quad (6.11)$$

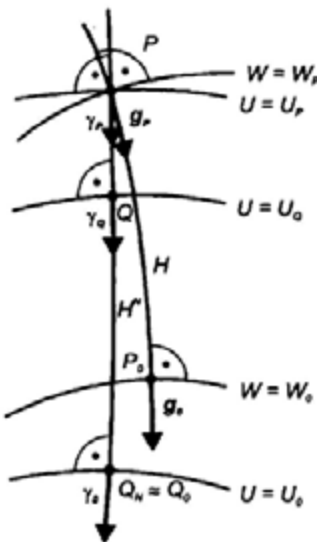


Fig. 6.2. Actual and normal gravity

\mathbf{g} can be measured on the earth's surface and in the exterior space. The calculation of γ_P , on the other hand, presupposes the knowledge of the geodetic coordinates of P , which is not assumed in the classical geodetic boundary value problem, cf. [6.5.1]. Consequently, gravity field modeling generally employs the *gravity anomaly*

$$\Delta \mathbf{g}_P = \mathbf{g}_P - \boldsymbol{\gamma}_Q, \quad (6.12)$$

with the magnitude

$$\Delta g_P = g_P - \gamma_Q . \quad (6.13)$$

Again, Q is related to P by the condition (6.6). γ_Q can be calculated by (4.63), starting from normal gravity γ_0 on the ellipsoid (4.41) and replacing h by H^N (3.107) as determined by leveling, cf. [3.4.3]. This free-air reduction is given by (4.61):

$$\delta g_F^N = -\frac{\partial \gamma}{\partial H^N} H^N . \quad (6.14)$$

The *free-air gravity anomaly*, defined on and outside the earth's surface according to Molodenski, reads

$$\Delta g_F^N = g + \delta g_F^N - \gamma_0 . \quad (6.15)$$

In many applications, $\partial \gamma / \partial H^N$ is approximated by $-3.086 \mu \text{ms}^{-2}/\text{m}$.

The determination of the *geoid* requires that the gravity anomalies are given everywhere on that level surface. In order to apply the Laplace equation, the masses outside the geoid have to be removed. Several types of gravity reductions are available for this purpose. The methods differ by the manner in which the topographical masses are displaced, cf. [6.5.3]. The gravity anomaly on the geoid is defined as the difference between the gravity on the geoid g_0 , and the normal gravity γ_0 on the ellipsoid (Fig. 6.2):

$$\Delta g = g_0 - \gamma_0 . \quad (6.16)$$

The difference (vector quantity) between the directions of the actual plumb line and a reference direction in the normal gravity field is called *deflection of the vertical* (Fig. 6.3). With respect to the reference direction, we distinguish between (JEKELI 1999):

- The deflection of the vertical θ^N defined on the surface or the exterior of the earth, with the direction of the normal plumb line at Q as a reference (*Molodenski definition*). The reference direction practically coincides with the surface normal to $U = U_P$ at P ,
- The deflection of the vertical θ at the earth's surface, referring to the ellipsoidal normal at P (*Helmert definition*). It differs from θ^N only by the slight curvature (effect of a few $0.1''$) of the normal plumb line, cf. [4.2.3]. This definition is preferred generally, as the ellipsoidal normal is provided by the geodetic coordinates,

- The deflection of the vertical θ_0 defined on the geoid (*Pizetti* definition). It is given by the difference between the actual plumb line on the geoid and the ellipsoidal normal. It differs from the previous definitions by the curvature of the actual plumb line and is of importance for the determination of the geoid.

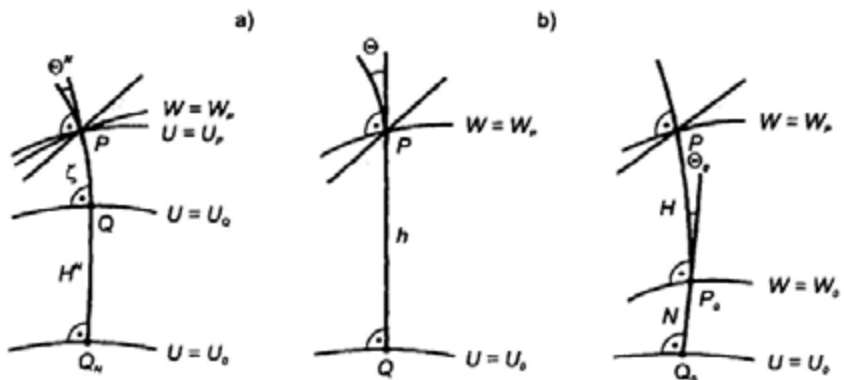


Fig. 6.3. Deflection of the vertical according to a) Molodenski, b) Helmert, c) Pizetti

The deflection of the vertical is expressed either by its magnitude θ and its azimuth α_θ or, more generally, by its components in the north-south and east-west directions. A geometric derivation follows from spherical trigonometry on the unit sphere around the definition point P (Fig. 6.4). Here, we assume that the minor axis of the reference ellipsoid is parallel to the Z -axis of the global reference system and that the ellipsoidal initial meridian is parallel to the X -axis. These conditions are practically fulfilled with modern reference systems and well approximated by classical geodetic systems, cf. [6.2.2]. After parallel displacement, we identify N as the point of intersection of the Z -axis with the unit sphere and Z_a and Z_g as the directions to the astronomic and the geodetic zenith respectively. The deflection of the vertical represents the spherical distance between Z_a and Z_g ; its azimuth is denoted by α_θ . The deflection is decomposed into the meridional component ξ (positive when Z_a is north of Z_g) and the component in the prime vertical η (positive when Z_a is east of Z_g). Along the azimuth α to a target point P_i , we have the vertical deflection component ε .

From spherical trigonometry we get

$$\sin \varphi = \cos \eta \sin(\Phi - \xi), \quad \sin \eta = \cos \varphi \sin(\Lambda - \lambda),$$

and with

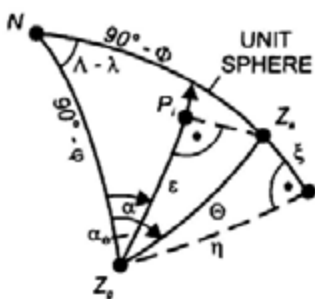


Fig. 6.4. Vertical deflection components

$$\cos \eta \approx 1, \quad \sin \eta \approx \eta, \quad \sin(\Lambda - \lambda) \approx \Lambda - \lambda,$$

the components are given by (linear approximation)

$$\xi = \Phi - \varphi, \quad \eta = (\Lambda - \lambda) \cos \varphi. \quad (6.17)$$

According to Fig. 6.4, the component ε in the azimuth α is composed by two parts:

$$\varepsilon = \xi \cos \alpha + \eta \sin \alpha. \quad (6.18)$$

These relations can also be derived by differencing (3.45) and (4.36), after linearization, cf. [6.2.2].

Equations (6.17) and (6.18) are valid for all definitions of the deflection of the vertical.

The residual gravity field quantities depend on the geodetic earth model used for approximating the gravity field and on its orientation with respect to the earth, cf. [6.2.2]. If referred to a geocentric mean earth ellipsoid, they are designated as absolute quantities, otherwise they are relative only. The r.m.s. scatter of absolute height anomalies and geoid heights is ± 30 m (maximum values about 100 m). The free-air gravity anomalies vary by about $\pm 400 \mu\text{ms}^{-2}$ (maximum values of a few $1000 \mu\text{ms}^{-2}$) and the deflections of the vertical by $\pm 7''$ (maximum $30''$ to $1'$ in the high mountains).

6.1.3 Statistical Description of the Gravity Field, Interpolation

The residual gravity field can be viewed as a realization of a stochastic process and treated by statistical methods (MORITZ 1962, 1970). The gravity anomaly is used as a fundamental gravity-field parameter in this aspect, as gravity data are available with high resolution on the continents and on the oceans.

We assume that the *mean value* of the gravity anomalies Δg over the earth is zero, cf. [6.5.4]:

$$M\{\Delta g\} = \frac{1}{4\pi} \iint_{\sigma} \Delta g \, d\sigma = 0, \quad (6.19)$$

where $M\{\}$ is the mean value operator and σ represents the unit sphere. The surface element can be expressed in spherical coordinates ϑ, λ by

$$d\sigma = \sin \vartheta \, d\vartheta \, d\lambda. \quad (6.20)$$

The statistical behavior of Δg is described by the *covariance function*

$$C(\psi) = \text{cov}(\Delta g, \Delta g', \psi) = M\{\Delta g \cdot \Delta g'\}_{\psi} = \frac{1}{4\pi} \iint_{\sigma} \Delta g \Delta g' \, d\sigma. \quad (6.21)$$

It is calculated as the mean value of all products of gravity anomalies at the points P and P' , having constant spherical distance ψ on the unit sphere. $C(\psi)$ shall only depend on ψ and not depend on the position (homogeneity of the anomalous gravity field) and the azimuth (isotropy), GRAFAREND (1976). $C(\psi)$ describes the mutual correlation of the gravity anomalies, which decreases with increasing distance. For $\psi=0$, we have $\Delta g = \Delta g'$, and the covariance transforms into the *variance*

$$\sigma^2(\Delta g) = M\{\Delta g^2\} = \frac{1}{4\pi} \iint_{\sigma} \Delta g^2 \, d\sigma. \quad (6.22)$$

From the theory of stochastic processes, the statistical properties should be derived from an infinite number of process realizations. As only one realization of the gravity field is available, the hypothesis of ergodicity is necessary, which states that the statistical quantities may also be calculated from mean values over one realization (MORITZ 1980, p.269).

As shown in [6.6.1], Δg as a functional of T can be expanded into spherical harmonics. On the earth's surface ($r=R$) the abbreviated form of this expansion reads

$$\Delta g(\vartheta, \lambda) = \sum_{l=2}^{\infty} \Delta g_l(\vartheta, \lambda), \quad (6.23)$$

with Δg_l = Laplace's surface harmonics, cf. [3.3.2]. Again the terms of degree 0 and 1 are missing. As a consequence of (6.23), $C(\psi)$ also can be expanded into spherical harmonics in the definition range $0 \leq \psi \leq \pi$:

$$C(\psi) = \sum_{l=2}^{\infty} c_l P_l(\cos \psi), \quad (6.24)$$

with $P_l(\cos \psi)$ = Legendre polynomials. Because of isotropy, only zonal terms exist in (6.24). The harmonic coefficients c_l are derived by inversion

$$c_l = \frac{2l+1}{2} \int_0^{\pi} C(\psi) P_l(\cos \psi) \sin \psi d\psi, \quad (6.25)$$

according to potential theory. Equation (6.25) can be solved for a known covariance function by numerical integration. By inserting (6.21) into (6.25), and taking (6.23) into account, we obtain

$$c_l = M\{\Delta g_l^2\} = \sigma_l^2(\Delta g). \quad (6.26)$$

Hence, the coefficients are given by the *anomaly degree variances* defined as mean values over the squares of Δg_l .

Based on a global set of point free-air anomalies, KAULA (1959) first gave an estimate for the covariance function. TSCHERNING and RAPP (1974) derived a covariance function and a degree variance model that are often applied. The model is based on satellite-derived harmonic coefficients for the degrees 2 to 10 and a set of 1° equal area anomalies (approximately quadratic compartments with constant area $110\text{ km} \times 110\text{ km}$). The variance of the point anomalies is

$$\sigma^2(\Delta g) = (424 \mu\text{ms}^{-2})^2$$

and that of the mean anomalies

$$\sigma^2(\overline{\Delta g})_{1^\circ} = (303 \mu\text{ms}^{-2})^2.$$

The correlation of the anomalies approaches zero at a spherical distance of about 30° to 40° (Fig. 6.5). The anomaly degree variance model reads

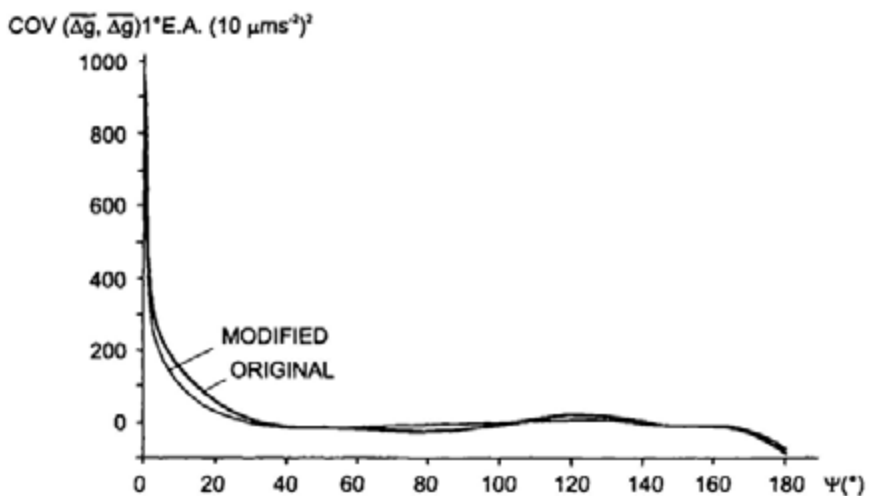


Fig. 6.5. Global covariance function of gravity anomalies, model TSCHERNING and RAPP (1974)

$$\sigma_l^2(\Delta g) = \begin{cases} 0 & \text{for } l = 0, 1 \\ 754 & \text{for } l = 2 \\ \frac{A(l-1)}{(l-2)(l+B)} \sigma_0^{l+2} & \text{for } l \geq 3 \end{cases} \quad (6.27)$$

with $A = 42\,528$ and $B = 24$. $\sigma_0 = (R_B/R)^2 = 0.999\,617$ is the ratio between the radii of the Bjerhammar sphere, cf. [3.3.2], and the earth, Fig. 6.6.

For regional applications, a covariance function may be derived by subtracting the long-wave part of the gravity field, which results in a decrease in the variance and in the correlation length. Local interpolation is even possible by a plane covariance function, e.g., the Gauss function

$$C(\psi) = C_0 \exp(-A^2 \psi^2), \quad (6.28)$$

Fig. 6.7, TORGÉ et al. (1984).

It should be noted that covariance functions have to be positive definite. This condition is fulfilled for (6.24), as all coefficients according to (6.26) are non-negative.

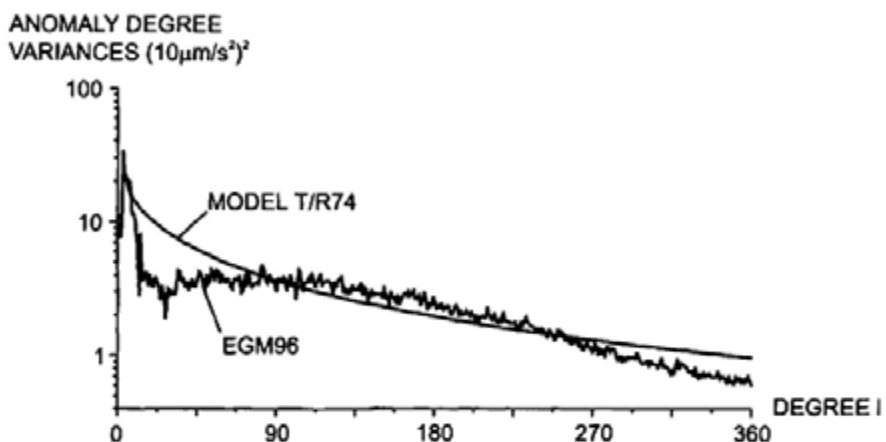


Fig. 6.6. Anomaly degree variances, model TSCHERNING and RAPP (1974) and geopotential model EGM96 (LEMOINE et al. 1998)

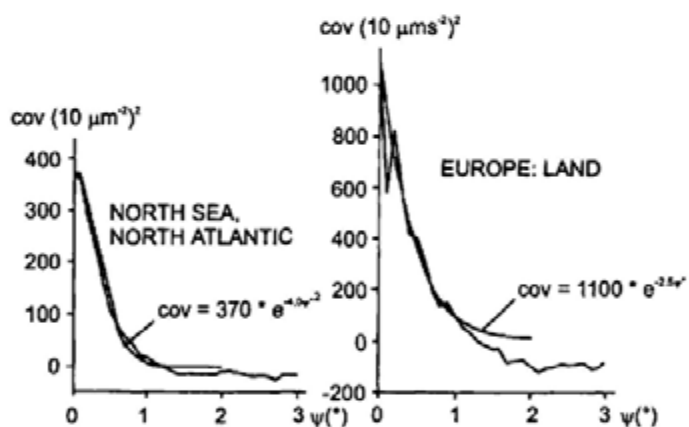


Fig. 6.7. Local covariance functions of trend-removed 6×10^4 mean free air anomalies (TORGE et al. 1984)

An important application of the anomaly covariance function is the *interpolation* of gravity anomalies at points not surveyed. Simple interpolation methods such as the manual construction of isoanomaly maps or the geometric interpolation using adjacent data are not ideal and do not deliver optimum results. *Least squares prediction* utilizes the statistical information inherent in the covariance function and takes the errors of the observations into account.

In the usual *linear* prediction, the gravity anomaly at the point P is estimated by a linear function of the anomalies observed at the points P_i ($i=1,\dots,n$). We assume that, in addition to the covariance function of the anomalies, an *error covariance function* is also available. Such a function can be derived from a priori error and error correlation estimates, although generally only error variances are known. The following covariances, for any distance ψ , can be calculated:

$C_{pi} = M\{\Delta g_p \cdot \Delta g_i\}$: crosscovariance of Δg_p with the observation Δg_i ,

$C_{ii} = M\{\Delta g_i \cdot \Delta g_i\}$: autocovariance of the observations,

$D_{ii} = M\{n_i \cdot n_i\}$: autocovariance of the observational errors (noise n),

and combined into

$$\mathbf{c}_p^T = (C_{p1}, \dots, C_{pi}, \dots, C_{pn}) \\ \mathbf{C} = \begin{pmatrix} C_{11} & \cdots & \cdots & \cdots & C_{1n} \\ \vdots & \ddots & & & \vdots \\ \vdots & & C_{ii} & & \vdots \\ \vdots & & & \ddots & \vdots \\ C_{n1} & \cdots & \cdots & \cdots & C_{nn} \end{pmatrix}, \quad \mathbf{D} = \begin{pmatrix} D_{11} & \cdots & \cdots & \cdots & D_{1n} \\ \vdots & \ddots & & & \vdots \\ \vdots & & D_{ii} & & \vdots \\ \vdots & & & \ddots & \vdots \\ D_{n1} & \cdots & \cdots & \cdots & D_{nn} \end{pmatrix}. \quad (6.29)$$

Now, the prediction error is introduced, being the difference between the true gravity anomaly and the predicted value $\hat{\Delta g}$. The requirement of a minimum prediction error variance, in analogy to least squares adjustment, leads to the result of least squares prediction

$$\hat{\Delta g}_p = \mathbf{C}_p^T \bar{\mathbf{C}}^{-1} \Delta \mathbf{g}, \quad (6.30)$$

where the observed anomalies have been collected in the vector

$$\Delta \mathbf{g}^T = (\Delta g_1, \dots, \Delta g_i, \dots, \Delta g_n). \quad (6.31)$$

Under the assumption that the gravity anomalies and their errors are not correlated, the corresponding matrices \mathbf{C} and \mathbf{D} can be added element by element, leading to

$$\bar{\mathbf{C}} = \mathbf{C} + \mathbf{D}. \quad (6.32)$$

The prediction of point free-air anomalies is successful only for very densely surveyed areas, as these anomalies strongly depend on height. A smoother gravity anomaly field is obtained by averaging over larger surface elements (e.g., $5' \times 5'$, $30' \times 30'$) or reduction of the effect of the topographic masses, where the Bouguer anomalies are especially well suited for interpolation, cf. [6.5.3]. As well known from least-squares adjustment theory, the predicted values of the gravity anomalies are relatively independent from the choice of the covariance function, while the error estimates strongly depend on it. Realistic prediction results can be expected only within the correlation length defined by a covariance of $1/2\sigma^2(\Delta g)$.

6.2 Three-dimensional Positioning

Three-dimensional positioning is generally carried out in a Cartesian coordinate system; the use of ellipsoidal coordinates results in more complicated models [6.2.1]. The Geodetic Datum provides the orientation of a three-dimensional model with respect to the global geocentric system [6.2.2]. Three-dimensional modeling has been investigated by WOLF (1963a, b), GRAFAREN (1978), and TORGE (1980a) among others.

The *observation equations* relate the observed quantities to the unknown station coordinates and other parameters (functional model). By "observations," we mean geometric quantities that result from preprocessing of the original measurements, such as signal travel time, phase and frequency, and readings on graduated circles or staffs. We also assume that instrumental corrections have been applied (e.g., calibration) and that influences from the atmosphere (refraction) and the gravity field (earth tides) have been taken into account. The observations equations are mostly non-linear. They have to be linearized for the subsequent least squares adjustment, which also includes the errors of the observations (stochastic model). The theory of errors and adjustment methods are discussed in textbooks by GRAFAREN and SCHAFFRIN (1993), WOLF (1997), and KOCH (1999).

6.2.1 Observation Equations

The observations used for three-dimensional positioning may be divided into satellite and terrestrial measurements.

Satellite observations include

- Spatial directions, cf. [5.2.4],
- Ranges derived from GPS and laser distance measurements, cf. [5.2.5], [5.2.6],

- Range rates from Doppler measurements, cf. [5.2.4].

We add

- Baseline vectors obtained from VLBI, cf. [5.3.4].

Satellite and VLBI networks generally are adjusted separately. The resulting

- Cartesian coordinates and
- Cartesian coordinate differences

can then be introduced as "observed" parameters into subsequent combined adjustments, together with other satellite networks or with terrestrial data.

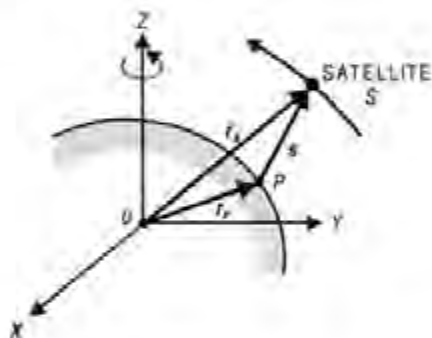


Fig. 6.8. Satellite tracking principle

Satellite observations provide the components of the *topocentric observation vector* \mathbf{s} directed from the station P to the satellite S (Fig. 6.8). The vector \mathbf{s} is related to the geocentric station vector \mathbf{r}_p and the radius vector \mathbf{r}_s of the satellite by

$$\mathbf{r}_p + \mathbf{s} - \mathbf{r}_s = \mathbf{0}, \quad (6.33a)$$

with

$$\mathbf{r}_p = \begin{pmatrix} X_p \\ Y_p \\ Z_p \end{pmatrix}, \quad \mathbf{r}_s = \begin{pmatrix} X \\ Y \\ Z \end{pmatrix}, \quad \mathbf{r}_s - \mathbf{r}_p = \begin{pmatrix} \Delta X_p^s \\ \Delta Y_p^s \\ \Delta Z_p^s \end{pmatrix}. \quad (6.33b)$$

The observation vector is formed by the distance and the spatial direction to the satellite given in the hour angle system:

$$\mathbf{s} = s \begin{pmatrix} \cos h_{Gr} \cos \delta \\ \sin h_{Gr} \cos \delta \\ \sin \delta \end{pmatrix}, \quad (6.34)$$

where δ is the declination and

$$h_{Gr} = \text{GAST} - \alpha \quad (6.35)$$

is the Greenwich hour angle, cf. [2.4.1].

Inserting (6.34) into (6.33) and solving for the components of \mathbf{s} yields the observation equations

$$\left. \begin{aligned} h_{Gr} &= \arctan \frac{\Delta Y_p^s}{\Delta X_p^s} \\ \delta &= \arctan \frac{\Delta Z_p^s}{\sqrt{\Delta X_p^{s2} + \Delta Y_p^{s2}}} \\ s &= \sqrt{\Delta X_p^{s2} + \Delta Y_p^{s2} + \Delta Z_p^{s2}} \end{aligned} \right\}. \quad (6.36)$$

Range rates to the satellite positions (i, j) are given by

$$s_j - s_i = \sqrt{\Delta X_p^{j2} + \Delta Y_p^{j2} + \Delta Z_p^{j2}} - \sqrt{\Delta X_p^{i2} + \Delta Y_p^{i2} + \Delta Z_p^{i2}}, \quad (6.37a)$$

with

$$\Delta X_p^j = X_j - X_p \text{ etc., } \Delta X_p^i = X_i - X_p, \text{ etc.} \quad (6.37b)$$

If the directions to the quasars are known, VLBI observations deliver the *baseline vector* between two terrestrial stations P_1 and P_2 (5.65):

$$\mathbf{b}_{1,2} = \mathbf{r}_2 - \mathbf{r}_1 = \begin{pmatrix} X_2 - X_1 \\ Y_2 - Y_1 \\ Z_2 - Z_1 \end{pmatrix}. \quad (6.38)$$

The relations of the original measurements to the geometrical quantities introduced in (6.36) to (6.38) are given by (5.42) for Doppler counts, (5.43) and (5.45) for GPS, (5.48) for satellite laser ranging, and (5.65) for VLBI.

The observation equations contain a large number of parameters in addition to the station coordinates. Among them are the earth orientation parameters, parameters describing earth tide effects and crustal deformation, as well as the satellite coordinates and the coefficients of the gravitational field and other "disturbing" forces. There are two strategies to handle the large amount of data and unknown parameters.

The first one consists in estimating most of the unknowns in *one* adjustment and to adopt only a few parameters (e.g., the earth orientation parameters) from other sources. This leads to "satellite-only" earth models, which provide a global set of station coordinates and the harmonic coefficients of the gravitational field, cf. [6.6.2].

In positioning, only a limited number of parameters, mainly the station coordinates, are introduced as unknowns, while numerical values for the other parameters are taken from models. Highly accurate orbital parameters are available for GPS and laser satellites and are disseminated by operational services. Parameter corrections taken from models are small and can easily be introduced into the adjustment. Examples include the orbital improvement for short arcs (less than one revolution) through corrections to the six Keplerian elements, the introduction of a local tropospheric "scale factor," and the determination of clock biases.

Several error influences are eliminated or greatly reduced when *simultaneous* measurements are carried out from two or more ground stations to the same satellites (relative positioning). This is due to the high error correlation between neighboring stations. By differencing the measurements, a large part of the errors cancel. Since the absolute orientation is lost with this strategy, the absolute coordinates of at least one station have to be provided.

Exact simultaneous measurements lead to a purely *geometric method* of evaluation. The satellite is regarded as a high-altitude target, and short-arc orbital fitting can improve the results (WOLF 1967, SCHWARZ 1969). Geometric satellite networks were established by stellar triangulation and by trilateration from the 1960's to the 1970's. The global network of the U.S. National Geodetic Survey (1966-1970, 45 stations) was determined by direction measurements with Wild BC4 cameras to the Pageos satellite, cf. [5.2.4]. The scale of this network was derived from long traverses measured with electronic distance meters; an accuracy of ± 4 to 5 m was achieved (SCHMID 1974).

Different methods have been developed for the evaluation of *simultaneously* observed *GPS networks* by forming linear combinations of the observations (WELLS et al. 1987, TEUNISSEN and KLEUSBERG 1998b). As a standard, "*single differences*" $s_1^A - s_2^A$ between the distances measured simultaneously from two receivers P_1, P_2 to the satellite A at epoch t , are formed (Fig. 6.9). Thereby, the satellite clock errors are eliminated and refraction and orbital errors are reduced.

"Double differences" are formed by differencing two single differences taken to different satellites A, B at the same epoch t_i : $(s_i^A - s_i^B) - (s_i^B - s_i^B)$. With double difference, the receiver clock errors vanish and refraction and orbital errors are further reduced. *"Triple differences"* are constructed by differencing two double differences taken at the epochs t_i and t_j . The ambiguity which enters into carrier phase measurements cancels in the observation equation. Due to the loss of information, triple differences allow reduced-accuracy positioning only but are useful for the removal of cycle slips, cf. [5.2.5].

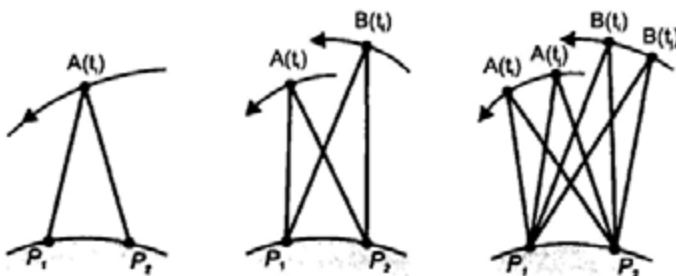


Fig. 6.9. GPS single, double and triple differences

Sophisticated software packages are available for the *adjustment* of satellite networks; for GPS networks we mention WÜBBENA (1989), BEUTLER et al. (1996a), WEBB and ZUMBERGE (1997). The adjustment delivers the Cartesian coordinates or coordinate differences of the ground stations and their full variance-covariance matrix, which has to be taken into account for further processing, e.g., for the combination with terrestrial data. If the orientation of the networks to be combined is not identical, a corresponding transformation (datum shift) has to be included in the adjustment, cf. [6.2.3].

Terrestrial measurements include

- Astronomic azimuths, latitudes, and longitudes, cf. [5.3.2],
- Horizontal directions (azimuths without orientation) and horizontal angles (differences of azimuths), cf. [5.5.1],
- Zenith angles, cf. [5.5.1],
- Distances, cf. [5.5.2],
- Leveled height differences, cf. [5.5.3].

By substituting (2.20) into (2.29) and taking (2.30) into account, we obtain the *observation equations* for azimuths A , zenith angles z , and distances s :

$$\left. \begin{aligned} A &= \arctan \frac{-\sin \Lambda \Delta X + \cos \Lambda \Delta Y}{-\sin \Phi \cos \Lambda \Delta X - \sin \Phi \sin \Lambda \Delta Y + \cos \Phi \Delta Z} \\ z &= \arccos \frac{\cos \Phi \cos \Lambda \Delta X + \cos \Phi \sin \Lambda \Delta Y + \sin \Phi \Delta Z}{(\Delta X^2 + \Delta Y^2 + \Delta Z^2)^{1/2}} \\ s &= (\Delta X^2 + \Delta Y^2 + \Delta Z^2)^{1/2} \end{aligned} \right\}, \quad (6.39)$$

with

$$\Delta X = X_2 - X_1, \quad \Delta Y = Y_2 - Y_1, \quad \Delta Z = Z_2 - Z_1.$$

Astronomic latitude Φ and astronomic longitude Λ enter as orientation parameters in (6.39). They relate the local astronomic to the global geocentric system and are treated as additional unknown parameters. If observed latitudes and longitudes are available, they are introduced as observed parameters in the adjustment.

Least squares adjustment requires linear relations between the observations and the unknowns. Corresponding *differential relations* are derived by numerical or analytical differentiation of (6.39). Analytical expressions for the partial derivatives $\partial A / \partial X$, etc. are found in WOLF (1963b) and HEISKANEN and MORITZ (1967, p.217).

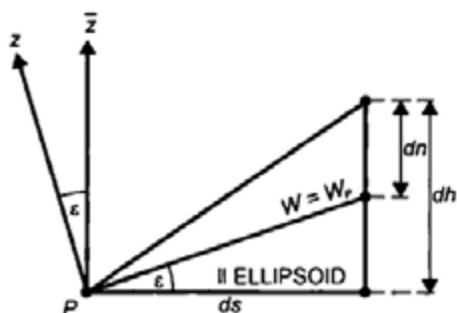


Fig. 6.10. Geometric-astronomic leveling

Geometric leveling can be incorporated into three-dimensional computations after transformation of the leveled height difference $\delta n \approx dn$ (5.111) into the geocentric coordinate system. An ellipsoidal height difference dh is obtained by reducing dn for the effect of the (surface) deflection of the vertical (Fig. 6.10). In the azimuth of the leveling line, the component ϵ (6.18) is effective, which gives

$$dh = dn - \varepsilon ds. \quad (6.40)$$

The negative sign prefixing εds is based on the sign definitions inherent in (6.17) and (6.7) resp. (6.8). A differential relationship between the ellipsoidal height and X, Y, Z is provided by (4.26a) and (4.27). With

$$d\bar{\mathbf{r}}_Q = \mathbf{0},$$

and replacing φ, λ with Φ, Λ , we obtain

$$dh = \bar{\mathbf{n}}^T \cdot d\mathbf{r} = \cos \Phi \cos \Lambda dX + \cos \Phi \sin \Lambda dY + \sin \Phi dZ. \quad (6.41)$$

Again, we have assumed that the axes of the ellipsoidal and the geocentric system are parallel:

$$d\bar{X} = dX, \quad d\bar{Y} = dY, \quad d\bar{Z} = dZ.$$

Integration of (6.40) yields the ellipsoidal height difference

$$\Delta h_{1,2} = h_2 - h_1 = \int_1^2 dn - \int_1^2 \varepsilon ds, \quad (6.42)$$

which can be included as an “observation” in spatial computations: *Geometric-astronomic leveling* (HEITZ 1973). It is noted that both integrals in (6.42) have to be formed over the same path. The differential relation for (6.42) follows from differencing (6.41) for the points P_1 and P_2 :

$$d(\Delta h_{1,2}) = dh_2 - dh_1. \quad (6.43)$$

The first integral in (6.42) can be easily computed by summing the leveled height differences. The evaluation of the second integral poses difficulties, as vertical deflections are generally only available at larger station distances (several 10 km in classical networks). This introduces the problem of the interpolation of deflections of the vertical, cf. [6.7.4]. In flat and hilly areas, with an average distance of the vertical deflection stations of 25 km, an accuracy of ± 0.1 m/100 km can be achieved for the ellipsoidal height differences (BÄUMKER 1984), while “cm” accuracy requires station distances of 5 to 10 km and sophisticated interpolation methods (TORGE 1977).

The three-dimensional concept was already introduced by VILLARCEAU (1868) and BRUNS (1878). Bruns suggested a pointwise determination of the earth's surface by a spatial polyhedron constructed from terrestrial measurements and orientated by astronomical observations. The

feasibility of this concept was demonstrated in some test networks (TORGE and WENZEL 1978, HRADILEK 1984), but large-scale application was prevented due to the uncertainties of trigonometrical height transfer over larger distances and the problems with reducing geometric leveling.

Ellipsoidal coordinates φ, λ , and sometimes h , cf. [4.1.3], are used for many applications in geodesy, cartography, and navigation. They can be easily derived from the Cartesian coordinates by the transformation (4.28). Network adjustments in the φ, λ, h -system are more complicated and restricted to special cases. Nevertheless, differential relations between the observations and the ellipsoidal coordinates are useful for certain problems, e.g., deriving reductions onto the ellipsoid and for two-dimensional ellipsoidal calculations, cf. [6.3.2], [6.3.3].

Equations (4.27) provide the fundamental relations between the φ, λ, h and the X, Y, Z -systems. Differentiation yields

$$\begin{pmatrix} d\bar{X} \\ d\bar{Y} \\ d\bar{Z} \end{pmatrix} = \bar{\mathbf{A}} \begin{pmatrix} (M+h)d\varphi \\ (N+h)\cos\varphi d\lambda \\ dh \end{pmatrix}, \quad (6.44)$$

where $\bar{\mathbf{A}}$ is given by (4.32). Again we assume parallelism of the ellipsoidal and the Cartesian coordinate systems. Equation (6.44) can be immediately used if satellite derived coordinates or coordinate differences are to be adjusted in the φ, λ, h -system. Differential formulas for the terrestrial observations A, z, s are obtained by inserting (6.44) into the differential relations for Cartesian coordinates and reordering (WOLF 1963b, HEISKANEN and MORITZ 1967), cf. [6.3.2].

We finally mention the straightforward transformation from the "natural" coordinates Φ, Λ, H (orthometric height) or H^N (normal height) to ellipsoidal coordinates φ, λ, h , where H and H^N are derived from the gravity potential W by (3.106) resp. (3.107). According to (6.17), the deflection of the vertical (ξ, η) transforms from the plumb line direction to the ellipsoidal normal:

$$\varphi = \Phi - \xi, \quad \lambda = \Lambda - \frac{\eta}{\cos\varphi}. \quad (6.45a)$$

If *normal* geodetic coordinates φ^N, λ^N (4.73) are required, the curvature of the normal plumb line has to be taken into account by $\delta\varphi^N$ (4.74):

$$\varphi^N = \Phi - (\xi + \delta\varphi^N) = \Phi - \xi^N, \quad \lambda^N = \lambda = \Lambda - \frac{\eta}{\cos \varphi}. \quad (6.45b)$$

The relation between h and H resp. H^N is given by, see Fig. 6.2:

$$h = H + N = H^N + \zeta. \quad (6.46)$$

where we have neglected the small (sub mm-order of magnitude) effect of the plumb line curvature. Gravimetric evaluation techniques allow calculation of the deflection of the vertical and the geoid height or the height anomaly from gravity data, cf. [6.7]. Equations (6.45) and (6.46) thus would allow us to establish a geocentric system of ellipsoidal coordinates (HEISKANEN 1951).

Since Φ and Λ can be determined only with an accuracy of $\pm 0.1''$ (corresponding to 3 m in horizontal position) or less, this method is no longer of interest for horizontal positioning. The height transformation (6.46), on the other hand, is most useful, as it permits connection of GPS-derived ellipsoidal heights with heights determined by geometric leveling, cf. [6.4.3].

6.2.2 Geodetic Datum

The *geodetic datum* describes the orientation of any geodetic system with respect to the global geocentric system, cf. [2.5.1]. Nowadays, networks established by satellite methods are tied to the ITRF, cf. [2.5.3], and hence geocentric. Larger deviations occur with classical geodetic networks, which were orientated by astronomical observations, cf. [6.3.3].

In the most general case, a non-geocentric $\bar{X}, \bar{Y}, \bar{Z}$ -system is transformed to the X, Y, Z -system by a *similarity transformation* in space, i.e., by three translations, three rotations, and a change in scale (Fig. 6.11):

$$\mathbf{r} = \mathbf{r}_0 + (1+m)\mathbf{R}(\varepsilon_{\bar{x}}, \varepsilon_{\bar{y}}, \varepsilon_{\bar{z}})\bar{\mathbf{r}}. \quad (6.47)$$

Here, $\mathbf{r}^T = (X, Y, Z)$ and $\bar{\mathbf{r}}^T = (\bar{X}, \bar{Y}, \bar{Z})$ are the position vectors in the two systems, and $\mathbf{r}_0^T = (X_0, Y_0, Z_0)$ contains the coordinates of the origin \bar{O} of the $\bar{X}, \bar{Y}, \bar{Z}$ -system with respect to the geocenter O . We assume that the scale of the $\bar{X}, \bar{Y}, \bar{Z}$ -system differs only slightly from the scale of the global reference frame and that the axes of the two systems are approximately parallel. Consequently, m is a small scale correction, and the rotation matrix is composed of three small Eulerian angles; it takes the form

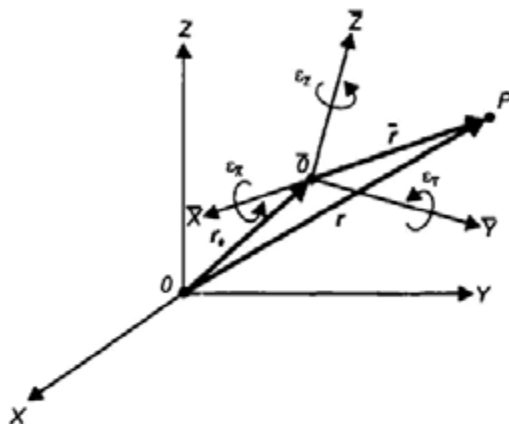


Fig. 6.11. Transformation between 3D-Cartesian coordinate systems

$$\mathbf{R}(\varepsilon_{\bar{x}}, \varepsilon_{\bar{y}}, \varepsilon_{\bar{z}}) = \begin{pmatrix} 1 & \varepsilon_{\bar{z}} & -\varepsilon_{\bar{y}} \\ -\varepsilon_{\bar{z}} & 1 & \varepsilon_{\bar{x}} \\ \varepsilon_{\bar{y}} & -\varepsilon_{\bar{x}} & 1 \end{pmatrix}. \quad (6.48)$$

In order to determine the seven parameters of the transformation (6.47), at least three points with coordinates given in both systems are required.

After converting the Cartesian coordinates into ellipsoidal ones, (6.47) can be expressed in ellipsoidal coordinates φ, λ, h . The datum parameters in that case also have to include the geometric parameters of the ellipsoid, i.e., the semimajor axis a and the flattening f . Of practical interest are the *changes* of the *ellipsoidal coordinates* that result from translation, rotation, change in scale, and change of the parameters of the ellipsoid. We insert (4.27) into (6.47) and take the total differential. As the real position of P does not change, we have $d\mathbf{r} = 0$. Neglecting the linear scale factor and substituting the differentials by (small) differences, a spherical approximation ($M + h = N + h = a, f = 0$) yields (MERRY and VANIČEK 1974, Torge 1980b):

$$\begin{pmatrix} a \delta\varphi \\ a \cos\varphi \delta\lambda \\ \delta h \end{pmatrix} = -\bar{\mathbf{A}}^{-1} \delta\mathbf{r}_0 + \mathbf{C} \begin{pmatrix} \delta\varepsilon_{\bar{x}} \\ \delta\varepsilon_{\bar{y}} \\ \delta\varepsilon_{\bar{z}} \end{pmatrix} + \mathbf{F} \begin{pmatrix} \delta a \\ a \delta f \end{pmatrix}, \quad (6.49a)$$

where $\bar{\mathbf{A}}^{-1}$ is given by (4.34) and

$$\mathbf{C} = a \begin{pmatrix} \sin \lambda & -\cos \lambda & 0 \\ -\sin \varphi \cos \lambda & -\sin \varphi \sin \lambda & \cos \varphi \\ 0 & 0 & 0 \end{pmatrix}, \quad \mathbf{F} = \begin{pmatrix} 0 & \sin 2\varphi \\ 0 & 0 \\ -1 & \sin^2 \varphi \end{pmatrix}. \quad (6.49b)$$

Equation (6.49) can be used for estimating the changes of the coordinates if the changes of the parameters of the geodetic datum are known. All differences are formed in the sense geocentric – non-geocentric, e.g., $\delta a = a(\text{geocentric}) - a(\text{non-geocentric})$. Formulas which take the flattening into account are given by EHLERT (1991), and ABD-ELMOTAAL and EL-TOKHEY (1995).

Classical geodetic networks have been orientated by the ellipsoidal coordinates of an *initial (fundamental) point* P_F and by condition equations for the parallelism of the axes with respect to the geocentric system. If we apply (6.49) at a running point P and at the fundamental point P_F , the translation can be expressed in changes $\delta\varphi_F, \delta\lambda_F, \delta h_F$ of the fundamental point (TORGE 1980b). By differentiating (6.45) and (6.46), and considering that $d\Phi = d\Lambda = dH = 0$, we obtain

$$\delta\xi = -\delta\varphi, \quad \delta\eta = -\cos\varphi \delta\lambda, \quad dN = dh. \quad (6.50)$$

Corresponding equations hold for the “normal” geodetic coordinates, cf. [4.2.3]. Hence, the coordinate changes at any point also can be expressed as *changes of the deflection of the vertical and the geoid height* (or height anomaly), in dependence on the corresponding changes in the fundamental point (VENING-MEINESZ 1950). Spherical approximation yields (HEISKANEN and MORITZ 1967, p.208)

$$\begin{aligned} d\xi &= (\cos\varphi_F \cos\varphi + \sin\varphi_F \sin\varphi \cos(\lambda - \lambda_F)) d\xi_F \\ &\quad - \sin\varphi \sin(\lambda - \lambda_F) d\eta_F \\ &\quad - (\sin\varphi_F \cos\varphi - \cos\varphi_F \sin\varphi \cos(\lambda - \lambda_F)) \\ &\quad \times \left(\frac{dN_F}{a} + \frac{da}{a} + \sin^2 \varphi_F df \right) - 2 \cos\varphi (\sin\varphi - \sin\varphi_F) df \quad (6.51) \\ d\eta &= \sin\varphi_F \sin(\lambda - \lambda_F) d\xi_F + \cos(\lambda - \lambda_F) d\eta_F \\ &\quad + \cos\varphi_F \sin(\lambda - \lambda_F) \left(\frac{dN_F}{a} + \frac{da}{a} + \sin^2 \varphi_F df \right) \end{aligned}$$

$$\begin{aligned}
 dN = & -a(\cos\varphi_F \sin\varphi - \sin\varphi_F \cos\varphi \cos(\lambda - \lambda_F))d\xi_F \\
 & -a\cos\varphi \sin(\lambda - \lambda_F)d\eta_F \\
 & +(\sin\varphi_F \sin\varphi + \cos\varphi_F \cos\varphi \cos(\lambda - \lambda_F)) .(6.51 \text{ continued}) \\
 & \times(dN_F + da + a\sin^2\varphi_F df) - da \\
 & +(\sin^2\varphi - 2\sin\varphi_F \sin\varphi)a df
 \end{aligned}$$

These relations have played a role in the optimum fitting of horizontal control networks to the geoid, cf. [7.1.2].

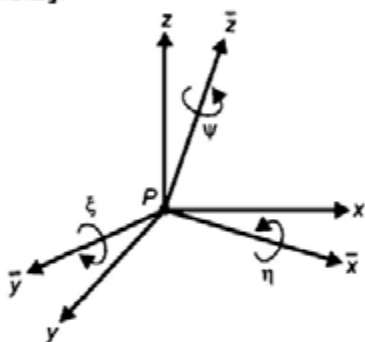


Fig. 6.12. Rotations between the local ellipsoidal and the local astronomic system

We now investigate how the (approximate) *parallelism of the axes* of classical geodetic networks with respect to the geocentric system has been achieved.

We describe the deviation between the local astronomic x,y,z -system (2.20) and the local ellipsoidal \bar{x},\bar{y},\bar{z} -system (4.29) by three Eulerian angles, after reflection of the y and \bar{y} -axes (producing right-handed systems), Fig. 6.12:

$$\mathbf{x} = \mathbf{R}(\xi, \eta, \psi) \bar{\mathbf{x}}, \quad (6.52a)$$

with the rotation matrix

$$\mathbf{R}(\xi, \eta, \psi) = \begin{pmatrix} 1 & \psi & -\xi \\ -\psi & 1 & \eta \\ \xi & -\eta & 1 \end{pmatrix}. \quad (6.52b)$$

The Eulerian angles are the components of the *deflection of the vertical*, cf. [6.1.2], in the meridian (ξ), in the prime vertical (η), and in the horizontal plane

(ψ). If the axes of the global X, Y, Z and $\bar{X}, \bar{Y}, \bar{Z}$ -systems are not parallel, the following relations hold, according to (2.26), (4.20), (6.47), and (6.52):

$$\Delta \mathbf{x} = \mathbf{Ax} = \mathbf{AR}(\xi, \eta, \psi) \bar{\mathbf{x}} = \mathbf{R}(\varepsilon_{\bar{x}}, \varepsilon_{\bar{y}}, \varepsilon_{\bar{z}}) \bar{\mathbf{A}} \bar{\mathbf{x}} \quad (6.53)$$

or

$$\mathbf{R}(\varepsilon_{\bar{x}}, \varepsilon_{\bar{y}}, \varepsilon_{\bar{z}}) \bar{\mathbf{A}} = \mathbf{AR}(\xi, \eta, \psi). \quad (6.54)$$

After inserting $\bar{\mathbf{A}}$ (4.32) and \mathbf{A} (2.28), the evaluation of (6.54) results in nine equations. Three of the nine equations are independent from each other (orthogonality relations). After Taylor expansion of the trigonometrical functions (Φ, Λ) inherent in (2.28) at the point (φ, λ) , we obtain the components (linear approximation) of the *deflection of the vertical* if the axes of the global systems are not parallel:

$$\left. \begin{aligned} \xi &= \Phi - \varphi + \sin \lambda \varepsilon_{\bar{x}} - \cos \lambda \varepsilon_{\bar{y}} \\ \eta &= (\Lambda - \lambda) \cos \varphi - \sin \varphi (\cos \lambda \varepsilon_{\bar{x}} + \sin \lambda \varepsilon_{\bar{y}}) + \cos \varphi \varepsilon_{\bar{z}} \\ \psi &= (\Lambda - \lambda) \sin \varphi + \cos \varphi (\cos \lambda \varepsilon_{\bar{x}} + \sin \lambda \varepsilon_{\bar{y}}) + \sin \varphi \varepsilon_{\bar{z}} \end{aligned} \right\}, \quad (6.55)$$

where the equations for η and ψ depend on each other.

We also generalize the equations for the *azimuth* and the *zenith angle* given in the local astronomic and the local ellipsoidal system. From (6.53) we have

$$\mathbf{Ax} = \mathbf{R}(\varepsilon_{\bar{x}}, \varepsilon_{\bar{y}}, \varepsilon_{\bar{z}}) \bar{\mathbf{A}} \bar{\mathbf{x}}.$$

Inserting (2.20) and (4.29) yields, after linearization of the trigonometrical functions of A, z at α, ζ :

$$\begin{aligned} A - \alpha &= (\Lambda - \lambda) \sin \varphi + ((\Phi - \varphi) \sin \alpha - \cos \varphi (\Lambda - \lambda) \cos \alpha) \cot \zeta \\ &\quad + \cos \varphi (\cos \lambda \varepsilon_{\bar{x}} + \sin \lambda \varepsilon_{\bar{y}}) + \sin \varphi \varepsilon_{\bar{z}} \end{aligned}, \quad (6.56a)$$

$$\begin{aligned} z - \zeta &= -((\Phi - \varphi) \cos \alpha + \cos \varphi (\Lambda - \lambda) \sin \alpha) \\ &\quad - (\cos \alpha \sin \lambda - \sin \alpha \sin \varphi \cos \lambda) \varepsilon_{\bar{x}} \\ &\quad + (\cos \alpha \cos \lambda + \sin \alpha \sin \varphi \sin \lambda) \varepsilon_{\bar{y}} \\ &\quad - \cos \varphi \sin \alpha \varepsilon_{\bar{z}} \end{aligned} \quad (6.56b)$$

With the global rotations

$$\varepsilon_{\bar{x}} = \varepsilon_{\bar{y}} = \varepsilon_{\bar{z}} = 0,$$

we obtain condition equations for the parallelism of the axes, which was presupposed when introducing the deflections of the vertical, cf. [6.1.2]:

$$\left. \begin{array}{l} \xi = \Phi - \varphi, \quad \eta = (\Lambda - \lambda) \cos \varphi \\ \psi = (\Lambda - \lambda) \sin \varphi \end{array} \right\}. \quad (6.57)$$

After inserting (6.57) into (6.56), the condition equations for the azimuth and the zenith angle read

$$A - \alpha = \eta \tan \varphi + (\xi \sin \alpha - \eta \cos \alpha) \cot \zeta \quad (6.58)$$

and

$$z - \zeta = -(\xi \cos \alpha + \eta \sin \alpha). \quad (6.59)$$

Equation (6.58) is known as *Laplace's equation of orientation*, while (6.59) furnishes the component ε of the deflection of the vertical in the azimuth α (6.18), VANIČEK and WELLS (1974).

A geometric interpretation of the condition equations (6.58) and (6.59) reveals that they prevent rotations about the vertical and the horizontal axis of a theodolite. In addition, a rotation about the line of sight must be forestalled to guarantee the parallelism of the global and the ellipsoidal system. This can be accomplished if, in addition to (6.58) and (6.59), another zenith angle equation is introduced at the fundamental point, possibly with an azimuth which differs by 90° . Due to the problems of vertical refraction, classical networks generally employed only the Laplace equation for orientation. A three-dimensional network then would need at least three *Laplace azimuths* at points well distributed over the network.

Two-dimensional positioning utilizes (6.58) for the reduction of observed azimuths and horizontal directions onto the ellipsoid, cf. [6.3.2], and (6.59) enters into trigonometric height determination, cf. [6.4.2].

6.3 Horizontal Positioning

In classical geodetic networks, horizontal positioning has been separated from height determination. This is due to the fact that ellipsoidal height differences

derived from geometric leveling or zenith angles are affected by greater uncertainties, which enter through the reductions of the gravity field and vertical refraction, but especially because users require heights defined in the gravity field.

With the ellipsoid as a reference surface, two-dimensional positioning requires ellipsoidal trigonometry [6.3.1] and reductions of the observed positional quantities onto the ellipsoid [6.3.2]. Ellipsoidal "observation" equations allow the calculation of coordinates, after proper orientation [6.3.3]. Ellipsoidal geodesy is found in textbooks such as GROSSMANN (1976), BOMFORD (1980), and HECK (1995).

6.3.1 Ellipsoidal Trigonometry

In order to carry out computations on the ellipsoidal surface, points on the ellipsoid are connected by surface curves. The arc of the normal section and the geodesic are employed primarily.

The *normal section* is defined by the curve of intersection of the vertical plane with the ellipsoid. Azimuths and distances, after being reduced to the ellipsoid, refer to normal sections. Since the surface normals of two points on the ellipsoid are in general skewed to each other, the reciprocal normal sections from P_1 to P_2 and from P_2 to P_1 do not coincide (Fig. 6.13). The differences in azimuth (less than $0.1''$ for $S = 100$ km) and in distance (less than 1 μm for $S = 100$ km) are small and can be taken into account easily (BOWRING 1971).

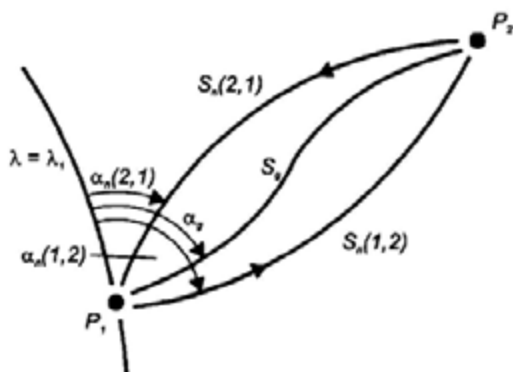


Fig. 6.13. Normal sections and geodesic

Normally, because of its favorable properties, the *geodesic* is used for ellipsoidal calculations. It is uniquely defined as the shortest connection between two points and is generally bounded by the two normal sections. This

definition is equal to the condition that the geodetic curvature (curvature of the normal projection of a surface curve onto the tangential plane) equals zero.

As known from differential geometry, the geodetic curvature k_g is represented by the triple scalar product

$$k_g = (\mathbf{r}' \times \mathbf{r}'') \cdot \mathbf{n}. \quad (6.60)$$

Here, $\mathbf{r}' = d\mathbf{r}/dS$ is the tangent vector and $\mathbf{r}'' = d^2\mathbf{r}/dS^2$ is the curvature vector. Also, S = arc length of the geodesic, and \mathbf{n} designates the normal vector to the surface. With $k_g = 0$, we obtain a second-order vectorial *differential equation* for the geodesic:

$$(\mathbf{r}' \times \mathbf{r}'') \cdot \mathbf{n} = 0; \quad (6.61)$$

the local projection of the geodesic onto the ellipsoid is a straight line. We introduce the φ, λ -system of ellipsoidal coordinates (Fig. 6.14) and express the geodesic by $\lambda = \lambda(\varphi)$. Corresponding evaluation of (6.61) yields the *scalar* differential equations

$$\left. \begin{aligned} p^2 \frac{d^2\lambda}{d\varphi^2} + 2p \frac{dp}{d\varphi} \frac{d\lambda}{d\varphi} &= 0 \\ M \frac{dM}{d\varphi} - p \frac{dp}{d\varphi} \left(\frac{d\lambda}{d\varphi} \right)^2 &= 0 \end{aligned} \right\}, \quad (6.62)$$

with $p = N \cos \varphi$ = radius of the circle of latitude (4.6) and the principal radii of curvature M and N (4.13), (4.15). From Fig. 6.14, we take the relations

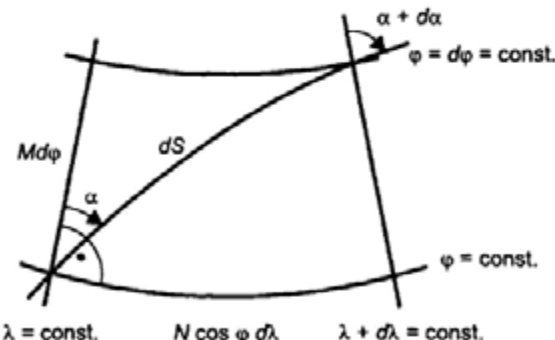


Fig. 6.14. Ellipsoidal (geodetic) surface coordinates

$$\frac{d\varphi}{dS} = \frac{\cos\alpha}{M}, \quad \frac{d\lambda}{dS} = \frac{\sin\alpha}{N \cos\varphi}, \quad (6.63)$$

which are valid for any surface curve. We form $d\lambda/d\varphi$ and the second derivative and insert them into (6.62). Integration yields *Clairaut's equation*

$$N \cos\varphi \sin\alpha = \text{const.} \quad (6.64)$$

The constant corresponds to the radius of the parallel circle at which the geodesic has a 90° azimuth. By differentiation with respect to S , and taking (6.63) into account, (6.64) is transformed into

$$\frac{d\alpha}{dS} = \frac{\sin\alpha \tan\varphi}{N}. \quad (6.65)$$

Equations (6.63) and (6.64) resp. (6.65) form a system of *first-order* differential equations for the geodesic. The solution of this system leads to elliptic integrals which cannot be solved elementarily, cf. [6.3.3].

Two-dimensional positioning on the ellipsoid implies the solution of *ellipsoidal triangles*, bounded by geodesics. As the curvature of surface curves changes according to (4.18), the solution of a triangle not only requires three geometric elements (angles, distances) but also the orientation parameters latitude and azimuth.

At point distances less than 100 km (classical terrestrial networks) the ellipsoid may be approximated by the Gaussian osculating sphere (4.23), with a latitude calculated as an arithmetic mean of the latitudes of the triangle vertices. Closed *spherical formulas* then can be used for the solution of triangles (HECK 1995, p.366), e.g., the spherical law of sines

$$\frac{\sin\alpha}{\sin\beta} = \frac{\sin(a/R)}{\sin(b/R)}, \quad (6.66)$$

with the spherical angles α, β and sides a, b , and R = radius of the Gaussian sphere. Errors due to the spherical approximation remain less than $0.002''$ for the angles and less than 1 mm for the distances. We finally mention the *spherical excess* which plays a role in spherical trigonometry. It is defined as the surplus over 180° of the angle sum of a spherical triangle. The excess is proportional to the area F of the triangle:

$$\varepsilon = \frac{F}{R^2} . \quad (6.67)$$

For an equilateral triangle with $S = 50$ km, the excess amounts to $5.48''$.

6.3.2 Reductions to the Ellipsoid

In order to carry out a transfer of ellipsoidal coordinates on the ellipsoid, observed azimuths and distances have to be reduced to the ellipsoidal quantities α and S , which refer to the geodesic.

The reduction of the *astronomic azimuth A* is composed of three parts. Laplace's equation (6.58) takes the effect of the *deflection of the vertical* into account. The corresponding reduction to the normal section reads

$$\alpha - A = -(\eta \tan \varphi + (\xi \sin \alpha - \eta \cos \alpha) \cot \zeta). \quad (6.68)$$

The first term in (6.68) is the azimuthal component of the deflection of the vertical. It does not depend on the azimuth and corresponds to a twist in the observed directions; horizontal angles are not affected. The second term can be viewed as an "error" in setting up the theodolite, by orientating it along the plumb line direction instead of the ellipsoidal normal. While the first term reaches the order of magnitude of the vertical deflections and more, a strong reduction takes place in the second term due to $\cot \zeta$. Hence, this direction dependent term is of the order of a few $0.1''$ in flat areas only but may reach some arcsec in the mountains.

If the target point is not situated on the ellipsoid but at a height h_2 , a further reduction has to be applied. Namely, the vertical plane formed by the ellipsoidal normal at P_1 and the target point P_2 , in general, does not contain the ellipsoidal

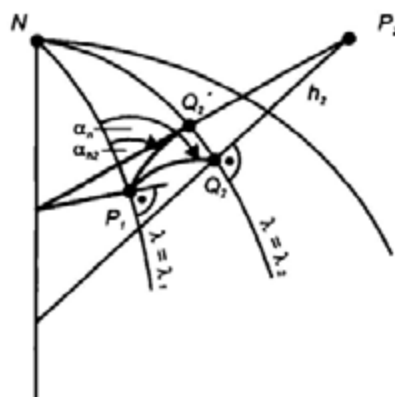


Fig. 6.15. Skew-normal reduction of the azimuth

normal through P_2 (Fig. 6.15). Therefore, the ensuing normal section does not pass through the footpoint Q_2 , but through Q'_2 , which requires a reduction by the angle $Q'_2 P Q_2$. This *skew-normal* reduction can be derived from the partial derivative $\partial A / \partial h_2$, formed for the adjustment in the φ, λ, h -system, cf. [6.2.1]; it reads

$$\alpha_n - \alpha_{h_2} = \frac{e^2}{2b} \cos^2 \varphi \sin 2\alpha h_2, \quad (6.69)$$

where e is the first eccentricity and b the semiminor axis of the ellipsoid, cf. [4.1.1]. For $\varphi = 0^\circ$ and $\alpha = 45^\circ$, the reduction attains only $0.11''$ at $h_2 = 1000$ m.

Finally, the azimuth has to be reduced from the *normal section* to the *geodesic*:

$$\alpha_g - \alpha_n = -\frac{e^2}{12a^2} \cos^2 \varphi \sin 2\alpha S^2. \quad (6.70)$$

At $\varphi = 0^\circ$ and $\alpha = 45$, this reduction reaches only $0.028''$ for $S = 100$ km.

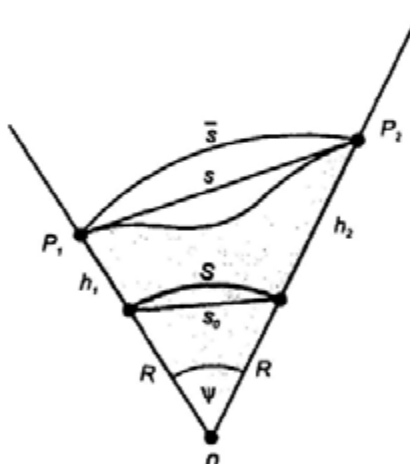


Fig. 6.16. Reduction of the spatial distance on the ellipsoid

The reduction of the chord *distance* s to the ellipsoid is a purely geometric problem, as distances do not depend on the gravity field. We assume that the effects of atmospheric refraction have been reduced beforehand, cf. [5.5.2]. From Fig. 6.16 we read

$$s^2 = (R + h_1)^2 + (R + h_2)^2 - 2(R + h_1)(R + h_2)\cos\psi$$

$$s_0 = 2R\sin\frac{\psi}{2}, \quad S = R\psi$$

which gives closed formulas for the reduction to the normal section

$$s_0 = \sqrt{\frac{s^2 - (h_2 - h_1)^2}{(1+h_1/R)/(1+h_2/R)}}, \quad S = 2R\arcsin\frac{s_0}{2R}, \quad (6.71a)$$

where R is taken from Euler's formula (4.18). After series expansion, the different contributions to the reduction become apparent:

$$S - s = -\frac{h_1 + h_2}{2R}s - \frac{(h_2 - h_1)^2}{2s} + \frac{s_0^3}{24R^2}. \quad (6.71b)$$

The first term in (6.71b) corresponds to a reduction from the mean height to the ellipsoid. It reaches the meter-order of magnitude in the mountains at distances of several km. The second term takes the inclination of the distance into account. It generally remains below the meter-order of magnitude in the lowland but may attain large values in the high mountains. The magnitude of these reduction terms does not allow substitution of the ellipsoidal heights by orthometric or normal heights, otherwise relative errors of 10^{-5} have to be expected. The last term in (6.71b) provides the transition from the ellipsoidal chord to the normal section and reaches the cm-order only at larger distances.

The reduction from the *normal section* to the *geodesic* is given by

$$S_g - S_n = -\frac{e^4}{360a^4}\cos^4\varphi\sin^22\alpha S^5. \quad (6.72)$$

The magnitude reaches the meter-order only at distances of several 1000 km and can be neglected in classical network computations.

6.3.3 Computations on the Ellipsoid

The importance of ellipsoidal calculations has decreased, since the results of three-dimensional positioning in Cartesian coordinates can easily be transformed into ellipsoidal coordinates, see (4.28). Azimuths and distances derived from Cartesian coordinates, see (6.39), can be reduced to the ellipsoid according to [6.3.2]. Nevertheless, computations on the ellipsoid are still of significance in navigation, and they have been the basis for the calculation of classical horizontal control networks, which are still in use today.

The *geodetic datum* of two-dimensional systems has been established by the deflection of the vertical and the geoid height at a fundamental point, cf. [6.2.2], and the parameters of the reference ellipsoid. Equation (6.57) then allows transformation of observed astronomical latitude and longitude into the corresponding ellipsoidal quantities, and (6.46) provides the height relation between the geoid and the ellipsoid. Having reduced the horizontal directions and the distances onto the ellipsoid, only one rotation about the ellipsoidal normal in the fundamental point is possible. This rotation is fixed by applying the Laplace equation on the astronomic azimuth observed at the fundamental point. Equations (6.57) and (6.58) thus provide the parallelism of the axes of the ellipsoidal system with respect to the global geocentric system.

The accuracy of the parallelism of axes depends on the accuracy of the astronomical observations entering into (6.57) and (6.58), and hence is about one to two arcsec or better. The origin of the classical systems may deviate by some 100 m from the geocenter. This is due to the fact that one arcsec in astronomical positioning corresponds to 30 m in horizontal position, but is especially due to the use of only *relative* deflections of the vertical and geoid heights, cf. [7.1.2].

Having fixed the ellipsoidal coordinates and one geodetic azimuth at the fundamental point, ellipsoidal coordinate transfer can be carried out with the ellipsoidal "observations" referring to the geodesic. Here, it is assumed that the ellipsoidal network is errorless; for adjustment strategies see [7.1.2].

We distinguish between

- The *direct problem*, i.e., to compute the ellipsoidal coordinates φ_2, λ_2 of the point P_2 , as well as the azimuth α_2 , given the coordinates φ_1, λ_1 of point P_1 , the azimuth α_1 , and the distance S ,
- The *inverse problem*, i.e., to compute the azimuths α_1, α_2 and the distance S , given the coordinates φ_1, λ_1 and φ_2, λ_2 of P_1 and P_2 .

The direct and the inverse problem correspond to the solution of the ellipsoidal polar triangle P_1NP_2 (Fig. 6.17), EHLERT (1993). With the geodesic introduced as a surface curve connecting P_1 and P_2 , elliptic integrals appear in the solutions, cf. [6.3.1], hence no closed solutions are available.

Numerous solutions of the direct and the inverse problem have been developed. They are based either on series expansions or on numerical integration (KNEISSL 1958/1959, SCHNÄDELBACH 1974).

A Taylor series expansion of latitude, longitude, and azimuth as a function of the arc length was given early on by *Legendre* (1806):

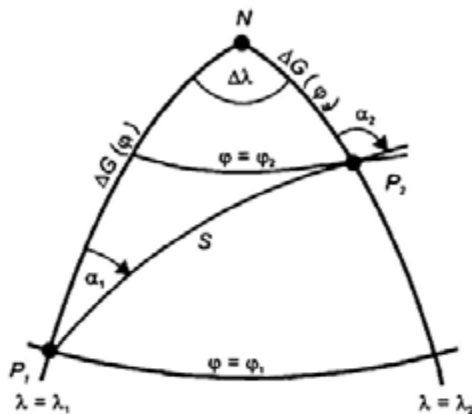


Fig. 6.17. Ellipsoidal polar triangle

$$\begin{aligned}\varphi_2 - \varphi_1 &= \left(\frac{d\varphi}{dS} \right)_1 S + \frac{1}{2} \left(\frac{d^2\varphi}{dS^2} \right)_1 S^2 + \dots \\ \lambda_2 - \lambda_1 &= \left(\frac{d\lambda}{dS} \right)_1 S + \frac{1}{2} \left(\frac{d^2\lambda}{dS^2} \right)_1 S^2 + \dots \\ \alpha_2 - \alpha_1 &= \left(\frac{d\alpha}{dS} \right)_1 S + \frac{1}{2} \left(\frac{d^2\alpha}{dS^2} \right)_1 S^2 + \dots\end{aligned}\quad (6.73)$$

where the first-order derivatives are provided by (6.63) and (6.65). The higher-order derivatives are calculated according to

$$\frac{d^2\varphi}{dS^2} = \frac{\partial}{\partial\varphi} \left(\frac{d\varphi}{dS} \right) \frac{d\varphi}{dS} + \frac{\partial}{\partial\alpha} \left(\frac{d\varphi}{dS} \right) \frac{d\alpha}{dS}, \quad (6.74)$$

where the equation of the geodesic enters through $d\alpha/dS$.

Since the Legendre series are expanded with respect to S , they converge slowly. An expansion to the fifth (φ, λ) resp. fourth-order (α) is necessary at mid-latitudes in order to provide an accuracy of $\pm 0.0001''$ and $\pm 0.001''$ resp., at distances of 100 km. Developments up to the tenth-order are available (KRACK 1982), and modifications of (6.73) improve the convergence and allow an efficient solution for lengths of several 100 km and more.

Series expansions suitable for very long geodesics have been developed by *Bessel* (1826) and improved by *Helmut* (1880). For this method, the ellipsoidal polar triangle is projected onto a concentric sphere with radius a (Fig. 6.18). The latitude φ is transformed to the reduced latitude β (4.10). Due to Clairaut's equation (6.64), which now reads

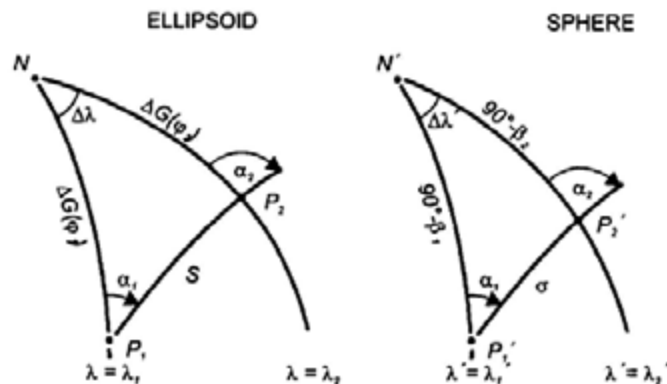


Fig. 6.18. Transfer of ellipsoidal coordinates: Bessel-Helmert solution

$$\cos \beta \sin \alpha = \text{const.},$$

the ellipsoidal azimuths are preserved if the azimuth α_i is transferred to the sphere. The relation between the ellipsoidal distance S and the spherical distance σ , as well as those between the ellipsoidal and the spherical longitude differences $\Delta\lambda$ and $\Delta\lambda'$, are given by differential formulas which correspond to (6.63):

$$\frac{d\beta}{d\sigma} = \cos \alpha, \quad \frac{d\lambda'}{d\sigma} = \frac{\sin \alpha}{\cos \beta}. \quad (6.75)$$

By combination with (6.63), the following relations are obtained:

$$dS = a\sqrt{1-e^2 \cos^2 \beta} d\sigma, \quad d\lambda = \sqrt{1-e^2 \cos^2 \beta} d\lambda'. \quad (6.76)$$

The elliptic integrals resulting from (6.76) are solved either by expanding the square roots in series and subsequent integration term by term or by numerical methods. As the series expansions are controlled by the (small) numerical eccentricity, they converge rapidly. After projection onto the sphere, the coordinate transfer is carried out by formulas of spherical trigonometry, and the results are then transformed back to the ellipsoid by inverse relations. Computations around the globe are possible with mm-accuracy (VINCENTY 1975, KLOTZ 1993).

Numerical methods are based either on a polynomial approximation of the integrals and subsequent integration (methods of Newton, Gauss, Simpson and others), SCHMIDT (1999), or an numerical integration. In the latter case, the length of the geodesic is subdivided into small increments, which are calculated using the differential formulas (6.63) and (6.64), Fig. 6.19. Clairaut's equation serves for keeping the increments on the direction of the geodesic. Summing the

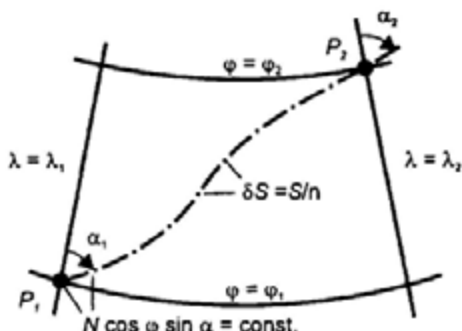


Fig. 6.19. Transfer of ellipsoidal coordinates: numerical solution

line elements provides a first approximation. By iteration with smaller increments and comparison of the results, a given error limit can be obtained. With increments of 100 m length, sub-cm accuracy can be achieved with geodesics of 10 000 km length (DORRER 1966, KIVIOJA 1971).

Inversion of the direct-problem solutions provides formulas for the *inverse problem* and is available for all methods. The adjustment of ellipsoidal networks would require *differential relations* $d\alpha/d\varphi$, $d\alpha/d\lambda$ and $dS/d\varphi$, $dS/d\lambda$. These relations can be derived from the corresponding differentials of a three-dimensional model reduced to the ellipsoid or by differentiating the solutions of the inverse problem (KNEISSL 1958, p.615, WOLF 1963b).

6.4 Height Determination

Precise height determination is based on the relative methods of geometric leveling, triangulation using zenith angles, and GPS heighting. Geometric leveling after applying small reductions provides heights defined in the gravity field [6.4.1]. Zenith angles deliver ellipsoidal heights if the influence of the gravity field is taken into account [6.4.2]. GPS heighting directly results in ellipsoidal heights, which have to be reduced to gravity field related quantities [6.4.3].

6.4.1 Heights from Geometric Leveling

The raw results of geometric leveling $\delta n \approx dn$ are transformed into potential differences by taking surface gravity g along the leveling line into account (5.113). If connected to the zero height surface (geoid, quasigeoid) geopotential numbers (3.104) are obtained:

$$C = W_0 - W_p = \int_0^P g \, dn . \quad (6.77)$$

In principle, the evaluation of (6.77) requires a *gravity* value at each leveling point, i.e., at distances of 100 m or less for precise leveling. This requirement can be diminished if we postulate the same relative accuracy for the influence of leveling and gravity on the geopotential differences:

$$\frac{dg}{g} = \frac{d(\Delta n)}{\Delta n} . \quad (6.78)$$

Assuming a leveling accuracy of 0.1 mm, gravity would only be needed with an accuracy of $\pm 100 \text{ } \mu\text{ms}^{-2}$ for $\Delta n = 10 \text{ m}$, and $\pm 10 \text{ } \mu\text{ms}^{-2}$ for $\Delta n = 100 \text{ m}$. Consequently, gravity values can be interpolated from gravity measurements carried out at station distances of 5 to 20 km in flat areas, and at 1 to 2 km in the mountains. Preferably, gravity stations should be established at sites where the gravity changes depart from linearity (variations in slope or direction of the leveling line, gravity anomalies). An average gravity value taken over a larger distance then can be used for transforming the leveled height difference into potential units.

Precise leveling in fundamental networks is carried out in closed loops, cf. [7.2]. The calculation of heights is performed by adjusting *potential differences*, with the condition, cf. [3.2.3],:

$$\oint dW = 0 . \quad (6.79)$$

Subsequent transformation yields metric heights, cf. [3.4.3].

An alternative approach, used classically, is to first convert the raw leveling results (with $\oint dn \neq 0$) into differences of the respective height system and then adjust *height differences*.

Dynamic height differences are obtained by differencing (3.105):

$$\Delta H_{1,2}^{\text{dyn}} = H_2^{\text{dyn}} - H_1^{\text{dyn}} = \Delta n_{1,2} + E_{1,2}^{\text{dyn}} , \quad (6.80a)$$

with the dynamic height reduction

$$E_{1,2}^{\text{dyn}} = \int_1^2 \frac{g - \gamma_0^{45}}{\gamma_0^{45}} dn. \quad (6.80\text{b})$$

For *orthometric heights*, we expand (3.106) by dynamic heights:

$$\Delta H_{1,2} = H_2 - H_1 = \Delta H_{1,2}^{\text{dyn}} + (H_2 - H_2^{\text{dyn}}) - (H_1 - H_1^{\text{dyn}}).$$

This leads to

$$\Delta H_{1,2} = \Delta n_{1,2} + E_{1,2}, \quad (6.81\text{a})$$

with the *orthometric height reduction*

$$E_{1,2} = \int_1^2 \frac{g - \gamma_0^{45}}{\gamma_0^{45}} dn + \frac{\bar{g}_1 - \gamma_0^{45}}{\gamma_0^{45}} H_1 - \frac{\bar{g}_2 - \gamma_0^{45}}{\gamma_0^{45}} H_2. \quad (6.81\text{b})$$

An analogue equation is valid for the transformation of leveled height differences into *normal height* differences, where \bar{g} is replaced by $\bar{\gamma}$ and H by H^N (3.107). The *normal height reduction* reads:

$$E_{1,2}^N = \int_1^2 \frac{g - \gamma_0^{45}}{\gamma_0^{45}} dn + \frac{\bar{\gamma}_1 - \gamma_0^{45}}{\gamma_0^{45}} H_1^N - \frac{\bar{\gamma}_2 - \gamma_0^{45}}{\gamma_0^{45}} H_2^N. \quad (6.81\text{c})$$

The dynamic height reduction only depends on the path. It attains values between a few mm (flat terrain) and some cm to dm (mountains). Hence, it has to be taken into account even in local surveys if the vertical reference system is based on dynamic heights. The orthometric and the normal height reduction include the dynamic reduction, and, in addition, contain two terms with the mean gravity values at the end points of the leveling line. The different effects substantially cancel each other, with the consequence that these reductions are below one mm in flat areas and only reach a few cm in the mountains.

Mean normal gravity $\bar{\gamma}$ can be calculated by (4.67) with the spherical approximation

$$\bar{\gamma} = \gamma_0 \left(1 - \frac{H^N}{R} \right). \quad (6.82)$$

Mean gravity \bar{g} , on the other hand, requires the knowledge of g along the plumb line between the geoid and the earth's surface. At any point P' with height H' , we have

$$g' = g - \int_{H'}^H \frac{\partial g}{\partial H} dH, \quad (6.83a)$$

where g is the surface gravity at P . The actual vertical gravity gradient is given by (3.71), where we may introduce (4.60) for the free-air part and 2670 kg/m^3 as a mean crustal density; this yields

$$g' = g + 0.848 \times 10^{-6} (H - H') \text{ ms}^{-2}. \quad (6.83b)$$

After inserting into (3.106) and integration between $H' = 0$ and $H' = H/2$, we obtain

$$\bar{g} = g + 0.424 \times 10^{-6} H \text{ ms}^{-2}. \quad (6.84)$$

Orthometric heights based on this estimate are also called *Helmert-heights*.

As shown in [6.5.3], the second term on the right side of (6.84) can be interpreted as a reduction of the surface gravity to actual gravity at $H/2$, with the Bouguer plate as a model of the topography. The effect of model errors remains small in flat terrain, but improved models that take actual topography and density into account are needed in the mountains (SUNKEL 1988).

6.4.2 Trigonometrical Heights

Zenith angles can be used for a trigonometrical height transfer if refraction effects have been reduced sufficiently, cf. [5.5.1], Fig. 6.20. The ellipsoidal zenith angle is obtained from the observed quantity z' by

$$\zeta = z' + \delta + \varepsilon = z + \varepsilon, \quad (6.85)$$

where δ is the angle of refraction (5.11) and ε the vertical deflection component in the azimuth of the line of sight (6.18). Using spherical trigonometry, the *ellipsoidal height difference* is given by (KNEISSL 1956, p.358):

$$\Delta h_{1,2} = h_2 - h_1 = S \left(1 + \frac{h_m}{R} \right) \cot \zeta_1 + \frac{S^2}{2R \sin^2 \zeta_1}. \quad (6.86)$$

S is the length of the ellipsoidal normal section, R the radius of curvature (4.18), and $h_m = (h_1 + h_2)/2$.

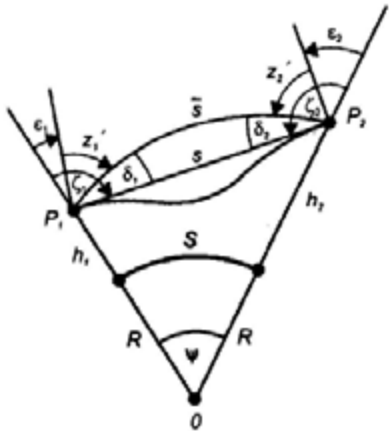


Fig. 6.20. Trigonometrical height transfer

The use of *reciprocal* zenith angles offers significant advantages. With the central angle ψ

$$\psi = \frac{S}{R} = \zeta_1 + \zeta_2 - \pi \quad (6.87)$$

taken from Fig. 6.20, we apply the law of tangents on the triangle P_1OP_2 . In connection with (6.85), the height difference is obtained:

$$\Delta h_{1,2} = S \left(1 + \frac{h_m}{R} + \frac{S^2}{12R^2} \right) \tan \frac{1}{2} ((z'_2 + \delta_2 + \epsilon_2) - (z'_1 + \delta_1 + \epsilon_1)). \quad (6.88)$$

Here, only differences in δ and ϵ appear. Symmetric refraction conditions may be expected with *simultaneous* observations, cf. [5.5.1], thus refraction effects will mostly cancel with the use of simultaneous reciprocal-zenith-angle measurements (KUNTZ and SCHMITT 1995). They also offer a possibility to determine the *coefficient of refraction*. Combining (5.11), (6.85), and (6.87), and neglecting the deflections of the vertical, yields

$$k = 1 - \frac{R}{S} (z'_1 + z'_2 - \pi). \quad (6.89)$$

An average value of $k = 0.13 \pm 0.04$ was obtained by Gauss for the arc measurements in the kingdom of Hannover. This value was confirmed by other surveys for lines of sight with a large ground clearance. Close to the ground, k may vary between -1 and $+1$. Network adjustment models may be extended by introducing individual refraction coefficients for each station or for

each line (HRADILEK 1984), and observed meteorological parameters may also contribute to the determination of actual values for k , cf. [5.1.2], [5.5.1]. In spite of these refinements, refraction irregularities strongly limit the application of trigonometrical heighting. A cm-order of accuracy can be obtained over distances of a few km, but errors of the dm-order of magnitude have to be expected with larger distances.

Trigonometric leveling significantly diminishes the errors of a trigonometrical height transfer, by reducing the lines of sight to 100 to 300 m (RÜEGER and BRUNNER 1982). Height differences are determined by measuring zenith angles and slope distances with a total station, cf. [5.5.2]. Either simultaneous reciprocal-observations are carried out using two reflector-equipped total stations or the method of leveling "from the middle" is applied, in analogy to geometric leveling, cf. [5.5.3]. Refraction effects are substantially reduced using this strategy. The reductions are largely due to the short distances and the fact that the lines of sight run approximately parallel to the earth's surface. In this way, a favorable error propagation over larger distances is obtained (accuracies of ± 1 to 2 mm per km). The efficiency of the method can be increased by motorized procedures (BECKER 1987). By using short lines of sight, trigonometric leveling resembles the procedure employed in geometric leveling. Hence, the results represent a reasonable approximation to leveled height differences.

Trigonometric height determination with long lines played an important role in the establishment of classical horizontal networks by triangulation, as it simultaneously provided heights for reduction onto the ellipsoid and for the construction of topographical maps. Today, it is restricted to special applications, e.g., to the height determination of inaccessible sites. Trigonometric leveling, on the other hand, has been employed successfully for surveying vertical control networks of large extension (WHALEN 1985).

6.4.3 Heights from GPS

The Global Positioning System (GPS), cf. [5.2.5], provides global Cartesian coordinates and, more accurately, coordinate differences, which can easily be transformed to ellipsoidal coordinates, see (4.28), DODSON (1995). Ellipsoidal height differences can be achieved with cm-accuracy over distances up to some 100 km or more, applying differential methods and long (e.g., 24 hours) observation times. For short distances, even sub-cm accuracy can be obtained (GÖRRES and CAMPBELL 1998). Consequently, GPS heighting may support or substitute time-consuming geometric leveling, at least for distances larger than about 10 km. This strategy requires that the reduction of ellipsoidal heights to normal or orthometric heights can be performed with a similar accuracy (TORGE 1990). According to (6.46), quasigeoid or geoid differences provide the necessary reductions:

$$\Delta H^N = \Delta h - \Delta \zeta, \quad \Delta H = \Delta h - \Delta N. \quad (6.90)$$

Today, global quasigeoid or geoid models have relative accuracies of a few decimeters, and regional models may reach the cm to decimeter accuracy, cf. [6.6], [6.7]. The use of these models for the reduction of GPS heights presupposes that the model describes the same surface as used as zero height surface for the height system, cf. [3.4.3]. This demand can be fulfilled by fitting the model to quasigeoid or geoid heights at control points where GPS and leveled heights are available. The fitting also reduces long and medium-wave model errors.

Following the method of least squares collocation, cf. [6.8.2], the discrepancies found at the control points can be modeled as follows (MILBERT 1995, DENKER et al. 2000):

$$h_{\text{gps}} - H^N - \zeta_{\text{mod}} = t + s + n, \quad (6.91a)$$

where t describes a trend component, s is a stochastic signal part, and n represents the random noise of all types of observations involved (GPS, leveling, geopotential model). A simple trend function may consist of a three-parameter datum shift according to (6.41):

$$t = \cos \varphi \cos \lambda \Delta X + \cos \varphi \sin \lambda \Delta Y + \sin \varphi \Delta Z. \quad (6.91b)$$

Equivalently, the function may describe a change in the ellipsoidal coordinates of some initial point, which corresponds to a vertical shift and tilts in the NS and the EW-direction. The signal part is derived from an empirical covariance function of the de-trended residuals and modeled e.g., by an exponential function, cf. [6.1.3].

Using trend reduction only, the r.m.s. discrepancies between regional and local quasigeoid models and GPS/leveling control points have been reduced to the dm-order of magnitude over a few 1000 km and to a few centimeter over several 100 km (TORGE et al. 1989). By including also a signal part, cm-accuracy may be obtained over distances up to 1000 km, which corresponds to the accuracy of classical leveling networks (DENKER 1998).

For *local* (several 10 km) applications, gravity field related heights may be estimated by purely mathematical interpolation between GPS/leveling control points, employing, e.g., low-order surface polynomials or splines (ILLNER and JÄGER 1995). If a dense net of control points is available, and if the gravity field is sufficiently smooth, cm-accuracy can be achieved (COLLIER and CROFT 1997). The accuracy strongly decreases in rough topography, and a topographic reduction is necessary then, cf. [6.5.3].

With the further improvement of quasigeoid/geoid models, "GPS leveling" will become even more important.

6.5 Fundamentals of Gravity Field Modeling

Gravity field modeling is part of the geodetic boundary-value problem [6.5.1]. Topography plays an important role in the solution of this problem [6.5.2]. Gravity reductions serve for reducing observed gravity field data onto the geoid and also provide different kind of gravity anomalies for field interpolation and geophysical interpretation [6.5.3]. While the orientation of the gravimetrically derived geoid is uniquely defined, the scale has to be determined by distance measurements [6.5.4].

6.5.1 The Geodetic Boundary-Value Problem

The geodetic boundary-value problem comprises the determination of the surface of the earth and of its external gravity field from observations on or close to the earth's surface (SANSÒ and RUMMEL 1997). The surface to be determined is either the geoid (*Stokes'* problem) or the physical surface of the earth (*Molodenski's* problem), SANSÒ (1995).

Based on Green's third identity and the generalized Laplace equation (3.49), the problem may be formulated by a non-linear integral equation of the second kind in the gravity potential W (MOLODENSKI 1958, MOLODENSKI et al. 1962):

$$\begin{aligned} -2\pi W + \iint_S \left(W \frac{\partial}{\partial n_s} \left(\frac{1}{l} \right) - \frac{1}{l} \frac{\partial W}{\partial n_s} \right) dS \\ + 2\pi \omega^2 (X^2 + Y^2) + 2\omega^2 \iiint_v \frac{dv}{l} = 0 \end{aligned} \quad (6.92)$$

Here n_s is the outer surface normal to the surface S , v is the volume of the earth and ω its rotational velocity, and l denotes the distance between the source point and the point of calculation. If W were known on S , then the geometry of the surface would remain as the only unknown quantity. After the determination of S , an upward continuation of W would deliver the external gravity field.

The problem is *linearized* by approximating the earth's surface by the telluroid (physical surface) or the ellipsoid (geoid) and by approximating the actual potential W by the normal potential U , cf. [6.1.1]. As the centrifugal part is well-known, (6.92) then transforms into an *integral equation* for T

$$-2\pi T + \iint_{\Sigma} \left(T \frac{\partial}{\partial n_{\Sigma}} \left(\frac{1}{l} \right) - \frac{1}{l} \frac{\partial T}{\partial n_{\Sigma}} \right) d\Sigma = 0. \quad (6.93)$$

The integration is performed over the known telluroid Σ . As the surface normal n_{Σ} deviates from the direction of the plumb line, $\partial T / \partial n_{\Sigma}$ not only depends on the gravity anomaly but also on the deflection of the vertical and the slope of the terrain, cf. [6.7.2]. If applied to the geoid as a boundary surface, this dependence reduces to the gravity anomaly.

Instead of the integral equation (6.93), the geodetic boundary-value problem can be formulated by Laplace's differential equation (6.2):

$$\Delta T = 0. \quad (6.94)$$

The residual gravity field parameters observed on the earth's surface, or reduced to the geoid, then enter into boundary conditions for the solution of (6.94). The primary "observables" are the height anomalies resp. the geoid heights, and the gravity anomalies. Deflections of the vertical and gravity gradient components play a role only in local calculations.

A Taylor development of U in the telluroid point Q gives

$$U_p = U_Q + \left(\frac{\partial U}{\partial \bar{n}} \right)_Q \zeta_p + \dots, \quad (6.95a)$$

with \bar{n} = normal to $U = U_Q$ and with normal gravity

$$\gamma_Q = - \left(\frac{\partial U}{\partial \bar{n}} \right)_Q. \quad (6.95b)$$

Inserting (6.95) into (6.1) yields the *height anomaly*

$$\zeta_p = \frac{T_p - (W_p - U_Q)}{\gamma_Q}. \quad (6.96a)$$

With the condition (6.6), we obtain

$$\zeta_p = \frac{T_p}{\gamma_Q}. \quad (6.96b)$$

Equation (6.96) is called *Brun's theorem*. If applied to the geoid it delivers the *geoid height*

$$N = \frac{T - (W_0 - U_0)}{\gamma_0}. \quad (6.97a)$$

Under the condition $U_0 = W_0$, it reads

$$N = \frac{T}{\gamma_0}. \quad (6.97b)$$

T now refers to the geoid, and γ_0 is normal gravity on the ellipsoid (4.41).

The *deflection of the vertical* is the horizontal derivative of ζ resp. N (Fig. 6.21). Taking (6.96) and (6.97) into account, the components in the direction of the meridian and the prime vertical, cf. [6.1.2], are given by

$$\xi = -\frac{1}{\gamma(M+h)} \frac{\partial T}{\partial \varphi}, \quad \eta = -\frac{1}{\gamma(N+h)\cos\varphi} \frac{\partial T}{\partial \lambda}, \quad (6.98a)$$

where the ellipsoidal arc elements are provided by (4.20). The negative sign follows from the sign conventions for the quasigeoid (geoid) and the vertical deflection, see (6.40).

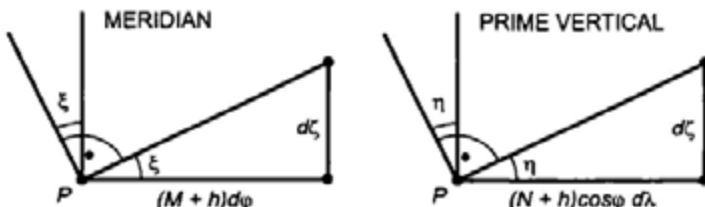


Fig. 6.21. Deflection of the vertical components and height anomaly

In spherical approximation we obtain

$$\xi = -\frac{1}{\gamma r} \frac{\partial T}{\partial \varphi}, \quad \eta = -\frac{1}{\gamma r \cos\varphi} \frac{\partial T}{\partial \lambda}. \quad (6.98b)$$

The *gravity disturbance* (6.11) is related to T by

$$\delta g_p = g_p - \gamma_p = -\left(\frac{\partial W}{\partial n}\right)_p - \left(-\frac{\partial U}{\partial \bar{n}}\right)_p = -\left(\frac{\partial T}{\partial n}\right)_p, \quad (6.99)$$

where again we have neglected the deflection of the vertical. We develop γ_p at the telluroid point Q :

$$\gamma_p = \gamma_Q + \left(\frac{\partial \gamma}{\partial \bar{n}}\right)_Q \xi_p + \dots \quad (6.100)$$

Inserting into (6.99) and taking (6.96b) into account yields the *gravity anomaly*

$$\Delta g_p = g_p - \gamma_Q = -\left(\frac{\partial T}{\partial n}\right)_p + \frac{1}{\gamma_Q} \left(\frac{\partial \gamma}{\partial \bar{n}}\right)_Q T_p. \quad (6.101a)$$

With the spherical approximation, cf. [4.2.2],

$$\frac{\partial \gamma}{\partial \bar{n}} = \frac{\partial \gamma}{\partial r} = -2 \frac{\gamma}{r},$$

we obtain

$$\Delta g = -\frac{\partial T}{\partial r} - \frac{2}{r} T. \quad (6.101b)$$

Equations (6.97), (6.98), and (6.101) represent boundary conditions for the solution of the Laplace equation. Because of the importance of (6.101), this first-order partial differential equation in T is known as the fundamental equation of physical geodesy.

High-precision gravity-field modeling (e.g., geoid determination with cm-accuracy) requires some refinements in the formulation and solution of the geodetic boundary-value problem (MORITZ 1974, HECK 1991). This includes the transition to an ellipsoidal approximation by developing the potential in ellipsoidal harmonics or by applying ellipsoidal corrections to the spherical approximation (JEKELI 1988b, WANG 1999). The mass of the atmosphere has to be taken into account by a corresponding reduction, cf. [4.3], and the topography has to be smoothed by a terrain correction, cf. [6.5.3].

The geodetic boundary-value problem resembles the third boundary-value problem of potential theory, namely to determine a harmonic function given a linear combination of the function and its normal derivative on a bounding surface. It differs from the classical problem, as the bounding surface is supposed to be unknown: free boundary-value problem. At the physical surface of the

earth, gravity data do not provide potential derivatives along the surface normal but rather refer to the plumb line: free and oblique boundary-value problem (GRAFAREN and NIEMEIER 1971). The horizontal components of the surface position vector cannot be determined with sufficient accuracy from gravimetric data, cf. [6.2.1], consequently the geometric part of the problem generally is restricted to the determination of heights: scalar free gravimetric boundary-value problem (HECK 1997).

With the rapid progress in satellite positioning, the geometry of the earth's surface can be assumed to be known with increasing accuracy; the only remaining unknown then is the external gravity potential. Hence, a fixed boundary-value problem can be formulated, which employs gravity disturbances as boundary values (KOCH and POPE 1972, BJERHAMMAR and SVENSSON 1983). This corresponds to the second (*Neumann*) boundary-value problem of potential theory, which is to determine a harmonic function from its derivative on the bounding surface. Finally, a mixed altimetric-gravimetric boundary-value problem may be set up, taking into account that altimetric geoid heights and gravity anomalies are the main data sets available on a global scale (SANSØ 1981, MARTINEC 1998).

6.5.2 Gravitation of Topography

The short wavelength part of the gravitational field is dominated by the effect of the topographical masses. By reducing this effect, the gravity field is smoothed significantly, which simplifies gravity field interpolation and transformation. For the determination of the geoid, the topography has to be removed in order to establish the geoid as a boundary surface (FORSGÅRD and TSCHERNING 1997).

The effect of the topographic masses on gravity field parameters is calculated by the law of gravitation. The evaluation of (3.10) and corresponding integrals for other parameters poses problems, as topography is rather irregular in geometry (heights) and, to a lesser extent, also in density. Therefore, the topographic masses are subdivided into elementary bodies for which closed solutions of the mass integrals exist. Rectangular *prisms* of constant density are especially appropriate, as the heights of the topography nowadays are provided in gridded form by digital elevation models. Vertical *cylindrical columns* with constant density and height have been used extensively in the past.

In a system of three-dimensional Cartesian coordinates, the gravitational potential of the topography is expressed by

$$V_{\text{top}} = G\rho \iiint_v \frac{dv}{l} = G\rho \int_{x_1}^{x_2} \int_{y_1}^{y_2} \int_{z_1}^{z_2} \frac{1}{l} dx dy dz, \quad (6.102)$$

with $l = \sqrt{x^2 + y^2 + z^2}$. The topographic effects on the deflection of the vertical, the gravity disturbance, and the gravity anomaly follow from differentiation, according to (6.98), (6.99), and (6.101). The integration over a *rectangular*

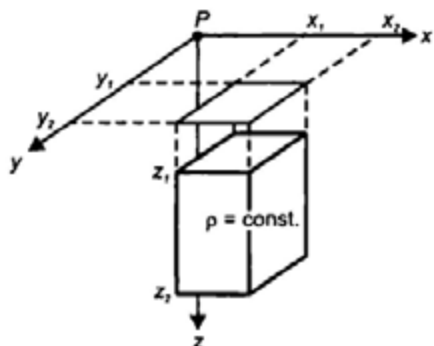


Fig. 6.22. Gravitation of topography: rectangular prism method

prism delivers closed formulas for the potential and its derivatives (FORSBERG 1984, NAGY et al. 2000). As an example, for a point located at the origin of the x,y,z -system, the *vertical component of the gravitation* is given by (NAGY 1966), Fig. 6.22:

$$b_z = G\rho \left| \left| x \ln(y+l) + y \ln(x+l) - z \arctan \frac{xy}{zl} \right|_{x_1}^{x_2} \right|_{y_1}^{y_2} \left|_{z_1}^{z_2} \right|. \quad (6.103)$$

The total effect of topography results from the sum over the gravitation of the individual elementary bodies:

$$\delta g_{\text{top}} = \sum b_z. \quad (6.104).$$

For heights given in a regular grid, Fast Fourier Transform (FFT) techniques provide a powerful tool for the efficient calculation of topographic effects (FORSBERG 1985, SIDERIS 1985, SCHWARZ et al. 1990).

Digital elevation models (DEM), also called digital terrain models, are available on global and regional scale. They are primarily based on digitized topographic and bathymetric maps. Space techniques contribute increasingly to the improvement of DEM's. Satellite radar altimetry serves for the height determination of the Greenland and Antarctica ice sheets and provides bathymetric information, due to the correlation between the ocean surface and the ocean bottom (SMITH and SANDWELL 1994). Space and airborne interferometric synthetic aperture radar (INSAR) has become an efficient method for the development of high resolution DEM's (ZEBKER and GOLDSTEIN 1986, NIELSEN et al. 1998).

Among the global DEM's are the ETOPO5 ($5' \times 5'$ gridded land and seafloor elevations) and the GLOBE (global land one-kilometer base elevation) models provided by the NOAA National Geophysical Data Center. GLOBE is given in a $30'' \times 30''$ grid; the accuracy depends on the data

quality and varies between ± 20 m and a few 100 m (HASTINGS et al. 2000). The NASA/NIMA Shuttle Radar Topography Mission (SRTM, February 2000) collected a global (between $\pm 60^\circ$ latitude) INSAR data set, which will be used for a DEM with 30 m mean resolution, accurate to ± 10 to 20 m. Regional DEM's have been developed in many countries with resolutions down to one arcsec (SMITH and ROMAN 2000).

For large-region applications, a mean density value of 2670 kgm^{-3} (corresponding to the density of granite) generally is introduced for the topographic masses. More refined density models have been used for local studies, where the density values are estimated from geological information, rock samples, and gravity profiles exploiting the density-dependent relation between gravity and height (*Nettleton method*, e.g., TORGE 1989).

Spherical harmonic models of the topography have been derived from global DEM's (PAVLIS and RAPP 1990). They serve for the development of topographic-isostatic models, cf. [8.2.2], which may be used for the prediction of mean gravity anomalies in unsurveyed areas, cf. [6.5.3].

6.5.3 Gravity Reductions to the Geoid

In order to determine the geoid as a boundary surface in the gravity field, the topographic masses have to be removed, and the observed gravity values have to be reduced to the geoid. This is done by *gravity reductions*, which provide gravity anomalies on the geoid.

Depending on how the topographic masses are displaced, different types of gravity anomalies are obtained. Uncertainties of the topographic model propagate into the calculation of the geoid. This has to be taken into account in the calculation of orthometric heights (3.106), where the same density model has to be employed.

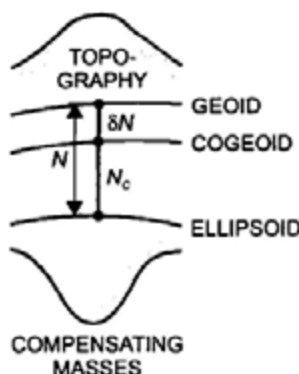


Fig. 6.23. Geoid and cogeoid

The displacement of the topographical masses changes the gravitational field of the earth, including the potential of the geoid. The level surface which possesses the geoid potential after the displacement is called *cogeoid*: *indirect effect* of the gravity reductions (WICHENCHAROEN 1982, MARTINEC 1998). The following steps may be distinguished in the calculation of the geoid (Fig. 6.23):

- Reduction of the *direct effect* of the topography on gravity and adding of the *direct effect* of the dislocated masses if necessary, both to be calculated by the law of gravitation, cf. [6.5.2],
- Calculation of the *primary indirect effect* on the potential, caused by the removal of the topography and the dislocation of the topographic masses. The calculation is performed according to some rule of compensation:

$$\delta V = V_{\text{top}} - V_c, \quad (6.105)$$

with V_{top} = potential of the topography and V_c = potential of the compensating masses,

- Calculation of the *vertical distance* between the geoid and the cogeoiod according to (6.97b):

$$\delta N = \frac{\delta V}{\gamma}, \quad (6.106)$$

- Reduction of the gravity values from the geoid to the cogeoiod: *secondary indirect effect*. Here, a free-air reduction (6.101) is sufficient:

$$\delta g_c = 2 \frac{\gamma}{r} \delta N, \quad (6.107)$$

- Calculation of the heights N_c of the *cogeoid* above the ellipsoid, cf. [6.6], [6.7],
- Calculation of the *geoid* heights according to

$$N = N_c + \delta N. \quad (6.108)$$

In principle, every kind of gravity reduction could serve for the calculation of the geoid according to this scheme. Naturally, the indirect effect should be small in order to avoid laborious and error susceptible computations. Other criteria for the selection of gravity reductions include the smoothness of the resulting gravity anomalies, which facilitates interpolation, and their geophysical significance, which would allow interpretation. Under these aspects, we may distinguish between the effects of (homogeneous) topography,

density anomalies within the topography and the earth's crust, and isostatic compensation masses, cf. [8.2.2].

The *free-air anomaly* is generally used for the calculation of the geoid, with the assumption that no masses exist above the geoid. The *free-air reduction*

$$\delta g_F = -\frac{\partial g}{\partial H} H \quad (6.109)$$

(H = orthometric height) provides the reduction of the surface gravity to the geoid, and the *simple free-air anomaly* on the geoid is given by

$$\Delta g_F = g + \delta g_F - \gamma_0. \quad (6.110)$$

According to (6.109), the correct reduction to the geoid requires the knowledge of the actual vertical gravity gradient. Splitting the gradient into a normal and an anomalous part gives

$$\frac{\partial g}{\partial H} = \frac{\partial \gamma}{\partial H} + \frac{\partial (\Delta g)}{\partial H}. \quad (6.111)$$

The actual and the normal part may differ by 10% or more. The normal gravity gradient can be calculated by (4.61). The calculation of the anomalous part corresponds to the downward continuation of a harmonic function. It can be formulated by Poisson's integral, which is a solution of the first (Dirichlet) boundary-value problem of potential theory, and solved by an integration over the surface gravity anomalies, cf. [6.7.2]. If the gravity anomaly depends linearly on elevation, the anomalous gradient corresponds to the terrain correction (MORITZ 1980, p.421), see below. Due to the assumptions made in (6.110), it equals the direct effect of the topographic and the dislocated masses on gravity (SIDERIS 1990). A discrete solution of this problem has been given by BJERHAMMAR (1969, 1985), which takes into account that gravity data are given only at discrete points. This solution satisfies all given data and generates missing data, and it is harmonic down to an internal sphere (Bjerhammar sphere), cf. [3.3.2].

The free-air anomaly on the *geoid* should be clearly distinguished from the free-air anomaly defined on the *surface* of the earth (6.15) where the normal gravity gradient is used for reduction.

The *terrain correction* removes irregularities of the topography. It creates a plate (spherical or planar) of constant thickness and density (Bouguer plate) by filling mass deficits below P and removing excess masses above the plate (Fig. 6.24). For planar approximation (Bouguer plate extending to infinity), both measures increase gravity at P ; the terrain correction then is always positive. It can be calculated from digital elevation models, cf. [6.5.2], and attains values of 1 to 10 μms^{-2} in flat areas, reaching several 100 μms^{-2} in the mountains. From (6.102) we obtain

$$\delta g_T = G\rho \int_{-\infty}^{\infty} \int_{-\infty}^{\infty} \int_{z=H_p}^{z=H} \frac{z - H_p}{l^3} dx dy dz . \quad (6.112a)$$

For small surface slopes, the distance

$$l = \sqrt{(x - x_p)^2 + (y - y_p)^2 + (z - z_p)^2}$$

may be approximated by

$$l_0 = \sqrt{(x - x_p)^2 + (y - y_p)^2} .$$

The linear approximation of the terrain correction then reads

$$\delta g_T = \frac{1}{2} G\rho \int_{-\infty}^{\infty} \int_{-\infty}^{\infty} \frac{(H - H_p)^2}{l_0^3} dx dy , \quad (6.112b)$$

where H resp. H_p are the orthometric heights of the terrain and the point of calculation (FORSBERG and TSCHERNING 1997).

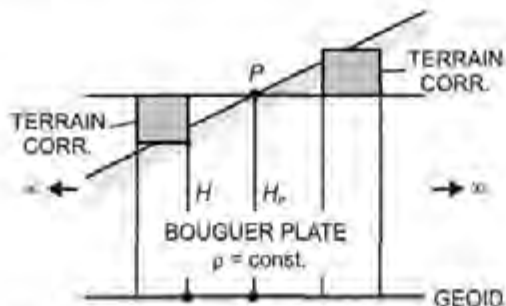


Fig. 6.24. Bouguer plate and terrain correction

By including the terrain correction into (6.110), we obtain the *terrain-corrected free-air anomaly*, called *Faye-anomaly*. The shift of the topographic masses now corresponds to a compensation of the Bouguer plate on the geoid (Helmert's *compensation method*). Here, the *surface density*

$$\mu = \frac{dm}{ds} = \rho \frac{dv}{ds} = \rho H \quad (6.113)$$

replaces the volume density ρ and takes the height of topography into account.

As the mass displacement is slight, the indirect effect of the free-air and the compensation reduction remains small. It reaches at most a few meters in the absolute sense and is of the cm to dm-order for geoid differences. As the height-dependent effect of the topography has not been removed, free-air anomalies are strongly correlated with height. Therefore, point free-air anomalies are not suited for interpolation and cannot be geophysically interpreted. For limited areas, the height-dependence can be described by linear regression, which corresponds to the application of the Bouguer plate reduction (see below). Interpolation and calculation of mean gravity anomalies is then facilitated (GROten and REINHART 1968).

By removing the effect of topography explicitly through a *topographic reduction* δg_{top} , we obtain the *Bouguer gravity anomaly* Δg_B . After the removal of the masses the surface gravity again is reduced to the geoid by the free-air reduction and compared with the normal gravity γ_0 (Fig. 6.24):

$$\Delta g_B = g - \delta g_{\text{top}} + \delta g_F - \gamma_0. \quad (6.114)$$

The topographic reduction is calculated from digital elevation models, cf. [6.5.2].

In most cases, the topographic reduction is decomposed into the Bouguer plate reduction δg_p and the terrain correction δg_T . The *Bouguer plate reduction* accounts for the gravitation of an infinitely extended horizontal plate with constant density. Its thickness is given by the height of the computation point. The gravitational effect of the Bouguer plate is derived from the attraction of a circular cylinder on a point located on the cylinder axis (GARLAND 1979, MILITZER and WEBER 1984). By extending the cylinder radius to infinity, one obtains

$$\delta g_p = 2\pi G \rho H = 0.000\,419 \rho H \mu\text{ms}^{-2}, \quad (6.115)$$

where ρ is taken in kg/m^3 and H in m. The *terrain correction* reduces the topography to the Bouguer plate (see above). The *Bouguer anomaly* then reads

$$\Delta g_B = g - \delta g_p + \delta g_T + \delta g_F - \gamma_0. \quad (6.116)$$

For large-region applications (e.g., national gravimetric surveys), a spherical Bouguer plate and a corresponding terrain correction is used frequently, with a calculation extending 170 km from the computation point and conventional density being 2670 kg/m^3 .

Due to the removal of the height-dependent part of topography, Bouguer anomalies display smooth long-wave variations only. Hence, they are well suited for interpolation. Revealing density anomalies below the geoid, the Bouguer anomalies are of considerable significance in geophysics and geology, cf. [8.2.4]. On the other hand, since the topographic masses are

completely removed and not restored (i.e. shifted to infinity), the indirect effect is very large (several 100 m). Hence, Bouguer anomalies are not used for geoid computations.

The Bouguer plate model allows a simple calculation of the *mean gravity* \bar{g} along the plumb line required for the computation of the orthometric height H (3.106), (6.81). If we assume a linear change of g along the vertical, \bar{g} will be found at the height $H/2$. Hence it can be derived from surface gravity by removing a Bouguer plate of thickness $H/2$, a free-air reduction from H to $H/2$, and a subsequent restoration of the Bouguer plate above $H/2$. Removing and restoring the Bouguer plate has the same (negative) effect on gravity; so we obtain

$$\bar{g} = g - \delta g_p(H) + \delta g_F(H/2). \quad (6.117)$$

Evaluation with (6.115) and (6.109), and introducing the density value 2670 kg/m³, leads to (6.84).

Equation (6.117) also provides an important interpretation of the difference between the heights of the geoid and the quasigeoid resp. the normal and the orthometric height. With the mean normal gravity

$$\bar{\gamma} = \gamma_0 - \delta g_F(H/2), \quad (6.118)$$

the *mean gravity anomaly* (6.9) is identified as the Bouguer anomaly (terrain correction neglected)

$$\bar{g} - \bar{\gamma} = g - \delta g_p(H) + \delta g_F(H) - \gamma_0 = \Delta g_B. \quad (6.119)$$

This fact permits a simple transformation from the quasigeoid to the geoid, cf. [6.7.2].

Isostatic anomalies are formed by not only removing the effect of topography but by also restoring compensation masses in the earth's crust below the geoid, according to some isostatic model. In this way, the crust is regularized, obtaining constant thickness and density, cf. [8.2.2]. The gravitational effect of the compensating masses is taken into account by an *isostatic reduction* δg_I , to be calculated from the isostatic model according to [6.5.2]. The isostatic anomaly then is given by

$$\Delta g_I = g - \delta_{top} + \delta g_I + \delta g_F - \gamma_0. \quad (6.120)$$

The largest part of the earth's topography is isostatically compensated. Hence, isostatic anomalies are small and vary smoothly about zero, with the exception of uncompensated areas. They may be

successfully employed for gravity prediction, and they are of great value for geophysical and geodynamic interpretation, cf. [8.2.4]. The compensating masses are arranged more remote from topography than in the free-air reduction (see above). Therefore, the indirect effect is larger and may reach 10 meters. Because of this, isostatic anomalies are rarely used for geoid calculations.

6.5.4 Orientation and Scale of Gravity Field Models

The following *assumptions* were made for the spherical harmonic expansion of the disturbing potential and the transformation to the quasigeoid resp. geoid, cf. [6.1.1], [6.5.1]:

- The level ellipsoid and the earth have the same mass:

$$M_{\text{Ell}} = M . \quad (6.121)$$

Hence, no zero-degree term T_0 appeared in the expansion (6.4),

- The center of the ellipsoid and the earth's center of mass (origin of the global coordinate system) coincide; no first-degree term entered into (6.4), cf. also [3.3.4],
- The normal potential U and the actual potential W are related by

$$U_Q = W_P , \quad (6.122a)$$

which corresponds to the condition

$$U_0 = W_0 \quad (6.122b)$$

between the potential of the level ellipsoid and the geoid.

A first-degree term in the spherical harmonic expansion would not affect the gravity anomaly, as the corresponding expansion (6.135) contains the factor $(l-1)$. Hence, the ellipsoid may be positioned in the geocenter without changing the gravity field: the gravimetric method yields "absolute" results.

Because of residual uncertainties in the determination of the mass and the potential, small differences between the values for the geoid and the ellipsoid have to be admitted:

$$\delta M = M - M_{\text{Ell}}, \quad \delta W = W_0 - U_0 . \quad (6.123)$$

The spherical harmonic expansion of T then must be extended by

$$T_0 = \frac{G \delta M}{R}, \quad (6.124)$$

and Bruns' formula must take T_0 and the potential difference into account:

$$N_0 = \frac{G \delta M}{\gamma R} - \frac{\delta W}{\gamma}. \quad (6.125)$$

For spherical approximation, the constant N_0 corresponds to a change in scale of the geoid. The expansion of the gravity anomaly (6.135), according to (6.101), has to be extended by (HEISKANEN and MORITZ 1967, p. 100 ff)

$$\Delta g_0 = -\frac{T_0}{R} + \frac{2}{R} \delta W = -\frac{G \delta M}{R^2} + \frac{2}{R} \delta W. \quad (6.126)$$

With the usual assumption of equality of mass and potential, the gravimetric solution of the boundary-value problem delivers results which refer to a best-fitting ellipsoid, where the equatorial radius ("scale") remains unknown by N_0 .

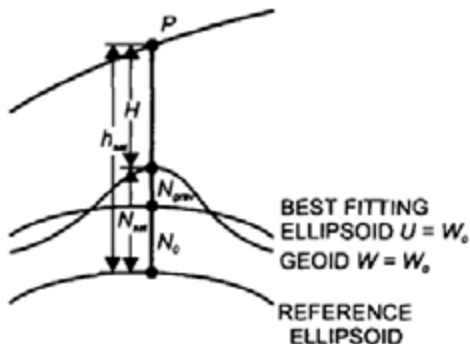


Fig. 6.25. Gravimetric geoid and geodetic reference ellipsoid

The *zero-degree undulation* N_0 can be determined by comparing gravimetrically computed geoid heights with geoid values derived by differencing distances that refer either to the geoid or to the ellipsoid. The primary data sets used are from satellite altimetry on the oceans and GPS heights on the continents (RAPP and BALASUBRAMANIA 1992, JEKELI 1998), Fig. 6.25). The geoid height from these satellite techniques is given by

$$N_{\text{sat}} = h_{\text{sat}} - H, \quad (6.127)$$

where h_{sat} stands for the ellipsoidal height of the altimeter or the GPS height, and H is the height of the altimeter above the geoid (result of the altimeter measurements) or the orthometric height derived from leveling. The zero-degree term is obtained by

$$N_0 = N_{\text{sat}} - N_{\text{grav}}. \quad (6.128)$$

It can be used to derive the semimajor axis of the best-fitting ellipsoid to which the gravimetric geoid heights refer:

$$a_{\text{grav}} = a_{\text{sat}} + N_0. \quad (6.129)$$

Generally, the ellipsoid adopted as part of a geodetic reference system, cf. [4.3], is kept unchanged. The gravimetrically determined geoid heights are then corrected in order to refer to that reference ellipsoid (e.g., the GRS80 ellipsoid):

$$N_{\text{ref}} = N_{\text{sat}} = N_{\text{grav}} + N_0. \quad (6.130)$$

Classically, best-fitting ellipsoids have been determined by comparing horizontal distances measured on the geoid with the ellipsoidal distances obtained by calculation, cf. [7.1.2]. A separation between δM and δW in principle would be possible using (6.126), together with (6.125), using the condition $\Delta g_0 = 0$ (6.19). However, deficiencies in the global gravity coverage still prevent use of this method. On the other hand, the geocentric gravitational constant GM is known today with high accuracy from space probes and high-flying satellites (GROTE 2000). The determination of N_0 thus provides the potential of the geoid. From Topex/Poseidon altimeter data, the equatorial radius of an ellipsoid that best fits the zero-tide geoid, cf. [3.4.1], has been estimated to $6\,378\,136.49 \pm 0.1$ m (RAPP 1995c).

6.6 Global Gravity Field Modeling

Global gravity field modeling is required for large-scale problems including the determination of satellite orbits, inertial navigation, and development of geophysical and geodynamic models. The geoid is required for establishing a global vertical reference system and for deriving sea surface topography. Finally, global models provide the long wavelength part of the gravity field for local gravity field approximation, cf. [6.7].

Global gravity models are based on spherical harmonic expansions [6.6.1]. The low frequency part of these series expansions stems from the analysis of satellite orbits [6.6.2]. Expansions of higher degree are achieved by combining

the low-degree models with the results of terrestrial gravimetry and satellite altimetry [6.6.3], BOUMAN (1997), NEREM et al. (1995), RAPP (1998).

6.6.1 Spherical Harmonic Expansions

Equations (6.3) to (6.5) provide the development of the disturbing potential T into spherical harmonics. A gravity field model thus is represented by the *spherical harmonic coefficients*. The functional relations between T and other relevant gravity field parameters, cf. [6.5.1], also allow spherical harmonic expansions for the height anomaly, the geoid height, and the gravity anomaly. These expansions generally employ fully normalized spherical harmonics, cf. [3.3.2].

By inserting (6.4) into Bruns' theorem (6.96b), we obtain the spherical harmonic expansion for the *height anomaly*

$$\zeta(r, \vartheta, \lambda) = \frac{GM}{r\gamma} \sum_{l=2}^{\infty} \left(\frac{a}{r} \right)^l \sum_{m=0}^l (\Delta \bar{C}_{lm} \cos m\lambda + \Delta \bar{S}_{lm} \sin m\lambda) \bar{P}_{lm}(\cos \vartheta). \quad (6.131)$$

Here, the fully normalized coefficients and spherical harmonics are indicated by bars. Equation (6.97b) delivers the corresponding expansion for the *geoid height*, which can be also be derived from (6.131), taking (6.9) into account:

$$N(r, \vartheta, \lambda) = \zeta(r, \vartheta, \lambda) + \frac{\Delta g_B}{\bar{\gamma}} H. \quad (6.132)$$

Differentiation of (6.4) with respect to r gives the spherical harmonic expansion for the *gravity disturbance* (6.99):

$$\delta g = -\frac{\partial T}{\partial r} = \frac{1}{r} \sum_{l=2}^{\infty} (l+1) \left(\frac{a}{r} \right)^{l+1} T_l(\vartheta, \lambda). \quad (6.133)$$

Inserting (6.4) and (6.133) into (6.101b) yields the expansion of the *gravity anomaly*

$$\Delta g(r, \vartheta, \lambda) = \frac{1}{r} \sum_{l=2}^{\infty} (l-1) \left(\frac{a}{r} \right)^{l+1} T_l(\vartheta, \lambda). \quad (6.134)$$

Substituting T_l from (6.5) gives

$$\Delta g(r, \vartheta, \lambda) = \frac{GM}{r^2} \sum_{l=2}^{\infty} (l-1) \left(\frac{a}{r} \right)^l \sum_{m=0}^l (\Delta \bar{C}_{lm} \cos m\lambda + \Delta \bar{S}_{lm} \sin m\lambda) \bar{P}_{lm}(\cos \vartheta). \quad (6.135)$$

By comparing the abbreviated form

$$\Delta g(r, \vartheta, \lambda) = \sum_{l=2}^{\infty} \left(\frac{a}{r} \right)^{l+1} \Delta g_l(\vartheta, \lambda) \quad (6.136)$$

with (6.134), we obtain the relation between the surface spherical-harmonics of T and Δg :

$$\Delta g_l(\vartheta, \lambda) = \frac{l-1}{r} T_l(\vartheta, \lambda). \quad (6.137)$$

Corresponding equations can be derived for the deflection of the vertical and for higher derivatives of T (WENZEL 1985). Due to the scarcity of terrestrial data of these types, these expansions are of limited importance. Second-order derivatives of T obtained from satellite gravity gradiometry, on the other hand, will be of great importance for future gravity field modeling (RUMMEL et al. 1993).

Equations (6.131) to (6.135) permit the harmonic coefficients to be determined from "observations", by *least-squares adjustment*, cf. [6.6.2], [6.6.3]. The coefficients can also be determined by *quadrature* over the observations. Taking the orthogonality relations and the properties of the fully normalized harmonics into account, the inversion of (6.131) and (6.135) yields (JEKELI 1998):

$$\begin{Bmatrix} \Delta \bar{C}_{lm} \\ \Delta \bar{S}_{lm} \end{Bmatrix} = \frac{1}{4\pi GM} \iint_{\sigma} r \gamma \left(\frac{r}{a} \right)^l N \bar{P}_{lm}(\cos \vartheta) \begin{Bmatrix} \cos m\lambda \\ \sin m\lambda \end{Bmatrix} d\sigma \quad (6.138a)$$

and

$$\begin{Bmatrix} \Delta \bar{C}_{lm} \\ \Delta \bar{S}_{lm} \end{Bmatrix} = \frac{1}{4\pi GM} \iint_{\sigma} \frac{r^2}{l-1} \left(\frac{r}{a} \right)^l \Delta g \bar{P}_{lm}(\cos \vartheta) \begin{Bmatrix} \cos m\lambda \\ \sin m\lambda \end{Bmatrix} d\sigma. \quad (6.138b)$$

The integration is extended over the unit sphere σ . In contrast to least squares adjustment, the quadrature approach only allows exploitation of one type of data for the determination of the harmonic coefficients.

Global data sets do not cover the earth homogeneously, and they have a limited spatial resolution. Consequently, *mean* geoid heights and mean gravity anomalies over surface compartments are introduced in gravity field modeling, where the surface blocks generally are bounded by meridians and parallels. The mean values are calculated according to

$$\bar{N} = \frac{1}{\Delta\sigma} \iint_{\Delta\sigma} N d\sigma, \quad \Delta\bar{g} = \frac{1}{\Delta\sigma} \iint_{\Delta\sigma} \Delta g d\sigma. \quad (6.139)$$

The block size $\Delta\sigma$ depends on the data distribution, cf. [6.6.3]. The maximum gravity field resolution which can be achieved is $\sqrt{\Delta\sigma}$. This corresponds to a maximum degree of the spherical harmonic expansion $l_{\max} = 180^\circ/\text{resolution}^\circ$, cf. [3.3.3]. The introduction of mean values causes a local smoothing of the gravity field, which also leads to smoothed harmonic coefficients. This fact has to be taken into account by damping factors (≤ 1), which depend on the degree and the dimension of the compartment (KATSAMBALOS 1979).

The truncation of the spherical harmonic expansion at l_{\max} produces an *omission error* due to the neglected part of the gravity field. This error can be estimated from the degree variances of the gravity field parameters. Degree variance models have been derived for gravity anomalies, see (6.27). They are based on the covariance function of the gravity anomalies (6.25), but can also be calculated from Laplace's surface harmonics Δg_l , (6.26). In spherical approximation ($r = a = R$), (6.137) gives

$$\Delta g_l = \frac{GM}{R^2} (l-1) \sum_{m=0}^l (\Delta \bar{C}_{lm} \cos m\lambda + \Delta \bar{S}_{lm} \sin m\lambda) \bar{P}_{lm}(\cos \vartheta). \quad (6.140)$$

Inserting (6.140) into (6.26) and evaluating yields the anomaly degree-variances as a function of the harmonic coefficients:

$$\sigma_l^2(\Delta g) = \left(\frac{GM}{R^2} \right)^2 (l-1)^2 \sum_{m=0}^l (\Delta \bar{C}_{lm}^2 + \Delta \bar{S}_{lm}^2). \quad (6.141)$$

This relation can especially be used to calculate the low-degree variances from the harmonic coefficients obtained from satellite orbit analysis.

The functional relations between the gravity field parameters, cf. [6.5.1], also permit the calculation of degree variances for geoid heights, deflections of the vertical, and higher-order derivatives (TSCHERNING and RAPP 1974, TSCHERNING 1976). With $\gamma = GM/r^2$, a comparison between (6.131) and (6.135) gives the geoid degree variance

$$\sigma_l^2(N) = \left(\frac{R}{\gamma(l-1)} \right)^2 \sigma_l^2(\Delta g). \quad (6.142)$$

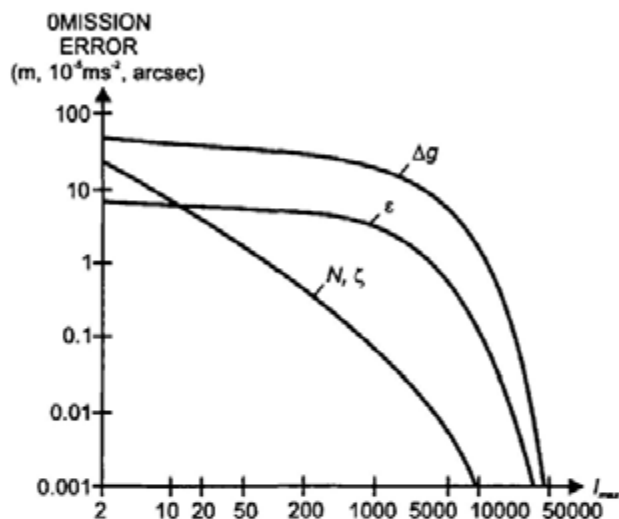


Fig. 6.26. Omission error for geoid heights (height anomalies), vertical deflections, and gravity anomalies (degree variance model TSCHERNING and RAPP 1974)

The omission error for geoid heights, gravity anomalies, and deflections of the vertical is shown in Fig. 6.26. For the presently usual truncation at degree 360, it amounts to $\pm 0.23 \text{ m}$, $\pm 253 \mu\text{ms}^{-2}$, and $\pm 3.8''$. An expansion to $l = 7200$, corresponding to a spatial resolution of 2.8 km, would reduce these errors to $\pm 0.002 \text{ m}$, $\pm 27 \mu\text{ms}^{-2}$, and $\pm 0.4''$.

6.6.2 Low-degree Gravity Field Models

Low-degree gravity field models are required for precise satellite orbit calculation, positioning of tracking stations, and long-wave geoid representation. They are primarily based on *satellite tracking data*, which are analyzed with respect to the deviations of the actual orbit from a precalculated reference orbit, cf. [5.2.2]. "Satellite-only" models use tracking data exclusively. In some cases, they have been utilized for the precise orbit determination of a specific satellite, especially by taking into account observations to that satellite ("tailored" models).

The "perturbing" gravitational potential (5.34) changes the Keplerian orbit elements with time (5.35). As the gravitational potential is modeled by a spherical harmonic expansion, the harmonic coefficients enter as unknowns into the observation equations of satellite geodesy, cf. [6.2.1]. In order to resolve the

gravitational field to a certain degree, satellites in different altitudes and with different inclinations are required, in addition to a good global distribution of the tracking stations and a sufficiently long observation time. The attenuation of the gravity field with height and the decrease of the harmonic coefficients at higher degrees, together with deficiencies in the geometry of the satellite orbits and the ground stations, limits the resolution of "satellite-only" models. With the satellites presently available (altitudes of 800 km and more), developments up to degree 70 have been carried out. Satellite-to-satellite tracking and satellite gravity gradiometry at orbital altitudes of about 300 km will extend this range up to degree 150 to 200, cf. [5.2.8], RUMMEL 1979.

We now regard the influence of the gravitational field on the satellite orbit. We distinguish between secular (linear), long-periodic (few days to months), and short-periodic (periods less than one day or one satellite revolution) perturbations (KAULA 1966, SEEBER 1993). The relationship between the perturbations of the orbital elements and the harmonic coefficients is obtained by transforming the spherical coordinates of the expansion (3.89) into the Keplerian elements, forming the derivatives of the perturbing potential with respect to the elements, and inserting them into (5.35).

Determination of the secular and long-periodic perturbations requires the integration over long arcs (several days). Here, short-periodic perturbations with periods of one or several revolutions are already eliminated. Furthermore, the influence of the tracking station coordinates becomes smaller with longer integration intervals, so that the stations may be even introduced as known. For the low-degree zonal coefficients, the integration over one satellite revolution yields the following variations for the orbital elements of main interest:

$$\left. \begin{aligned} \Delta\Omega &= -3\pi \left(\frac{a_e}{\bar{p}} \right)^2 \cos i J_2 + \dots \\ \Delta\omega &= 6\pi \left(\frac{a_e}{\bar{p}} \right)^2 \left(1 - \frac{5}{4} \sin^2 i \right) J_2 + \dots \\ \Delta e &= -3\pi (1-e^2) \left(\frac{a_e}{\bar{p}} \right)^3 \left(1 - \frac{5}{4} \sin^2 i \right) \sin i \cos \omega J_3 + \dots \\ \Delta i &= 3\pi \left(\frac{a_e}{\bar{p}} \right)^2 \left(1 - \frac{5}{4} \sin^2 i \right) \cos i \cos \omega e J_3 + \dots \end{aligned} \right\}, \quad (6.143)$$

with $\bar{p} = a(1-e^2)$ and a_e = semimajor axis of the earth ellipsoid.

J_2 and higher even-zonal-coefficients cause *secular* perturbations in Ω and ω . For $i < 90^\circ$, Ω decreases in time (westward regression of the nodal line). The

change in ω corresponds to a rotation of the orbital ellipse in the orbital plane (Fig. 5.5). This rotation produces *long-periodic* perturbations in the quantities e and i , as they depend on ω . The even zonals thus can be determined primarily from the perturbations in Ω and ω , while the odd zonals are obtained from i and e . If the perturbations are added to the orbital elements of the initial epoch, one obtains the orbital elements at a specific epoch as a function of the zonal harmonics. Substitution into (6.33) provides a system of observation equations for the determination of the zonal harmonic coefficients. As mentioned earlier, the coefficients depend particularly on the inclination but also on the semimajor axis and the eccentricity.

The *tesseral* harmonics are responsible for small-amplitude (a few 100 m) short-periodic perturbations, especially in the elements i , Ω , ω . They can be determined only from dense observations over short arcs. Weather-independent microwave measurements are particularly suitable for this purpose.

Several tesseral terms of higher degree and order can be determined by *resonance* effects, arising after days to weeks. These effects occur if the ratio of the mean angular velocity of the satellite to the rotational velocity of the earth is an integer number, which produces an enhancement of perturbation in a repeat orbit.

Recent "satellite-only" models employ several million records of tracking data. Laser distance and microwave range and range-rate measurements form the bulk of the data, but optical directions still are included and assist in stabilizing the solutions. Spaceborne positioning systems, including GPS, increasingly contribute to the data set. The observations to more than 30 satellites are generally used, with altitudes varying between 800 and 20 000 km and inclinations between 40° and 110°.

While limitations in computational facilities previously forced zonal, tesseral and resonant terms to be computed separately, the harmonic coefficients can now be rigorously determined by a common least squares adjustment, together with the coordinates of the tracking stations, ocean tidal parameters, polar motion and earth rotation. Sometimes the horizontal station velocities and the variations of the low-degree coefficients with time are also included in the adjustment (BOUMAN 1997).

Weighting of data and modeling of systematic effects poses a special problem for these complex adjustments. As the accuracy estimates generally are too optimistic, the calculated standard deviations often are "scaled", e.g., by a factor of 5 (SCHWINTZER et al. 1997).

In most cases, "satellite-only" models are improved and stabilized by *combining* them with satellite altimetry and surface gravity data. Mean values for $1^\circ \times 1^\circ$ blocks are introduced as "observations" and calculated either from point or smaller block values, cf. [6.6.3]. The observation equations for satellite

altimetry are given by (5.49), after inserting (6.131) for the altimetric geoid heights and taking a low-degree spherical harmonic model of sea surface topography into account. The observation equation for the gravity anomalies is given by (6.135). The normal equations of these data sets are added to the normal equations of the satellite-only model (RAPP 1997). Tab. 6.1 gives the values for the low degree-and-order harmonic coefficients, as derived from a recent combination solution.

Tab. 6.1. Fully normalized harmonic coefficients ($\times 10^6$), GRIM4-C4 model (SCHWINTZER et al. 1997)

| l | m | \bar{C}_{lm} | \bar{S}_{lm} |
|-----|-----|----------------|----------------|
| 2 | 0 | -484.1656 | |
| | 2 | 2.4393 | -1.4000 |
| 3 | 0 | 0.9573 | |
| | 1 | 2.0301 | 0.2484 |
| | 2 | 0.9050 | -0.6194 |
| | 3 | 0.7213 | 1.4143 |
| 4 | 0 | 0.5402 | |
| | 1 | -0.5353 | -0.4735 |
| | 2 | 0.3509 | 0.6626 |
| | 3 | 0.9910 | -0.2011 |
| | 4 | -0.1883 | 0.3088 |
| 5 | 0 | 0.0687 | |
| 6 | 0 | -0.1506 | |
| 7 | 0 | 0.0906 | |
| 8 | 0 | 0.0505 | |
| 9 | 0 | 0.0282 | |
| 10 | 0 | 0.0517 | |

The relative accuracy of the harmonic coefficients derived from low-degree spherical harmonic expansions decreases with increasing degree, from about 10^{-7} at $l=2$ to about 1% at $l=10$ and approaches 100% at $l=30$ to 40 (satellite-only models) resp. at $l=65$ to 70 (combination models). The long-wave part of the marine geoid is accurate to about ± 0.8 m (satellite-only) and ± 0.25 m (combination). Orbit determination for dedicated satellites (TOPEX/POSEIDON, ERS-1) is possible with an accuracy of a few cm with these models.

The first gravity field information from space came from Sputnik I (1957), with the dynamic form factor J_2 (polar flattening); and from Vanguard I (1958), with the coefficient J_3 (unequal flattening at the north and south pole). The Smithsonian Astrophysical Observatory (SAO) Standard Earth I provided a model complete to degree and order 8 (LUNDQUIST and VEIS 1966). Among the recent low-degree solutions are the NASA Goddard Space Flight Center (GSFC) earth model GEM T3 (satellite-only and combination with GEOS-3, Seasat, and GEOSAT altimetry

and $1^\circ \times 1^\circ$ surface gravity anomalies, complete to degree and order 50, resolved also for the coordinates of about 400 tracking stations and ocean tides, polar motion and earth rotation parameters, LERCH et al. 1994); the joint (GSFC, University of Texas, Ohio State University, CNES France) gravity model JGM-2S (satellite-only, complete to degree and order 70, NEREM et al. 1994); and the JGM-3 (70,70, including Doris and GPS-tracking, TAPLEY et al. 1996), which was developed primarily for the TOPEX/POSEIDON mission. The GRIM4 models (Geoforschungszentrum Potsdam and Groupe de Recherches de Géodésie Spatiale, Toulouse) include a satellite-only (60,60) and a combination (72,72) solution and also solve for a large number of additional parameters (SCHWINTZER et al. 1997), see also BOUMAN (1997), RAPP (1998).

6.6.3 High-degree Gravity Field Models

Parameters of high-degree gravity-field models are restricted to the harmonic coefficients and do not include other unknowns: *geopotential models*. Degree and order of the spherical harmonic expansion depend on the spatial resolution of the gravity field data available and on their global distribution. Of particular interest is the high-resolution quasigeoid resp. geoid needed for the establishment of a global vertical datum, cf. [3.4.3], as a reference for satellite altimetry in the determination of sea surface topography, cf. [3.4.2], and for the transformation of GPS-heights to normal or orthometric heights, cf. [6.4.3].

The models combine low-degree gravity-field models with surface gravity anomalies and altimetric geoid heights. Hence, they utilize:

- The harmonic coefficients of a “satellite-only” model (sometimes a combination model is used), with the full error covariance matrix,
- Mean free-air anomalies from terrestrial gravimetry on land and sea,
- Mean geoid heights from satellite altimetry. Some solutions use mean gravity anomalies derived from the geoid heights, with a transformation based either on an integral formula, cf. [6.7.1], or on least squares collocation, cf. [6.8.2].

Mean *free-air anomalies* are calculated from point anomalies collected e.g., at the Bureau Gravimetrique International or the U.S. National Imagery and Mapping Agency (NIMA). Least squares prediction is employed for interpolation to gridded values, where Bouguer anomalies are used as intermediate gravity field quantities, cf. [6.5.3], RAPP (1997). $1^\circ \times 1^\circ$ mean values based on measurements are available for a large part of the world (about 80%). On the continents, $30' \times 30'$ mean anomalies have also been derived for large regions, but great gaps exist on the oceans and in antarctica. The accuracy of the mean anomalies amounts to about ± 50 to ± 200 μms^{-2} (KIM and RAPP 1990, KENYON 1998).

Mean *altimetric geoid heights* are derived from individual measurements to the sea surface, after least squares adjustment of the crossover discrepancies and reduction of the sea surface topography by an oceanographic model. Data sets of high accuracy and resolution are available

from the GEOSAT and ERS-1 geodetic missions, which cover the oceans between $\pm 72^\circ$ resp. 82° latitude with an equatorial track spacing of 4 resp. 8 km. Mean geoid heights, and by inversion $30 \times 30'$ mean gravity anomalies, have been calculated from mean values derived for smaller block sizes, cf. [6.7.1], where the accuracy of the altimetric gravity anomalies is about $\pm 20 \mu\text{m s}^{-2}$ and more homogeneous than surface gravity.

By combining the mean anomalies from surface gravimetry and altimetry, only a few percent of the earth's surface remain uncovered. These gaps are filled either by some low-degree model values and/or isostatic anomalies calculated from topographic-isostatic models (PAVLIS and RAPP 1990).

High-degree geopotential models are calculated either by least squares adjustment or by quadrature methods (RAPP 1997).

A *least squares adjustment*, in principle, would utilize all available data in order to determine the full set of potential coefficients (130 321 coefficients at $l,m = 360,360$; 3.24 million coefficients at $1800,1800$), together with the error variance/covariance matrix. Currently, computational limitations still prevent a rigorous adjustment of these quantities. Consequently, non-optimum solutions have been developed, which, for instance, presuppose a complete data coverage on a grid and homogeneous and uncorrelated errors. Special arrangements of the normal equation matrix (block-diagonal technique) then allow an efficient computation by iterative procedures (COLOMBO 1981, WENZEL 1985, PAVLIS et al. 1996).

The *quadrature* approach employs the integration over the gravity anomalies according to (6.138). As a global and homogeneous data set is required, altimetric geoid heights have to be transformed into gravity anomalies and data gaps have to be filled by model values. After the calculation of the harmonic coefficients from the gravity anomalies, they are combined by adjustment with the coefficients of a low-degree gravity model (COLOMBO 1981, RAPP and PAVLIS 1990).

The long-wave structures of the *free-air anomalies* and the *geoid*, as derived from a recent geopotential model, are shown in Figs. 6.27 and 6.28. The free air anomalies vary rather irregularly about zero, but a correlation with extended mountain chains (Cordilleras, Himalaya) can be recognized. The principal features of the geoid include the maxima near New Guinea (+80 m), in the North Atlantic, the southwestern Indian Ocean, and in the Andes, as well as the minima at Sri Lanka (-105 m), in Antarctica, to the west of California, and near Puerto Rico.

Early spherical harmonic expansions are due to Jeffreys (1941-1943), Zhongolovich (1952), and Uotila (1962). Sparse surface gravity data coverage limited these expansions to the low-degree harmonics. Kaula (1959) introduced a constraint from satellite orbit analysis in order to develop a

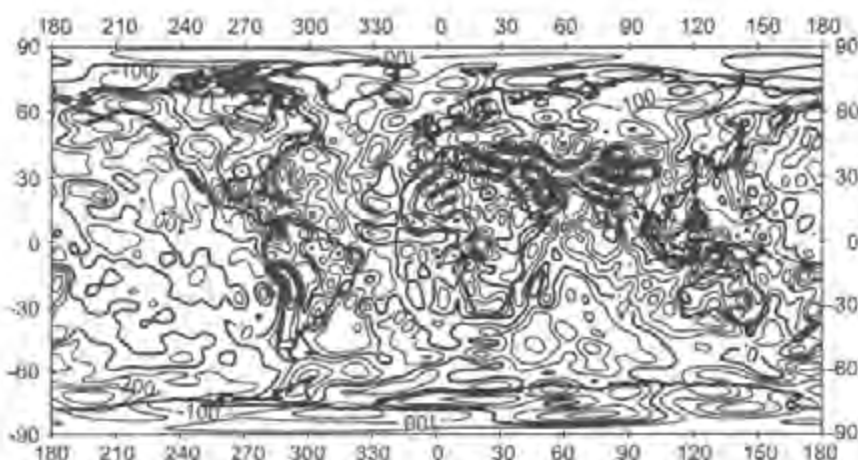


Fig. 6.27. EGM96 gravity anomalies, spherical harmonic expansion truncated at degree and order 36, contour line interval $100 \mu\text{m s}^{-2}$ (LEMOINE et al. 1998)

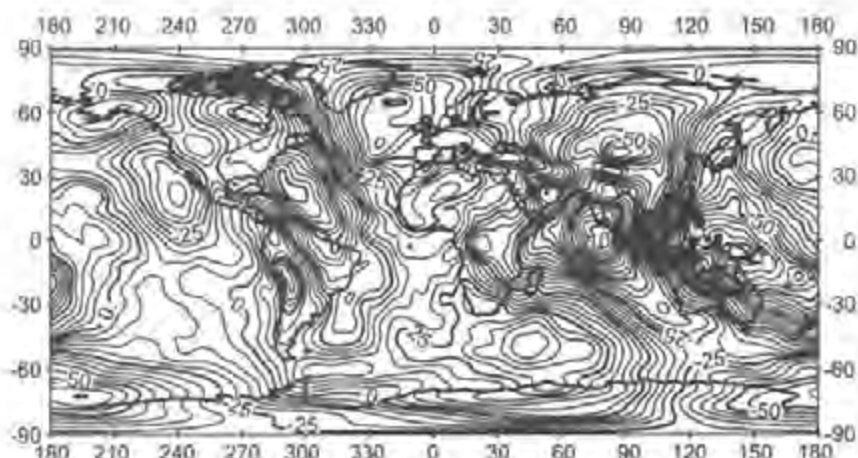


Fig. 6.28. EGM96 geoid heights, spherical harmonic expansion truncated at degree and order 36, contour line interval 5 m (LEMOINE et al. 1998)

8.8 geoid model (RAPP 1998). Among the recently developed geopotential models are the Ohio State University (OSU) model OSU91 (combination of the GEM-T2 36,36 model with $1^\circ \times 1^\circ$ and $30^\circ \times 30^\circ$ gravity anomalies from surface gravimetry and altimetry, quadrature method, RAPP et al. 1991) and the Geoforschungszentrum Potsdam (GFZ) model GFZ96 (combination of the GRIM-4 60,60 and 72,72 models with terrestrial anomalies and ERS-1 geoid heights, least squares iteration, GRUBER et al. 1997), both complete to degree and order 360.

Most complete sets of satellite tracking data (including altimetry in the form of tracking), gravity anomalies, and recent satellite altimetry (GEOSAT, ERS-1 in the polar regions) have been utilized in the NASA/GSFC and NIMA joint geopotential (360,360) model EGM96 (LEMOINE

et al. 1997, 1998). The model is composed of a 70,70 combination model (least squares adjustment resolving for tidal parameters and a 20,20 model of sea surface topography, as well as for station coordinates) and $30' \times 30'$ mean anomalies. Up to degree and order 359, a block-diagonal solution was performed, and the degree 360 coefficients were calculated by quadrature. Geoid accuracy estimates are between ± 0.5 m (oceans) and ± 1 m (land).

A 1800,1800 ultra-high spherical harmonic model GPM98 was developed by WENZEL (1999) by combining EGM96 with $5' \times 5'$ mean gravity anomalies collected from surface gravity and altimetry for about 75% of the earth's surface (the remaining areas being filled by larger block size values), where integral formulas were applied for the calculation of the coefficients. In areas well covered by high-resolution data, this solution provides a relative geoid accuracy of a few cm and gravity anomalies accurate to several $10 \mu\text{m s}^{-2}$.

Tailored geopotential models have been developed in order to better approximate the gravity field in a certain region (WEBER and ZOMORODIAN 1988, KEARSLEY and FORSBERG 1990). Here, a global high-resolution spherical harmonic expansion is used as a starting model, and higher degree coefficients are modified and extended so as to better reproduce high resolution gravity anomalies in the region. Among these models are a 360,360 solution for Europe (BAŠIĆ et al. 1989), a 500,500 solution for Canada (LI and SIDERIS 1994), and a 720,720 solution for China (LU et al. 2000).

6.7 Local Gravity Field Modeling

Local gravity field approximation is especially useful for the determination of geoid or quasigeoid heights with high accuracy, as needed for the reduction of GPS heights, cf. [6.4.3]. Integral formulas allow a pointwise calculation of gravity field quantities, and thus provide the possibility of an arbitrarily high gravity field resolution which depends only on data coverage and quality (SANSO and RUMMEL 1997).

Utilizing gravity anomalies as the primary data set, classical solutions aim at the determination of geoid heights and geoidal deflections of the vertical [6.7.1]. Reduction to the geoid is avoided in the calculation of the corresponding surface quantities, where the quasigeoid plays a special role [6.7.2]. Once the gravity field is known on the geoid or on the physical surface of the earth, an upward continuation provides gravity field quantities in space [6.7.3]. Astronomically determined deflections of the vertical furnish differences of geoid or quasigeoid heights and may locally support or substitute gravimetric solutions [6.7.4].

An alternative approach to the integral formulas is least squares collocation which will be discussed under the more general aspect of "integrated geodesy" in [6.8.2].

6.7.1 Gravimetric Geoid Heights and Deflections of the Vertical

The series expansion (6.4) for the disturbing potential T can also be represented by a surface integral. By inserting (6.137) into (6.3), this expansion reads

$$T(r, \vartheta, \lambda) = \sum_{l=2}^{\infty} \frac{r}{l-1} \left(\frac{a}{r} \right)^{l+1} \Delta g_l(\vartheta, \lambda). \quad (6.144)$$

As known from potential theory, the surface spherical harmonics Δg_l are derived by inversion of (6.136), as a surface integral of the gravity anomalies over the unit sphere σ :

$$\Delta g_l = \frac{2l+1}{4\pi} \iint_{\sigma} \Delta g P_l(\cos \psi) d\sigma, \quad (6.145)$$

where $P_l(\cos \psi)$ are the Legendre polynomials. Inserting into (6.144) yields the *disturbing potential on the geoid in spherical approximation*:

$$T(\vartheta, \lambda) = \frac{R}{4\pi} \iint_{\sigma} S(\psi) \Delta g d\sigma, \quad (6.146)$$

where the integral kernel

$$S(\psi) = \sum_{l=2}^{\infty} \frac{2l+1}{l-1} P_l(\cos \psi) \quad (6.147a)$$

can be expressed in closed form:

$$S(\psi) = \frac{1}{\sin \frac{\psi}{2}} + 1 - 5 \cos \psi - 6 \sin \frac{\psi}{2} - 3 \cos \psi \ln \left(\sin \frac{\psi}{2} + \sin^2 \frac{\psi}{2} \right). \quad (6.147b)$$

This integral formula has been derived by STOKES (1849); it is called *Stokes' formula*. If an accuracy of the cm-order of magnitude is required, *ellipsoidal* corrections have to be applied (SÜNKEL 1997).

By inserting (6.146) into Bruns' theorem (6.97b), we obtain the *geoid height*

$$N = \frac{R}{4\pi \gamma_m} \iint_{\sigma} S(\psi) \Delta g d\sigma, \quad (6.148)$$

where γ_m is a mean gravity value over the earth. Stokes' formula can also be derived as a solution of the integral equation (6.93), if applied to the geoid.

Stokes' function $S(\psi)$ acts as a weighting function on the gravity anomalies. It depends on the spherical distance ψ between the point of computation and the surface element $d\sigma$ with the gravity anomaly Δg . $S(\psi)$ decreases with ψ until a first zero at $\psi = 39^\circ$, and then oscillates with large values until $\psi = 180^\circ$ (Fig. 6.29). The *neighborhood* of the computation point requires particular attention, as $S(\psi)$ becomes infinite at $\psi = 0^\circ$. The contribution of the innermost zone can be estimated in planar approximation (e.g., with a radius $s_i = 5$ km), by expanding Δg in a Taylor series and performing integration term by term. To a first approximation, the effect of the *inner zone* on the geoid height depends on the gravity anomaly in the computation point:

$$N_i = \frac{s_i}{\gamma_m} \Delta g_p + \dots \quad (6.149)$$

The components of the *deflection of the vertical* are obtained by differentiating T in north-south and east-west direction (6.98). This can be realized by expressing ψ in (6.146) in spherical coordinates of the computation point and the source point (the corresponding formulas of spherical trigonometry are taken from the spherical polar triangle, see Fig. 2.14), differentiation, and resubstitution of ψ . We obtain

$$\begin{Bmatrix} \xi \\ \eta \end{Bmatrix}_0 = \frac{1}{4\pi\gamma_m} \iint_{\sigma} \frac{dS(\psi)}{d\psi} \Delta g \begin{Bmatrix} \cos \alpha \\ \sin \alpha \end{Bmatrix} d\sigma, \quad (6.150)$$

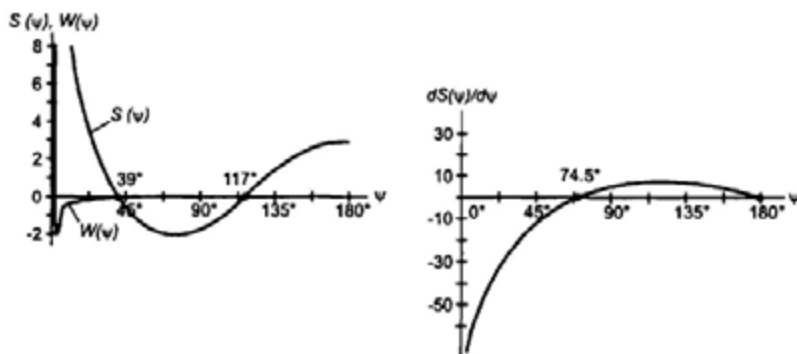


Fig. 6.29. Original and modified Stokes' function

Fig. 6.30. Vening-Meinesz function

where α is the azimuth of the great circle from the computation point to the source point. Equation (6.150) was derived by VENING-MEINESZ (1928).

The *Vening-Meinesz function*

$$\frac{dS}{d\psi} = -\frac{\cos(\psi/2)}{2\sin^2(\psi/2)} + 8\sin\psi - 6\cos(\psi/2) - 3\frac{1-\sin(\psi/2)}{\sin\psi} + 3\sin\psi \ln[\sin(\psi/2) + \sin^2(\psi/2)] \quad (6.151)$$

is infinite at $\psi = 0^\circ$ and then decreases rapidly, attaining only small values after $\psi = 50^\circ$ to 60° (Fig. 6.30). The contribution of the *innermost zone* depends primarily on the horizontal gradient of the gravity anomalies:

$$\begin{Bmatrix} \xi \\ \eta \end{Bmatrix}_i = -\frac{s_i}{2\gamma_m} \begin{Bmatrix} \partial(\Delta g)/\partial x \\ \partial(\Delta g)/\partial y \end{Bmatrix}_p + \dots \quad (6.152)$$

Stokes' and Vening-Meinesz' formulas allow a *pointwise* calculation of the geoid height and the deflection of the vertical, by integrating the gravity anomalies given on the surface of the geoid, cf. [6.5.3]. The properties of Stokes' function require high resolution gravity data all over the earth, while the effect of remote zones is small in the calculation of vertical deflections and can be estimated by low-degree global gravity field models. The inner zone may contribute some cm to the geoid height, this is well accounted for at gravity station distances of 1 to 5 km, depending mainly on the roughness of topography. The effect of the inner zone on the deflection of the vertical can reach several arcsec, especially in the mountains. A dense gravity survey and/or the calculation of the effect of topography is needed in order to achieve an accuracy better than one arcsec.

In practice, the integrals (6.148) and (6.150) are solved by a summation of finite surface elements. For this purpose, either a set of gridded point anomalies is formed from the observed data, using e.g., least squares prediction or spline interpolation, or mean values over surface blocks delineated by meridians and parallels are calculated. The latter case also requires the integration of the Stokes or Vening-Meinesz function over the block. After gridding, a very efficient solution is obtained in the spectral domain using Fast Fourier Transform (FFT) techniques. The convolution required in (6.148) and (6.150) becomes a simple multiplication, and the results are easily retransformed to the space domain by the inverse FFT (SCHWARZ et al. 1990, HAAGMANS et al. 1993, SÜNKEL 1997).

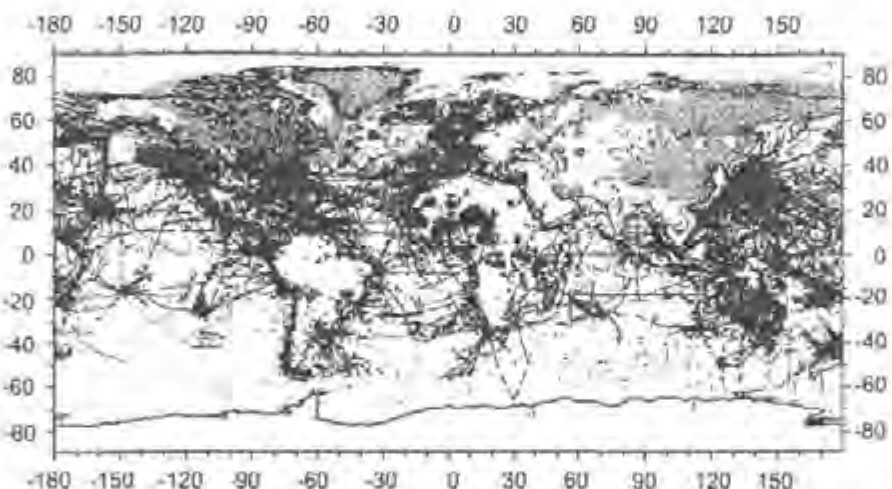


Fig. 6.31. Global distribution of terrestrial gravity data, from IAG (1997)

Point gravity anomalies (or mean gravity anomalies for some countries) are collected and kept at a few global *gravity data bases* (U.S. National Imagery and Mapping Agency NIMA: about 30 mill. point values, Bureau Gravimétrique International: about 13 mill. data freely available, Fig. 6.31). The accuracy of point anomalies derived from land, sea and airborne gravimetry varies between ± 5 and $\pm 50 \mu\text{ms}^{-2}$, cf. [5.4.4]. In order to avoid long-wave systematic errors in gravity field modeling, the anomalies have to refer to the same gravity (IGSN71), horizontal (ITRF, GRS80) and vertical reference systems, where the global vertical datum poses a special problem, cf. [3.4.3], HECK (1990).

The data gaps still existing in large parts of the oceans can be filled by the results of *satellite altimetry*, cf. [5.2.7]. For this purpose, the altimetrically derived geoid heights are transformed to gravity anomalies either by least squares collocation, cf. [6.8.2], or by a surface integral resulting from the inversion of Stokes' formula (6.148), taking (6.101b) into account (LELGEMANN 1976):

$$\Delta g_p = -\frac{\gamma_m}{R} N_p - \frac{\gamma_m}{16\pi R} \iint_{\sigma} \frac{N - N_p}{\sin^3(\psi/2)} d\sigma. \quad (6.153)$$

Here, N and N_p are the altimetric geoid heights at a particular surface element $d\sigma$ and at the computation point P , respectively. Due to the properties of the integral kernel, the influence of the more remote zones on Δg decreases rapidly. Hence, by combining the altimetric geoid heights with a global geopotential model, the integration can be restricted to a radius of a few degrees.

Altimetric gravity anomalies have been calculated for block sizes down to $5' \times 5'$ and $2' \times 2'$ from high resolution altimetry as provided by the geodetic missions of Geosat and ERS-1 (SANDWELL and SMITH 1997, ANDERSEN and KNUDSEN 1998).

Purely gravimetric or gravimetric/altimetric calculations of geoid heights and deflections of the vertical suffer from the data gaps at the polar caps, in some continental areas, and at coastal zones. They are also hampered by long-wave systematic data errors and by inhomogeneous spatial resolution and accuracy of the gravity data. Free-air anomalies on land, in addition, are rather irregular due to the gravitation of topography.

Global geopotential models, on the other hand, provide the long-wave part of the gravity field, cf. [6.6.3], and dense gravity data with station distances down to 1 to 3 km are available in many regions, usually together with high-resolution digital elevation models, cf. [6.5.2]. This leads to solutions that *combine* the global model with the gravity data in a limited region, where data smoothing techniques are used by considering the terrain effect.

Combination solutions apply the *remove-restore technique* (FORSBERG and TSCHERNING 1981, DENKER et al. 1986), which includes the following steps:

- Reduction of the gravity anomalies Δg by the anomaly part of the global model Δg_M ,
- Smoothing of the anomalies by some kind of terrain reduction Δg_T (see below),
- Gridding of the residual gravity anomalies

$$\Delta g_{\text{res}} = \Delta g - \Delta g_M - \Delta g_T, \quad (6.154)$$

- Application of Stokes' formula (6.148) on the residual gravity anomalies, resulting in residual geoid heights N_{res} ,
- Restoration of the effects of the global model and the terrain to the residual geoid heights:

$$N = N_{\text{res}} + N_M + N_T. \quad (6.155)$$

The remove-restore technique can also be applied on the deflections of the vertical or any other gravity field quantity. It has been used successfully also with least squares collocation, but for large-scale geoid modeling, integral formulas together with FFT is the only practicable technique to date.

Since the residual gravity anomalies no longer contain the long and short-wave parts of the gravity field, they are considerably smaller and smoother than the original data, and they possess (approximately) homogeneity and isotropy properties, cf. [6.1.3]. With global models complete to

degree and order 360, the integration area can be restricted to the region with dense data coverage and a narrow edge zone around it.

As only a small radius of integration is required for the remove-restore technique, a *planar approximation of Stokes' formula* is permitted. Stokes' function then reduces to

$$S(\psi) \approx \frac{1}{\sin(\psi/2)} \approx \frac{2}{\psi} \approx 2 \frac{R}{l_0}, \quad (6.156a)$$

with $l_0 = \sqrt{(x - x_p)^2 + (y - y_p)^2}$ and x_p, y_p = plane coordinates of the computation point. The spherical surface element is replaced by the planar element

$$dS = R^2 d\sigma. \quad (6.156b)$$

Inserting (6.156a) and (6.156b) into (6.148) yields *Stokes' formula in planar approximation*

$$N = \frac{1}{2\pi Y_m} \iint_S \frac{\Delta g}{l_0} dS, \quad (6.156c)$$

which is very convenient to evaluate by FFT techniques; the integration can be restricted to spherical distances of a few degrees.

Different strategies can be pursued for the application of *terrain reductions* (FORSBERG and TSCHERNING 1997).

When *Helmut's condensation method* is employed, terrain-corrected Bouguer anomalies are used for gridding, cf. [6.5.3]. After restoring the Bouguer plate term ("condensation"), Faye anomalies reduced by the effect of the global model serve for the calculation of residual geoid heights.

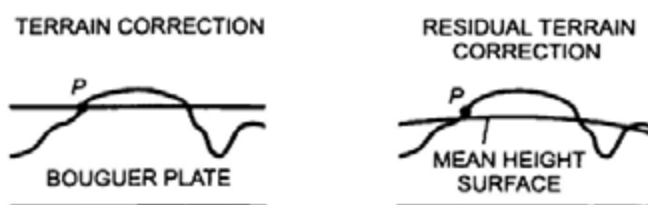


Fig. 6.32. Bouguer plate with terrain correction and residual terrain correction

With the *residual terrain correction*, only the high-frequency part of topography is taken into account in the remove-restore process, as the long-wave part has been subtracted already with the global model (FORSBERG and TSCHERNING 1981). It is calculated from a residual terrain model (RTM) which refers to a reference topography, as provided by a global topographic model (spherical harmonic expansion of the same degree and order as the geopotential model, RUMMEL et al. 1988) or the moving average over mean heights of $15' \times 15'$ or $30' \times 30'$ blocks. This procedure produces a balanced set of positive and negative anomalies (Fig. 6.32). The prism method is used generally for the calculation of the residual terrain correction, cf. [6.5.2].

If applied to Stokes' formula, the remove-restore technique implies that the complete spectrum of the geoid heights is computed from the gravity anomalies in the integration area, augmented by the values of the global model outside this region. In the case of long-wave discrepancies between the terrestrial gravity data and the global model, this leads to a distortion of the long wavelengths of the geoid. This problem is avoided by *least squares spectral combination* (SJÖBERG 1979, WENZEL 1982). Here, the long-wave spectral components of the global model and of the gravity anomalies are combined within the area of integration, using a least squares adjustment with spectral weights

$$w_i = \frac{\sigma_i^2(\varepsilon_M)}{\sigma_i^2(\varepsilon_M) + \sigma_i^2(\varepsilon \Delta g)}. \quad (6.157a)$$



Fig. 6.33. Gravimetric Geoid99 of the U.S.A., contour line interval 2 m (SMITH and ROMAN 2001), courtesy D.A. Smith, National Geodetic Survey/NOAA

The error degree variances $\sigma_i^2(\varepsilon_M)$ of the potential coefficients of the global model are estimated in analogy to (6.142), and the error degree variances of the terrestrial anomalies $\sigma_i^2(\varepsilon_{\Delta g})$ are derived from an error covariance function (WEBER 1984), in analogy to (6.25). Here, Stokes' function is extended by the spectral weights to form an optimum integral kernel

$$W(\psi) = \sum_{l=2}^{\infty} \frac{2l+1}{l-1} w_l P_l(\cos \psi). \quad (6.157b)$$

This function is no longer infinite at $\psi = 0^\circ$, and it converges to zero more rapidly than the original Stokes' function, see Fig. 6.33.

Early gravimetric geoid calculations with Stokes' formula are due to *Hirvonen* (1934) and *Tanni* (1948). Based on isostatic anomalies, the "Columbus Geoid" was calculated at the Ohio State University (HEISKANEN 1957). A combination of a low-degree satellite model (Goddard GEM-6, degree and order 16) with $1^\circ \times 1^\circ$ free-air gravity anomalies (integration radius 10°) was presented by *MARSH* and *VINCENT* (1974). Among the recent regional solutions is the gravimetric geoid for the U.S.A.. It is based on a $2' \times 2'$ grid of Faye anomalies, constructed from Bouguer anomalies, and employs the EGM96 model as a global reference, cf. [6.6.3], Fig. 6.33. This geocentric geoid, accurate to about 0.2 m, also has been fitted to the North American vertical datum, cf. [7.2], *SMITH* and *MILBERT* (1999). Least squares spectral combination has been applied in the calculation of a European quasigeoid, cf. [6.7.2].

6.7.2 Gravimetric Height Anomalies and Surface Deflections of the Vertical

The geodetic boundary-value problem for the *physical* surface of the earth has been formulated by *M.S Molodenski*, through the integral equation (6.92), MOLODENSKI et al. (1962). By introducing the telluroid Σ as an approximation to the earth's surface, an integral equation for the disturbing potential was obtained (6.93). In contrast to the derivative $\partial T / \partial n$ (n = normal to the level surface), the derivative $\partial T / \partial n_\Sigma$ (n_Σ = normal to the telluroid) now not only depends on the gravity anomaly but also on the deflection of the vertical and the inclination of the terrain. Inserting $\partial T / \partial n_\Sigma$ into (6.93) yields (HEISKANEN and MORITZ 1967, p.299)

$$\left. \begin{aligned} & T - \frac{1}{2\pi} \iint_{\Sigma} \left(\frac{\partial}{\partial n_\Sigma} \left(\frac{1}{l} \right) - \frac{1}{\gamma} \frac{\partial \gamma \cos \beta}{\partial h} \right) T d\Sigma \\ & = \frac{1}{2\pi} \iint_{\Sigma} \frac{1}{l} \left(\Delta g - \gamma (\xi \tan \beta_x + \eta \tan \beta_y) \cos \beta \right) d\Sigma \end{aligned} \right\}, \quad (6.158)$$

with β_x, β_y = angle of terrain inclination in NS and EW-direction, β = angle of maximum inclination, and ξ, η = vertical deflection components.

A simpler integral equation can be derived by expressing T as the potential of an infinitely thin *surface layer* condensed on the telluroid. With the surface density μ (6.113), the law of gravitation (3.10) yields

$$T = G \iint_{\Sigma} \frac{\mu}{l} d\Sigma. \quad (6.159)$$

As the potential of a surface layer is harmonic outside the surface, Laplace's equation is fulfilled, and we may introduce (6.159) and its normal derivative into (6.101). This strategy results in an integral equation which only depends on Δg and on the terrain inclination. It can be solved by successive approximation, leading to a series expansion for T (MORITZ 1971). With Bruns' formula (6.96), the corresponding development for the height anomaly ζ is obtained. In spherical approximation (σ = unit sphere, R = earth's radius), and limiting the series to its first two terms, the *height anomaly* is given by

$$\zeta = \frac{R}{4\pi\gamma} \iint_{\sigma} (\Delta g + G_1) S(\psi) d\sigma + \dots, \quad (6.160a)$$

where $S(\psi)$ is Stokes' function (6.147). The main term corresponds to Stokes' formula as applied to the surface gravity anomalies (6.14). The first correction term, in close approximation, is

$$G_1 = \frac{R^2}{2\pi} \iint_{\sigma} \frac{H^N - H_r^N}{l_0^3} \Delta g d\sigma, \quad l_0 = 2R \sin \frac{\psi}{2}. \quad (6.160b)$$

It depends on the terrain inclination (H^N = normal height) and on gravity anomalies. Assuming a linear correlation of the gravity anomalies with height, G_1 can be approximated by the gravimetric terrain correction (6.112), MORITZ (1968b), SIDERIS (1990). Hence, Faye anomalies, cf. [6.5.3], are well suited for the computation of height anomalies.

Since the integral kernel in (6.160b) decreases rapidly with increasing spherical distance ψ , the integration can be restricted to a limited area. Higher-order terms in (6.160) contain the tangent of the terrain inclination and can be neglected generally. In order to ensure convergence of Molodenski's series expansion, extreme inclinations and singularities (steep slopes) need to be removed by some smoothing procedure. The Molodenski correction terms reach the dm-order of magnitude in the high mountains and remain at the cm-order in the lowlands. If the remove-restore technique, cf. [6.7.1], is applied, the corrections reduce by about one-order of magnitude and the series convergence is significantly improved.

Molodenski's problem has been thoroughly investigated by MORITZ (1971) and others, and the existence and uniqueness of the solution was proved by HÖRMANDER (1976) and SANSØ (1988).

A very efficient method for calculating the height anomaly is provided by the "gradient solution" (MORITZ 1980). Here, the surface gravity anomalies are first reduced to sea level (geoid or quasigeoid); then Stokes' integral is applied, leading to height anomalies on sea level. An upward continuation finally gives the surface height anomaly:

$$\zeta = \frac{R}{4\pi\gamma} \iint_{\sigma} \left(\Delta g - \frac{\partial(\Delta g)}{\partial H} H \right) S(\psi) d\sigma + \frac{\partial \zeta}{\partial H} H. \quad (6.161a)$$

The radial derivative of Δg is given by

$$\frac{\partial(\Delta g)}{\partial H} = \frac{R^2}{2\pi} \iint_{\sigma} \frac{\Delta g - \Delta g_p}{l_0^3} d\sigma \quad (6.161b)$$

and again can be approximated by the terrain correction (see above). The vertical gradient of ζ results from (6.96) and (6.101):

$$\frac{\partial \zeta}{\partial H} = \frac{\partial}{\partial H} \left(\frac{T}{\gamma} \right) = \frac{1}{\gamma} \left(\frac{\partial T}{\partial H} - \frac{1}{\gamma} \frac{\partial \gamma}{\partial H} T \right) = -\frac{\Delta g}{\gamma}, \quad (6.161c)$$

where Δg is the surface gravity anomaly. If the surface anomalies are reduced to the level of the computation point P , H in (6.161a) has to be substituted by $H - H_p$. The last term in (6.161a) then vanishes, as H outside the integral means H_p :

$$\zeta = \frac{R}{4\pi\gamma} \iint_{\sigma} \left(\Delta g - \frac{\partial(\Delta g)}{\partial H} (H - H_p) \right) S(\psi) d\sigma. \quad (6.161d)$$

These solutions are particularly well suited for FFT techniques (FORSBERG and TSCHERNING 1997).

The *surface deflection of the vertical* (see Molodenski's definition in [6.1.2]) is derived from (6.160) by differentiation according to (6.98):

$$\begin{Bmatrix} \xi^N \\ \eta^N \end{Bmatrix} = \frac{1}{4\pi\gamma} \iint_{\sigma} (\Delta g + G_i) \frac{dS(\psi)}{d\psi} \begin{Bmatrix} \cos \alpha \\ \sin \alpha \end{Bmatrix} d\sigma - \frac{\Delta g}{\gamma} \begin{Bmatrix} \tan \beta_x \\ \tan \beta_y \end{Bmatrix}. \quad (6.162)$$

The principal term is Vening-Meinesz' formula (6.150), and the Molodenski correction terms again take the effect of the terrain into account, reaching a few arcsec.

Molodenski's problem is characterized by the fact that no assumptions on the density distribution within the earth are necessary, in contrast to the geoid determination using Stokes' formula. By the relation (6.9) between the geoid and the quasigeoid, a simple method is available to derive geoid heights from height anomalies:

$$N = \zeta + \frac{\Delta g_s}{\gamma} H$$

Data reductions onto the geoid and calculations of indirect effects are avoided by this strategy, and density hypotheses enter only through the Bouguer anomaly Δg_s . On a large scale, the Bouguer anomalies are negative on the continents, cf. [8.2.4], hence the quasigeoid generally is above the geoid. The differences between the geoid and the quasigeoid are of the cm to dm-order of magnitude in flat and hilly regions but may assume one meter and more in the mountains. As the quasigeoid is highly correlated with the height, the quasigeoid mirrors the topography.

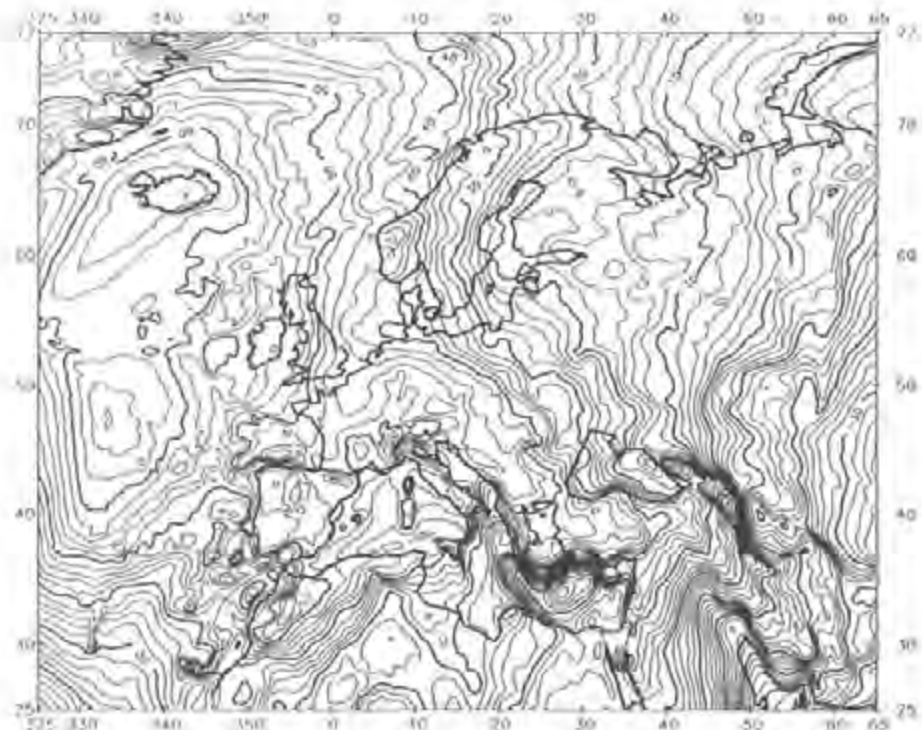


Fig. 6.34. European gravimetric quasigeoid EGG97 (DENKER and TORGE 1998): contour line interval 2 m

One example for a large-region quasigeoid determination is the European Gravimetric Quasigeoid EGG97 (DENKER and TORGE 1998). It is based on a high-resolution data set of point and mean gravity anomalies derived from surface gravimetry and satellite altimetry in the marine areas. The remove-restore technique was applied using the EGM96 geopotential model and a $15' \times 15'$ moving average reference topography. Gridded $1' \times 1.5'$ residual gravity anomalies were transformed to height anomalies by least squares spectral combination, cf. [6.7.1]. The main part of EGG97 (Fig. 6.34) stems from the global model, but the contributions from terrestrial gravity data and topography still amount to ± 0.4 m (maximum 4 m) and ± 0.03 m (maximum 0.8 m), respectively. The error estimates (\pm a few cm/100 km to ± 0.1 m/1000 km) were confirmed by comparisons with GPS/leveling control points, e.g., on the European NS-GPS-traverse between Munich and Tromsø (TORGE et al. 1989).

6.7.3 The External Gravity Field

The gravity field outside the earth is modeled by *upward continuation* from the boundary surface, either globally or locally.

Global modeling employs the spherical harmonic expansion of the disturbing potential (6.4) and the corresponding expansions for the height anomaly (6.131) and the gravity anomaly (6.135). These expansions converge outside a sphere enclosing the earth, cf. [3.3.2]. They are especially useful for the orbit determination of satellites, but the present limited spatial resolution makes them less suited for low altitudes, e.g., for airborne applications.

For *local modeling*, we start with the *free-air anomaly* Δg , where according to (6.134) the function

$$r \Delta g = \sum_{l=2}^{\infty} (l-1) \left(\frac{a}{r} \right)^{l+1} T_l(\vartheta, \lambda) \quad (6.163)$$

is harmonic in space. The calculation of gravity anomalies in space from boundary values thus corresponds to the first boundary-value problem (*Dirichlet problem*) of potential theory. The solution is given by *Poisson's integral*. In spherical approximation we have

$$\Delta g_p = \frac{R^2 (r_p^2 - R^2)}{4\pi r_p} \iint_{\sigma} \frac{\Delta g}{l^3} d\sigma, \quad (6.164)$$

where Δg_p refers to the point P in space and Δg are the surface anomalies on the spherical boundary surface. The integral kernel decreases rapidly with ψ , which allows restriction of the integration area on a limited zone around the computation point.

By inserting (6.164) into (6.101b) we obtain

$$\Delta g = -\frac{\partial T}{\partial r} - \frac{2}{r} T, \quad (6.165)$$

which now represents a differential equation in *space*. The solution leads to a spatial extension of Stokes' formula for the *disturbing potential*, which was derived by *Pizetti*:

$$T(r, \vartheta, \lambda) = \frac{R}{4\pi} \iint_{\sigma} S(r, \psi) \Delta g \, d\sigma, \quad (6.166a)$$

where

$$S(r, \psi) = \frac{2R}{l} + \frac{R}{r} - \frac{3Rl}{r^2} - \frac{R^2}{r^2} \cos \psi \left(5 + 3 \ln \frac{r - R \cos \psi + l}{2r} \right), \quad (6.166b)$$

with

$$l = \sqrt{r^2 + R^2 - 2Rr \cos \psi}, \quad (6.166c)$$

is the extended Stokes' function.

Bruns' theorem finally gives the separation between the geopotential surface $W = W_p$ and the spheropotential surface $U = U_q = W_p$ (*height anomaly* in space):

$$\zeta(r, \vartheta, \lambda) = \frac{R}{4\pi\gamma} \iint_{\sigma} S(r, \psi) \Delta g \, d\sigma. \quad (6.167)$$

Corresponding relations can be derived for the gravity disturbance and the deflection of the vertical, using (6.98) and (6.99).

6.7.4 Astrogeodetic Geoid and Quasigeoid Determination

Geoid and quasigeoid height *differences* can be obtained from deflections of the vertical, determined according to (6.17) from astronomic and geodetic latitudes and longitudes.

In *astronomic leveling*, the deflections of the vertical are integrated along the path, either on the geoid or on the earth's surface (Fig. 6.35). On the *geoid*, we have

$$dN = -\varepsilon_0 ds, \quad (6.168a)$$

where ε_0 is the vertical deflection component in the azimuth of the path (6.18), reduced to the geoid according to Pizetti's definition, cf. [6.1.2]. Integration between P_1 and P_2 yields the geoid height difference

$$\Delta N_{1,2} = N_2 - N_1 = - \int_1^2 \varepsilon_0 ds. \quad (6.168b)$$

The negative sign follows from the sign conventions for the geoid height (6.8) and the deflection of the vertical (6.17).

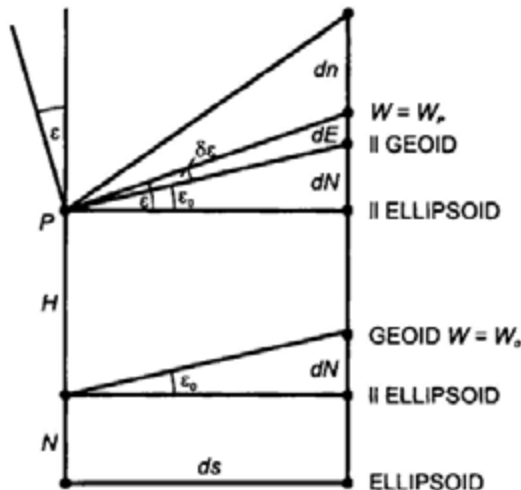


Fig. 6.35. Astronomic leveling

The *geoidal deflection of the vertical* is obtained by *reducing* the observed astronomic latitude and longitude onto the geoid:

$$\Phi_0 = \Phi + \delta\Phi, \quad \Lambda_0 = \Lambda + \delta\Lambda, \quad (6.169)$$

where Φ_0 and Λ_0 are the astronomic coordinates on the geoid (Fig. 6.36). The reductions follow from the integration of the plumb line curvature κ_x , κ_y , between the earth's surface and the geoid (3.74):

$$\delta\Phi = - \int_0^H \kappa_x dH, \quad \delta\Lambda = - \int_0^H \kappa_y dH, \quad (6.170a)$$

H = orthometric height. Inserting (3.67) and (3.70) yields

$$\delta\Phi = -\frac{1}{R} \int_0^H \frac{1}{g} \frac{\partial g}{\partial \Phi} dH, \quad \delta\Lambda = -\frac{1}{R \cos \Phi} \int_0^H \frac{1}{g} \frac{\partial g}{\partial \Lambda} dH, \quad (6.170b)$$

R = mean radius of the earth. With (6.17), the NS and EW-components of the vertical deflection are given by

$$\xi_0 = \xi + \delta\Phi, \quad \eta_0 = \eta + \cos \Phi \delta\Lambda, \quad (6.171a)$$

and the azimuthal component reads

$$\varepsilon_0 = \xi_0 \cos \alpha + \eta_0 \sin \alpha. \quad (6.171b)$$

In order to evaluate (6.170), the gravity and the horizontal gravity gradient along the plumb line are required. Digital terrain models allow estimation of these quantities with an accuracy between $0.1''$ and $1''$, but errors may be larger in the high mountains. The angle of plumb line curvature itself attains values of a few $0.1''$ in the lowlands and may reach $10''$ and more at high mountain stations.

Instead of integrating the deflections of the vertical on the geoid, the *surface* vertical deflections (definitions from Helmert or from Molodenski) may be used. *Helmert* deflections of the vertical are given by

$$\varepsilon = \varepsilon_0 - \delta\varepsilon, \quad (6.172)$$

where the components of $\delta\varepsilon$ are obtained from (6.170b). Inserting into (6.168b) yields

$$\Delta N_{1,2} = N_2 - N_1 = - \int_1^2 \varepsilon ds - \int_1^2 \delta\varepsilon ds. \quad (6.173a)$$

As seen from Fig. 6.36, the second term on the right side equals the orthometric height reduction E known from geometric leveling (6.81b); the angle of plumb line curvature is the horizontal derivative of E . We thus have

$$\Delta N_{1,2} = - \int_1^2 \varepsilon ds - E_{1,2}. \quad (6.173b)$$

For *height anomalies*, the difference follows from the differential (MORITZ 1983)

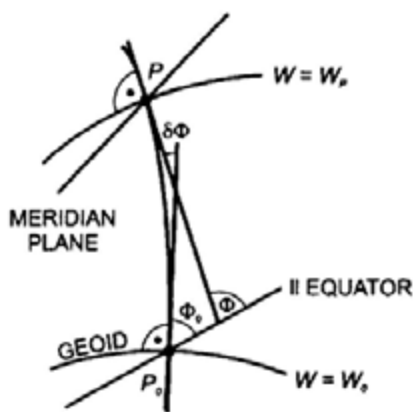


Fig. 6.36. Plumb line curvature in the meridian plane

$$d\zeta = \frac{d\zeta}{ds} ds + \frac{d\zeta}{dh} dh . \quad (6.174)$$

The first term describes the effect of Molodenski's vertical deflection. The second term enters because the physical surface of the earth is not a level surface. Using (6.161c) and integration along the path yields Molodenski's astronomic leveling of height anomalies

$$\Delta\zeta_{1,2} = \zeta_2 - \zeta_1 = - \int_1^2 \varepsilon^N ds - \int_1^2 \frac{\Delta g}{\gamma} dh . \quad (6.175)$$

The relation between geoid and quasigeoid height differences follows from (6.9) and (6.81):

$$\Delta\zeta_{1,2} = \Delta N_{1,2} + E_{1,2} - E_{1,2}^N \quad (6.176a)$$

or when taking (6.173b) into account

$$\Delta\zeta_{1,2} = - \int_1^2 \varepsilon ds - E_{1,2}^N , \quad (6.176b)$$

where $E_{1,2}^N$ is the normal height reduction.

As the small corrections in (6.173), (6.175), and (6.176) can be derived easily from surface gravity and a digital terrain model, the integration of surface vertical deflections is of advantage compared to the tedious reductions onto the geoid required in (6.168).

The line integrals of astronomic leveling presuppose that the deflections of the vertical are given continuously along the path. In reality, vertical deflections are available only at larger distances (several 10 km or more), which is due to the time-consuming astronomic observations. This poses the problem of *interpolation* between the vertical deflection points (in the following we do not distinguish between the vertical deflections on the geoid and on the earth's surface). Interpolation can be carried out by purely mathematical methods or supported by additional information on the gravity field behavior.

In the simplest case of *mathematical interpolation*, a linear change of the deflections of the vertical between the stations P_1 and P_2 is assumed. The integration then yields

$$\Delta N_{1,2} = -\frac{\varepsilon_1 + \varepsilon_2}{2} s, \quad (6.177)$$

where s is the distance between P_1 and P_2 .

The linear interpolation model is adequate in flat areas and where the distances between the vertical deflection points are not too large (some km to some 10 km). An area with sufficient control point coverage can be evaluated either by forming triangles and adjusting the geoid height misclosures or by a surface polynomial approximation to the geoid (VANIČEK and MERRY 1973). The polynomial coefficients are determined from the corresponding series expansions of the vertical deflection components, which result from (6.98) and Bruns' formula

$$\xi = -\frac{1}{R} \frac{\partial N}{\partial \varphi}, \quad \eta = -\frac{1}{R \cos \varphi} \frac{\partial N}{\partial \lambda}, \quad (6.178)$$

where the condition of integrability of a potential field, cf. [3.1.5] must be heeded:

$$\frac{\partial \xi}{\cos \varphi \partial \lambda} = \frac{\partial \eta}{\partial \varphi}. \quad (6.179)$$

Least squares prediction, cf. [6.1.3], offers another efficient interpolation method (HEITZ 1969), while least squares collocation, cf. [6.8.2], even allows direct estimation of geoid heights from the vertical deflections, thus providing an alternative to the integral formulas.

Additional *gravity field information* between the vertical deflection points can be supplied by terrain models, gravity anomalies, and zenith angles.

A digital *terrain model* (possibly also taking density variations into account) can be used to calculate the effect of topography on the deflections of the vertical. For more extended calculation areas, the effect of isostatically

compensating masses should also be considered, cf. [6.5.2]. By subtracting these effects from the observations, the vertical deflection field is smoothed, and mathematical interpolation methods may be applied. The interpolated residual deflections of the vertical are augmented by the effects of topography and isostasy, leading to a densified network of vertical deflection points. This remove-restore method has proved to be efficient especially in mountainous areas; an interpolation accuracy of 1 to 2 arcsec can be achieved.

If a dense field of gravity stations around the vertical deflection points is available, it can be utilized for a *gravimetric* interpolation. Here, gravimetric deflections of the vertical are computed according to (6.150) by integrating the gravity anomalies over a limited area (e.g., three times the distance between the vertical deflection points). This gravimetric part is then removed from the observations, and a systematic difference between the astrogeodetic and the gravimetric vertical deflections has to be taken into account (different reference systems, effect of the zones neglected in the calculation of the gravimetric vertical deflections). The residual deflections of the vertical thus obtained are smooth and easy to interpolate. This method has been extended to *astrogravimetric leveling*, with a gravimetric “correction” to quasigeoid differences obtained from linear interpolation of surface deflections of the vertical (MOLODENSKI et al. 1962). Gravimetric interpolation allows calculation of geoid or quasigeoid height differences with cm to dm accuracy, even at larger spacing of the vertical deflection points.

Reciprocal *zenith angles* deliver differences of the vertical deflection components ε in the line of sight. According to (6.85), the observed zenith angles z and the ellipsoidal quantities ζ are related by (Fig. 6.20)

$$\zeta_1 = z_1 + \varepsilon_1, \quad \zeta_2 = z_2 + \varepsilon_2.$$

Inserting the above relations into (6.87), and taking sign conventions into account, yields

$$\varepsilon_2 - \varepsilon_1 = z_1 + z_2 - \frac{S}{R} - \pi, \quad (6.180)$$

where S = spherical distance between P_1 and P_2 . Starting at a vertical deflection point, these differences can be used for the interpolation of deflections of the vertical. The method has found limited application in mountainous areas, where an interpolation accuracy of about one arcsec has been achieved (GLEINSVIK 1960).

The advantage of the astrogeodetic method of geoid determination consists in its independence from data outside the area of calculation, in contrast to the

gravimetric method where a global coverage with gravity data is needed. In addition, the demands on the accuracy of the point heights are less stringent as with the formation of gravity anomalies. On the other hand, the establishment of a vertical deflection point requires substantially more time than a gravity measurement. A station spacing of 10 to 20 km is available only in few regions, and even distances of up to 30 to 50 km are limited to well surveyed countries. Large parts of the continents are covered only sparsely, with concentration on profiles along first-order triangulation chains, cf. [7.1.1]. Thus, the *accuracy* of astronomic leveling depends entirely on the quality of interpolation. In densely surveyed areas, an accuracy of \pm a few cm to 0.1 m over some 100 km can be achieved (BÄUMKER 1984, ELMIGER and GURTNER 1983). The accuracy can be increased by topographic-isostatic reductions, including geological information on rock densities. By fitting the results to GPS/leveling control points, the geoid heights are referred to the national vertical datum and systematic effects are reduced, which increases the accuracy to \pm 0.01 to 0.02 m over several 100 km (GROTE 1996).

The superior efficiency of gravimetric methods has greatly reduced the application of astronomic leveling. It is now restricted to areas or profiles which are not well covered by gravity data or where the coverage is not representative, as in the mountains where gravity stations are typically concentrated along the roads.

Astronomic leveling was introduced by HELMERT (1884) and first applied in the Harz mountains, Germany. From the 1950's to the 1970's, astrogeodetic geoid determinations were carried out in a number of countries, using astronomic observations on the first-order triangulation points (HEITZ 1969). Deflections of the vertical, and the resulting geoid, referred to the national geodetic datum and served for the reduction of horizontal angles and chord distances onto the national reference ellipsoid, cf. [6.3.2], [7.1.2]. Large-scale solutions included the "Bomford" geoid for Europe (LEVALLOIS and MONGE 1975) and the continent-wide geoid determination by FISCHER et al. (1968), with an average accuracy of a few meters. High precision astrogeodetic geoid models have been developed in Switzerland and Austria, based on a densified net of vertical deflection points and high-resolution digital terrain models and employing remove-restore techniques (ERKER 1987, MARTI 1997).

6.8 Combined Methods for Positioning and Gravity Field Determination

Combined evaluation methods permit simultaneous determination of positions and the gravity field. These quantities are eventually combined with systematic model parameters within *one* mathematical model. By introducing geometrical and gravity field observations, the information content of the data is more completely exhausted. On the other hand, the large amount of data and

unknown parameters raises serious problems with respect to proper weighting of the observations, modeling of systematic effects, and data processing. Hence, the application of the combination methods is still restricted to a limited number of parameters and observations.

A functional combination model is based on the observation equations for all relevant data and uses least squares adjustment for the determination of earth models and optimum earth parameters [6.8.1]. In least squares collocation, a stochastic model for gravity field estimation is added, which leads to a very general method of combination [6.8.2].

6.8.1 Earth Models and Optimum Earth Parameters

"Earth models" are determined by rigorous least squares adjustment from satellite tracking data, either alone or in combination with satellite altimetry and surface gravity. They contain the coordinates of the tracking stations and station velocities, the parameters of a low-degree gravity field model, as well as ocean tidal and earth rotation parameters, cf. [6.6.2].

Using the latest supercomputers, present earth models include about 5000 geopotential coefficients and about 10000 parameters in total. The coordinates of the tracking stations are determined with cm-accuracy, and station velocities are accurate to a few mm/a. The long-wave part of the geoid (wavelength > 550 km) is accurate to about ± 0.9 m on the continents and ± 0.3 m on the oceans.

Combination solutions also provide *actual* values of a *model earth*, as represented by a level ellipsoid with optimum approximation to the geoid and the external gravity field, cf. [4.2.1]. These actual values must not be confused with the parameters of a geodetic reference system, recommended as a standard for a longer time interval, cf. [4.3]. The best estimates (1999) for the defining parameters of a level ellipsoid are as follows (GROTE 2000):

- The *geocentric gravitational constant*

$$GM = (398\,600.442 \pm 0.001) \times 10^8 \text{ m}^3\text{s}^{-2}$$

including the mass of the atmosphere. This value is derived from orbit analyses of satellites and space probes. A variation of GM with time has not been found,

- The *equatorial radius* of the earth

$$a = 6\,378\,136.6 \pm 0.1 \text{ m}.$$

The radius is determined by an optimal fit between ellipsoidal heights and orthometric heights, as obtained for satellite tracking stations on the continents, and from satellite altimetry on the oceans, applying the minimum condition

$$\iint_{\sigma} N^2 \, d\sigma = \min . \quad (6.181)$$

on the geoid heights. According to [6.5.4], the *geoid potential* W_0 could also be introduced as a defining parameter if GM and a are known:

$$W_0 = 62\,636\,856.0 \pm 0.5 \text{ m}^2\text{s}^{-2} .$$

a and W_0 are given in the zero-tide system, which contains the indirect tidal distortion, cf. [3.4.1]. The equatorial radius and the geoid potential can be assumed constant with time.

- The second-degree zonal harmonic coefficient (*dynamical form factor*)

$$J_2 = (1082.6267 \pm 0.0001) \times 10^{-6}$$

in the tide-free system and

$$J_2 = (1082.6359 \pm 0.0001) \times 10^{-6}$$

in the zero-tide system. J_2 is obtained from global gravity models, cf. [6.6]. A long-term temporal change of J_2 was found from the analysis of satellite orbits over long time intervals:

$$\dot{J}_2 = dJ_2/dt = -(2.6 \pm 0.3) \times 10^{-9} / \text{cy} .$$

- The mean angular velocity of the *earth's rotation*

$$\omega = 7.292\,115 \times 10^{-5} \text{ rad s}^{-1}$$

is provided by the International Earth Rotation Service, cf. [2.2.2]. It experiences a long-term variation

$$\dot{\omega} = d\omega/dt = (-4.5 \pm 0.1) \times 10^{-22} \text{ rad s}^{-2} ,$$

which may be decomposed into a component due to tidal dissipation ($-6.1 \times 10^{-22} \text{ rad s}^{-2}$) and a non-tidal part ($+1.6 \times 10^{-22} \text{ rad s}^{-2}$) probably reflecting the postglacial rebound of the earth's crust and mantle.

Among the quantities derived from the defining parameters we have

- The reciprocal flattening

$$1/f = 298.25642 \pm 0.000\,01$$

and

- The *normal gravity* at the equator

$$\gamma_a = 9.780\,327 \pm 0.000\,001 \text{ ms}^{-2}.$$

The *minimum conditions* for the deflections of the vertical

$$\iint_{\sigma} (\xi^2 + \eta^2) d\sigma = \min \quad (6.182)$$

and the gravity anomalies

$$\iint_{\sigma} \Delta g^2 d\sigma = \min, \quad (6.183)$$

in principle, could also serve to derive the parameters of a best approximating ellipsoid (HEISKANEN and MORITZ 1967, p.216). While (6.182) has been used for the determination of local reference ellipsoids in classical national geodetic surveys, cf. [7.1.2], (6.183) has not been exploited due to lacking global gravity coverage.

6.8.2 Least Squares Collocation

Least squares collocation combines the calculation of station coordinates and other deterministic unknowns (harmonic coefficients, earth ellipsoid and earth orientation parameters, calibration and drift coefficients, etc.) with the estimation of gravity field quantities of unsurveyed points, utilizing many types of observables (KRARUP 1969, MORITZ 1973). The general form of the *observation equation* reads

$$\mathbf{l} = \mathbf{Ax} + \mathbf{s} + \mathbf{n}, \quad (6.184)$$

where \mathbf{l} is the linearized vector of observations. It is composed of the deterministic part \mathbf{Ax} (\mathbf{x} = parameter vector, \mathbf{A} = design matrix containing the differential relations between observations and parameters) and two random parts. The signal vector \mathbf{s} contains the residual gravity field quantities at any point, either observed or to be predicted. It may include, in contrast to least squares prediction, any kind of gravity field quantities such as residual harmonic coefficients, geoid or quasigeoid heights, gravity anomalies, deflections of the vertical, etc. The noise vector \mathbf{n} represents the observational errors. Each of the random quantities is supposed to have a mean value of zero. The statistical behavior is described by the covariance matrix \mathbf{C} of the signals and the covariance matrix \mathbf{D} of the noise, where mutual independence of signal and noise is assumed, cf. [6.1.3].

After linearization with a geodetic earth model, all geodetic observations can be expressed in the form (6.184). The observation equations for leveled heights, gravity, astronomic latitudes, longitudes, and azimuths, satellite tracking data, VLBI observations, zenith angles, and spatial distances are found in the corresponding sections of [6]. While all observations depend on position (described by the geodetic coordinates in connection with the parameters of the ellipsoid), a dependence on the gravity field does not exist with VLBI observations and spatial distances. A complete set of observation equations is given by GRAFarend (1978).

Least squares collocation is an overdetermined problem with respect to the parameters (number of observations exceeds the number of parameters) and an underdetermined problem with respect to the gravity field signal (more signals have to be predicted than have been observed). It is solved by applying a least squares minimum condition on the weighted quadratic sum of the signal part and the noise, thus combining least squares adjustment with least squares prediction (MORITZ 1980). The solution for the *parameter vector* is given by

$$\mathbf{x} = (\mathbf{A}^T \bar{\mathbf{C}}^{-1} \mathbf{A})^{-1} \mathbf{A}^T \bar{\mathbf{C}}^{-1} \mathbf{l}, \quad (6.185)$$

with $\bar{\mathbf{C}} = \mathbf{C} + \mathbf{D}$. The component of the *signal vector* predicted in an unsurveyed point results in

$$\hat{\mathbf{s}}_p = \mathbf{C}_p^T \bar{\mathbf{C}}^{-1} (\mathbf{l} - \mathbf{Ax}), \quad (6.186)$$

where the covariance vectors and matrices are explained in [6.1.3] but now may include heterogeneous signals.

The simultaneous determination of station coordinates and gravity field quantities has been designated as "integrated" or "operational" geodesy (EEG and KRARUP 1973, HEIN 1986). The main problem in its practical application is the solution of a system of equations with a dimension equal to the number of

observations for the inversion of the covariance matrix $\bar{\mathbf{C}}$. By separation into subsystems with low correlation (e.g., horizontal positioning on the one hand, and height respectively gravity field determination on the other), the dimension of the system of equations can be reduced significantly. This strategy leads to least squares adjustment for the deterministic part, and offers an efficient and flexible solution for gravity field determination, which is used extensively in various applications.

If applied to *gravity field estimation*, the elements of the signal covariance matrix \mathbf{C} are required, describing the correlation between heterogeneous residual gravity field quantities. Since all these quantities belong to the same gravity field, the covariances have to be derived from a basic covariance function through covariance propagation. The *covariance function* of the *disturbing potential* T is selected for this purpose, as all residual gravity field quantities are related to T in a simple manner. This covariance function is defined in analogy to the covariance function of the gravity anomalies (6.21). It is considered to be the mean value of the products of T in the points P and P' for a constant spherical distance ψ and assumes homogeneity and isotropy. The function is given by:

$$K(\psi) = \text{cov}(T, T', \psi) = M\{T \cdot T'\}_\psi. \quad (6.187)$$

Covariance propagation is well known from the theory of errors and is applied here to gravity field signals. As demonstrated by (6.96) to (6.101), the residual gravity field quantities (either observed or to be predicted) can be expressed as a linear functional of T . For an *observation* l_i , we thus have

$$l_i = L_i^P T(P'), \quad (6.188)$$

where L_i is the functional to be applied to T in order to transform T into the observed quantity. The covariance between T and l_i is obtained by applying L_i on the covariance function $K(\psi) = K(P, P')$, which can be expressed as a function of the coordinates of P and P' in space:

$$C_{pi} = M\{T \cdot l_i\} = L_i^P K(\psi). \quad (6.189)$$

For different types of observation at P and P' , the covariance results from a subsequent application of the functionals L valid for the transformation of T into the respective observation:

$$C_{ij} = M\{l_i \cdot l_j\} = L_i^P L_j^{P'} K(\psi). \quad (6.190)$$

The same rules have to be followed if heterogeneous signals shall be estimated.

A statistical description of the earth's gravity field is available by anomaly degree variance models, cf. [6.1.3]. The relation of these models to the basic covariance function can be derived by applying the mean value operator (6.187) on the spherical harmonic expansion of the disturbing potential (6.4). This yields

$$K(\psi) = \sum_{l=2}^{\infty} \sigma_l^2(T) \left(\frac{R^2}{rr'} \right)^{l+1} P_l(\cos\psi), \quad (6.191a)$$

where the potential degree variances are defined in analogy to (6.26):

$$\sigma_l^2(T) = M\{T_l^2\}. \quad (6.191b)$$

Equation (6.142) provides the relation between the degree variances of the disturbing potential and the gravity anomalies:

$$\sigma_l^2(T) = \left(\frac{R}{l-1} \right)^2 \sigma_l^2(\Delta g), \quad (6.192)$$

where we have taken Bruns' formula $N = T/\gamma$ into account. Inserting (6.192) into (6.191) yields

$$K(\psi) = R^2 \sum_{l=2}^{\infty} \frac{1}{(l-1)^2} \sigma_l^2(\Delta g) \left(\frac{R^2}{rr'} \right)^{l+1} P_l(\cos\psi), \quad (6.193)$$

which enables the calculation of the basic covariance function from an anomaly degree variance model. For local applications, the covariance function has to be fit to the gravity field behavior in the area of calculation, cf. [6.1.3].

The advantage of least squares collocation is the flexibility in estimating any kind of gravity field quantity from different types of gravity field observations, at surveyed and unsurveyed points. The data can be processed as discrete values and need not be continuous, as required for the application of integral formulas, cf. [6.7]. Neither gridding of the data nor reduction to some reference level is required. For homogeneous and continuously distributed data, least squares collocation transforms into the integral formulas (MORITZ 1976). On the other hand, the amount of data that can be handled is still limited by computing facilities. Applications have therefore been restricted to limited areas and data sets. By introducing some restrictions on the data, computing time can be

reduced and larger data sets evaluated: fast collocation (BOTTONI and BARZAGHI 1993, GROTE 1996).

Least squares collocation has been applied especially for local and regional geoid determination (RAPP 1978, ARABELOS 1980, TSCHERNING and FORSBERG 1986, DENKER 1988), but also for the estimation of gravity anomalies from altimetric geoid heights and for downward continuation problems. Remove-restore techniques are used generally, cf. [6.7.1], which reduces the data collection area.

7 Geodetic and Gravimetric Networks

Geodetic and gravimetric networks consist of monumented control points that provide the reference frames for positioning and gravity-field determination at all scales. Global networks allow realization of the reference systems defined by international conventions. Regional networks form the fundamental basis for national or supranational (continental) geodetic and gravimetric surveys, which are the basis of geo-information systems and map series. Local networks are typically established for engineering and exploration projects and for geodynamic investigations.

In the sequel we concentrate on regional networks, which are increasingly integrated into global reference-frames established for positioning, navigation, cf. [2.5.3], and gravity, cf. [5.4.3]. Horizontal and vertical control networks have been established separately, following the classical treatment of positioning and heighting; these networks still are the basis of national geodetic systems [7.1], [7.2]. Geodetic space methods allow establishment of three-dimensional networks within the geocentric reference system and are now superseding the classical control networks [7.3]. Gravity networks serve the needs of geodesy and geophysics, with the reference provided either by a global network or by absolute gravimetry [7.4].

If reobserved after a certain time span, geodetic and gravimetric networks can be utilized for the investigation of long-term changes of position and gravity with time. Specially designed networks have been set up on global, regional, and local scale in order to monitor geodynamic processes of different origins, cf. [8.3.3].

The establishment of geodetic networks is treated in textbooks on geodesy and geodetic surveying (BOMFORD 1980, KAHMEN and FAIG 1988, HECK 1995, LEICK 1995); for gravity networks see TORGE (1989, 1998).

7.1 Horizontal Control Networks

National horizontal control networks were established from the 18th century until the 1960's, with the networks' design, observation, and computation changing with the available techniques [7.1.1]. Computations were carried out on a reference ellipsoid fitted to the survey area. Since the 1960's, spatial geodetic methods have allowed orientation of the classical networks with respect to the global reference system [7.1.2].

7.1.1 Design and Observation

Horizontal control networks are realized by *trigonometric* (triangulation) points, which in principle should be distributed evenly over the country. One distinguishes between different *orders* of trigonometric points, from first order or primary (station separation 30 to 60 km) to second order (about 10 km) to fourth or even fifth order (down to one to two km) stations. The maximum distance between first-order points was determined by the terrestrial measurement methods, which required intervisibility between the network stations. Consequently, first and some second-order stations were established on the top of hills and mountains; observation towers (wooden or steel constructions with heights of 30 m and more) were erected especially in flat areas. The stations have been permanently marked by underground and surface monuments (stone plates, stone or concrete pillars, bolts in hard bedrock). Eccentric marks have been set up in order to aid in the recovery and verification of the center mark.

Classical first and second-order horizontal control networks have been observed by the methods of triangulation, trilateration, and traversing.

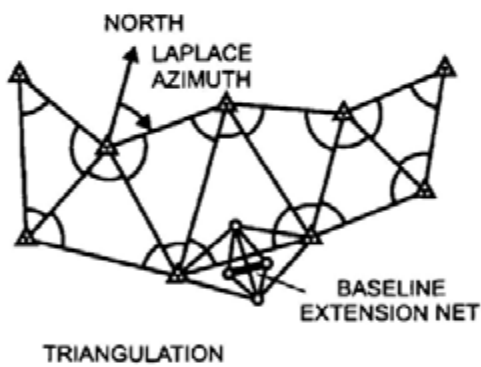


Fig. 7.1. Triangulation with baseline extension net and Laplace azimuth (principle)

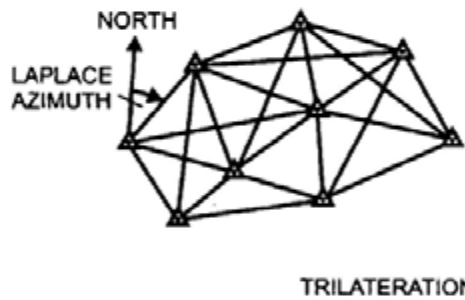


Fig. 7.2. Trilateration with Laplace azimuth (principle)

In *triangulation*, all angles of the triangles formed by the trigonometric points are observed with a theodolite (Fig. 7.1). The instrument is set up on the observation pillar or tower; at large distances the targets are made visible by light signals. Either directions (successive observation of all target points) or angles (separate measurement of the two directions comprising one angle) are observed in several sets (i.e., in both positions of the telescope), distributed over the horizontal circle of the theodolite. The scale of a triangulation network is obtained from the length of at least one triangulation side, either derived from a

short *base line* through a base line extension net or measured directly by a distance meter, cf. [5.5.2]. Astronomic observations provide the orientation of the network, cf. [7.1.2], whereas an astronomic azimuth is needed for the horizontal orientation according to Laplace's equation (6.58): *Laplace station*. In extended networks, base lines and Laplace stations often were established at distances of a few 100 km in order to control the error propagation through the network with respect to scale and orientation (effects of lateral refraction).

Trilateration employs electromagnetic distance meters in order to measure the lengths of all triangle sides of a network, including diagonals (Fig. 7.2). At least one Laplace azimuth is needed for the orientation of the net. Electromagnetic distance measurements put less demands on the stability of observation towers as compared to angular measurements, and the use of laser light and microwaves makes the method more independent from weather conditions.

Traverses combine distance and angular measurements, where the traverse stations are arranged along a profile (Fig. 7.3). Again, a Laplace azimuth is required in order to orientate the traverse. Traversing represents a very effective and flexible method for establishing horizontal control networks, with no more need to establish stations on hilltops. It has been employed primarily for the densification of higher order networks, with the coordinates of the existing control points providing orientation.

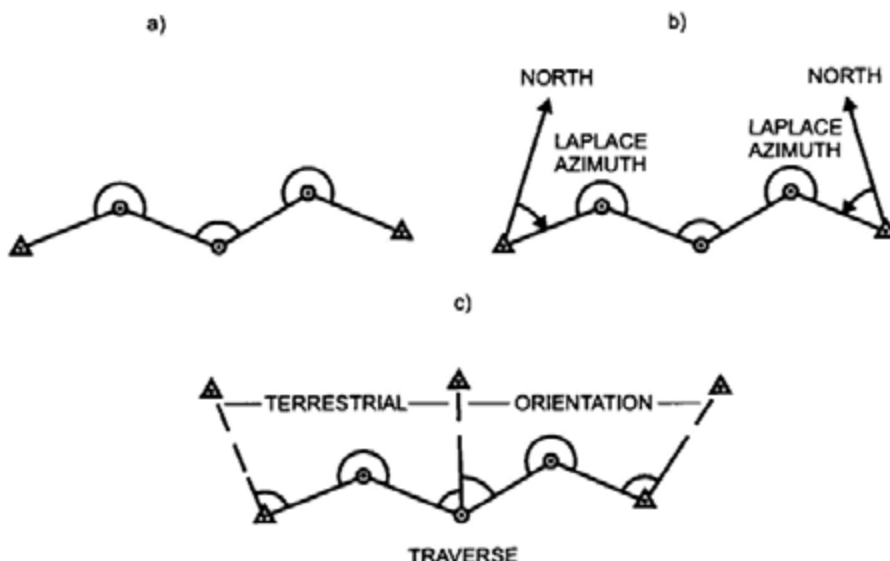


Fig. 7.3. Traverse connecting two control points (principle): a) without additional orientation, b) with orientation by Laplace azimuths, c) with orientation by directions to control points

Horizontal control networks can also be formed by *combining* the methods of triangulation, trilateration, and traversing. Such networks are very stable in design, and allow establishment of first and second-order control simultaneously. *Optimization* methods have been developed for the design and survey of trigonometric networks. Starting from the demands on accuracy and reliability, these methods provide information on the optimum point configuration and the distribution of the measurements in the network given the limitations of available equipment and the maximum allowable cost of the survey (BOSSLER et al. 1973, GRAFAREN and SANSÒ 1985).

Triangulation as part of a national geodetic survey started in France (1733-1750: *Carte géométrique de la France*, under the direction of *Cassini de Thury*) and in Great Britain (since about 1780 triangulation by the Ordnance Survey, under *W. Roy* and others). It continued to be the method for establishing horizontal control networks in the 19th and 20th century until the introduction of electromagnetic distance measurements. Triangulation often started with chains (in many cases established along meridians and parallels) composed of triangles or quadrilaterals with diagonals tied together every few 100 km. The meshes of this framework then were filled by first or second-order areal triangulation. The triangulations of Bavaria (1808-1828, *J.G. Soldner*) and of Prussia (since 1875, *O. Schreiber*) brought significant improvements in measurement and calculation techniques, which also influenced other national geodetic surveys. Large-scale networks (chains and filling nets) were developed in the U.S.A. (since about 1830, *J.F. Hayford*, *W. Bowie*) and in the former Soviet Union (since the 1930's, *T.N. Krassovski*), cf. [7.1.2]. *Trilateration* was applied from the 1950's to the 1970's for strengthening, extending, and densifying triangulation networks. Airborne microwave methods were employed for the rapid survey of regions with difficult access and for bridging water areas (a few m to 10 m accuracy over some 100 km). *Traversing* has been used mainly for network densification since the 1960's, but first-order geodimeter traverses also strengthened continental networks (U.S.A.) or even established them (Australia). From the 1960's to the 1980's, *satellite methods* were utilized to control the quality of horizontal control networks and especially to determine the orientation of the ellipsoidal systems with respect to the global geocentric system (Doppler positioning).

7.1.2 Computation and Orientation

Classical first and some second-order horizontal control networks have been calculated on a reference ellipsoid within the system of ellipsoidal coordinates, cf. [4.1]. Lower order networks are primarily calculated in planar Cartesian coordinates, after conformal mapping of the ellipsoid onto the plane (LEE 1974, GROSSMANN 1976, KUNTZ 1990, HOOIJBERG 1997).

The observed horizontal angles, directions, and spatial distances were *reduced* to the ellipsoid first, cf. [6.3.2]; the gravity-field-related reductions (deflections of the vertical, geoid height) were not considered during earlier surveys. The network *adjustment* was carried out either by the method of conditions or by variation of the coordinates, with redundancy resulting from triangle misclosures, diagonals in trilateration quadrilaterals, and additional base lines

and Laplace azimuths. For the method of conditions, the geometry of the network was adjusted first. The *coordinates transfer* from an initial point (see below) was then carried out using the solutions of the direct problem on the ellipsoid; while for the method of variation of the coordinates, ellipsoidal "observation equations" were derived from the solution of the inverse problem, cf. [6.3.3]. Among the deficiencies of this classical "development method" are the neglecting of the deflections of the vertical, the inadequate reduction of distances on the ellipsoid, and especially the step by step calculation of larger networks, with junction constraints when connecting a new network section to an existing one. This led to network distortions of different type, with regionally varying errors in scale ($\pm 10^{-5}$) and orientation (\pm a few arcsec). Relative coordinate errors with respect to the initial point increased from a few decimeters over about 100 km to about one meter over several 100 km and reached 10 meters and more at the edges of extensively extended networks.

The *geodetic datum* of a horizontal control network comprises the parameters of the reference ellipsoid and of the network's orientation with respect to the earth's body, cf. [6.3.3].

Conventional ellipsoids, as computed by the adjustment of several arc measurements, were introduced during earlier geodetic surveys, cf. [1.3.3]. Some more recent surveys refer to locally *best-fitting ellipsoids*, as derived from a minimum condition on the vertical deflections, according to (6.182):

$$\Sigma(\xi^2 + \eta^2) = \min., \quad (7.1)$$

using the equations (6.51). Topographic-isostatically reduced deflections of the vertical have been used for larger networks in order to eliminate short and medium-wave effects. The ellipsoid parameters of a geodetic reference system, cf. [4.3], have been used recently. Tab. 7.1 gives the parameters of some

Tab. 7.1. Parameters of reference ellipsoids (rounded values), NIMA (2000)

| Name, year | semimajor axis a (m) | reciprocal flattening $1/f$ |
|-----------------|------------------------|-----------------------------|
| Airy 1830 | 6 377 563 | 299.3 |
| Everest 1830 | 6 377 276 | 300.8 |
| Bessel 1841 | 6 377 397 | 299.15 |
| Clarke 1866 | 6 378 206 | 294.98 |
| Clarke 1880 | 6 378 249 | 293.47 |
| Hayford 1909 | 6 378 388 | 297.0 |
| = Int.Ell.1924 | | |
| Krassovski 1940 | 6 378 245 | 298.3 |
| GRS 67 | 6 378 160 | 298.247 |
| GRS 80 | 6 378 137 | 298.257 |

reference ellipsoids that have been used for national geodetic surveys (STRASSER 1957, NIMA 2000).

The ellipsoids of Airy (applied in Great Britain), Everest (India etc.), Bessel (Germany, Austria, Japan etc.), Clarke 1866 (U.S.A., Canada etc.), and Clarke 1880 (France etc.) are based on the adjustment of arc measurements distributed over the continents. The Hayford ellipsoid fits best to the vertical deflection field in the U.S.A., it has been introduced in a number of countries. The Krassovski ellipsoid resulted from a fit to the Russian triangulation, with additional data from western Europe and the U.S.A. The ellipsoids of the geodetic reference systems GRS67 (Australia etc.) and GRS 80 represent optimum approximations to the geoid.

The *orientation* of the ellipsoid was realized by defining the ellipsoidal coordinates of a fundamental (initial) point, also called network origin, and by conditions for the parallelism of the axes of the ellipsoidal and the global geocentric systems, cf. [6.3.3].

In earlier surveys, the coordinates of the *fundamental point* were fixed by postulating equality between observed astronomic latitude, longitude, and orthometric height and the corresponding ellipsoidal quantities. This is identical to setting the deflection of the vertical and the geoid height of the fundamental point to zero:

$$\xi_F = \eta_F = N_F = 0. \quad (7.2)$$

This strategy provides a good approximation of the ellipsoid to the geoid close to the origin, but may lead to larger deviations at more remote areas (Fig. 7.4). If

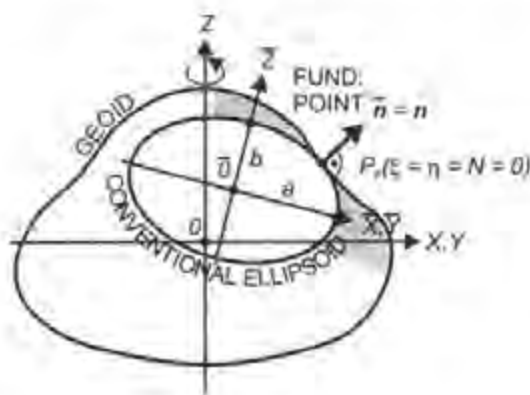


Fig. 7.4. Locally fitting "conventional" ellipsoid

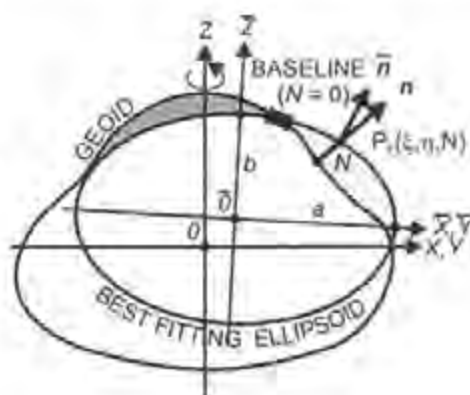


Fig. 7.5. Regionally best fitting ellipsoid

a sufficient number of vertical deflection points were available and well distributed over the area of calculation, the minimum condition (7.1) was used. This condition permits determination of the deflection of the vertical in the fundamental station and, eventually, the parameters of a best-fitting ellipsoid. This procedure led to an *optimum fitting* over the whole area, and kept the deflections of the vertical small. In many cases, the geoid height of the origin point was defined indirectly by reducing the base lines onto the geoid and treating them as ellipsoidal quantities (Fig. 7.5). The minimum condition for the geoid heights (6.181)

$$\Sigma N^2 = \min. \quad (7.3)$$

was occasionally applied using relative geoid heights calculated from astronomic leveling, cf. [6.7.4], and utilizing the last equation of (6.51). The *parallelism* of the axes was achieved by the condition equations (6.57) and (6.58) for the deflection of the vertical and the azimuth (Laplace equation); these were applied to the observations at the fundamental point and eventually at additional Laplace stations. Some recent geodetic datums utilize the ellipsoid parameters of a Geodetic Reference System, cf. [4.3], with optimum approximations to the geoid (mean earth ellipsoid), Fig. 7.6. Tab. 7.2 lists the ellipsoids and the origin points used for some geodetic datums (HOOIJBERG 1997, NIMA 2000).

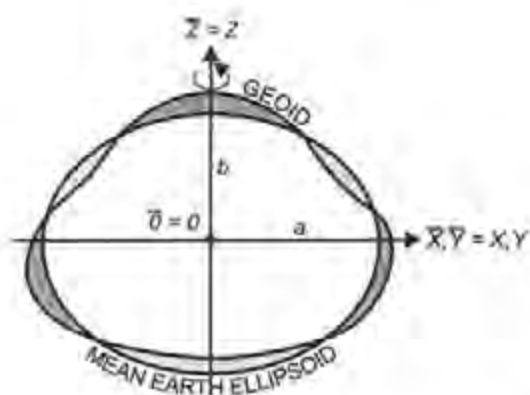


Fig. 7.6. Mean earth ellipsoid

Tab. 7.2. Reference ellipsoids and origin points of some geodetic datums

| Geodetic Datum | Reference Ellipsoid | Name of Origin | Latit. | Longit. | Origin |
|--|--------------------------|----------------------|---------|---------|--------|
| Australian Geodetic 1984 (AGD84) | GRS67 | Johnston | -25°57' | 133°13' | |
| Deutsches Hauptdreiecksnetz (DHDN), Germany | Bessel 1841 | Rauenberg/Berlin | 52°27' | 13°22' | |
| European Datum 1950 (ED50) | Intern.Ellipsoid 1924 | Potsdam, Helmertturm | 52°23' | 13°04' | |
| Indian | Everest 1830 | Kalianpur | 24°07' | 77°39' | |
| North American 1927 (NAD27) | Clarke 1866 | Meades Ranch, Kansas | 39°13' | 261°27' | |
| North American 1983 (NAD83) | GRS80 | geocentric | | | |
| Ordnance Survey of Great Britain 1936 (OSGB36) | Airy 1830 | Herstmonceux | 50°52' | 0°21' | |
| Pulkovo 1942, former Soviet Union | Krassovski 1940 | Pulkovo | 59°46' | 30°20' | |
| South American 1969 (SAD69) | GRS67 | Chua, Brazil | -19°46' | 311°54' | |

The horizontal control network of the U.S.A. was constructed by triangulation chains with mesh sizes of about 500 km. Nodal nets at the junctions of the chains were treated as constraints in the adjustment, and areal networks later filled the meshes (BAKER 1974). A conventional ellipsoid (Clarke 1866) was introduced, with the orientation obtained from the minimum condition for vertical deflections (7.1): *North American Datum 1927* (NAD27), see Tab.7.2. This system has been replaced by the North American *Datum of 1983* (NAD83), which combines the horizontal control networks of the U.S.A., Canada, Greenland, Mexico, and Central America by a rigorous adjustment (SCHWARZ 1989, SCHWARZ and WADE 1990), Fig.7.7. The observations include terrestrial data (horizontal directions, azimuths, distances), Doppler stations (large-scale control and reference to the geocenter), and VLBI baselines (scale and orientation). The adjustment (about 1.8 million observations, more than 900 000 unknowns and 266 000 stations) was performed by Helmert-blocking (WOLF 1978) and utilized a height-constrained three-dimensional procedure, cf. [6.2], (VINCENTY 1980, 1982). The two-dimensional results refer to the Geodetic Reference System 1980, with a geocentric position accurate to about ± 2 m. The relative station uncertainty is a few cm to a few dm for distances between 10 and 300 km (SNAY 1990). Deflections of the vertical and geoid heights were calculated for all stations by gravimetric methods, cf. [6.7.1].

Since the 1950's, attempts have been made in Europe to establish a unified *European triangulation network* (RETrig). A central European network formed by selected triangulation



Fig. 7.7. Horizontal control network of the U.S.A. (NAD83), with first and second order triangulation, and traverses, courtesy National Geodetic Survey, National Ocean Service, NOAA

chains was calculated first and later augmented by blocks in the southwest, southeast, and north (WHITTEN 1952); *European Datum 1950* (ED50), see Tab.7.2. The International Ellipsoid 1924 served as the reference surface and was orientated by the minimum condition (7.1), which provided vertical deflection components ($\xi = 3.36''$, $\eta = 1.78''$) for the origin Potsdam, Helmertturm. The base lines, reduced to the geoid, indirectly provided the geoid height ($N = 0.4$ m) at the origin (WOLF 1987). For western Europe, a rigorous readjustment of all first-order triangulation nets was carried out later, including electromagnetic distance measurements, VLBI, satellite laser ranging, and Doppler observations: *European Datum 1987* (ED87), PODER and HORNIK (1989). The system is more homogeneous than ED50, with improved parallelism of the axes (better than 0.1 arcsec) and scale (0.1×10^{-6}). The International Ellipsoid 1924 was preserved as a reference surface, and the translation was taken from ED50 by adopting the ED50 coordinates for the station Munich, Frauenkirche ($X_0 = -83$ m, $Y_0 = -97$ m, $Z_0 = -117$ m). While ED50 was introduced in several countries, and served as the NATO military system until the 1990's, no practical application was found for ED87. In the former Soviet Union, the triangulation chains were adjusted on the Krassovski 1940 ellipsoid: *Pulkovo Datum 1942*, IZOTOV (1959). Parameters and orientation of the ellipsoid were derived from the minimum condition (7.1), with the geoid height set to zero at the origin Pulkovo. Reductions to the ellipsoid became possible by observed and gravimetrically interpolated deflections of the vertical and quasigeoid heights from astrogravimetric leveling, cf. [6.7.4]. After extension to the eastern European countries and inclusion of new measurements, a new adjustment was carried out leading to the astrogeodetic net 1983.

The primary triangulation net of Germany, developed since the 1870's, is an example of a local horizontal control network. The northwestern part, between the rivers Elbe and Main, was

covered by triangulation chains and densification nets between 1870 and 1895 as part of the geodetic survey of Prussia. A conventional ellipsoid (Bessel 1841) was introduced for the calculation and orientated by the condition (7.2) at the origin Rauenberg/Berlin, whereby the geoid height was fixed indirectly through the reduction of five base lines, one of them located near Berlin. The Laplace azimuth from Rauenberg to Berlin, Marienkirche provided the network's orientation on the ellipsoid. After the network adjustment, the ellipsoidal coordinates were calculated according to the development method, where the horizontal directions were not reduced for the vertical deflections. The eastern parts of Prussia and the triangulations of the southern German states were later tied to this "Schreiber's block" utilizing common points at the networks' margins: *Deutsches Hauptdreiecksnetz* (DHDN), see Tab. 7.2. In western Germany, the DHDN has been locally improved since the 1950's by additional horizontal directions and electromagnetic distance measurements, without changing the original datum. While the relative accuracy over some 10 to 100 km is at the dm order of magnitude, distortions up to 1 m have been found between different parts of the network. In eastern Germany, a complete retriangulation was carried out after 1950 and calculated within the common adjustment of the eastern European triangulations (see above): Staatliches Trigonometrisches Netz 1942/1983 (STN42/83), IHDE und LINDSTROT (1995). Due to the different datum definitions, DHDN and STN42/83 differ systematically by about 2" in latitude and 4" in longitude. The DHDN90 thus consists of three blocks observed over a time span of more than 100 years with different orientation (SCHMIDT 1995), Fig. 7.8. Local transformations between the two systems have been performed for practical applications, and a complete recalculations will be carried out together with the transformation to the three-dimensional system DREF 1991, which is part of the European Reference Frame EUREF, cf. [7.3.2].

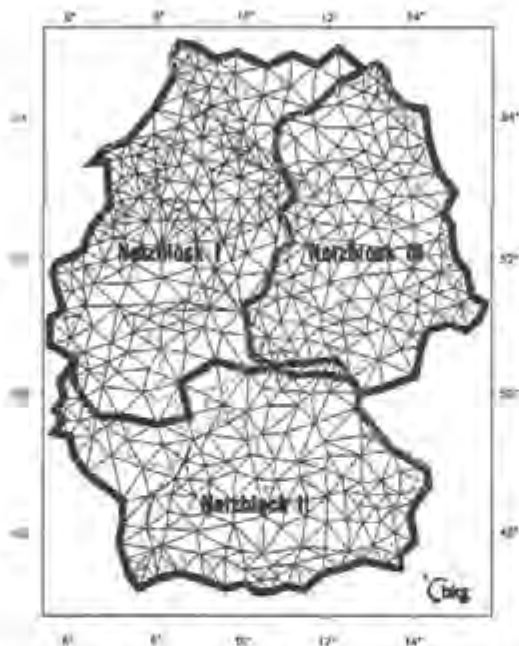


Fig. 7.8. Primary triangulation net of Germany (DHDN90), courtesy Bundesamt für Kartographie und Geodäsie (BKG), Frankfurt a.M., Germany

Satellite positioning was employed early to control the quality of horizontal-control networks and to determine the *datum transformation* parameters with respect to the geocentric system, ASHKENAZI et al. (1988). Equations (6.47) were used to calculate translation, rotation, and scale factor from identical stations coordinated in the global system (especially in the WGS84) and in the local or regional geodetic datum. The results are mean values for the respective geodetic datum, depending strongly on the distribution of the identical points. Tab. 7.3 provides the translations, rotations, and scale factors for some geodetic datums.

Tab. 7.3. Translation, rotation, and scale factors for some geodetic datums (mean values), DMA (1987), NIMA (2000), DHDN and Pulkovo 1942 (STN42/83); IHDE and LINDSTROT (1995)

| Geodetic Datum (see Tab. 7.2) | 7-Parameter-Transformation | | | | | | 3-Parameter-Transf. | | | |
|-------------------------------------|----------------------------|-------|-------|-------------------|--------------|--------------|------------------------------------|----------------------|---------|---------|
| | Translation (m) | | | Rotation (arcsec) | | | Scale Factor $m \times 10^6$ | Translation only (m) | | |
| | X_0 | Y_0 | Z_0 | ϵ_x | ϵ_y | ϵ_z | | X_0 | \circ | \circ |
| AGD84 | -127 | -50 | 153 | 0.0 | 0.0 | -0.1 | 1.2 | -134 | -48 | 149 |
| DHDN | 582 | 105 | 414 | -1.0 | -0.4 | 3.1 | 8.3 | | | |
| ED50 | -102 | -102 | -129 | 0.4 | -0.2 | 0.4 | 2.5 | -87 | -98 | -121 |
| Indian | 227 | 803 | 274 | -0.4 | -0.6 | -0.4 | 6.6 | 295 | 736 | 257 |
| NAD27 | -4 | 166 | 183 | -0.3 | 0.3 | -0.1 | 0.4 | -8 | 160 | 176 |
| OSG36 | 446 | -99 | 544 | -0.9 | -0.3 | -0.4 | -20.9 | 375 | -111 | 431 |
| Pulkovo 42 | 24 | -123 | -94 | 0.0 | 0.2 | 0.1 | 1.1 | 28 | -130 | -95 |
| SAD69 | -56 | -3 | -38 | 0.1 | -0.6 | -0.2 | -0.6 | -57 | 1 | -41 |

Remark: Pulkovo 42 7-Parameter-Transformation values are valid for eastern Germany (STN42/83); 3-Parameter-Transformation values are valid for Russia.

The translation values are at the order of magnitude of the deflections of the vertical. They are larger when conventional ellipsoids have been used and decrease with best-fitting ellipsoids. The rotation angles mirror the accuracy of the astronomic observations and are usually not significant. While the scale errors for older networks reach 10^{-5} and more; they attain only 10^{-6} and less in recent systems, characterizing the progress in length determination. Due to network distortions, local datum-shift values may differ significantly from the mean values, e.g., by 5 to 10 m and more for the translation parameters. If a three-parameter solution (translation only) is carried out, the translation values for older networks experience considerable changes.

The *transformation* from a local geodetic datum to the geocentric system can be done either by a complete readjustment including spatial observations (example: NAD83) or by mean or local (more accurate) transformation parameters. The regional behavior of the translation parameters may also be

modeled by low-order polynomials and provided in the form of datum shift contour charts (DMA 1987). Of special interest is the transformation of ellipsoidal coordinates, which includes the transition from a conventional or best-fitting ellipsoid to a geocentric one. From (6.49) we obtain the changes in the ellipsoidal latitude, longitude, and height (spherical approximation, rotations neglected, ellipsoidal formulas are given by DMA 1987, EHLERT 1991):

$$\begin{aligned}\Delta\varphi &= -\sin\varphi\cos\lambda \cdot X_0 - \sin\varphi\sin\lambda \cdot Y_0 + \cos\varphi \cdot Z_0 + \sin 2\varphi \cdot \Delta f \\ \cos\varphi \Delta\lambda &= -\sin\lambda \cdot X_0 + \cos\lambda \cdot Y_0 \\ \Delta h &= \cos\varphi\cos\lambda \cdot X_0 + \cos\varphi\sin\lambda \cdot Y_0 + \sin\varphi \cdot Z_0 - \Delta a + a\sin^2\varphi \cdot \Delta f\end{aligned}\quad (7.4a)$$

Here, the sign of the translation vector

$$\mathbf{X}_0 = \begin{pmatrix} X_0 \\ Y_0 \\ Z_0 \end{pmatrix} = \begin{pmatrix} X - \bar{X} \\ Y - \bar{Y} \\ Z - \bar{Z} \end{pmatrix} \quad (7.4b)$$

has been changed (reduction!). All differences are formed in the sense "geocentric – local system", resulting in the transformation

$$\begin{aligned}\varphi &= \bar{\varphi} + \Delta\varphi, \lambda = \bar{\lambda} + \Delta\lambda, h = \bar{h} + \Delta h \text{ and} \\ a &= \bar{a} + \Delta a, f = \bar{f} + \Delta f.\end{aligned}\quad (7.4c)$$

Again, the changes in φ, λ, h can be modeled and given in contour charts, provided a sufficiently large number of identical points have been used. The accuracy of these transformations depends on the area and the number of points available in both systems. A few m accuracy has been achieved for continent-wide networks.

Classical horizontal control networks form the basis for many applications in surveying and mapping. They suffer from network distortions, also they are not geocentric and typically do not use modern geodetic standard-ellipsoids. Within the near future, they will be transformed and integrated into the global geocentric three-dimensional reference frame, cf. [7.3.2].

7.2 Vertical Control Networks

Vertical control networks have been established separately from horizontal control nets. This is due to the demand that heights have to refer to the gravity field rather than the ellipsoidal system used for horizontal positioning.

Vertical control networks are determined by *geometric leveling* and occasionally by hydrostatic leveling, cf. [5.5.3], the control points being designated as *bench marks*. According to the leveling procedure and the accuracy achieved, national geodetic surveys distinguish between different orders of leveling. First-order leveling is carried out in closed loops (loop circumferences of some 100 km) following the rules for precise leveling. The loops are composed of leveling lines connecting the nodal points of the network (Fig. 7.9). The lines, in turn, are formed by leveling runs that connect neighboring benchmarks (average spacing 0.5 to 2 km and more). The first-order leveling network is densified by second to fourth-order leveling.

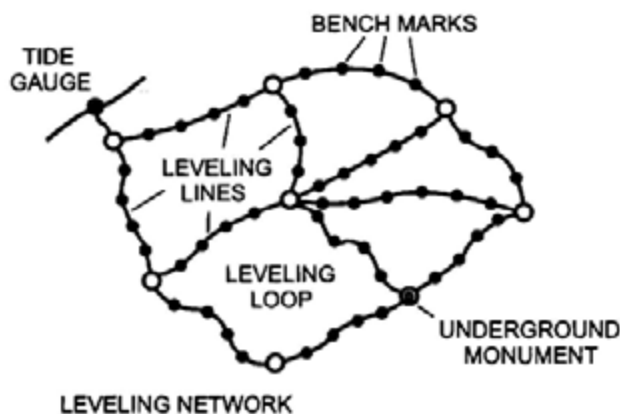


Fig. 7.9. Leveling network (principle)

Leveling lines generally follow main roads, railway lines, and waterways. The benchmarks consist of bolts in buildings, bedrock, or on concrete posts. Long pipes are set up in alluvial regions. Underground monuments are established in geologically stable areas in order to secure the network stability with respect to variations with time. An accuracy of about 1 mm per km is achieved for first-order networks. They should be reobserved at time intervals of some 10 years, as regional and local height changes can reach 1 mm/year and more, especially in areas which experience crustal motion, cf. [8.3.3].

Prior to the adjustment of a leveling network, the observed raw height differences have to be transformed either to geopotential differences or to

differences of normal or orthometric heights by considering surface gravity, cf. [6.4.1]. The adjustment then utilizes the loop misclosure condition of zero and is carried out either by the method of condition equations or, preferably, by the method of parameter variation.

First-order leveling networks were established in many countries between the 1860's and the 1930's when surface gravity along the leveling lines was not available. Hence, gravity reductions were either neglected completely or actual gravity was approximated by normal gravity, leading to *normal* or *spheroidal* orthometric heights. These path-dependent heights may differ from normal or orthometric heights by some mm (flat terrain) to some dm (mountains). With gravity data being generally available now, gravity can be taken into account in calculations of modern leveling networks (WOLF 1974).

The *vertical datum* (zero height surface) is defined by mean sea level (MSL) as derived from tide gauge records. National height systems may differ by some dm to 1 m, and more, between each other. They may also differ from the geoid as a global reference surface, which is due to the effect of sea surface topography, cf. [3.4.3]. Network distortions arise if the vertical datum is constrained to MSL of more than one tide gauge.

Estimates of the vertical datum differences between different height systems are available from satellite positioning and global geoid models and from continental-wide leveling connected to tide gauges (RAPP 1995b, IHDE et al. 1998). For instance, the zero height surface of the North American Vertical Datum of 1988 is about 0.7 m below MSL at Amsterdam, which was used for the European leveling network. In Europe, the national vertical datums have been derived from MSL records in the Mediterranean, the North Sea, and the Baltic Sea. Taking MSL in Amsterdam (used, e.g., in the Netherlands and in Germany) as reference, MSL in Kronstadt (near St.Petersburg, Russia) is about 15 cm higher, and tide gauges along the Mediterranean (Marseille: France, Genoa: Italy, Trieste: Austria) give a MSL that is about 0.4 to 0.5 m lower (SACHER et al. 1999).

In North America, a previous adjustment of first-order leveling provided the *North American Vertical Datum of 1929* (NAVD29), which was constrained to the MSL of 26 tide gauges in the U.S.A. and Canada (BAKER 1974). After replacing destroyed bench marks and extensive releveling, a new adjustment of the leveling data of the U.S.A., Canada, Mexico, and Central America was carried out in geopotential numbers: *North American Vertical Datum of 1988* (NAVD88). Heights are given as orthometric heights according to Helmert (6.84) and refer to MSL of one primary bench mark (Father Point/ Rimouski, Quebec, Canada), ZILKOSKI et al. (1992).

The *United European Leveling Net* (UELN) is formed by first-order leveling lines of the European countries (Fig.7.10). Periodic adjustments have been carried out since 1954, with continuous improvement and extension by including new data. The adjustments are performed in geopotential numbers, and normal heights are available. The average accuracy (UELN95) of the leveling is ± 1.1 mm/km, and the standard deviations related to Amsterdam remain less than ± 0.1 .



Fig. 7.10. United European Leveling Net (UELN95), courtesy BKG, Frankfurt a.M., Germany



Fig. 7.11. Primary leveling network of Germany (DHHN92), courtesy BKG, Frankfurt a.M., Germany

in. The vertical datum is taken from MSL of the North Sea as determined in the period 1940 to 1958 at Amsterdam (Normal Amsterdamsch Peil NAP of 1950). The UELN is connected to a large number of tide gauges, which permits determination of sea surface topography around Europe. In the future, UELN will be extended to a kinematic height system by including vertical point velocities (ADAM et al. 2000a).

First-order leveling in Germany started around 1865 and first led to a height system calculated from the raw leveling data. Complete resurveys were carried out from 1912 to 1960 and from 1980 to 1985 (western Germany, including gravity measurements). These networks were adjusted as normal-orthometric heights: *Deutsches Haupthöhennetz* (DHHN). The vertical datum was derived by leveling from the Amsterdam normal tide gauge, representing MSL for the period 1683/1684 (WAALEWIJN 1986). The zero height surface (*Normal-Null*, N.N.) was fixed by a standard bench mark, established 37.000 m above N.N. at the former Berlin observatory and, since 1912, by underground marks about 40 km east of Berlin. In eastern Germany, releveling was carried out in the 1970's and adjusted as normal heights. The vertical datum was taken from MSL at the tide gauge in Kronstadt: *Höhennull* (HN). Due to the different definitions of the vertical datum and the heights, systematic height differences between 8 and 16 cm occurred at the boundary between western and eastern Germany. A readjustment was performed in geopotential numbers, where the vertical datum is defined by the geopotential number of the nodal point Wallenhorst taken from the UELN86 adjustment and thus refers to MSL at Amsterdam (Fig. 7.11); DHHN92. Normal heights have been introduced as official heights, referring to the reference surface (quasigeoid) *Normalhöhennull* (NHN), WEBER (1995).

Leveling networks are characterized by high accuracy, but systematic errors may accumulate over large distances. Due to the time-consuming measurement procedure, repetition surveys are feasible only after long time intervals. A more rapid establishment of vertical control networks can be achieved by trigonometric leveling, cf. [6.4.2], and a drastic change is to be expected by GPS-heighting in connection with precise geoid or quasigeoid models, cf. [6.4.3]. In this way, vertical control networks will be integrated into three-dimensional control systems, cf. [7.3.2]. Geometric leveling will maintain its importance over short distances, and especially in areas of recent crustal movements, such as regions of land subsidence and zones of earthquake or volcanic activity, cf. [8.3.3].

7.3 Three-dimensional Networks

Geodetic space methods deliver three-dimensional coordinates with cm-accuracy in the global geocentric system on global, regional, and local scale. Global networks realize the terrestrial reference system and provide reference stations for the establishment of continent-wide networks, wherein GPS plays a fundamental role [7.3.1]. Further network densification is carried out nearly exclusively by GPS, with subsequent integration of existing classical control nets [7.3.2].

7.3.1 Global and Continental Networks

The *International Terrestrial Reference Frame* (ITRF) represents the global basis for three-dimensional positioning. It is defined by the geocentric Cartesian coordinates and the horizontal velocities of a global set of space geodetic observing sites, given for a certain epoch, with an accuracy of about ± 1 cm and ± 1 to 3 mm/year respectively, cf. [2.5.3]. The ITRF results are based on observations obtained by global networks employing different space techniques, which are combined within the frame of the International Earth Rotation Service (IERS), cf. [2.3].

Nowadays, the *Global Positioning System* (GPS) is the primary technique used in all scales for positioning and navigation. The GPS results refer to the *World Geodetic System 1984* (WGS84). The underlying global network is comprised of a limited number of GPS tracking stations, determined with an accuracy of about 5 cm. At this accuracy level, WGS84 also agrees with ITRF, cf. [5.2.5].

The *International GPS Service* (IGS), established by IAG, has been operational since January 1, 1994. It consists of a global network of more than 200 permanently operating GPS stations equipped with geodetic, two-frequency GPS receivers and several data and analysis centers (BEUTLER et al. 1996b).

IGS products include highly accurate (\pm a few cm) GPS satellite ephemerides, clock corrections, earth rotation parameters provided on a daily basis, and weekly solutions for the station coordinates (sub-cm accuracy in horizontal position, ± 1 to 2 cm in height) and velocities. In addition, the raw GPS tracking data (phase and pseudorange observations), station clock, ionospheric, and tropospheric information are available. By using ITRF positions and velocities for a subset of IGS stations, the IGS network is connected to ITRF and contributes significantly to it. On the other hand, IGS stations and products serve for densifying ITRF on continental scale.

The establishment of continent-wide *fundamental networks* with GPS began at the end of the 1980's; an approximate homogeneous station-coverage is generally the goal. Station distances are several 100 km, and at least three stations per country are generally selected as a reference for further densification and for the transformation of existing control networks, cf. [7.1.2], [7.3.2]. The *station sites* are selected according to the requirements of GPS observations (no visibility obstructions between 5° to 15° and 90° elevation, absence of multipath effects, no radio wave interference). Generally the stations are monumented by concrete pillars, providing a forced centering for the GPS antenna and a height reference mark. Eccentric marks are established in order to locally control horizontal-position and height. Existing first-order control points may be used if they fulfill the GPS requirements, otherwise the GPS stations should be connected to the existing control networks by local surveys.

Dedicated *GPS campaigns* are carried out for the determination of the station coordinates, employing relative positioning, cf. [5.2.5]. This strategy requires the inclusion of at least one reference station with coordinates given in the ITRF. Practically all ITRF and IGS stations in the survey region are introduced as reference ("fiducial") stations. Temporary reference stations may be established through baseline connections to IGS stations in order to improve the connection of the network to the ITRF. Depending on the number of stations and available GPS receivers (two-frequency geodetic type), either all stations are observed simultaneously or the network is divided into blocks that are observed sequentially (Fig. 7.12). All observations made simultaneously during a given time interval are called a "session" (SNAY 1986). The duration of one session is typically 24 hours, which permits determination of the ambiguity unknowns and a simultaneous solution for the station coordinates and tropospheric correction parameters. The results of *one* session are highly correlated. Consequently, several sessions are generally carried out, leading to a total observation time of some days to one week.

By referencing the network to IGS stations and applying the IGS precise orbital data, the effect of reference station and orbital errors on the station coordinates is only at the few mm level. When different type GPS receivers are employed in one campaign, corrections have to be applied for antenna phase-center

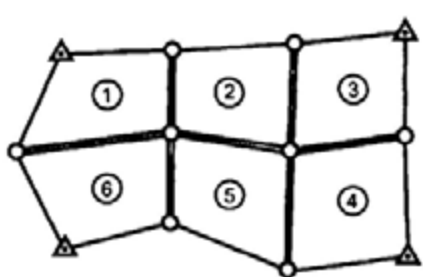


Fig. 7.12. GPS network constructed from individual blocks (principle)



Fig. 7.13. GPS network constructed from baselines to permanent GPS stations (principle)

differences. In addition, phase-center variations have to be taken into account by calibration (SEEBER et al. 1998). Longer observation periods increase the accuracy of the results, due to the changing satellite geometry and the reduction of residual tropospheric, multipath, and antenna effects. This is especially valid for the height component, where small satellite elevations improve the geometry of the solution but introduce larger tropospheric errors. Continent-wide GPS networks can be determined with an accuracy of about ± 1 cm.

Permanent ("active") GPS stations have increasingly been established since the 1990's at regional and local scales. They are equipped with geodetic GPS receivers that continuously track all available satellites. Undisturbed visibility to the satellites is achieved by installing the antennas several m to 10 m above the ground on concrete pillars, steel grid masts, etc., or on the top of buildings. Permanent stations provide the raw GPS tracking data, clock corrections, atmospheric information, and daily to weekly solutions for the station coordinates with a precision of a few mm. They serve primarily for the maintenance of the GPS reference system realized by the fundamental network, by controlling variations with time due to plate tectonics and other geodynamic activities. The establishment of GPS control points is facilitated by differential GPS using baselines to the permanent stations and exploiting the data made available for these stations. Thus, a single receiver can be used for precise positioning (Fig. 7.13).

Fundamental GPS networks with permanent stations densify ITRF and IGS on a continental scale and provide the reference for national systems. Following the ITRF strategy, reference epochs are defined for the station coordinates of the fundamental networks, which may differ from the epoch of the ITRF stations introduced and from the time of the observation campaign. Consequently, reductions have to be applied which take the station velocities between the different epochs into account.

A *European Reference Frame* (EUREF) has been built up since the end of the 1980's, as realization of a European Terrestrial Reference System (ETRS). The EUREF stations were determined by successive GPS campaigns that included ITRF and IGS stations and generally covered several countries (SEEGER et al. 1998, ADAM et al. 2000b). The Reference System was defined for the epoch 1989.0 and realized through the European Terrestrial Reference Frame 1989 (ETRF89), which agrees with the definition of ITRF89. In 1999, the ETRF comprised about 200 stations, with distances between 300 and 500 km (Fig. 7.14). ETRF89 shall rotate with the stable part of the European tectonic plate, which allows the frame to remain unchanged over a longer time interval. About 90 permanent GPS stations serve for maintaining ETRS and densifying the IGS network. Further applications include investigations of recent geodynamics, sea level monitoring, and contributions to weather prediction, utilizing the tropospheric zenith path delays (BRUYNINX 1999), cf. [5.1.2].



Fig. 7.14. European Reference Frame (EUREF89/97) with permanent GPS stations (status 1999), courtesy BKG, Frankfurt a.M., Germany

A *European Vertical Reference Network* (EUVN) is under construction in order to unify, at a few-cm accuracy level, the different height systems used in the European countries. The network comprises about 200 stations determined in dedicated GPS campaigns (1997) using one-week observation times. It includes EUREF sites, nodal points of the European leveling net UELN, tide gauges, and a number of permanent GPS stations. Three-dimensional coordinates, geopotential numbers, and normal heights will be calculated; hence EUVN will provide fiducial points in order to fit the European quasigeoid to a unified European height system, cf. [6.4.3]. By extension to a kinematic height system, EUVN shall be used for monitoring large-scale, vertical crustal movements and sea level changes (ADAM et al. 2000a).

In South America, a *Sistema de Referencia Geocentrico para America del Sur* (SIRGAS) was established in 1995 by simultaneous GPS observations (10 days) on some 60 stations well distributed over the sub-continent (HOYER et al. 1998)). Referring to ITRF94, SIRGAS provides the basis for the transformation of the national networks to the global reference system. Within the frame of SIRGAS, another GPS campaign was carried out in 2000 (including Central and North America) on SIRGAS stations, leveling benchmarks, and tide gauges in order to derive a unified vertical height system.

7.3.2 National Networks

National geodetic control-networks have been established by GPS since the 1990's and now supersede the classical horizontal (and possibly vertical) control networks (AUGATH 1997). Although the strategies for establishing and maintaining these three-dimensional reference networks are still under discussion and differ from country to country, the following directions clearly can be identified:

- establishment of a large-scale, three-dimensional network with station distances between 10 and 50 km,
- installation of permanent GPS stations with distances of 50 to 100 km,
- transformation of the existing horizontal control network, eventually using additional GPS control.

A *three-dimensional network* is established by dedicated GPS campaigns using relative positioning, either as a densification of existing continental reference networks or by connection to ITRF and IGS stations, cf. [7.3.1]. Station sites are selected so that they coincide with first and second-order trigonometric points, or are located close to them. GPS observation criteria have to be taken into account, and monuments set below ground are beneficial for the long-term preservation of the network. A separation into a fundamental network with station distances of several 10 km (corresponding to the first-order trigonometric points) and densification nets with distances down to 10 km (second-order triangulation) may be useful for larger countries. Precise leveling benchmarks and tide gauges may be included into these networks in order to incorporate the existing vertical control system. While all stations can be observed simultaneously in smaller networks, a separation into observation blocks with subsequent GPS campaigns will generally be necessary. Each station is occupied at least two times on different days, with session durations between 8 and 24 hours. IGS precise orbital data is used in the network adjustment. Nearby global and continental reference stations are used as "fiducial stations". A "multi-station" adjustment utilizes all data collected during one session, while the "multi-session" adjustment combines the results of several sessions. The national network is transformed to a certain ITRS epoch. Accuracies of ± 1 cm and better are achieved for the horizontal components, and ± 1 to 2 cm for the heights.

Permanent GPS stations are established at distances of 50 to 100 km or more. The permanent stations are used to maintain the national reference frame with respect to recent crustal movements, but they also serve as reference for all types of GPS surveys which employ differential GPS (DGPS), WANNINGER (1996). The stations are equipped with geodetic GPS receivers; they track all visible GPS satellites at a high data rate (e.g., 1 s). Site selection and delivery of data products (raw tracking data, station coordinates, atmospheric corrections, etc.) follows the rules developed for permanent stations in continental networks, cf. [7.3.1].

By connecting the three-dimensional network stations to first and second-order trigonometric points, the existing horizontal control networks can be *transformed* into the three-dimensional reference frame. Additional GPS control points may be needed if the classical networks contain larger distortions; the selection of the control points depends on the network peculiarities, cf. [7.1.2]. A 7-parameter transformation may suffice for homogeneous networks of high precision, but usually more sophisticated transformation models will be necessary, including polynomial, least squares, or spline approximation (MORITZ 1978). In this way, the local cm-accuracy of classical networks will be kept, and the effect of the network distortions can be reduced to the order of a few cm to dm over distances of some 10 to 100 km.

After the introduction of a three-dimensional reference frame, *GPS-positioning* can be carried out in the relative mode by connection to the reference stations in the survey area. Two or more GPS receivers are required; one (or more) generally serve as a temporary reference with continuous satellite tracking. If a network of permanent GPS stations is operated by a national GPS service, with telemetry data transfer to the users, DGPS can be applied (SEEBER 1993, WANNINGER 2000). Positioning is now possible with one receiver only, depending on the baselines between the new station and the permanent stations. For short (few to 10 km) baselines, a relative cm-accuracy can be achieved in quasi real-time after proper ambiguity solution. For longer baselines, the results are degraded by the distance-dependent errors of GPS, cf. [5.2.5]. By connecting to an array of at least three permanent stations, the known geometry can be used to rapidly determine the ambiguities and to calculate baseline corrections for ionospheric, tropospheric, and orbit effects. Post-processing of DGPS can yield relative sub-cm accuracy. After the completion of the transformation to a three-dimensional reference frame, the classical horizontal networks of lower order will no longer be maintained.

By including first-order leveling benchmarks in the three-dimensional network, the differences between the ellipsoidal heights and the heights of the national height system can be determined (geoid heights, quasigeoid heights). These GPS/leveling control points allow the national height system to be fit to a geoid

or quasigeoid model, and they can be used to derive gravity-field related heights (orthometric heights, normal heights) for all three-dimensional reference stations, cf. [6.4.3]. This will lead to a large-scale *vertical control system* identical with the three-dimensional reference frame and not restricted to the leveling lines. Depending on the accuracy of the geoid-/quasigeoid "reduction" of GPS heights, the application of geometric leveling will be reduced to more local problems where mm-accuracy is required.



Fig. 7.15. German GPS Reference Net 1991(DREF91) with EUREF stations (black circles), courtesy BKG, Frankfurt a.M., Germany

In Germany, a three-dimensional network was established in 1991: Deutsches Referenznetz 1991 (DREF91). It consists of 109 stations that are mostly collocated with first or second-order trigonometric points (Fig. 7.15). The network comprises the ITRF and EUREF stations and represents the national reference frame embedded in the ETRF, cf. [7.3.1]. Two independent GPS campaigns were carried out (8-hour observation time per session), and the adjusted coordinates (accuracy ± 1 cm for the horizontal component and ± 1 to 2 cm for the height) were transformed to ETRF89 (LINDSTROT 1999). The network is maintained by about 20 permanent stations operated by BKG and the state survey agencies. DREF densification nets (station distances 15 to 25 km) are under construction by the state survey agencies, which also operate a DGPS service: Satellitenpositionierungsdienst der deutschen Landesvermessung (SAPOS). About 200 permanent GPS stations are planned, which will store the GPS signals and provide them to users in RINEX (receiver independent exchange) format, together with other products. Different accuracy levels are available for real-time and post-processing applications (HANKEMEIER 1996). With SAPOS being fully operational, the lower order trigonometric control networks will not be further maintained. Other examples of national three-dimensional reference networks are found in GUBLER and HORNIK (1999) and GUBLER et al. (1999).

Permanent GPS networks play an increasing role in regions of earthquake activity, cf. [8.3.3]. In Japan, a country-wide network of more than 1000 stations is operated by the Geographical Survey Institute, which continuously monitor strain accumulation and tectonic movements.

7.4 Gravity Networks

Gravity networks provide the frame for gravimetric surveys on global, regional, or local scales. They consist of gravity stations where gravity has been determined by absolute or relative methods. On a global scale, the gravity standard is realized by the *International Gravity Standardization Net 1971* (IGSN71), but *absolute gravimeters* now allow independent establishment of the gravity standard, cf. [5.4.3]. A global, absolute-gravity base-station network has been established primarily for the investigation of long-term gravity variations with time, cf. [8.3.4].

National gravimetric surveys are based on a primary or base network, which in most cases is densified by lower order nets. The gravity *base-network* stations should be evenly distributed over the area; station distances of a few 100 km are typical for larger countries. The station sites should be stable with respect to geological, hydrological, and microseismic conditions, and they should be located at permanent locations (observatories etc.). Eccentric stations serve for securing the center station and for controlling local height and mass changes. The stations of the subsequent densification networks may be collocated with horizontal and vertical control points. Horizontal position and height of the network stations should be determined with m and mm to cm-accuracy, respectively.

Absolute gravimeters are increasingly employed for the establishment of base networks, partly in combination with relative gravity-meters. Densification networks are observed primarily with relative instruments. *Relative* gravimeters need to be calibrated, and repeated measurements are necessary in order to determine the instrumental drift. The use of several instruments reduces residual systematic effects, cf. [5.4.2]. Relative gravimetry requires at least two absolute stations in order to derive the gravity "datum" and corrections to the linear calibration coefficient that was determined by the manufacturer or on a calibration line. A network optimization is beneficial for obtaining maximum accuracy and reliability for given restrictions (WENZEL 1977).

The establishment of gravity networks for *geophysical* and *geodynamic* applications follows the same rules, but the distribution of the gravity stations is determined by the geological structures or the geodynamic processes under investigation, cf. [8.3.4].

Gravity networks are generally *adjusted* by the method of parameter variation. Gravity values and - for relative gravimeters - drift and calibration coefficients are the parameters to be determined. Absolute gravity data and relative gravimeter readings, or reading differences, are introduced as observations. The *observation equation* for an *absolute* gravity measurement on the station i reads

$$\bar{z}_i = g_i, \quad (7.5)$$

where \bar{z}_i represents the station mean value corrected for polar motion and earth tides and reduced to ground level, cf. [5.4.1]. For *relative* gravity measurements, the observation equation follows from (5.90) and (5.92). If we restrict ourselves to the linear terms of the drift and the calibration function, the relative gravimeter reading z_i (after approximate calibration and application of the earth tides reduction) on the station i (time t_i) is transformed to gravity by

$$Y_i z_i - d_i t_i + N_0 = g_i, \quad (7.6a)$$

which leads to the observation equation

$$z_i = g_i - N_0 - Y_i z_i + d_i t_i. \quad (7.6b)$$

Here, d_i = linear drift coefficient, $Y_i = 1 + y_i$ = linear calibration coefficient, y_i = scale correction, N_0 = level unknown. In most applications, reading differences between the stations i and j are introduced as observations, hereby eliminating the level unknowns (TORGE 1993):

$$\Delta z_{ij} = z_j - z_i = g_j - g_i - y_i(z_j - z_i) + d_i(t_j - t_i). \quad (7.7)$$

The *accuracy* of primary gravity networks, established by absolute gravimeters or by a combination of absolute and relative gravimetry, is about $\pm 0.1 \mu\text{m s}^{-2}$ and may reach $\pm 0.05 \mu\text{m s}^{-2}$.

In Germany, gravity base networks and densifying networks were established beginning in the 1930's. The first base-network was observed with relative pendulum instruments; relative gravimeters have contributed since the 1950's. These networks were tied to the Potsdam absolute gravity value, cf. [5.4.3], accuracy increased from some $\pm 1 \mu\text{m s}^{-2}$ to \pm a few $0.1 \mu\text{m s}^{-2}$. Absolute gravimetry was introduced in 1976/1977 in order to establish a combined absolute/relative base-network in western Germany: *Deutsches Schwerergrundnetz 1976* (DSGN76), SIGL et al. (1981). This base network was extended to eastern Germany and completely remeasured in 1994/1995: DSGN94. The network consists of 30 stations (one center and at least two eccentric points) that were observed with an absolute gravimeter FG5. Repeated observations and relative ties (several gravimeters of type LaCoste and Romberg and Scintrex) served for investigations of accuracy

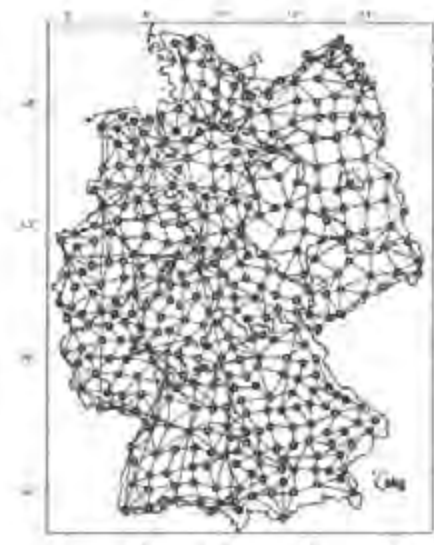


Fig. 7.16. Primary gravity net of Germany (DHSN96), with German gravity base net (DSGN94) stations (black circles), courtesy BKG, Frankfurt a.M., Germany



Fig. 7.17. Gravity network of Uruguay, with absolute stations (black triangles), relative stations, and earth tide station (black circle), after SUBIZA et al. (1998)

($\pm 0.05 \mu\text{m s}^{-2}$) and reliability (TORGE et al. 1999a). A first-order densification net (average station distance 30 km) was observed with several relative gravimeters (1978–1982, 1994, accuracy better than $\pm 0.01 \mu\text{m s}^{-2}$), Fig. 7.16. Further densification down to a few km has been realized or is in progress (WEBER 1998). The gravity network of Uruguay is an example of a combined adjustment of a few absolute stations and relative measurements carried out mainly along leveling lines, Fig. 7.17 (SUBIZA et al. 1998).

In the U.S.A., absolute gravity measurements have primarily been carried out within the frame of dedicated projects (investigation of recent vertical crustal movements, establishment of gravimeter calibration lines, etc.) by NOAA/NGS and other agencies, covering the country by more than 150 stations in 2000. A gravity network established in 1976/1979 by LaCoste and Romberg gravimeters (more than 200 sites) has been constrained to the absolute standard (PETER et al. 1989).

8 Structure and Dynamics of the Earth

Geodesy, within the frame of the geosciences (geophysics, geology, petrology, mineralogy, geochemistry), deals with the determination of the figure and the external gravity field of the earth. The results of geodetic work provide boundary conditions for the development of static and dynamic geophysical earth models. These models, in turn, provide significant information for the planning and implementation of geodetic operations.

Geophysical earth models are based on a radial structure of physical properties, and presuppose hydrostatic equilibrium [8.1]. These assumptions are not valid for the upper layers of the earth, where geodynamic processes play an important role [8.2]. Geodesy contributes to geodynamic research by monitoring the actual variations of the orientation, the physical surface, and the gravity field of the earth [8.3].

From the extensive geophysical literature we mention the classical work of JEFFREYS (1970) and the recent textbooks by BERCKHEMER (1990), STACEY (1992), LOWRIE (1997) and FOWLER (1999). The interrelations between geodesy and geophysics are treated especially in HEISKANEN and VENING-MEINESZ (1958), LAMBECK (1988), and MORITZ (1990). The actual state of geophysical data collection and parameter estimation is given in AHRENS (1995).

8.1 The Geophysical Earth Model

Various observations show that the earth does not possess a *homogeneous* structure:

- The *mass* M of the earth as derived from the geocentric gravitational constant GM , cf. [6.8.1], and the constant of gravitation G , cf. [2.1], amounts to $M = 5.974 \times 10^{24} \text{ kg}$. With the volume of the earth ellipsoid $1083 \times 10^{18} \text{ m}^3$, we obtain the *mean density*

$$\rho_m = 5.515 \times 10^3 \text{ kg m}^{-3}.$$

- As the density of the earth's crust only amounts to $2.7 \dots 2.9 \times 10^3 \text{ kg m}^{-3}$, density must increase toward the interior of the earth.
- Astronomic observations of the lunisolar precession, cf. [2.4.2], deliver the *dynamic (mechanical) ellipticity*

$$H = \frac{C - A}{A}, \quad (8.1)$$

with a value of $1/305.45$. With the dynamical form factor provided by satellite geodesy, cf. [6.8.1],

$$J_2 = \frac{C - A}{a^2 M}, \quad (8.2)$$

(C and A being the polar and the mean equatorial moment of inertia, respectively) we obtain the *moment of inertia* with respect to the *rotational axis*

$$C = 0.3307 a^2 M.$$

If the earth were a homogeneous sphere, we would have $C = 0.4a^2 M$. This again indicates a density increase with depth.

- Seismology shows that the earth has a *shell-like* construction, with the shell boundaries being defined by discontinuities of the seismic waves velocities.

With the velocities of the seismic waves being known, and under the assumption of hydrostatic equilibrium, density, gravity, and pressure inside a spherically layered earth model can be calculated as a function of the radial distance from the earth's center of mass.

The assumption of hydrostatic pressure in the earth's interior is justified by the fact that the earth originally existed in a liquid state. In which case, the pressure depended only on the weight of the masses lying above, and it increased toward the center of the earth.

Seismology determines the *velocities* of the primary (compression) and the secondary (shear) seismic waves, v_p and v_s . From these velocities the *seismic parameter*

$$\Phi = \frac{K}{\rho} = v_p^2 - \frac{4}{3}v_s^2 \quad (8.3)$$

is derived, where K is the bulk modulus (compressibility) and ρ is density. K is defined as the ratio between the hydrostatic pressure and the dilation experienced by a body under this pressure. The relationship between changes of *pressure* p and *density* is given by

$$d\rho = \frac{1}{\Phi} dp . \quad (8.4)$$

Under hydrostatic equilibrium, the increase of *pressure* with *depth* depends on the weight of the additional vertical mass column. With the radial distance r , the fundamental hydrostatic equation reads

$$dp = -g(r)\rho(r)dr , \quad (8.5)$$

where the minus-sign indicates that pressure decreases with increasing radius. Finally, from (8.4) and (8.5) we obtain the relation between *height* and *density* changes (*Adams-Williamson* equation):

$$\frac{d\rho}{dr} = -\frac{g(r)\rho(r)}{\Phi} . \quad (8.6)$$

According to (3.52), the radial change of the gravity potential W is given by

$$dW = -g(r)dr . \quad (8.7)$$

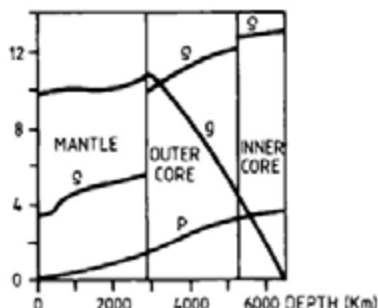


Fig. 8.1. Density ρ (10^3 kg/m^3), gravity g (m/s^2), and pressure p (10^{11} Pa) inside a spherically symmetric earth model, after DZIEWONSKI and ANDERSON (1981)

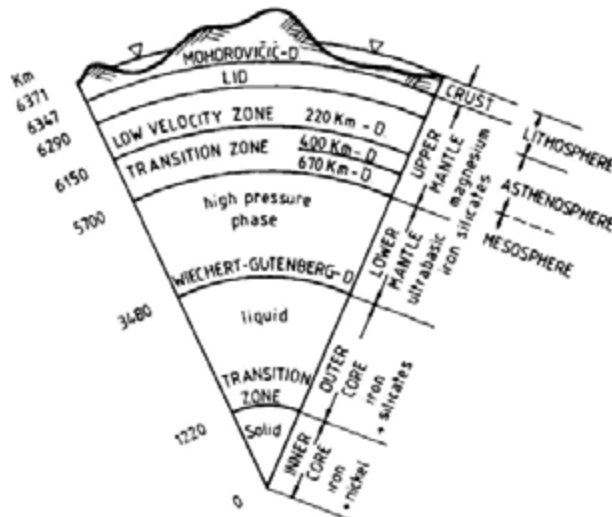


Fig. 8.2. Spherical earth model, with homogeneous shells separated by discontinuity zones (D.), not to scale, after DZIEWONSKI and ANDERSON (1981)

Inserting (8.7) into (8.5) yields

$$dp = \rho(r)dW. \quad (8.8)$$

Hence, the surfaces of equal pressure (isobaric surfaces) coincide with equipotential surfaces and, after (8.4), also with surfaces of equal density.

Starting from density and gravity values on the earth surface, density, pressure and gravity inside the earth can be calculated iteratively, using (8.3), (8.4) and (3.22), (3.23). Here we use the total mass and the polar moment of inertia as boundary conditions. Corresponding spherically symmetric *earth models* consist of several layers characterized by chemical and physical properties (composition, pressure, temperature), BULLEN (1975), DZIEWONSKI and ANDERSON (1981). The velocities, or the velocity gradients, of the seismic waves change abruptly at the boundaries of the layers (discontinuity surfaces or zones), as does density (Fig.8.1). Inside one layer, density increases smoothly and reaches about 13000 kg m^{-3} at the earth's center. Gravity remains nearly constant within the earth's mantle and decreases almost linearly to zero in the core. Pressure increases continuously with depth.

The layered structure of the earth is shown in Fig.8.2. The earth's *crust* (average thickness over the continents and the oceans about 24 km) is the uppermost layer and is characterized by a complex structure. It is separated from the *upper mantle* by the *Mohorovičić-discontinuity*. Lateral density variations are pronounced in the crust, but are found also in the upper mantle, cf. [8.2.1]. The crust and the uppermost part of the mantle (also called lid of the low-velocity layer beneath it) behave rigidly and are affected by plate tectonic motions, cf. [8.2.3]. The *lower mantle* starts at a depth of 650 to 670 km and is separated from the core at 2890 km depth, through the *Wiechert-Gutenberg-discontinuity*. The liquid *outer core* extends to 5150 km, followed by the solid *inner core*.

The density distribution of these earth models can also be tested by comparing its *elasticity* parameters with the results obtained from the observation of natural oscillations and (to a limited extent) earth tides, cf. [8.3.5]. The free oscillations especially provide an important constraint on the models.

More refined models have to take the *deviations from spherical symmetry* into account, as well as departures from hydrostatic equilibrium. These deviations are clearly indicated by the odd zonal and the tesseral harmonic coefficients of the gravity potential, cf. [3.3.4], and by other geophysical observations. Seismic tomography especially revealed large-scale lateral variations of the P and S-wave velocities in the mantle, correlated with zones of density and temperature anomalies (DZIEWONSKI and WOODHOUSE 1987). A global deviation from

hydrostatic equilibrium is indicated by the flattening of a rotating spheroidal body in equilibrium, composed of density layers that are approximately ellipsoidal. According to *Clairaut*, the following relation holds between the polar moment of inertia C , the mass M , the ellipsoidal quantities a and m (4.50), and the hydrostatic flattening f_h :

$$\frac{C}{a^2 M} = \frac{2}{3} \left(1 - \frac{2}{5} \sqrt{\frac{5m}{2f_h} - 1} \right). \quad (8.9)$$

Inserting the observed values results in *hydrostatic flattening* values of about 1/299.7, which differ significantly from 1/298.25 derived directly from satellite orbit analyses, cf. [6.8.1], DENIS (1989).

The larger actual flattening may be attributed to a “fossil” flattening of the lower mantle, which developed when the earth’s rotational velocity was larger and which is not yet compensated. The still incomplete recovery of the ancient ice loads at the polar caps may be another explication.

Refined geophysical earth models that take the ellipsoidal form and the rotation of the earth into account may use the level ellipsoid as a good approximation for the external boundary surface, cf. [4.2.1].

8.2 The Upper Layers of the Earth

Large deviations from the spherically symmetric earth model are found in the earth’s crust and upper mantle [8.2.1]. Topographic mass excesses (mountains) and deficiencies (oceans) are, to a large part, compensated by the underlying masses, which leads to isostatic equilibrium [8.2.2]. The theory of plate tectonics introduces (nearly) rigid lithospheric plates that move against each other, causing crustal deformations, especially at the plate boundaries [8.2.3]. Since the gravity field reflects the distribution of the terrestrial masses, it provides an essential constraint in the development of crust and mantle models [8.2.4].

8.2.1 Structure of the Earth’s Crust and Upper Mantle

The heterogeneous structure of the uppermost layers of the earth is recognized directly by the distribution and composition of the *topographic* masses. There is a pronounced difference between the mean elevation of the continents (about 0.5 km) and the mean depth of the oceans (about 4.5 km). Ocean depths increase with growing distance from the ocean ridges (mean depth around 2.5 km) due to thermal cooling and contraction of the oceanic lithosphere with sea-floor spreading, cf. [8.2.3]. Consequently, the age of the oceanic crust is at most

200 million years, while the continental crust dates back 4 billion years (CAZENAVE 1995).

The *crust* is composed of a variety of sedimentary, igneous (effusive and intrusive), and metamorphic rocks. Density changes occur primarily between different types of rock, but larger density variations are also found within the same rock material, especially in sediments. Density estimates are based on surface rock samples, borehole probes, and the relationship between density and seismic wave velocities (ST. MUELLER 1974). The *upper mantle* has been investigated by seismic methods especially, and three-dimensional models are now available from seismic tomography (WOODHOUSE and DZIEWONSKI 1984).

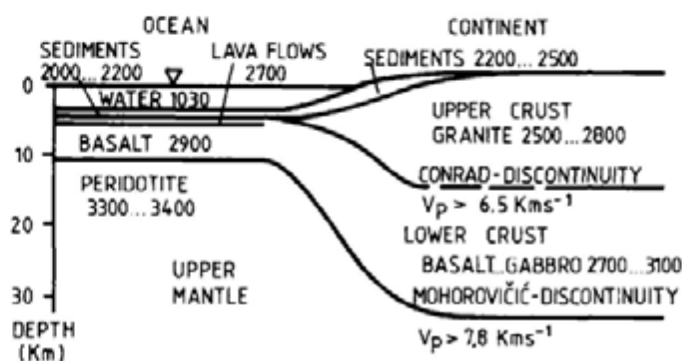


Fig. 8.3. Structure of the earth's crust with rock densities (kg/m^3) and velocities of seismic primary waves, after TORGE (1989)

The *structure of the earth's crust and upper mantle* may be briefly described as follows (Fig.8.3):

A *sediment* layer with highly varying thickness is found in the uppermost stratum in large parts of the *crust*. Seismic wave velocities and rock densities (average value 2400 kg m^{-3} for consolidated sandstone) vary considerably in this zone. In *continental* areas, the next lower layer of the upper crust consists mainly of acidic rocks such as granite (mean density 2700 kg m^{-3}); primary wave velocities vary between 5.9 and 6.3 km s^{-1} . The lower crust is composed of basic rocks such as basalt and gabbro (mean density 2700 kg m^{-3}). Wave velocities exceed 6.5 km s^{-1} and gradually increase to more than 7 km s^{-1} . The boundary between the upper and the lower crust (*Conrad – discontinuity*) is marked only in some parts of the continents, at depths of 10 to 20 km. Beneath the *oceans*, consolidated sediments and basalt lava flows are found in the upper part of the crust above a basaltic layer of 6 to 7 km thickness (TANIMOTO 1995).

A sharp (over a few km) change in seismic velocity ($v_p > 7.8 \text{ km s}^{-1}$) is found at an average depth of 35 km on the continents and 10 km on the oceans. This

Mohorovičić-discontinuity (Moho) defines the boundary between crust and mantle. Ultrabasic rocks (peridotite, with olivine as the main mineral constituent) are assumed to be located below the Moho, with a density of 3300 to 3400 kg m^{-3} . The depth of the Moho is closely related to topography. On the continents, it may be less than 20 km (Afar hotspot), reaching about 30 to 40 km at shields and platforms. Cenozoic mountain belts (Alps, Rocky Mountains, Himalaya) are characterized by a crustal thickness of 60 to 80 km. On the oceans, the crustal thickness is more constant. An extremely thin crust of a few km is found at slow spreading and fracture zones, while a thick crust of about 20 km appears where hotspots (mantle plumes) are located under ridge axes, as in southern Iceland. These variations of crustal thickness are mainly due to isostasy and plate tectonics, cf. [8.2.2], [8.2.3].

A global description of the Moho-depth is provided by a spherical harmonic expansion up to degree and order 20 (SOLLER et al. 1982). More detailed studies on the depth of the Moho are available for the U.S.A. (ALLENBY and SCHNETZLER 1983) and for Europe (MEISSNER et al. 1987), among others. Three-dimensional models are available for the crust (MOONEY et al. 1998) and for the upper mantle.

8.2.2 Isostasy

When considering the topographic masses and ocean waters as deviations from hydrostatic equilibrium, the removal of topography and the filling of the oceans should create an equilibrium figure, with a gravity field coinciding with the normal gravity field, cf. [4.2.2]. However, from the systematic behavior of the residual gravity field quantities, it follows that the visible mass excesses and deficiencies are, to a large part, compensated by a corresponding mass distribution in the interior of the earth (HEISKANEN and VENING-MEINESZ 1958).

During the arc measurement in Peru, cf. [1.3.2], Bouguer discovered that the *deflections of the vertical* as computed from the masses of the mountains were larger than the observed values. In the 19th century, the Survey of India (*G. Everest*) revealed significant differences between observed and calculated deflections of the vertical caused by the Himalaya Mountains, the computed values being several times larger than the observed ones. This observation was the basis for the theory of isostasy developed by Airy and Pratt (see below).

The large-scale behavior of the *Bouguer anomalies*, cf. [6.5.3], is another indication for the compensation of the visible mass anomalies. In mountainous areas, the Bouguer anomalies are generally negative, reaching values as low as $-2000 \mu\text{m s}^{-2}$, while positive values (up to $4000 \mu\text{m s}^{-2}$) are common over the oceans. A correlation with the mean height or depth (mean over several 100 km) can be demonstrated and approximated by a regression of $-1000 \mu\text{m s}^{-2}/1000 \text{ m height}$, and $+1000 \mu\text{m s}^{-2}/1000 \text{ m depth}$.

Finally, the *geoid heights* produced by the topographic masses would reach values of up to about 500 m (HELMERT 1884), whereas the observed values remain below 100 m.

The model of *isostasy* is used to explain these observations. It postulates that the topographic masses are compensated in such a way that hydrostatic pressure is achieved at a certain depth of compensation. The compensation depends on the dimension of the topographic load and may be achieved by different mechanisms. Loads of several 10 to 100 km dimensions are supported by the strength of the lithosphere and are not isostatically compensated. Larger loads may lead to an elastic flexure of the lithosphere. Large-scale topographic features of several 100 km dimension, and more, are generally in isostatic equilibrium, at least for the major part of the earth, the exceptions being areas of postglacial isostatic rebound (see below) and the deep-sea trenches, cf. [8.2.3].

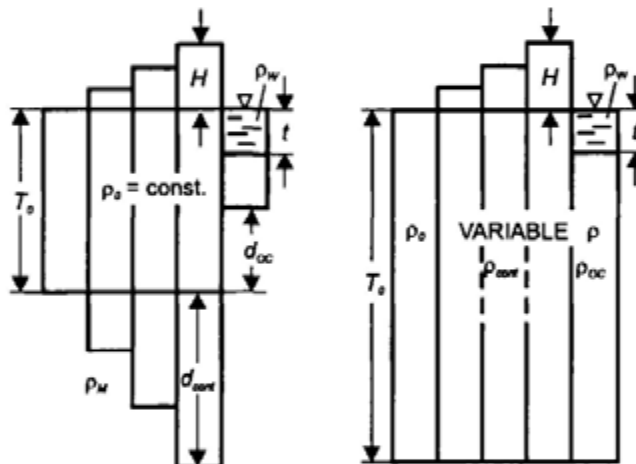


Fig. 8.4. Isostatic model of Airy

Fig. 8.5. Isostatic model of Pratt

The classical isostasy models of *Airy* and *Pratt* are based on the assumption that isostatic compensation takes place locally in vertical columns only. Utilizing the hydrostatic equation (8.5), the condition of isostasy then reads (with $g = \text{const.}$)

$$\int_{H+T}^H \rho dz = \text{const.}, \quad (8.10)$$

with z = depth, H = height of topography, T = depth of compensation. The model developed by G.B. *Airy* in 1855 (also designated Airy-Heiskanen model) is based on a crust of constant density ρ_0 and varying thickness, where the "normal" column of height $H=0$ has the thickness T_0 (Fig. 8.4). The continental topography ($H > 0$) forms mountain "roots" (thickness d_{out}), while

"antiroots" (thickness d_{∞}) are found beneath the oceanic columns. The ocean depth is denoted as t . In this way, the crust penetrates with varying depths into the upper mantle: floating equilibrium. Neglecting the earth's curvature, the following equilibrium conditions hold for the continental and the oceanic columns:

$$\begin{aligned} (\rho_M - \rho_0) d_{\text{cont}} &= \rho_0 H \\ (\rho_M - \rho_0) d_{\infty} &= (\rho_0 - \rho_w) t, \end{aligned} \quad (8.11)$$

with ρ_0 = density of the crust, ρ_M = density of the upper mantle, ρ_w = sea water density. With the conventional values $\rho_0 = 2670 \text{ kg m}^{-3}$, $\rho_M = 3270 \text{ kg m}^{-3}$, $\rho_w = 1030 \text{ kg m}^{-3}$, the thickness of the root and the antiroot is given by

$$d_{\text{cont}} = 4.45 H, d_{\infty} = 2.73 t. \quad (8.12)$$

The thickness T_0 of the normal column can be estimated from isostatic gravity anomalies calculated on the basis of a certain depth of compensation, cf. [6.5.3]. For $T_0 = 30$ to 40 km , these anomalies generally do not depend on the height of the topography. Hence, the depth of compensation is in good agreement with the depth of the Moho as obtained from seismology, cf. [8.2.1].

The isostatic model of *J.H. Pratt* (1855, also called Pratt-Hayford model) assumes a crustal layer of constant thickness T_0 and allows lateral changes in density in order to obtain isostatic equilibrium (Fig. 8.5). With the density ρ_0 for the normal column ($H = 0$), continental columns generate densities smaller than ρ_0 , while oceanic columns are denser. The equilibrium conditions for the continents and the oceans are:

$$\begin{aligned} \rho_{\text{cont}} (T_0 + H) &= \rho_0 T_0 \\ \rho_w t + \rho_{\infty} (T_0 - t) &= \rho_0 T_0. \end{aligned} \quad (8.13)$$

with $\rho = 2670 \text{ kg m}^{-3}$ and $\rho_w = 1030 \text{ kg m}^{-3}$ the densities of the continental and the oceanic columns are given by

$$\rho_{\text{cont}} = 2670 \frac{T_0}{T_0 + H}, \quad \rho_{\infty} = \frac{2670 T_0 - 1030 t}{T_0 - t}. \quad (8.14)$$

The depth of compensation can be estimated from the behavior of residual gravity field quantities calculated with depth dependent assumptions. By utilizing topographic-isostatically reduced deflections of the vertical in the U.S.A., *Hayford* obtained minimum values for a compensation depth of 113.7 km . This value is close to the thickness of the continental lithosphere, cf. [8.2.3].

A refined isostatic model was proposed by VENING-MEINESZ (1931). It admits *regional isostatic compensation* by assuming that the upper layer behaves like an elastic plate overlying a weak fluid. A surface load causes a flexure of the plate, with a regional bending over a horizontal distance wider than the load dimension (Fig. 8.6). The amount of flexure depends on the distance from the load and can be calculated from the load, the density contrast between the plate and the substratum, and the elastic parameters (Young's modulus, Poisson's ratio) of the plate (ABD-ELMOTAAL 1995).

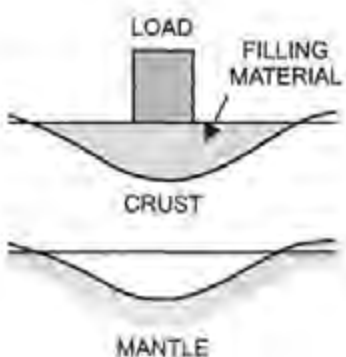


Fig. 8.6. Regional isostatic model of Vening-Meinesz

Globally, the models of Airy respectively Vening-Meinesz describe the dominating isostatic features, but lateral density variations (Pratt model) also contribute to isostasy in some regions. In the compensated parts of the earth, isostatic anomalies vary non-uniformly about zero (maximum values of about $500 \mu\text{m s}^{-2}$), and they clearly indicate areas which are not in isostatic equilibrium. On the other hand, they are not very sensitive with respect to a change of the model or variations of the model parameters, which makes discerning of different models and estimating the absolute depth of the compensation level difficult. Utilizing global models of the topography, cf. [6.5.2], spherical harmonic expansions of the topographic-isostatic potential have been developed (SÜNKEL 1936b). These models can be used for gravity field interpolation and for the analysis of the observed gravity field (RUMMEL et al. 1988).

Incomplete isostatic compensation is found in some mountainous regions and in the areas of strong pleistocene glaciation (Canada, Fennoscandia, Greenland, Antarctica). Mountains may become overcompensated by large erosion, and as a consequence a vertical uplift will occur. The melting of the ice masses after the pleistocene glaciation has caused an isostatic imbalance, which has since been compensated by postglacial rebound. This phenomenon has been especially well investigated in Fennoscandia, where recent uplift rates reach 1 cm/year (KAKKURI 1986). As the rate of uplift depends on the viscosity of the

mantle, corresponding observations contribute to the determination of this geophysical parameter (LAMBECK et al. 1998), cf. [8.3.3].

8.2.3 Plate Tectonics

The theory of plate tectonics synthesizes a multitude of individual observations of geological and geophysical nature. The theory integrates the concepts of *continental drift* (WEGENER 1915) and *sea-floor spreading* (DIETZ 1961, HESS 1962). According to this model, new oceanic crust is formed by uprising basaltic magma at the axes of the mid-oceanic ridges, and it spreads out to both sides of the rift system. The spreading sea-floor is characterized by stripes of interchanging positive and negative magnetic anomalies aligned parallel to the ridges, which indicate the reversal of the earth's magnetic field occurring irregularly at intervals of tens of thousands to tens of million years (VINE and MATTHEWS 1963). Radiometric age determinations of the oceanic rocks show that the age of the ocean floor increases with the distance from the ridge axes and does not exceed 200 million years.

Before that time (Permian and Triassic), the supercontinent Pangaea, postulated by Wegener, united all present land masses. Break up started during the Jurassic period, when Pangaea rifted into Laurasia (today North America and Eurasia) and Gondwana (today South America, Africa, India, Antarctica and Australia), with the Tethys Sea between them. This rifting process finally led to the present distribution of the continents and oceans.

The spreading rates of the ocean floor (referring to geological time spans) can be derived from the spacing of the magnetic anomalies and the rock age. They vary between 2 cm/year (e.g., at the Reykjanes Ridge south of Iceland) and 15 cm/year at the East Pacific Rise, MINSTER and JORDAN (1978).

Plate tectonics (McKENZIE and PARKER 1967, MORGAN 1968) postulates seven larger (Pacific, North and South American, Eurasian, African, Indian-Australian, Antarctic) and more than 20 smaller, nearly rigid lithospheric plates which move against each other on the asthenosphere. The *lithosphere* includes the earth's crust and the uppermost part of the mantle; it possesses a thickness of 70 to 100 km under the deep oceans and 100 to 150 km under the continents. The *asthenosphere* is characterized by low viscosity (resistance to flow within a fluid), which allows a viscous flow on geological time scales (LE PICHON et al. 1973). The plate boundaries can be identified by an accumulation of seismic (earthquakes) and volcanic activity, where the boundary zones vary in width between some 10 to some 100 km and more (Fig.8.7).

The movement of the tectonic plates can be described as follows (LE PICHON et al. 1973, LOWRIE 1997), Fig.8.8:



Fig. 8.7. Main lithospheric plates and direction of plate movements, AN = Anatolian, AR = Arabian, CA = Caribbean, CO = Cocos, NA = Nazca, PH = Philippines, SO = Somalia plate, after TORGE (1989)

The mid-ocean ridges represent *diverging* (constructive) plate boundaries where new lithospheric material is formed from magma uprising from the asthenosphere and pressed apart. When colliding with another plate, the cooled, heavier oceanic plate is forced to sink into the upper mantle (subduction) where it is consumed at depths of around 700 km: *converging* (destructive) plate boundary. This process creates deep-sea trenches and island arcs (e.g., at the western and northern Pacific, subduction rate of about 9 cm/year at the Japan trench) or mountain ranges (e.g., the Andes). The collision of two continental plates leads to the formation of mountain chains (e.g., the Himalaya and the Alps). *Transform faults* with relative motion parallel to the strike of the fault are usually found between ridge segments, but also occur where two plates meet with shear movements (e.g., San Andreas Fault, California, shear movements of several cm/year): *conservative* plate boundary. About 85 percent of the earth's surface is covered by the (nearly) rigid plates, while deformations are concentrated on the plate boundary zones. Thermic *convection* (heat transfer by movement of molecules) flows in the mantle are assumed to be the driving mechanism for the plate movements (RUNCORN 1962). Different theories exist on the size and the location of the convection cells (whole-mantle or layered mantle convection).

The *motions* of the lithospheric plates on the spherical earth can be described as a rotation of a spherical cap about an axis through a fixed point (pole of rotation) with a certain angular velocity (GORDON 1995). From these parameters, the *relative* plate motion (direction and magnitude) can be calculated for any location. Geologically-recent (average over the last few million years) plate velocities have been estimated from the spacing of the

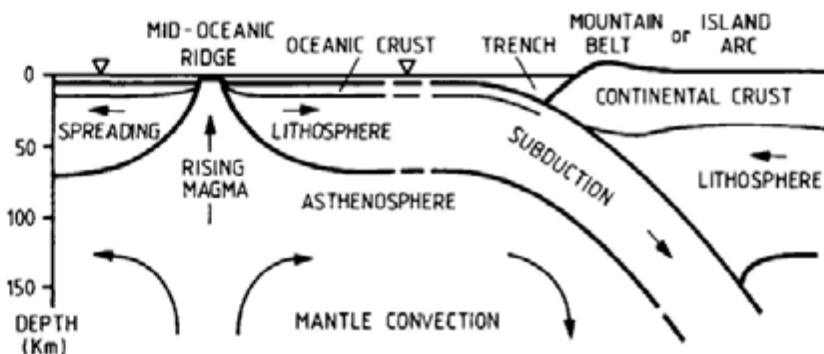


Fig. 8.8. Motion of lithospheric plates at diverging and converging plate boundaries, vertical scale exaggerated, after TORGE (1989)

magnetic anomalies across the mid-ocean ridges and from the azimuths of submarine transform faults and slips from large earthquakes. Recent models such as NUVEL-1 (DE METS et al. 1990) and NUVEL-1A (DE METS et al. 1994) include the major plates (about 15), keeping either one plate fixed (NUVEL-1: Pacific plate), or referencing the motions to a rotation-free system coupled with the earth: no-net rotation (NUVEL-1A). An *absolute* plate motion can be derived by reference to the hotspots (SOLOMON and SLEEP 1974). Here, hot material is rising from deep mantle plumes that do not participate in the plate tectonic motions. Hotspots are characterized by surface volcanism and high heat flow; examples are Hawaii, Iceland, and Afar (Ethiopia).

It has to be noted that the plate velocities derived from these models represent the average over geological time spans. Furthermore, they suffer from the choice of the plates used, from strong deformations occurring at the converging plate boundaries, and from the existence of intra-plate deformations, as well as from the assumption of non-moving hotspots. Geodetic measurements allow determination of the actual plate motions and identification of local and regional deformations at the plate boundaries and inside the plates, cf. [8.3.3].

8.2.4 Interpretation of the Gravity Field

The observed gravity field reflects the integrated effect of the mass distribution inside the earth and reveals deviations from spherical symmetry and hydrostatic equilibrium, cf. [8.1]. Static and dynamic geophysical earth models must fulfill the constraints imposed by the gravity field. The *inverse problem*, i.e., the determination of the density distribution from the external gravity field, on the other hand, cannot be solved uniquely (SKEELS 1947, MARTINEC 1994). This fact is seen in Stokes' theorem, where the external gravity field of an equipotential surface is completely determined without knowing the distribution of the internal masses, cf. [4.2.1]. Consequently, gravity field interpretation requires additional information through geophysical and geological data, where

seismically derived depths of bounding surfaces and the composition and density of the masses play the major role.

Gravity field interpretation is based on *residual* gravity field quantities obtained by reducing the effect of the normal gravity field, cf. [6.1], and eventually also on the well-known gravitation of the uppermost layers of the earth, cf. [6.5.3]. The primary gravity-field parameters used for interpretation are gravity anomalies and, to a limited extent, deflections of the vertical, as well as geoid heights. The effect of the masses on gravity anomalies and vertical deflections is inversely proportional to the square of the distance, while geoid heights depend on the reciprocal distance to the masses. Consequently, *gravity anomalies* and *deflections of the vertical* are more suited for investigating the density distribution in the upper layers of the earth. Gravity anomalies react primarily to vertically extended masses, while vertical deflections reflect the effect of horizontal layers, hence they especially support local investigations. *Geoid heights* reveal deeper seated mass anomalies, which generally have large dimensions.

The spectral decomposition of the gravity field as provided by the *spherical harmonic expansion*, cf. [6.6.1], is especially appropriate for global and regional interpretation. Degree variance models for the gravity anomalies (6.27) and the geoid heights (6.142) show that about 95 percent of the geoid variance is concentrated in degrees 2 to 10 (corresponding to wavelengths of 20000 to 4000 km), while this long-wave spectral part attains only 9 percent of the gravity anomalies. Medium (degree 2 to 180) and short (degree 181 to 2000) wavelengths, on the other hand, each contribute more than 40 percent to the anomaly variance. Nearly 10 percent of the anomaly variance still stem from wavelengths less than 20 km (degrees > 2000), reflecting small structures in the upper crust (e.g., salt domes). Deflections of the vertical show a spectral distribution similar to that of the gravity anomalies.

Hence, the interpretation of the *geoid* concentrates on the long and medium-wave part of the spectrum. Density and/or temperature anomalies are thought to produce the low degrees of the spherical harmonic expansion, while mantle convection and lithospheric structures are seen in wavelengths of thousands of kilometers (PHILLIPS and LAMBECK 1980, BOWIN 2000). Shorter wavelengths of a few 100 to 1000 km can be correlated with diverging and converging plate boundaries and with hotspots (CAZENAVE 1994). Areas of postglacial rebound or significant crustal thinning are also reflected in this spectral part.

Slow-spreading ridges and hotspots may exhibit relative geoid maxima of several meters. Deep-sea trenches are characterized by narrow zones of geoid depression up to 5 to 20 m, followed by a geoid rise along the island arcs (Fig. 8.9). Postglacial land uplift areas show a geoid depression (up to 10 m in Fennoscandia), which is correlated with present uplift rates (BJERHAMMAR 1981).

Fig. 8.10. The Ivrea body (western Alps) is an example of a local geoid rise (up to 9 m) due to the

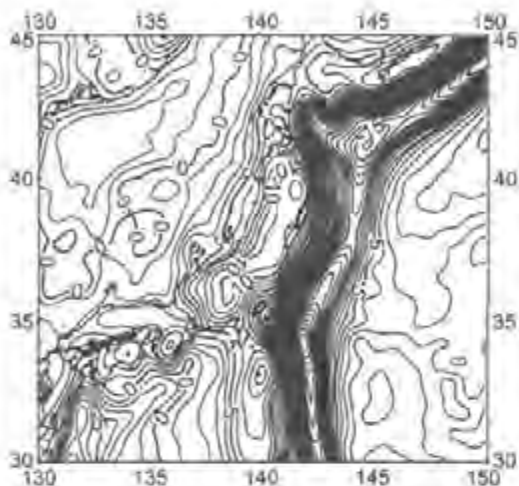


Fig. 8.9. Geoid structures at the Japan subduction zone, EGM96 geoid model, spectral part degree 11 to 360, contour line interval 1 m, after LEMOINE et al. (1998)

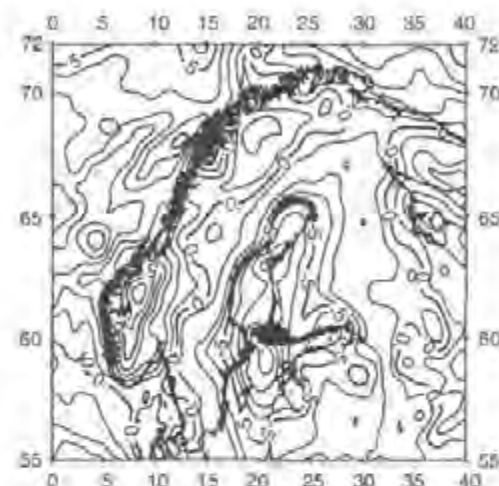


Fig. 8.10. Geoid structure at the Fennoscandian land uplift area, EGM96 geoid model, spectral part degree 11 to 360, contour line interval 1 m, after LEMOINE et al. (1998)

shifting of lower crustal/upper mantle material to a shallow level (BÜRKI 1989).

Modelling of the long-wave geoid structures can be based on equivalent point masses arranged primarily around the bounding surfaces as determined by seismology, cf. [8.1], BOWIN (1994). The solutions strongly depend on the choice of the spectral part to be modeled, the distribution of the masses, and the introduced density differences.

The interpretation of *gravity anomalies* uses either the spherical harmonic expansion (global and large-scale investigations) or local models based on observed or gridded data. Different types of gravity anomalies can be used for regional and local investigations.

Point *free-air anomalies* depend strongly on height and are not suited for interpretation. The long and medium-wave part provided by global models, or corresponding mean anomalies, on the other hand, can be exploited, due to the smoothing of the high frequencies. The free-air anomalies then may be interpreted as isostatic anomalies with a compensation depth of zero. Structures of plate tectonics (e.g., subduction zones) and postglacial rebound can be identified, where proper filtering again may be necessary.

Bouguer anomalies are employed for regional and local investigations, as they are free from the effect of topography, cf. [6.5.3]. They mainly reflect density

anomalies in the crust and upper mantle and can be correlated with tectonic structures such as ocean ridges, deep-sea trenches, continental grabens, young-folded mountains, and with upper mantle structures (KOGAN and McNUTT 1993). Isostatic compensation is indicated by the large-scale systematic behavior of the Bouguer anomalies, with negative values in the mountains and positive values in the oceans, cf. [8.2.2], Fig. 8.11. Bouguer anomalies play an important role in geophysical prospecting (DOBRIN 1976).



Fig. 8.11. Regional Bouguer gravity anomaly map of the United States, composed of wavelengths longer than 250 km, referred to IGSN71 and GRS67, rock density 2670 kg/m^3 , contour line interval $200 \mu\text{m/s}^2$, after KANE and GODSON (1985)

More detailed investigations of the deeper regions of the crust are made possible by further reducing the effects of known or assumed mass distributions. *Isostatic anomalies* take the effect of the compensating masses into account; deviations from zero indicate areas of isostatic imbalance and are often correlated with geological features (SIMPSON et al. 1986). The reduction of geologically known structures ("crustal stripping") allows, among others, the estimation of the depth of sedimentary basins and of the crust-mantle boundary (HAMMER 1963, TOMODA and FUJIMOTO 1981).

Gravity anomalies have been used for modeling a variety of crust and mantle structures of local and regional extent. Here, a starting model is iteratively improved by varying the geometry and densities of the masses, taking the constraints from seismic data and geology into account. We mention the

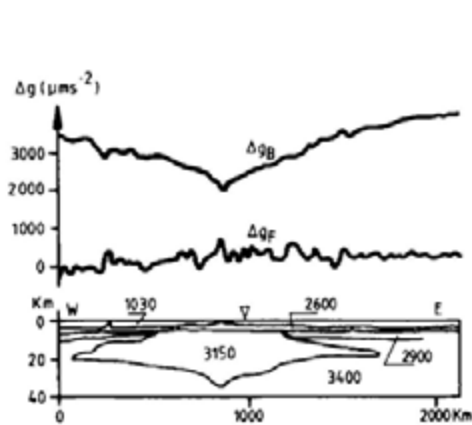


Fig. 8.12. Bouguer and free-air anomalies across the Mid-Atlantic ridge and crustal density model, with oceanic layers (2600 kg/m^3), low-density zone (3150 kg/m^3), and upper mantle (3400 kg/m^3), after TALWANI et al. (1965)

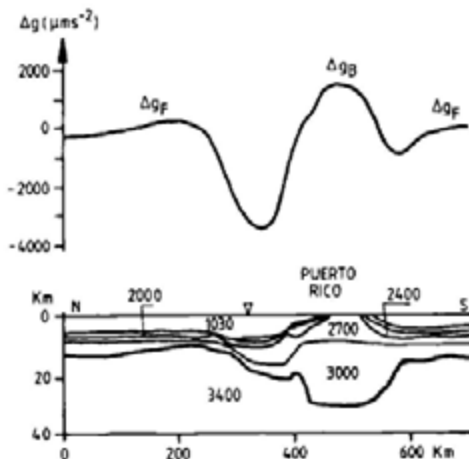


Fig. 8.13. Generalized free-air anomalies (Bouguer anomalies on land) across the Puerto Rico trench and crustal density model, with unconsolidated (2000 kg/m^3) and consolidated (2400 kg/m^3) sediments, upper (2700 kg/m^3) and lower (3000 kg/m^3) crust, and upper mantle (3400 kg/m^3), after TALWANI et al. (1959)

following from the relationships found between the gravity field and crustal structures (KAULA 1992, NEREM et al. 1995):

- *Oceanic ridges* show negative Bouguer anomalies (up to $-2000 \mu\text{ms}^{-2}$) due to high anomalous mantle material, while free-air anomalies deviate only slightly from zero, Fig.8.12.
- *Deep-sea trenches* are characterized by strong, negative free-air anomalies (up to $-4000 \mu\text{ms}^{-2}$), which are explained in part by thick sedimentary layers and sea floor topography. Further inland, large positive anomalies occur due to cooling of the subtracted material, Fig.8.13.
- *Continental grabens* are correlated with strong negative Bouguer anomalies due to sedimentary layers and/or anomalous mantle material; local highs may occur through crustal thinning.
- *Young, folded-mountains* arising at continental collision zones exhibit negative Bouguer anomalies, indicating isostatic compensation. Isostatic anomalies may differ from zero due to recent tectonic processes and incomplete compensation.
- *Postglacial rebound* areas are characterized by negative free-air anomalies.

8.3 Geodesy and Recent Geodynamics

From repeated measurements, geodetic and gravimetric techniques allow detection of temporal variations of the orientation, surface, and gravity field of the earth. The observed changes are used for modeling the effects on geodetic data and for referring the data to common reference epochs. The variations contain, on the other hand, valuable information on geodynamic processes of global, regional, and local scales. Geodesy thus contributes to research in *geodynamics*, in collaboration with astronomy, oceanography, meteorology, solid earth geophysics, and geology.

In order to obtain significant results for geodynamic modeling, the temporal and spatial resolution of the observations as well as their accuracy must be tuned to the frequencies and amplitudes of the signals to be detected. For this reason, observation stations and platforms must remain stable in position over time, or their changes accurately monitored.

Space-geodetic observations provide changes of the earth rotation due to the redistribution of masses in the atmosphere, the hydrosphere, and the solid earth [8.3.1]. Satellite altimetry, together with tide gauge measurements, represents a powerful tool for the study of sea level variations [8.3.2]. Recent crustal movements are observed by space and terrestrial techniques; they serve as constraints for the modeling of geodynamic processes and as precursor phenomena [8.3.3]. Observed gravity variations contain the integral effect of terrestrial mass redistributions and support and supplement the geodetic observations [8.3.4]. Continuous records of geodetic and gravimetric data are especially useful for earth tide research [8.3.5].

Extensive treatises on the contributions of geodesy to geodynamics research are found in LAMBECK (1988) and MUELLER and ZERBINI (1989).

8.3.1 Changes in Earth Rotation

Temporal changes of the earth rotation vector with respect to the earth's body are described by polar motion and variations of the length of the day (LOD). These changes proceed at different time scales and reach the $0.1''$ respectively ms order of magnitude. The integral effect of the LOD variations over time leads to larger deviations of the rotational time UT1 from the atomic time TAI (DICKEY 1995), cf. [2.5.2]. VLBI and satellite techniques, including GPS, allow determination of the earth rotation changes with a resolution of a few hours and an accuracy of better than $0.001''$ respectively 0.01ms (ROTHACHER et al. 1999), cf. [2.3].

The observed rotation changes mirror the combined effects of terrestrial mass redistributions, which affect the inertia tensor of the earth, and of the related *motion*, which acts on the respective angular momentum of the layer (e.g., atmosphere, oceans, continental waters, mantle, core). The law of the conservation of the *total* angular momentum of the earth then requires corresponding changes of the rotational vector. The integral effect of the redistribution of masses can be recovered by repeated gravity field observations, cf. [8.3.4].

From the many sources of rotational changes, only a limited number have been clearly identified. The mass redistribution mainly affects polar motion, while LOD variations are dominated by the mass motions (CHAO 1994).

Secular effects have been found in polar motion (redistribution of ice masses and postglacial rebound) and in LOD (tidal friction in the oceans). *Decadal* effects could be due to core/mantle processes but also to long-term atmospheric variations. *Interannual* variations are especially pronounced in LOD; they are produced by changes in the atmospheric angular momentum. The *Chandler wobble* in polar motion is excited from atmospheric mass redistributions, but strong earthquakes may also play a role (CHAO et al. 1996). *Annual*, *semiannual*, and *seasonal* effects stem mainly from mass shifts in the atmosphere and in the oceans, together with changes in the groundwater layers, in ice/snow coverage, and in the water level of large lakes.

An outstanding example of a large-scale interannual effect is the El Niño phenomenon. It manifests itself by strong disturbances of the atmospheric and oceanic states in the tropical Pacific (atmospheric pressure, wind, ocean temperature, sea level inclination in west-east direction due to ocean warming and shift of water masses), with effects reaching far beyond the Pacific. It recurs after two to seven years with varying intensity; the last strong occurrence happened in 1997/1998. El Niño effects have been clearly identified in LOD (increase of several 0.1 to 1 ms) and in irregular perturbations of polar motion (SALSTEIN et al. 1999).

Diurnal and *subdiurnal* effects, as well as more *irregular* variations in earth rotation, are excited primarily by processes in the atmosphere and hydrosphere and by earthquakes as well. *Tidal* deformations of the solid earth and the oceans cause maximum rotation changes of a few 0.001" respectively some 0.1 ms; they can be modeled with sufficient accuracy.

By using reasonable models to reduce the effects (tidal effects, atmospheric circulation, ocean circulation, etc.), the residual part of polar motion and LOD can be analyzed, providing information on further geophysical processes and model deficiencies (WILSON 1995), Fig. 8.14.

The *nearly diurnal free wobble* (also free-core nutation) is a case of special interest (ZÜRN 1997b). Because the rotational axes of the fluid outer core and the earth's mantle are slightly

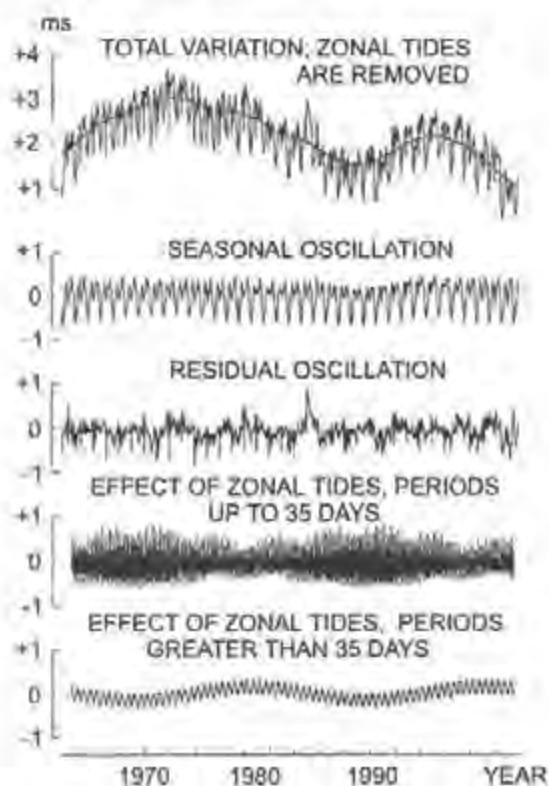


Fig. 8.14. Length of day (LOD) variations, and separation of tidal and seasonal effects, after IERS annual report 1998

misaligned, restoring forces occur at the elliptic core/mantle boundary that try to realign the axes. This leads to a damped wobble of the rotational axis around the figure axis, with nearly diurnal frequency in retrograde (opposite to the earth's rotation) direction and an amplitude of $0.00017''$. In space, this corresponds to a nutation of the rotational axis around the axis of total angular momentum. The effect has been observed with VLBI (HERRING and DONG 1994) and is also recognized through resonant terms in the tidal analysis of gravity observations, cf. [8.3.5]. The results are utilized for the improvement of the nutation theory, cf. [2.4.2], and for modeling the earth's deep interior.

8.3.2 Sea Level Variations

Variations of sea level with time are relevant in geodesy for the definition and realization of height reference surfaces, especially the geoid, cf. [3.4.3]. The determination and interpretation of sea level changes, on the other hand, is of fundamental importance in order to better understand the ocean-atmosphere interactions and their influence on climate. An acceleration of the global sea level rise would especially indicate climate changes related to global warming. The study of sea level variations thus requires close collaboration between oceanography, meteorology, and geodesy.

Sea level changes occur at a wide range of temporal and spatial scales, with amplitudes at the 0.1 to 1 m order of magnitude (LISITZIN 1974). Tide gauge measurements and satellite altimetry allow a *direct* determination of these changes, while oceanographic modeling utilizes meteorological and oceanographic data, cf. [3.4.2]. Observed variations of the earth rotation and of the earth's gravity field contain *indirect* information about the redistribution of the oceanic water masses, cf. [8.3.1], [8.3.4].

Tide gauge records can be evaluated for the determination of the oceanic tides and other short and medium-term phenomena, including the effects of atmospheric pressure changes, storm surges, and meltwater inflow. Averaging over long time intervals reveals long-term water level variations. For the 20th century, an average global rise of 0.1 to 0.2 m/100 years has been found, with large regional and local scatter and decadal variations (WOODWORTH 1997), Fig. 8.15.

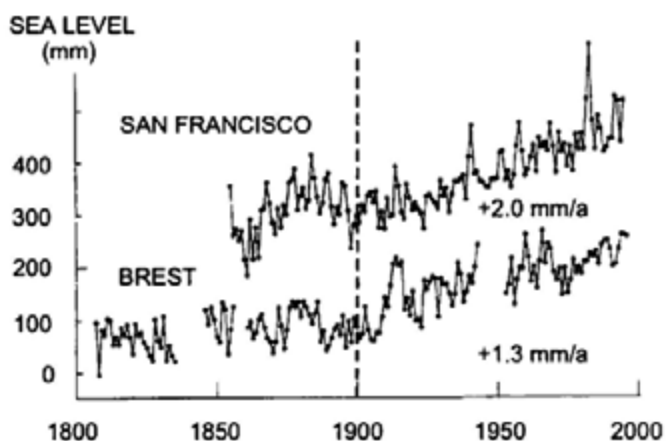


Fig. 8.15. Sea level records for San Francisco and Brest (vertical offset applied), and trend for the 20th century, after WOODWORTH (1997)

It must be emphasized that tide gauge data only provide *relative* water level changes, by a superposition of absolute water level changes and vertical movements of the mareograph. Vertical crustal movements are at the mm/year order of magnitude and may reach several mm/year and more in areas of postglacial land uplift, cf. [8.3.3]; hence a long-term height control with mm-accuracy is required for tide gauges. This is achieved locally by leveling between bench marks and globally by repeated GPS heighting. GPS sampling rates of a half to one year are typical, and connection should be made to the International Terrestrial Reference Frame (ITRF). Repeated absolute gravimetry represents an independent method for the determination of height changes and delivers additional information about the internal mass redistribution, cf. [8.3.4], CARTER et al. (1989).

Satellite altimetry provides a nearly global and quasi-continuous monitoring of the sea level with cm-accuracy. Recent ocean tide models allow reduction of the tidal effects with cm-accuracy (SHUM et al. 1997). The analysis of long-term (several years) observation series improved the ocean tide models (SMITH et al. 2000b) and revealed a number of other phenomena, with variations of 0.1 to 0.3 m (NEREM et al. 1997). This includes ocean basin-wide decadal and interannual fluctuations, probably due to the shift of water masses (BOSCH 2001), Fig. 8.16. The annual cycle has a 180° phase shift between the northern and the southern hemisphere caused by thermal expansion and contraction. Interannual and seasonal variations can be correlated with the variability of ocean currents such as the Gulf Stream meandering and eddies and the El Niño phenomenon (sea level rise in the eastern and subsidence in the western Pacific), TAPLEY et al. (1994).

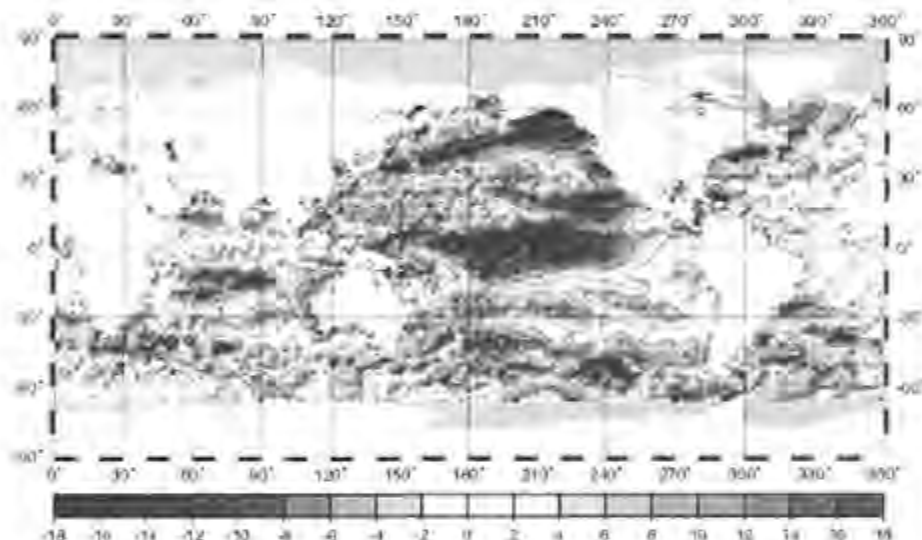


Fig. 8.16. Mean drift rate (mm/year) of sea level change determined between 1992 and 2000 from TOPEX/Poseidon altimetry, from BOSCH (2001)

The combination of tide gauge data and satellite altimetry leads to significant improvements. Here, the tide gauge data serve as ground truth and can be used to remove biases in the altimetric results, which may be affected by altimeter drift, systematic orbit errors, and differences between the tracking station's reference systems. By combining the results of different altimetry missions the spatial resolution is improved. Oceanographic and meteorological data such as sea surface temperature, salinity, current velocities, and air pressure may also be integrated.

8.3.3 Recent Crustal Movements

Recent crustal movements (horizontal and vertical) are determined by repeated geodetic measurements carried out at certain epochs, or continuously. The observation sites have to be monumented, and their local stability over time, with respect to changes caused of geological, hydrological, and man-made phenomena, must be controlled. Present-day sub-centimeter accuracies require reductions for the influence of body tides and ocean tide loading (DUCARME and JANSSEN 1990), atmospheric pressure loading (VAN DAM and WAHR 1987), and earth's rotation changes (GIPSON and MA 1998).

On a *global* scale, space-geodetic networks (VLBI, SLR, GPS, DORIS) provide geocentric coordinates for certain epochs and station velocities with mm/year to cm/year accuracy (PLAG et al. 1998), where GPS plays an increasing role (LARSON et al. 1997). The network solutions are combined by the IERS, and the annual station velocities are then part of the International Terrestrial Reference Frame ITRF, cf. [2.5.3]. The horizontal velocities are primarily due to the motions of the tectonic plates (ROBBINS et al. 1993), while the detection and interpretation of vertical motions is still in its infancy (SOUDARIN et al. 1999). For stations located in the interior region of the tectonic plates, the recently observed horizontal velocities generally agree well with the velocities given by geological/geophysical models as mean values over the past 3 to 10 million years, cf. [8.2.3]. Larger discrepancies are found at the plate boundaries, as the local deformations are not taken into account in the models, Fig. 8.17.



Fig. 8.17. Recent plate motions as determined from geodetic observations (APKIM 10.0 model) and the geophysical model NNR NUVEL-1A, courtesy Deutsches Geodätisches Forschungsinstitut (DGFI), München

By combining global geodetic data sets, geodetic Actual Plate Kinematic Models (APKIM) have been developed (DREWES et al. 1992). These models assume the plates' interior as being rigid and rotating on the earth's surface. They admit deformation zones at the plate boundaries that result from the forces exerted by the adjacent plates. By interpolation, the actual velocity field is provided in a $1^\circ \times 1^\circ$ grid, with the condition that the integrated velocities over the whole earth's surface are zero.

Regional crustal movements are derived from the repeated survey of national or continental control networks and from dedicated networks set up in areas of geodynamic activity.

Triangulation and leveling networks established in large parts of the world between the end of the 19th and the second half of the 20th century are valuable for the detection of long-term crustal movements (KAKKURI 1993b). Systematically repeated surveys of these classical networks have been carried out in high earthquake risk areas such as California and Japan. Higher repetition rates became possible with Laser distance measurements and mobile VLBI and SLR-systems; this led to the detection of medium-term crustal movements (STEIN 1987). GPS receivers are now the primary tool for investigations of recent crustal movements, where measurement campaigns are carried out at different epochs or permanent stations are operated (BEVIS et al. 1997). After strain analysis, the geodetic results can be correlated or combined with geological and geophysical data (HOLT et al. 2000) and thus contribute to the development of global or regional stress maps (ZOBACK 1992).

We mention some examples of large-scale monitoring of plate-boundary and intraplate deformation. Triangulation began in Iceland (diverging plate boundary) in 1938, followed by repeated angular and distance measurements, and GPS epoch observations have been carried out since 1986 (VÖLKSEN 2000). In Japan (converging plate boundary), a continuously operating GPS network with an average station distance of 25 km has been established (TSUJI et al. 1995), and permanent GPS arrays are also in operation in California (shear movements at the San Andreas Fault), BOCK et al. (1997). The strain field in the plate collision zones of southeast Asia (Eurasian, Pacific/Philippine, and Australian plates, WILSON et al. 1998) and the eastern Mediterranean (Eurasian, African, and Arabian plates, KAHLE et al. 2000) have been derived by repeated GPS campaigns.

Large-scale *vertical* crustal movements are found in areas of postglacial rebound, recent mountain building, continental erosion, and sedimentary subsidence. While geometric leveling only allowed repetition rates of several decades, GPS-heighting (epoch measurements or permanent stations) offers the possibility to determine elevation changes with high temporal resolution. Repeated gravity measurements can also be employed, cf. [8.3.4].

Leveling and GPS-heighting refer to different reference surfaces (geoid and ellipsoid, respectively). As the geoid is affected by mass redistributions, the leveling results should be

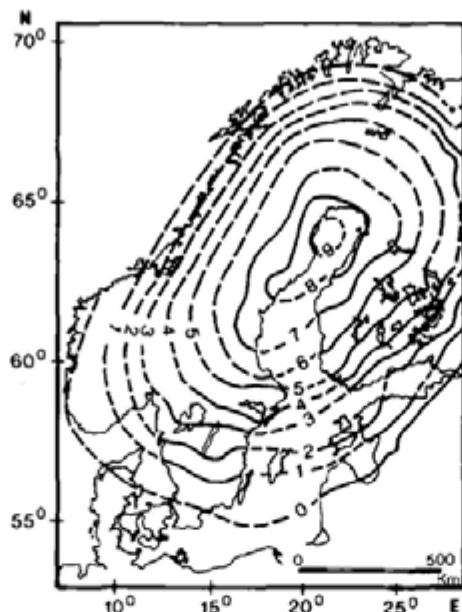


Fig. 8.18. Land uplift (relative to sea level) in mm/year, as determined from repeated geodetic leveling, after KAKKURI (1986)

reduced accordingly, applying the formulas for gravity field modeling on estimated or observed gravity variations with time, cf. [6.6.1], [6.7.1]. Even with large mass shifts, as in Fennoscandia, this reduction remains significantly below 10% of the height changes and can generally be neglected (EKMAN 1993).

Fennoscandia is among the examples of well-surveyed areas of recent vertical movement, where the postglacial land uplift has been investigated by leveling, sea level data, and gravimetry. The apparent land uplift reaches a maximum of 9 mm/year with respect to mean sea level (Fig. 8.18) and is associated with a viscous inflow of mass in the upper mantle (EKMAN and MÄKINEN 1996), cf. [8.2.4]. Repeated leveling in the Swiss Alps revealed mountain uplift rates of 1 mm/year and more. These uplifts were caused partly by isostatic rebound after erosion and partly by compression at the European/African plate boundary (GUBLER et al. 1981). From leveling along the German North Sea coast, a land subsidence of 0.5 to 1 mm/year is suspected, with significant local effects at the river estuaries (LEONHARD 1987).

Local investigations in earthquake and volcanic risk areas have generally employed a multitude of techniques (terrestrial distance measurements, leveling, GPS, strain and tilt measurements, gravimetry) in order to detect precursor phenomena and to monitor surface deformations during and after activity phases (RIKITAKE 1982). In seismotectonically active zones, the data provide information on the accumulation of strain energy, its release during an earthquake, and the relaxation that follows the quake (LARSON 1995, HUDDNUT 1995). Significant deformations have been found in connection with larger earthquakes (BOCK et al. 1993). Preseismic uplift has been explained as the

result of the generation of dilatancies, which occur through the opening of micro-cracks and the subsequent filling with underground water. With *volcanoes*, crustal deformation due to magma injection and outflow is easier to detect, and the detection plays an important role in forecasting volcanic eruptions. Continuous strain and tilt measurements could indicate precursor effects shortly before a phase of activity but may be strongly deteriorated by meteorological and hydrological disturbances (TAKEMOTO 1991). The combination of pointwise measurements (GPS) and interferograms generated from synthetic aperture radar (SAR) images taken at different times (e.g., at the 35 days repeat cycle of the ERS satellites) is a promising tool for obtaining surface information related to vertical ground deformation (MASSONNET et al. 1993).

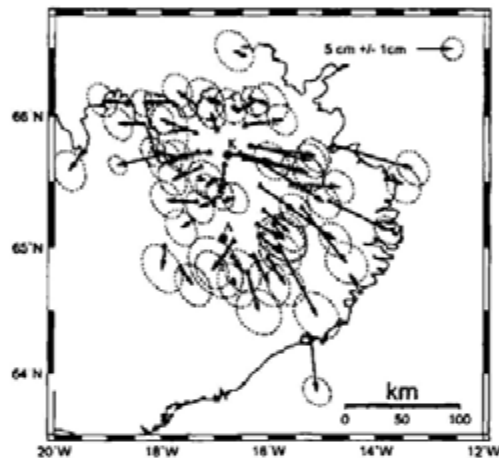


Fig. 8.19. Horizontal crustal deformations 1987 - 1990 in northwestern Iceland, as determined from repeated GPS measurements , with (assumed) non-movable stations in the Krafla fissure swarm, A = Askja volcano, K = Krafla volcano, after VÖLKSEN (2000)

The *San Andreas Fault*, California, is among the earthquake areas where co and inter-seismic slip rates are regularly determined by geodetic methods (SAVAGE et al. 1987, GAN et al. 2000). The *Krafla* (northern Iceland) *rifting episode* (1975-1984) and the following period of relaxation has been monitored by terrestrial measurements, GPS, and gravimetry (TRYGGVASSON 1994). The rifting process was triggered by the in and outflow of magma in a shallow magma reservoir, which caused repeated inflation and deflation of the Krafla volcano (BJÖRNSSON 1985). During the rifting episode, large horizontal (several m) and vertical (up to 1m and more) crustal movements have been observed, which decreased to a few cm/year along a narrow zone around the Krafla fissure swarm during the stress relaxation phase that followed. Eventually, the motions approached the average plate-spreading rate of 2 cm/year (JAHN et al. 1994), Fig.8.19. Satellite radar interferometry identified a post-rifting subsidence (several mm to 2 cm/year) above the magma chamber and along the spreading segment, due to cooling contraction and ductile flow of material away from the spreading axis (SIGMUNDSSON et al. 1997). Geodetic monitoring of

volcanoes is described by DVORAK (1995). Among the routinely surveyed active volcanoes are the Kilauea and Mauna Loa, Hawaii (OWEN et al. 2000), Long Valley, California (RUNDLE and WHITCOMB 1986), and Mount Etna, Italy (BONACCORSO et al. 1995).

Man-made vertical crustal movements are related to the exploitation of natural gas, oil, and geothermal fields, the withdrawal of groundwater, mining, and load changes in water reservoirs. They are of more local character and generally result in surface subsidence. Monitoring is carried out by leveling and GPS-heighting, and gravimetry also contributes, cf. [8.3.4].

8.3.4 Gravity Variations with Time

Gravity variations with time result from a multitude of sources, cf. [3.5]. Here we consider only the variations that are caused by the redistribution of terrestrial masses and thus provide information on geodynamic processes, cf. [3.5.3]. Gravimetric tidal effects will be discussed within the frame of earth tides, cf. [8.3.5]. More details are found in TORGE (1989).

Global gravity variations can be determined by comparing the harmonic coefficients of the gravitational field obtained from the analysis of satellite orbits of different epochs, cf. [6.6.2]. Changes of the low degree zonal harmonics (up to degree 5) have been found from laser satellites (Lageos, Starlette, Ajisai) over time intervals of 10 to 20 years (NEREM and KLOSKO 1996). The change of the dynamical form factor $J_2 = dJ_2/dt = -2.7 \times 10^{-11}/a$ is especially pronounced and suspected to result from postglacial rebound. Annual and semiannual variations of the second-degree harmonics are related to mass redistributions in the atmosphere, the oceans, and the continental groundwater (CHENG and TAPLEY 1999). If the harmonics of degree one are included in the evaluation, variations indicate the movement of the geocenter with respect to the terrestrial reference frame realized by the coordinates of the tracking stations, cf. [2.5.2], [3.3.4].

A *terrestrial* network of absolute gravity stations well distributed over the earth's surface and repeatedly observed at time intervals of 10 years or more could also provide long-term global gravity changes (MATHER et al. 1977). This is intended by the *International Absolute Gravity Basestation Network* (IAGBN) proposed by IAG (BOEDECKER and FRITZER 1986). The majority of the 36 scheduled stations have been installed, but only a few observation have been repeated.

Terrestrial absolute and relative gravity measurements are required in order to detect *regional* and *local* gravity changes with time. Corresponding investigations concentrate on areas where recent height changes occur, caused by postglacial uplift, mountain building, earthquake and volcanic activity, and man-made land subsidence, cf. [8.3.3].

In order to detect and analyze the small gravity changes associated with geodynamic phenomena, a high observational accuracy and the adequate reduction of tidal effects and local disturbances is required. Present gravimetric earth tide models allow sufficient reduction of the tidal effects for most parts of the continents, cf. [8.3.5]. *Polar motion* only affects absolute gravimetry and can be reduced. This is also valid for the effect of *atmospheric pressure* changes, which can be modeled by a Bouguer plate, modified through the deformation caused by the load of the atmospheric masses (SPRATT 1982), cf. [5.4.1]. For relative gravity measurements, atmospheric pressure effects generally cancel, but they must be taken into account for continuous gravity recording, cf. [8.3.5]. Temporal variations of the *ground water* level and *soil moisture* mainly occur seasonally, with superimposed short-term fluctuations of a few hours to a few days. They may produce maximum gravity changes of 50 to 100 nms^{-2} (seasonal) and several 100 nms^{-2} (strong rainfall). For simple hydrological structures, a reduction is possible by applying the Bouguer plate model

$$\delta g_{\text{groundwater}} = 4.2 \cdot P \cdot \delta H \text{nms}^{-2}, \quad (8.15)$$

with P = pore volume (%), and δH = change of groundwater level in m. A corresponding relation holds for the soil moisture reduction. The lack of groundwater and soil moisture data, as well as deficiencies of this simple model, generally prevent an adequate reduction of these hydrological effects (MÄKINEN and TATTARI 1988).

Observed *gravity changes* contain the combined effect of internal mass redistributions and a vertical shift of the observer, provided that earth tides, atmospheric pressure, and groundwater/soil moisture effects have been reduced properly. Hence, they can be transformed to *height changes* if a reasonable model for the internal mass redistribution is available (STRANG VAN HEES 1977, BIRO 1983). Assuming a linear relationship between gravity and height changes, the conversion factor may vary between -1.5 and $-3.5 \mu\text{m s}^{-2}/\text{m}$ (JACHENS 1978). The free-air relation of $-3 \mu\text{m s}^{-2}/\text{m}$ is often found locally and corresponds to a vertical shift without mass changes (e.g., dilating sphere). For larger areas, the Bouguer-plate relation of $-2 \mu\text{m s}^{-2}/\text{m}$ is more typical, indicating internal mass displacements according to the Bouguer plate model, cf. [6.5.3]. Simultaneous measurements of gravity and height variations allow the conversion factor to be determined. Gravity data can then be used for the determination of height changes, and the geophysical model for the internal mass redistribution can be verified (TORGE 1986).

Postglacial uplift has been monitored in Fennoscandia for some decades by relative gravimetry in connection with leveling, resulting in a mean conversion factor of $-2 \text{nms}^{-2}/\text{mm}$ (EKMAN and

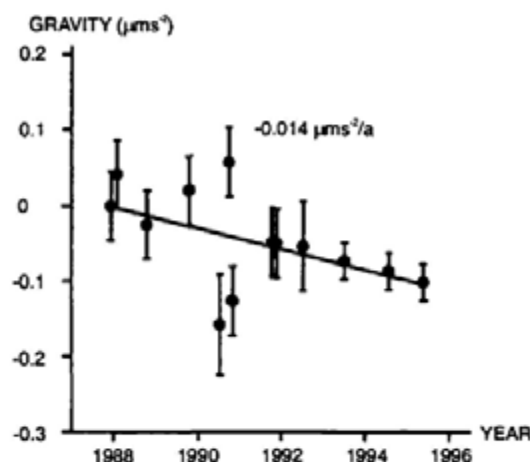


Fig. 8.20. Absolute gravity variations from 1987 to 1995 at Churchill, Manitoba, Canada, after LAMBERT et al. (1996)

MÄKINEN 1996), cf. [8.3.3]. In Canada, repeated absolute gravity measurements yielded gravity changes of -10 to $-20 \text{ nms}^{-2}/\text{year}$, in agreement with geophysical rebound models (LAMBERT et al. 1996), Fig. 8.20.

Gravimetric networks established in the Central Andes (subduction of the Nazca plate) and in the Venezuelan Andes (Caribbean/South American plate boundary) are examples of investigations at *tectonic plate boundaries* (BECKER and GROTE 1998, DREWES et al. 1991). While local effects (subsidence of sedimentary basins, variations related to the rainy and the dry season) have been identified, long-term gravity changes caused by plate tectonic processes are still difficult to extract over time spans of several years.

Gravimetry is extensively employed in areas of *seismotectonic* and *volcanic* activity, as in California (JACHENS et al. 1983) and in Japan (SATOMURA et al. 1986); the results are, in many cases, well correlated with changes in elevation and strain. An absolute gravity network established in Yunnan (collision zone of the Indian and the Eurasian plates) and observed several times between 1990 and 1995 is intended to monitor long-term changes at this region of high earthquake risk (TORGE et al. 1999). The Krafla rifting phenomena in northern Iceland mirrored itself in gravity and height variations with significant correlation, but forerunners are hard to detect (TORGE et al. 1992), Fig. 8.21, cf. [8.3.3]. Occasionally, gravity changes of a few $\mu\text{m s}^{-2}$ have been observed before strong *earthquakes*, one example being the 1976 Tangshan/China ($M=7.8$) earthquake (LI et al. 1989). *Volcano* monitoring, in many cases, includes gravimetry, which has proved to be an efficient tool for detecting magma inflation and deflation and to contribute to eruption forecasting and observation of the phase of activity (RYMER and LOCKE 1995).

Repeated gravity measurements also contribute to the investigation of land subsidence caused by *man-made* activities. This includes the exploitation of geothermal fields (ALLIS and HUNT 1986), of natural gas and oil (VAN GELDEREN et al. 1999), the withdrawal of groundwater, and the

effects of mining (LYNESS 1985).

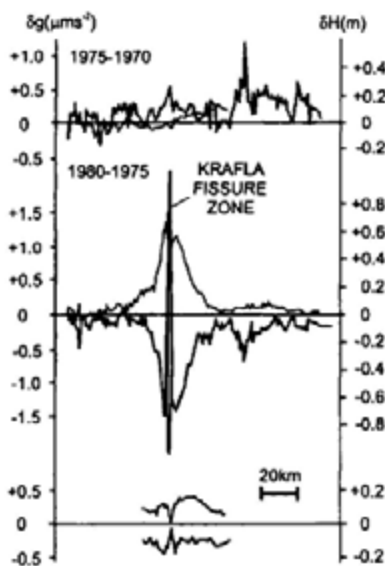


Fig. 8.21. Long-term gravity and height changes along an EW-profile ($\phi = 65^{\circ}40'$) in northern Iceland, related to the Krafla rifting episode, after TORGE et al. (1992)

8.3.5 Earth Tides

Tidal effects on a *rigid* earth can be calculated from the ephemerides of the moon, the sun, and the planets, cf. [3.5.2]. In reality, the *solid* earth reacts to the tidal forces like an elastic body: *Earth tides* (also body tides). The *ocean* tides follow the law of hydrodynamics, with strong disturbances occurring in the adjacent seas and along the coast lines. Tidal phenomena, especially earth tides, are discussed extensively in MELCHIOR (1983), BAKER (1984), and WILHELM et al. (1997).

The tidal response of a *spherically symmetric, non-rotating, oceanless* earth can be described by applying the dimensionless *Love numbers* h, k, l (l also called *Shida* number) to the individual terms of the series expansion of the tidal potential V_t (3.116), WAHR (1995).

The *vertical deformation* of the earth's surface is given by (Fig. 8.22)

$$\Delta r_{\text{el}} = h \cdot \Delta r_t, \quad (8.16a)$$

where the shift of the level surface follows from (3.52):

$$\Delta r_t = \frac{V_t}{g}. \quad (8.16b)$$

The *horizontal* displacement in NS and EW-direction is obtained by

$$\Delta x_{el} = \frac{l}{g} \cdot \frac{\partial V_t}{\partial \bar{\varphi}}, \Delta y_{el} = \frac{l}{g} \cdot \frac{\partial V_t}{\cos \bar{\varphi} \partial \lambda}, \quad (8.17)$$

with $\bar{\varphi}, \lambda$ = geocentric latitude and longitude.

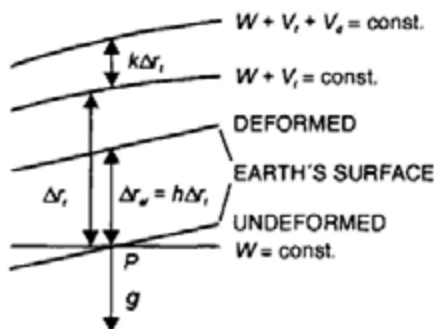


Fig. 8.22. Vertical shift of a level surface and the physical surface of the earth caused by the tides

The tidal-induced mass shift causes an additional *deformation potential* which is proportional to the tidal potential:

$$V_d = k \cdot V_t. \quad (8.18)$$

The *Love numbers* depend on density and elastic properties (compressibility, rigidity) of the earth's body, and they are functions of the radial distance from the earth's center. Restricting ourselves to the dominant (about 98%) term of degree two in the spherical harmonic expansion, we have for a spherical earth model with solid mantle, liquid outer and solid inner core, cf. [8.1]:

$$h = 0.60, l = 0.08, k = 0.30.$$

The *gravitational potential* on the earth's surface experiences a tidal-induced change which is composed of the direct attraction (3.117), the deformation part (8.18), and the potential change due to the vertical shift of the surface (8.16):

$$V_{el} = V_t + V_d - g \cdot \Delta r_{el} = V_t (1 + k - h). \quad (8.19)$$

Differentiating with respect to the radial distance r delivers the *vertical component* of the tidal *acceleration*. According to (3.117), (3.118) we have

$$b_r = \frac{\partial V_t}{\partial r} = 2 \frac{V_t}{r}. \quad (8.20a)$$

Expressing the deformation potential through a spherical harmonic expansion of degree two (3.89), and with (8.18) we obtain

$$\frac{\partial V_d}{\partial r} = -\frac{3}{r} V_d = -\frac{3}{r} k V_t. \quad (8.20b)$$

Inserting (8.20) into (8.19) and taking (3.118) and (8.16) into account yields the vertical acceleration component

$$b_{r(\text{el})} = \left(1 - \frac{3}{2}k + h\right) b_r, \quad (8.21a)$$

with the *gravimetric (amplitude) factor*

$$\delta = 1 - \frac{3}{2}k + h \quad (8.21b)$$

already introduced in (5.97).

The *horizontal* component of the tidal acceleration and its relation to the corresponding component on a rigid earth (3.119) follows from

$$b_{v(\text{el})} = -\frac{\partial V_d}{r \partial \psi} = (1 + k - h) b_v, \quad (8.22a)$$

with the *tilt (amplitude) factor*

$$\gamma = 1 + k - h. \quad (8.22b)$$

With the above model values for the love numbers h and k we obtain

$$\delta = 1.15, \gamma = 0.69.$$

Hence, the gravity change observed on an elastic earth is larger than on a rigid one, which is due to the vertical shift of the observer. The tilt factor mirrors the flexibility of the earth's surface with respect to the tidal force.

Rotation and *ellipticity* of the earth cause a slight latitude dependence of the tidal parameters (WAHR 1981). Mantle *anelasticity* results in a frequency dependent amplitude increase and a phase delay of the tidal response (DEHANT 1987); lateral *inhomogeneities* should be visible, with a dependence on position. The *resonance* effect caused by the liquid outer core (nearly diurnal free wobble, cf. [8.3.1]), is reflected in the diurnal tidal band by a frequency dependence of the Love numbers. The deviations from a spherically symmetric earth model remain below 0.1%.

Earth tide observations include the effect of the *ocean tides*, which is composed of the direct attraction and the loading effect of the water masses (JENTZSCH 1997). The ocean tide effects are especially pronounced in the semidiurnal tides and reach several percent at stations located in the continents' interior. Close to the coast, they may assume up to 10% in the gravimetric tidal signal, several 10% in strain, and 100% and more in tilt, with corresponding phase shifts.

The gravitational and the loading part of the *oceanic tidal effect* can be calculated from ocean tide models, cf. [3.4.2]. Here, the ocean load is considered as a surface layer and expanded into spherical harmonics where a development up to degree 10000 is required. The reaction of the earth's surface to the load is described by load Love numbers, which depend on the underlying earth model (FARRELL 1972). A convolution of the ocean tidal model and Green's functions (load Love numbers weighted according to the distance from the load) provides the loading effects in gravity, strain, and tilt for each partial tide.

Tidal perturbations on the earth's surface reach $1 \text{ to } 2 \mu\text{ms}^{-2}$ in gravity, $0.01''$ to $0.02''$ in tilt, and 10^{-7} to 10^{-8} in strain, see the estimates for a rigid earth in [3.5.2]. Hence, they are clearly visible in geodetic data series and, after an earth tide analysis, can be evaluated in order to

- derive *tidal reductions* for geodetic (VLBI, SLR, LLR, GPS, precise leveling etc.) and gravimetric measurements,
- verify and improve *global earth models* with respect to deviations from spherical symmetry, after subtraction of the oceanic tidal effects,
- verify *ocean tide models* after subtraction of the body tides,
- investigate local changes in the tidal parameters associated with earthquakes and volcanic activity.

While a relative *accuracy* of about $\pm 1\%$ and $\pm 0.5^\circ$ generally suffices for tidal reductions, $\pm 0.1\%$ respectively $\pm 0.05^\circ$ and better is required for model verification and geodynamic investigations.

Gravimetric earth tide observations especially contribute to tidal analysis (WENZEL 1997b). Here, elastic-spring type gravimeters provide the short-periodic partial tides (Fig. 8.23), and superconducting instruments also deliver long-periodic tides and the pole tide (Fig. 8.24), cf. [5.4.6].

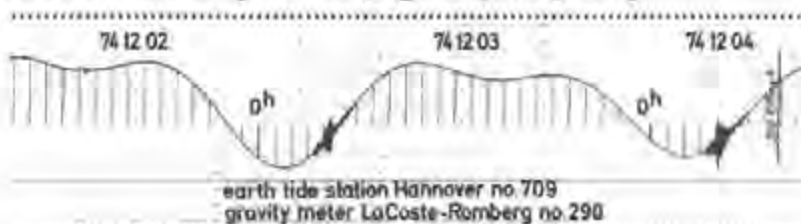


Fig. 8.23. Gravimetric earth tide record, obtained with Lacoste and Romberg gravimeter G298, Institut für Erdmessung (IfE), University of Hannover

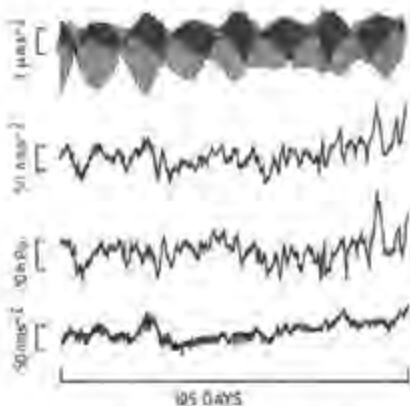


Fig. 8.24. GWR superconducting gravimeter drift, with (top to bottom) raw gravimeter signal, earth tides reduced signal, atmospheric pressure, and gravity residuals after removal of earth tides and atmospheric pressure effects, courtesy GWR-Instruments, Inc., San Diego, CA, U.S.A.

As an example, Tab. 8.1 contains the gravimetric tidal parameters for a selected number of partial tides (out of a total number of 57 analyzed wave groups) from a long-term observation with a superconducting gravimeter (DITTFELD 2000), cf. [3.5.2].

The main results of the gravimetric earth tide analysis are (WENZEL 1997b):

- The average *noise level* amounts to a few 0.01 nms^{-2} for the short-periodic tides and may reach 10 nms^{-2} for the annual tide, which characterizes the high observational precision.
- The separation of the small S1 wave mirrors the quality of the *analysis*, as the diurnal tides are strongly contaminated by meteorological effects.

Tab. 8.1. Adjusted Gravimetric Earth Tide Parameters (selection, rounded values), Earth Tide Station No.765, GFZ/Potsdam ($\phi = 52.38^\circ \text{N}$, $\lambda = 13.07^\circ \text{E}$, $H = 81\text{m}$), Superconducting Gravimeter GWR TT70 No.018, recording time June 1992 to October 1998 (2250 days), after DITTFELD (2000)

| Tide Symbol | Period | Amplitude nms^{-2} | Ampl. Factor δ | Phase Lead $\Delta\Phi$ |
|----------------------|----------|--------------------------------|--------------------------|----------------------------|
| Long-periodic | | | | |
| Sa | 365.26 d | 18.4 | 4.4 | -40° |
| Ssa | 182.62 d | 29.7 | 1.13 | -2° |
| Mm | 27.55 d | 34.0 | 1.14 | 0.6° |
| Mf | 13.66 d | 64.4 | 1.14 | -3° |
| Diurnal | | | | |
| Q1 | 26.87 h | 66.0 | 1.146 | -0.22° |
| O1 | 25.82 h | 345.6 | 1.150 | -0.13° |
| P1 | 24.07 h | 160.9 | 1.150 | 0.12° |
| S1 | 24.00 h | 4.2 | 1.28 | 2.0° |
| K1 | 23.93 h | 480.6 | 1.137 | 0.2° |
| ψ_1 | 23.87 h | 4.2 | 1.26 | 0.6° |
| φ_1 | 23.80 h | 7.1 | 1.18 | -0.1° |
| Semidiurnal | | | | |
| N2 | 12.66 h | 63.2 | 1.179 | 1.99° |
| M2 | 12.42 h | 332.3 | 1.186 | 1.36° |
| S2 | 12.00 h | 154.6 | 1.186 | 0.21° |
| K2 | 11.97 h | 42.0 | 1.186 | 0.45° |
| Terdiurnal | | | | |
| M3 | 8.28 h | 3.6 | 1.073 | 0.3° |

Standard deviation (short and long-periodic tides adjusted): $\pm 9 \text{nms}^{-2}$, only short-periodic tides: $\pm 0.8 \text{nms}^{-2}$. Air pressure regression coefficient $-2.776 \text{nms}^{-2}/\text{hPa}$, pole-tide δ -factor 1.13.

- The standard deviations of the adjusted *tidal parameters* are approximately inversely proportional to the amplitude of the waves. The amplitude factor of the principal waves (O1, P1, K1, M2, S2) can be obtained with a relative accuracy of about $\pm 0.01\%$ and the phase lead with $\pm 0.01^\circ$, and better. The long-periodic tides (Mm, Mf) are accurate to a few % and a few degrees.
- After reduction of the oceanic tidal effects, the tidal parameters are in close agreement with advanced geophysical *earth models*. A dependence on latitude, lateral heterogeneities, or heat flow has not been clearly recognizable (BAKER et al. 1996, ZÜRN 1997a),

- The *resonance effect* of the liquid outer core can be clearly identified in the diurnal tides (ψ_1, φ_1) and used for model verification.
- *Ocean tide* effects manifest themselves in the semidiurnal waves and provide useful constraints for oceanic tidal models (DUCARME and MELCHIOR 1983).
- *Free oscillations* (vertical component) of the earth with periods between 10 s and 54 min. as excited by strong earthquakes have been analyzed from high resolution records and can be used for the support of global seismic networks.

World-wide *synthetic gravity tide parameters* have been calculated for a $1^\circ \times 1^\circ$ grid, based on the WAHR (1981)/DEHANT (1987) body tide and the SCHWIDERSKI (1980) ocean tide models. With the exception of strongly disturbed coastal zones, the synthetic parameters agree well with the gravimetric earth tide observations and provide the gravimetric tidal reductions with the desired accuracy (see above), TIMMEN and WENZEL (1994b).

The *Global Geodynamics Project* (GGP, 1997 – 2003) comprises about 20 stations equipped with superconducting gravimeters that collect gravity data with a sampling rate of 1 to 10 s and an accuracy of $\pm 1\text{nms}^{-2}$. The results will be used for improving earth and ocean models, should provide information on geodynamic phenomena, and serve as ground truth for the GRACE mission, cf. [5.2.8], CROSSLEY et al. (1999).

Strain and *tiltmeter* measurements fail to reliably determine the global or regional tidal response of the earth, which is due to strong distortion by local heterogeneities. But these measurements contribute significantly to local investigations, cf. [5.5.4]. Long-term *space-geodetic* observations such as VLBI, SLR, and GPS allow for direct monitoring of tidal displacements of the station sites. Thus they can be used to directly derive the Love numbers h and l , the resonance parameters in the diurnal tidal band, and the ocean loading effects (MATHEWS et al. 1997, SCHUH and HAAS 1998).

References

Abbreviations frequently used:

- Allg. Verm. Nachr. = Allgemeine Vermessungsnachrichten, Wichmann-Huthig, Heidelberg.
- Boll. Geof. teor. appl. = Bollettino di Geofisica teorica ed applicata. Osservatorio Geofisico Sperimentale, Trieste.
- Bull. Géod. = Bulletin Géodesique. Springer, Berlin-Heidelberg-New York.
- DGK = Veröffentlichungen der Deutschen Geodätischen Kommission bei der Bayerischen Akademie der Wissenschaften, München und Frankfurt a.M.
- EOS = Transactions American Geophysical Union, Washington, D.C.
- J. Geod. = Journal of Geodesy. Springer, Berlin-Heidelberg-New York.
- JGR = Journal of Geophysical Research. American Geophysical Union, Washington, D.C.
- Man. Geod. = Manuscripta Geodaetica. Springer, Berlin-Heidelberg-New York.
- Mitt. BKG = Mitteilungen de Bundesamtes für Kartographie und Geodäsie, Frankfurt a.M.
- OSU Rep. = Reports of the Department of Civil and Environment Engineering and Geodetic Science, Geodetic Science and Surveying, The Ohio State University, Columbus, Ohio.
- Unisurv G = Univ. of New South Wales, Geodesy Reports, Kensington, N.S.W.
- Wiss. Arb. Univ. Hannover = Wissenschaftliche Arbeiten der Fachrichtung Vermessungswesen der Universität Hannover.
- ZfV = Zeitschrift für Vermessungswesen. K. Wittwer, Stuttgart.

- ABD-ELMOTAAL, H.A. (1995): Theoretical background of the Vening-Meinesz isostatic model. In Sünkel and Marson (1995): 268-277.
- ABD-ELMOTAAL, H.A., M. EL-TOKHEY (1995): Does the spherical approximation affect the datum transformation ? In Sünkel and Marson (1995): 472-483.
- ADAM, J., W. AUGATH, F. BROUWER et al. (2000a): Status and development of the European height system. In Schwarz (2000b) : 55-60.
- ADAM, J., W. AUGATH, C. BOUCHER et al. (2000b): The European Reference System coming of age. In Schwarz (2000b): 47-54.
- AGNEW, D.C. (1986): Strainmeters and tiltmeters. Rev. Geophys. 24: 579-624.
- AHRENS, T.J., ed. (1995): Global Earth Physics: A Handbook of Physical Constants. AGU ref. shelf 1, Washington, D.C.
- ALASIA, F., L. CANNIZZO, G. CERUTTI, I. MARSON (1982): Absolute gravity acceleration measurements: Experiences with a transportable gravimeter. Metrologia 18: 221-229.

- ALLENBY, R.J., C.C. SCHNETZLER (1983): United States crustal thickness. *Tectonophysics* 93: 13-31.
- ALLIS, R.G., T.M. HUNT (1986): Analysis of exploitation-induced gravity changes at Wairakei geothermal field. *Geophysics* 51: 1647-1660.
- ANDERLE, R.J. (1986): Doppler satellite measurements and their interpretation. In A.J. Anderson and A. Cazenave, eds. (1986), *Space geodesy and geodynamics*: 113-167. Academic Press, London etc.
- ANDERSEN, N. (1992): The hydrostatic levelling across Fehmarn Belt in 1987. *Kort- og Matrikelstyrelsen*, Publ. 4. Series, vol. 2, Kobenhavn, Denmark.
- ANDERSEN, O.B., P. KNUDSEN (1998): Global marine gravity field from the ERS-1 and Geosat geodetic mission altimetry. *JGR* 103: 8129-8137.
- ANDERSEN, O.B., P.L. WOODWORTH, R.A. FLATHER (1995): Intercomparison of recent ocean tide models. *JGR* 100: 25261-25282.
- ANDERSEN, P.H., S. AKSNES, H. SKONNORD (1998): Precise ERS-2 orbit determination using SLR, PRARE and RA observations. *J. Geod.* 72: 421-429.
- ANDERSON, J.M., E.M. MIKHAIL (1998): Surveying - theory and practice. 7.ed., McGraw-Hill, New York etc.
- ANGUS-LEPPAN, P.V. (1984): Refraction in geodetic leveling. In Brunner (1984a): 163-180.
- ANZENHOFER, M., T. GRUBER, M. RENTSCH (1996): Global high resolution mean sea surface based on ERS-1 35- and 168-days cycles and Topex data. In Rapp et al. (1996): 208-217..
- ARABELOS, D. (1980): Untersuchungen zur gravimetrischen Geoidbestimmung, dargestellt am Testgebiet Griechenland. *Wiss. Arb. Univ. Hannover* 98.
- ARIAS, E.F., P. CHARLOT, M. FEISSEL, J.-F. LESTRADE (1995): The extragalactic reference system of the International Earth Rotation Service. *Astronomy and Astrophysics* 303: 604-608.
- ASHKENAZI, V., T. MOORE, M.E. NAPIER, C. DE LA FUENTE (1988): Using GPS to control a triangulation network. *Survey Review* 29: 287-294.
- AUGATH, W. (1997): GPS-gestützte Netzverdichtung in der Landesvermessung. DVW Schriftenreihe 28: 154-169, Wittwer, Stuttgart.
- BAKER, L.S. (1974): Geodetic networks in the United States. *Canadian Surveyor* 28: 445-451.
- BAKER, T.F. (1984): Tidal deformations of the earth. *Sci. Progr.*, Oxford 69: 197-233.
- BAKER, T.F., D.J. CURTIS, H. DODSON (1996): A new test of earth tide models in central Europe. *Geophys. Res. Letters* 23: 3559-3562.
- BANNISTER, A., S. RAYMOND, R. BAKER (1998): Surveying. 7.ed., Longman, Harlow, Essex, England.
- BARTHELEMY, J., B. DUCARME, P. MELCHIOR, eds. (1995): New challenges for geodesy in volcanoes monitoring. *Cahiers du Centre Européen de Géodynamique et de Séismologie* 8, Luxembourg.
- BASIC, T., H. DENKER, P. KNUDSEN, D. SOLHEIM, W. TORGE (1990): A new geopotential model tailored to gravity data in Europe. In Rummel and Hipkin (1990): 109-118.
- BÄUMKER, M. (1984): Zur dreidimensionalen Ausgleichung von terrestrischen und Satellitenbeobachtungen. *Wiss. Arb. Univ. Hannover* 130.

- BECKER, J.-M. (1987): The experiences with new levelling techniques ML and MTL. In Pelzer and Niemeier (1987): 159-174.
- BECKER, M., E. GROTHEN (1998): Präzisionsgravimetrische Beobachtungen in den Zentralen Anden 1984-1990. *ZfV* 123: 37-42.
- BECKER, M., G. BERRINO, A.G. CAMACHO et al. (2000): Results of the relative gravimetric measurements at the ICAG97 intercomparison. *Bull. d'Inf. Bur.Gravim.Int.* 85: 61-71.
- BELL, R.E., A.B. WATTS (1986): Evaluation of the BGM-3 sea gravity meter onboard R/V Conrad. *Geophysics* 51: 1480-1493.
- BENDER, P.L. (1992): Atmospheric refraction and satellite laser ranging. In De Munck and Spoelstra (1992): 117-125.
- BENDER, P.L., D.G. CURRIE, R.H. DICKE et al. (1973): The lunar laser ranging experiment. *Science* 182: 229-238.
- BERCKHEMER, H. (1990): Grundlagen der Geophysik. Wiss. Buchgesellschaft Darmstadt.
- BERGER, J., J. LEVINE (1974): The spectrum of earth strain from 10^{-8} to 10^2 Hz. *JGR* 79: 1210-1214.
- BEUTLER, G., W. GURTNER, I. BAUERSIMA, M. ROTHACHER (1987): Correlation between simultaneous GPS double difference carrier phase observations in the multistation mode. Implementation, considerations and first experiences. *Man. Geod.* 12: 40-44.
- BEUTLER, G., E. BROCKMANN, S. FRANKENHAUSER et al. (1996a): Bernese GPS Software Version 4.0. Doc., Astronomical Institute, Univ. of Bern, Switzerland.
- BEUTLER, G., I.I. MUELLER, R.E. NEILAN (1996b): The International GPS Service for Geodynamics (IGS): the story. In Beutler et al. (1996c): 3-13.
- BEUTLER, G., G.W. HEIN, W.G. MELBOURNE, G. SEEBER, eds. (1996c): GPS trends in precise terrestrial, airborne, and spaceborne applications. IAG Symp. Proceed. 115, Springer, Berlin-Heidelberg-New York.
- BEVIS, M., S. BUSINGER, T.A. HERRING, CH. ROCKEN, A. ANTHES, R.H. WARE (1992): GPS meteorology: Remote sensing of atmospheric water vapor using the Global Positioning System. *JGR* 97: 15787-15801.
- BEVIS, M., Y. BOCK, P. FANG, R. REILINGER, T. HERRING, J. STOWELL, R.J. SMALLEY (1997): Bending old and new approaches to regional GPS geodesy. *EOS* 78: 61, 64, 66.
- BEYER, L.A., R.E. VON HUENE, T.H. McCULLOH, J.R. LOVETT (1966): Measuring gravity on the seafloor in deep water. *JGR* 71: 2091-2100.
- BIALAS, V. (1982): Erdgestalt, Kosmologie und Weltanschauung. Wittwer, Stuttgart.
- BILLS, B.G., S.P. SYNNOTT (1987): Planetary geodesy. *Rev. Geophys.* 25: 833-839.
- BIPM (1991): Le Système International d'Unités (SI). Bureau International des Poids et Mesures, Sèvres, France.
- BIRARDI, G. (1976): The establishment of a net of vertical deflection points in Italy by means of a photo-astronomical procedure. *Boll. di Geod. e Scienze Affini* 35: 113-152.
- BIRO, P. (1983): Time variation of height and gravity. Wichmann, Karlsruhe.
- BJERHAMMAR, A. (1969): On the boundary value problem of physical geodesy. *Tellus* 21: 451-516.

- BJERHAMMAR, A. (1981): The uplift process in Fennoscandia and the corresponding potential field from satellites. Proceed. 4th Int. Symp Geodesy and Physics of the Earth, Veröff. Zentralinstitut Physik der Erde 63/III: 554-581.
- BJERHAMMAR, A. (1985): A robust approach to global problems in physical geodesy. Bull. Géod. 59: 303-315.
- BJERHAMMAR, A., L. SVENSSON (1983): On the geodetic boundary value problem for a fixed boundary surface – a satellite approach. Bull. Géod. 57: 382-393.
- BJÖRNSSON, A., (1985): Dynamics of crustal rifting in NE Iceland. JGR 90: 10151-10162.
- BKG (1998): Geodätische Vernetzung Europas. Mitt. d. Bundesamtes für Kartographie und Geodäsie, Bd.1, Frankfurt a. M.
- BLAKELEY, R.J. (1996): Potential theory in gravity and magnetic applications. Cambridge Univ. Press.
- BOCCALETI, D., G. PUCACCO (1996/1999): Theory of orbits. Springer, Berlin-Heidelberg-New York.
- BOCK, Y., D.C. AGNEW, P. FANG et al. (1993): Detection of crustal deformation from the Landers earthquake sequence using continuous geodetic measurements. Nature 361: 337-340.
- BOCK, Y., S. WDOWINSKI, P. FANG et al. (1997): Southern California permanent GPS geodetic array: continuous measurements of regional crustal deformation between the 1992 Landers and 1994 Northridge earthquakes. JGR 102: 18013-18033.
- BÖDECKER, G., TH. FRITZER (1986): International Absolute Gravity Basestation Network. Veröff. Bayer. Komm. für die Internat. Erdmessung, Astron.-Geod. Arb. 47, München.
- BOMFORD, G. (1980): Geodesy. 4.ed., Clarendon Press, Oxford.
- BONACCORSO, A., R. VELARDITA, L. VILLARI (1995): Magma uprising and intrusion at Mount Etna (Sicily, Italy): Some insight from ground deformation modelling. In Barthelemy et al. (1995): 231-243.
- BONVALOT, S., M. DIAMENT, G. GABALDA (1998): Continuous gravity recording with Scintrex CG-3M meters: a promising tool for monitoring active zones. Geophys. J. Int. 135: 470-494.
- BORKOWSKI, K.M. (1989): Accurate algorithms to transform geocentric to geodetic coordinates. Bull. Géod. 63: 50-56.
- BOSCH, W. (2001): EOF-Analysen der Meeresspiegelschwankungen im Pazifik. ZfV 126 (in press).
- BOSSLER, J.D. E. GRAFARENDS, R. KELM (1973): Optimal design of geodetic nets 2. JGR 78: 5887-5897.
- BOSSLER, J.D., C.C. GOAD, P.L. BENDER (1980): Using the Global Positioning System (GPS) for geodetic positioning. Bull. Géod. 54: 553-563.
- BOTTONI, G.P., R. BARZAGHI (1993): Fast collocation. Bull. Géod. 67: 119-126.
- BOUCHER, C. (1987): GPS receiver technology. In Turner (1987), Applied Geodesy: 11-15, Springer, Berlin-Heidelberg-New York.
- BOUCHER, C., Z. ALTAMINI, P. SILLARD (1999): The 1997 International Terrestrial Reference Frame (ITRF97). IERS Techn. Note 27, Paris.
- BOUMAN, J. (1997): A survey of global gravity models. Delft Inst. for Earth-oriented Space Research (DEOS) Rep. 97.1, TU Delft.

- BOWIN, C. (1994): The geoid and deep earth mass anomaly structure. In Vaniček and Christou (1994): 203-219.
- BOWIN, C. (2000): Mass anomalies and the structure of the earth. *Phys. Chem. Earth (A)* 25: 343-353.
- BOWIN, C., TH.C. ALDRICH, R.A. FOLINSBEE (1972): VSA Gravity Meter System: Tests and recent developments. *JGR* 77: 2018-2033.
- BOWRING, B.R. (1971): The normal section – forward and inverse formulae at any distance. *Survey Review no.161*: 131-136.
- BOWRING, B.R. (1985): The accuracy of geodetic latitude and height equations. *Survey Review* 28: 202-206.
- BROSCHÉ, P., H. SCHUH (1999): Neue Entwicklungen in der Astrometrie und ihre Bedeutung für die Geodäsie. *ZfV* 124: 343-350.
- BROSCHÉ, P., W.R. DICK (1996): GAIA für Gää? – Zur geowissenschaftlichen Nutzung eines geplanten Astrometrie-Satelliten. *ZfV* 121: 577-580.
- BROUWER, D., G.M. CLEMENCE (1961): Methods of celestial mechanics. Academic Press, New York.
- BROWN, L.D., R. DANIELL, Jr., M.W. FOX, J.A. KLOBUCHAR, P.H. DOHERTY (1991): Evaluation of six ionospheric models as predictors of total electron content. *Radio Science* 26: 10007-10015.
- BROZENA, J.M., M.F. PETERS (1995): State-of-the-art airborne gravimetry. In Sünkel and Marson (1995): 187-197.
- BRUNNER, F.K., ed. (1984a): Geodetic refraction. Springer, Berlin-Heidelberg-New York.
- BRUNNER, F.K. (1984b): Modelling of atmospheric effects on terrestrial geodetic measurements. In Brunner (1984a): 143-162.
- BRUNNER, F.K., ed. (1998): Advances in positioning and reference frames. IAG Symp. Proceed. 118, Springer, Berlin-Heidelberg-New York.
- BRUNNER, F.K., CHR. RIZOS, eds. (1990): Developments in four-dimensional geodesy. Lecture Notes in Earth Sciences 29, Springer, Berlin-Heidelberg-New York.
- BRUNS, H. (1878): Die Figur der Erde. Publ. Königl. Preuß. Geod. Inst., Berlin.
- BRUYNINX, C. (1999): Status and prospects of the permanent EUREF network. In Gubler et al. (1999): 42-46.
- BULLEN, K.E. (1975): The earth's density. Chapman and Hall, London.
- BÜRKI, B. (1989): Integrale Schwerefeldbestimmung in der Ivrea-Zone und deren geophysikalische Interpretation. *Geod. geophys. Arbeiten in der Schweiz* 40, Schweiz. Geod. Komm., Zürich.
- BURSA, M. (1995): Special Commission SC3 "Fundamental Constants" Report. In *Travaux de l'Assoc. Int. de Géod.*, Tome 30: 370-384, Paris.
- CAMPBELL, J., B. WITTE (1978): Grundlagen und geodätische Anwendung der Very Long Baseline Interferometry. *ZfV* 103: 10-20.
- CAMPBELL, J., A. NOTHNAGEL, H. SCHUH (1992): VLBI-Messungen für geodynamische Fragestellungen. *ZfV* 117: 214-227.
- CANNON, M.E., G. LACHAPELLE, eds. (1997): Proceed. Int. Symp. on Kinematic Systems in Geodesy, Geomatics and Navigation, Banff 1997, Univ. of Calgary.
- CARTER, W.E., D.S. ROBERTSON, J.R. MACKAY (1985): Geodetic radio interferometric surveying: application and results. *JGR* 90: 4577-4587.

- CARTER, W.E., D.G. AUBREY, T. BAKER et al. (1989): Geodetic fixing of tide gauge bench marks. Woods Hole Oceanographic Institution Report WHOI-89-31/CRC-89-5, Woods Hole, Mass., U.S.A.
- CARTWRIGHT, D.E., J. CREASE (1963): A comparison of the geodetic reference levels of England and France by means of the sea surface. Proc. Roy. Soc. London, A 273: 558-580.
- CARTWRIGHT, D.E., A.C. EDDEN (1973): Corrected tables of tidal harmonics. Geophys. J. R. Astr. Soc. 33: 253-264.
- CARTWRIGHT, D.E., R.J. TAYLER (1971): New computations of the tide-generating potential. Geophys. J. R. Astr. Soc. 23: 45-74.
- CAZENAVE, A. (1994): The geoid and oceanic lithosphere. In Vaniček and Christou (1994): 255-283.
- CAZENAVE, A. (1995): Geoid, topography and land forms. In Ahrens (1995): 32-39.
- CHADWELL, D., F. SPIESS, J. HILDEBRAND, L. YOUNG, G. PURCELL jr., H. DRAGERT (1998): Deep-sea geodesy: monitoring the ocean floor. GPS World 9(9): 44-55.
- CHAO, B.F. (1994): The geoid and earth rotation. In Vaniček and Christou (1994): 285-298.
- CHAO, B.F., R. GROSS, Y. YAN (1996): Seismic excitation of the polar motion 1977-1993. Pageoph 146: 407-419.
- CHEN, J.Y. (1982): Geodetic datum and Doppler positioning. Mitt. Geod. Inst. TU Graz, Folge 39.
- CHENEY, R.E. et al. (1995): TOPEX/POSEIDON: Scientific results. JGR 100: 24893-25382.
- CHENG, M., B.D. TAPLEY (1999): Seasonal variations in low degree zonal harmonics of the earth's gravity field from satellite laser ranging observations. JGR 104: 2667-2681.
- CLARK, T.A., D. GORDON, W.E. HINRICH, C. MA, A. MALLAMA, J.W. RYAN (1987): Determination of relative site motions in the western United States using MKIII Very Long Baseline Interferometry. JGR 92: 12741-12750.
- COCHRAN, J.R., D.J. FORNARI, B.J. COAKLEY, R. HERR, M.A. TIVEY (1999): Continuous near-bottom gravity measurements made with a BGM-3 gravimeter in DSV Alvin on the East Pacific Rise crest near 9°31'N and 9°50'N. JGR 104: 10841-10861.
- COHEN, S.C., R.W. KING, R. KOLENKIEWICZ, R.D. ROSEN, B.E. SCHUTZ, eds. (1985): Lageos scientific results. JGR 90: 9215-9438.
- COLLIER, P.A., M.J. CROFT (1997): Height from GPS in an engineering environment. Survey Review 34: 11-18.
- COLOMBO, O. (1981): Numerical methods for harmonic analysis on the sphere. OSU Rep. 310, Columbus, Ohio.
- COLOMBO, O.L. (1989): Advanced techniques for high-resolution mapping of the gravitational field. In Sansò and Rummel (1989): 335-372.
- COLOMBO, O.L., ed. (1992): From Mars to Greenland: Charting gravity with space and airborne instruments. IAG Symp. Proceed. 110, Springer, New York-Berlin-Heidelberg.
- COOK, A.H. (1959): The external gravity field of a rotating spheroid to the order of e^3 . Geophys. J. R. Astr. Soc. 2: 199-214.

- COORS, S., R. HEER, H. HUSTEDT, V. SCHWIEGER (1998): Zur Leistungsfähigkeit der Empfangssysteme GePos RD24 und Trimble 4000 SSi. ZfV 123: 403-414.
- CROSSLEY, D., J. HINDERER, G. CASULA et al. (1999): Network of superconducting gravimeters benefits a number of disciplines. EOS 80: 121, 125-126.
- DASSING, R.W. SCHLÜTER, U. SCHREIBER (1992): Das neue Laserentfernungsmeßsystem der Fundamentalstation Wettzell. ZfV 117: 180-188.
- DAVIS, J.L., M.L. COSMO, G. ELGERED (1996): Using the Global Positioning System to study the atmosphere of the earth: overview and prospect. In Beutler et al. (1996c): 233-242.
- DE METS, C., R.G. GORDON, D.F. ARGUS, S. STEIN (1990): Current plate motions. Geophys. J. Int. 101: 425-478.
- DE METS, C., R.G. GORDON, D.F. ARGUS, S. STEIN (1994): Effect of recent revisions to the geomagnetic reversal time scale on estimates of current plate motions. Geophys. Res. Letters 21: 2191-2194.
- DE MUNCK, J.C., T.A.TH. SPOELSTRA, eds. (1992): Proceed. of the Symp. on refraction of transatmospheric signals in geodesy. Neth. Geod. Comm., Publ. on Geodesy, New Series No. 36, Delft.
- DEHANT, V. (1987): Tidal parameters for an inelastic earth. Phys. Earth Planet. Inter. 49: 97-116.
- DEHLINGER, P. (1978): Marine gravity. Elsevier Scient. Publ., Amsterdam etc.
- DEICHL, K. (1975): Zur Messung mit Pendelastrolabien und ihrer Auswertung. ZfV 100: 499-509.
- DENIS, C. (1989): The hydrostatic figure of the earth. In Teisseyre (1989): 111-186.
- DENKER, H. (1988): Hochauflösende regionale Schwerefeldbestimmung mit gravimetrischen und topographischen Daten. Wiss. Arb. Univ. Hannover 156.
- DENKER, H. (1998): Evaluation and improvement of the EGG97 quasigeoid model for Europe by GPS and leveling data. Rep. Finn. Geod. Inst. 98.4: 53-61.
- DENKER, H., W. TORGE (1998): The European gravimetric quasigeoid EGG97 – an IAG supported continental enterprise. In Forsberg et al. (1998): 249-254.
- DENKER, H., D. LELGEMANN, W. TORGE, G. WEBER, H.G. WENZEL (1986): Strategies and requirements for a new European geoid determination. Proceed. Int. Symp. on the Definition of the Geoid, vol.1: 207-222, Ist. Geogr. Ital., Firenze.
- DENKER, H., W. TORGE, G. WENZEL, J. IHDE, U. SCHIRMER (2000): Investigation of different methods for the combination of gravity and GPS/levelling data. In Schwarz (2000b): 137-142.
- DEUMLICH, F. (1982): Surveying instruments. De Gruyter, Berlin-New York.
- DEUMLICH, F., R. STAIGER (2001): Instrumentenkunde. 9. Aufl., Wichmann/Hüthig, Heidelberg.
- DICKEY, J.O. (1995): Earth rotation. In Ahrens (1995): 356-368.
- DIETZ, R.S. (1961): Continent and ocean evolution by spreading of the sea floor. Nature 190: 854-857.
- DIRAC, P.A.M. (1938): A new basis for cosmology. Proc. Roy. Soc. London, A 165: 199-208.
- DITTFELD, H.-J. (2000): Final results of the SG-registration in Potsdam. In Ducarme and Barthelemy (2000): 11-24.

- DIVIS, D.A. (1999): Galileo- enthusiasm and money propel Europe's GNSS. *GPS World* 10 (11): 12-19.
- DMA (1987): Department of Defense World Geodetic System 1984. DMA Technical Report TR 8350.2 and Supplement TR 830.2-A,B, Washington, D.C.
- DOBRIN, M.B. (1976): Introduction to geophysical prospecting. McGraw-Hill, New York etc.
- DODSON, A.H. (1995): The status of GPS for height determination. *Survey Review* 34: 66-76.
- DODSON, A.H., P. FLEMING (1988): The Geomensor CR204: Baseline test results. *Survey Review* 29: 351-357.
- DONG, D., J.O. DICKEY, Y. CHAO, M.K. CHENG (1997): Geocenter variations caused by atmosphere, ocean and surface ground water. *Geophys. Res. Letters* 24: 1867-1870.
- DOODSON, A.I. (1921): The harmonic development of the tide-generating potential. *Proc. Roy. Soc. London, A* 100: 305-329.
- DORRER, E. (1966): Direkte numerische Lösung der geodätischen Hauptaufgaben auf Rotationsflächen. DGK, C 90, München.
- DREWES, H., W. TORGE, R.H. RÖDER, C. BADELL, D. BRAVO, O. CHOURIO (1991): Absolute and relative gravimetric surveys of national and geodynamic networks in Venezuela. *J. South American Earth Sciences* 4: 273-286.
- DREWES, H., C. FÖRSTE, C. REIGBER (1992): Ein aktuelles plattenkinematisches Modell aus Laser- und VLBI- Auswertungen. *ZfV* 117: 205-214.
- DUCARME, B., J. BARTHELEMY, eds. (2000): High precision gravity measurements with application to geodynamics and second GGP workshop. Cahiers du Centre Européen de Géodynamique et de Séismologie 17, Luxembourg.
- DUCARME, B., B. JANSEN (1990): Changes of station coordinates with earth tides and ocean loading. In Paquet et al. (1990): 39-45.
- DUCARME, B., P. MELCHIOR (1983): A prediction of tidal ocean loading and attraction effects on gravity measurements in continents. *Bull. d'Inf. Bur. Gravim. Int.* 52: 77-85.
- DUCARME, B., P. PAQUET, eds. (1998): Proceedings of the Thirteenth International Symposium on Earth Tides. Obs. Royal de Belgique, Serie Geophysique, Bruxelles.
- DVORAK, J.J. (1995): Volcano geodesy: results of 100 years of surveillance. In Barthelemy et al. (1995): 1-119.
- DZIEWONSKI, A.M., D.L. ANDERSON (1981): Preliminary reference earth model (PREM). *Phys. Earth Planet. Int.* 25: 297-356.
- DZIEWONSKI, A.M., J.H. WOODHOUSE (1987): Global images of the earth's interior. *Science* 236: 37-48.
- ECKER, E., E. MITTERMAYER (1969): Gravity corrections for the influence of the atmosphere. *Boll. Geof. teor. appl.* 11: 70-80.
- EEG, J., T. KRARUP (1973): Integrated geodesy. *Dan. Geod. Inst., int. rep.* 7, Copenhagen.
- EHLERT, D. (1991): Differentielle Verschiebungen und Drehstreckungen in dreidimensionalen Koordinatensystemen. DGK, B 295, Frankfurt a.M.
- EHLERT, D. (1993): Methoden der ellipsoidischen Dreiecksberechnung. DGK, B 292, Frankfurt a.M.

- EICHHORN, H. (1974): Astronomy of star positions. Ungar Publ., New York.
- EKMAN, M. (1989): Impacts of geodynamic phenomena on systems for height and gravity. *Bull. Géod.* 63: 281-296..
- EKMAN, M. (1993): Postglacial rebound and sea level phenomena, with special reference to Fennoscandia and the Baltic Sea. In *Kakkuri* (1993a): 7-70.
- EKMAN, M., J. MÄKINEN (1996): Recent postglacial rebound, gravity change and mantle flow in Fennoscandia. *Geophys. J. Int.* 126: 229-234.
- ELMIGER, A., W. GURTNER (1983): Astrogeodätische Geoidbestimmung und Lotabweichungsinterpolation in der Schweiz. Inst. für Geodäsie und Photogrammetrie. ETH Zürich, Nr. 74.
- ERKER, E. (1987): The Austrian geoid – local geoid determination using modified conservative algorithms. *Geod. Arb. Österreichs f.d. Intern. Erdmessung*, N.F. IV: 19-46, Graz.
- FALK, R. (1995): Erste Erfahrungen mit dem automatischen Gravimeter SCINTREX CG-3M Autograv. *ZfV* 120: 26-34.
- FALLER, J.E., I. MARSON (1988): Ballistic methods of measuring g – the direct free-fall and symmetrical rise- and fall methods compared. *Metrologia* 25: 49-55.
- FALLER, J.E., Y.G. GUO, J. GSCHWIND, T.M. NIEBAUER, R.L. RINKER, J. XUE (1983): The JILA portable absolute gravity apparatus. *Bull. d'Inf. Bur. Gravim. Int.* 53: 87-97.
- FARRELL, W.E. (1972): Deformation of the earth by surface loads. *Rev. Geophys. Space Physics* 10: 761-797.
- FEIST, W., B. DONATH, M. GÖRING, M. KÖHLER, M. SEEGER, L. MONZ (1998): Elta S10 und Elta S20 von Carl Zeiss, Systemtachymeter einer neuen Generation. *Verm.wesen und Raumordnung* 60: 104-127.
- FINETTI, I., C. MORELLI (1973): Geophysical exploration of the Mediterranean Sea. *Boll. Geof. teor. appl.* 15: 263-344.
- FISCHBACH, E., C.L. TALMADGE (1999): The search for non-Newtonian gravity. Springer, New York.
- FISCHER, I. (1975): The figure of the earth – changes in concepts. *Geophys. Surveys* 2: 3-54.
- FISCHER, I. (1977): Mean sea level and the marine geoid – an analysis of concept. *Marine Geodesy* 1: 37-59.
- FISCHER, I., M. SLUTSKY et al. (1968): New pieces in the picture puzzle of an astrogeodetic geoid map of the world. *Bull. Géod.* no. 88: 199-221.
- FLACH, D. (1976): The Askania borehole tiltmeter in field operation. Proceed. 7th Int. Symp. on Earth Tides, Sopron 1973: 243-247, Budapest.
- FORSBERG, R. (1984): A study of terrain reductions, density anomalies and geophysical inversion methods in gravity modelling. OSU Rep. 355, Columbus, Ohio.
- FORSBERG, R. (1985): Gravity field terrain effect computations by FFT. *Bull. Géod.* 59: 342-360.
- FORSBERG, R., J.M. BROZENA (1993): The Greenland airborne gravity project – comparison of airborne and terrestrial gravity data. In Montag and Reigber (1993): 171-175.
- FORSBERG, R., C.C. TSCHERNING (1981): The use of height data in gravity field approximation. *JGR* 86: 7843-7854.

- FORSBERG, R., C.C. TSCHERNING (1997): Topographic effects in gravity field modelling for BVP. In F. Sansò and R. Rummel (1997): 241-272.
- FORSBERG, R., M. FEISSEL, R. DIETRICH, eds. (1998): Geodesy on the move: Gravity, geoid, geodynamics, and Antarctica. IAG Symp. Proceed. 119, Springer, Berlin-Heidelberg-New York.
- FOWLER, C.M.R. (1999): The solid earth. Cambridge Univ. Press.
- FRANCIS, O. (1997): Calibration of the CO21 superconducting gravimeter in Membach (Belgium) using 47 days of absolute gravity measurements. In Segawa et al. (1997): 212-219.
- FRICKE, W., H SCHWAN, T. LEDERLE, eds. (1988): Fifth Fundamental Catalogue (FK5). Veröff. Astron. Recheninstitut Heidelberg 32, Braun, Karlsruhe.
- FROOME, K.D. (1971): Mekometer III: EDM with sub-millimeter resolution. Survey Review 21: 98-118.
- FU, L.-L., J. CHRISTENSEN, C. YAMARONE et al. (1994): TOPEX-POSEIDON mission overview. JGR 99: 24369-24381.
- GAN, W., J.L. SVARC, J.C. SAVAGE, W.H. PRESCOTT (2000): Strain accumulation across the Eastern California Shear Zone at latitude 36°30'N. JGR 105: 16229-16236.
- GARLAND, G.D. (1979): Introduction to geophysics. Saunders, Philadelphia.
- GERARDY, TH. (1977): Die Anfänge von Gauss' geodätischer Tätigkeit. ZfV 102: 1-20.
- GERSTBACH, G. (1996): CCD und geodätische Astronomie – Zur Nutzbarkeit von CCD für Lot- und Azimutmessungen. Österr. Z.f.Verm. u. Geoinf. 96: 63-68.
- GILLIES, G.T. (1987): The Newtonian Gravitational Constant. Metrologia 24 (suppl.): 1-56.
- GIPSON, J.M., C. MA (1998): Site displacement due to variation in earth rotation. JGR 103: 7337-7350.
- GLEINSVIK, P. (1960): Studien über die Ermittlung der Geoidform und die Bestimmung von Meereshöhen aus Höhenwinkeln. Mitt. Nr.7, Geod. Inst., ETH Zürich.
- GOODKIND, J.M. (1991): The superconducting gravimeters: principle of operation, current performance and future prospects. In Poitevin (1991): 81-90, Luxembourg.
- GOPALAPILLAI, S. (1974): Non-global recovery of gravity anomalies from a combination of terrestrial and satellite altimetry data. OSU Rep. 210, Columbus, Ohio.
- GORDON, R.G. (1995): Present plate motions and plate boundaries. In Ahrens (1995): 66-87.
- GÖRRES, B., J. CAMPBELL (1998): Bestimmung vertikaler Punktbewegungen mit GPS. ZfV 123: 222-230.
- GRABOWSKI, J. (1987): Hydrostatic levelling over long distances. In Pelzer and Niemeier (1987): 271-287.
- GRAFAREND, E.W. (1972): Three-dimensional geodesy and gravity gradients. OSU Rep. 174, Columbus, Ohio.
- GRAFAREND, E.W. (1976): Geodetic applications of stochastic processes. Phys. Earth Planet. Int. 12: 151-179.
- GRAFAREND, E.W. (1978): Operational geodesy. In Moritz and Sünkel (1978): 235-284.
- GRAFAREND, E.W. (1986): Differential geometry of the gravity field. Man.Geod. 11: 29-37.

- GRAFarend, E.W., W. NIEMEIER (1971): The free nonlinear boundary value problem of physical geodesy. *Bull. Géod.* no. 101: 243-262.
- GRAFarend, E.W., F. SANSØ, eds. (1985): Optimization and design of geodetic networks. Springer, Berlin-Heidelberg.
- GRAFarend, E.W., B. SCHAFFRIN (1993): *Ausgleichungsrechnung in linearen Modellen*. BI Wissenschaftsverlag, Mannheim.
- GRONWALD, W. (1963): "Das Einheitliche Europäische Nivellementsnetz" und der "Mittlere Meeresspiegel". *ZfV* 88: 141-153.
- GROSSMANN, W. (1976): *Geodätische Rechnungen und Abbildungen in der Landesvermessung*. 3.Aufl., Wittwer, Stuttgart.
- GROTE, TH. (1996): Regionale Quasigeoidmodellierung aus heterogenen Daten mit cm-Genauigkeit. *Wiss. Arb. Univ. Hannover* 212.
- GROTN, E. (1979): Geodesy and the earth's gravity field. Dümmler, Bonn.
- GROTN, E. (2000): Parameters of common relevance of astronomy, geodesy, and geodynamics. *J. Geod.* 74: 134-140.
- GROTN, E., E. REINHART (1968): Gravity prediction in mountainous areas. *Boll. Geof. teor. appl.* 10: 28-43.
- GRUBER, TH., M. ANZENHOFER, M. RENTSCH, P. SCHWINTZER (1997): Improvements in high resolution gravity field modeling at GFZ. In Segawa et al (1997): 445-452.
- GUBLER, E., H. HORNIK, eds. (1999): IAG Section I, Comm. X, Subcomm. for Europe (EUREF), Publ. No. 9, Mitt. BKG 6, Frankfurt a.M.
- GUBLER, E., H.G. KAHLE, E. KLINGELE, ST. MUELLER, R. OLIVIER (1981): Recent crustal movements in Switzerland and their geophysical interpretation. *Tectonophysics* 71: 125-152.
- GUBLER, E., J.A. TORRES, H. HORNIK, eds. (1999): IAG, Section I, Comm.X, Subcomm. for Europe (EUREF), Publ. No. 8, Veröff. Bayer. Komm. f.d. Internat. Erdmessung Nr.60, München.
- GUMERT, W.R. (1995): Third generation aerogravity system. Proceed. Int. Symp.on Kinematic Systems in Geodesy, Geomatics, and Navigation: 163-169.
- HAAGMANS, R., E. DE MIN, M. VAN GELDEREN (1993): Fast evaluation of convolution integrals on the sphere using 1D FFT, and a comparison with existing methods for Stokes' integral. *Man. Geod.* 18: 227-241.
- HAASBROEK, N.D. (1968): Gemma Frisius, Tycho Brahe and Snellius and their triangulation. *Publ. Netherl. Geod. Comm.*, Delft.
- HAKE, G., D. GRÜNREICH (1994): *Kartographie*. 7. Aufl., de Gruyter, Berlin- New York.
- HAMMER, S. (1963): Deep gravity interpretation by stripping. *Geophysics* 28: 369-378.
- HAMMER, S. (1979): Relative precision of vertical and horizontal gravity gradients measured by gravimeter. *Geophysics* 44: 99-101.
- HAMMER, S. (1983): Airborne gravity is here. *Geophysics* 48: 213-223.
- HANKEMEIER, P. (1996): The DGPS-Service for the FRG: Concept and status. In Beutler et al (1996c): 75-84.
- HANNAH, J. (1989): A long term sea level change scenario and its implications for geodetic networks. *Marine Geodesy* 13: 91-100.

- HARNISCH, M., G. HARNISCH (1993): Helmert's Arbeiten zur physikalischen Geodäsie. In F.R. Helmert, Akademievorträge, Nachr. a.d. Karten- und Verm.wesen 109: 37-77, Inst. f. Angew. Geodäsie, Frankfurt a.M.
- HARRISON, J.C. (1976): Cavity and topographic effects in tilt and strain measurements. *JGR* 81: 319-328.
- HARTMANN, T., H.-G. WENZEL (1995): The HW95 tidal potential catalogue. *Geophys. Res. Letters* 22: 3553-3556.
- HASTINGS, D.A., P.K. DUNBAR, A.M. HITTELMAN (2000): Assessing the global land one-km base elevation DEM. In Schwarz (2000b): 101-106.
- HECK, B. (1990): An evaluation of some systematic error sources affecting terrestrial gravity anomalies. *Bull. Géod.* 64: 88-108.
- HECK, B. (1991): On the linearized boundary value problem of physical geodesy. OSU Rep. 407, Columbus, Ohio.
- HECK, B. (1995): Rechen- und Auswertemodelle der Landesvermessung. 2.Aufl., Wichmann, Heidelberg.
- HECK, B. (1997): Formulation and linearization of boundary value problems: From observables to mathematical models. In Sansò and Rummel (1997): 121-160.
- HEIN, G.W. (1986): Integrated geodesy – state of the art 1986 reference text. In Sünkel (1986a): 505-548.
- HEISKANEN, W.A. (1951): On the world geodetic system. *Publ. Isostat. Inst., Int. Ass. Geod.*, 26, Helsinki.
- HEISKANEN, W.A. (1957): The Columbus Geoid. *EOS* 38: 841-848.
- HEISKANEN, W.A., H. MORITZ (1967): Physical geodesy. Freeman and Co., San Francisco and London.
- HEISKANEN, W.A., F.A. VENING-MEINESZ (1958): The earth and its gravity field. McGraw-Hill, New York.
- HEITZ, S. (1969): An astro-geodetic determination of the geoid for West Germany. *Nachr. a.d. Karten- und Verm.wesen* II 24, Frankfurt a.M.
- HEITZ, S. (1973): Ein dreidimensionales Berechnungsmodell für Punktbestimmungen mit Berücksichtigung orthometrischer Höhen. *ZfV* 98: 479-485.
- HEITZ, S. (1988): Coordinates in geodesy. Springer, Berlin-Heidelberg-New York.
- HELMERT, F.R. (1880/1884): Die mathematischen und physikalischen Theorien der höheren Geodäsie. Teubner, Leipzig (reprint Minerva GmbH, Frankfurt a.M. 1961).
- HERRING, T.A., D. DONG (1994): Measurement of diurnal and semidiurnal rotational variations and tidal parameters of earth. *JGR* 99: 18051-18071.
- HESS, H.H. (1962): History of ocean basins. In A.E. Engel, H.L. James, B.F. Leonard, eds., Petrological studies – Buddington Memorial Volume: 599-620, Geol. Soc. Am., New York, N.Y.
- HINDERER, J., D. CROSSLEY, H. XU (1994): A two-year comparison between the French and Canadian superconducting gravimeter data. *Geophys. J. Int.* 116: 252-266.
- HINZE, W.J., ed. (1985): The utility of regional gravity and magnetic anomaly maps. Society of Exploration Geophysicists, Tulsa, Oklahoma.
- HIPPARCOS (1995). *Astronomy and Astrophysics* 304: 34-316.
- HIRVONEN, R.A. (1960): New theory of the gravimetric geodesy. *Publ. Isostat. Inst., Int. Ass. Geod.*, 32, Helsinki.

- HOFMANN-WELLENHOF, B., H. LICHTENEGGER, J. COLLINS (1997): Global Positioning System: Theory and practice. 5th ed., Springer, Berlin-Heidelberg-New York.
- HOLT, W.E., N. CHANNOT-ROOKE, X. LE PICHON, A.J. HAINES, B. SHEN-TU, J. REN (2000): Velocity field in Asia inferred from Quaternary fault slip rates and Global Positioning System observations. *JGR* 105: 19185-19209.
- HOOIJBERG, M. (1997): Practical geodesy. Springer, Berlin-Heidelberg-New York.
- HOPCKE, W. (1965): Eine Studie über die Korrelation elektromagnetisch gemessener Strecken. *Allg. Verm. Nachr.* 72: 140-147.
- HOPCKE, W. (1966): On the curvature of electromagnetic waves and its effects on measurement of distance. *Survey Review* 18: 298-312.
- HOPFIELD, H. (1969): Two-quartic tropospheric refractivity profile for correcting satellite data. *JGR* 74: 4487-4499.
- HÖRMANDER, L. (1976): The boundary value problem of physical geodesy. *Archive for Rat. Mechanics and Analysis* 62: 1-52.
- HOTINE, M. (1969): Mathematical geodesy. ESSA Monogr.2, Washington, D.C.
- HOYER, M., S. ARGINIEGAS, K. PEREIRA, H. FAGARD, R. MATURANA, R. Torchetti, H. DREWES, M. KUMAR, G. SEEGER (1998): The definition and realization of the reference system in the SIRGAS project. In Brunner (1998): 168-173.
- HRADILEK, L. (1984): Threedimensional terrestrial triangulation – applications in surveying engineering. Wittwer, Stuttgart.
- HUDNUT, K.W. (1995): Earthquake geodesy and hazard monitoring. *Rev. Geophys.*, Suppl.: 249-255.
- HUGGETT, G.R., L.W. SLATER (1975): Precision electromagnetic distance-measuring instrument for determining secular strain and fault movement. *Tectonophysics* 29: 19-27.
- IAG (1971): Geodetic Reference System 1967. *Publ. Spec. 3*, IAG Central Bureau, Paris.
- IAG (1997): Science Services: International Association of Geodesy (IAG) / Federation of Astronomical and Geophysical Services (FAGS). Dep.of Civil and Environmental Engineering and Geodetic Science, The Ohio State Univ, Columbus, Ohio, and IAG Central Bureau, c/o Dep. of Geophysics, Copenhagen, Denmark.
- IERS (1995): Missions and goals for 2000. IERS Central Bureau, Paris.
- IHDE, J., W. LINDSTROT (1995): Datumstransformation zwischen den Bezugssystemen ETRF/WGS, DHDN und System 42. *ZfV* 120: 192-196.
- IHDE, J., W. SCHLÜTER, J. ADAM, W. GURTNER, B.G.HARSSON, G. WÖPPELMANN (1998): Konzept und Status des European Vertical Reference Network (EUVN). In *BKG* (1998): 53-67.
- ILIFFE, J.C., A.H. DODSON (1987): Refraction effects on precise EDM observations. *Survey Review* 29: 181-190.
- ILK, K.H. (2000): Envisaging a new era of gravity field research. In Rummel et al (2000a): 53-62.
- ILLNER, M., R. JÄGER (1995): Integration von GPS-Höhen ins Landesnetz – Konzept und Realisierung im Programmsystem HEIDI. *Allg. Verm. Nachr.* 102: 1-18.
- INGENSAND, H. (1990): Das Wild NA 2000, das erste digitale Nivellier der Welt. *Allg. Verm. Nachr.* 97: 201-210.

- IZOTOV, A.A. (1959): Reference-ellipsoid and the standard geodetic datum adopted in the USSR. *Bull. Géod.* no.53: 1-6.
- JACHENS, R.C. (1978): Temporal gravity changes as applied to studies of crustal deformation. In Proceed. of Conf. VII Stress and Strain Measurements Related to Earthquake Prediction. U.S. Geological Survey Open-File Report 79-370.
- JACHENS, R.C., W. THATCHER, C.W. ROBERT, R.S. STEIN (1983): Correlation of changes in gravity, elevation, and strain in southern California. *Science* 219: 1215-1217.
- JAHN, C.-H., G. SEEBER, G.R. FOULGER, P. EINARSSON (1994): GPS epoch measurements spanning the Mid-Atlantic plate boundary in northern Iceland 1987-1990. In Schutz et al. (1994): 109-123.
- JANES, H.W., R.B. LANGLEY, S.P. NEWBY (1991): Analysis of tropospheric delay prediction models: comparison with ray-tracing and implications for GPS relative positioning. *Bull. Géod.* 65: 151-161.
- JEFFREYS, SIR HAROLD (1970): The earth - its origin, history and physical constitution. 5.ed., Cambridge Univ. Press.
- JEKELI, C. (1988a): The gravity gradiometer survey system (GGSS). *EOS* 69: 105, 116-117.
- JEKELI, C. (1988b): The exact transformation between ellipsoidal and spherical harmonic expansion. *Man. Geod.* 13: 106-113.
- JEKELI, C. (1995): Airborne vector gravimetry using precise, position-aided inertial measurements. *Bull. Géod.* 69: 1-11.
- JEKELI, C. (1998): The world of gravity according to Rapp. In Forsberg et al. (1998): 79-91.
- JEKELI, C. (1999): An analysis of vertical deflections derived from high-degree spherical harmonic models. *J. Geod.* 73: 10-22.
- JEKELI, C. (2001): Inertial navigation systems with geodetic applications. De Gruyter, Berlin-New York.
- JELSTRUP, J. (1955): Crossing of fjords with precise levelling. *Bull. Géod.* no. 38: 55-63.
- JENTZSCH, G. (1997): Earth tides and ocean tidal loading. In Wilhelm et al. (1997): 145-167.
- JGR (1998): Advances in oceanography and sea ice research using ERS observations. JGR special issue 103 (C4).
- JOECKEL, R., M. STOBER (1999): Elektronische Entfernung- und Richtungsmessung. 3.Aufl., Wittwer, Stuttgart.
- KÄÄRIÄINEN, J. (1979): Observing the earth tides with a long water-tube tiltmeter. Publ. Finn. Geod. Inst. 88, Helsinki.
- KAHLE, H.-G., M. COCARD, Y. PETER, A. GEIGER, R. REILINGER, A. BARKA, G. VEIS (2000): GPS-derived strain rate field within the boundary zones of the Eurasian, African and Arabian plates. *JGR* 105: 23353-23370.
- KAHMEN, H. (1978): Elektronische Meßverfahren in der Geodäsie. 3. Aufl., Wichmann, Karlsruhe.
- KAHMEN, H. (1997): Vermessungskunde. 19. Aufl., de Gruyter, Berlin- New York.
- KAHMEN, H., W. FAIG (1988): Surveying. De Gruyter, Berlin-New York.
- KAKKURI, J. (1966): Versuche mit dem automatischen Doppelinstrument Zeiss Ni2 beim Stromübergangsnivellement. *ZfV* 91: 160-164.

- KAKKURI, J. (1986): Newest results obtained in studying the Fennoscandian land uplift phenomenon. *Tectonophysics* 130: 327-331.
- KAKKURI, J., ed. (1993a): Geodesy and geophysics. *Publ. Finn. Geod. Inst.* 115, Helsinki.
- KAKKURI, J. (1993b): The stress phenomenon in the Fennoscandian shield. In Kakkuri (1993a): 71-86.
- KANE, M.F., R.H. GODSON (1985): Features of a pair of long-wavelength (> 250 km) and short wavelength (< 250 km) Bouguer gravity maps of the United States. In Hinze (1985): 46-61.
- KANNIGIESER, E. (1983): Genauigkeitssteigerungen in der Relativgravimetrie. *ZfV* 108: 180-189.
- KANNIGIESER, E., K. KUMMER, W. TORGE, H.-G. WENZEL (1983): Das Gravimeter-Eichsystem Hannover. *Wiss. Arb. Univ. Hannover* 120.
- KATSAMBALOS, K.E. (1979): The effect of the smoothing operator on potential coefficient determination. *OSU Rep.* 287, Columbus, Ohio.
- KAULA, W.M. (1959): Statistical and harmonic analyses of gravity. *JGR* 64: 2401-2421.
- KAULA, W.M. (1966): Theory of satellite geodesy. Blaisdell Publ., London.
- KAULA, W.M. (1992): Properties of the gravity fields of terrestrial planets. In Colombo (1992): 1-10.
- KAULA, W.M. (1993): Higher order statistics of planetary gravities and topographies. *Geophys. Res. Letters* 20: 2583-2586.
- KEARSLEY, A.H.W., R. FORSBERG (1990): Tailored geopotential models – applications and short-comings. *Man. Geod.* 15: 151-158.
- KELLOGG, O.D. (1929): Foundations of potential theory. Springer, Berlin (reprint 1967).
- KENYON, S.C. (1998): The development by the National Imagery and Mapping Agency of a global surface gravity anomaly database for the EGM96 geopotential model and future applications. In Forsberg et al. (1998): 99-104.
- KIM, J.-H., R.H. RAPP (1990): The development of the July 1989 $1^\circ \times 1^\circ$ and $30' \times 30'$ terrestrial mean free-air anomaly data base. *OSU Rep.* 403, Columbus, Ohio.
- KING, G.C.P., R.G. BILHAM (1973): Strain measurement instrumentation and technique. *Phil. Trans. Roy. Soc. London, A* 274: 209-217.
- KING, G.C.P., R.G. BILHAM (1976): A geophysical wire strainmeter. *Bull. Seism. Soc. Am.* 66: 2039-2047.
- KIVIOJA, L.A. (1971): Computation of geodetic direct and indirect problems by computers accumulating increments from geodetic line elements. *Bull. Géod.* no. 99: 53-63.
- KLEUSBERG, A. (1998): Atmospheric models from GPS. In Teunissen and Kleusberg (1998a): 599-623.
- KLINGELÈ, E.E., M. COCARD, H.-G. KAHLE, M. HALLIDAY (1997): GPS as a source for airborne gravity reduction in the airborne gravity survey of Switzerland. *JGR* 102: 7705-7715.
- KLOBUCHAR, J.A. (1991): Ionospheric effects on GPS. *GPS World* 2 (4): 48-51.
- KLOPPING, F. G., SASAGAWA, D., WINESTER et al. (1997): Report on the 1995 Table-Mountains international absolute-gravity-meter intercomparison. In Segawa et al. (1997): 40-46.

- KLOTZ, J. (1993): Die Transformation zwischen geographischen Koordinaten und geodätischen Polar- und Parallel-Koordinaten. ZfV 118: 217-227.
- KNEISSL, M. (1956): Höhenmessung-Tachymetrie. Jordan-Eggert-Kneissl, Handbuch der Vermessungskunde, Band III, Metzler, Stuttgart.
- KNEISSL, M. (1958/1959): Mathematische Geodäsie (Landesvermessung). Jordan-Eggert-Kneissl, Handbuch der Vermessungskunde, Band IV 1/2, Metzler, Stuttgart.
- KNUDSEN, P. (1993): Altimetry for geodesy and oceanography. In Kakkuri (1993a): 87-129.
- KOCH, K.R. (1989): Der erste europäische Fernerkundungssatellit ERS-1 und seine geodätische Nutzungsmöglichkeit. ZfV 114: 342-345.
- KOCH, K.R. (1999): Parameter estimation and hypothesis testing in linear models. 2nd ed., Springer, Berlin-Heidelberg-New York..
- KOCH, K.-R., A.J. POPE (1972): Uniqueness and existence of the geodetic boundary value problem using the known surface of the earth. Bull. Géod. no. 106: 467-476.
- KOGAN, M.G., M.K. McNUTT (1993): Gravity field over northern Eurasia and variations in the strength of the upper mantle. Science 259: 473-479.
- KOHL, M., J. LEVINE (1995): Measurement and interpretation of tidal tilts in Southern California. JGR 100: 3929-3942.
- KOUBA, J.A. (1983): A review of geodetic and geodynamic satellite Doppler positioning. Rev. Geophys. 21: 41-50.
- KOVALEVSKY, J. (1989): Lectures in celestial mechanics. In Sansò and Rummel (1989): 69-114, Springer, Berlin-New York.
- KOVALEVSKY, J. (1995): Modern astrometry. Springer, Berlin-Heidelberg-New York.
- KOVALEVSKY, J. et al. (1997): The HIPPARCOS catalogue as a realization of the extragalactic reference system. Astronomy and Astrophysics 323: 620-633.
- KOVALEVSKY, J., I.I. MUELLER, B. KOLACZEK, eds. (1989): Reference frames in astronomy and geophysics. Kluwer Acad. Publ., Dordrecht-Boston-New York.
- KRACK, K. (1982): Rechnergestützte Ableitung der Legendreschen Reihen und Abschätzung ihrer ellipsoidischen Anteile zur Lösung der ersten geodätischen Hauptaufgabe auf Bezugsellipsoiden. ZfV 107: 118-125.
- KRARUP, T. (1969): A contribution to the mathematical foundation of physical geodesy. Publ. Danish Geod. Inst. 44, Copenhagen.
- KRAUS, K. (1992/1997): Photogrammetry. Vol.1/ Vol.2, Dümmler, Bonn.
- KRAUS, K., W. SCHNEIDER (1988/1990): Fernerkundung. Dümmler, Bonn.
- KRIEG, L.A. (1981): Mathematical modelling of the behaviour of the LaCoste and Romberg "G" gravity meter for use in gravity network adjustments and data analyses. OSU Rep. 321, Columbus, Ohio.
- KUKKAMÄKI, T.J. (1938): Über die nivellitische Refraktion. Publ. Finn. Geod. Inst. 25, Helsinki.
- KUKKAMÄKI, T.J. (1949): Tidal correction of the levelling. Publ. Finn. Geod. Inst. 36: 143-152.
- KUKKAMÄKI, T.J. (1980): Errors affecting levelling. Proceed. NAD-Symp. Ottawa: 1-10.
- KUNTZ, E. (1990): Kartennetzentwurfslehre. 2.Aufl., Wichmann/ Hüthig, Heidelberg.

- KUNTZ, E., G. SCHMITT (1995): Präzisionshöhenmessung durch Beobachtung gleichzeitig gegenseitiger Zenitdistanzen. *Allg. Verm. Nachr.* 92: 427-434.
- KUTTERER, H. (1998): Effiziente Berechnung von Meridianbogenlängen. *Allg. Verm. Nachr.* 105: 96-98.
- LAMBECK, K. (1980): The earth's variable rotation. Cambridge Univ. Press.
- LAMBECK, K. (1988): Geophysical geodesy. Clarendon Press, Oxford.
- LAMBECK, K., C. SMITHER, P. JOHNSTON (1998): Sea-level change, glacial rebound and mantle viscosity for northern Europe. *Geophys. J. Intern.* 134: 102-144.
- LAMBERT, A., T.S. JAMES, J.O. LIARD, N. COURTIER (1996): The role and capability of absolute gravity measurements in determining the temporal variations in the earth's gravity field. In Rapp et al. (1996): 20-29.
- LANGBEIN, J.O., M.F. LINKER, A.F. McGARR (1987): Precision of two-color geodimeter measurements: Results from 15 months of observations. *JGR* 92: 11644-11656.
- ANGLEY, R.B. (1997a): GLONASS: review and update. *GPS World* 8(7): 46-51.
- ANGLEY, R.B. (1997b): GPS receiver system noise. *GPS World* 8(6): 40-45.
- ANGLEY, R.B. (1998): Propagation of the GPS signals. In Teunissen and Kleusberg (1998a): 111-149.
- ANGLEY, R.B. (1999): Dilution of precision. *GPS World* 10(5): 52-59.
- LARSON, K., J. LEVINE (1999): Carrier-phase time transfer. *IEEE Trans. on Ultrasonics, Ferroelectrics, and Frequency Transfer Control* 46: 1001-1012.
- LARSON, K.M. (1995): Crustal deformation. *Rev. Geophys., Suppl.*: 371-377.
- LARSON, K.M., J.T. FREYMUELLER, S. PHILIPSEN (1997): Global plate velocities from the Global Positioning System. *JGR* 102: 9961-9981.
- LE PICHON, X., J. FRANCHETEAU, J. BONNIN (1973): Plate tectonics. Developm. In *Geotectonics* vol. 6, Elsevier, Amsterdam-London-New York
- LEDERSTEGER, K. (1956/1969): Astronomische und Physikalische Geodäsie (Erdmessung). Jordan-Eggert-Kneissl, Handbuch der Vermessungskunde, Band V, Metzler, Stuttgart.
- LEE, L.P. (1974): The computation of conformal projections. *Survey Review* 22: 245-256.
- LEICK, A. (1995): GPS satellite surveying. 2nd ed., Wiley and Sons, New York etc.
- LELGEMANN, D. (1976): On the recovery of gravity anomalies from high precision altimeter data. *OSU Rep.* 239, Columbus, Ohio.
- LEMOINE, F.G., D.E. SMITH, L. KUNZ et al. (1997): The development of the NASA GSFC and NIMA joint geopotential model. In Segawa et al. (1997): 461-469.
- LEMOINE, F.G., S.C. KENYON et al. (1998): The development of the Joint NASA GSFC and the National Imagery and Mapping Agency (NIMA) Geopotential Model EGM96. *NASA/TP-1998-206861*, Goddard Space Flight Center, Greenbelt, Maryland.
- LEONHARD, T. (1987): Vertical crustal movements in northern Germany. In Pelzer and Niemeier (1987): 525-538.
- LERCH, F.J., R.S. NEREM, B.H. PUTNEY et al. (1994): A geopotential model from satellite tracking, altimeter, and surface gravity data: GEM-T3. *JGR* 99: 2815-2839.
- LEVALLOIS, J.J. (1980): The history of the International Association of Geodesy. *Bull. Géod.* 54: 249-313.

- LEVALLOIS, J.J. (1988): Mésurer la terre – 300 ans de géodésie Francaise. Association Francaise de Topographie, Paris.
- LEVALLOIS, J.J., H. MONGE (1978): Le geoid Européen, version 1978. Proc. Int. Symp. on the Geoid in Europe and Mediterranean Area, Ancona 1978: 153-164.
- LEVITUS, S. (1982): Climatological atlas of the world ocean. NOAA, Geophys. Fluid Lab., Profess. Paper 13, Dep. of Commerce, Washington, D.C.
- LI RUIHAO, SUN HEPING, HU YENCHANG (1989): Investigation of gravity variation associated with crustal deformation of the Tianjin area before and after the Tangshan earthquake. Tectonophysics 167: 341-347.
- LI, Y., M. SIDERIS (1994): Minimizationand estimation of geoid undulation errors. Bull. Géod. 68: 201-219.
- LINDSTROT, W., ed. (1999): Das Deutsche Referenznetz 1991 (DREF91). Mitt. BKG 9, Frankfurt a.M.
- LISITZIN, E. (1974): Sea level changes. Elsevier, Amsterdam etc.
- LISTING, J.B. (1873): Über unsere jetzige Kenntnis der Gestalt und Größe der Erde. Nachr.d. Kgl. Gesellsch. d. Wiss. und der Georg-August-Univ., Göttingen: 33-98.
- LOWRIE, W. (1997): Fundamentals of geophysics. Cambridge Univ. Press.
- LU, Y., H.T. HSU, F.Z. JIANG (2000): The regional geopotential model to degree and order 720 in China. In Schwarz (2000b): 143-148.
- LUCHT, H. (1972): Korrelation im Präzisionsnivelllement. Wiss. Arb. Univ. Hannover 48.
- LUNDQUIST, C.A., G. VEIS (1966): Geodetic parameters for a 1966 Smithsonian Institution Standard Earth. Smithsonian Astrophysical Obs., Spec. Rep. 200.
- LYNESS, D. (1985): The gravimetric detection of mining subsidence. Geophysical Prospecting 33: 567-576.
- MA, C. et al. (1998): The International Celestial Reference Frame as realized by Very Long Baseline Interferometry. The Astronomical J. 116: 516-546.
- MA, C., M. FEISSEL, eds. (1997): Definition and realization of the International Reference System by VLBI astrometry of extragalactic objects. IERS Techn. Note 23, Paris.
- MÄKINEN, J., S. TATTARI (1988): Soil moisture and ground water: Two sources of gravity variations. Bull. d'Inf. Bur. Gravim. Int. 62: 103-110.
- MARKOWITZ, W. (1973): SI, the international system of units. Geophys. Surveys 1: 217-241.
- MARSH, J.G., S. VINCENT (1974): Global detailed geoid computation and model analysis. Geophys. Surveys 1: 481-511.
- MARSON, I., J.E. FALLER (1986): g – the acceleration of gravity: its measurement and its importance. J. Phys.E. Sci. Instrum.19: 22-32.
- MARTI, U. (1997): Geoid der Schweiz. Geod. geophysik. Arbeiten in der Schweiz 56, Schweiz. Geod. Komm., Zürich.
- MARTINEC, Z. (1994): Inversion techniques. In Vaniček and Christou (1994): 125-145.
- MARTINEC, Z. (1998): Boundary-value problems for gravimetric determination of a precise geoid. Lecture Notes in Earth Sciences 73, Springer, Berlin-Heidelberg-New York.
- MARUSSI, A. (1949): Fondements de géometrie differentielle absolue du champ potential terrestre. Bull. Géod. no. 14: 411-439.

- MARUSSI, A. (1985): Intrinsic geodesy. Springer, Berlin-Heidelberg-New York.
- MARUSSI, A., H. MORITZ, R.H. RAPP, R.O. VICENTE (1974): Ellipsoidal density models and hydrostatic equilibrium. *Phys. Earth Planet. Inter.* 9: 4-6.
- MASSONNET, D., M. ROSSI, C. CARMONA, F.ADRAGNA, G. PELTZER, K. FIEGL, T. RABAUTE (1993): The displacement field of the Landers earthquake mapped by radar interferometry. *Nature* 364: 138-142.
- MATHER, R.S. (1973): Four dimensional studies in earth space. *Bull. Géod.* no. 108: 187-209.
- MATHER, R.S. (1978): The role of the geoid in four-dimensional geodesy. *Marine Geodesy* 1: 217-252.
- MATHER, R.S., E.G. MASTERS, R. COLEMAN (1977): The role of non-tidal gravity variations in the maintenance of reference systems for secular geodynamics. *Unisur G* 26: 1-25.
- MATHEWS, P.M., V. DEHANT, J.M. GIPSON (1997): Tidal station displacements. *JGR* 102: 20469-20447.
- McADOO, D.C., D.T. SANDWELL (1988): GEOSAT's exact repeat mission. *EOS* 69: 1569.
- McCARTHY, D.D., ed. (1996): IERS Conventions (1996). IERS Techn. Note 21, Paris.
- McDONALD, K. (1999): Opportunity knocks: Will GPS modernization open doors? *GPS World* 10(9): 36-46.
- McKENZIE, D.P., R.L. PARKER (1967): The North Pacific: an example of tectonics on a sphere. *Nature* 216: 1276-1280.
- MEIER, D., R. LÖSER (1986): Das Mekometer ME 5000 - Ein neuer Präzisionsdistanzmesser. *Allg. Verm. Nachr.* 93: 82-90.
- MEIER-HIRMER, B., R. MEIER-HIRMER (1997): Untersuchungen zur intrinsischen Genauigkeit der Digitalnivelliere NA2000/NA3000 und DiNi20/DiNi10. *Verm.wesen und Raumordnung* 59: 286-295.
- MEISSNER, R., TH. WEVER, E.R. FLÜH (1987): The Moho in Europe- implications for crustal development. *Annales Geophysicae* 5: 357-364.
- MELCHIOR, P. (1983): The tides of the planet earth. Pergamon Press, Oxford etc.
- MELCHIOR, P. (1994): A new data bank for tidal gravity measurements (DB92). *Phys. Earth Planet. Inter.* 82: 125-155.
- MENGE, F., G. SEEBER, C. VOLKSEN, G. WÜBBENA, M. SCHMITZ (1998): Results of absolute field calibration of GPS antenna PCV. Proceed. 11th Intern. Techn. Meeting of the Satellite Division of the Institute of Navigation ION GPS-98: 31-38, Nashville, Tennessee.
- MERRIAM, J.B. (1992): Atmospheric pressure and gravity. *Geophys. J. Int.* 109: 488-500.
- MERRY, C.L., P. VANÍČEK (1974): The geoid and datum translation components. *The Canadian Surveyor* 28: 56-62.
- MILBERT, D.G. (1995): Improvement of a high resolution geoid model in the United States by GPS heighting on NAVD88 benchmarks. *Bull. d'Inf. Bur. Gravim. Int.* 77 and *Int. Geoid Service Bull.* 4, *New geoids in the world:* 13-36, Milan/Toulouse.
- MILITZER, H., F. WEBER (1984): Angewandte Geophysik. Springer, Wien-New York.
- MINSTER, J.B., T.H. JORDAN (1978): Present-day plate motions. *JGR* 83: 5331-5354.

- MINSTER, J.-F., C. BROSSIER, PH. ROGEL (1995): Variations of the mean sea level from TOPEX/POSEIDON data. *JGR* 100: 25153-25162.
- MISRA, P.N., R.J. ABBOT (1994): SGS 85 – WGS 84 transformation. *Man Geod.* 19: 300-308.
- MITCHUM, G. (1994): Comparison of TOPEX sea surface heights and tide gauge sea level. *JGR* 99: 24541-24553.
- MOLODENSKI, M.S. (1958): Grundbegriffe der geodätischen Gravimetrie. Transl. from Russian (1945), VEB Verlag Technik, Berlin 1958.
- MOLODENSKI, M.S., V.F. YEREMEYEV, M.I. YURKINA (1962): Methods for study of the external gravitational field and figure of the earth. Transl. From Russian (1960), Israel. Program for Scient. Transl., Jerusalem.
- MONTAG, H., CH. REIGBER, eds. (1993): Geodesy and physics of the earth. IAG Symp. Proceed. 112, Springer, Berlin-Heidelberg-New York.
- MOONEY, W.D., M.G. LASKE, T.G. MASTERS (1998): CRUST 5.1: a global crust model at 5°x5°. *JGR* 103: 727-748.
- MORELLI, C., C. GANTAR, T. HONKASALO, R.K. McCONNELL, J.G. TANNER, B. SZABO, U. UOTILA, C.T. WHALEN (1974): The International Gravity Standardization Net 1971 (IGSN71). I.U.G.G.-I.A.G.-Publ.Spec. 4, Paris.
- MORGAN, W.J. (1968): Rises, trenches, great faults, and crustal blocks. *JGR* 73: 1959-1982.
- MORITZ, H. (1962): Interpolation and prediction of gravity and their accuracy. OSU Rep. 24, Columbus, Ohio.
- MORITZ, H. (1968a): Mass distributions for the equipotential ellipsoid. *Boll. Geof. teor. appl.* 10: 59-65.
- MORITZ, H. (1968b): On the use of the terrain correction in solving Molodensky's problem. OSU Rep. 108, Columbus, Ohio.
- MORITZ, H. (1968c): Kinematical geodesy. DGK, A 59, München.
- MORITZ, H. (1970): Least-squares estimation in physical geodesy. DGK, A 69, München (OSU Rep. 130, Columbus, Ohio).
- MORITZ, H. (1971): Series solution of Molodensky's problem. DGK, A 70, München.
- MORITZ, H. (1973): Least squares collocation. DGK, A 75, München.
- MORITZ, H. (1974): Precise gravimetric geodesy. OSU Rep. 219, Columbus, Ohio.
- MORITZ, H. (1976): Integral formulas and collocation. *Man. Geod.* 1: 1-40.
- MORITZ, H. (1977): Der Begriff der mathematischen Erdgestalt seit Gauß. *Allg. Verm. Nachr.* 84: 133-138.
- MORITZ, H. (1978): Introduction to interpolation and approximation. In Moritz and Sünkel (1978): 1-45.
- MORITZ, H. (1980): Advanced physical geodesy. Wichmann, Karlsruhe.
- MORITZ, H. (1983): Local geoid determination in mountain regions. OSU Rep. 352, Columbus, Ohio.
- MORITZ, H. (1990): The figure of the earth. Wichmann, Karlsruhe.
- MORITZ, H. (2000): Geodetic Reference System 1980. *J. Geod.* 74: 128-133.
- MORITZ, H., B. HOFMANN-WELLENHOF (1993): Geometry, relativity, geodesy. Wichmann, Karlsruhe.
- MORITZ, H., I.I. MUELLER (1987): Earth rotation. Ungar Publ., New York.
- MORITZ, H., H. SÜNKEL (1978): Approximation methods in geodesy. Wichmann, Karlsruhe.

- MUELLER, I.I. (1969): Spherical and practical astronomy. Ungar Publ., New York.
- MUELLER, I.I. (1988): Reference coordinate systems, an update. OSU Rep. 394, Columbus, Ohio.
- MUELLER, I.I., O. HOLWAY III, R.R. KING jr. (1963): Geodetic experiment by means of a torsion balance. OSU Rep. 30, Columbus, Ohio.
- MUELLER, I.I., S. ZERBINI, eds. (1989): The interdisciplinary role of space geodesy. Lecture Notes in Earth Sciences 22, Springer, Berlin etc.
- MUELLER, ST., ed. (1974): The structure of the earth's crust based on seismic data. Elsevier, Amsterdam etc.
- NAGY, D. (1966): The gravitational attraction of a right angular prism. *Geophysics* 31: 362-371.
- NAGY, D., G. PAPP, J. BENEDEK (2000): The gravitational potential and its derivative for the prism. *J. Geod.* 74: 552-560.
- NASA (1983): The Geodynamics Program: An overview. NASA Techn. Paper 2147, Washington, D.C.
- NAT. ACAD. SCIENCES (1978): Geodesy: Trend and prospects. Nat. Acad. of Sciences, Comm. on Geodesy, Washington, D.C.
- NEREM, R.S. (1995a): Terrestrial and planetary gravity fields. *Rev. of Geophys.*, Suppl.: 469-476.
- NEREM, R.S. (1995b): Measuring global mean sea level variations using TOPEX/POSEIDON altimeter data. *JGR* 100: 25135-25151.
- NEREM, R.S., S.M. KLOSKO (1996): Secular variations of the zonal harmonics and polar motion as geophysical constraints. In Rapp et al. (1996): 152-163.
- NEREM, R.S., F.J. LERCH, J.A. MARSHALL et al. (1994): Gravity model development for TOPEX/POSEIDON: Joint gravity models 1 and 2. *JGR* 99: 24421-24447.
- NEREM, R.S., C. JEKELI, W.M. KAULA (1995): Gravity field determination and characteristics: Retrospective and prospective. *JGR* 100: 15053-15074.
- NEREM, R.S., K.E. RACHLIN, B.D. HUGHES (1997): Characterization of global mean sea level variations observed by TOPEX/POSEIDON using empirical orthogonal functions. *Surv.Geophys.* 18: 293-302.
- NEUMEYER, J., H.-J. DITTFELD (1997): Results of three year observation with a superconducting gravimeter at the GeoforschungsZentrum Potsdam. *J. Geod.* 71: 97-102.
- NEUMEYER, J., K. HEHL (1995): State-of-the-art and future sensor technology for airborne gravimetry. In Sünkel and Marson (1995): 151-160.
- NIEBAUER, T.M. (1988): Correcting gravity measurements for the effects of local air pressure. *JGR* 93: 7989-7991.
- NIEBAUER, T.M. (1989): The effective measurement height of free-fall absolute gravimeters. *Metrologia* 26: 115-118.
- NIEBAUER, T.M., G.S. SASAGAWA, J.E. FALLER, R. HILT, F. KLOPPING (1995): A new generation of absolute gravimeters. *Metrologia* 32: 159-180.
- NIELL, A.E. (1996): Global mapping functions for the atmospheric delay of radio wavelengths. *JGR* 101: 3227-3246.
- NIELSEN, C.S., R. FORSBERG, S. EKHOLM, J.J. MOHR (1998): SAR interferometry for improved terrain corrections in surface and airborne gravimetry. In Forsberg et al. (1998): 529-534.

- NIMA (2000): Department of Defense World Geodetic System 1984. National Imagery and Mapping Agency Technical Report TR 8350.2, 3.ed., Washington, D.C.
- NOAA (1966): US Standard Atmosphere Supplements, 1966. Nat. Techn. Inf. Service, US Dept. of Comm., Springfield, Va., U.S.A.
- NOAA (1976): US Standard Atmosphere 1976. Nat. Techn. Inf. Service, US Dept. of Comm., Springfield, Va., U.S.A.
- OWEN, S., P. SEGALL, M. LISOWSKI, A. MIKLIUS, R. DENLINGER, M. SAKO (2000): Rapid deformation of Kilauea volcano: Global Positioning System measurements between 1990 and 1996. *JGR* 105: 18983-18998.
- PAIK, H.J., J.-S. LEUNG, S.H. MORGAN, J. PARKER (1988): Global gravity survey by an orbiting gravity gradiometer. *EOS* 69: 1601, 1610-1611.
- PAIK, H.J., E.R. CANAVAN, M.V. MOODY (1997): Airborne/Shipborne SGG Survey System. In Cannon and Lachapelle (1997): 565-570.
- PAQUET, P., J. FLICK, B. DUCARME, eds. (1990): GPS for geodesy and geodynamics. Cahiers du Centre Européen de Géodynamique et de Séismologie 2, Luxembourg.
- PAUL, M.K. (1978): Recurrence relations for the integrals of associated Legendre functions. *Bull. Géod.* 52: 177-190.
- PAVLIS, N.K., R.H. RAPP (1990): The development of an isostatic gravitational model to degree 360 and its use in global gravity field modeling. *Geophys. J. Int.* 100: 369-378.
- PAVLIS, N.K., J.C. CHAN, F. LERCH (1996): Alternative estimation techniques for global high-degree modeling. In Rapp et al. (1996): 111-120.
- PELZER, H., ed. (1980): Geodätische Netze in Landes- und Ingenieurvermessung. Wittwer, Stuttgart.
- PELZER, H., W. NIEMEIER, eds. (1987): Determination of heights and height changes. Dümmler, Bonn.
- PESCHEL, H. (1974): Das motorisierte Präzisionsnivelllement – leistungsfähigstes Verfahren genauer Höhenmessungen. *Vermessungstechnik* 22: 57-64.
- PETER, G., R.E. MOOSE, C.W. WESSELS, J.E. FALLER, T.M. NIEBAUER (1989): High-precision absolute gravity observations in the United States. *JGR* 94: 5659-5674.
- PHILLIPS, R.J., K. LAMBECK (1980): Gravity fields of the terrestrial planets: Long-wavelength anomalies and tectonics. *Rev. Geophys.* 18: 27-76.
- PICK, M., J. PICHA, V. VYSCOCIL (1973): Theory of the earth's gravity field. Elsevier Scient. Publ. Co., Amsterdam-London-New York..
- PLAG, H.P., B. AMBROSIUS, T.F. BAKER et al. (1998): Scientific objectives of current and future WEGENER activities. In Zerbini et al. (1998): 177-223.
- PODER, K., H. HORNIK, eds. (1989): The European Datum 1987 (ED87). IAG RETRIG Subcomm., Publ. No.18, München.
- POITEVIN, C., ed. (1991): Proceed. of the Workshop: Non tidal gravity changes - Intercomparison between absolute and superconducting gravimeters. Cahiers du Centre Européen de Géodynamique et de Séismologie3, Luxembourg.
- POITEVIN, C., ed. (1995): Proceed. of the Second Workshop: Non tidal gravity changes – Intercomparison between absolute and superconducting gravimeters. Cahiers du Centre Européen de Géodynamique et de Séismologie 11, Luxembourg.
- RAPP, R.H. (1978): Results of the application of least-squares collocation to selected geodetic problems. In H. Moritz and H. Sünkel (1978): 117-156.

- RAPP, R.H. (1983a): The need and prospects for a world vertical datum. In Proceed. IAG Symp. XVIII, IUGG Gen. Ass. Hamburg 1983, vol. 2 : 432-445, Dep. of Geod. Science and Surveying, The Ohio State Univ., Columbus, Ohio.
- RAPP, R.H. (1983b): Tidal gravity computations based on recommendations of the Standard Earth Tide Committee. Bull. d'Inf. Marées Terrestres 89: 5814-5819.
- RAPP, R.H. (1995a): A world vertical datum proposal. Allg. Verm. Nachr. 102: 297-304.
- RAPP, R.H. (1995b): Separation between reference surfaces of selected vertical datums. Bull. Géod. 69: 26-31.
- RAPP, R.H. (1995c): Equatorial radius estimates from Topex altimeter data. In: Erwin Groten 60 Festschrift:90-97, Publ. Inst. of Geodesy and Navigation, University FAF Munich.
- RAPP, R.H. (1997): Global models for the 1 cm geoid – present status and near term prospects. In Sansò and Rummel (1997): 273-311.
- RAPP, R.H. (1998): Past and future developments in geopotential modelling. In Forsberg et al. (1998): 58-78.
- RAPP, R.H., N. BALASUBRAMANIA (1992): A conceptual formulation of a world height system. OSU Rep. 421, Columbus, Ohio.
- RAPP, R.H., N.K. PAVLIS (1990): The development and analysis of geopotential coefficient models to spherical harmonic degree 360. JGR 95: 21885-21911.
- RAPP, R.H., Y. YI (1997): Role of ocean variability and dynamic ocean topography in the recovery of the mean sea surface and gravity anomalies from satellite altimeter data. J. Geod. 71: 617-629.
- RAPP, R.H., Y.M. WANG, N. PAVLIS (1991): The Ohio State 1991 geopotential and surface topography harmonic coefficient models. OSU Rep. 410, Columbus, Ohio.
- RAPP, R.H., A.A. CAZENAVE, R.S. NEREM, eds. (1996): Global gravity field and its temporal variations. IAG Symp. Proceed. 116, Springer, Berlin-Heidelberg-New York.
- RAY, J., ed. (1999): IERS analysis campaign to investigate motions of the geocenter. IERS Techn. Note 25, Paris.
- REIGBER, C., M. FEISSEL (1997): IERS missions, present and future. Report on the 1996 IERS workshop. IERS Techn. Note 22, Paris.
- REIGBER, CH., H. LÜHR, P. SCHWINTZER (2000): Status of the CHAMP mission. In Rummel et al. (2000a): 63-65.
- RICHTER, B. (1987): Das supraleitende Gravimeter. DGK, C 329, Frankfurt a.M.
- RICHTER, B. (1995): Cryogenic gravimeters: Status report on calibration, data acquisition and environmental effects. In Poitevin (1995): 125-146, Luxembourg.
- RICHTER, B., H. WILMES, I. NOWAK (1995): The Frankfurt calibration system for relative gravimeters. Metrologia 32: 217-223.
- RICHTER, B.U. (1995): Die Parametrisierung der Erdorientierung. ZfV 120: 109-119.
- RIKITAKE, T. (1982): Earthquake forecasting and warning. Center for Acad. Publ. Japan/Tokyo-Reidel Publ. Co., Dordrecht-Boston-London.
- RINNER, K. (1977): Über geometrische Aufgaben der Meeresgeodäsie. ZfV 102: 354-366.

- RIZOS, C. (1982): The role of the geoid in high precision geodesy and oceanography. DGK, A 96, München.
- ROBBINS, J.W., D.E. SMITH, C. MA (1993): Horizontal crustal deformation and large scale plate motions inferred from space geodetic techniques. In Smith and Turcotte (1993): 21-36.
- ROBERTSON, D.S., W.E. CARTER, J. CAMPBELL, H. SCHUH (1985): Daily earth rotation determinations from IRIS very long baseline interferometry. *Nature* 316: 424-427.
- ROBERTSSON, L., O. FRANCIS, T. VAN DAM et al. (2001): Results from the fifth international comparison of absolute gravimeters, ICAG'97. *Metrologia* (in press).
- RÖDER, R.H., M. SCHNÜLL, H.-G. WENZEL (1985): Gravimetry with an electrostatic feedback system. *Bull. d'Inf. Bureau Gravim. Int.* 57: 72-81.
- RÖDER, R.H., M. SCHNÜLL, H.-G. WENZEL (1988): SRW feedback for LaCoste-Romberg gravimeters with extended range. *Bull. d'Inf. Bureau Gravim. Int.* 62: 46-50.
- ROTHACHER, M., G. BEUTLER, T.A. HERRING, R. WEBER (1999): Estimation of nutation using the Global Positioning System. *JGR* 104: 4835-4859..
- RÜEGER, J.M. (1997): Electronic distance measurements, an introduction. 4.ed., Springer, Berlin-Heidelberg-New York.
- RÜEGER, J.M., F.K. BRUNNER (1982): EDM-height traversing versus geodetic leveling. *The Canadian Surveyor* 36: 69-88.
- RÜEGER, J.M., F.K. BRUNNER (2000): On system calibration and type testing of digital levels. *ZfV* 125: 120-130.
- RUMMEL, R. (1979): Determination of short-wavelength component of the gravity field from satellite-to-satellite tracking or satellite gradiometry – an attempt to an identification of problem areas. *Man. Geod.* 4: 107-148.
- RUMMEL, R. (1986): Satellite gradiometry. In Sünkel (1986a): 317-363.
- RUMMEL, R., R.G. HIPKIN, eds. (1990): Gravity, gradiometry, and gravimetry. IAG Symp. Proceed. 103, Springer, New York-Berlin-Heidelberg.
- RUMMEL, R., K.H. ILK (1995): Height datum connection – the ocean part. *Allg. Verm. Nachr.* 102: 321-330.
- RUMMEL, R., P. TEUNISSEN (1988): Height datum definition, height datum connection and the role of the geodetic boundary value problem. *Bull. Géod.* 62: 477-498.
- RUMMEL, R., CH. REIGBER, K.H. ILK (1978): The use of satellite-to-satellite tracking for gravity parameter recovery. Proc. ESA Workshop on Space Oceanography, Navigation and Geodynamics (SONG), ESA-SP-137: 151-161.
- RUMMEL, R., R.H. RAPP, H. SÜNKEL, C.C. TSCHERNING (1988): Comparison of global topographic-isostatic models to the earth's observed gravity field. OSU Rep. 388, Columbus, Ohio.
- RUMMEL, R., F. SANSÒ, M. VAN GELDEREN et al. (1993): Spherical harmonic analysis of satellite gradiometry. Netherl. Geodetic Comm., Publ. on Geodesy, New Series 39, Delft.
- RUMMEL, R., H. DREWES, W. BOSCH, H. HORNIK, eds. (2000a): Towards an integrated global geodetic observing system (IGGOS). IAG Symp. Proceed. 120, Springer, Berlin-Heidelberg-New York.

- RUMMEL, R., J. MÜLLER, H. OBERNDORFER, N. SNEEUW (2000b): Satellite gravity gradiometry with GOCE. In Rummel et al. (2000a): 66-72.
- RUNCORN, S.K. (1962): Convection currents in the earth's mantle. *Nature* 195: 1248-1249.
- RUNDLE, J.B., J.H. WHITCOMB (1986): Modeling gravity and trilateration data in Long Valley, California, 1983-1984. *JGR* 91: 12675-12682..
- RYMER, H., C.A. LOCKE (1995): Microgravity and ground deformation precursors to eruption: a review. In Barthelemy et al. (1995): 21-39.
- SAASTOMAINEN, J. (1972/1973): Contributions to the theory of atmospheric refraction. *Bull. Géod.* 105: 279-298, 106: 383-397, 107: 13-34.
- SACHER, M., J. IHDE, H. SEEGER (1999): Preliminary transformation relations between national European height systems and the United European Levelling Network (UELN). In Gubler et al. (1999): 80-86.
- SAKUMA, A. (1983): An industrialized absolute gravimeter: Type GA 60. *Bull.d'Inf. Bureau Gravim. Int.* 53: 114-118.
- SALSTEIN, D.A., B. KOLACZEK, D. GAMBIS, eds. (1999): The impact of El Niño and other low-frequency signals on earth rotation and global earth system parameters. *IERS Techn. Note* 26, Paris.
- SANDWELL, D., W. SMITH (1997): Marine gravity anomaly from Geosat and ERS-1 altimetry. *JGR* 102: 10039-10054.
- SANSÒ, F. (1981): Recent advances in the theory of the geodetic boundary value problem. *Rev. Geophys. and Space Physics* 19: 437-449.
- SANSÒ, F. (1988): The Wiener integral and the overdetermined boundary value problems of physical geodesy. *Man. Geod.* 13: 75-98.
- SANSÒ, F. (1995): The long road from measurements to boundary value problem in physical geodesy. *Man. Geod.* 20: 326-344.
- SANSÒ, F., R. RUMMEL, eds. (1989): Theory of satellite geodesy and gravity field determination. *Lecture Notes in Earth Sciences* 25, Springer, Berlin-New York.
- SANSÒ, F., R. RUMMEL, eds. (1997): Geodetic boundary-value problems in view of the one centimeter geoid. *Lecture Notes in Earth Sciences* 65, Springer, Berlin-Heidelberg-New York.
- SATO, T., J.C. HARRISON (1990): Local effects on tidal strain measurements at Esashi, Japan. *Geophys. J. Int.* 102: 513-526.
- SATOMURA, M., I. NAKAGAWA, H. TSUKAMOTO, T. HIGASHI, Y. FUKUDA, K. NAKAMURA (1986): Secular changes of gravity observed in Kinki district, Japan. *Bull. d'Inf. Bur. Gravim. Int.* 59: 215-223.
- SAVAGE, J.C., W.H. PRESCOTT, M. LISOWSKI (1987): Deformation along the San Andreas Fault 1982-1986 as indicated by frequent geodolite measurements. *JGR* 92: 4785-4797.
- SCHERER, M. (1985): Der Präzisionsdistanzmesser CR204 Geomensor - Funktionsprinzip und erste Felderprobungen. *ZfV* 110: 135-145..
- SCHLEMMER, H. (1984): A new technique to produce precise graduation on invar tape. In H. Pelzer and W. Niemeier, eds. (1984), *Precise leveling*: 119-125, Dümmler, Bonn.
- SCHLEMMER, H. (1996): Grundlagen der Sensorik. Wichmann-Hüthig, Heidelberg.
- SCHMID, H. (1974): Worldwide geometric satellite triangulation. *JGR* 79: 5349-5376.

- SCHMIDT, H. (1999): Lösung der geodätischen Hauptaufgaben auf dem Rotationsellipsoid mittels numerischer Integration. *ZfV* 124: 121-128, 169.
- SCHMIDT, R. (1995): Referenz- und Koordinatensysteme in der deutschen Grundlagenvermessung. *Nachr. a.d. öffentl. Verm.wesen Nordrhein-Westfalen*: 23-67.
- SCHNÄDELBACH, K. (1974): Entwicklungstendenzen in Rechenverfahren der mathematischen Geodäsie. *ZfV* 99: 421-430.
- SCHNEIDER, M. (1988): *Satellitengeodäsie*. BI Wissenschaftsverlag, Mannheim-Wien-Zürich.
- SCHNEIDER, M. (1992/1993): *Himmelsmechanik* Bd.I(3.Aufl.1992)/Bd.II(1993). BI Wissenschaftsverlag, Mannheim-Leipzig-Wien-Zürich.
- SCHÖDLBAUER, A. (2000): *Geodätische Astronomie*. De Gruyter, Berlin-New York.
- SCHUH, H., R. HAAS (1998): Earth tides in VLBI observations. In Ducarme and Paquet (1998): 101-110.
- SCHÜLER, R., G. HARNISCH, H. FISCHER, R. FREY (1971): Absolute Schweremessungen mit Reversionspendeln in Potsdam 1968-1969. *Veröff. Zentralinst. Physik der Erde* 10, Potsdam.
- SCHUTZ, B.E., A. ANDERSON, C. FROIDEVAUX, M. PARKE, eds. (1994): *Gravimetry and space techniques applied to geodynamics and ocean dynamics*. *Geophys. Monograph* 82, IUGG vol.17, AGU/IUGG, Washington, D.C.
- SCHWARZ, C.R. (1969): The use of short arc orbital constraints in the adjustment of geodetic satellite data. *OSU Rep.* 118, Columbus, Ohio.
- SCHWARZ, C.R. (1989): North American Datum of 1983. *NOAA Profess. Paper NOS 2*, Nat. Geod. Survey, Rockville, Md.
- SCHWARZ, C.R., E.B. WADE (1990): The North American Datum of 1983: Project methodology and execution. *Bull. Géod.* 64: 28-62.
- SCHWARZ, K.-P. (1975): Zur Erdmessung des Eratosthenes. *Allg. Verm. Nachr.* 82: 1-12.
- SCHWARZ, K.-P., ed. (1986): *Inertial technology for surveying and geodesy*. Proc. Third Intern. Symp, Banff, Canada 1985. The Division of Surveying Eng., The Univ. of Calgary.
- SCHWARZ, K.-P. (2000a): An analysis of the current IAG structure and some thoughts on an IAG focus. In Schwarz (2000b): 407-414.
- SCHWARZ, K.-P., ed. (2000b): *Geodesy beyond 2000: The challenges of the first decade*. IAG Symp. Proceed. 121, Springer, Berlin-Heidelberg-New York.
- SCHWARZ, K.-P., M.G. SIDERIS, R. FORSBERG (1990): The use of FFT techniques in physical geodesy. *Geophys. J. Int.* 100: 485-514.
- SCHWIDERSKI, E.W. (1980): On charting global ocean tides. *Rev. Geophys.* 18: 243-268.
- SCHWIDERSKY, E.W. (1983): Atlas of ocean tidal charts and maps, part I: The semidiurnal principal lunar tide M2. *Marine Geodesy* 6: 219-266.
- SCHWINTZER, P., C. REIGBER, A. BODE et al. (1997): Long-wavelength global gravity field models: GRIM4-S4, GRIM4-C4. *J. Geod.* 71: 189-208.
- SEEBER, G. (1993): *Satellite geodesy*. De Gruyter, Berlin-New York.
- SEEBER, G., W. TORGE (1985): Zum Einsatz transportabler Zenitkameras für die Lotabweichungsbestimmung. *ZfV* 110: 439-450.

- SEEBER, G., D. EGGE, M. HOYER, H.W. SCHENKE, K.H. SCHMIDT (1982): Einsatzmöglichkeiten von Doppler-Satellitenmessungen. Allg. Verm. Nachr. 89: 373-388.
- SEEBER, G., D. EGGE, A. SCHUCHARDT, J. SIEBOLD, G. WÜBBENA (1985): Experiences with the TI 4100 NAVSTAR Navigator at the University of Hannover, Proceed. First Int. Symp. on Positioning and GPS, I: 215-226, Rockville, Md.
- SEEBER, G., F. MENGE, C. VÖLKSEN, G. WÜBBENA, M. SCHMITZ (1998): Precise GPS positioning improvements by reducing antenna and site dependent effects. In Brunner (1998): 237-244.
- SEEBER, H., Y. ALTINER, G. ENGELHARDT, P. FRANKE, H. HABRICH, W. SCHLÜTER (1998): EUREF - 10 Jahre Aufbauarbeit an einem neuen geodätischen Bezugssystem für Europa. BKG Mitt. Band 1 Geodätische Vernetzung Europas: 9-51, Frankfurt a.M.
- SEGAWA, J., H. FUJIMOTO, S. OKUBO, eds. (1997): Gravity, geoid and marine geodesy. IAG Symp. Proceed. 117, Springer, Berlin-Heidelberg-New York.
- SEIDELMANN, K.P., ed. (1992): Explanatory supplement to the astronomical almanac. Univ. Science Books, Mill Valley, Cal., U.S.A.
- SHUM, C.K., P.L. WOODWORTH, O.B. ANDERSEN et al. (1997): Accuracy assessment of recent ocean tidal models. JGR 102: 25173-25194.
- SIDERIS, M. (1985): A fast Fourier transform method for computing terrain corrections. Man. Geod. 10: 66-71.
- SIDERIS, M.G. (1990): Rigorous gravimetric terrain modelling using Molodensky's operator. Man. Geod. 15: 97-106.
- SIGL, R. (1985): Introduction to potential theory. Abacus Press, Cambridge.
- SIGL, R., W. TORGE, H. BEETZ, K. STUBER (1981): Das Schwergrundnetz 1976 der Bundesrepublik Deutschland (DSGN76). DGK, B 254, München.
- SIGMUNDSSON, F., H. VADON, D. MASSONET (1997): Readjustment of the Krafla spreading segment to crustal rifting measured by Satellite Radar Interferometry. Geophys. Res. Letters 24: 1843-1846.
- SILVERBERG, E.C. (1978): Mobile satellite ranging. In I.I. Mueller, ed. (1978), Applications of geodesy to geodynamics, OSU Rep. 280: 41-46, Columbus, Ohio.
- SIMPSON, R.W., R.C. JACHENS, R.J. BLAKELEY (1986): A new isostatic residual gravity map of the conterminous United States with a discussion on the significance of isostatic residual anomalies. JGR 91: 8348-8372.
- SJÖBERG, L.E. (1979): Integral formulas for heterogeneous data in physical geodesy. Bull. Géod. 53: 297-315.
- SJÖBERG, L.E. (1999): An efficient iterative solution to transform rectangular geocentric coordinates to geodetic coordinates. ZfV 124: 295-297.
- SKEELS, D.C. (1947): Ambiguity in gravity interpretation. Geophysics 12: 43-56.
- SLATER, L.E. (1983): A long-baseline two-fluid tiltmeter. EOS 64: 208.
- SLATER, J.A., S. MALYS (1998): WGS 84 - past, present and future. In Brunner (1998): 1-7.
- SMITH, J.R. (1986): From plane to spheroid. Landmark Enterprises, Rancho Cordova, CA, U.S.A.
- SMITH, D.A., D.G. MILBERT (1999): The GEOID96 high resolution geoid model for the United States. J. Geod. 73: 219-236.

- SMITH, D.A., D.R. ROMAN (2000): Recent advances in the acquisition and use of terrain data for geoid modelling over the United States. In Schwarz (2000b): 107-111.
- SMITH, D.A., D.R. ROMAN (2001): GEOID99 and G99SSS: One arc-minute geoid models for the United States. *J. Geod.* (in press).
- SMITH, W.H., D.T. SANDWELL (1994): Bathymetric prediction from dense satellite altimetry and sparse shipboard bathymetry. *JGR* 99: 21803-21824.
- SMITH, D., D. TURCOTTE, eds. (1993): Contributions of space geodesy to geodynamics: Crustal dynamics. AGU, Washington, D.C.
- SMITH, D.E., R. KOLENKIEWICZ, P.J. DUNN, M.H. TORRENCE (2000): Earth scale below a part per billion from satellite laser ranging. In Schwarz (2000b): 3-12.
- SNAY, R.A. (1986): Network design strategies applicable to GPS surveying using three or four receivers. *Bull. Géod.* 60: 37-50.
- SNAY, R.A. (1990): Accuracy analysis for the NAD83 Geodetic Reference System. *Bull. Géod.* 64: 1-27.
- SNEEUW, N., K.H. ILK (1997): The status of spaceborne gravity field mission concepts: a comparative simulation study. In Segawa et al. (1997): 171-178.
- SOLLER, D.R., R.D. RAY, R.D. BROWN (1982): A new global crustal thickness map. *Tectonics* 1: 125-149.
- SOLOMON, S.C., N.H. SLEEP (1974): Some simple physical models for absolute plate motions. *JGR* 79: 2557-2567.
- SOUDARIN, L., J.F. CRETAUX, A. CAZENAVE (1999): Vertical crustal motions from the DORIS space-geodesy system. *Geophys. Res. Letters* 26: 1207-1210.
- SPRATT, R.S. (1982): Modelling the effect of atmospheric pressure variations on gravity. *Geophys. J. R. Astr. Soc.* 71: 173-186.
- STACEY, F.D. (1992): Physics of the earth. Brookfield Press, Brisbane.
- STEIN, R.S. (1987): Contemporary plate motion and crustal deformation. *Rev. Geophys.* 25: 855-863.
- STEPHENSON, F.R., L.V. MORRISON (1994): Long-term fluctuations in the earth's rotation: 700 BC to AD 1990. *Phil. Trans. Royal Soc. London, A* 313: 47-70.
- STOKER, J.J. (1969): Differential geometry. Wiley-Interscience, New York.
- STOKES, G.G. (1849): On the variation of gravity on the surface of the earth. *Trans. Cambridge Phil. Soc.* 8: 672-695.
- STRANG VAN HEES, G.L. (1977): Zur zeitlichen Änderung von Schwere und Höhe. *ZfV* 102: 444-450.
- STRASSER, G. (1957): Ellipsoidische Parameter der Erdfigur. DGK, A 19, München.
- STRYKOWSKI, G. (1998): Geoid and mass density- why and how. In Forsberg et al. (1998): 237-242.
- STURGES, W. (1974): Sea level slopes along continental boundaries. *JGR* 79: 825-830.
- SUBIZA, W.H., W. TORGE, L. TIMMEN (1998): The national gravimetric network of Uruguay. In Forsberg et al. (1998): 51-57.
- SÜNKEL, H., ed. (1986a): Mathematical and numerical techniques in physical geodesy. Lecture Notes in Earth Sciences 7, Springer, Berlin-Heidelberg-New York.
- SÜNKEL, H. (1986b): Global topographic-isostatic models. In Sünkel (1986a): 417-462.
- SÜNKEL, H. (1988): Digital height and density model and its use for orthometric height and gravity field determination for Austria. *Boll. di Geod. e Scienze Affini* 47: 139-144.

- SÜNKEL, H. (1997): GBVP-classical solutions and implementation. In Sansò and Rummel (1997): 219-237.
- SÜNKEL, H., I. MARSON, eds. (1995): Gravity and geoid. IAG Symp. Proceed. 113, Springer, Berlin-Heidelberg-New York.
- TAKEMOTO, S. (1991): Some problems on detection of earthquake precursors by means of continuous monitoring of crustal strains and tilts. JGR 96: 10377-10390.
- TALWANI, M., G.H. SUTTON, J.L. WORZEL (1959): A crustal section across the Puerto Rico trench. JGR 64: 1545-1555.
- TALWANI, M., X. LE PICHON, M. EWING (1965): Crustal structure of the mid-ocean ridges. 2: Computed model from gravity and seismic refraction data. JGR 70: 341-352.
- TANIMOTO, T. (1995): Crustal structure of the earth. In Ahrens (1995): 214-224.
- TAPLEY, B.D., G.H. BORN, M.E. PARKE (1982): The Seasat altimeter data and its accuracy assessment. JGR 87: 3179-3188.
- TAPLEY, B.D., D.P. CHAMBERS, C.K. SHUM, R.J. EANES, J.C. RIES, R.H. STEWART (1994): Accuracy assessment of the large-scale dynamic ocean topography from TOPEX/POSEIDON altimetry. JGR 99: 24605-24617.
- TAPLEY, B.D., J.C. RIES, G.W. DAVIS et al. (1995): Precise orbit determination for TOPEX/POSEIDON. JGR 99: 24383-24404.
- TAPLEY, B.D., M.M. WATKINS, J.C. RIES et al. (1996): The Joint Gravity Model 3. JGR 101:28029-28049.
- TEISSEYRE, R., ed. (1989): Gravity and low-frequency geodynamics. Elsevier, Amsterdam etc.
- TEUNISSEN, P.J.G., A. KLEUSBERG, eds. (1998a): GPS for geodesy. 2nd ed., Springer, Berlin-Heidelberg-New York.
- TEUNISSEN, P.J.G., A. KLEUSBERG (1998b): GPS observations and positioning concepts. In Teunissen and Kleusberg (1998a): 187-229.
- THAYER, G.D. (1974): An improved equation for the radio refractive index of air. Radio Science 9: 803-807.
- TIMMEN, L., H.-G. WENZEL (1994a): Improved gravimetric earth tide parameters for station Hannover. Bull. d'Inf. Marées Terrestres 119: 8834-8846.
- TIMMEN, L., H.-G. WENZEL (1994b): Worldwide synthetic gravity tide parameters available on INTERNET. Bull. d'Inf. Bur. Gravim. Int. 73: 32-40.
- TIMMEN, L., G. BOEDECKER, U. MEYER (1998): Flugzeuggestützte Vermessung des Erdschwerefeldes. ZfV 123: 378-384.
- TODHUNTER, I. (1873): A history of the mathematical theories of attraction and the figure of the earth. Macmillan and Co. (reprint Dover Publ., New York 1962).
- TOLKATCHEV, A. (1996): Global Sea Level Observing System (GLOSS). Marine Geodesy 19: 21-62.
- TOMODA, Y., H. FUJIMOTO (1981): Gravity anomalies in the western Pacific and geophysical interpretation. J. Phys. Earth 29: 387-419.
- TORGE, W. (1977): Untersuchungen zur Höhen- und Geoidbestimmung im dreidimensionalen Testnetz Westharz. ZfV 102: 173-186.
- TORGE, W. (1980a): Drei- und zweidimensionale Modellbildung. In Pelzer (1980): 113-130.
- TORGE, W. (1980b): Geodätisches Datum und Datumstransformation. In Pelzer (1980): 131-140.

- TORGE, W. (1984): Observation strategy and -technique in gravimetry. In B.G. Harsson, ed. (1984), Optimization of geodetic operations: 126-210, Norges Geografiske Oppmåling, Publ.3.
- TORGE, W. (1986): Gravimetry for monitoring vertical crustal movements: potential and problems. *Tectonophysics* 130: 385-393.
- TORGE, W. (1989): Gravimetry. De Gruyter, Berlin-New York.
- TORGE, W. (1990): Approaching the "cm-geoid" – strategies and results. *Mitt. Geod. Inst. TU Graz* 67: 1-9.
- TORGE, W. (1991): The present state of absolute gravimetry. In Poitevin (1991): 9-22, Luxembourg.
- TORGE, W. (1993): Gravimetry and tectonics. In Kakkuri (1993a): 131-172.
- TORGE, W. (1996): The International Association of Geodesy (IAG) – More than 130 years of international cooperation. *J. Geod.* 70: 840-845.
- TORGE, W. (1997): Von Gauss zu Baeyer und Helmert – Frühe Ideen und Initiativen zu einer europäischen Geodäsie. In H. Junius und K. Kröger (eds.), Europa wächst zusammen: 39-65, Wittwer, Stuttgart.
- TORGE, W. (1998): The changing role of gravity reference networks. In Forsberg et al. (1998): 1-10.
- TORGE, W., H.-G. WENZEL (1978): Dreidimensionale Ausgleichung des Testnetzes Westharz. DGK, B 234, München.
- TORGE, W., G. WEBER, H.-G. WENZEL (1984): 6×10^4 free air gravity anomalies of Europe including marine areas. *Marine Geophys. Res.* 7: 93-111.
- TORGE, W., R.H. RÖDER, M. SCHNÜLL, H.-G. WENZEL, J.E. FALLER (1987): First results with the transportable absolute gravity meter JILAG-3. *Bull. Géod.* 61: 161-176.
- TORGE, W., T. BASIC, H. DENKER, J. DOLIFF, H.-G. WENZEL (1989): Long range geoid control through the European GPS traverse. DGK, B 290, München.
- TORGE, W., T. GROTE, R.H. RÖDER, M. SCHNÜLL, H.-G. WENZEL (1992): Introduction of absolute gravimetric techniques into a high-precision gravity and vertical control system in northern Iceland. DGK, B 297, München.
- TORGE, W., R. FALK, A. FRANKE, E. REINHART, B. RICHTER, M. SOMMER, H. WILMES (1999a): Das Deutsche Schweregrundnetz 1994 (DSGN94). DGK, B 309, München.
- TORGE, W., M. SCHNÜLL, L. TIMMEN, JIA MINYU, XING CANFEI, LI HUI (1999b): Absolute and relative gravimetry 1990/1992/1995 in the Western Yunnan Earthquake Prediction Experimental Area. DGK, B 307, München.
- TRYGGVASON, E. (1994): Surface deformation at the Krafla volcano, North Iceland, 1982-1992. *Bull. of Volcanology* 56: 98-107.
- TSCHERNING, C.C. (1976): Covariance expressions for second and lower order derivatives of the anomalous potential. OSU Rep. 225, Columbus, Ohio.
- TSCHERNING, C.C., R. FORSBERG (1986): Geoid determination in the Nordic countries from gravity and height data. Proceed. Int. Symp. on the Definition of the Geoid, vol. 1: 325-352, Ist. Geogr. Ital., Firenze.
- TSCHERNING, C.C., R.H. RAPP (1974): Closed covariance expressions for gravity anomalies, geoid undulations, and deflections of the vertical implied by anomaly degree variance models. OSU Rep. 208, Columbus, Ohio.

- TSCHERNING, C.C., R.H. RAPP, C.C. GOAD (1983): A comparison of methods for computing gravimetric quantities from high degree spherical harmonic expansions. *Man. Geod.* 8:249-272.
- TSUJI, H., Y. HATANAKA, T. SAGIYA, M. HASHIMOTO (1995): Coseismic crustal deformation from the 1994 Hokkaido-Toho-Oki earthquake monitored with a nationwide continuous GPS array in Japan. *Geophys. Res. Lett.* 22: 1669-1672.
- TURNER, S., ed. (1987): Applied geodesy. Springer, Berlin-Heidelberg-New York.
- VÄISÄLÄ, Y. (1946): An astronomic method of triangulation. *Sitz. Ber. Finn. Akad. der Wiss.schaften* 8: 99-107.
- VAN DAM, T.M., J.M. WAHR (1987): Displacement of the earth's surface due to atmospheric loading: effects on gravity and baseline measurements. *JGR* 92: 1281-1286.
- VAN GELDEREN, M., R. HAAGMANS, M. BILKER (1999): Gravity changes and natural gas extraction in Groningen. *Geophysical Prospecting* 47: 979-994.
- VAN GYSEN, H., R. COLEMAN (1997): On the satellite crossover problem. *J. Geod.* 71: 83-96.
- VAN RUYMBEKE, M. (1976): Sur un pendule horizontal équipé d'un capteur de déplacement à capacité variable. *Bull. Géod.* 50: 281-290.
- VANIČEK, P., N.T. CHRISTOU (1994): Geoid and its geophysical interpretations. CRC Press, Boca Raton etc.
- VANIČEK, P., E.J. KRAKIWSKY (1986): Geodesy: The concepts. 2.rev. ed., Elsevier Science Publ., Amsterdam-New York.
- VANIČEK, P., C.L. MERRY (1973): Determination of the geoid from deflections of the vertical using a least squares surface fitting technique. *Bull. Géod.* no. 109: 261-280.
- VANIČEK, P., D.E. WELLS (1974): Positioning of horizontal geodetic datums. *The Canadian Surveyor* 28: 531-538.
- VASCO, D.W., C. TAYLOR (1991): Inversion of airborne gravity gradient data, southwestern Oklahoma. *Geophysics* 56: 90-101.
- VENING-MEINESZ, F.A. (1928): A formula expressing the deflection of the plumb-lines in the gravity anomalies and some formulae for the gravity field and the gravity potential outside the geoid. *Proc. Koninkl. Akad. Wetenschap* 31: 315-331, Amsterdam.
- VENING-MEINESZ, F.A. (1931): Une nouvelle méthode pour la réduction isostasique régionale de l'intensité de la pesanteur. *Bull. Géod.* no. 29:33-51.
- VENING-MEINESZ, F.A. (1950): New formulas for systems of deflections of the plumb-line and Laplace's theorem.-Changes of deflections of the plumb-line brought about by a change of the reference ellipsoid. *Bull. Géod.* no. 15: 33-51.
- VILLARCEAU, Y. (1868): Nouveau théorème sur les attractions locales. *Compt. Rend. Hebd. des Séances de L'Acad. des Sciences* 67: 1275-1281, Paris.
- VINCENTY, T. (1975): Direct and inverse solutions of geodesics on the ellipsoid with application of nested equations. *Survey Review* 23: 88-93.
- VINCENTY, T. (1980): Height-controlled three-dimensional adjustment of horizontal networks. *Bull. Géod.* 54: 37-43.
- VINCENTY, T. (1982): Methods of adjusting space systems data and terrestrial measurements. *Bull. Géod.* 56: 231-241.

- VINE, F.J., D.H. MATTHEWS (1963): Magnetic anomalies over ocean ridges. *Nature* 199: 947-949.
- VIRTANEN, H. (2000): On the observed hydrological environmental effects on gravity at the Metsähovi station, Finland. In Ducarme and Barthelemy (2000): 169-175, Luxembourg.
- VÖLKSEN, C. (2000): Die Nutzung von GPS für die Deformationsanalyse in regionalen Netzen. *Wiss. Arb. Univ. Hannover* 237.
- WAALEWIJN, A. (1964): Hydrostatic levelling in the Netherlands. *Survey Review* 17: 212-221, 267-276.
- WAALEWIJN, A. (1986): Der Amsterdamer Pegel. *Österr. Z. für Verm.wesen und Photogrammetrie* 74: 264-270.
- WAGNER, C.A., D.C. McADOO (1986): Time variations in the earth's gravity field detectable with Geopotential Research Mission intersatellite tracking. *JGR* 91: 8373-8386.
- WAHR, J. (1981): Body tides on an elliptical, rotating, elastic and oceanless earth. *Geophys. J. R. Astr. Soc.* 64: 677-704.
- WAHR, J. (1995): Earth tides. In Ahrens (1995): 40-46.
- WANG, Y.M (1999): On the ellipsoidal corrections to gravity anomalies using the inverse Stokes integral. *J. Geod.* 73: 29-34.
- WANNINGER, L. (1995): Enhancing differential GPS using regional ionospheric error models. *Bull. Géod.* 69: 283-291.
- WANNINGER, L. (1996): Präzise GPS-Positionierung in regionalen Netzen permanenter Referenzstationen. *ZfV* 121: 441-454.
- WANNINGER, L. (2000): Präzise Positionierung in regionalen GPS-Referenzstationsnetzen. DGK, C 508, München.
- WARBURTON, R.J., E.W. BRINTON (1995): Recent developments in GWR instruments' superconducting gravimeters. In Poitevin (1995): 23-56, Luxembourg.
- WEBB, F.H., J.F.ZUMBERGE (1997): An introduction to GIPSY/OASIS -II- precision software for the analysis of data from the Global Positioning System. Doc., Jet Propulsion Laboratory, California Institute of Technology, Pasadena, Cal., U.S.A.
- WEBER, D. (1995): Berechnung des Deutschen Haupthöhennetzes 1992 abgeschlossen. *ZfV* 120: 196-200.
- WEBER, D. (1998): Die Schweremessungen der Landesvermessung in Deutschland. *ZfV* 123: 370-378.
- WEBER, G. (1984): Hochauflösende mittlere Freiluftanomalien und gravimetrische Lotabweichungen für Europa. *Wiss. Arb. Univ. Hannover* 135.
- WEBER, G., H. ZOMORRODIAN (1988): Regional geopotential improvement for the Iranian geoid determination. *Bull Géod.* 62: 125-141..
- WEGENER, A. (1915): Die Entstehung der Kontinente und Ozeane. 4. Aufl., Vieweg und Sohn, Braunschweig 1962.
- WEI, M., K.P. SCHWARZ (1998): Flight test results from a strapdown airborne gravity system. *J. Geod.* 72: 323-332.
- WELLS, W.C. ed. (1984): Spaceborne gravity gradiometers. NASA Conf. Publ. 2305 (Proceed. of a workshop held at NASA GSFC, Greenbelt, Md., 1983.
- WELLS, D.E., ed. (1986): Guide to GPS positioning. Canadian GPS Associates, Fredericton, N.B.

- WENZEL, H.-G. (1976): Zur Genauigkeit von gravimetrischen Erdgezeitenbeobachtungen. *Wiss. Arb. Univ. Hannover* 67.
- WENZEL, H.-G. (1977): Zur Optimierung von Schwerenetzen. *ZfV* 102: 452-457.
- WENZEL, H.-G. (1982): Geoid computation by least-squares spectral combination using integral kernels. *Proceed. Gen. Meeting IAG, Special Issue J. Geod. Soc. of Japan*: 438-453, Tokyo.
- WENZEL, H.-G. (1985): Hochauflösende Kugelfunktionsmodelle für das Gravitationspotential der Erde. *Wiss. Arb. Univ. Hannover* 137.
- WENZEL, H.-G. (1989): On the definition and numerical computation of free air gravity anomalies. *Bull.d'Inf. Bur.Gravim. Int.* 64: 23-31..
- WENZEL, H.-G. (1996): The nanogal software: Earth tide data processing package ETERNA 3.30. *Bull. d'Inf. Marees Terrestres* 124: 9425-9439.
- WENZEL, H.-G. (1997a): Tide-generating potential for the earth. In Wilhelm et al. (1997): 9-26.
- WENZEL, H.-G. (1997b): Analysis of earth tide observations. In Wilhelm et al. (1997): 59-75.
- WENZEL, H.-G. (1999): Schwerefeldmodellierung durch ultra-hochauflösende Kugelfunktionsmodelle. *ZfV* 124: 144-154.
- WHALEN, C.T. (1985): Trigonometric motorized leveling at the National Geodetic Survey. In D.B. Zilkoski, ed. (1985), *Proceed. Third Intern. Symp. on the North American Vertical Datum (NAVD'85)*: 65-80. Nat. Geod. Inform. Center, NOAA, Rockville, Md.
- WHITTEN, C.A. (1952): Adjustment of European triangulation. *Bull. Géod.* no.24: 187-203.
- WICHENCHAROEN, C. (1982): The indirect effects on the computation of geoid undulations. *OSU Rep.* 336, Columbus, Ohio.
- WIELEN, R., H. SCHWAN, C. DETTBARN, A. LENHARDT, H. JAHREISS, R. JÄHRLING (1999): Sixth catalogue of fundamental stars (FK6). Veröff. Astron. Rechen-Institut Heidelberg No. 35, Braun, Karlsruhe.
- WILHELM, H., W. ZURN, H.-G. WENZEL, eds. (1997): Tidal phenomena. Springer, Berlin-Heidelberg-New York.
- WILLIAMS, D.C., H. KAHMEN (1984): Two wavelength angular refraction measurements. In Brunner (1984a): 7-31.
- WILSON, C.R. (1995): Earth rotation and global change. *Rev. Geophys., Suppl.*: 225-229.
- WILSON, P., J. RAIS, C. Reigber, H. SEEGER et. al. (1998): The GEODYSSSEA project: an investigation of the geology of south and south-east Asia. *EOS* 79: 545, 548-549.
- WOLF, H. (1963a): Dreidimensionale Geodäsie. Herkunft, Methodik und Zielsetzung. *ZfV* 88: 109-116.
- WOLF, H. (1963b): Die Grundgleichungen der dreidimensionalen Geodäsie in elementarer Darstellung. *ZfV* 88: 225-233.
- WOLF, H. (1967): Computation of satellite triangulation by spatial fitting of the orbit. *DGK, B* 153: 75-92.
- WOLF, H. (1974): Über die Einführung von Normalhöhen. *ZfV* 99: 1-5.
- WOLF, H. (1978): The Helmert-block method, ist origin and development. Proceed. 2nd Int. Symp. on Problems Related to the Redefinition of North American Geodetic

- Networks, Arlington, Va.: 319-326. Nat. Geod. Inform. Branch, NOAA, Rockville, Md.
- WOLF, H. (1987): Datums-Bestimmungen im Bereich der deutschen Landesvermessung. *ZfV* 112: 406-413.
- WOLF, H. (1993): Friedrich Robert Helmert – sein Leben und Wirken. *ZfV* 118: 582-590.
- WOLF, H. (1997): Ausgleichungsrechnung nach der Methode der kleinsten Quadrate. 3.Aufl., F.Dümmler, Bonn.
- WOODHOUSE, J.H., A.M. DZIEWONSKI (1984): Mapping the upper mantle: three dimensional modelling of earth structure by inversion of seismic waveforms. *JGR* 89: 5953-5986.
- WOODWORTH, P.L. (1997): The Permanent Service for Mean Sea Level and the Global Sea Level Monitoring System. In IAG (1997): 55-58.
- WÜBBELMANN, H. (1992): Das hydrodynamische Nivellement am Beispiel eines Pegelnetzes am Fehmarn-Belt. *Wiss. Arb. Univ. Hannover* 176.
- WÜBBENA, G. (1989): The GPS adjustment software package GEONAP- Concepts and models. Proc. Fifth Int. Geod. Symp.on Satellite Positioning: 452-461, Las Cruces, New Mexico, U.S.A.
- WYATT, F., D.C. AGNEW, H.O. JOHNSON (1990): Pinyon Flat Observatory: Comparative studies and geophysical investigations. U.S. Geol. Survey, open-file report 90-380: 242-248.
- YODER, O.F. (1995): Astrometric and geodetic properties of earth and the solar system. In Ahrens (1995): 1-31.
- YUNCK, T.P., W.G. MELBOURNE (1996): Spaceborne GPS for earth science. In Beutler et al. (1996c): 113-122.
- ZAHEL, W. (1997): Ocean tides. In Wilhelm et al. (1997): 113-143.
- ZARRAO, N. W. MAI, E. SARDON, A. JUNGSTAND (1998): Preliminary evaluation of the Russian GLONASS system as a potential geodetic tool. *J. Geod.* 72: 356-363.
- ZEBKER, H.A., R.M. GOLDSTEIN (1986): Topographic mapping from interferometric synthetic aperture radar observations. *JGR* 91: 4993-4999.
- ZERBINI, S., L. BASTOS, H.-P. PLAG, B. RICHTER, eds. (1998): WEGENER: An interdisciplinary contribution to unraveling the geodynamics of the European and Mediterranean arc. *Tectonophysics* 294, nos. 3-4.
- ZILKOSKI, D.B., J.H. RICHARDS, G.M. YOUNG (1992): Results of the general adjustment of the North American Vertical Datum of 1988. *Surveying and Land Information Systems* 52: 133-149.
- ZILKOSKI, D.B., J.H. RICHARDS, G.M. YOUNG (1995): A summary of the results of the general adjustment of the North American vertical datum of 1988. *Allg. Verm. Nachr.* 102: 310-321.
- ZOBACK, M.L. (1992): First- and second-order patterns of stress in the lithosphere: The world stress map project. *JGR* 97: 11703-11728.
- ZUMBERGE, M.A. (1981): A portable apparatus for absolute measurements of the earth's gravity. Ph.D. thesis, Univ. of Colorado, Dep. of Physics, Boulder, Col.
- ZUMBERGE, M.A., E.L. CANUTESON (1995): An ocean bottom absolute gravity meter. In Sünkel and Marson (1995): 7-16.
- ZURN, W. (1997a): Earth tide observations and interpretation. In Wilhelm et al. (1997): 77-94.

- ZÜRN, W. (1997b): The nearly-diurnal free wobble-resonance. In Wilhelm et al. (1997): 95-109.
- ZÜRN, W., H. WILHELM (1984): Tides of the earth. In Landolt-Börnstein, New Series V, vol.2: 259-299, Springer, Heidelberg-New-York.
- ZÜRN, W., D. EMTER, E. HEIL, J. NEUBERG, W. GRÜNINGER (1986): Comparison of short and long- baseline tidal tilts. In Viera, R., ed.: Proceed. Tenth Intern. Symp. on Earth Tides, Madrid 1985: 61-70, Madrid.

Index

Names of the authors cited in the text are not included in the index

- Aberration 166, 169
- Acoustic waves 120, 206
- Adams-Williamson equation 335
- Airborne
 - gravimetry 186, 188, 190
 - microwave methods 311
- Air drag 134
- Airy 313, 340
- Al-Mámân* 6
- Almucantar 160
- Altimetry, *see* Satellite altimetry
- Ambiguity problem 149
- Angle
 - horizontal 40, 196, 230
 - vertical 196
 - zenith 6, 40, 159, 196, 230, 238, 252
- Angle measurement 6, 196, 309
- Angular velocity
 - earth rotation 23, 54, 103, 115, 145, 302
 - satellites 131
- Anomalous potential, *see* Disturbing potential
- Anomaly
 - eccentric 131
 - mean 131
 - true 131
- Arc measurement 5, 8, 10, 312
- Argument of perigee 132
- Aristarchus of Samos* 7
- Aristotle* 5
- Astatization 180
- Asthenosphere 343
- Astrogeodetic systems
 - datum 236, 312
 - ellipsoids 312, 314
 - origin 236, 313, 315
- Astronomic almanac 167
- Astronomic horizon, *see* Celestial horizon
- Astronomic parallel curve 64
- Astrometric positioning 64, 162
- Astrometric system
 - equatorial 26, 132
 - global 38, 65
 - local 39, 59, 65, 159, 186, 237
- Astrometric triangle 41
- Atmosphere
 - density 120
 - mass 51, 72, 116
 - model 127, 135
- Atomic clock 20, 139, 142, 174
- Atomic time 20, 35, 350
- Azimuth
 - astronomic 40, 165, 197, 230, 243
 - ellipsoidal, *see* - geodetic
 - geodetic 97, 101, 243, 246
 - Laplace 239, 243, 309, 310
- Azimuth determination 165
- Azimuth reductions 243
- Baeyer* 11, 14
- Balloon satellite 139
- Base line
 - terrestrial 6, 199, 310
 - VLBI 228
- Bench mark 320
- Bergstrand* 201
- Bessel* 10, 11, 247, 313
- BIH zero meridian 35, 116
- Bjerhammar* sphere 72, 223, 264
- Bomford* geoid 300
- Bouguer* 9, 266, 339
- Bouguer* (gravity) anomaly 266, 287, 292, 339, 347
- Bouguer* plate 264, 266
- Boundary-value problem
 - geodetic 2, 256, 289
 - potential theory 259, 264, 293
- Bowie* 311
- Brillouin* sphere 72

- Brun's* 12, 59, 232
 — equation 64, 110
 — spheroid 104
 — theorem 258, 282, 290, 294
- Bulk modulus** 334
- Bureau Gravimetrique International (BGI)** 15, 278, 285
- Bureau International de l'Heure (BIH)** 19, 25
- Bureau International des Poids et Mesures (BIPM)** 15, 18, 186
- C/A-code (GPS)** 143, 145, 148, 150
- Calibration line**
 — distance meter 199, 202
 — gravimeter 184, 185, 332
- Camera**
 — astronomic 139
 — ballistic 139
 — zenith 159, 161, 164
- Carrier phase measurements**
 — GPS 149
 — terrestrial 200
- Cartesian coordinate system**
 — global 26, 32, 231
 — local 39, 59, 196, 231
- Cassini de Thury* 9, 10, 311
- Cassini, J.* 9.
- Cassini, J.D.* 7, 9
- Cassinis* 115
- Cavendish* 20
- Cavity effect** 212
- Celestial**
 — Ephemeris Pole (CEP) 29, 35
 — equator 22, 26, 29
 — horizon 41
 — Intermediate Pole (CIP) 29
 — meridian 27, 37
 — parallel 26
 — pole 26, 37
 — reference frame 30
 — reference system 30, 37
 — sphere 26
- Centrifugal**
 — acceleration 54, 214
 — force 54
 — potential 55, 72, 105
- CHAMP satellite** 157
- Chandler*
 — period 34
 — wobble 34, 351
- Chronograph** 162
- Circle of latitude** 93, 98
- Clairaut* 9, 59, 103, 109
 — equation 242, 247, 248
 — theorem 9, 106, 108
- Clarke* 313
- Code measurement (GPS)** 148
- Cogeoid** 263
- Colatitude**, *see* Polar distance
- Collocation**, *see* Least squares collocation
- Conrad discontinuity** 338
- Continental drift** 343
- Control network**
 — horizontal 11, 309
 — threedimensional 12, 323
 — vertical 11, 320
- Convection current**, *see* Mantle convection
- Conventional Inertial System (CIS)** 25, 30
- Conventional International Origin (CIO)** 35, 116
- Conventional Terrestrial Pole** 23, 32
- Cook* 177
- Coordinates**
 — astronomic (geographic) 38, 162, 231
 — ellipsoidal 104
 — ellipsoidal (geographic), *see* - geodetic
 — ellipsoidal (local) 101, 237
 — geodetic 93, 99, 114, 246, 311
 — natural 64
 — normal geodetic 111, 114, 233
 — spherical 27, 32, 48, 67
- Copernicus* 7
- Covariance function**
 — disturbing potential 305
 — error 225
 — gravity anomaly 221, 223
- Cross coupling effect** 188
- Crustal movements** 13, 355
- Curvature**
 — geodetic 241
 — light ray 122, 126, 205

- meridian 95
- microwave 127
- normal 60, 244
- normal plumb line 113
- plumb line 61, 295
- prime vertical 96
- principal 61, 113
- Cycle slip (GPS) 149
- Danjon astrolabe 160
- Day
 - mean sidereal 23
 - mean solar 12, 19, 23
 - TAI 20
 - universal, *see* — mean solar
- Declination 27, 41, 228
- Deflection of the vertical 10, 218, 238, 283, 291, 295, 297, 312
 - components 219, 283, 291
 - interpolation 298
- Degree variance
 - anomaly 222, 273, 306
 - disturbing potential 306
- Delambre* 10
- Density 47, 265
 - crust 57, 262, 333, 338
 - mantle 339
 - mean earth 333
 - surface 265, 290
- Deutsches
 - Hauptdreiecksnetz (DHDN) 317
 - Haupthöhenhennetz (DHHN) 322
 - Referenznetz (DREF) 329
 - Schweregrundnetz (DSGN) 331
- Development method 312
- Differential GPS (DGPS) 148, 151, 229, 328
- Digital elevation (terrain) model 261, 298
- Direct geodetic problem 246
- Direction measurement
 - satellite 138, 139, 228, 276
 - terrestrial 196, 309
- Discontinuity surface 336
- Dispersion 120, 198, 204
 - angle 198
- Distance 40, 101, 205, 228, 230, 244
- Distance measurements
 - electromagnetic 12, 140, 142, 199
 - laser 151, 202
 - mechanical 199
 - reductions 204, 244
- Distance meter
 - calibration 203
 - electro-optical 201
 - microwave 201
 - two/three wavelengths 203
- Disturbing potential 214, 282
 - integral equation 257, 289
 - spherical harmonic expansion 215
- Doodson* 86
- Doppler measurements 138, 140, 148
- Doppler positioning 140, 311
- DORIS 24, 138, 141, 156
- Downward continuation 77
- Drift, *see* Gravimeter - drift
- Dynamic height, *see* Height - dynamic
- Dynamic ocean topography, *see* Sea surface topography
- Dynamical ellipticity 333
- Dynamical form factor 75, 277, 302, 334, 359
- Dynamical time 21
- Earth
 - core 336
 - crust 336, 338
 - mantle 336, 338
 - mass 333
- Earth ellipsoid
 - mean 4, 103, 301
- Earth model
 - ellipsoidal 7, 103
 - geodetic 4, 114, 301
 - geophysical 29, 103, 336, 362
 - homogeneous 50, 103
 - spherical 4, 98
- Earth orientation parameters (EOP) 25, 36, 350
- Earth rotation 13, 19, 23, 33, 302, 350
- Earth satellites 136
- Earth surface
 - mathematical 3
 - physical 2
- Earth tides 13, 89, 362

- analysis 195, 366
- measurements 193
- Eccentricity
 - first 92, 131
 - linear 92
 - second 92
- Ecliptic 22, 28, 29
- Electromagnetic waves 119
 - velocity 123
- Electron density 128
- Ellipsoid
 - *Bessel* 312
 - best-fitting 11, 270, 312
 - *Clarke* 312
 - Conventional 11, 312
 - curvature 95
 - equipotential, *see Level ellipsoid*
 - Geodetic reference system 115, 270
 - *Hayford* 115, 316
 - homogeneous 8, 104
 - International (1924), *see - Hayford*
 - Level, *see Level ellipsoid*
 - *Krassowski* 312, 316
 - mean earth, *see Earth ellipsoid - mean*
 - rotational 4, 91
 - triaxial 104
 - WGS84 145
- Eötvös*
 - reduction 187
 - tensor 63, 191
 - unit 191
- Ephemeris time 20
- Equatorial
 - plane 22, 32
 - radius 91, 115, 116, 270, 301
 - system 26, 132
- Equilibrium
 - figure 8, 103, 104, 337
 - hydrostatic 103, 335, 337
 - surface 58, 103
 - tide 87
- Equipotential
 - ellipsoid, *see Level ellipsoid*
 - surface, *see Level surface*
- Eratosthenes* 5
- ERS satellites 155, 277, 279, 280
- Essen and Froome* formula 126
- Euler* period 34
- Euler's* formula 97
- European
 - Datum (ED) 316
 - leveling net (EULN) 321
 - Terrestrial Reference Frame (ETRF) 326
 - triangulation net (RETRIG) 315
 - Vertical Reference Network (EUVN) 326
- Everest* 11, 312, 339
- Extensometer, *see Strainmeter*
- Faller* 177
- Faye* anomaly 265, 287, 290
- Feedback system 181, 193
- Fermat's* principle 120
- Fernel* 6
- Figure of the earth 2, 3, 10
- Flattening
 - geometric 8, 92, 302
 - gravimetric 107
 - hydrostatic 337
- Free-air (gravity) anomaly 218, 264, 278, 293, 347
- Free-air reduction 218, 263
- Free-fall method 172
- Free oscillations 336, 368
- Frisius* 6
- Fundamental Catalogue (FK) 25, 30
- Fundamental equation of physical geodesy 259
- Fundamental point 236, 246, 312
- Fundamental star 30
- Furtwängler*, *see Kühnen*
- Gal 171
- Galilei* 7, 171
- GALILEO 146
- GAST, *see Greenwich Sidereal Time*
- Gauss 3, 10, 11, 14, 76
- Gauss' integral formula 53
- Gaussian osculating sphere 98, 242
- Geocenter 26, 28, 36
- Geocentric system 32, 36
- Geodesic 240
 - reduction to 243

- Geodesy
 - four-dimensional 4, 13
 - integrated 304
 - lunar 1
 - planetary 1
 - three-dimensional 13, 232
- Geodetic astronomy 41, 159
- Geodetic datum 115, 234, 246, 312, 318
- Geodetic Reference System (GRS) 114, 116, 314
 - GRS80 116, 145
- Geodetic surveys 1, 14
- Geoid 3, 76, 262, 279, 295
 - mean 77
 - non-tidal 77
 - zero 77
- Geoid height 216, 236, 258, 282, 340, 346
 - mean 273, 278
- Geoid potential 268, 270, 302
- Geoid undulation, *see* Geoid height
- Geopotential model 145, 278, 286
 - EGM96 280, 281
 - tailored 274, 281
- Geopotential number 80, 249, 320
- Geopotential surface, *see* Level surface
- GEOS satellite 155, 157, 277
- GEOSAT satellite 155, 277, 279, 280, 286
- Global Geodynamics Project (GGP) 368
- Global Positioning System (GPS) 12, 24, 142
 - heighting 254
 - network 229, 324, 327
 - permanent station 325, 328
 - positioning 148, 151
 - pseudorange 142
 - receiver 138, 146, 324
 - session 324
 - station 324
- GLONASS 145
- GMST, *see* Greenwich Sidereal Time
- GOCE satellite 159
- Goddard Earth Models 277
- Godin 9
- GPS, *see* Global Positioning System
- GPS time 145
- GRACE satellite 158
- Gravimeter
 - absolute 171, 330
 - airborne 188
 - bore-hole 182
 - calibration 183, 185, 194, 331
 - drift 182, 331
 - force-balanced 189
 - recording 193
 - relative 178, 330
 - sea 188, 190
 - superconducting 193
 - tare 182
 - underwater 182
 - vibrating string 189
- Gravimetric (amplitude) factor 195, 364
- Gravimetric method 10
- Gravitation
 - acceleration 46
 - force 45
 - potential 46, 50, 70
 - spherical earth model 48
- Gravitational constant 19, 45, 83
- geocentric 116, 270, 301
- Gravity
 - acceleration 55, 58, 65
 - gradient, *see* Gravity gradient
 - normal, *see* Normal gravity
 - potential 38, 56, 64
- Gravity anomaly 217, 259, 271, 285, 346
- altimetric 285
- covariance function, *see* Covariance function
- degree variance, *see* Degree variance
- interpolation 224
- interpretation 347
- mean 221, 273, 276, 278
- Gravity field
 - external 1, 2, 3, 107, 110, 293
 - internal 336
- Gravity gradient 40, 63, 158, 191
 - horizontal 63, 191
 - vertical 64, 173, 192
- Gravity gradiometer 138, 158, 191
- Greenwich meridian 12, 25, 32
- Greenwich Sidereal Time 22, 37
- Grimaldi and Riccioli 6

- GRIM earth models 278
 Gyrotheodolite 197
- Halley* 8
 Harmonic analysis (earth tides) 195, 365
 Harmonic coefficients, *see* Spherical harmonic coefficients
 Harmonic function 51
Hayford 115, 311, 341
 Height
 — dynamic 81, 250
 — ellipsoidal 99, 252
 — orthometric 82, 251, 321
 — normal 82, 112, 251, 322
 — normal orthometric 321
 — spheroidal orthometric, *see* — normal orthometric
 Height anomaly 215, 236, 257, 271, 290, 294
Heiskanen 115
Helmert 1, 10, 218, 247
 — compensation method 287
 — height 252
 — projection 99
 — spheroid 104
 HIPPARCOS satellite 30
Hirvonen 289
Homer 4
 Horizon system 41
 Horizontal
 — angle, *see* Angle – horizontal
 — direction 40
 Horizontal control network 308
 — Europe 315
 — Germany 316
 — U.S.A. 315
 Horizontal pendulum 211
 Horizontal plane 4
Horrebow-Talcott method 163
 Hotspot 339, 345, 346
 Hour angle 27, 41
 Hour angle system 27
 Hour circle 26
Huygens 8
 Hydrostatic
 — equation 79, 335
 — equilibrium 103, 335, 336, 337
- Inclination (orbital plane) 132, 137
 Index of refraction 120, 123, 128
 Indirect effect (gravity reduction) 263
 Inertial gravimetry 188
 Inertial surveying 196
 Inertial system 25, 30
 Initial point, *see* Fundamental point
 INSAR 261
 Interference comparator 199
 Interferometry
 — absolute gravimeter 174
 — Very Long Baseline, *see* Very Long Baseline Interferometry
 International Absolute Gravity Standardization Net 1971 (IGSN71) 184, 330
 International Association of Geodesy (IAG) 14, 114
 International Astronomical Union (IAU) 24, 29, 30
 International Celestial Reference Frame (ICRF) 30, 37
 International Celestial Reference System (ICRS) 30
 International Center for Earth Tides (ICET) 15
 International Earth Rotation Service (IERS) 15, 24
 International Geoid Service (IgeS) 15
 International GPS Service (IGS) 15, 150, 323
 International Gravity Basestation Network (IAGBN) 359
 International Laser Ranging Service (ILRS) 15
 International Latitude Service (ILS) 25
 International Polar Motion Service (IPMS) 25
 International Terrestrial Reference Frame (ITRF) 36, 323, 355
 International Terrestrial Reference System (ITRS) 36
 International Union of Geodesy and Geophysics (IUGG) 15, 24, 114
 International VLBI Service for Geodesy and Astrometry (IVS) 15
 Intrinsic geodesy 66

- Inverse problem
 - geodetic (three-dimensional) 100
 - geodetic (two-dimensional) 246, 249
 - potential theory 345
- Ionosphere 127, 129, 149, 156
- Isostasy 340
- Isostatic (gravity) anomaly 267, 348
- Isostatic (gravity) reduction 267
- Isostatic models
 - Airy (-Heiskanen) 340
 - Pratt (-Hayford) 341
 - Vening-Meinesz (regional) 342
- Isozenithal line 64
- Jacoby* 204
 - ellipsoid, *see* Ellipsoid - homogeneous
- Jäderin* 199
- Jeffreys* 279
- Julian Century 20
- Kater* 172
- Kepler* 7, 131
 - equation 132
 - laws 131
- Keplerian elements 3, 229
- Kilogram 18, 19
- Krassowski 311, 312, 316
- Kühnen and Furtwängler 184
- Küstner 13
- LaCaille* 9
- LaCondamine* 9
- Lageos satellite 152, 359
- LaHire* 9
- Lambdon* 11
- Laplace* 10
 - azimuth 239
 - differential equation 51, 215
 - equation 239, 243, 310, 314
 - perturbation equation 134
 - station 310
 - surface spherical harmonics, *see* Spherical harmonics
 - tidal equation, *see* Tidal equation
- Laser distance measurements
 - moon 154
- satellites 138, 152, 153
- terrestrial 202
- LAST, *see* Sidereal Time
- Latitude
 - astronomic 38, 41, 42, 64, 162
 - ellipsoidal, *see* - geodetic
 - geocentric 32, 94
 - geodetic 93, 114, 233, 246
 - normal geodetic 112, 114, 233
 - reduced 94, 104
- Latitude arc measurement 9
- Least squares
 - collocation 303
 - prediction 224, 298
 - spectral combination 288
- Legendre* 10, 246
 - functions, associated 68
 - polynomials 67, 222
- Length of day (LOD) 35, 350
- Level ellipsoid 103, 106, 268
- Leveling
 - astrogravimetric 299
 - astronomic 294, 297, 300
 - dynamic, *see* - geostrophic
 - geometric (spirit) 40, 206, 231, 249, 320
 - geometric-astronomic 232
 - geostrophic 79, 210
 - hydrodynamic, *see* - geostrophic
 - hydrostatic 210
 - motorized 210
 - reciprocal 210
 - steric 79
 - trigonometric 254
- Leveling instrument (level) 206
- Leveling network 83, 250, 320
- Level spheroid 104
- Level surface 3, 39, 57, 59, 64, 79
- Lever spring balance 179
- Light velocity 19
- Light waves 119, 125
- Lithosphere 343
- Longitude
 - astronomic 22, 38, 41, 42, 64, 163
 - ellipsoidal, *see* - geodetic
 - geodetic 93, 114, 233, 246
- Longitude arc measurement 9

- Love*
 — load numbers 365
 — numbers 362, 364, 368
 Lunar laser ranging (LLR) 154
- MacLaurin* 59, 103
- Mantle convection 344
- Mareograph, *see* Tide gauge
- Marussi tensor 63, 65, 114
- Maupertuis* 9
- Mean curvature
 — ellipsoid 97
 — level surface 61, 64
- Mean position 29, 166
- Mean radius (earth) 98
- Mean sea level (MSL) 78, 321
- Méchain* 10
- Mechanical ellipticity, *see* Dynamical ellipticity
- Meridian
 — astronomic 64
 — geodetic 93
- Meridian arc 97
- Meridian ellipse 94
- Meridian plane
 — astronomic 27, 38
 — ellipsoidal 93, 99
- Meteorological parameters 124, 203
- Meter 10, 12, 18, 19
- Meusnier*
 — theorem 96
- Mitteleuropäische Gradmessung 11, 14
- Mohorovičić discontinuity 336, 339
- Molodenski* 218, 256, 289
 — correction 290, 292
- Moment of inertia
 — earth 75, 335
- Multipath effects (GPS) 150
- Nadir 41
- Nankung Yüeh and I-Hsing* 6
- Navigation message (GPS) 144
- NAVSTAR Global Positioning System,
see Global Positioning System (GPS)
- Navy Navigation Satellite System (NNSS)
 141
- Nearly diurnal free wobble 351, 365, 368
- Network
 — geodynamic 330, 355, 356
 — national 315, 321, 327, 331
- Network adjustment 311, 320, 327, 331
- Network optimization 311, 330
- Newton* 7, 103
 — equation of motion 21, 25, 131, 133, 186
 — law of gravitation 25, 45
- Normal gravity 81, 105, 106, 109, 115, 117, 217, 251, 266
 — gradient 110, 114
 — potential 105, 107, 112, 214
- Normal gravity formula 106, 108, 109, 110
- international (1930) 115
 — *Newton* 108
 — Geodetic Reference System 1980 116
 — *Somigliana* 106
- Normal height, *see* Height – normal
- Normal height reduction 251, 297
- Normalhöhen-Null (NHN) 322
- Normal-Null (N.N.) 322
- Normal section 97, 240
- North American Datum
 — horizontal (NAD27, NAD 83) 315
 — vertical (NAVD88) 321
- Norwood* 6
- Nutation 28, 37, 166
- Ocean floor control points 206
- Ocean loading Ocean tides 78, 89, 362, 365
- Off-leveling effect (gravimetry) 188
- Omission error 273
- Orbital elements, *see* Keplerian elements
- Orbital system 132
- Orbital velocity
 — satellite 136
- Orientation
 — geodetic networks 236, 238, 246, 312
- Origin point, *see* Fundamental point
- Orthogonality relations (spherical harmonics) 69
- Orthometric height, *see* Height – orthometric
- Orthometric height reduction 251, 296

- Pageos satellite 139, 229
 Parallactic angle 41, 165
 Parallax 166
 Parallel
 — astronomic 26
 — celestial, *see* - astronomic
 — geodetic 93, 99
 Partial tides 89, 366
 P-code (GPS) 143
 PDOP (GPS) 150
 Pendulum
 — horizontal, *see* Horizontal pendulum
 — mathematical 171
 — physical 172
 — reversible 172
 — vertical, *see* Vertical pendulum
 Pendulum measurements
 — absolute 171
 — relative 178
 Perigee 132
 Permanent Service for Mean Sea Level 15
 Perturbations
 — satellite orbit 133, 275
 Perturbing potential 133, 274
 Phase lead (earth tides) 195
 Phase measuring method, *see* Carrier phase measurements
Picard 7, 9
Pizetti 103, 218, 294
 — theorem 106, 108
 Plane surveying 1
 Planetary geodesy 1
 Plate boundary 343, 344, 361
 Plate motion 343, 355
 Plate tectonics 36, 343, 355
 Plumb line 10, 38, 56, 58, 61, 218, 296
 — fluctuation 87, 209
 — normal 111
 Poisson's differential equation 53, 72
 Poisson's integral 293
 Polar distance 32
 Polar motion 33, 167, 175, 351
 Polar radius of curvature 96, 117
 Polar triangle
 — astronomic, *see* Astronomic triangle
 — ellipsoidal 242
 Polar wander 34
 Pole
 — IERS Reference 35, 167
 — mean 32
 — north 6, 32, 41
Posidonius 6
 Position
 — apparent 166
 — mean, *see* Mean position
 — true, *see* True position
 Position lines, method 164
 Postglacial rebound 13, 346, 349, 356, 360
 Potential function, *see* Harmonic function
 Potsdam Gravity System 184
 PRARE 138, 156
Pratt 339, 341
 Precession 28, 37, 166
 Precise leveling 208, 321
 Prediction, least squares, *see* Least squares prediction
 Prime vertical 96
 Prism astrolabe 160
 Product of inertia
 — earth 75
 Proper motion 30, 166
Ptolemy 7
 Pulkovo Datum 316
 Pulse measuring method 152, 199
Pythagoras 5
 Quartz clock 139
 Quasar 30, 167
 Quasigeoid 82, 112, 216
 Radar distance measurement 138, 154
 Radian 19
 Radiation pressure 135
 Radio source
 — extragalactic 30, 167
 — system 30
 Radio telescope 167, 170
Rebeur-Paschwitz 13
 Recording gravimeter, *see* Gravimeter - recording
 Reduced pendulum length 172
 Reference ellipsoid 114, 312
 Reference surface 3

- height 80, 249, 321
- Reference system 3
 - earth-fixed 31
 - ellipsoidal 102
 - gravity-field related 38
 - space-fixed 25
- Refraction
 - astronomic 165
 - atmospheric 119
 - horizontal 122, 310
 - ionospheric 127, 149, 156
 - lateral, *see* - horizontal
 - tropospheric 124, 149, 169
 - vertical 122, 209
- Refraction angle 123, 198
- Refraction coefficient 122, 126, 253
- Remove-restore method 286, 307
- Repsold* 172
- Resonance effect
 - outer core 368
 - satellite orbit 276
- Reversible pendulum, *see* Pendulum - reversible
- Riccioli*, *see* Grimaldi
- Richer* 7
- Right ascension 26, 41
 - ascending node 132
- Rise-and-fall method 173, 177
- Rotational axis (earth) 26, 28, 32
- Rotational ellipsoid, *see* Ellipsoid – rotational
- Rotational variations (earth) 33, 83, 302, 350
- Roy* 311
- Runge-Kraruup* theorem 72
- Sakuma 177
- SAPOS 329
- Satellite altimetry 79, 154, 285, 354
- Satellite geodesy 12, 130
- Satellite gravity gradiometry 158
- Satellite laser ranging (SLR) 24, 151
- Satellite-only model 229, 274, 278
- Satellite refraction 139
- Satellite-to-Satellite tracking (SST) 157
- Satellite triangulation 140, 229
- Satellite trilateration 140
- Schreiber* 311
- Schumacher* 11
- Sea floor spreading 343
- Sea level variations 78, 352
- Seasat satellite 155
- Sea surface topography 78, 155
- Second 18
- Secor method 140
- Seismic parameter 334
- Selective availability (SA) 144
- Shida* number 362
- Short arc method 229
- Sidereal time 22, 41
- SIRGAS 327
- SI-System 18
- Skew normal reduction 244
- Snellius* 6, 9
- Solar time 23
- Soldner* 11, 311
- Somigliana* 106
- Spherical excess 242
- Spherical harmonic coefficients 70, 72, 117, 137, 271, 275
- Spherical harmonic expansion
 - geoid 271
 - gravitational potential 69
 - gravity anomaly 271
 - gravity disturbance 271
 - gravity potential 72
 - height anomaly 271
 - normal gravity potential 107
 - reciprocal distance 67
 - tidal potential 86
- Spherical harmonic functions 71
 - fully normalized 71
 - solid 70
 - surface 69, 73, 215, 272
- Spheroid 104
- Spheropotential surface 111
- Star catalogue 30
- Star position 29, 165
- Stellar system 30
- Stellar triangulation 12
- Sterneck, von* 178
- Stokes* 256
 - constants, *see* Spherical harmonic coefficients

- formula 282, 287
- function 282, 294
- inverse formula 285
- Poincaré theorem 103, 345
- Strainmeter 212, 368
- Struve* 11
- Subduction zone 344
- Sun
 - mean 23
- Surface
 - equal pressure (isobaric) 79, 336
 - equilibrium, *see* Equilibrium Surface
 - equipotential, *see* Level surface
- Surface density, *see* Density - surface
- Surface layer 290
- Surveying
 - geodetic 1
- Tanni* 289
- Telluroid 112, 216, 257, 289
- Temperature gradient 125
- Tenner* 11
- Terrain correction 264, 266, 290
 - residual 288
- Terrestrial reference frame 36
- Terrestrial reference system 36
- Terrestrial Time (TT) 21
- Thales of Milet* 4
- Theodolite 197, 309
- Tidal acceleration 84, 86, 364
- Tidal constant (*Doodson*) 86
- Tidal deformation 351, 362
- Tidal reduction (leveling) 209
- Tidal equation 88
- Tidal friction 35, 351
- Tidal potential 85
- Tidal model
 - ocean 78
 - solid earth 88, 368
- Tide gauge 79, 321, 353
- Tilt (amplitude) factor 364
- Tiltmeter 211, 368
- Time measurement 139, 162
- Time signal 24
- TOPEX/Poseidon satellite 79, 156, 270, 278
- Topocenter 41
- Topographic reduction 266
- Topography 260, 337
- Torsion
 - geodetic 60, 113
- Torsion balance 192
- Total electron content (TEC) 128
- Total station 202
- Transit satellite, *see* Navy Navigation Satellite System
- Traverse 310
- Triangulation 6, 309
- Trigonometric height determination 252
- Trigonometric point 309
- Trilateration 310
- Tycho de Brahe* 6, 131
- Universal instrument 160
- Universal time 23, 35
- Uotila* 279
- Upward continuation 291, 293
- Väissälä* 199
- Vening-Meinesz* 188
 - equations (datum shift) 236
 - formula (vertical deflection) 283
 - function 284
- Vernal equinox 22, 26, 28, 29
- Vertical, *see* Plumb line direction
- Vertical datum 82, 321
- Vertical deflection, *see* Deflection of the vertical
- Vertical deflection point 314
- Vertical pendulum 211
- Very Long Baseline Interferometry (VLBI) 24, 167
- Viscosity (mantle) 343
- Volet* 177
- Wadley* 201
- Water-tube tiltmeter 211
- Wave velocity (seismic) 334
- Wegener* 343
- Wiechert-Gutenberg discontinuity 336
- World Geodetic System
 - 1972 (WGS72) 141
 - 1984 (WGS84) 141, 145, 323
- Zenith 27, 39, 41, 101

- Zenith angle, *see* Angle – zenith
- ellipsoidal, *see* - geodetic
- geodetic 101, 252
- reciprocal 6, 198, 253, 299
- Zenith camera, transportable, *see* Camera
 - zenith
- Zenith distance, *see* Zenith angle
- Zenith tube, photographic 159
- Zero method (gravimetry) 181
- Zhongolovich 279
- Zöllner 211